Numerical Solutions of Problems of Bearing Capacity and Settlement of Loaded Clay Layers.

Lo, K. W

NUMERICAL SOLUTIONS OF PROBLEMS OF BEARING CAPACITY AND SETTLEMENT OF LOADED CLAY LAYERS

Submitted as a thesis for the degree of Ph.D. in Soil Mechanics of the Faculty of Engineering, University of London,

by

K.W. Lo, M.Sc., M.I.C.E.,

Department of Civil Engineering,

King's College London.

November, 1975

To my dear wife May for her patience, understanding and encouragement

CONTENTS

Page

ACKNOWLEDGEMENTS

It is a great pleasure to be able to record my gratitude to Professor R.E. Gibson who has been a constant source of inspiration and whose supervision has been invaluable in every respect. It has been a great privilege to have had the opportunity to carry out this research under his guidance.

My thanks also to Mr. K.R.F. Andrews who gave advice and encouragement generously.

ABSTRACT

The advent of the Finite Element Method, in association with the digital computer, has provided the means for analysing almost any boundary value problem based on rationally conceived constitutive relations. Thus, the oversimplified analytical models of soil mechanics textbooks may be extended to include more realistic parameters so that less demands are made on engineering judgement. The temptation to incorporate every conceivable parameter of any relevance is to be avoided since models that are too complex may be extremely difficult to interpret and thus become ineffectual. A more profitable approach is to start with a simple model and then introduce significant parameters individually to assess their relative importance and obtain a "feel" for the problem.

Parametric studies on the bearing capacity and settlement of loaded clay layers are conducted here with these considerations in mind.

An understanding of soil behaviour in the intermediate loading range, although important to safe and economical design, has hitherto been largely neglected. Here, the traditional linear elastic and rigid-plastic materials are combined to provide the means for studying soil behaviour from low working to collapse load conditions.

The Initial Stress Method, based on the finite element analysis, is employed to deal with the elastoplastic materials.

A novel assembly procedure termed "Stack Addition" has been devised to aid economy of computation. "Stack Addition" is adapted to deal with the vertical cut problem, and guidelines are set out for solving problems of consolidation and other boundary-value problems of significance in soil mechanics.

Finally, suggestions are made on possible approaches to other important soil mechanics topics, in the present context of parametric studies.

INTRODUCTION

In recent years, there has been considerable research aimed at redressing the anomalies inherent in the traditional textbook approach to the analysis of bearing capacity and settlement of soil bodies subject to external loading as well as under self-weight. An excellent account of some of the more serious deficiencies may be found in a paper by Roscoe (1). On the one hand, efforts have been made to improve the ideal constitutive relations for soil. Notable amongst these are the work done on the critical state (1) and stress-dilatancy (2) models by Cambridge and Manchester Universities respectively.

These models are, however, as yet in a comparatively early stage of development and thus strictly applicable to somewhat idealised soils under equally idealised conditions only (1 , 2).

Despite this, limitations in the models have already been brought to light during application to some plane strain problems (3). Thus, at present, their predictive power on behaviour in the field may be very little greater than that of the simple materials of the traditional approach (4 , 5).

On the other hand, numerous parametric studies have been conducted to improve the overall analytical model whilst more or less adhering to the simple constitutive relations of the traditional approach.

These studies have two important attributes, namely:-

(a) The analytical models are relatively simple so that they may be readily interpreted without undue costs.

(b) The models are a natural development of the traditional approach so that previous experience on the latter basis is still relevant.

In the past, it has been customary to rely on a few solutions to simple problems of bearing capacity and settlement with consequent heavy demands made on engineering judgement to allow for differences between the analytical models and reality. The advent of the Finite Element Method (6), in conjunction with the availability of large digital computers, has now provided the means whereby almost any problem in continuum mechanics based on rationally conceived constitutive relations may be analysed - at least in principle.

In soil mechanics, this has led to improvements in the oversimplified analytical models hitherto available by means of parametric studies (7).

Owing to the present day availability of powerful computers, there is a temptation to strive to build analytical models to account for every conceivable relevant parameter. However, if these models are too complex, their interpretation may become extremely difficult so that they are ineffectual. It would be better tactics, in the writer's opinion, to start with a simple model and then introduce parameters of likely significance one at a time to assess their relative

importance as well as to obtain a "feel" for the problem. The parametric studies on bearing capacity and settlement of loaded clay layers of the present thesis are conducted on this basis. For this purpose the linear elastic and rigid-plastic materials of the traditional approach are combined to provide various simple idealisations of soil behaviour that are applicable from low working to collapse load conditions. The means is thus available for the study of soil behaviour in the intermediate loading range which, although of importance to safe and economical design, has hitherto been largely neglected. To deal with the above elastoplastic behaviour, the Initial Stress Method (8), which is an extension of the well-established Finite Element approach to elastic analysis, has been employed.

Chapter 1 provides a detailed account of the analytical models to be employed in the parametric studies of the following chapter. A novel procedure for assembling finite elements to facilitate accurate computation without corresponding increase in cost - i.e. "Stack Addition" - is presented. The elastoplastic stress-strain increment relations for a Tresca material are derived. All analytical models are fully defined with the aid of flow charts.

In Chapter 2, several parametric studies on the bearing capacity and settlement of a saturated clay layer subject to undrained strip loading are carried out. This is preceeded by satisfactory preliminary checks on the numerical approach via comparisons with known solutions.

In Chapter 3, the necessary adaptations to the analytical models of Chapter 2 to implement alternative Mohr-Coulomb behaviour are presented to pave the way for similar parametric studies on drained behaviour. Some encouraging results are obtained for a simple example of a drained model thereby justifying further study.

For the same reasons, the modifications to "Stack Addition" to deal with the vertical cut problem are given and a simple example is solved to show that good results may be achieved.

To further increase the scope of parametric studies along present lines, the procedures for dealing with consolidation and various boundary value problems of significance in soil mechanics are indicated.

Finally, some suggestions are made on possible approaches to other soil mechanics topics of relevance, in the present context.

CHAPTER 1

SOME ELASTIC AND ELASTOPLASTIC MODELS FOR STUDYING THE BEHAVIOUR OF CLAY LAYERS AND EXTENSIVE CLAY BODIES SUBJECT TO STRIP LOADING

1.1. Introduction

The present chapter develops several elastic and elastoplastic models, based on the Finite Element Method, for numerical solution using a digital computer.

These models are used in Chapter 2 to conduct some parametric studies on strip loading on clay layers and extensive clay bodies, with particular emphasis on the settlement and bearing capacity of clay layers under undrained conditions.

As a convenient starting point, a rectangular assemblage of linear elastic, triangular finite elements in plane strain is presented. By keeping its overall dimensions general, a half-space, or a layer overlying a rigid base may be idealised. The elastic properties of individual elements are arbitrary so that the model is, effectively, random inhomogeneous. A uniform strip load is applied mid-way along the horizontal surface.

To obtain an accurate solution, a fine mesh is provided around the loaded area. A large number of elements is thus adopted and a solution cannot be obtained via direct inversion of the stiffness matrix of the

entire assemblage (maximum size of 4470 by 4470).

To overcome this problem, a technique called "Stack Addition" is used, whereby only a line of joints need be considered at a time.

The method was first introduced in another work (9), but it has been necessary to make certain changes to deal with asymmetry of loading or material properties about the centre of the loaded area.

Its purely physical approach, in contrast with other similar techniques, has obvious engineering appeal.

By using only a few component elements as the basis for systematic assembly into a highly uniform mesh, further reduction in computer usage can result.

This general elastic model is then adapted to evolve several other elastic models with lesser degrees of inhomogeneity and non-uniform loading.

Next, the Initial Stress Method (8) is applied to the model to simulate an elastoplastic material. A particular category of plastic behaviour is adopted which obeys the Tresca yield criterion and its associated flow rule. It is assumed that the elements are linear elastic (as before) and linear work hardening (constant) at yield. The plane strain elastoplastic relations are derived according to the formulation required by the Initial Stress Method.

The model has a random distribution of elastic properties as before, and also a random strength distribution. The degree of work hardening is the same for all elements.

This general elastoplastic model is then adapted to evolve several

other elastoplastic models with lesser degrees of inhomogeneity and non-uniform loading.

Finally, an extension to the Initial Stress Method is presented whereby a variable degree of work hardening (or softening), as the material flows plastically, may be handled in any of the elastoplastic models thus modified.

The material properties of all models are assumed to be isotropic.

1.2. The linear elastic finite element model for uniform strip loading on the surface of an isotropic, random inhomogeneous half-space or layer overlying a rigid base

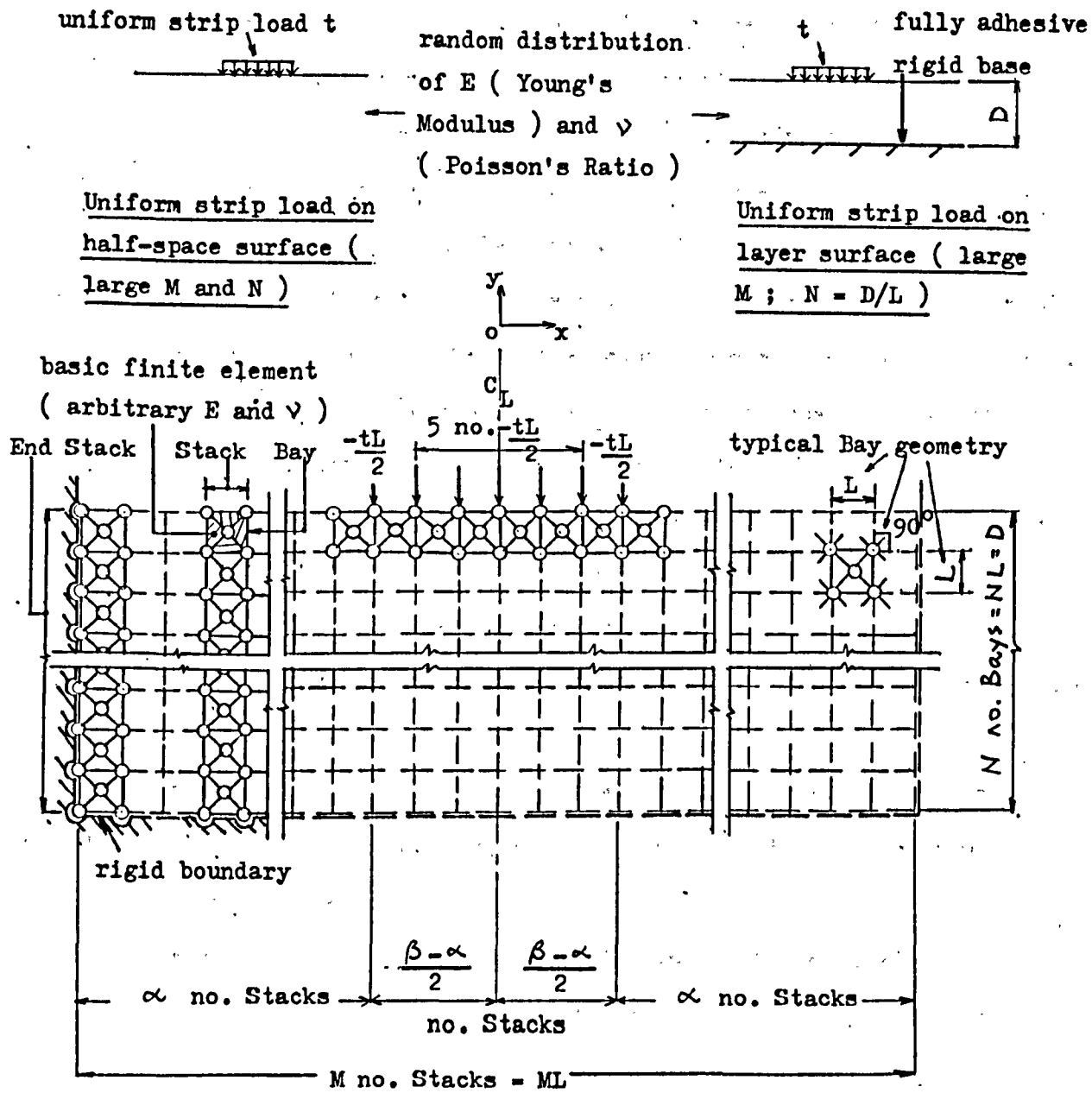

Fig. 1. Boundary value problems and finite element idealisation

Fig. 1 illustrates a finite element idealisation for strip loading on the horizontal surface of a linear elastic half-space or layer overlying a fully adhesive rigid base (for a frictionless base, the joints at the bottom boundary are mounted on rollers; however, on the premise that soil mechanics problems are generally better represented by the adhesive condition (10), only full fixture is considered).

Random inhomogeneity of Young's Modulus (E) and Poisson's Ratio (ν) in both bodies is idealised by attributing arbitrary values of these elastic properties to individual elements.

For the half-space, both lateral and bottom boundaries have to be sufficiently remote from the loaded area. For the layer, only the lateral boundaries are far removed; the bottom boundary is set to the layer depth.

To simplify the discussion, square Bays are assumed throughout the assemblage. In the actual models adopted in Chapter 3, these are generally used to produce a fine mesh in the vicinity of the loaded area; near the boundaries where the influence of the load is small, rectangular Bays are used so that less elements are required to keep the boundaries remote.

A brief description suffices to adapt the model to include rectangular Bays in the latter part of the discussion.

It was found that by adopting the width of the strip load as shown in Fig. 1, sufficient accuracy can be expected in both elastic as well as elastoplastic models.

More will be said about accuracy of solution in Chapter 3.

Starting with a brief resume of the Finite Element Method, the assemblage is then systematically built up, via a single component

triangular finite element - the basic finite element. This element generates the Bay which, in turn, generates the Stack. The Stacks are then joined together to form the final mesh - see Fig. 1.

The solution of the given boundary value problem is then effected in an essentially reverse process.

Flow charts are presented to supplement the theory as well as showing how the computer program is written.

Brief accounts of the modifications required to deal with lesser degrees of inhomogeneity and non-uniform loading are next presented.

Finally, the adaptation of the general model to deal with rectangular Bays is discussed.

The aim of this chapter is to keep the format problem-orientated. The references provided may be used as further reading.

A working knowledge of the stiffness method in structural analysis is assumed.

1.2.1. The Finite Element Method

The particular finite element formulation adopted is known as the Displacement Method and is based on the Rayleigh-Ritz procedure.

This procedure obtains approximate solutions to self-adjoint (i.e., can be deduced from a variational principle) elliptic boundary value problems such as the static problems in elasticity considered here.

The variational principle concerned is that of minimum potential energy; it states that of all geometrically acceptable patterns of displacements for any given problem, the true one is that which leads to minimum potential energy.

In applying the Rayleigh-Ritz procedure, one begins by simply choosing to approximate the true solution of the displacement field by some combination of "trial functions"; the Finite Element Method is unique in the manner by which it provides an automatic procedure for obtaining these functions. Thus, the continuum is discretised into an assemblage of finite elements which are interconnected at their nodes; a set of "displacement functions" are chosen which uniquely define the state of displacement within each element in terms of its nodal displacements, the unknown paramters of the problem.

For this approximate displacement field to be geometrically acceptable, however, it must satisfy any prescribed displacements on the boundary ("essential conditions") as well as remain at a finite energy level; otherwise, no meaningful solution would result.

Next, the toal potential energy of the domain and any associated loading is derived, the minimisation of which should lead to the best approximation of the displacements (and hence, strains and stresses) that the choice of trial functions can provide.

By increasing the fineness of subdivision of the continuum into finite elements, the constraint of the assumed displacement pattern reduces as it develops a greater degree of freedom; in the limit, the exact solution will be obtained - with complete equilibrium - provided certain convergence criteria are satisfied. These are that:

(a) no straining occurs in the elements as a result of rigid body displacement,

(b) constant strain conditions, when they exist, should be manifested and

(c) strains at the interface between elements should be finite - i.e. the displacement field must be compatible.

In general, it will be found that the equilibrium conditions are satisfied in the overall sense only; local violation of equilibrium on element boundaries occur.

Also, the total strain energy of the domain will be underestimated in its general picture; this means the same will be found for displacements, strains and stresses. However, this is obviously not true for all elements.

The following derivation deals specifically with a linear elastic material subject to plane strain conditions. The continuum is discretised as an assemblage of triangular finite elements interconnected at their joints.

Reference (6) provides an excellent account for further reading.

1.2.2. Strain energy of the basic linear elastic, triangular finite element in plane strain

1.2.2.1. Theory

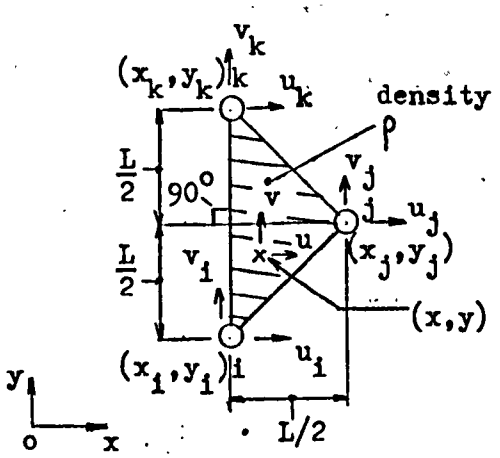

Note: u (along x direction) and v (along y direction) are displacement components at any point (x,y) within the assemblage

Fig. 2. The basic finite element

Fig. 2 illustrates the finite element which constitutes the building block of the final assemblage. It is of unit thickness (in the z direction - i.e. into the paper); its Young's Modulus is E and Poisson's Ratio ν .

The joints located at its corners are i, j and k, with displacements, (u_i,v_i), (u_j,v_j) and (u_k,v_k), respectively.

The geometry and positive directions of displacements are as shown; tensile stresses and strains are positive.

Assuming a linear displacement field for the assemblage, we have,

$$\{\bar{u}\} = \begin{Bmatrix} u \\ v \end{Bmatrix} = \begin{bmatrix} 1 & x & y & 0 & 0 & 0 \\ 0 & 0 & 0 & 1 & x & y \end{bmatrix} \{a\} \quad \ldots\ldots (1), \text{ where}$$

$\{a\}$ is a 6x1 vector of arbitrary constants.

For the element, these constants may be eliminated in favour of the joint displacements, $\{\bar{u}_c\}$, by substituting the coordinates of the corner joints into Eqn. 1 as follows:

$$\{\bar{u}_c\} = \begin{Bmatrix} u_i \\ u_j \\ u_k \\ v_i \\ v_j \\ v_k \end{Bmatrix} = \begin{bmatrix} 1 & x_i & y_i & 0 & 0 & 0 \\ 1 & x_j & y_j & 0 & 0 & 0 \\ 1 & x_k & y_k & 0 & 0 & 0 \\ 0 & 0 & 0 & 1 & x_i & y_i \\ 0 & 0 & 0 & 1 & x_j & y_j \\ 0 & 0 & 0 & 1 & x_k & y_k \end{bmatrix} \{a\}$$

$$= \begin{bmatrix} [g] & [0] \\ [0] & [g] \end{bmatrix} \{a\}, \text{ whereupon,}$$

$$\{a\} = \begin{bmatrix} [g^{-1}] & [0] \\ [0] & [g^{-1}] \end{bmatrix} \{\bar{u}_c\} = [G']\{\bar{u}_c\} \quad \ldots\ldots (2).$$

Now substitute Eqn. 2 into Eqn. 1 and we have,

$$\{\bar{u}\} = \begin{bmatrix} 1 & x & y & 0 & 0 & 0 \\ 0 & 0 & 0 & 1 & x & y \end{bmatrix} [G'] \{\bar{u}_c\} \quad \ldots\ldots (3)..$$

Eqn. 3 is applicable, in form, to all elements of the assemblage, and by substituting for the relevant joint coordinates, the value of $\{\bar{u}\}$ can be obtained in terms of $\{\bar{u}_c\}$ for the appropriate element.

Thus, $\{\bar{u}\}$ consists of two continuous functions that vary throughout an element and along its edges in a way that is fixed by its joint displacements.

Since any two adjacent elements have the same displacements at their common joints, they will also have the same displacements at every point along their common edge. Thus, the condition of compatibility (i.e., continuity) is satisfied for the displacement field chosen.

Also, because the field is linear in any one element, $\frac{\partial}{\partial x}\{\bar{u}\}$ and $\frac{\partial}{\partial y}\{\bar{u}\}$ will be constant and thus finite throughout the assemblage.

To satisfy the essential (i.e. boundary) conditions on $\{\bar{u}\}$, only problems where (i) the boundaries are polygonal and (ii) any prescribed displacements that occur vary linearly, are admissible.

For this slightly restricted range of problems, the geometric conditions mentioned in Section 1.2.1. will be satisfied.

Thus, the entire displacement field of the domain is expressed in terms of the joint displacements of the component elements; the values of some of these will be fixed by the essential conditions and the problem solved approximately by minimising the total potential energy of the domain and any associated loading, with respect to the rest.

To do this, we first return to the basic finite element, and

proceed to derive an expression for its strain energy in the following.

From Eqn. 3, we obtain the strain vector

$$\{\gamma\} = \begin{Bmatrix} \varepsilon_x \\ \varepsilon_y \\ \gamma_{xy} \end{Bmatrix} = \begin{bmatrix} \partial/\partial x & 0 \\ 0 & \partial/\partial y \\ \partial/\partial y & \partial/\partial x \end{bmatrix} \{\bar{u}\}$$

$$= \begin{bmatrix} 0 & 1 & 0 & 0 & 0 & 0 \\ 0 & 0 & 0 & 0 & 0 & 1 \\ 0 & 0 & 1 & 0 & 1 & 0 \end{bmatrix} [G'] \{\bar{u}_c\} = [A][G']\{\bar{u}_c\} \quad \ldots\ldots (4).$$

Now let

$$\{\bar{u}_c'\} = \begin{Bmatrix} u_i \\ v_i \\ u_j \\ v_j \\ u_k \\ v_k \end{Bmatrix} = \begin{bmatrix} 1 & 0 & 0 & 0 & 0 & 0 \\ 0 & 0 & 1 & 0 & 0 & 0 \\ 0 & 0 & 0 & 0 & 1 & 0 \\ 0 & 1 & 0 & 0 & 0 & 0 \\ 0 & 0 & 0 & 1 & 0 & 0 \\ 0 & 0 & 0 & 0 & 0 & 1 \end{bmatrix} \{\bar{u}_c\} = [p]\{\bar{u}_c\} \quad ;$$

$[p]$ is a permutation matrix re-ordering the component joint displacements to facilitate subsequent assembly (dealing with $\{\bar{u}_c\}$ means that only $[g]$, rather than a 6x6 matrix need be inverted).

We can thus re-write Eqn. 4 as

$$\{\gamma\} = [A][G'][p]\{\bar{u}_c'\} = [\Gamma]\{\bar{u}_c'\} \quad \ldots\ldots (5),$$

where $[\Gamma]$ is a matrix of constants, and therefore, all points

within the element are under constant strain. Further, it can be shown that nodal displacements caused by rigid body displacement will not lead to straining of the element; taken in combination with compatibility of the displacement field (pg. 15), the convergence criteria (pg. 12) are thus satisfied.

For a linear elastic material in plane strain, the stress vector

$$\{\sigma\} = \begin{Bmatrix} \sigma_x \\ \sigma_y \\ \tau_{xy} \end{Bmatrix} = [\bar{E}]\{\gamma\} = [\bar{E}][\Gamma]\{\bar{u}_c'\} \quad \ldots\ (6),$$ where

the elasticity matrix $$[\bar{E}] = \frac{E(1-\nu)}{(1+\nu)(1-2\nu)} \begin{bmatrix} 1 & \nu/(1-\nu) & 0 \\ \nu/(1-\nu) & 1 & 0 \\ 0 & 0 & (1-2\nu)/2(1-\nu) \end{bmatrix},$$

E being the Young's Modulus and ν the Poisson's Ratio.

Thus, the strain energy of the element $U = \int_{A_E} \frac{1}{2}\{\gamma\}^T\{\sigma\}\, dA_E$

$= \frac{1}{2}\{\bar{u}_c'\}^T[\Gamma]^T[\bar{E}][\Gamma]\{\bar{u}_c'\} A_E = \frac{1}{2}\{\bar{u}_c'\}^T[H]\{\bar{u}_c'\}$ .... (7), where

A_E is its area ($= L^2/4$) and $[H] = [\Gamma]^T[\bar{E}][\Gamma]A_E$, a matrix of constants.

Although, for plane strain, $\sigma_z = \nu(\sigma_x + \sigma_y)$ .... (8), since $\varepsilon_z = 0$ .... (9), there is no contribution to U from stresses in the z direction (note that the particular condition, $\varepsilon_z = 0$ is applicable throughout the present work when discussing plane strain, rather than the general plane strain condition, ε_z = constant).

The above expressions which have been derived for the basic finite element are equally applicable to all elements in principle as Eqn. 3 applies throughout the assemblage (see also pg. 15) .

Also, E and ν may be set to arbitrary values according to the degree of uniformity prescribed for the assemblage.

1.2.2.2. Flow chart for computing $[H]$ (to be read in conjunction with Master Flow Chart in Appendix) - similar for all elements

Block D4

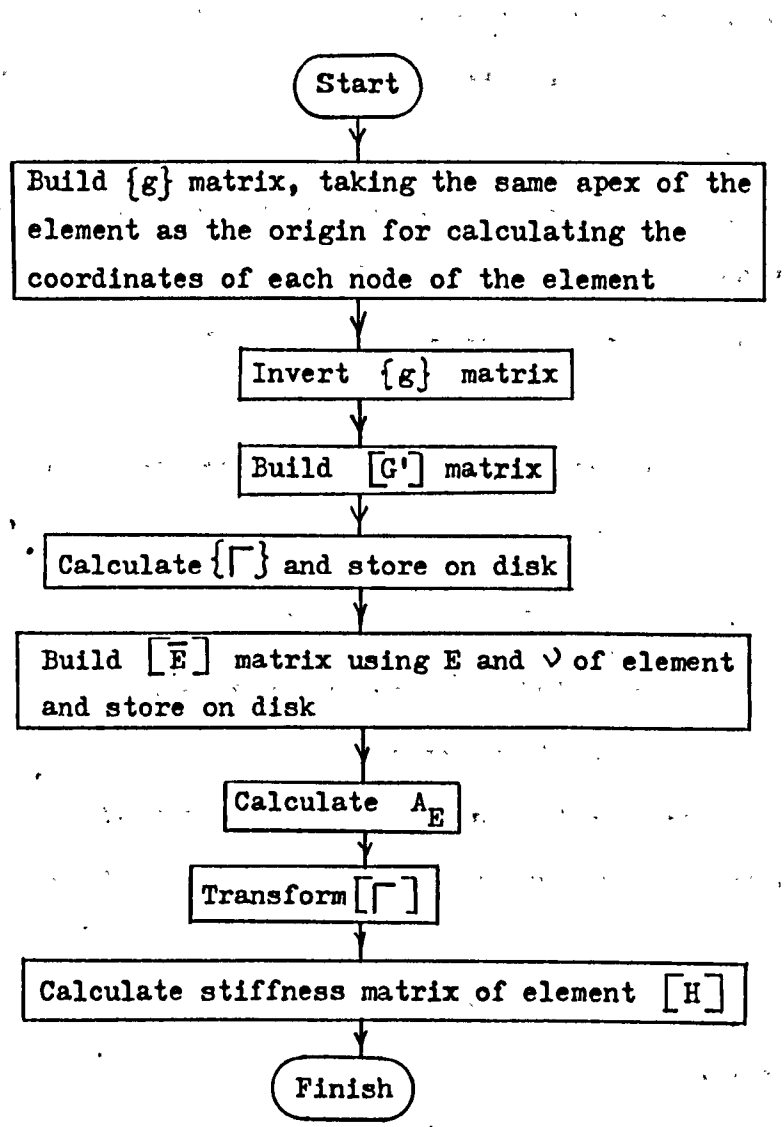

1.2.3. The stiffness equation of the assemblage

Before proceeding with assembling, it is necessary to establish the analogy of a finite element assemblage to a structural framework so that a stiffness equation can be assumed to apply to any part (or the whole) of the assemblage, as in the stiffness method in structural analysis.

By inspection of the strain energy expression of Eqn. 7, $[H]$ is seen to be analogous to the stiffness matrix of a pin-ended member, albeit for three corner joints of the element rather than just the two of the member.

Since a similar expression holds for all other elements (see pg. 18), the total strain energy of the assemblage can be simply expressed as $\overline{U} = \frac{1}{2} \{q\}^T [K] \{q\}$ .... (10), where $\{q\}$ is a vector of the joint displacements, ordered in accordance with the incidence vector, and $[K]$ the overall stiffness matrix of the assemblage, obtained by adding the submatrices of the individual element matrices like $[H]$ into locations within $[K]$, mapped by the incidence vector.

The consequence of not adopting the analogy is that a much larger matrix, $[A] [\tilde{H}] [A]$, would have to be handled in place of $[K]$.

Fig. 6 provides an illustration of the mapping procedure; for present purposes, it suffices simply to state Eqn. 10 .

So far, only the total strain energy of the assemblage has been derived; the Rayleigh-Ritz procedure requires that the total potential

energy of the assemblage and associated loading be derived, as a prelude to applying the variational principle.

Thus, the next step is to derive expressions for the potential energy due to the loading. This is divided into three types:-

(i) Body forces - for the assemblage, the potential energy due to body forces $\{b\}$ ($= \begin{Bmatrix} b_x \\ b_y \end{Bmatrix}$, the components along the x and y directions, respectively, relevant to plane strain),

$\bar{V}_B = -\int_A \{\bar{u}\}^T \{b\}\, dA$, where A is the total area of the domain.

$\bar{V}_B$ can be broken up into a sum of individual integrals, each over one element only; for the basic element for example, the potential energy

$$V_B = -\int_{A_E} \{\bar{u}\}^T \{b\}\, dA_E = -\{\bar{u}_c'\}^T \int_{A_E} [p]^T [G']^T \begin{bmatrix} 1 & 0 \\ x & 0 \\ y & 0 \\ 0 & 1 \\ 0 & x \\ 0 & y \end{bmatrix} \begin{Bmatrix} b_x \\ b_y \end{Bmatrix} dA_E$$

(see Eqn. 3) $$= -\{\bar{u}_c'\}^T \{\bar{p}_B\} \quad \ldots\ (11)\ .$$

In particular, when the weight of the element is considered (see Chapter 3., Section 3.3.),

$$\{\bar{p}_B\} = -\int_{A_E} [p]^T [G']^T \begin{bmatrix} 1 & 0 \\ x & 0 \\ y & 0 \\ 0 & 1 \\ 0 & x \\ 0 & y \end{bmatrix} \begin{bmatrix} 0 \\ -\rho g \end{bmatrix} = \frac{A_E}{3} \begin{bmatrix} 0 \\ -\rho g \\ 0 \\ -\rho g \\ 0 \\ -\rho g \end{bmatrix} \quad \ldots\ldots (12),$$

where ρ is the density (uniform) of the element - the weight acts in the opposite direction to v (see Fig. 2) .

The structural analogy is again evident in Eqn. 11 and since similar expressions will apply to other elements - see pg. 16, we can write, for the assemblage,

$\bar{V}_B = -\{q\}^T \{p_B\}$ .... (13), for which $\{p_B\}$ is obtained by adding contributions from vectors like $\{\bar{p}_B\}$ into positions indicated by the incidence vector, as for $[K]$ (pg. 20), except that this time, only row mapping, rather than the whole of the square matrix, need be done. Fig. 6 provides the general procedure for mapping.

(ii) Surface tractions - for the assemblage, the potential energy due to surface tractions $\{T\}$ (= $\begin{Bmatrix} T_x \\ T_y \end{Bmatrix}$, the components along the x and y directions, respectively, relevant to plane strain.),

$\bar{V}_T = -\int_{S_T} \{\bar{u}\}^T \{T\}\, dS_T$, where S_T is that part of the boundary on which $\{T\}$ is specified.

Such tractions exist only on elements having one or two edges on the boundary where they occur.

To obtain $\bar{V}_T$, it is best to proceed element by element, and edge by edge. Thus, for the basic element, for example, the potential energy $V_T = -\int_{S_{T(e)}} \{\bar{u}\}^T \{T\} \, dS_{T(e)}$, where $S_{T(e)}$ represents the edge or edges subject to traction.

Assuming, for the purpose of this exercise, that edge i-k (Fig. 3 - is subject to traction, $\{T\} = \{T(s)\}$ where s is a convenient variable to use such that

$\{\bar{u}\} = \{\bar{u}_c'\}_i + s\,(\{\bar{u}_c'\}_k - \{\bar{u}_c'\}_i)$ $(0 \leqslant s \leqslant 1)$ for $\{\bar{u}_c'\}_i = \begin{Bmatrix} u_i \\ v_i \end{Bmatrix}$ and $\{\bar{u}_c'\}_k = \begin{Bmatrix} u_k \\ v_k \end{Bmatrix}$, we can re-write,

$$V_T = -L\int_0^1 (\{\bar{u}_c'\}_i^T + s[\{\bar{u}_c'\}_k^T - \{\bar{u}_c'\}_i^T])\{T(s)\}\, ds$$

$$= -\left\{\{\bar{u}_c'\}_i^T \{\bar{u}_c'\}_k^T\right\} \begin{Bmatrix} \{\bar{p}_T\}_i \\ \{\bar{p}_T\}_k \end{Bmatrix} \quad \ldots\ (14)$$ - since $\frac{dS_{T(e)}}{ds} = L$,

where $\{\bar{p}_T\}_i = L\int_0^1 (1-s)\{T(s)\}\, ds$, and $\{\bar{p}_T\}_k = L\int_0^1 s\{T(s)\}\, ds$.

In particular, when a uniform pressure t is applied to the edge i-k , and the element rotated anticlockwise through 90° , $\{T(s)\} = \begin{Bmatrix} 0 \\ -t \end{Bmatrix}$ (the traction acting in the opposite direction to v) and therefore

$$\{\bar{p}_T\}_i = \{\bar{p}_T\}_k = \begin{Bmatrix} 0 \\ \frac{-tL}{2} \end{Bmatrix} \quad \ldots\ (15)\ .$$

This form of loading forms the basis for idealising a uniform strip load, as shown in Fig. 1.

As for the body forces, the structural analogy applies here and we obtain, in the same way, the potential energy of the loading on the assemblage as $\bar{V}_T = -\{q\}^T \{p_T\}$ .... (16), $\{p_T\}$ being obtained from contributions from vectors like $\{\bar{p}_T\}_i$ and $\{\bar{p}_T\}_k$.

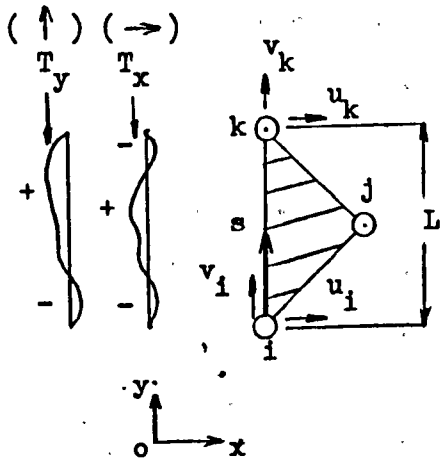

Fig. 3. Surface tractions on edge i-k of the basic element

(iii) Concentrated loads on joints at the boundary - for the assemblage, the potential energy due to concentrated loads acting on the boundary joints is obviously $\bar{V}_P = -\{q\}^T \{p_P\}$ .... (17), $\{p_P\}$ being a vector of the concentrated loads thenselves, ordered according to the incidence vector of the joint displacements $\{q\}$ which are coincident with the lines of action of the respective loads (given as x and y components).

This is identical to the expression for a structural framework.

A single load of this type in appropriate orientation and

position would constitute line loading when applied to the model in Fig. 1 .

We are now in a position to express the total potential energy of the assemblage and associated loading as

$$\bar{U} + \bar{V}_B + \bar{V}_T + \bar{V}_P = \tfrac{1}{2}\{q\}^T[K]\{q\} - \{q\}^T\{p_B\} - \{q\}^T\{p_T\} - \{q\}^T\{p_P\} \quad .$$

Applying the principle of minimum potential energy, we have,

$\frac{\partial}{\partial\{q\}_r}\left(\bar{U} + \bar{V}_B + \bar{V}_T + \bar{V}_P\right) = 0$ for r=1 to n, where $\{q\}_r$ are the rth joint displacements (x and y components) and n the total number of joints in the assemblage.

Substituting Eqns. 10, 13, 16 and 17 accordingly, we obtain,

$\{p_B\} + \{p_T\} + \{p_P\} = [K]\{q\}$ .... (18) which is a set of nx2 linear simultaneous equations.

Since $\{p_B\}$, $\{p_T\}$, $\{p_P\}$ and $[K]$ are known, $\{q\}$ can thus be solved.

However, for a large number of joints, a direct inversion procedure would be prohibitive in terms of computer usage and the analogy between a finite element assemblage and a structural framework, evident by inspection of Eqn. 18, will be used in the following sections to systematically build up the assemblage and solve for joint displacements, a set at a time.

Thus, it will be assumed that in assembling any number of finite elements, an equation like Eqn. 18 may be written for "equilibrium" at their joints when subject to "concentrated loads", $\{p_B\}$, $\{p_T\}$ and $\{p_P\}$.

1.2.4. The stiffness equation of the Condensed Bay

1.2.4.1. Theory

The present section deals with the first stage of assembly whereby the basic finite element and three other similar elements are interconnected to form the Bay - see Fig. 5 .

To begin with, the stiffness matrices of the other three elements have to be determined. This may be done by substituting the relevant joint coordinates into Eqn. 1 and proceeding to obtain a matrix such as $[H]$, the stiffness metrix of the basic element.

Alternatively, the same result can be achieved, for a homogeneous Bay, via the transformation of the displacement system u-v to system u"-v" , whilst maintaining the same relative orientation to the basic finite element as it rotates through angle θ - see Fig. 4 .

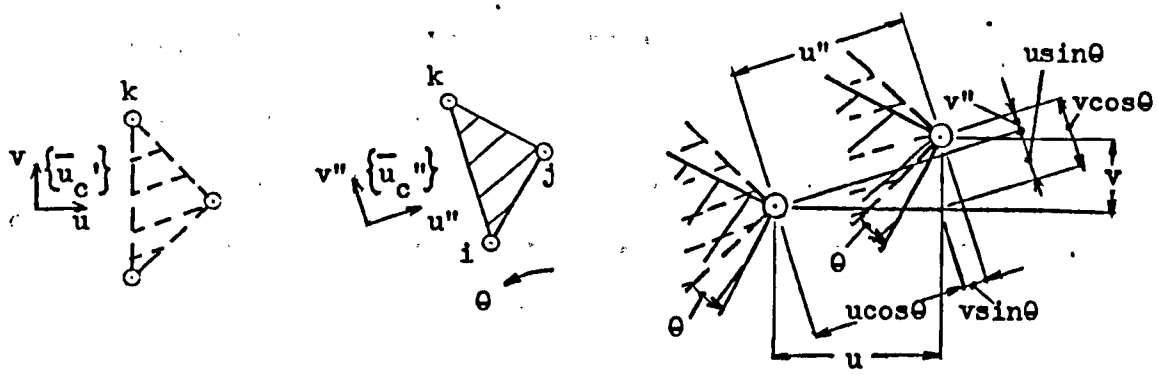

The basic element - see Fig. 2 | The re-orientated element | Component joint displacements - both systems

Fig. 4. Transformation from system $\{\bar{u}_c'\}$ to system $\{\bar{u}_c''\}$

By doing so, $[H]$ will still be applicable to the re-orientated element whose strain energy may therefore be given by

$$U'' = \tfrac{1}{2} \{\bar{u}_c''\}^T [H] \{\bar{u}_c''\} \quad \text{(see Eqn. 7) .}$$

Nevertheless, for the purpose of assembly, it is necessary to work to a consistent displacement system, and retaining the $\{\bar{u}_c'\}$ system as the reference system, we can substitute

$$\{\bar{u}_c''\} = [R_{(\theta)}] \{\bar{u}_c'\} \quad , \text{ where}$$

$$[R_{(\theta)}] = \begin{bmatrix} \cos\theta & \sin\theta & 0 & 0 & 0 & 0 \\ -\sin\theta & \cos\theta & 0 & 0 & 0 & 0 \\ 0 & 0 & \cos\theta & \sin\theta & 0 & 0 \\ 0 & 0 & -\sin\theta & \cos\theta & 0 & 0 \\ 0 & 0 & 0 & 0 & \cos\theta & \sin\theta \\ 0 & 0 & 0 & 0 & -\sin\theta & \cos\theta \end{bmatrix} \text{ - see Fig. 4 ,}$$

into the expression for U'' , giving,

$$U'' = \tfrac{1}{2} \{\bar{u}_c'\}^T [R_{(\theta)}]^T [H][R_{(\theta)}] \{\bar{u}_c'\} = \tfrac{1}{2} \{\bar{u}_c'\}[H'_{(\theta)}] \{\bar{u}_c'\} \quad ,$$

where $[H'_{(\theta)}] = [R_{(\theta)}]^T [H][R_{(\theta)}]$ .... (19) .

Thus, $[H'_{(\theta)}]$ effectively replaces $[H]$ as the stiffness matrix for the re-orientated element.

From the foregoing, it is evident that mere translation of the basic element will not alter its stiffness matrix, as for a structural member.

Fig. 5 shows how, by substituting $\theta = \frac{\pi}{2}$, π and $\frac{3\pi}{2}$, respectively, the stiffness matrices of the three component finite elements (other than the basic element for which $\theta = 0$) - $[H(\pi/2)]$, $[H(\pi)]$ and $[H(3\pi/2)]$, respectively - of the Bay may be computed using Eqn. 19 .

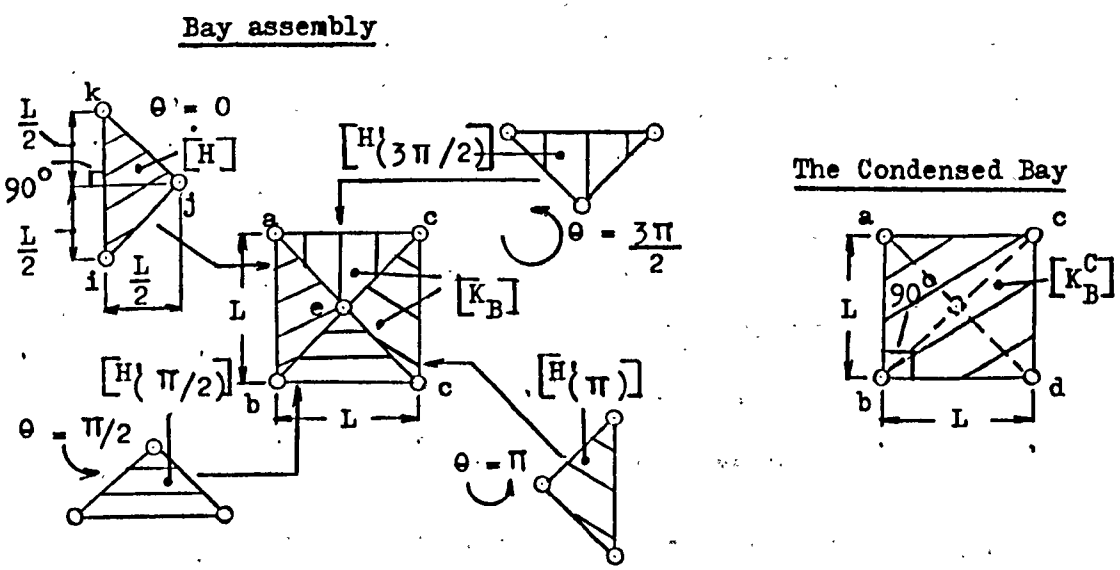

Fig. 5. Assembling component finite elements to form Condensed Bay

Next, the elements of the stiffness matrix, $[K_B]$, of the Bay are mapped by adding the submatrices of the stiffness matrices of the

component finite elements into the locations of $[K_B]$, according to the incidence vector, as shown in Fig. 6 which is self-explanatory.

Note: all $[h]$'s and $[k_B]$'s are 2x2 submatrices; where more than one $[h]$ submatrix is mapped into a $[k_B]$ position, the former are summed

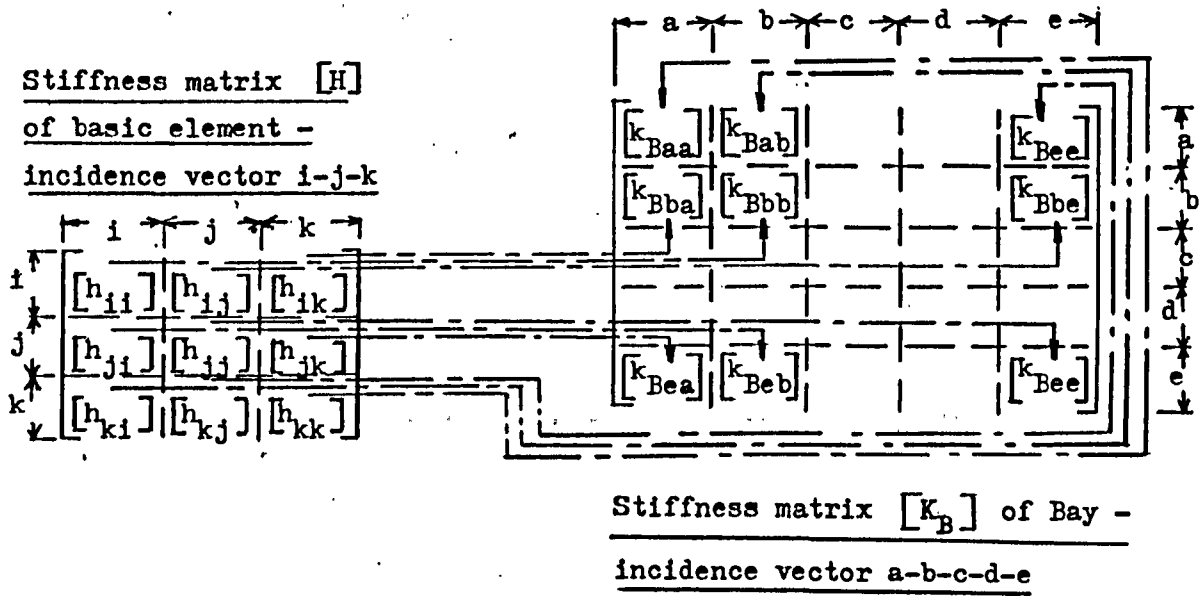

Fig. 6. Typical procedure for mapping the elements of the stiffness matrix of a component finite element into the stiffness matrix of the Bay - similar for other three component elements

The Bay is then "condensed"; i.e., the stiffness matrix, $[K_B]$, modified to relate to the four corner joints only. This is a necessary

prelude to assembling the Stack - see Section 1.2.5.

Fig. 7 shows how the stiffness equation of the Bay may be subdivided into convenient submatrices to facilitate derivation of the stiffness matrix $\left[K_B^C\right]$ of the Condensed Bay - see also Fig. 5 .

Note: the $\{p\}$'s and $\{q\}$'s are 2x1 submatrices of the loads at (see pg. 25), and displacements of the respective joints - x component followed by y component - ordered according to the incidence vector a-b-c-d-e

$$\begin{Bmatrix} \{p_a\} \\ \{p_b\} \\ \{p_c\} \\ \{p_d\} \\ \{p_e\} \end{Bmatrix} = \begin{Bmatrix} \{P\} \\ \vdots \\ \{p_e\} \end{Bmatrix} = \left[\begin{array}{c|c} [X] & [Y] \\ \hline [Z] & [k_{Bee}] \end{array}\right] \begin{Bmatrix} \{Q\} \\ \hline \{q_e\} \end{Bmatrix}, \text{ where } \{Q\} = \begin{Bmatrix} \{q_a\} \\ \{q_b\} \\ \{q_c\} \\ \{q_d\} \end{Bmatrix}$$

Fig. 7. Subdividing the stiffness equation of the Bay

From Fig. 7 , we have,

$$\{P\} = [X]\{Q\} + [Y]\{q_e\} \quad \ldots\ (20) \text{ and}$$

$$\{p_e\} = [Z]\{Q\} + [k_{Bee}]\{q_e\} \quad \ldots\ (21) .$$

Eqn. 21 gives, $\{q_e\} = [k_{Bee}]^{-1} (\{p_e\} - [Z]\{Q\}) \ldots$ (22) and therefore, substituting for $\{q_e\}$ in Eqn. 20, we have,

$\{P\} = ([X] - [Y][k_{Bee}]^{-1} [Z]) \{Q\} + [Y][k_{Bee}]^{-1} \{p_e\}$, or, alternatively,

$\{P^C\} = [K_B^C]\{Q\}$, which is the stiffness equation of the Condensed Bay, incidence vector a-b-c-d .

Thus, the stiffness matrix of the Condensed Bay

$[K_B^C] = [X] - [Y][k_{Bee}]^{-1}[Z]$ .... (23) , and the load vector

$\{P^C\} = \{P\} - [Y][k_{Bee}]^{-1}\{p_e\}$ .... (24) ; it can be seen that a further requirement for condensation is that the load vector, $\{P\}$, of the Bay has to be modified to $\{P^C\}$ (which includes the effect of loading on joint e of the Bay, now that only the corner joints are considered) .

1.2.4.2. Flow chart for computing $[K_B^C]$ (to be read in conjunction with Master Flow Chart in Appendix)

Block D7

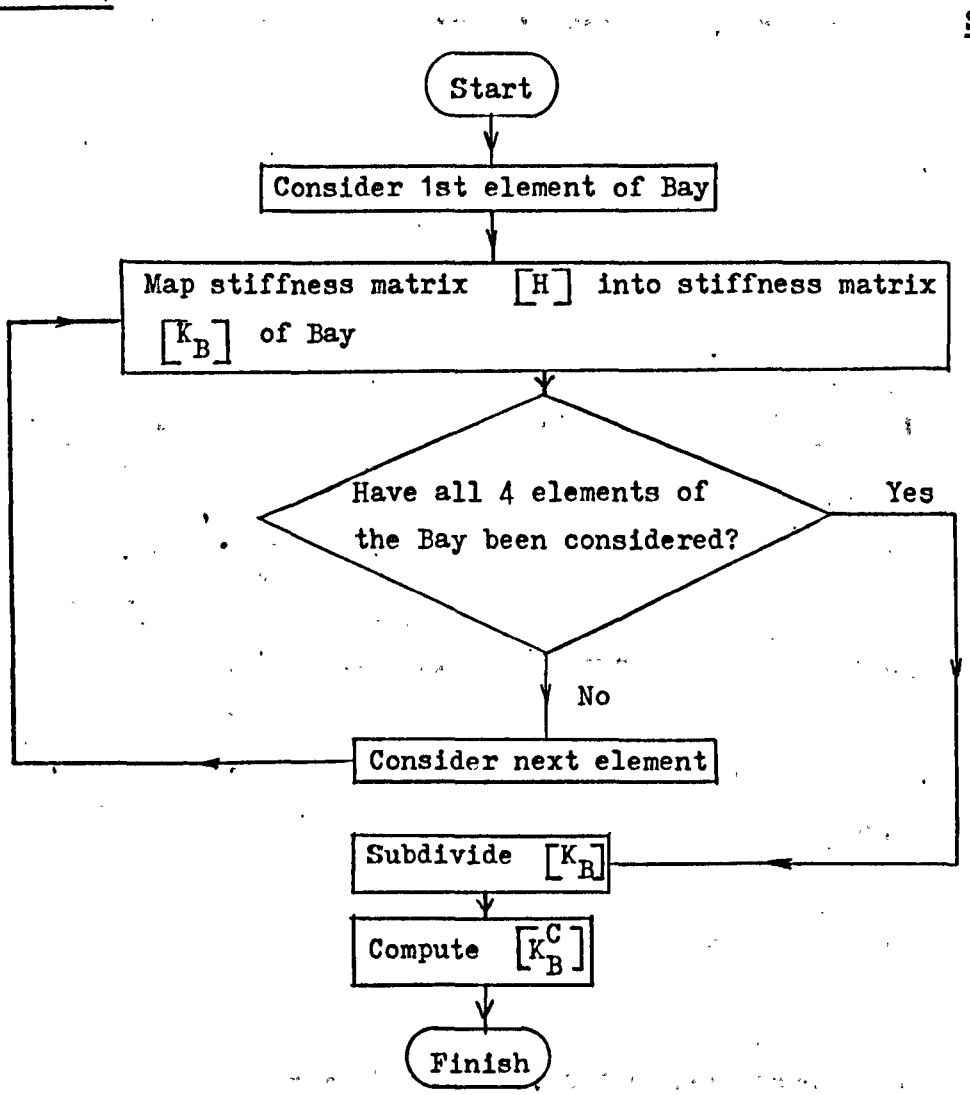

1.2.5. The stiffness equation of the Stack and End Stack

1.2.5.1. Theory

The next stage of assembly, whereby N (Fig. 1) number Condensed Bays are interconnected to form the Free Stack, is illustrated in Fig. 8.

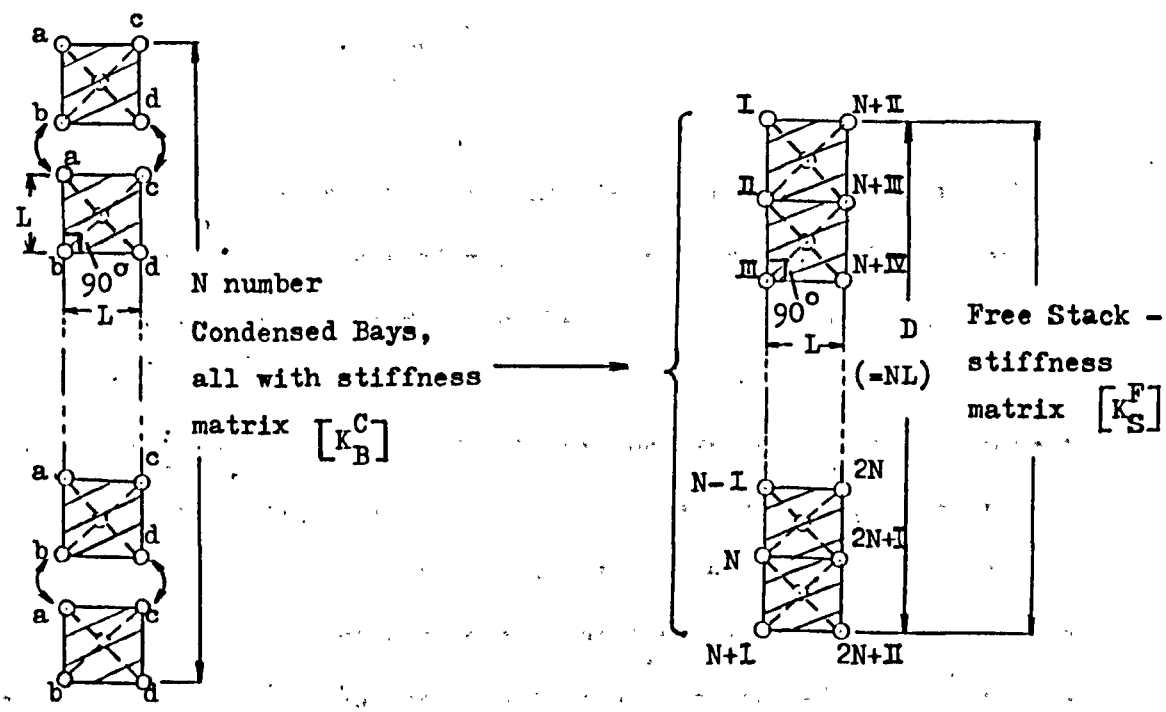

Fig. 8. Assembling component Condensed Bays to form Free Stack

The stiffness matrix, $[K_S^F]$, of the Free Stack is mapped by adding the submatrices of the stiffness matrices, $[K_B^C]$, of the

component Condensed Bays into the locations of $\left[K_S^F\right]$ according to the incidence vector I- II- ... -2N+I -2N+II , a procedure similar to that shown in Fig. 6 .

Thus, the stiffness equation of the Free Stack may be written as

$$\begin{Bmatrix} \{p_I\} \\ \{p_{II}\} \\ \vdots \\ \{p_{2N+I}\} \\ \{p_{2N+II}\} \end{Bmatrix} = \left[K_S^F\right] \begin{Bmatrix} \{q_I\} \\ \{q_{II}\} \\ \vdots \\ \{q_{2N+I}\} \\ \{q_{2N+II}\} \end{Bmatrix} \quad \ldots\ldots (25)$$

, for which the $\{p\}$'s and $\{q\}$'s are 2x1 submatrices of the loads at, and the displacements of the respective joints (x component followed by y component), ordered according to the incidence vector I- II- ... 2N+I -2N+II , as for the Bay.

When mapping the elements of the load vectors of the component Condensed Bays into the locations of the load vector of the Free Stack, the term $\{P^C\}$ (Eqn. 24), rather than $\{P\}$ (Fig. 7) should be used; the latter accounts solely for the cumulative effect of the relevant body forces, surface traction and concentrated boundary loads (pgs. 21 to 25) whereas the former includes the effect of loading on joint e (Fig. 5), on the corner joints.

Mapping is simply a mechanical procedure for establishing the equilibrium relations at the joints - in this case, of the Free Stack; since the equilibrium of the corner joints of the component Condensed

Bays is dependent on loading at the joints, e , these cannot be ignored.

Next, Eqn. 25 has to be modified to account for end fixity - see Fig. 9 - of the Stack.

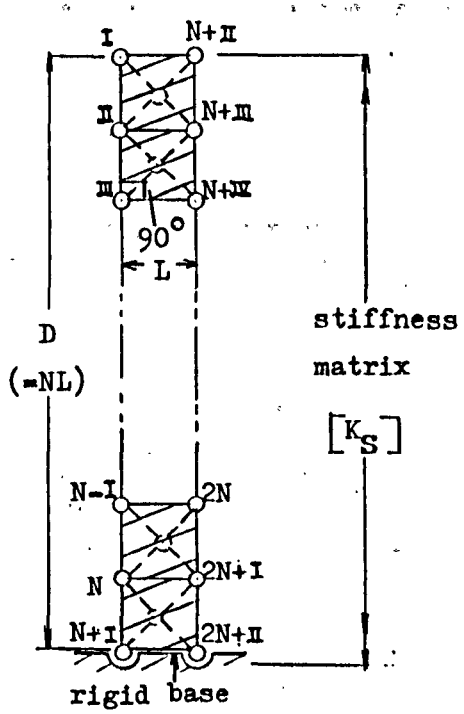

Fig. 9. The Stack - including end fixity

Thus, the conditions, $\{q_{N+I}\} = \{q_{2N+II}\} = \begin{Bmatrix} 0 \\ 0 \end{Bmatrix}$, have to be incorporated into Eqn. 25, as shown in Fig. 10.

The form depicted is for convenience of computation.

By examining Eqn. 3, it is obvious that fixing the bottom joints also restrains the lower edge of the bottom element (since there is no relative movement of the joints at either end), thereby adhering to the prescribed boundary conditions.

Note: only the modifications to the load vector and the stiffness matrix are shown; their remaining elements, and the displacement vector do not alter

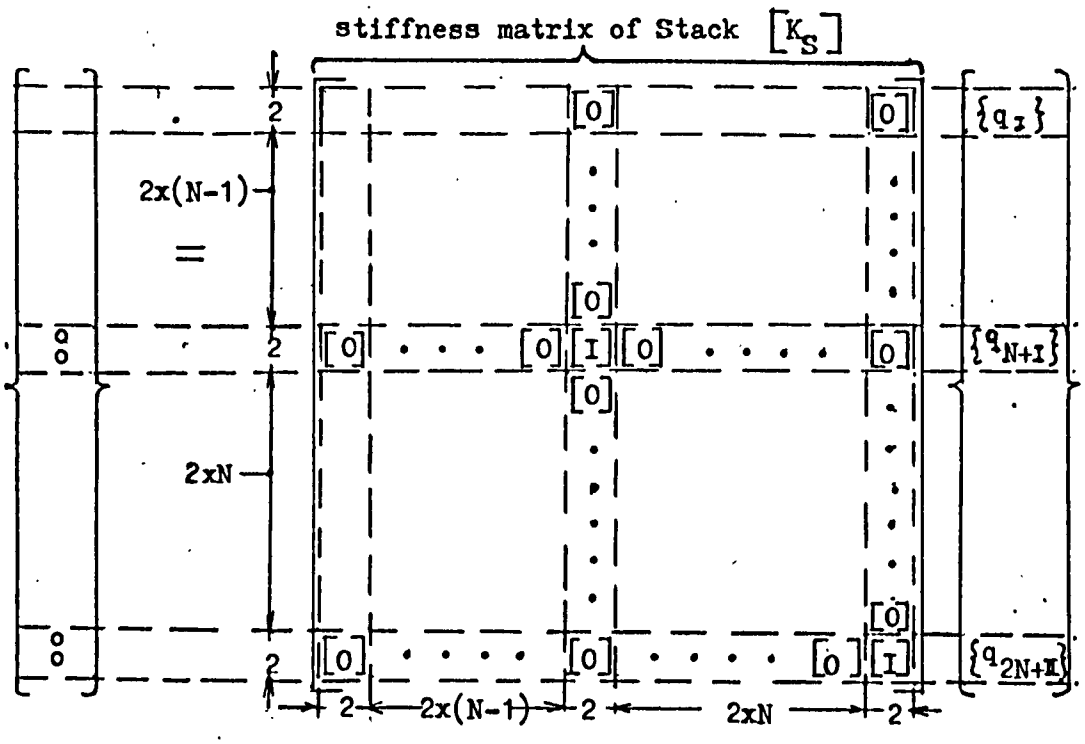

$0 = \begin{bmatrix} o & o \\ o & o \end{bmatrix}$ and $I = \begin{bmatrix} 1 & o \\ o & 1 \end{bmatrix}$; typically, $[0] \cdots [0]$ ← all $[0]$'s between →

Fig. 10. Modifications to Eqn. 25 to obtain stiffness equation of Stack

Similar modifications also apply to the End Stacks (see Fig. 1) as shown in Fig. 11.

As already pointed out in Section 1.2., although Fig. 1 depicts the fully adhesive condition which is of interest in soil problems, the provision of roller joints at the base of the Free Stack leads to a frictionless base. This simply entails adding the conditions,

$\{q_{N+I}\} = \begin{Bmatrix} u_{N+} \\ o \end{Bmatrix}$ and $\{q_{2N+II}\} = \begin{Bmatrix} u_{2N+II} \\ o \end{Bmatrix}$, in place of those for the fully adhesive case, with corresponding modifications to the stiffness equation of the Free Stack as before.

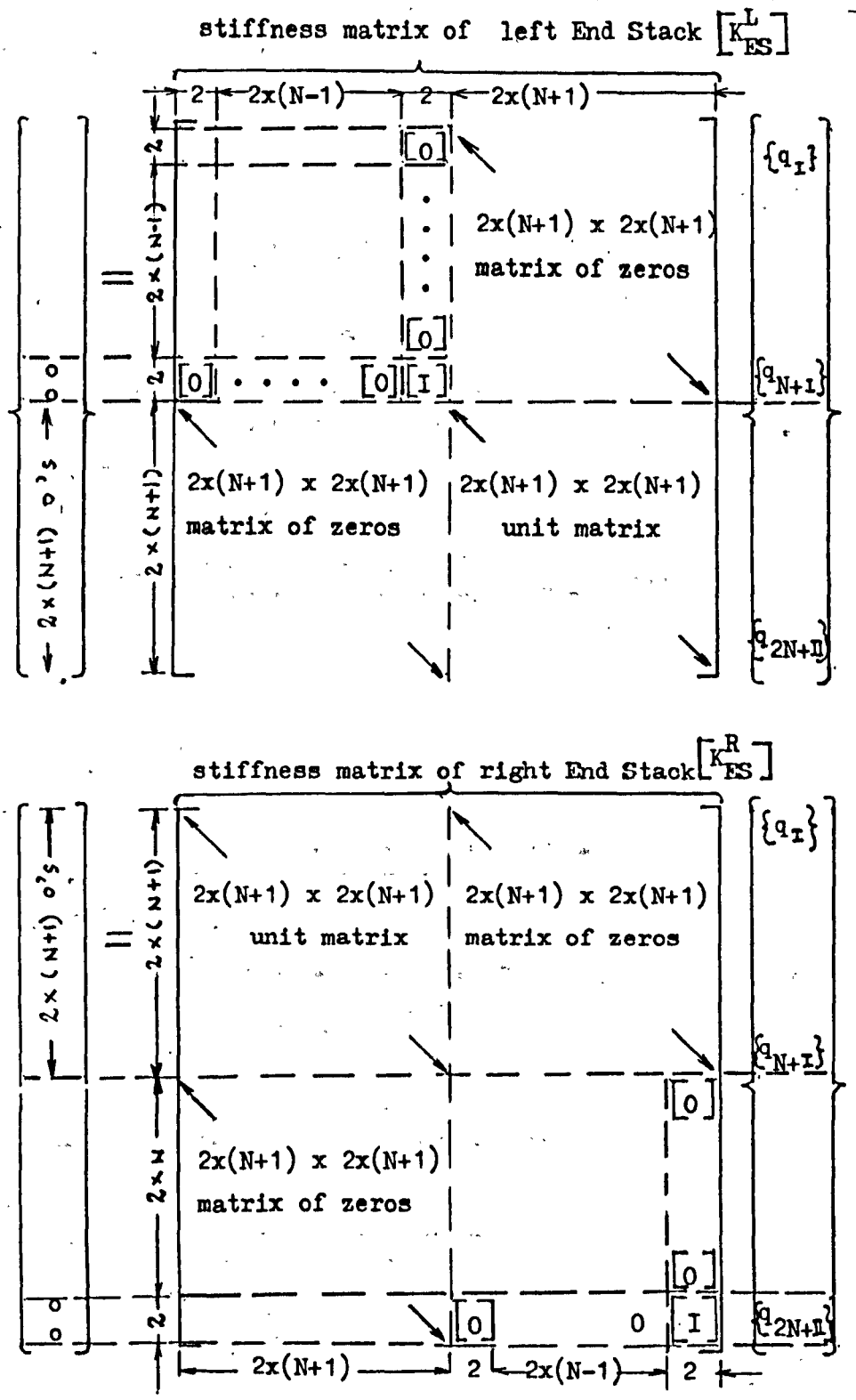

Fig. 11. Modifications to Eqn. 25 to obtain the stiffness equations of the End Stacks (note in Fig. 10 applicable)

1.2.5.2. Flow chart for computing $[K_s]$ (to be read in conjunction with Master Flow Chart in Appendix)

Block D10

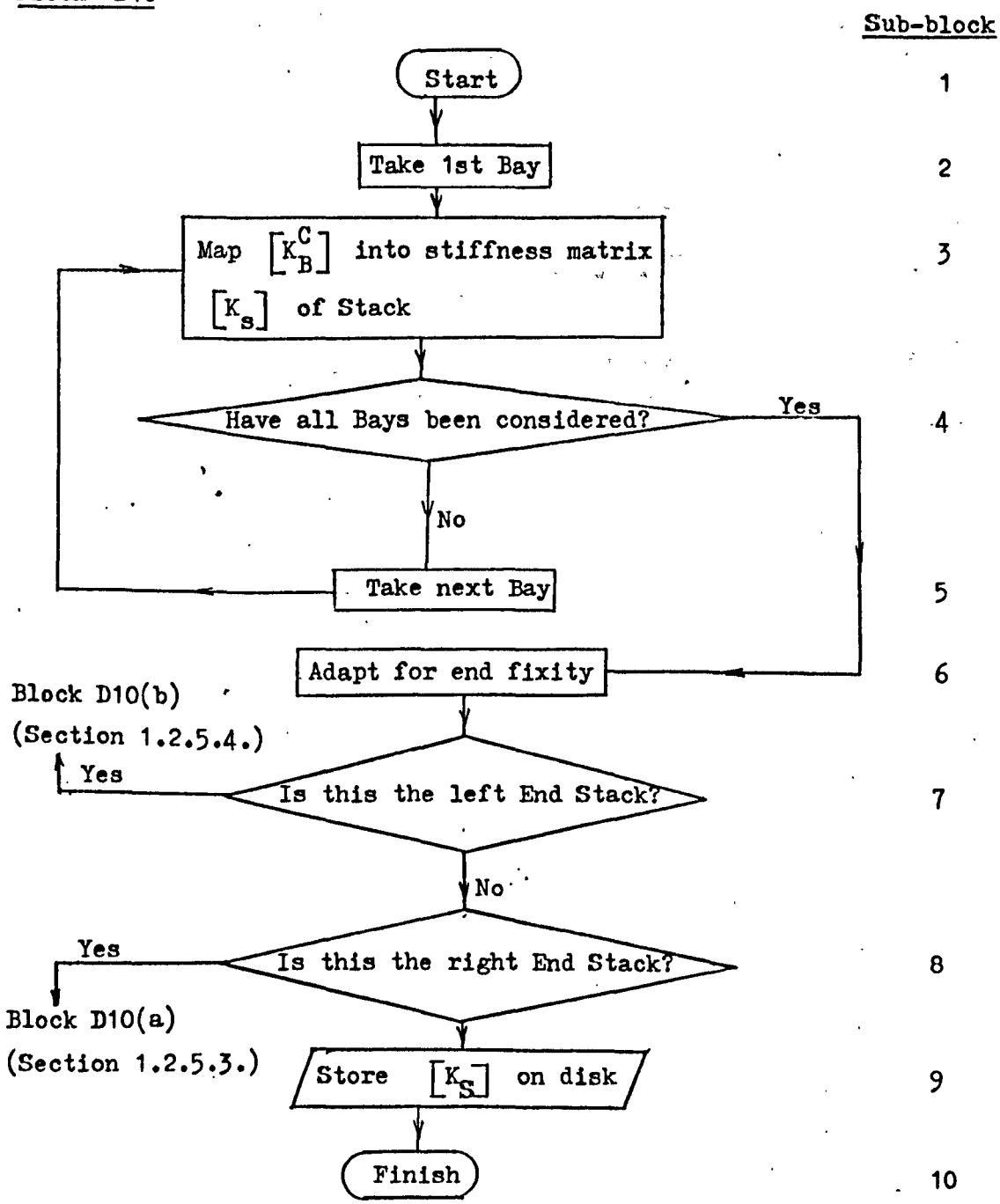

1.2.5.3. Flow chart for computing $\left[K_{ES}^{R}\right]$ (to be read in conjunction with Master Flow Chart in Appendix)

Block D10(a)

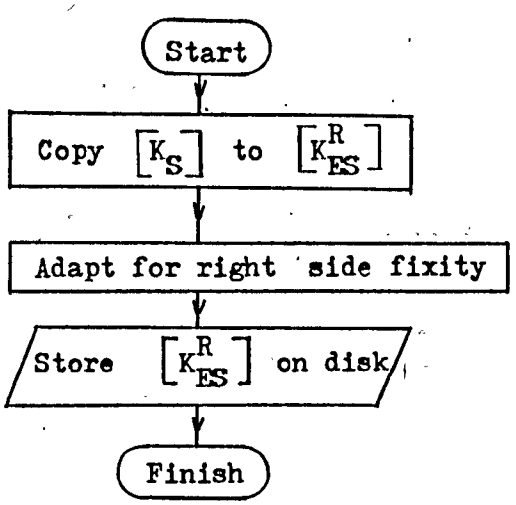

Sub-block

1
2
3
4
5

1.2.5.4. Flow chart for computing $\left[K_{ES}^{L}\right]$ (to be read in conjunction with Master Flow Chart in Appendix)

Block D10(b)

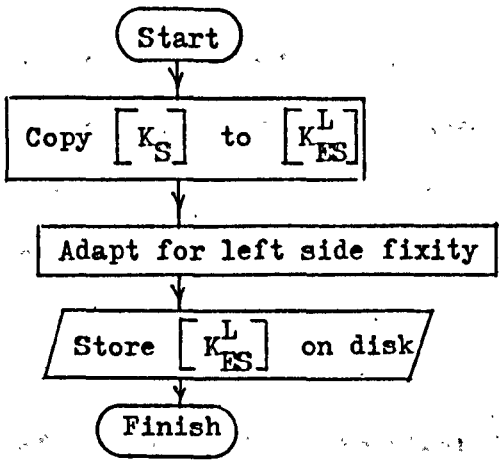

Sub-block	
1	
2	
3	
4	
5	

1.2.6. Solution of the displacement field, etc., for the model in Section 1.2. via "Stack Addition"

1.2.6.1. Theory - part 1

As shown in Fig. 12, the stiffness equation of the Stack may be subdivided into submatrices so that the result is analogous to the stiffness equation of a pin-ended structural member; thus, the Stack can be thought of as an equivalent member.

Notes: L refers to the left joint and R to the right joint; since a stiffness matrix is symmetric, $[K_{LR}] = [K_{RL}]^T$

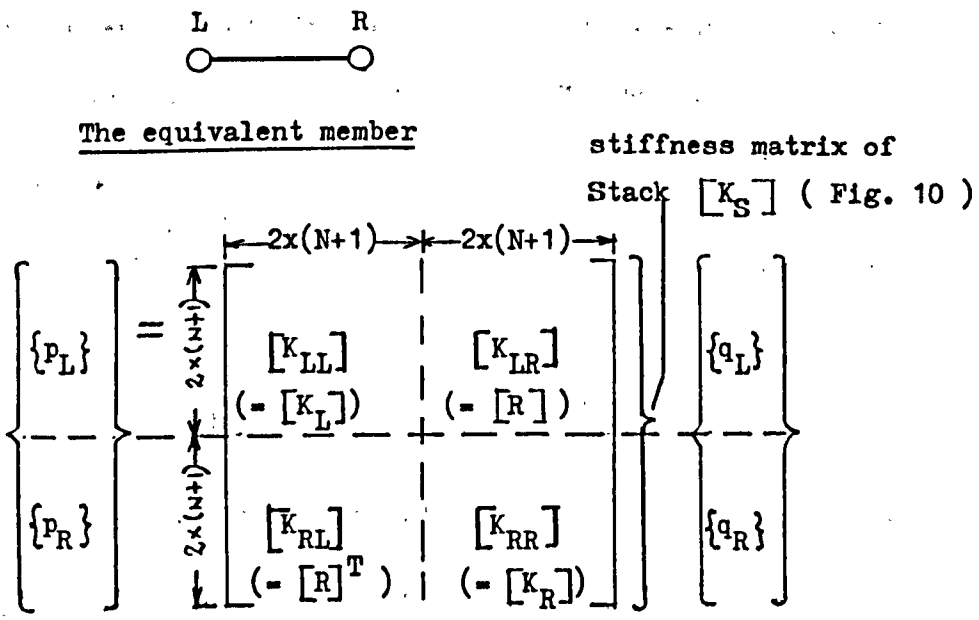

Fig. 12. Transformation of stiffness equation of Stack to that of equivalent member

By similar procedures, the stiffness equations of equivalent members for the End Stacks - see Fig. 11 - may be obtained.

The interconnection of Stacks and End Stacks (where applicable) leads to the formation of the assemblage of finite elements depicted in Fig. 1, and the procedure would be greatly simplified by considering the analogy to a linear assembly of their equivalent members - see Fig. 13. The following discussion is conducted in these "equivalent" terms.

Thus, for joint r to be in equilibrium (see equations in Fig. 13), $\{p_r\} = [R_{(r-1)}]^T\{q_{r-1}\} + [K_{R(r-1)}]\{q_r\} + [K_{L(r)}]\{q_r\} + [R_{(r)}]\{q_{r+1}\}$ .... (26) . Therefore, substituting r=0 into Eqn. 26, we have, for joint 0 ,

$\{p_0\} = [R_{(-1)}]^T\{q_{-1}\} + [K_{R(-1)}]\{q_0\} + [K_{L(0)}]\{q_0\} + [R_{(0)}]\{q_1\}$;

however, since member (-1) and joint -1 do not exist, we re-write,

$\{p_0\} = [K_{L(0)}]\{q_0\} + [R_{(0)}]\{q_1\}$, whereupon,

$\{q_0\} = [K_{L(0)}]^{-1}\,(\,\{p_0\} - [R_{(0)}]\{q_1\}\,)$ .... (27) .

Further, let $[K_{L(0)}]^{-1} = [F_{(0)}]$ .... (28),

$\{p_0\} = \{h_0\}$ .... (29) and

$-[F_{(0)}][R_{(0)}] = [T_{(1,0)}]$ .... (30) ;

substituting Eqns. 28. 29 and 30 into Eqn. 27, we have,

$\{q_0\} = [F_{(0)}]\{h_0\} + [T_{(1,0)}]\{q_1\}$ .... (31) .

Next, proceeding to joint 1 , we substitute r=1 in

$$\begin{Bmatrix} \{p_1\} \\ \{p_2\} \end{Bmatrix} = \begin{bmatrix} [K_{L(1)}] & [R_{(1)}] \\ [R_{(1)}]^T & [K_{R(1)}] \end{bmatrix} \begin{Bmatrix} \{q_1\} \\ \{q_2\} \end{Bmatrix} \qquad \begin{Bmatrix} \{p_{r-1}\} \\ \{p_r\} \end{Bmatrix} = \begin{bmatrix} [K_{L(r-1)}] & [R_{(r-1)}] \\ [R_{(r-1)}]^T & [K_{R(r-1)}] \end{bmatrix} \begin{Bmatrix} \{q_{r-1}\} \\ \{q_r\} \end{Bmatrix}$$

$$\begin{Bmatrix} \{p_0\} \\ \{p_1\} \end{Bmatrix} = \begin{bmatrix} [K_{L(0)}] & [R_{(0)}] \\ [R_{(0)}]^T & [K_{R(0)}] \end{bmatrix} \begin{Bmatrix} \{q_0\} \\ \{q_1\} \end{Bmatrix} \qquad \begin{Bmatrix} \{p_r\} \\ \{p_{r+1}\} \end{Bmatrix} = \begin{bmatrix} [K_{L(r)}] & [R_{(r)}] \\ [R_{(r)}]^T & [K_{R(r)}] \end{bmatrix} \begin{Bmatrix} \{q_r\} \\ \{q_{r+1}\} \end{Bmatrix}$$

$$\begin{Bmatrix} \{p_{n-2}\} \\ \{p_{n-1}\} \end{Bmatrix} = \begin{bmatrix} [K_{L(n-2)}] & [R_{(n-2)}] \\ [R_{(n-2)}]^T & [K_{R(n-2)}] \end{bmatrix} \begin{Bmatrix} \{q_{n-2}\} \\ \{q_{n-1}\} \end{Bmatrix} \qquad \begin{Bmatrix} \{p_{n-1}\} \\ \{p_n\} \end{Bmatrix} = \begin{bmatrix} [K_{L(n-1)}] & [R_{(n-1)}] \\ [R_{(n-1)}]^T & [K_{R(n-1)}] \end{bmatrix} \begin{Bmatrix} \{q_{n-1}\} \\ \{q_n\} \end{Bmatrix}$$

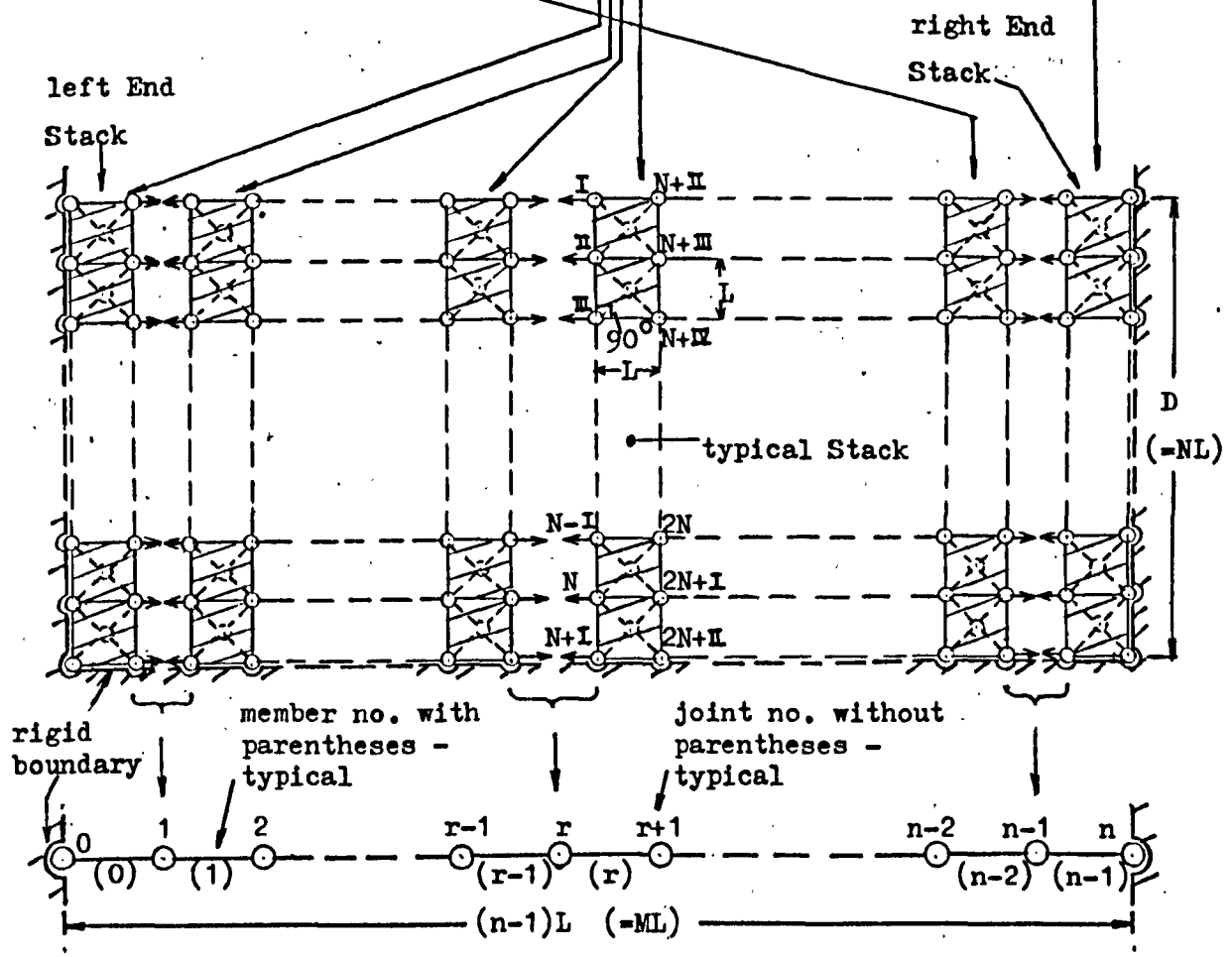

Fig. 13. "Stack Addition" as linear assembly of equivalent members

Eqn. 26, giving,

$$\{p_1\} = [R_{(0)}]^T \{q_0\} + [K_{R(0)}]\{q_1\} + [K_{L(1)}]\{q_1\} + [R_{(1)}]\{q_2\} \quad .$$

Substituting Eqn. 31 into the above, we have,

$$\{p_1\} = [R_{(0)}]^T ([F_{(0)}]\{h_0\} + [T_{(1,0)}]\{q_1\}) + ([K_{L(1)}] + [K_{R(0)}])\{q_1\}$$

$$+ [R_{(1)}]\{q_2\} = ([K_{L(1)}] + [K_{R(0)}] + [R_{(0)}]^T [T_{(1,0)}]) \{q_1\} -$$

$$[T_{(1,0)}]^T \{h_0\} + [R_{(1)}]\{q_2\} \quad (\text{since } [F_{(0)}] \text{ is a symmetric matrix });$$

re-arranging, we have,

$$\{q_1\} = [F_{(1)}] (\{p_1\} + [T_{(1,0)}]^T \{h_0\}) - [F_{(1)}][R_{(1)}]\{q_2\} \quad (\text{where}$$

$$[F_{(1)}] = ([K_{L(1)}] + [K_{R(0)}] + [R_{(0)}]^T [T_{(1,0)}])^{-1} \quad \ldots\ldots (32) \quad)$$

$$= [F_{(1)}]\{h_1\} + [T_{(2,1)}]\{q_2\} \quad \ldots\ldots (33), \text{ where}$$

$$\{h_1\} = \{p_1\} + [T_{(1,0)}]^T \{h_0\} \quad \ldots\ldots (34), \text{ and}$$

$$[T_{(2,1)}] = - [F_{(1)}] [R_{(1)}] \quad \ldots\ldots (35) .$$

Similarly, for joint 2 , r=2 in Eqn. 26, giving,

$$\{p_2\} = [R_{(1)}]^T \{q_1\} + [K_{R(1)}] \{q_2\} + [K_{L(2)}]\{q_2\} + [R_{(2)}]\{q_3\} \quad ,$$

which is of the same form as that for joint 1 ; thus, by analogy,

$$\{q_2\} = [F_{(2)}] \{h_2\} + [T_{(3,2)}] \{q_3\} \quad \ldots\ldots (36), \text{ where}$$

$$[F_{(2)}] = ([K_{L(2)}] + [K_{R(1)}] + [R_{(1)}]^T [T_{(2,1)}])^{-1} \quad \ldots\ldots (37),$$

$$\{h_2\} = \{p_2\} + [T_{(2,1)}]^T \{h_1\} \quad \ldots\ldots (38), \text{ and}$$

$$[T_{(3,2)}] = - [F_{(2)}] [R_{(2)}] \quad \ldots\ldots (39) .$$

By inductive reasoning, the following expressions may now be deduced for a general joint r:-

$$\{q_r\} = [F_{(r)}]\{h_r\} + [T_{(r+1,r)}]\{q_{r+1}\} \quad \ldots\ldots (40), \text{ where}$$

$$[F_{(r)}] = ([K_{L(r)}] + [K_{R(r-1)}] + [R_{(r-1)}]^T [T_{(r,r-1)}])^{-1} \quad \ldots\ldots (41),$$

$$\{h_r\} = \{p_r\} + [T_{(r,r-1)}]^T \{h_{r-1}\} \quad \ldots\ldots (42), \text{ and}$$

$$[T_{(r+1,r)}] = -[F_{(r)}][R_{(r)}] \quad \ldots\ldots (43).$$

The stage is thus set for solution by computation (bearing in mind that the $[K_L]$, $[K_R]$ and $[R]$ matrices from the stiffness equations of the equivalent members - see Fig. 13 -- have already been determined as a result of Stack assembly) as follows:-

Starting with joint 0, we have, $[F_{(0)}] = [K_{L(0)}]^{-1}$ (Eqn. 28) and hence, $[T_{(1,0)}]$ may be computed using Eqn. 30.

A comparison of the stiffness equation of equivalent member (0) (Fig. 13) with Fig. 11 shows that $\{p_0\} = \{0\}$ where $\{0\}$ is a $2x(N+1)$th order vector of zeros. Thus, $\{h_0\} = \{0\}$ (Eqn. 29).

Next, by substituting the value of $[T_{(1,0)}]$ into Eqn. 32, $[F_{(1)}]$ may be computed for joint 1 and, following, $[T_{(2,1)}]$ obtained (Eqn. 35).

For the uniform strip load idealisation illustrated in Fig. 1, with which we are concerned, it is obvious that $\{p_1\}$ is simply a $2x(N+1)$th

order vector of zeros as no loading is applied to any one of the line of joints that constitute joint 1 .

Thus $\{h_1\} = \{0\}$ (Eqn. 34).

The procedure for joint 1 is subsequently repeated for successive joints until joint α is reached - see Fig. 1 - when the finite element idealisation of the uniform strip load requires that a concentrated load, $-tL/2$, in the y-direction, be applied to the surface joint of the line of joints that constitute joint α (see pg. 23). Therefore, $\{p_\alpha\} =$

$$\begin{bmatrix} 0 \\ \frac{-tL}{2} \\ 0 \\ \vdots \\ 0 \end{bmatrix} \quad 2\times(N+1)$$

(all zeros between)

and hence, substituting $r=\alpha$ in Eqn. 42, we have - since $\{h_{\alpha-1}\} = \{0\}$ as before, $\{h_\alpha\} = \{p_\alpha\} \cdot [F_{(\alpha)}]$ and hence, $[T_{(\alpha+1,\alpha)}]$ are computed in the usual manner using Eqns. 41 and 43, respectively.

For the next joint, $\alpha+1$, $\{p_{\alpha+1}\} =$

$$\begin{bmatrix} 0 \\ -tL \\ 0 \\ \vdots \\ 0 \end{bmatrix} \quad 2\times(N+1)$$

(all zeros between) by similar reasoning to that for joint α , and $\{h_{\alpha+1}\}$ may then be computed using Eqn. 42 with $r=\alpha+1$. $[F_{(\alpha+1)}]$ and $[T_{(\alpha+2,\alpha+1)}]$ are again computed in the usual way.

Similar procedures then apply to successive joints except that at joint β , $\{p_\beta\} = \{p_\alpha\}$, when the end of the loaded area is reached,

and for subsequent joints ($\beta+1$ to $n-1$ - see Figs. 1 and 13), $\{p_r\} = \{0\}$, as prior to reaching the loaded area.

At joint $n-1$, since $\{q_n\} = \{0\}$ due to complete fixture of the line of joints to the rigid boundary, we have, from Eqn. 40, and substituting $r=n-1$, $\{q_{n-1}\} = [F_{(n-1)}]\{h_{n-1}\}$ which is readily determined when $[F_{(n-1)}]$ and $\{h_{n-1}\}$ have been obtained in the usual way.

It is now possible to determine the displacements of the remaining joints in successive lines backwards using Eqn. 40 and suubstituting r for the relevant joint number, the $[F_{(r)}]$, $\{h_r\}$ and $[T_{(r+1,r)}]$ matrices having already been computed in the forward assembly. A useful check to $[T_{(1,0)}]$ is that $\{q_0\}$ should be equal to $\{0\}$.

The way in which the displacement field is solved, a line of joints at a time, obviates the necessity of inverting the stiffness matrix of the whole assemblage, thus enabling a large number of finite elements to be used to improve the accuracy of solution using only moderate resources.

1.2.6.2. Flow chart for computing $[F_{(r)}]$ (to be read in conjunction with Master Flow Chart in Appendix)

Block D13

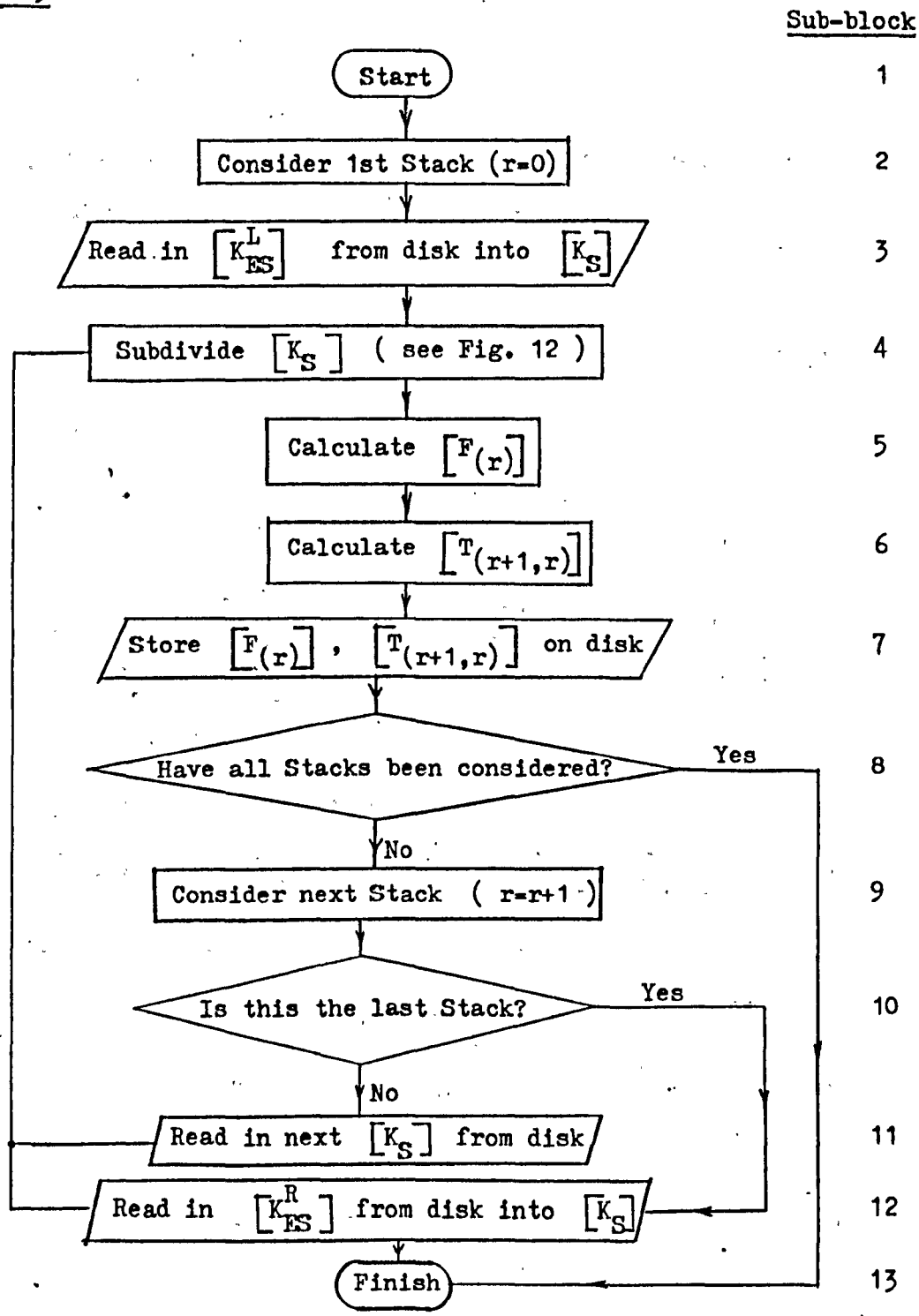

1.2.6.3. Flow chart for computing $[T_{(r+1,r)}]$ (to be read in conjunction with Master Flow Chart in Appendix)

- The flow chart is incorporated in that of Section 1.2.6.2. -

1.2.6.4. Flow chart for computing $\{h_r\}$ (to be read in conjunction with Master Flow Chart in Appendix)

Block F2

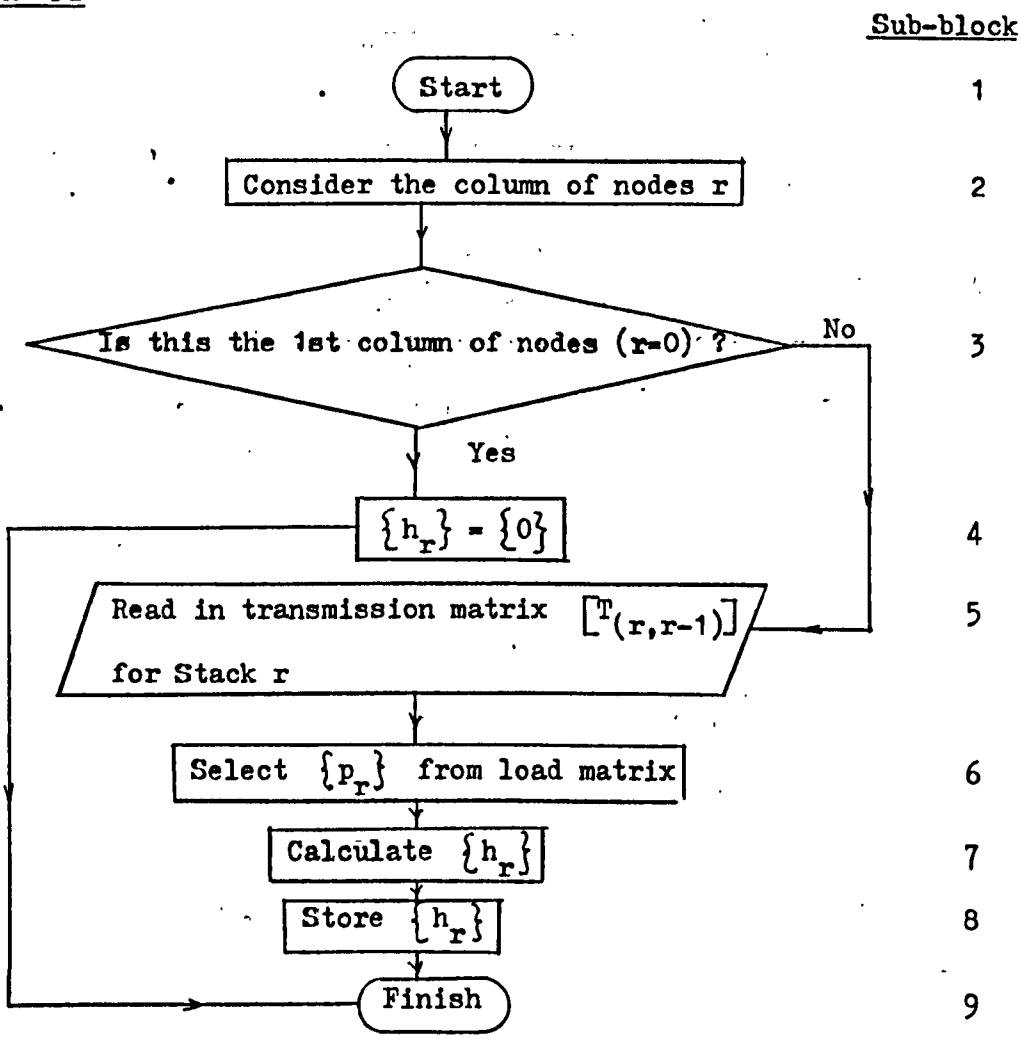

1.2.6.5. Flow chart for computing $\{q_r\}$ (to be read in conjunction with Master Flow Chart in Appendix)

Block F7

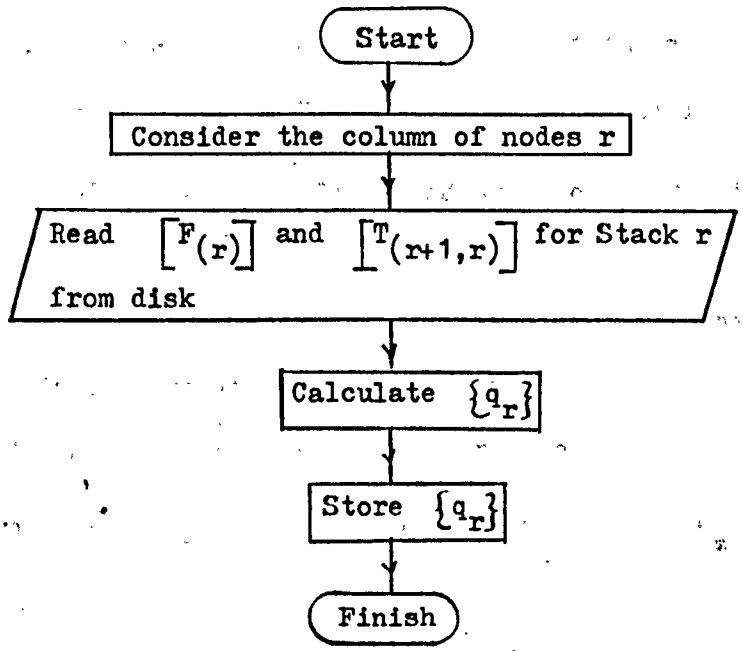

1.2.6.6. Theory - part 2

Having, by now, effectively obtained the values of the displacements of every Stack in the assemblage, the solution is completed by considering successively more basic components of it.

Thus, for the Bay, the displacements of the middle joint e (Fig. 5) may be computed using Eqn. 22 ; the load vector for joint e $\{p_e\}$ = $\{0\}$ for this case of surface loading, where $\{0\}$ is a second order vector of zeros.

Finally, for the individual finite elements whose corner joint displacements are now known, equations such as (3) , (5) and (6) (pg. 18) give the displacement, strain and stress values (e.g., $\{\bar{u}\}$, $\{\gamma\}$ and $\{\sigma\}$, respectively - σ_z and ε_z are given by Eqns. 8 and 9) .

Note, however, that for this model, the incompressible condition $\nu = \frac{1}{2}$ is untenable because it leads to an infinite denominator for the terms of the elasticity matrix (pg. 17) . Herrman (11) presented a method for dealing with incompressibility; however, for present purposes, $\nu = 0{\cdot}49999$ is an adequate alternative.

1.2.6.7. Flow chart for computing $\{q_e\}$, $\{\gamma\}$, $\{\sigma\}$ and σ_z (to be read in conjunction with Master Flow Chart in Appendix)

- similar procedure for all elements

Note: ξ_z set to zero (Eqn. 9)

Block F9

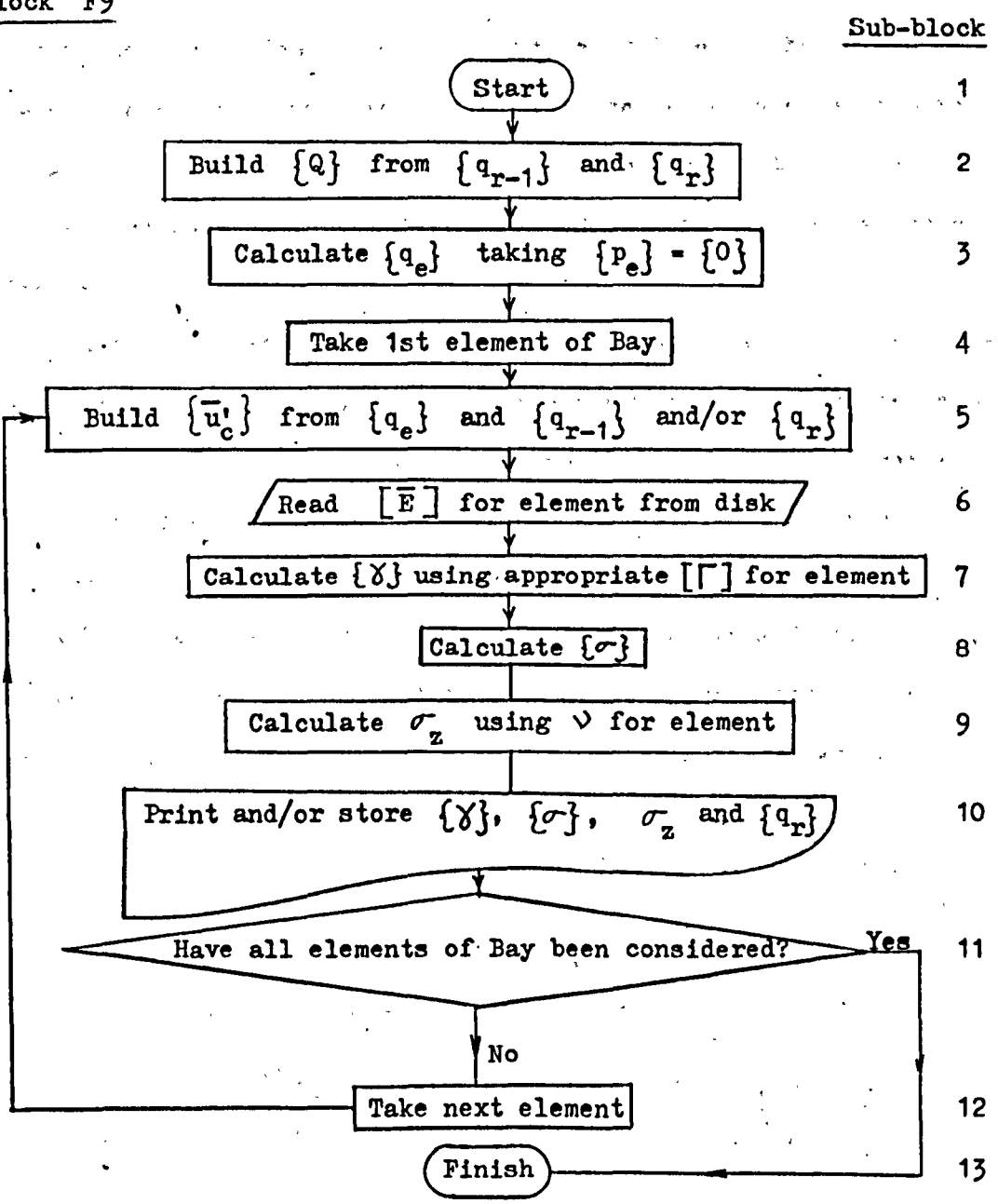

1.2.7. Adaptations to the general elastic model (Fig. 1) to evolve several elastic models of lesser degrees of inhomogeneity and to deal with linear varying strip loading

Since the only difference between the general elastic model and others of lesser degrees of inhomogeneity is in specifying the E and values of the individual finite elements, it suffices to replace the routine for random E and ν value generation to the relevant alternative routine that specifies how these values are distributed throughout the assemblage. The following flow charts therefore replace the "random" routine in the Master Flow Chart for the special cases indicated.

In the case of a linear varying strip load, Fig. 14 illustrates the two distributions studied. By referring to the derivation in pg. 23 for the uniform load, it can be shown that when T(s) varies linearly from zero to some value when s=1, i.e. a triangular distribution, the point loads at the joints when s=0 and when s=1 will be in the ratio 1:2 . For a parallelogram type distribution, the results of the uniform and triangular pressure distribution component parts are superposed since the material is linear elastic.

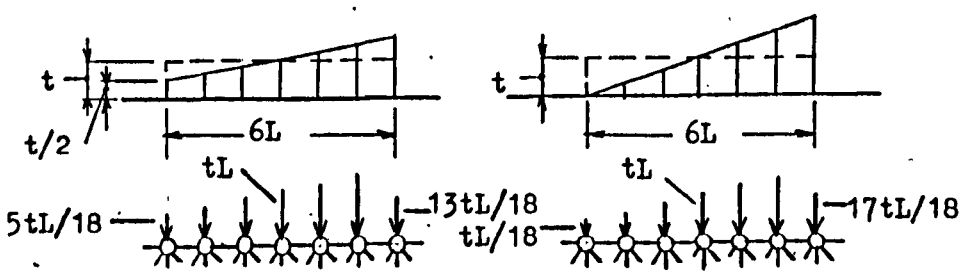

Fig. 14. Linear varying strip loads and their equivalent point loads

1.2.7.1. Adaptations to flow chart for general elastic model to obtain homogeneous model (to be read in conjunction with Master Flow Chart in Appendix - as for all other adaptations below)

Block	Adaptations
B1	Initialise ν of elements to a constant value
C1	Initialise E of elements to constant value

1.2.7.2. Adaptations to flow chart for general elastic model to obtain random E, ν constant model

Block	Adaptations
B1	Initialise ν of elements to a constant value

1.2.7.3. Adaptations to flow chart for general elastic model for inhomogeneity of E about centre of strip

Block	Adaptations
B1	Initialise ν of elements to a constant value
C1	Initialise E's of elements on either side of centre-line

1.2.7.4. Adaptations to flow chart for general elastic model for linear varying strip loading

Block	Adaptations
B1	Initialise ν of elements to a constant value
C1	Initialise E of elements to a constant value
E1	Set up load vectors of all columns of nodes for linear varying strip load, and store

1.2.7.5. Adaptations to flow chart for general elastic model for linear varying E with depth

Block	Adaptations
B1	Initialise ν of elements to a constant value
C1	Initialise linear varying E's with depth

1.2.7.6. Adaptations to flow chart of Section 1.2.7.5. for stiff crust problem

Block	Adaptations
C1	Initialise linear varying E's with depth but with stiff crust

1.2.7.7. Adaptations to flow chart for general elastic model for underlying soft layer problem

Block	Adaptations
B1	Initialise ν of elements to a constant value
C1	Initialise linear varying E's with depth with underlying soft layer

1.2.8. Modifications to general elastic model for rectangular Bays

It was mentioned in pg. 9 that rectangular Bays are required in order to keep the rigid boundaries of the elastic model sufficiently remote.

This is illustrated in Fig. 15 below for three such types of assemblages that are used in Chapter 2.

The preceding flow charts have been kept general so that rectangular Bays can be incorporated in the given procedures.

Concerning the outlined theory, the following modifications to two points are required:-

(i) The Bay geometry depicted in Fig. 1 is revised to those in Fig. 15 so that the dimensions of the triangular finite element in Fig. 2 are then $L_1/2$ and $L_2/2$ in place of $L/2$; thus, the area of the element A_E (pg. 17) becomes $L_1L_2 / 4$.

(ii) The stiffness matrices of the other component elements of the Bay have to be computed via the coordinates of the joints as for the basic element; i.e. the concept of rotational transformation (Fig. 5) is no longer valid.

Otherwise, the theory for the square Bays applies equally to rectangular Bays.

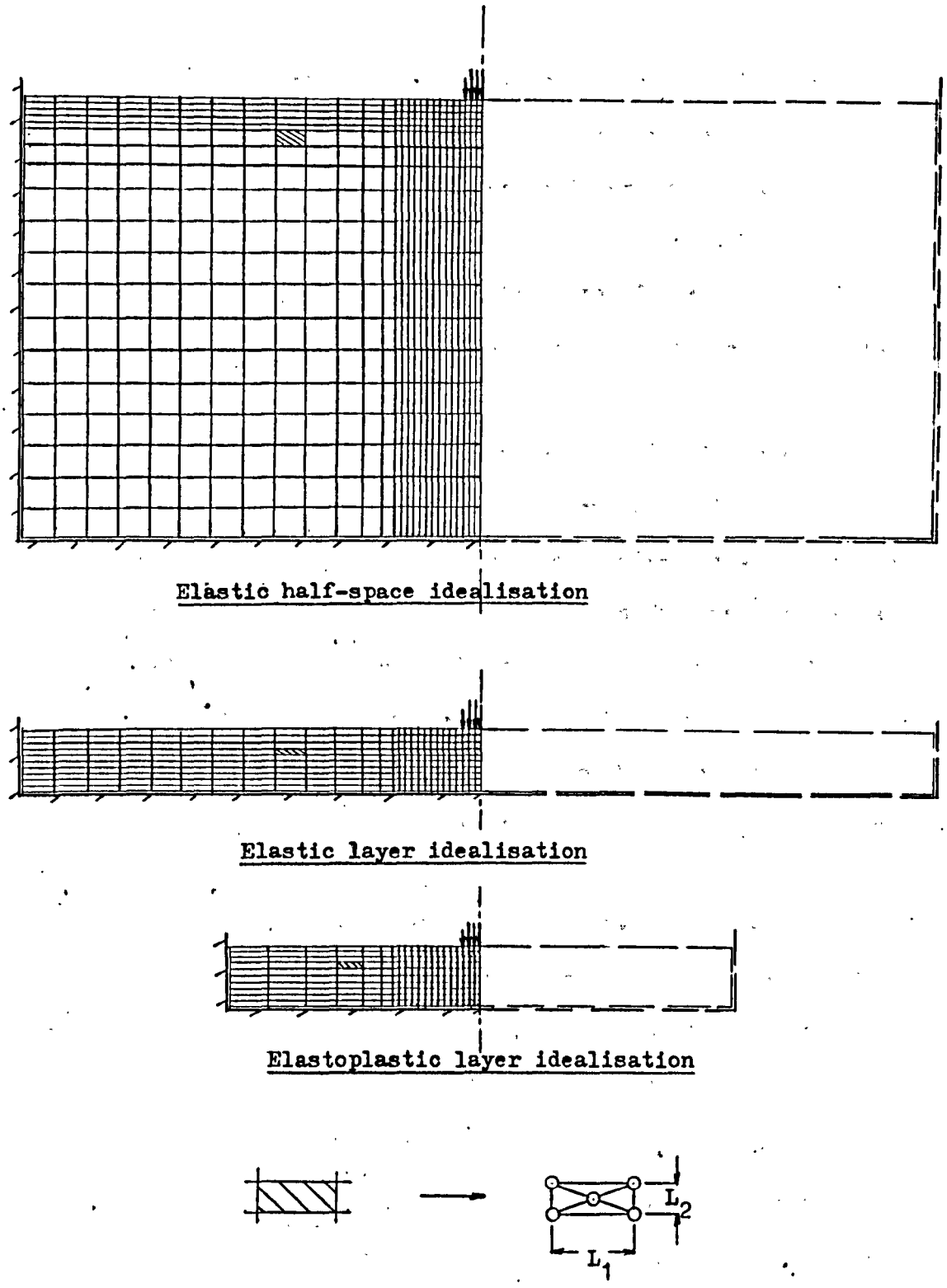

Fig. 15. Three assemblages used in the models of Chapter 2

1.3. The linear elastic, linear work hardening plastic (Tresca) model for uniform strip loading on the surface of an isotropic, random inhomogeneous half-space or layer overlying a rigid base

The present model retains the features of the general elastic model of Section 1.2., with the added facility for simulating plastic flow at yield.

Thus, a finite element is linear elastic until first yield. Additional loading causes linear work hardening as plastic flow occurs. Any unloading is accompanied by elastic strain recovery with further plastic flow after the last yield condition is attained on re-loading.

The elastic properties of the model have a random distribution as before and its strength is also random inhomogeneous. The degree of work hardening is assumed to be constant for all elements.

Fig. 16 illustrates the differences between this and the previous elastic model.

Several distinct categories of materials can be defined as plastic by virtue of certain well-known basic characteristics that they hold in common (12) ; some properties that distinguish the material under consideration may be stated as follows:-

The material satisfies the stability postulate formulated by Drucker (13) for which (i) the plastic strain increment vector is normal to the yield surface, and (ii) the yield surface is convex.

Condition (i) in turn implies the coincidence of the plastic

potential with the yield surface so that the plastic flow rule is associated with, or derivable from the yield conditions. Thus, the elastic phase of the material acts independently of the plastic phase.

The Tresca yield criterion is adopted and the material is assumed to work harden isotropically so that the shape of the yield surface does not alter during hardening.

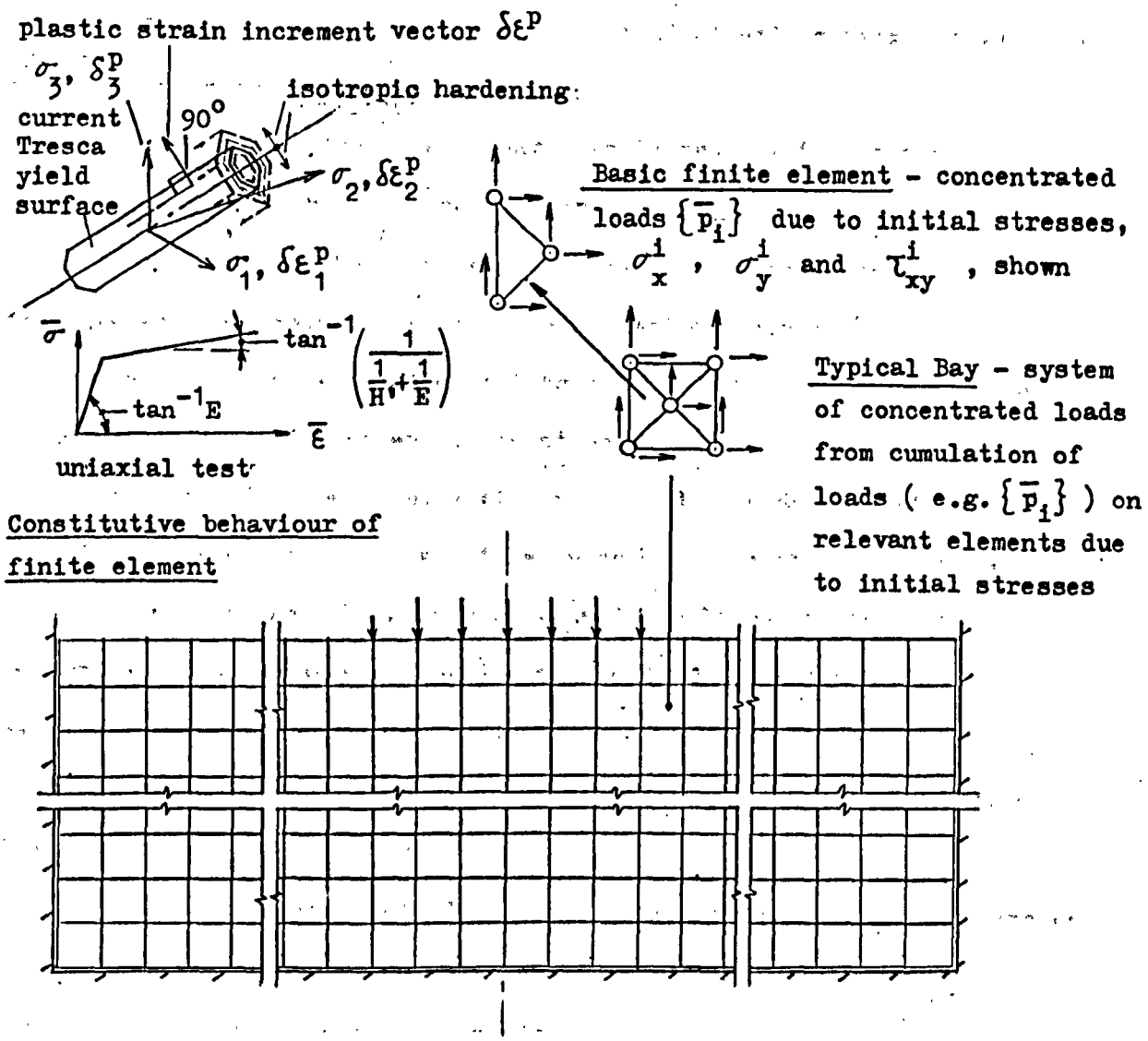

Fig. 16. Additions to the elastic model of Fig. 1 for the general elastoplastic model

To simulate plastic flow, the Initial Stress Method of Zienkiewicz et al. (8) is adopted; initial stresses are added to the elastic model in Fig. 1 so that the prescribed elastoplastic behaviour is adhered to at all times.

The method has several advantages over others that has led to its adoption.

Two main categories of numerical methods for dealing with elastoplastic as well as other non-linear constitutive behaviour have been developed under the headings of constant elastic matrix and variable elastic matrix processes (14) .

In the former, the same linear elastic problem is repeatedly solved; in the latter, different linear elastic problems are solved each time. In both cases, the solutions are modified by adjustments either to the stresses or strains to satisfy constitutive behaviour.

The Initial Stress Method belongs to the first category and the stresses are corrected at every iteration.

The method has been successfully applied to elastoplastic materials of differing yield criteria and flow rules (15) ; thus, for instance, stresses, strains and the growth of plastic enclaves are readily determined at all stages of loading and loading and unloading paths as well as varying degrees of hardening are simply dealt with. An advantage of the method is that the yield criterion is satisfied at all iterations.

The Initial Strain Method (also of first category but with strains corrected) is unable to deal with small degrees of hardening and is thus unsuitable for the present study.

Zienkiewicz et al. (8) presented a comparison between a variable elastic matrix method and the Initial Stress Method and showed the latter to be more stable and has better convergence. Smith (3) arrived at the same conclusion although Havner (16) showed there was little difference between them, in the example given.

Zienkiewicz et al. also showed that the Initial Stress Method is relatively insensitive to the magnitude of load increments; the conclusion drawn is that there is, as found by several authors in theoretical plasticity, little difference between an incremental and a deformation plasticity approach. On the other hand, a large load increment led to meaningless results in the variable elastic matrix method.

Recently, other numerical techniques have evolved. Smith (17) presented a procedure combining the above two categories. He also used an initial strain, followed by an "accelerated" initial stress procedure (3) as the optimum for solving the expanding cylinder problem, for Cam Clay.

The following sections present (i) the particular elastoplastic relations for the Tresca material in plane strain, in the form required by the Initial Stress Method, then (ii) the Initial Stress Method, whereby the general elastic model of Section 1.2. is adapted, via the application of initial stresses, to satisfy the elastoplastic model shown in Fig. 16.

A flow chart provides a detailed account of the Initial Stress Method, and the adaptations required for strength inhomogeneity of

varying degrees also shown.

Finally, a procedure for dealing with varying degrees of work hardening, as plastic flow occurs, is introduced. The procedure is also applicable to work softening.

By selecting the appropriate flow charts from Section 1.2. and this section, the required degree of inhomogeneity of both elastic and plastic phases of the assemblage as well as type of loading may be prescribed.

A working knowledge of the basic ideas of the theory of plasticity is assumed in the following account.

1.3.1. The elastoplastic stress increment / total strain increment relations for a Tresca material in plane strain

For generality, the elastoplastic stress increment / total strain increment relations are developed for a general yield surface in three-dimensional stress analysis, the departure to the particular case of the Tresca material in plane strain made at the appropriate stages.

Thus, consider the yield surface, $F(\{\bar{\sigma}\}, \kappa) = 0$ .... (44), in a six-dimensional hyperspace of stress, in three-dimensional stress analysis, where $\{\bar{\sigma}\} = \begin{Bmatrix} \sigma_x \\ \sigma_y \\ \sigma_z \\ \tau_{xy} \\ \tau_{yz} \\ \tau_{zx} \end{Bmatrix}$, and κ is the hardening (isotropic) parameter whose current value determines the position of the yield surface.

At any point in a body of elastoplastic material whose state of stress lies on this surface, the application of infinitesimal stress increments, $\delta\{\bar{\sigma}\}$ $\left(= \begin{Bmatrix} \delta\sigma_x \\ \delta\sigma_y \\ \delta\sigma_z \\ \delta\tau_{xy} \\ \delta\tau_{yz} \\ \delta\tau_{zx} \end{Bmatrix} \right)$, will lead to the corresponding infinitesimal total strain increments, $\delta\{\bar{\varepsilon}\}_t$ $\left(= \begin{Bmatrix} \delta\varepsilon_{x_t} \\ \delta\varepsilon_{y_t} \\ \delta\varepsilon_{z_t} \\ \delta\gamma_{xy_t} \\ \delta\gamma_{yz_t} \\ \delta\gamma_{zx} \end{Bmatrix} \right)$, that comprise the

two distinct components, namely, the elastic strain increments, $\delta\{\bar{\varepsilon}\}_e$ ($= \begin{Bmatrix} \delta\varepsilon_{x_e} \\ \delta\varepsilon_{y_e} \\ \delta\varepsilon_{z_e} \\ \delta\gamma_{xy_e} \\ \delta\gamma_{yz_e} \\ \delta\gamma_{zx} \end{Bmatrix}$), and the plastic strain increments, $\delta\{\bar{\varepsilon}\}_p$ ($= \begin{Bmatrix} \delta\varepsilon_{x_p} \\ \delta\varepsilon_{y_p} \\ \delta\varepsilon_{z_p} \\ \delta\gamma_{xy_p} \\ \delta\gamma_{yz_p} \\ \delta\gamma_{zx_p} \end{Bmatrix}$);

i.e., $\delta\{\bar{\varepsilon}\}_t = \delta\{\bar{\varepsilon}\}_e + \delta\{\bar{\varepsilon}\}_p$.

Since $\delta\{\bar{\varepsilon}\}_e = [D]^{-1}\,\delta\{\bar{\sigma}\}$, where $[D]$ is the elasticity matrix in three-dimensional stress analysis

$$\left(= \frac{E(1-\nu)}{(1+\nu)(1-2\nu)} \begin{bmatrix} 1 & \nu/1-\nu & \nu/1-\nu & 0 & 0 & 0 \\ & 1 & \nu/1-\nu & 0 & 0 & 0 \\ & & 1 & 0 & 0 & 0 \\ & & & \frac{1-2\nu}{2(1-\nu)} & 0 & 0 \\ & \text{- symmetric -} & & & \frac{1-2\nu}{2(1-\nu)} & 0 \\ & & & & & \frac{1-2\nu}{2(1-\nu)} \end{bmatrix} \right),$$

and $\delta\{\bar{\varepsilon}\}_p = \lambda\left\{\frac{\partial F}{\partial\{\bar{\sigma}\}}\right\}$, according to the flow rule (8) - where λ is a proportionality constant, we have, on substituting,

$$\delta\{\bar{\varepsilon}\}_t = [D]^{-1}\,\delta\{\bar{\sigma}\} + \lambda\left\{\frac{\partial F}{\partial\{\bar{\sigma}\}}\right\} \quad \ldots\ldots (45).$$

The expressions, λ and $\left\{\frac{\partial F}{\partial\{\bar{\sigma}\}}\right\}$ have thus yet to be determined to obtain explicit relations between the respective stress and total strain increments.

λ is conveniently considered in terms of a related variable A ; this is determined as follows: for a small change in the yield surface, Eqn. 44 may be differentiated to give $\frac{\partial F}{\partial \sigma_x}\delta\sigma_x + \frac{\partial F}{\partial \sigma_y}\delta\sigma_y +$

$\frac{\partial F}{\partial \sigma_z}\delta\sigma_z + \frac{\partial F}{\partial \tau_{xy}}\delta\tau_{xy} + \frac{\partial F}{\partial \tau_{yz}}\delta\tau_{yz} + \frac{\partial F}{\partial \tau_{zx}}\delta\tau_{zx} + \frac{\partial F}{\partial \kappa}\delta\kappa = 0$;

i.e., $\left\{\frac{\partial F}{\partial \{\bar{\sigma}\}}\right\}^T \delta\{\bar{\sigma}\} + A\lambda = 0$ .... (46) where $A = \frac{\partial F}{\partial \kappa} \cdot \frac{\delta\kappa}{\lambda}$.

For a work hardening material, the associated change in plastic work done $\delta\kappa = \sigma_x \delta\varepsilon_x^p + \sigma_y \delta\varepsilon_y^p + \sigma_z \delta\varepsilon_z^p + \tau_{xy}\delta\gamma_{xy}^p +$

$\tau_{yz}\delta\gamma_{yz}^p + \tau_{zx}\delta\gamma_{zx}^p$; i.e., substituting the flow rule, we have,

$$\delta\kappa = \{\bar{\sigma}\}^T \lambda \left\{\frac{\partial F}{\partial \{\bar{\sigma}\}}\right\} .$$

Therefore, substituting for $\delta\kappa$, we have, finally,

$A = \frac{\partial F}{\partial \kappa} \{\bar{\sigma}\}^T \left\{\frac{\partial F}{\partial \{\bar{\sigma}\}}\right\}$ .... (47) which is a determinate form since an explicit relationship between A and $\frac{\partial F}{\partial \kappa}$ can be obtained via the uniaxial test.

For a Tresca material, we may write

$F = (\sigma_1 - \sigma_3) - \bar{\sigma}$ .... (48) (18), where $\bar{\sigma}$ ($= \bar{\sigma}(\kappa)$ - see Eqn. 44) is the uniaxial stress at yield, and σ_1 and σ_3 the major

and minor principal stresses, respectively.

Thus, by differentiation, we have, $\frac{\partial F}{\partial \sigma_1} = 1$ and $\frac{\partial F}{\partial \sigma_2} = 0$

(σ_2 being the intermediate principal stress) and $\frac{\partial F}{\partial \sigma_3} = -1$;

confining the following discussion to the principal stress system, the validity of Eqn. 47 is unaffected by writing, $\left\{\frac{\partial F}{\partial \{\bar{\sigma}\}}\right\} = \begin{Bmatrix} \partial F/\partial \sigma_1 \\ \partial F/\partial \sigma_2 \\ \partial F/\partial \sigma_3 \end{Bmatrix}$

$= \begin{Bmatrix} 1 \\ 0 \\ -1 \end{Bmatrix}$, provided $\{\bar{\sigma}\}$ is, correspondingly, $\begin{Bmatrix} \sigma_1 \\ \sigma_2 \\ \sigma_3 \end{Bmatrix}$.

Thus, the value of $\{\bar{\sigma}\}^T \left\{\frac{\partial F}{\partial \{\bar{\sigma}\}}\right\}$ in Eqn. 47 becomes

$\{\sigma_1 \quad \sigma_2 \quad \sigma_3\} \begin{Bmatrix} 1 \\ 0 \\ -1 \end{Bmatrix} = \bar{\sigma}$, since the material is initially at yield (see Eqn. 46) and, by comparing Eqns. 44 and 48, $\sigma_1 - \sigma_3 = \bar{\sigma}$.

Consider next a uniaxial test performed on a specimen of the material at yield, under stress $\bar{\sigma}$; an infinitesimal stress increase leads to a corresponding plastic strain increment, $\delta \bar{\varepsilon}^p$, so that the plastic work done in the interval, $\delta K = \bar{\sigma}\, \delta \bar{\varepsilon}^p$.

Thus, $\frac{\delta \bar{\varepsilon}^p}{\delta K}_{(\delta K \to 0)} = \frac{d \bar{\varepsilon}^p}{dK} = \frac{1}{\bar{\sigma}}$ since $\bar{\sigma} = \bar{\sigma}(K)$

(Eqn. 48), and therefore, from the above, $\bar{\varepsilon}^p = \bar{\varepsilon}^p(K)$.

By differentiating Eqn. 48, we obtain, $\frac{\partial F}{\partial \bar{\sigma}} = -1$; therefore,

$$\frac{\partial F}{\partial \kappa} = \frac{\partial F}{\partial \bar{\sigma}} \frac{d\bar{\sigma}}{d\kappa} = -\frac{d\bar{\sigma}}{d\kappa} = -\frac{d\bar{\sigma}}{d\bar{\varepsilon}^p} \frac{d\bar{\varepsilon}^p}{d\kappa} .$$

Let $\frac{d\bar{\sigma}}{d\bar{\varepsilon}^p} = H'$ (i.e., the slope of the $\bar{\sigma} - \bar{\varepsilon}^p$ plot at any $\bar{\sigma}$ value) ; therefore, by further substitution, we obtain, $\frac{\partial F}{\partial \kappa} = -H' \frac{1}{\bar{\sigma}} = -\frac{H'}{\bar{\sigma}}$.

Combining this result with that derived on pg. 69, we finally have,

$$A = \frac{\partial F}{\partial \kappa} \{\bar{\sigma}\}^T \left\{\frac{\partial F}{\partial \{\bar{\sigma}\}}\right\} = -H' \quad \ldots . (49) .$$

The next step in determining the required stress increment - total strain increment relations is to obtain the values of $\left\{\frac{\partial F}{\partial \{\bar{\sigma}\}}\right\}$ for the the Cartesian stress system (see Eqn. 45) :-

By differentiating Eqn. 48, we obtain the following expressions for the plastic strain increments in the principal stress directions,

$$\delta\varepsilon_1^p = \lambda \frac{\partial F}{\partial \sigma_1} = \lambda , \quad \delta\varepsilon_2^p = \lambda \frac{\partial F}{\partial \sigma_2} = 0 \text{ and } \delta\varepsilon_3^p = \lambda \frac{\partial F}{\partial \sigma_3} = -\lambda .$$

according to the flow rule.

By comparing these with the traditional expressions for the plastic strain increments, viz., $\delta\varepsilon_1^p = \delta\varepsilon_p$, $\delta\varepsilon_2^p = 0$ and

$\delta\varepsilon_3^p = -\delta\varepsilon_p$ .... (50) - where $\delta\varepsilon_p$ is the effective plastic strain increment (either defined in terms of $\delta\kappa$ or by intuitive

reasoning (18)) and a function of the component plastic strain increments that reduces to the plastic strain increment, $\delta\bar{\varepsilon}^{p}$, of the uniaxial test (see pg. 69), it is apparent that, in fact, $\lambda = \delta\varepsilon_{p}$.

Eqn. 50 implies not only that the principal stress directions (1, 2 and 3) are coincident with those of the plastic strain increments but also that the relative magnitudes of the principal stresses are reflected in their corresponding plastic strain increments - i.e., $\delta\varepsilon_1^p < \delta\varepsilon_2^p < \delta\varepsilon_3^p$ in general.

This coincidence is implicit in the derivation of $\{\bar{\sigma}\}^{T}\left\{\frac{\partial F}{\partial\{\bar{\sigma}\}}\right\}$ with respect to the principal stress system (see pgs. 68 and 69).

At this stage, it is appropriate to particularise the discussion to the case of plane strain. Thus, the z direction is a principal direction.

It is commonly held that $\bar{\sigma}_z$ is, in addition, the intermediate principal stress. Hill (19a), however, set out certain provisions by which this viewpoint is tenable for the present material. These are (i) the material is rigid plastic, or (ii) $\nu = \frac{1}{2}$, or (iii) the plastic strains are at least a few times the elastic strains so that the latter are relatively insignificant; this is normally satisfied after comparatively small plastic distortion provided H' is small in relation to E, and no sharp bend occurs in the strain path so that the strain increment is of the order of the elastic strain increments (in

an example to support this viewpoint, Hill used the Prandtl-Reuss relations in conjunction with the Tresca yield criterion which Mendelson (18) has shown to be incompatible).

In view of the above considerations, and since the present work entails the use of arbitrary elastic parameters and degrees of hardening over the entire elastoplastic range, the simplification that σ_z is the intermediate stress is avoided.

We now proceed to determine $\left\{\frac{\partial F}{\partial \{\sigma\}}\right\}$ ($= \begin{Bmatrix} \partial F/\partial \sigma_x \\ \partial F/\partial \sigma_y \\ \partial F/\partial \tau_{xy} \end{Bmatrix}$)

and $\frac{\partial F}{\partial \sigma_z}$, which are the terms in $\frac{\partial F}{\partial \{\sigma\}}$ that are relevant in plane strain.

Let the two remaining principal stresses that occur in the x-y plane be denoted by σ_I and σ_{II}. These act in the I and II directions, respectively, and $\sigma_I > \sigma_{II}$ in general.

Also, let the plastic strain increments in the principal directions (of stress, and hence, also of plastic strain increment - see pg. 71) be given by $\delta\varepsilon^p_I = a\delta\varepsilon_p$, $\delta\varepsilon^p_{II} = b\delta\varepsilon_p$ and $\delta\varepsilon^p_z = c\delta\varepsilon_p$ .... (51

It follows, therefore, from the above discussion and Eqn. 50, that a, b and c can be any combination of the values, 1, 0 and -1, depending on which of the three principal directions, 1, 2 and 3, that I, II and z happen to coincide with at any given state of stress.

From pgs. 70 and 71, the equations indicate that $\frac{\partial F}{\partial \sigma_z} = c$ .... (52).

To obtain $\frac{\partial F}{\partial \sigma_x}$, $\frac{\partial F}{\partial \sigma_y}$ and $\frac{\partial F}{\partial \sigma_z}$, however, it is necessary firstly to determine the angle η between the principal and Cartesian systems. Fig. 17 illustrates how this is done and also provides expressions for σ_I and σ_{II}. The derivations are based on reference (20).

Notes: all stresses relate to point P; CPB is a small triangular prism extending into the paper - i.e. the z direction - in plane strain

By statics, $\sigma\, BC = \sigma_x\, BC \cos\theta \cos\theta + \sigma_y\, BC \sin\theta \sin\theta + \tau_{xy}\, BC \cos\theta \sin\theta + \tau_{xy}\, BC \sin\theta \cos\theta$;

i.e., $\sigma = \sigma_x (\cos 2\theta + 1)/2 + \sigma_y (1 - \cos 2\theta)/2 + \tau_{xy} \sin 2\theta$ .... (53).

Also, $\tau\, BC = \sigma_y\, BC \sin\theta \cos\theta - \sigma_x\, BC \cos\theta \sin\theta + \tau_{xy}\, BC \cos\theta \cos\theta - \tau_{xy}\, BC \sin\theta \sin\theta$;

i.e., $\tau = (\sigma_y - \sigma_x) \sin 2\theta/2 + \tau_{xy} \cos 2\theta$ .... (53A).

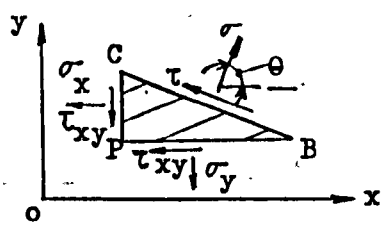

(a) Normal and shear stresses at general angle θ to Cartesian system

In the principal stress system, $\tau = 0$; i.e., $(\sigma_y - \sigma_x) \frac{\sin 2\theta}{2} + \tau_{xy} \cos 2\theta = 0$;

i.e., $\left.\begin{matrix}\eta \\ 90^{\circ}+\eta\end{matrix}\right\} = \frac{1}{2}\tan^{-1}\left(\frac{2\tau_{xy}}{(\sigma_x-\sigma_y)}\right)$ .... (54) .

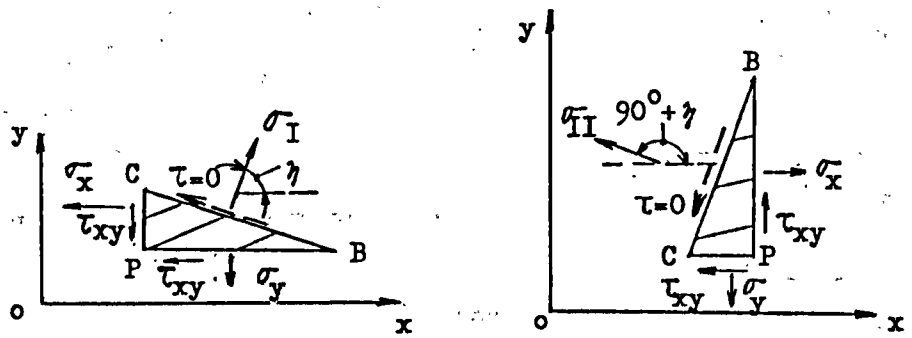

(b) Principal stresses at angles, η and $90^{\circ}+\eta$, to Cartesian system

Therefore, substituting Eqn. 54 into Eqn. 53, we have, for η ,

$$\sigma_I = \sigma_x\left[\frac{\frac{(\sigma_x-\sigma_y)}{2\sqrt{\left(\frac{\sigma_x-\sigma_y}{2}\right)^2+\tau_{xy}^2}}+1}{2}\right] + \sigma_y\left[\frac{1-\frac{(\sigma_x-\sigma_y)}{2\sqrt{\left(\frac{\sigma_x-\sigma_y}{2}\right)^2+\tau_{xy}^2}}}{2}\right]$$

$$+\tau_{xy}\left[\frac{2\tau_{xy}}{2\sqrt{\left(\frac{\sigma_x-\sigma_y}{2}\right)^2+\tau_{xy}^2}}\right] = \frac{\sigma_x+\sigma_y}{2} + \sqrt{\left(\frac{\sigma_x-\sigma_y}{2}\right)^2+\tau_{xy}^2} \quad \text{.... (55)}$$

- see expressions for trigonometric functions below. Similarly, for $90^{\circ}+\eta$,

$$\sigma_{II} = \sigma_x\left[\frac{\frac{-(\sigma_x-\sigma_y)}{2\sqrt{\left(\frac{\sigma_x-\sigma_y}{2}\right)^2+\tau_{xy}^2}}+1}{2}\right] + \sigma_y\left[\frac{1-\frac{-(\sigma_x-\sigma_y)}{2\sqrt{\left(\frac{\sigma_x-\sigma_y}{2}\right)^2+\tau_{xy}^2}}}{2}\right]$$

$$\tau_{xy}\left[\frac{-2\tau_{xy}}{2\sqrt{\frac{\sigma_x-\sigma_y}{2}^2+\tau_{xy}^2}}\right] = \frac{\sigma_x+\sigma_y}{2} - \sqrt{\left(\frac{\sigma_x-\sigma_y}{2}\right)^2+\tau_{xy}^2} \quad \text{.... (56) .}$$

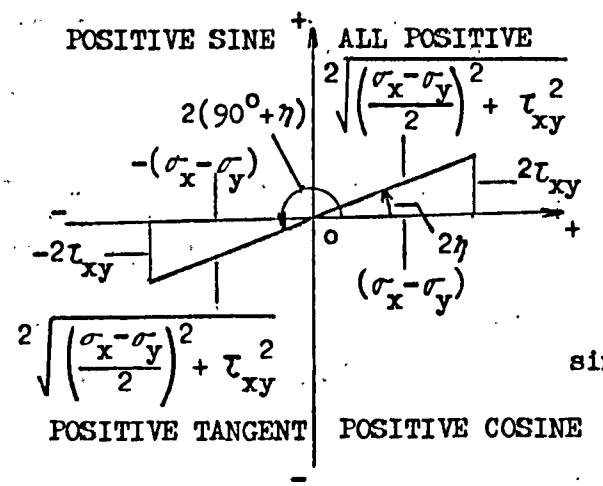

$$\sin 2\eta = \frac{2\tau_{xy}}{2\sqrt{\left(\frac{\sigma_x-\sigma_y}{2}\right)^2+\tau_{xy}^2}}$$

$$\cos 2\eta = \frac{(\sigma_x-\sigma_y)}{2\sqrt{\left(\frac{\sigma_x-\sigma_y}{2}\right)^2+\tau_{xy}^2}}$$

$$\sin 2(90^\circ+\eta) = \frac{-2\tau_{xy}}{2\sqrt{\left(\frac{\sigma_x-\sigma_y}{2}\right)^2+\tau_{xy}^2}}$$

$$\cos 2(90^\circ+\eta) = \frac{-(\sigma_x-\sigma_y)}{2\sqrt{\left(\frac{\sigma_x-\sigma_y}{2}\right)^2+\tau_{xy}^2}}$$

(c) Expressions for some trigonometric functions

Fig. 17. Derivation of principal stresses in the x-y plane and angle between principal and Cartesian systems

The principal stresses, σ_I and σ_{II}, are needed to establish what the relative magnitudes of the three principal stresses are at every iteration within a load increment so that the appropriate values of the plastic strain increment components (i.e. $\delta\varepsilon_p$, 0 or $-\delta\varepsilon_p$) may be relegated to the principal directions, I, II and z, respectively. Also, they are used in determining whether the material is in a state of yield. These points are further discussed in the following section - 1.3.2.

We now know , and consequently, the directions in which the plastic strain increments, $\delta\varepsilon_I^p$ and $\delta\varepsilon_{II}^p$, act.

Thus, the resolution of these strains into the Cartesian system may

be accomplished. To do this, the analogy between the re-orientation of stress and strain systems is exploited so that, by replacing σ_x , σ_y , τ_{xy} , σ_I and σ_{II} with $\delta\varepsilon_x^p$, $\delta\varepsilon_y^p$, $\delta\gamma_{xy}^p/2$, $\delta\varepsilon_I^p$ and $\delta\varepsilon_{II}^p$, respectively, the statical relationships shown in Fig. 17(a) applies equally to the strains (20).

Fig. 18 sets out the expressions for the plastic strain increments in the Cartesian system.

The notes in Fig. 17 apply, reading "strains" in place of "stresses"; substituting $\theta = 180^\circ - \eta$ in Eqn. 52 (noting that the re-orientation is now from principal to Cartesian system - i.e., in reverse), we have,

$$\delta\varepsilon_x^p = \delta\varepsilon_I^p \left(\frac{\cos 2(180^\circ-\eta)+1}{2}\right) + \delta\varepsilon_{II}^p \left(\frac{1-\cos 2(180^\circ-\eta)}{2}\right)$$

$$= \delta\varepsilon_I^p \frac{(\cos 2\eta + 1)}{2} + \delta\varepsilon_{II}^p \frac{(1-\cos 2\eta)}{2}$$

$$= \left(\frac{a(\cos 2\eta + 1)}{2} + \frac{b(1-\cos 2\eta)}{2}\right)\delta\varepsilon_p \quad \text{(see Eqn. 51).}$$

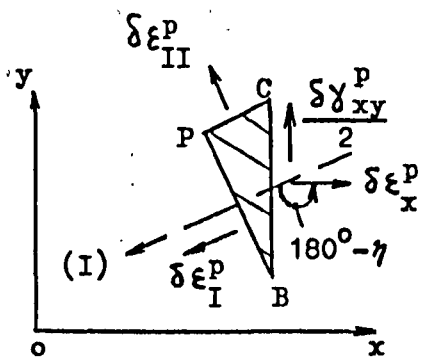

(a) Cartesian plastic strain increments, $\delta\varepsilon_x^p$ and $\delta\gamma_{xy}^p/2$, from principal strain increments (statical analogy)

Similarly, substituting $\theta = 270^\circ - \eta$, we have,

$$\delta\varepsilon_y^p = \delta\varepsilon_I^p \left(\frac{\cos 2(270^\circ-\eta)+1}{2}\right) + \delta\varepsilon_{II}^p \left(\frac{1-\cos 2(270^\circ-\eta)}{2}\right)$$

$$= \delta\varepsilon_I^p \frac{(1-\cos 2\eta)}{2} + \delta\varepsilon_{II}^p \frac{(\cos 2\eta + 1)}{2}$$

$$= \left(\frac{a(1-\cos 2\eta)}{2} + \frac{b(\cos 2\eta + 1)}{2}\right) \delta\varepsilon_p \ .$$

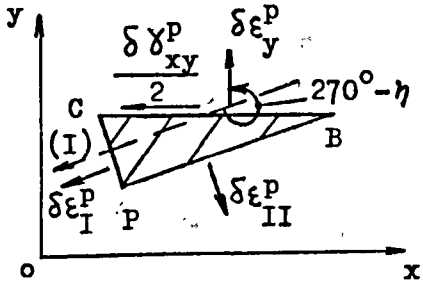

(b) Cartesian plastic strain increments, $\delta\varepsilon_y^p$ and $\delta\gamma_{xy}^p/2$, from principal strain increments (statical analogy)

Finally, substituting $\theta = 180^\circ - \eta$ in Eqn. 53, we have,

$$\frac{\delta\gamma_{xy}^p}{2} = (\delta\varepsilon_{II}^p - \delta\varepsilon_I^p)\frac{\sin 2(180^\circ-\eta)}{2} \ ; \ \text{i.e.,} \ \delta\gamma_{xy}^p = (\delta\varepsilon_I^p - \delta\varepsilon_{II}^p)\sin 2\eta$$

$$= \{(a-b)\sin 2\eta\}\delta\varepsilon_p \ .$$

Fig. 18. Derivation of the plastic strain increments in the Cartesian system

An examination of the expressions for the plastic strain increments in Fig. 18 indicates that, since $\lambda = \delta\varepsilon_p$ (pg. 71) ,

$$\frac{\partial F}{\partial \sigma_x} = \tfrac{1}{2}\{a(\cos 2\eta + 1) + b(1-\cos 2\eta)\} \ , \quad \frac{\partial F}{\partial \sigma_y} = \tfrac{1}{2}\{a(1-\cos 2\eta) + b(\cos 2\eta + 1)\}$$

and $\frac{\partial F}{\partial \tau_{xy}} = (a-b)\sin 2\eta$ .... (57) by the flow rule (pg. 67).

We have thus determined λ (indirectly, via A - see Eqn. 49) and the plane strain equivalents of $\left\{\frac{\partial F}{\partial \{\bar{\sigma}\}}\right\}$ (pg. 67) - $\frac{\partial F}{\partial \sigma_x}$, $\frac{\partial F}{\partial \sigma_y}$, $\frac{\partial F}{\partial \tau_{xy}}$ and $\frac{\partial F}{\partial \sigma_z}$ (Eqns. 52 and 57).

Therefore, the plane strain stress increment/total strain increment relations (cf. Eqn. 45) are now determinate.

These relations and Eqn. 46 (also modified for a Tresca material in plane strain) are summarised in matrix form below. Since, for plane strain, $\tau_{yz} = \tau_{zx} = \gamma_{yz} = \gamma_{zx} = 0$, the corresponding elastoplastic relations of Eqn. 45 concerning the y-z and z-x planes may be omitted without affecting the subsequent solution (by the same token, terms in yz and zx do not enter into the modified Eqn. 46). The condition $\varepsilon_z^t = 0$ is also imposed. Thus,

$$\begin{Bmatrix} \delta\varepsilon_x^t \\ \delta\varepsilon_y^t \\ \delta\gamma_{xy}^t \\ 0 \\ \hline 0 \end{Bmatrix} = \left[\begin{array}{cccc|c} \frac{1}{E} & -\frac{\nu}{E} & 0 & -\frac{\nu}{E} & \frac{1}{2}\{a(\cos 2\eta+1)+b(1-\cos 2\eta)\} \\ -\frac{\nu}{E} & \frac{1}{E} & 0 & -\frac{\nu}{E} & \frac{1}{2}\{a(1-\cos 2\eta)+b(\cos 2\eta+1)\} \\ 0 & 0 & \frac{1}{G} & 0 & (a-b)\sin 2\eta \\ -\frac{\nu}{E} & -\frac{\nu}{E} & 0 & \frac{1}{E} & c \\ \hline \multicolumn{4}{c|}{\text{symmetric}} & -H' \end{array}\right] \begin{Bmatrix} \delta\sigma_x \\ \delta\sigma_y \\ \delta\tau_{xy} \\ \delta\sigma_z \\ \hline \delta\varepsilon_p \end{Bmatrix} \quad \ldots\ (58)$$

(shear modulus $G = E / 2(1+\nu)$)

For the procedure in the Initial Stress Method, the stress increments are required in terms of the total strain increments, and this is derived

via further algebraic manipulation as follows:-

Firstly, the relations in Eqn. 58 may be re-written as

$$\begin{Bmatrix} \delta\varepsilon_x^t \\ \delta\varepsilon_y^t \\ \delta\gamma_{xy}^t \\ \hline 0 \end{Bmatrix} = \left[\begin{array}{c|c} [\bar{E}]^{-1} & \begin{matrix} \tfrac{1}{2}\{a(\cos 2\eta+1) + b(1-\cos 2\eta) + \nu c \\ \tfrac{1}{2}\{a(1-\cos 2\eta) + b(\cos 2\eta+1) + \nu c \\ (a-b)\sin 2\eta \end{matrix} \\ \hline \text{symmetric} & -H'-Ec^2 \end{array}\right] \begin{Bmatrix} \delta\sigma_x \\ \delta\sigma_y \\ \delta\tau_{xy} \\ \hline \delta\varepsilon_p \end{Bmatrix} \quad \ldots\ldots (59)$$

(where $[\bar{E}]$ is the plane strain elasticity matrix - see pg. 17) by substituting $-\frac{\nu}{E}\delta\sigma_x - \frac{\nu}{E}\delta\sigma_y + \frac{1}{E}\delta\sigma_z + c\,\delta\varepsilon_p = 0$ (row four of Eqn. 58); i.e., $\delta\sigma_z = \nu(\delta\sigma_x + \delta\sigma_y) - Ec\,\delta\varepsilon_p$ .... (60) .

By writing $\delta\{\sigma\} = \begin{Bmatrix} \delta\sigma_x \\ \delta\sigma_y \\ \delta\tau_{xy} \end{Bmatrix}$, $\delta\{\varepsilon\}_t = \begin{Bmatrix} \delta\varepsilon_x^t \\ \delta\varepsilon_y^t \\ \delta\gamma_{xy}^t \end{Bmatrix}$, $A' = H'+Ec^2$ and

$\left\{\frac{\overline{\partial F}}{\partial\{\sigma\}}\right\} = \begin{Bmatrix} \tfrac{1}{2}\{a(\cos 2\eta+1)+b(1-\cos 2\eta) + \nu c \\ \tfrac{1}{2}\{a(1-\cos 2\eta)+b(\cos 2\eta+1) + \nu c \\ (a-b)\sin 2\eta \end{Bmatrix}$ in Eqn. 59, we can write the equation as $\delta\{\varepsilon\}_t = [\bar{E}]^{-1}\delta\{\sigma\} + \delta\varepsilon_p\left\{\frac{\overline{\partial F}}{\partial\{\sigma\}}\right\}$ .... (61) and

$\left\{\frac{\overline{\partial F}}{\partial\{\sigma\}}\right\}^T \delta\{\sigma\} - A'\delta\varepsilon_p = 0$ .... (62) .

Next, by premultiplying Eqn. 61 by $[\bar{E}]$, we have,

$[\bar{E}]\delta\{\varepsilon\}_t = \delta\{\sigma\} + [\bar{E}]\delta\varepsilon_p\left\{\frac{\overline{\partial F}}{\partial\{\sigma\}}\right\}$ .... (63) ; further premultiplication by $\left\{\frac{\overline{\partial F}}{\partial\{\sigma\}}\right\}^T$ then gives,

$$\left\{\frac{\overline{\partial F}}{\partial\{\sigma\}}\right\}^T[\bar{E}]\delta\{\varepsilon\}_t = \left\{\frac{\overline{\partial F}}{\partial\{\sigma\}}\right\}^T\delta\{\sigma\} + \left\{\frac{\overline{\partial F}}{\partial\{\sigma\}}\right\}^T[\bar{E}]\,\delta\varepsilon_p\left\{\frac{\overline{\partial F}}{\partial\{\sigma\}}\right\} .$$

Substituting $\left\{\frac{\overline{\partial F}}{\partial\{\sigma\}}\right\}^T\delta\{\sigma\} = A'\delta\varepsilon_p$ from Eqn. 62 into the above, we have, $\left\{\frac{\overline{\partial F}}{\partial\{\sigma\}}\right\}^T[\bar{E}]\delta\{\varepsilon\}_t = A'\delta\varepsilon_p + \left\{\frac{\overline{\partial F}}{\partial\{\sigma\}}\right\}^T[\bar{E}]\,\delta\varepsilon_p\left\{\frac{\overline{\partial F}}{\partial\{\sigma\}}\right\}$, i.e,

$$\delta\varepsilon_p = \left(A' + \left\{\frac{\overline{\partial F}}{\partial\{\sigma\}}\right\}^T[\bar{E}]\left\{\frac{\overline{\partial F}}{\partial\{\sigma\}}\right\}\right)^{-1}\left\{\frac{\overline{\partial F}}{\partial\{\sigma\}}\right\}^T[\bar{E}]\delta\{\varepsilon\}_t \quad \ldots\ (64) .$$

Next, by substituting for $\delta\varepsilon_p$ in Eqn. 63 and re-arranging, we have,

$$\delta\{\sigma\} = [\bar{E}]\delta\{\varepsilon\}_t - [\bar{E}]\left\{\frac{\overline{\partial F}}{\partial\{\sigma\}}\right\}\left(A' + \left\{\frac{\overline{\partial F}}{\partial\{\sigma\}}\right\}^T[\bar{E}]\left\{\frac{\overline{\partial F}}{\partial\{\sigma\}}\right\}\right)^{-1}\left\{\frac{\overline{\partial F}}{\partial\{\sigma\}}\right\}^T[\bar{E}]\delta\{\varepsilon\}_t :$$

since $\left(A' + \left\{\frac{\overline{\partial F}}{\partial\{\sigma\}}\right\}^T[\bar{E}]\left\{\frac{\overline{\partial F}}{\partial\{\sigma\}}\right\}\right)^{-1}$ is a scalar, we can write,

$$\delta\{\sigma\} = \left([\bar{E}] - [\bar{E}]\left\{\frac{\overline{\partial F}}{\partial\{\sigma\}}\right\}\left\{\frac{\overline{\partial F}}{\partial\{\sigma\}}\right\}^T[\bar{E}]\left(A' + \left\{\frac{\overline{\partial F}}{\partial\{\sigma\}}\right\}^T[\bar{E}]\left\{\frac{\overline{\partial F}}{\partial\{\sigma\}}\right\}\right)^{-1}\right)\delta\{\varepsilon\}_t , \text{ or}$$

$$\delta\{\sigma\} = \left[\overline{D^*_{ep}}\right]\delta\{\varepsilon\}_t \quad \ldots\ (65), \text{ where}$$

$$\left[\overline{D^*_{ep}}\right] = \left([\bar{E}] - [\bar{E}]\left\{\frac{\overline{\partial F}}{\partial\{\sigma\}}\right\}\left\{\frac{\overline{\partial F}}{\partial\{\sigma\}}\right\}^T[\bar{E}]\left(A' + \left\{\frac{\overline{\partial F}}{\partial\{\sigma\}}\right\}^T[\bar{E}]\left\{\frac{\overline{\partial F}}{\partial\{\sigma\}}\right\}\right)^{-1}\right) .$$

Finally, $\delta\varepsilon_p$ (Eqn. 64) may be substituted into Eqn. 60, giving,

$$\delta\sigma_z = \nu(\delta\sigma_x + \delta\sigma_y) - Ec\left(A' + \left\{\frac{\overline{\partial F}}{\partial\{\sigma\}}\right\}^T[\bar{E}]\left\{\frac{\overline{\partial F}}{\partial\{\sigma\}}\right\}\right)^{-1}\left\{\frac{\overline{\partial F}}{\partial\{\sigma\}}\right\}^T[\bar{E}]\delta\{\varepsilon\}_t$$

$\ldots\ (66) .$

Eqns. 65 and 66 are the incremental elastoplastic relations used

in the Initial Stress Method of the following section.

Note that $\left[\overline{D^*_{ep}}\right]$ is an explicit expansion which is symmetric, positive definite and valid for a perfectly plastic material (i.e. with $H' = 0$) since its derivation does not entail either multiplication or division by H' .

Also, as will be apparent from the Initial Stress Method outlined in the following section, only the unique yield surface (Eqn. 44) and the expressions, A (Eqn. 47) and $\left\{\frac{\partial F}{\partial \{\bar{\sigma}\}}\right\}$ (pg. 67), which depend on its shape (15), are the sole distinctions between various types of elastoplastic material of the category considered here (pgs. 61 and 62).

1.3.2. Adaptations to the general elastic model (Fig. 1), via the Initial Stress Method, to simulate the general elastoplastic model (Fig. 16)

In Section 1.2., the general elastic model was solved numerically for displacements, stresses and strains. Here, the procedure is adapted, via the application of initial stresses, to solve the general elastoplastic model.

Although the elastoplastic relations presented in Section 1.3.1. are applicable to a material that work hardens in varying degrees, the procedure given here is similar to the one published (8) so that only a constant work hardening material can be dealt with.

However, a technique is later presented in Section 1.4. to overcome this limitation, and varying degrees of hardening as well as softening may thus be modelled.

The procedure here is applicable to all finite elements of the assemblage and it suffices to examine the response of a typical element, X (Fig. 19), referring to the assemblage as a whole as appropriate.

It is amply illustrated by examining the changes of state, O-A , B-C , D-E and F-G , caused by the corresponding uniform, finite load increments/decrement, $\Delta t_{(O-A)}$, $\Delta t_{(B-C)}$, $\Delta t_{(D-E)}$ and $\Delta t_{(F-G)}$, respectively, being applied to the general elastoplastic model.

As shown in Fig. 19(b), these states are conveniently represented in a plot of a composite measure of the stresses (effective stress σ_e) against a composite measure of the strains (ε) that occur in plane strain.

The effective stress may be defined as a positively increasing function of the stresses during plastic flow which determines whether plastic flow takes place or not. It also reduces to the uniaxial test stress. For a Tresca material, $\sigma_e = \sigma_1 - \sigma_3$ .... (67) (18) so that $(\sigma_1 - \sigma_3) \geq \bar{\sigma}$ for plastic flow to occur (see pg. 69 for the yield condition) .

For a perfectly plastic material, the condition, $(\sigma_1 - \sigma_3) = \bar{\sigma}$, is sufficient to cause plastic flow. Conversely, when $(\sigma_1 - \sigma_3) < \bar{\sigma}$, only elastic strain increments can occur.

The measure, ε , comprises two distinct components, namely, the elastic strain, σ_e / E , and the plastic strain, ε_p . ε_p is the cumulation of the effective plastic strain increments, $\delta\varepsilon_p$ (i.e. $\varepsilon_p = \int d\varepsilon_p$) , defined on pgs. 70 - 71).

By inference, therefore, the above plot is identical to the uniaxial test plot.

As the following discussion is for plane strain, there are no stresses or strains in the y-z and z-x planes so that these need not be further considered.

The infinitesimal stress and strain increments of Section 1.3.1., pertinent to incremental plasticity, are approximated to finite increments.

Load increments are kept in small steps for accuracy of solution; however, Zienkiewicz et al. (8) found that results from the Initial Stress Method are relatively insensitive to the magnitude of load increments. More will be said about this in the following chapters.

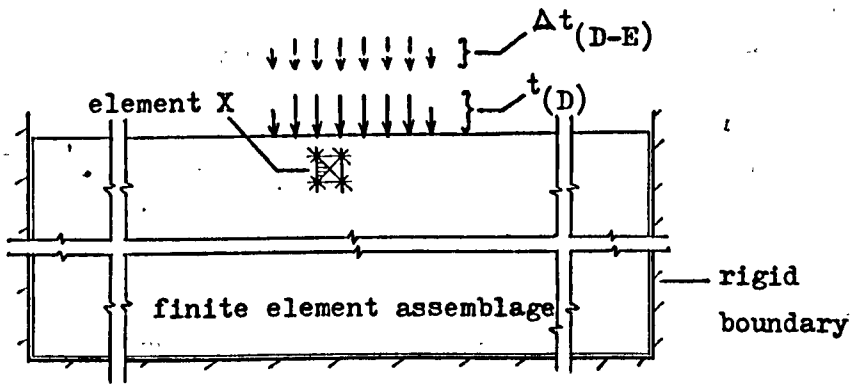

(a) Element X at state D, subject to load increment $\Delta t_{(D-E)}$ - typical

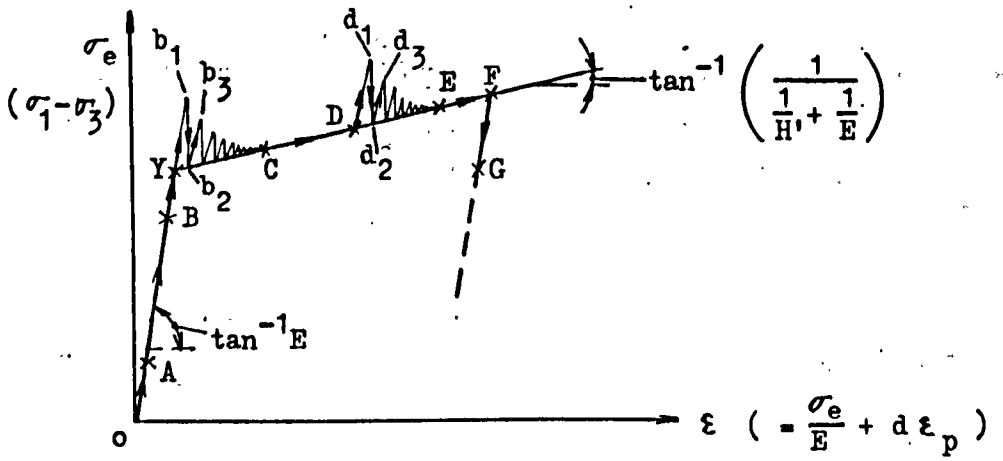

(b) Composite stress-strain plot of various states of element X

Fig. 19. Response of typical element X to finite load increments

Initially, element X is stress/strain free at state 0, prior to application of the strip load.

A small but finite uniform strip load, $\Delta t_{(0-A)}$, leads to an elastic state change, 0-A, with stress increments, $\Delta\sigma'_{x(0-A)}$, $\Delta\sigma'_{y(0-A)}$, $\Delta\tau'_{xy(0-A)}$ and $\Delta\sigma'_{z(0-A)}$, and strain increments, $\Delta\varepsilon'_{x(0-A)}$, $\Delta\varepsilon'_{y(0-A)}$, $\Delta\gamma'_{xy(0-A)}$ and $\Delta\varepsilon'_{z(0-A)}$, say.

These are deduced by solving the general elastic model of Section 1.2.1 with t (Fig. 1) $= \Delta t_{(0-A)}$, and using equations such as 5, 6, 8 and 9, reading σ_x as $\Delta\sigma'_{x(0-A)}$, σ_y as $\Delta\sigma'_{y(0-A)}$, τ_{xy} as $\Delta\tau'_{xy(0-A)}$, σ_z as $\Delta\sigma'_{z(0-A)}$, ε_x as $\Delta\varepsilon'_{x(0-A)}$, ε_y as $\Delta\varepsilon'_{y(0-A)}$, γ_{xy} as $\Delta\gamma'_{xy(0-A)}$ and ε_z as $\Delta\varepsilon'_{z(0-A)}$ ($= 0$).

The effective stress of the element, $\sigma_{e(A)}$, at state A is given by Eqn. 67. That is, $\sigma_{e(A)} = \sigma_{1(A)} - \sigma_{3(A)}$, where the major principal stress, $\sigma_{1(A)}$, and the minor principal stress, $\sigma_{3(A)}$, are the highest and lowest values, respectively, amongst the three principal stresses, $\sigma_{I(A)}$ ($= \frac{\Delta\sigma'_{x(0-A)} + \Delta\sigma'_{y(0-A)}}{2} + \sqrt{\left(\frac{\Delta\sigma'_{x(0-A)} - \Delta\sigma'_{y(0-A)}}{2}\right)^2 + \Delta\tau'^2_{xy(0-A)}}$, - see Eqn. 55); $\sigma_{II(A)}$ ($= \frac{\Delta\sigma'_{x(0-A)} + \Delta\sigma'_{y(0-A)}}{2} - \sqrt{\left(\frac{\Delta\sigma'_{x(0-A)} - \Delta\sigma'_{y(0-A)}}{2}\right)^2 + \Delta\tau'^2_{xy(0-A)}}$ - see Eqn. 56) and $\Delta\sigma'_{z(0-A)}$

- see pg. 72 .

Since the element has not attained first yield, it will be found that $\sigma_{e_{(A)}} < \sigma_{e_{(Y)}}$ ($= \bar{\sigma}_{(Y)}$, the uniaxial stress at first yield) - see pg. 83 . Thus, no plastic flow occurs in the element for the moment.

If, in addition, no plastic flow occurs in any of the other elements of the assemblage during the load increment, then state A is, indeed, the final state of the element under the strip load $\Delta t_{(O-A)}$; otherwise, further iterations are required as will be evident from the following.

Subsequent elastic changes in state due to the addition of small, finite load increments are treated similarly, except that (i) the element is no longer stress/strain free initially so that the initial stresses and strains have to be added to their elastic increments to obtain their values at the final state for the applied load increment and (ii) the elastic stress and strain increments need simply be determined by multiplying those for the state change O-A with the ratio of the current load increment to $\Delta t_{(O-A)}$, by the principle of superposition.- there is no need to solve the elastic model every time.

At state B, the element is subject to the stresses, $\sigma_{x_{(B)}}$, $\sigma_{y_{(B)}}$, $\tau_{xy_{(B)}}$ and $\sigma_{z_{(B)}}$, and the strains, $\varepsilon_{x_{(B)}}$, $\varepsilon_{y_{(B)}}$, $\gamma_{xy_{(B)}}$ and $\varepsilon_{z_{(B)}}$ ($= 0$), say.

A further increase in pressure, $\Delta t_{(B-C)}$, leads to the elastic state-change, B-b_1 , and the stress increments, $\Delta\sigma'_{x_{(B-b_1)}}$, $\Delta\sigma'_{y_{(B-b_1)}}$,

$\Delta\tau'_{xy_{(B-b_1)}}$ and $\Delta\sigma'_{z_{(B-b_1)}}$, and strain increments, $\Delta\varepsilon'_{x_{(B-b_1)}}$, $\Delta\varepsilon'_{y_{(B-b_1)}}$, $\Delta\gamma'_{xy_{(B-b_1)}}$ and $\Delta\varepsilon'_{z_{(B-b_1)}}$ (= 0), say. These are determined by multiplying the corresponding increments for state change O-A with the factor $\frac{\Delta t_{(B-C)}}{\Delta t_{(O-A)}}$ - see point (ii) of pg. 86.

As a result, the element attains state b_1, with stresses, $\sigma_{x_{(B)}} + \Delta\sigma'_{x_{(B-b_1)}} = \sigma_{x_{(b_1)}}$, say, $\sigma_{y_{(b_1)}}$ (= $\sigma_{y_{(B)}} + \Delta\sigma'_{y_{(B-b_1)}}$), $\tau_{xy_{(b_1)}}$ (= $\tau_{xy_{(B)}} + \Delta\tau'_{xy_{(B-b_1)}}$) and $\sigma_{z_{(b_1)}}$ (= $\sigma_{z_{(B)}} + \Delta\sigma'_{z_{(B-b_1)}}$), and strains, $\varepsilon_{x_{(b_1)}}$ (= $\varepsilon_{x_{(B)}} + \Delta\varepsilon'_{x_{(B-b_1)}}$), $\varepsilon_{y_{(b_1)}}$ (= $\varepsilon_{y_{(B)}} + \Delta\varepsilon'_{y_{(B-b_1)}}$), $\gamma_{xy_{(b_1)}}$ (= $\gamma_{xy_{(B)}} + \Delta\gamma'_{xy_{(B-b_1)}}$) and $\varepsilon_{z_{(b_1)}}$ (= $\varepsilon_{z_{(B)}} + \Delta\varepsilon'_{z_{(B-b_1)}}$ = 0).

The effective stress, $\sigma_{e_{(b_1)}}$ (= $\sigma_{1_{(b_1)}} - \sigma_{3_{(b_1)}}$, where $\sigma_{1_{(b_1)}}$ and $\sigma_{3_{(b_1)}}$ are the highest and lowest values, respectively, of

$$\frac{\sigma_{x_{(b_1)}} + \sigma_{y_{(b_1)}}}{2} + \sqrt{\left(\frac{\sigma_{x_{(b_1)}} - \sigma_{y_{(b_1)}}}{2}\right)^2 + \tau_{xy^2_{(b_1)}}},$$

$$\frac{\sigma_{x_{(b_1)}} + \sigma_{y_{(b_1)}}}{2} - \sqrt{\left(\frac{\sigma_{x_{(b_1)}} - \sigma_{y_{(b_1)}}}{2}\right)^2 + \tau_{xy^2_{(b_1)}}} \quad \text{and} \quad \sigma_{z_{(b_1)}}),$$

will now have exceeded the uniaxial stress at first yield. That is,

$\sigma_{e_{(b_1)}} > \sigma_{e_{(Y)}}$ ($= \bar{\sigma}_{y(Y)}$), so that some plastic flow can be expected to occur in element X.

However, B-b_1 is a purely elastic response so that state b_1 is incompatible with true constitutive behaviour.

The following correction is next applied to enforce agreement with the prescribed elastoplastic behaviour:-

Firstly, the element is taken up to state Y - i.e., first yield, using the principle of superposition. The corresponding stresses are thus

$$\sigma_{x_{(B)}} \times \frac{\sigma_{e_{(Y)}}}{\sigma_{e_{(B)}}} = \sigma_{x_{(Y)}}, \text{ say, } \sigma_{y_{(Y)}} \left(= \sigma_{y_{(B)}} \times \frac{\sigma_{e_{(Y)}}}{\sigma_{e_{(B)}}} \right),$$

$$\tau_{xy_{(Y)}} \left(= \tau_{xy_{(B)}} \times \frac{\sigma_{e_{(Y)}}}{\sigma_{e_{(B)}}} \right) \text{ and } \sigma_{z_{(Y)}} \left(= \sigma_{z_{(B)}} \times \frac{\sigma_{e_{(Y)}}}{\sigma_{e_{(B)}}} \right),$$

and the strains, $\varepsilon_{x_{(Y)}} \left(= \varepsilon_{x_{(B)}} \times \frac{\sigma_{e_{(Y)}}}{\sigma_{e_{(B)}}} \right)$, $\varepsilon_{y_{(Y)}} \left(= \varepsilon_{y_{(B)}} \times \frac{\sigma_{e_{(Y)}}}{\sigma_{e_{(B)}}} \right)$, $\gamma_{xy_{(Y)}} \left(= \gamma_{xy_{(B)}} \times \frac{\sigma_{e_{(Y)}}}{\sigma_{e_{(B)}}} \right)$ and $\varepsilon_{z_{(Y)}} \left(= \varepsilon_{z_{(B)}} \times \frac{\sigma_{e_{(Y)}}}{\sigma_{e_{(B)}}} \right)$ ($\frac{\sigma_{e_{(Y)}}}{\sigma_{e_{(B)}}} = 0$).

The remaining stress/strain increments in going from state Y to state b_1 are, therefore, $\sigma_{x_{(b_1)}} - \sigma_{x_{(Y)}} = \Delta\sigma'_{x_{(Y-b_1)}}$, say, $\Delta\sigma'_{y_{(Y-b_1)}}$

$(= \sigma_{y_{(b_1)}} - \sigma_{y_{(Y)}})$, $\Delta\tau'_{xy_{(Y-b_1)}}$ $(= \tau_{xy_{(b_1)}} - \tau_{xy_{(Y)}})$, $\Delta\sigma'_{z_{(Y-b_1)}}$ $(= \sigma_{z_{(b_1)}} - \sigma_{z_{(Y)}})$, $\Delta\varepsilon'_{x_{(Y-b_1)}}$ $(= \varepsilon_{x_{(b_1)}} - \varepsilon_{x_{(Y)}})$, $\Delta\varepsilon'_{y_{(Y-b_1)}}$ $(= \varepsilon_{y_{(b_1)}} - \varepsilon_{y_{(Y)}})$, $\Delta\gamma'_{xy_{(Y-b_1)}}$ $(= \gamma_{xy_{(b_1)}} - \gamma_{xy_{(Y)}})$ and $\Delta\varepsilon'_{z_{(Y-b_1)}}$ $(= \varepsilon_{z_{(b_1)}} - \varepsilon_{z_{(Y)}} = 0)$.

At the end of the above strain increments, the true state of the element is b_2, and the corresponding stress increments, $\Delta\sigma_{x_{1_{(Y-b_2)}}}$, $\Delta\sigma_{y_{1_{(Y-b_2)}}}$, $\Delta\tau_{xy_{1_{(Y-b_2)}}}$ and $\Delta\sigma_{z_{1_{(Y-b_2)}}}$, say, are given by Eqns. 65 and 66, by reading $\delta\{\sigma\}$ as $\begin{Bmatrix} \Delta\sigma_{x_{1_{(Y-b_2)}}} \\ \Delta\sigma_{y_{1_{(Y-b_2)}}} \\ \Delta\tau_{xy_{1_{(Y-b_2)}}} \end{Bmatrix}$, $\delta\sigma_z$ as $\Delta\sigma_{z_{1_{(Y-b_2)}}}$ and $\delta\{\varepsilon\}_t$ as $\begin{Bmatrix} \Delta\varepsilon'_{x_{(Y-b_1)}} \\ \Delta\varepsilon'_{y_{(Y-b_1)}} \\ \Delta\gamma'_{xy_{(Y-b_1)}} \end{Bmatrix}$, the stresses at state Y being used to determine a, b, c and η.

By adding the initial stresses, $\Delta\sigma_{x_{1_{(Y-b_2)}}} - \Delta\sigma'_{x_{(Y-b_1)}} = \Delta\sigma''_{x_{(b_1-b_2)}}$, say, $\Delta\sigma''_{y_{(b_1-b_2)}}$ $(= \Delta\sigma_{y_{1_{(Y-b_2)}}} - \Delta\sigma'_{y_{(Y-b_1)}})$, $\Delta\tau''_{xy_{(b_1-b_2)}}$ $(= \Delta\tau_{xy_{1_{(Y-b_2)}}} - \Delta\tau'_{xy_{(Y-b_1)}})$ and $\Delta\sigma''_{z_{(b_1-b_2)}}$ $(= \Delta\sigma_{z_{1_{(Y-b_2)}}} - \Delta\sigma'_{z_{(Y-b_1)}})$,

to those at state b_1 without altering the strains in the element, it will undergo the state change b_1-b_2 .

Thus, the element is currently at state b_2 with stresses,

$$\sigma_{x_{(Y)}} + \Delta\sigma_{x_1}{}_{(Y-b_2)} = \sigma_{x_{(b_2)}}, \text{ say, } \sigma_{y_{(b_2)}} \left(= \sigma_{y_{(Y)}} + \Delta\sigma_{y_1}{}_{(Y-b_2)} \right),$$

$$\tau_{xy_{(b_2)}} \left(= \tau_{xy_{(Y)}} + \Delta\tau_{xy_1}{}_{(Y-b_2)} \right) \text{ and } \sigma_{z_{(b_2)}} \left(= \sigma_{z_{(Y)}} + \Delta\sigma_{z_1}{}_{(Y-b_2)} \right),$$

and the strains unchanged from those at state b_1 .

The imposition of these initial stresses, however, leads to the addition of concentrated loads at the corner joints of the element so that a further elastic change of state b_2-b_3 occurs which is the total effect of these and any other such additions to elements of the assemblage that have similarly become plastic, on the elastic model.

To elaborate, we return to Eqn. 6 (the prior derivation remaining unchanged) for which the presence of initial stresses, σ^i_x, σ^i_y and τ^i_{xy} , say, requires an additional term, viz.,

$$= \begin{Bmatrix} \sigma^i_x \\ \sigma^i_y \\ \tau^i_{xy} \end{Bmatrix} + \left[\bar{E}\right] \left[\Gamma\right] \left\{\bar{u}_c'\right\} \quad \ldots\ldots (68).$$

This, in turn, leads to an additional strain energy term to be added to the expression for total potential energy in pg. 25, as the following shows:- The strain energy due to the initial stresses in the

element, $U_i = \int_{A_E} \{\gamma\}^T \begin{Bmatrix} \sigma_x^i \\ \sigma_y^i \\ \tau_{xy}^i \end{Bmatrix} A_E = \{\bar{u}_c'\}^T [\Gamma]^T \begin{Bmatrix} \sigma_x^i \\ \sigma_y^i \\ \tau_{xy}^i \end{Bmatrix} A_E = \{\bar{u}_c'\}^T \{\bar{p}_i\}$ .. (69) .

The similarity to the expression for the potential energy due to body forces (Eqn. 11) is evident and therefore, as for those, the total strain energy due to the presence of initial stresses in a number of finite elements of the assemblage may be deduced by row mapping of contributions from vectors like $\{\bar{p}_i\}$ (since Eqn. 69 is, in principle, applicable to all elements - cf. for $\{\bar{p}_B\}$) into the vector, $\{p_i\}$, of the expression, $\bar{U}_i = \{q\}^T \{p_i\}$ .... (70), ordered according to the incidence vector.

As before, $-\{p_i\}$ is analogous to a system of concentrated loads (x component followed by y component) acting at the joints of the assemblage (see pg. 25).

Thus, for element X, the concentrated loads applied to the corner joints due to initial stresses in it may be obtained by reading σ_x^i as $\Delta\sigma''_{x(b_1-b_2)}$, σ_y^i as $\Delta\sigma''_{y(b_1-b_2)}$ and τ_{xy}^i as $\Delta\tau''_{xy(b_1-b_2)}$ in the expression $-[\Gamma]^T \begin{Bmatrix} \sigma_x^i \\ \sigma_y^i \\ \tau_{xy}^i \end{Bmatrix} A_E$, the incidence vector being i-j-k (Fig. 2).

Similar expressions apply to the concentrated loads at the corner joints of other elements of the assemblage due to the presence of initial stresses.

The cumulative effect of these and the concentrated loads from the total strip load ($= \Delta t_{(O-A)} + \ldots + \Delta t_{(B-C)}$) constitute the current loading on the elastic model. Since this model gives a general treatment of load vectors, the solution procedure is unaltered by the initial stress load vectors. Solving, then, as usual, for the overall loading - except that equations like Eqn. 68 (the left hand term being the cumulative value of the initial stresses to date, the right hand term having the same connotation as before) rather than Eqn. 6 are used to determine the stresses, element X undergoes a further elastic change in state, b_2-b_3 , so that it attains state b_3 with stresses, $\sigma_{x_{(b_3)}}$, $\sigma_{y_{(b_3)}}$, $\tau_{xy_{(b_3)}}$ and $\sigma_{z_{(b_3)}}$, and strains, $\varepsilon_{x_{(b_3)}}$, $\varepsilon_{y_{(b_3)}}$, $\gamma_{xy_{(b_3)}}$ and $\varepsilon_{z_{(b_3)}}$ ($= 0$) , say.

Thus, the stress increments, $\sigma_{x_{(b_3)}} - \sigma_{x_{(b_2)}} = \Delta\sigma'_{x_{(b_2-b_3)}}$, say, $\Delta\sigma'_{y_{(b_2-b_3)}}$ ($= \sigma_{y_{(b_3)}} - \sigma_{y_{(b_2)}}$), $\Delta\tau'_{xy_{(b_2-b_3)}}$ ($= \tau_{xy_{(b_3)}} - \tau_{xy_{(b_2)}}$) and $\Delta\sigma'_{z_{(b_2-b_3)}}$ ($= \sigma_{z_{(b_3)}} - \sigma_{z_{(b_2)}}$), and the strain increments, $\Delta\varepsilon'_{x_{(b_2-b_3)}}$ ($= \varepsilon_{x_{(b_3)}} - \varepsilon_{x_{(b_2)}}$), $\Delta\varepsilon'_{y_{(b_2-b_3)}}$ ($= \varepsilon_{y_{(b_3)}} - \varepsilon_{y_{(b_2)}}$), $\Delta\gamma'_{xy_{(b_2-b_3)}}$ ($= \gamma_{xy_{(b_3)}} - \gamma_{xy_{(b_2)}}$) and $\Delta\varepsilon'_{z_{(b_2-b_3)}}$ ($= \varepsilon_{z_{(b_3)}} -$

$\varepsilon_{z_{(b_2)}} = 0$), form the basis for the second iteration, in the same way as $\Delta\sigma'_{x_{(Y-b_1)}}$, etc. (see pg. 88) did for the first.

However, it will be noted that $\Delta\sigma'_{z_{(b_2-b_3)}}$ is as yet undetermined; as for the other three stress components (Eqn. 68), extra terms are added, this time to Eqn. 8 of the elastic model, viz.,

$\sigma_z = \sigma^i_z + \nu(\sigma_x - \sigma^i_x) + (\sigma_y - \sigma^i_y)$ .... (71), where σ^i_z is the cumulative initial stress applied to the element in the z direction. (note the elastic contribution to the other stress components is used).

The application of these initial stresses, unlike the other initial stress components, leads to no additional energy term since there can be no straining (see Eqn. 9) in the z direction. Another way of looking at this is that no deformation arises from the application of an initial stress in the z direction, in the x-y plane which is of interest here. The same conclusion may be drawn for the other elements of the assemblage.

Thus, in the first iteration, we simply add the initial stress, $\Delta\sigma''_{z_{(b_1-b_2)}}$, to the stress in the z direction obtained via the usual elastic analysis but with concentrated loads added due to initial stresses.

Prior to executing the second iteration, the yield stress of the element must be updated. That is, in determining whether plastic flow occurs in the iteration, we compare the effective stress at state b_3 with $\sigma_{e_{(b_2)}}$ ($= \sigma_{1_{(b_2)}} - \sigma_{3_{(b_2)}}$, where $\sigma_{1_{(b_2)}}$ and $\sigma_{3_{(b_2)}}$ are the highest and lowest values, respectively, of $\sigma_{I_{(b_2)}}$ ($= \frac{\sigma_{x_{(b_2)}} + \sigma_{y_{(b_2)}}}{2}$

$$+\sqrt{\left(\frac{\sigma_{x_{(b_2)}} - \sigma_{y_{(b_2)}}}{2}\right)^2 + \tau_{xy^2_{(b_2)}}}\ ),\ \sigma_{II_{(b_2)}}\ (= \frac{\sigma_{x_{(b_2)}} + \sigma_{y_{(b_2)}}}{2}$$

$$-\sqrt{\left(\frac{\sigma_{x_{(b_2)}} - \sigma_{y_{(b_2)}}}{2}\right)^2 + \tau_{xy^2_{(b_2)}}}\ )\ \text{and}\ \sigma_{z_{(b_2)}}\ ).$$

Also, it may be noted that the strains that are considered in this procedure are total strains.

Following the second iteration, the third iteration will be b_4-b_5 -b_6 , and so on...

In all iterations that follow the first, all prior additional concentrated loads from initial stresses in elements are included with those from the total strip load as existing loads at the beginning of the iteration.

At some stage, it will be found that the additional loads from initial stresses generated in a current iteration make no significant change to the overall loading above, e.g., no single joint load increases by more than 1/1000 th its current value.

The element X is then assumed to have attained its final state (C) for the load increment $\Delta t_{(B-C)}$; this state is chosen to be that at the final iteration, subsequent to adding the true stress/strain increments to those at the initial state.

The same also applies to all other elements.

Moving on to state D, it is obvious that a load increment, $\Delta t_{(D-E)}$,

which leads to the final state E, is handled as a series of iterations, $D\text{-}d_1\text{-}d_2\text{-}d_3\text{-}\ \ldots$, via the same procedure as outlined for $Y\text{-}b_1\text{-}b_2\text{-}b_3\text{-}$ ...

Finally, we arrive at state F. A load decrement, $\Delta t_{(F\text{-}G)}$, will lead to elastic stress/strain decements from those at state F and it will be found that the effective stress at state G is less than that at state F (obtained by progressive updating from state Y).

Thus, the stresses and strains so obtained for state G are the final state results. This state change is essentially in reverse of O-A and, by the same token, continuous unloading leads to a procedure that is in reverse of first loading prior to yield; re-loading is then similar to first loading.

1.3.2.1. Flow chart for the Initial Stress Method of Section 1.3.2.

This flow chart has been incorporated into the Master Flow Chart in Appendix (Block G5 to Block L7).

1.3.3. Adaptations to the general elastoplastic model to evolve several elastoplastic models of lesser degrees of inhomogeneity and to deal with linear varying strip loading

As in Section 1.2.7., differences in degree of inhomogeneity simply entail replacement of the random material property generators by the pertinent routines reflecting the required degree of inhomogeneity.

Thus, by adopting the alternative flow chart subroutines given below, strength inhomogeneity of varying degrees replace the random strength distribution hitherto assumed.

The required degree of inhomogeneity of the elastic phase may be obtained by selecting the relevant flow charts of the previous section - 1.2. - as shown below.

Linear variation of strip pressure is treated in a similar fashion to that of Section 1.2.7.4.

1.3.3.1. Adaptations to flow chart for general elastoplastic model to obtain homogeneous model (to be read in conjunction with Master Flow Chart in Appendix - as for all other adaptations below)

Block	Adaptations
B1	Initialise ν of elements to a constant value
C1	Initialise E of elements to a constant value
G2	Initialise $\bar{\sigma}$ of elements to a constant value

1.3.3.2. Adaptations to flow chart for general elastoplastic model for inhomogeneity of rigidity and strength about centre of strip

Block	Adaptations
B1	Initialise ν of elements to a constant value
C1	Initialise E's of elements on either side of centre-line
G2	Initialise $\bar{\sigma}$'s of elements on either side of centre-line

1.3.3.3. Adaptations to flow chart for general elastoplastic model for linear varying strip loading

Block	Adaptations
B1	Initialise ν of elements to a constant value
C1	Initialise E of elements to a constant value
E1	Set up load vectors of all columns of nodes for linear varying strip load, and store
F9 (Sub-block 10)	Store $\{\gamma\}$, $\{\sigma\}$ and σ_z in $\{\Delta\varepsilon'\}$, $\{\Delta\sigma'\}$ and $\Delta\sigma'_z$, respectively
G1	Is this the 1st load increment? (Yes - G2 ; No - 4.3)
G2	Initialise $\bar{\sigma}$ of elements to a constant value
L3	Read next load increment
L4	Add load increment to load vectors
L5	Set up load vectors of all columns of nodes for linear varying strip load increment in a workarea
L6	Update $\bar{\sigma}$ for all elements
L7	Go to Block F1 and proceed using load vectors in the workarea

1.3.3.4. Adaptations to flow chart for general elastoplastic model for linear variation of rigidity and strength with depth

Block	Adaptations
B1	Initialise ν of elements to a constant value
C1	Initialise linear varying E's with depth
G2	Initialise linear varying $\bar{\sigma}$'s with depth

1.3.3.5. Adaptations to flow chart of Section 1.3.3.4. for stiff crust problem

Block	Adaptations
C1	Initialise linear varying E's with depth but with stiff crust
G2	Initialise linear varying $\bar{\sigma}$'s with depth but with stiff crust

1.3.3.6. Adaptations to flow chart for general elastoplastic model for underlying soft layer problem

Block	Adaptations
B1	Initialise ν of elements to a constant value
C1	Initialise linear varying E's with depth with underlying soft layer
G2	Initialise linear varying $\bar{\sigma}$'s with depth with underlying soft layer

1.4. A procedure for dealing with variable work hardening / work softening

In the Initial Stress Method outlined in Section 1.3.2., it was necessary to specify the value of H' (and hence, $[D^*_{ep}]$) at the start of every iteration so that, for the assumed total strain increments, the actual stress increments may be determined (pg. 89).

However, as the value of ξ (Fig. 19) at the final state of the iteration is not known a priori, only a constant value of H' can be used at the outset without requiring some information of the relative proportions of the elastic and plastic strain components.

Fig. 20 illustrates two cases of variable H' as the loading progresses. These permit better approximations to the constitutive behaviour encountered in actual soils via curve fits.

A procedure is presented by which a variable H' curve can be approximated to any desired degree of accuracy via a subsidiary set of iterations within each usual iteration of the Initial Stress Method.

It suffices to examine the procedure at a "kink" (Fig. 21) of a work hardening and a work softening material, respectively.

The work softening material is simply defined as one with a negative H'; the rest of the specification is as in Section 1.3.1.

However, the stability postulate of Drucker (pg. 61) is not obeyed by the resulting material.

Mroz (12), however, has shown two cases of materials that do

not obey the stability postulate and yet, when perfectly plastic, do obey the associated flow rule.

Hoeg (21) also adopted a similar material to the one here.

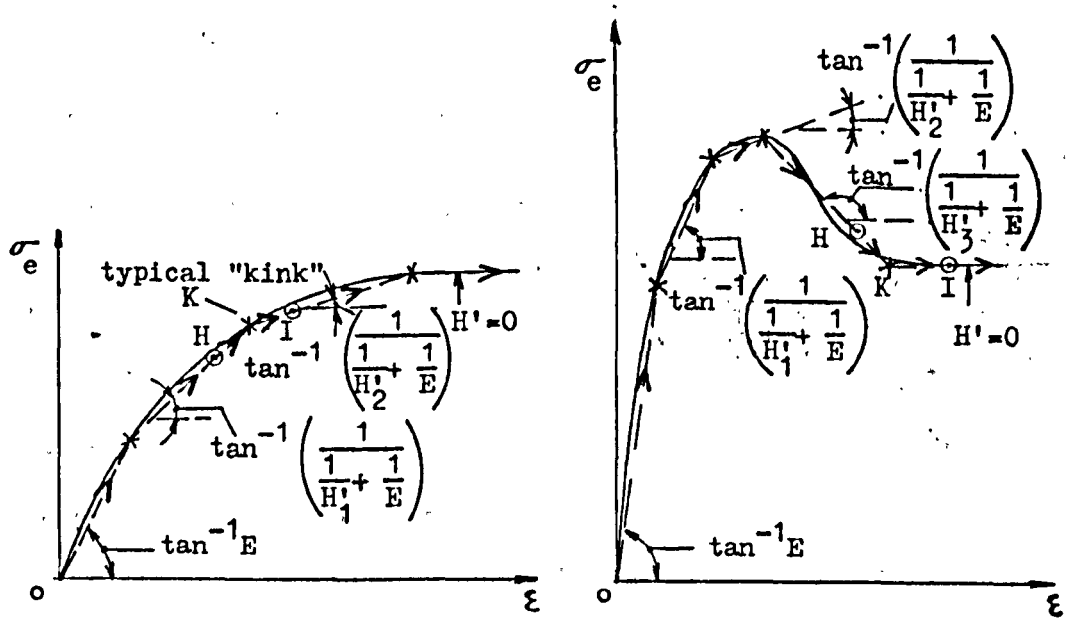

Fig. 20. Curve fitting for two elastoplastic materials with variable work hardening and softening

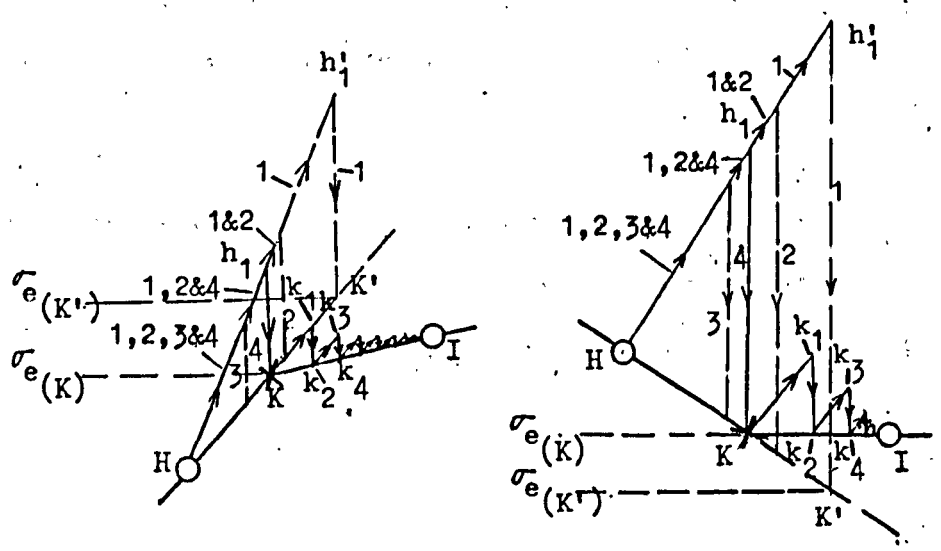

Fig. 21. The subsidiary iterative processes at two "kinks"

1.4.1. Adaptations to procedure of Section 1.3.2. for variations in H'

Consider the element X (Fig. 19) to be at some state H (Fig. 21), initially, and subjected to pressure increase, $\Delta t_{(H-I)}$.

By adopting the procedure in Section 1.3.2., the state path of the element in the first iteration ($\vec{1}$) is $H\text{-}h_1'\text{-}K'$ (cf. state change, $D\text{-}d_1\text{-}d_2$ - Fig. 19).

However, by comparing the effective stress, $\sigma_{e_{(K')}}$, at state K' with that at the "kink" K, i.e., $\sigma_{e_{(K)}}$, it can be seen that there is an overshoot from the elastoplastic curve.

Before proceeding with the usual second iteration (cf. $d_2\text{-}d_3\text{-}d_4$ of Fig. 19), it is therefore necessary to modify the procedure to take the state of the element to the "kink".

This is done by assuming one-half the total strain increments for $H\text{-}h_1'\text{-}K'$ and repeating the first iteration ($\vec{2}$) with these as the basis. Successive iteration along these lines will generally be required ($\vec{3}$, $\vec{4}$) until, at some stage, it is found that when comparing the effective stress at the end of a repeated iteration with $\sigma_{e_{(K)}}$, the difference is insignificant.

The halving process leads to an increase or decrease from the total strain increments of the previous iteration, depending on which side of the "kink" the final state lies during a subsidiary iteration of this

kind; if the final state is nearer state H than K, the average of the total strain increments of the previous and current iterations is used in the following iteration.

The adopted first iteration is thus H-h_1-K, and from there on, successive iterations are carried out as before, the value of H' post "kink" being used from the second iteration onwards. The initial stresses are dealt with as usual. Note that the difference in total strain increments between H-h_1'-K' and H-h_1-K is used in the second iteration.

The difference between a hardening and softening material is that the initial effective stress computed for the former will be greater than that at the "kink" , whilst it is less for the latter.

1.4.2. Adaptations to flow chart for general elastoplastic model for variable work hardening / work softening

Block	Adaptations
G3	Set up and store H' values for each portion of the elastoplastic curve
G3a	Initialise H' for each element
J8a	Is H' of the element = H' of the elastoplastic curve beyond the final kink? (Yes - J9 ; No - J8b)
J8b	From the H' of the element identify the next kink on the elastoplastic curve, say kink I
J8c	Set $\{\sigma\} = \{\sigma_o\} + \{\Delta\sigma_1\}$ and $\sigma_z = \sigma_{z_o} + \Delta\sigma_{z_1}$
J8d	Calculate the effective stress of the element using $\{\sigma\}$ and σ_z
J8e	Is the effective stress of the element > the effective stress at kink I? (Yes - J8f ; No - J9)
J8f	Is the effective stress of the element within +1% of the effective stress at kink I? (Yes - J8j ; No - J8g)
J8g	Set IP=1 to indicate this increment will be processed in 2 parts

Block	Adaptations
J8h	Obtain the next approximation of the total strain increment to take the state of the element to kink I by binary halving
J8i	Go to J7 and proceed
J8j	Set H' of the element to H' of the elastoplastic curve just beyond kink I
J10a	Is IP = 1? (Yes - J10b ; No - J11)
J10b	Calculate remainder of increment not processed and set $\{\Delta\varepsilon'\}$, $\{\Delta\sigma'\}$, $\Delta\sigma'_z$ accordingly
J10c	Set IP = 0
J10d	Calculate σ_{I_o} , σ_{II_o} , σ_{z_o}
J10e	Go to J2 and proceed

CHAPTER 2

SOME PARAMETRIC STUDIES ON THE SETTLEMENT AND BEARING CAPACITY OF A SATURATED CLAY LAYER SUBJECT TO UNDRAINED STRIP LOADING

2.1. Introduction

The elastoplastic models of Chapter 1 are employed here as idealisations for several parametric studies on the settlement and bearing capacity of a saturated clay layer subject to undrained strip loading. Some stress distributions obtained from these studies are also presented, to be subsequently used in 1- and psuedo 3-dimensional consolidation analyses as total stresses. A practical example consisting of uniform strip loading on a normally consolidated clay layer is devised as the basis for the above studies. To begin with, a working load is applied to a linear elastic, isotropic, homogeneous half-space idealising the soil conditions of the practical example. The adoption of a linear elastic material is in accordance with traditional approach to a working load problem. This idealisation is justified on the grounds that in the early portion of the triaxial stress-strain curve, a constant stress-strain modulus may be reasonably assumed. Also, in the present studies, the question of elastic recovery, which detracts from observed behaviour, does not arise since there is no

unloading. As there is no volume change, Poisson's ratio is taken to be approximately 0·5.

The existence of a classical solution to the stresses in the above half-space problem enables a check to be made on the accuracy attainable with the type of assemblage in general use here (the surface settlement is theoretically infinite, and thus cannot be modelled). It will be shown that with a suitable choice of assemblage, quite accurate stresses are computed, and the opportunity is thus taken to extend the work of Gibson and Sills (22) - in classical analysis - on stresses in a fully heterogeneous, linear elastic half-space, by studying the stresses in random inhomogeneous half-spaces using the adopted mesh.

Half-space idealisations such as the above are, however, better suited to the study of extensive soil masses. Next, therefore, a linear elastic, isotropic, homogeneous layer is adopted as a simple, initial assessment of the earlier practical example, assuming a working load. The choice of a suitable assemblage for this problem is based on a favourable check on the computed stresses and surface displacements against those obtained by Poulos (10) via numerical solution.

When studying the collapse of cohesive soil bodies - e.g. of saturated, undrained clays - that are subject to strip loading, it is customary to idealise the material as elastic-rigid, perfectly plastic, obeying the Tresca yield criterion and its associated flow rule. This is based on the premise that a soil element can

develop large, irrecoverable strains at failure, prior to which the strains are, by comparison, negligible. The yield surface and the associated flow rule as well as the initial rigid behaviour lead to the required zero volume change condition.

By combining the linear elastic and rigid plastic materials of the traditional approach to the problems of settlement and collapse respectively however, the resulting linear elastic, perfectly plastic material can provide the basis for studying the intermediate loading range. The latter material is a simple one that retains the important characteristics of the traditional materials so that experience built up around these is still relevant. For instance, the path independence of the collapse load of a perfectly plastic material (23a) ensures that earlier work on collapse is still applicable. This is entirely in keeping with the intention of the present parametric studies.

For some time solutions have been available only for strip loading on linear elastic uniform half-spaces and single and contiguous layers, and rigid plastic uniform half-spaces. The limit theorems (24), although providing a powerful means for studying collapse, can lead to unacceptable estimates of the collapse load - e.g. for parametric studies. Recently, however, there have been significant advances in parametric studies involving both linear elastic and rigid plastic half-spaces and layers (25 , 26 , 27 , 28 , 29) using classical as well as numerical methods of analysis. Further such studies are undertaken here, including the behaviour in the intermediate loading range, an understanding of which will be contributory to

safe and economical design.

To begin with, the earlier elastic working load layer model is replaced by a linear elastic, perfectly plastic, isotropic, homogeneous layer idealisation that is applicable throughout the entire loading range to collapse. The latter is, as before, a simple, initial assessment of the practical example, and thus serves as the basis for the following parametric studies.

A smaller mesh (i.e. laterally) than that of the elastic model is adopted for economy of computation. The reduction, however, has no significant effect on the accuracy of the elastic solution nor is the computed collapse load noticeably different from that for the initial layer mesh, as will be shown. The computed collapse load will be shown to be in excellent agreement with the well-known Prandtl result, $(\pi + 2)\, c_u$ (30), and to be relatively insentitive to reasonably-spaced rigid boundaries so that for a half-space mesh, the Prandtl result will be closely approximated. Thus in view of the accurate modelling of both elastic and elastoplastic behaviour attainable via the present numerical approach, the following parametric studies may be undertaken with some confidence.

To begin with, the effects of varying the thickness of the layer are examined.

Next, inhomogeneity of rigidity, and hence strength about the centre of the load is studied. This is bound to occur in the real situation to some degree even with a relatively uniform soil.

Similarly, asymmetry of loading is considered. The cases dealt with are also relevant to the eccentric loading of footings whereby a linear stress distribution of the subgrade reaction is assumed in design.

It is generally accepted, however, that the undrained rigidity and strength of a normally consolidated clay layer varies approximately linearly with depth due to increasing effective overburden pressure (25, 28). This thus provides the basis for an important parametric study.

A stiff crust can then form at the surface due, for example, to overconsolidation as a result of surface drying (28). The effect of this is also considered.

If, during sedimentation, the clay layer of the practical example on pp.113 was underlain by a layer of softer material, a "stepped" linear variation of rigidity and strength would be a better idealisation (31). This case is next studied.

Another problem considered is that of random inhomogeneity of rigidity and strength of the layer. An instance where such a distribution is appropriate may be construed as follows.-

Assume, say, the layer of the practical example to undergo heavy overconsolidation until its rigidity and strength become approximately constant at all points. Then, as a result of the consolidation of nearby structures, varying degrees of pore pressure build-up occur at different points so that the layer weakens non-uniformly.

Finally, the stress-strain curve of the triaxial test is more closely modelled by approximating it as a series of elastic, then elastoplastic lines. In one case the slopes of these lines decrease steadily with strain until peak strength is reached, when the material strains without further stress increase. It has been found from experiments, however, that some degree of "post-peak" softening is bound to occur for both normally and overconsolidated saturated clays under undrained loading (32). This then forms the basis for the other study in which a moderate sensitivity of the clay is assumed.

The studies undertaken in the present chapter as described above are presented in four main sections. In Part A, the practical example of undrained strip loading is outlined. The linear elastic finite element models of the practical example are then analysed and the computed stresses and displacements compared with known solutions to obtain a measure of the accuracy of these models. Some results of stresses in random inhomogeneous half-space models are also included. In Part B, the basic model, i.e. the linear-elastic, perfectly plastic, isotropic, homogeneous layer model of the practical example is examined in detail, thus providing some initial experience in the behaviour of the type of models that are used subsequently . In Part C, further parametric studies using similar elastoplastic models are undertaken. Finally, in Part D, a number of parametric studies are initiated to provide the basis for future studies.

PART A - A PRACTICAL EXAMPLE AND SOME ELASTIC MODELS

2.2. A practical example of undrained uniform strip loading on a normally consolidated, saturated clay layer and the soil mechanics idealisation

Fig. 22(a) illustrates a long warehouse at the end of construction, founded on a normally consolidated, saturated clay layer overlying a rough rock base. The warehouse is lightly framed and cladded so that the footing loads are small compared to the uniformly distributed storage load. The ground slab is thin in relation to its width since it is designed to enlist ground support. The problem is thus one of undrained uniform strip loading on a layer overlying a fully-adhesive, rigid base.

As suggested earlier, the clay is idealised as a linear elastic, perfectly plastic material. On this basis, it is further assumed that its undrained rigidity E_u and shear strength c_u vary linearly with depth (Fig. 22(c)); as already pointed out, this is a reasonable approximation, and reflects the influence of the increasing effective overburden pressure with depth.

The E_u and c_u distributions adopted are based on an example given by Duncan and Dunlop (33). Hoeg (21) also suggested using the relation : $E_u = 1000\ c_u$ for normally consolidated clays as well as lightly overconsolidated clays of low plasticity.

The deviator stress - axial strain curve from a standard triaxial compression test on a typical clay sample is shown in Fig. 22(b). The sample is consolidated under a cell pressure approximating the effective overburden pressure at the point from which it is taken, then sheared undrained.

The ideal linear elastic, perfectly plastic curve is obtained from the above plot as follows.

The linear elastic line OB is drawn from point O to intersect the triaxial plot at point A which corresponds to 65% of the maximum deviator stress - i.e. 65% of $2c_u$ since, following standard practice (34a), the triaxial and uniaxial tests are taken to be the same.

This procedure is based on the premise that, assuming a working load with a factor of safety of 3 against collapse, the maximum shear stress in the layer is unlikely to exceed 65% of the shear strength (Skempton - (35)). Duncan and Dunlop (33) appear to have used the same criterion. Thus, for a working load, it is reasonable to expect a factor of safety against local shear failure of about 1·5. Furthermore, the line OA is the best fit to the triaxial plot that is conservative; it generally approximates the plot fairly well.

Point B is taken to be the elastic limit since the maximum shear stress then equals the shear strength. For perfect plasticity, the ideal curve proceeds horizontally from that point, i.e. along BC.

Since the uniaxial and triaxial tests are the same, E_u is read as E and c_u as $\frac{\bar{\sigma}}{2}$ (for the Tresca material, the shear stress at

yield = 0·5 the uniaxial stress at yield (18)), in the notation of Chapter 1. Also the uniform strip load p is denoted as t in Chapter 1. Since the material is perfectly plastic, H' = 0.

The Tresca yield surface and its associated flow rule, coupled with a Poisson's ratio approximating 0·5, closely model the zero volume change requirement of undrained loading on the saturated clay layer.

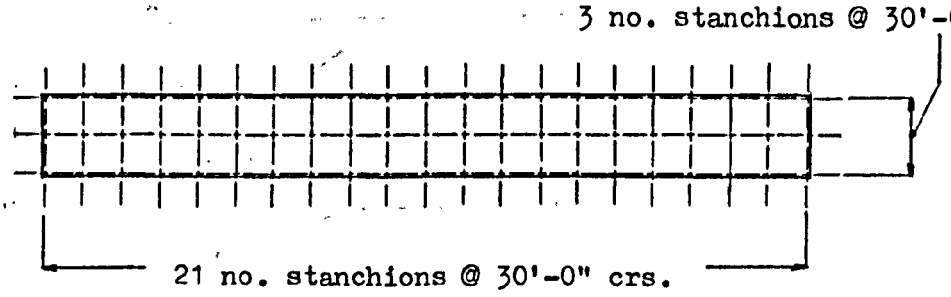

Plan of warehouse

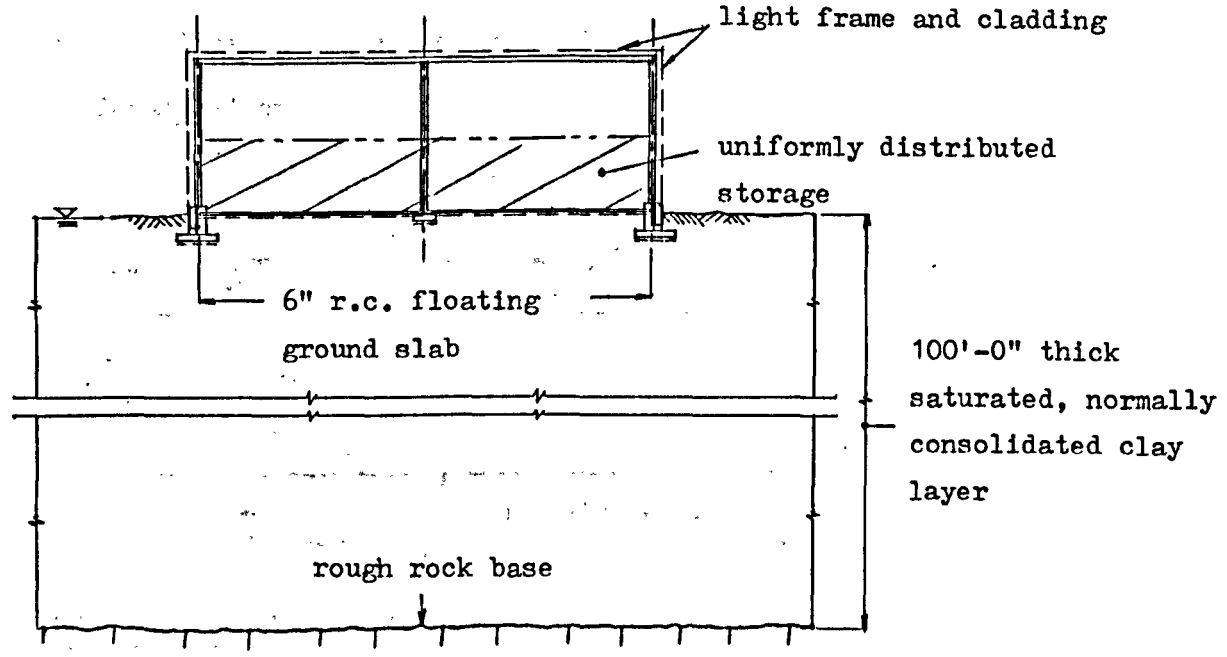

Typical cross-section through warehouse

(a) The practical example (applies to mid section of warehouse and at end of construction only)

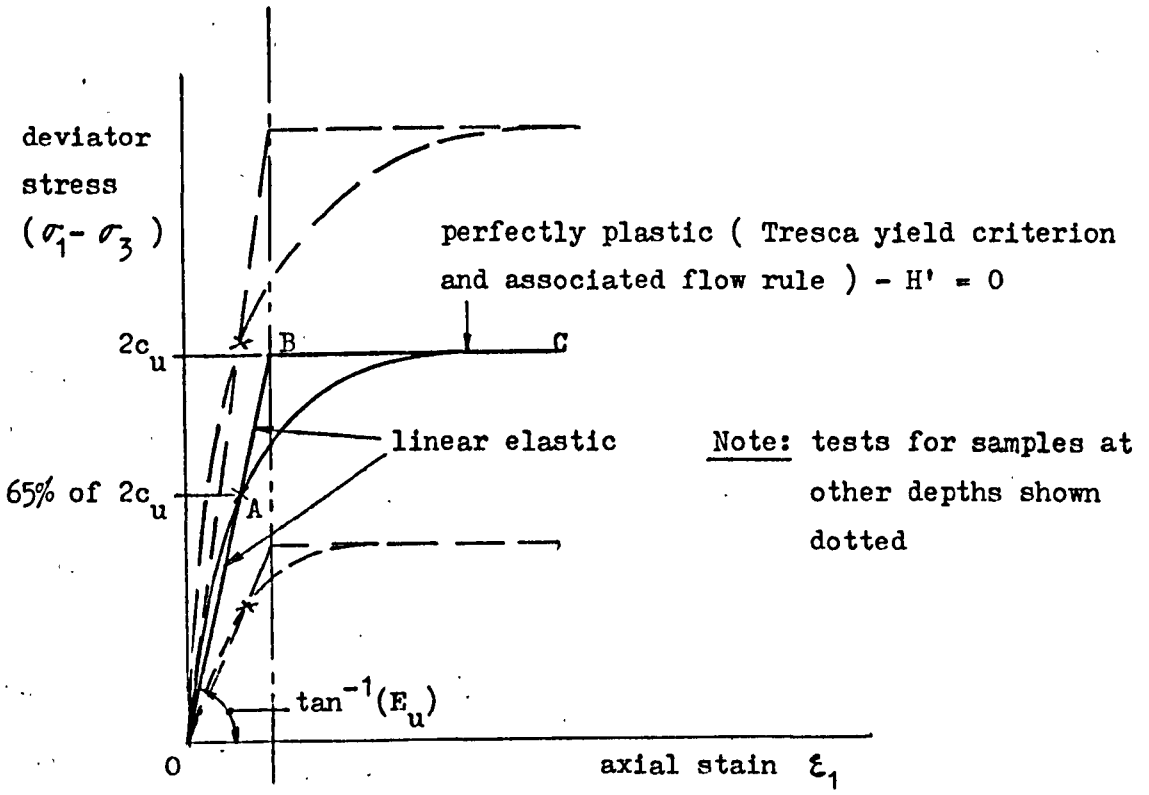

(b) Consolidated undrained triaxial compression test and elastoplastic idealisation

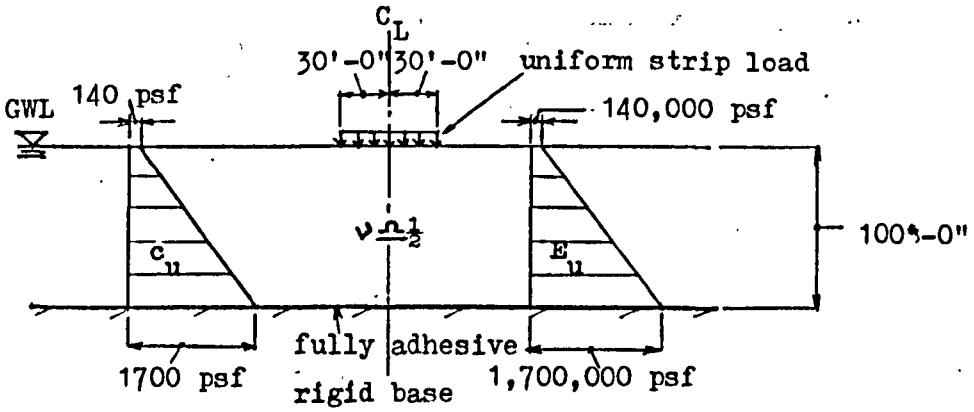

(c) The soil mechanics idealisation

Fig. 22. A practical example of undrained uniform strip loading on a normally consolidated, saturated clay layer and its idealisation

2.3. The linear elastic, isotropic, homogeneous half-space model (flow chart in Section 1.2.7.1.)

Fig. 23(a) shows a linear elastic, isotropic, homogeneous half-space idealisation for an extensive body of clay with the properties of the layer of Section 2.2., and subject to the same loading.

Since we are concerned here with the stresses, and these are theoretically independent of both Young's modulus and Poisson's ratio (37a), the choice of these parameters can be quite arbitrary. Nevertheless, the values at the average point (34b), which corresponds to the centre of the pressure bulb and has been taken as being representative of a soil body with some success (34b), are adopted.

The depth of the pressure bulb is approximately equal to that of the layer of Section 2.2. and thus, the elastic parameters of the average point are assumed to those at mid-depth in the layer. Incidentally, this depth coincides with the recommended minimum for a site investigation and thus the layer should be fully probed.

The collapse load for the half-space, assuming c_u to be the average point value, is given by Prandtl's expression, $(\pi + 2)\, c_u$. Thus, with a factor of safety of 3 against collapse, the working load is 1500 psf (c_u being 920 psf) - it will be shown in a later parametric study that this is excessive, although it suffices for the

present purpose.

Fig. 23(b) shows the finite element model adopted for the half-space idealisation. The mesh is the best choice amongst several trial assemblages from the point of view of accuracy and economy of computation. Christian and Carrier (29) used a similar configuration in their study of circular loading on a linear elastic half-space. They found that, to maintain accuracy of the computed displacements for a nearly incompressible material, a frictionless bottom boundary and a free lateral boundary are required. The mesh here is considerably larger, however, and the boundaries thereby more remote.

Also, as will be shown, it leads to reasonably accurate computed stresses, the only requirements for such accuracy being that (a) the mesh is reasonably fine in the vicinity of the load, (b) the Bays are of limited slenderness and (c) the boundaries are sufficiently remote. Indeed, the slenderness of some Bays adopted by Christian and Carrier are well beyond the recommended limit.

The fixed joints at the boundaries are justified on the grounds that when the latter are at infinity, the joint displacements are zero.

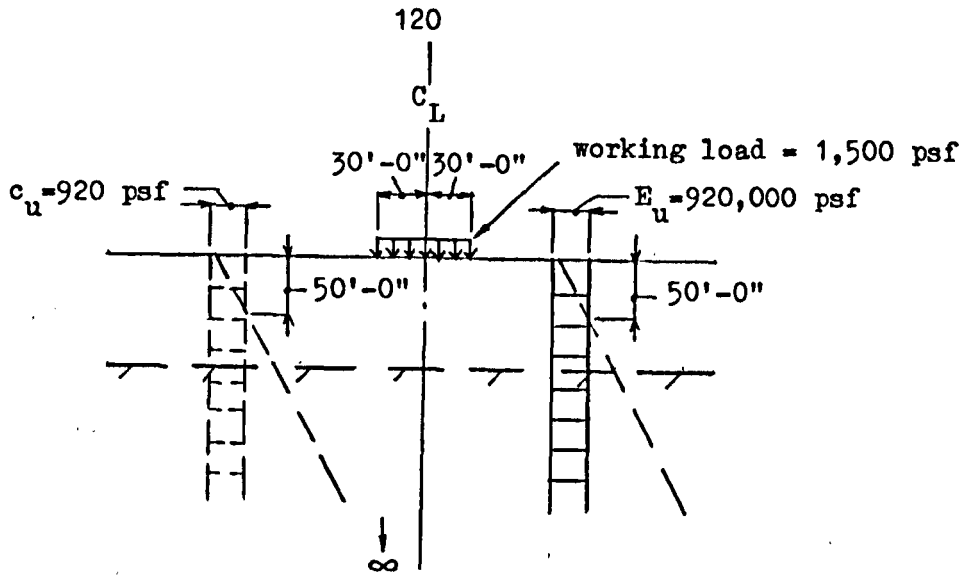

(a) The linear elastic, isotropic, homogeneous half-space idealisation

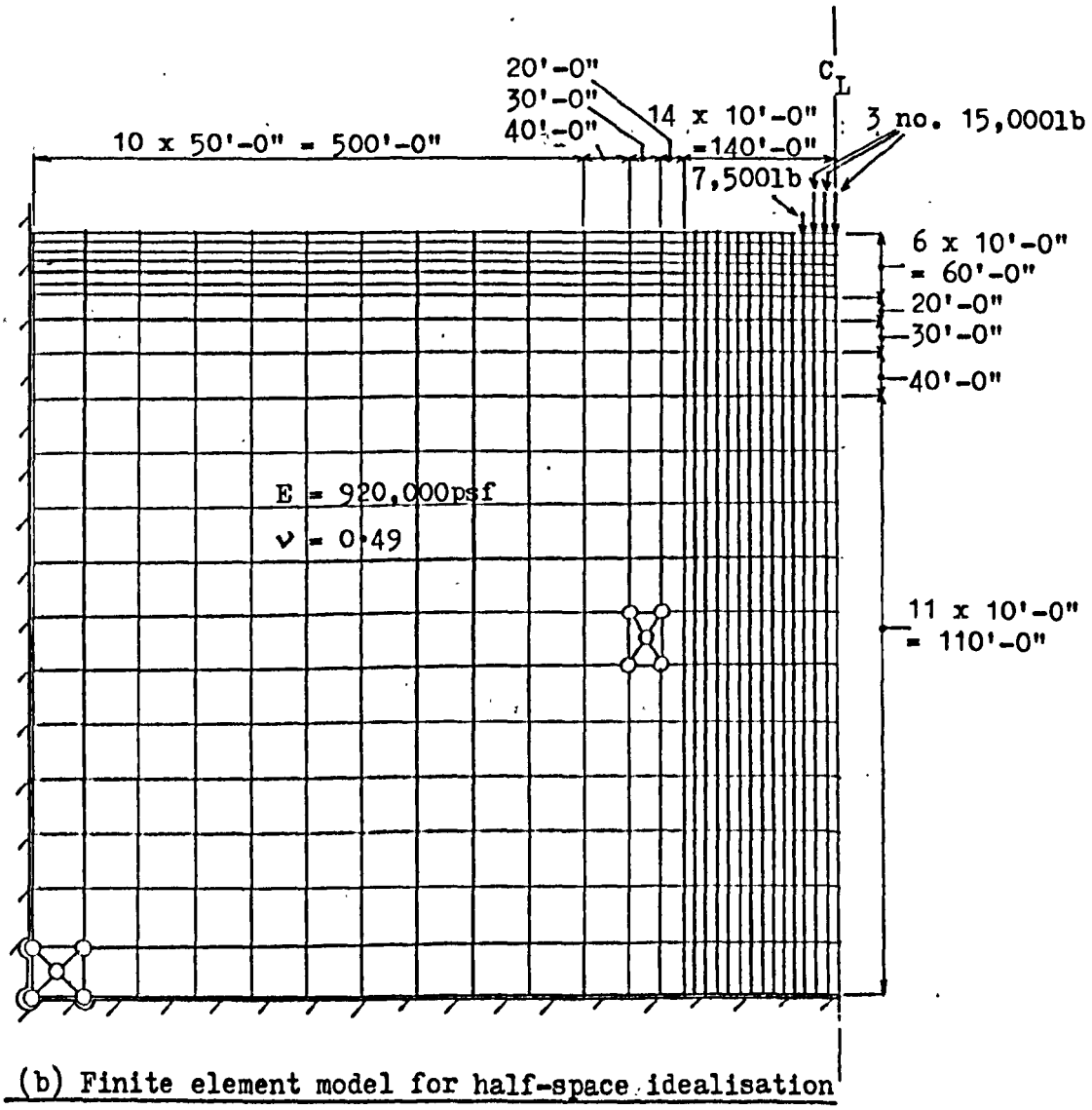

(b) Finite element model for half-space idealisation

Fig. 23. Half-space idealisation of an extensive clay body

2.3.1. Accuracy of stresses computed from the finite element model

Figs. 24 and 25 show the stresses down the centre and edge, respectively, of the strip load. The values given by classical solution (37a) as well as those computed via the finite element model are plotted. The latter are obtained as follows.

The stresses in the respective finite elements are assumed to act at their centroids. For neighbouring elements, these are then averaged and given equal weighting in determining the position of the resultant. Thus, as shown in Fig. 24, the average stresses generally occur at internal joints, except for the surface elements.

The above procedure thus effectively combines two suggested methods by Zienkiewicz and Cheung (38) to cater for the "jump" in stress values across the constant stress finite elements. The same procedure is applied to all subsequent stress plots, and where checks are made, will be shown to be generally quite successful. For the elastic solutions, only σ_x, σ_y and τ_{max} are plotted since these are sufficient to specify the state of stress at any given point.

Returning to the present problem, it can be seen from Figs. 24 and 25 that in general, close agreement between the stresses by classical solution and those computed, is obtained.

There are, however, two exceptions, namely:-

(a) For τ_{max} down the edge (Fig. 25(c)), the computed stresses depart from the classical solution, towards the surface. This is because the true stresses along the surface change too abruptly at the edge (i.e., $\frac{p}{\pi}$ at the edge and zero on either side of it, p being the uniform strip load) so that the constant stress finite elements are unable to model the stresses in the vicinity of the edge accurately. Other stress plots (including those of the elastic layer problem of Section 2.5.) do not undergo such abrupt changes and thus, there are no significant errors in the computed stresses. By further refining the mesh around the edge, the above error may be contained in a small, localised area.

(b) At greater depths, there can be significant differences between the computed stresses and those given by classical solution. This is due to the slenderness of the Bays there, and the inaccuracy is accentuated by the small stress values as well. However, because they are small, they are relatively unimportant in practice.

The stress contours over the half-space are also plotted, using the SYMAP package (39). The stresses are supplied as input data, the points at which they act having been specified a priori. The package then interpolates (or extrapolates) amongst points to determine the contours which are then produced on line-printer.

Fig. 26 shows the stress contours obtained by (i) classical

solution, (ii) classical solution and plotted with SYMAP, and (iii) computation and plotted with SYMAP. It can be seen from these plots that for the computed stresses, SYMAP gives a reasonable indication of general trends.

Further improvement - especially in the vicinity of the load - via (a) specification of more data points, and (b) better usage of SYMAP (e.g. by opting for particular routines rather than, as here, for default routines), is envisaged.

2.4. Stresses in linear elastic, isotropic, random inhomogeneous half-spaces (flow charts in Sections 1.2. and 1.2.7.2.)

The success with which the finite element model of the previous section is able to model stresses in the homogeneous half-space, and the obvious ease with which varying degrees of inhomogeneity may be attributed to the model leads to the present studies in random inhomogeneity.

These studies are prompted by an earlier paper by Gibson and Sills (22) where it was shown that the stresses in a linear elastic, isotropic, fully heterogeneous, incompressible half-space are identical to those of the linear elastic, isotropic, homogeneous half-space whose solution has been known for some time (37a).

The above finding posed the question as to whether the same result would be found for other space variations in the elastic moduli, provided these were sufficiently smooth.

Gibson and Sills found, however, that when the condition of incompressibility is relaxed in the fully heterogeneous case, the stresses do change, σ_x and τ_{max} being extremely sensitive to Poisson's ratio. This came as a surprise in view of the insensitivity of the stresses to Poisson's ratio in the homogeneous case.

Another possibility is that if the half-space is kept incompressible, the stresses may still be insensitive to varying

degrees of inhomogeneity of Young's modulus in the half-space. A stringent test of this possibility would seem to be to assume random inhomogeneity of Young's modulus.

Thus, in the first study, Poisson's ratio is taken to be 0·49 and Young's modulus allowed to take random values ranging from 500,000 to 5,000,000 psf, attributable to soft clay and shingle, respectively. In this study - as well as the next - the mesh and type of loading of Fig. 23(b) are the obvious choice; a strip load of 1500 psf continues to apply to provide a ready means of comparison of the computed stresses with those of the homogeneous case.

To ensure a truly random selection of Young's modulus, the ULCC RANF subroutine (40) is adopted: RANF generates values according to a rectangular distribution.

Figs. 24 and 25 show the computed stresses down the centre and left edge, respectively, of the strip load, for the above random distribution of Young's modulus. These stresses oscillate about the stress plots for the homogeneous half-space, which act as approximate mean plots. An examination of the corresponding SYMAP plots (Figs. 27 and 28) shows that this behaviour is generally applicable in that, whilst there are differences of detail between the plots, they do nevertheless exhibit similar general trends.

Thus, on the basis of the above evidence alone, the possibility that the stresses for random Young's modulus in an incompressible half-space agree with those of the homogeneous half-space remains open: it

could be argued that the differences of detail are attributable to non-smooth inhomogeneity through the use of finite elements with constant Young's modulus.

However, the author's view is that this interpretation is untenable. By it, the relaxation of incompressibility ought to lead to some distinct changes in the stress plots alike those shown by Gibson and Sills (22) for τ_{max}, instead of which, when a random distribution of Poisson's ratio in the half-space (from 0 to 0·49, also using RANF) is further assumed, the computed stress plots again follow the general trend of those of the homogeneous case, the differences being of detail (cf. Figs. 27 and 29; also see Figs. 24 and 25). Since the common ground in the above two cases is that both have random inhomogeneous distributions of material constants, a more attractive explanation for the above similarities in the stress plots may be advanced via an analogy to the physical behaviour of metals: for the latter, random inhomogeneity at the crystalline level can nevertheless lead to reasonable homogeneity at the macroscopic level.

By the same token, it can be argued that as the mesh is further reduced, the half-space becomes increasingly random inhomogeneous so that the differences of detail of the stress plots should thereby reduce. A completely random distribution would thus have the effect of a homogeneous medium. This argument is, in fact, contrary to the earlier notion that the differences of detail are caused by non-

smooth inhomogeneity.

It should, however, be recognised that explanations hitherto advanced for the behaviour of the stress plots are hypothetical. A fuller investigation involving variations in the degree of fineness of the mesh, adoption of different random distributions of the material constants, etc. is recommended. Further study along these lines is justifiable owing to the inherently highly non-uniform nature of soils.

It will be noted that the SYMAP plots shown here are obviously inaccurate around the surface. This is because data points were not specified at the surface, unlike the SYMAP plot of Fig. 26. However, they do serve the present purpose adequately.

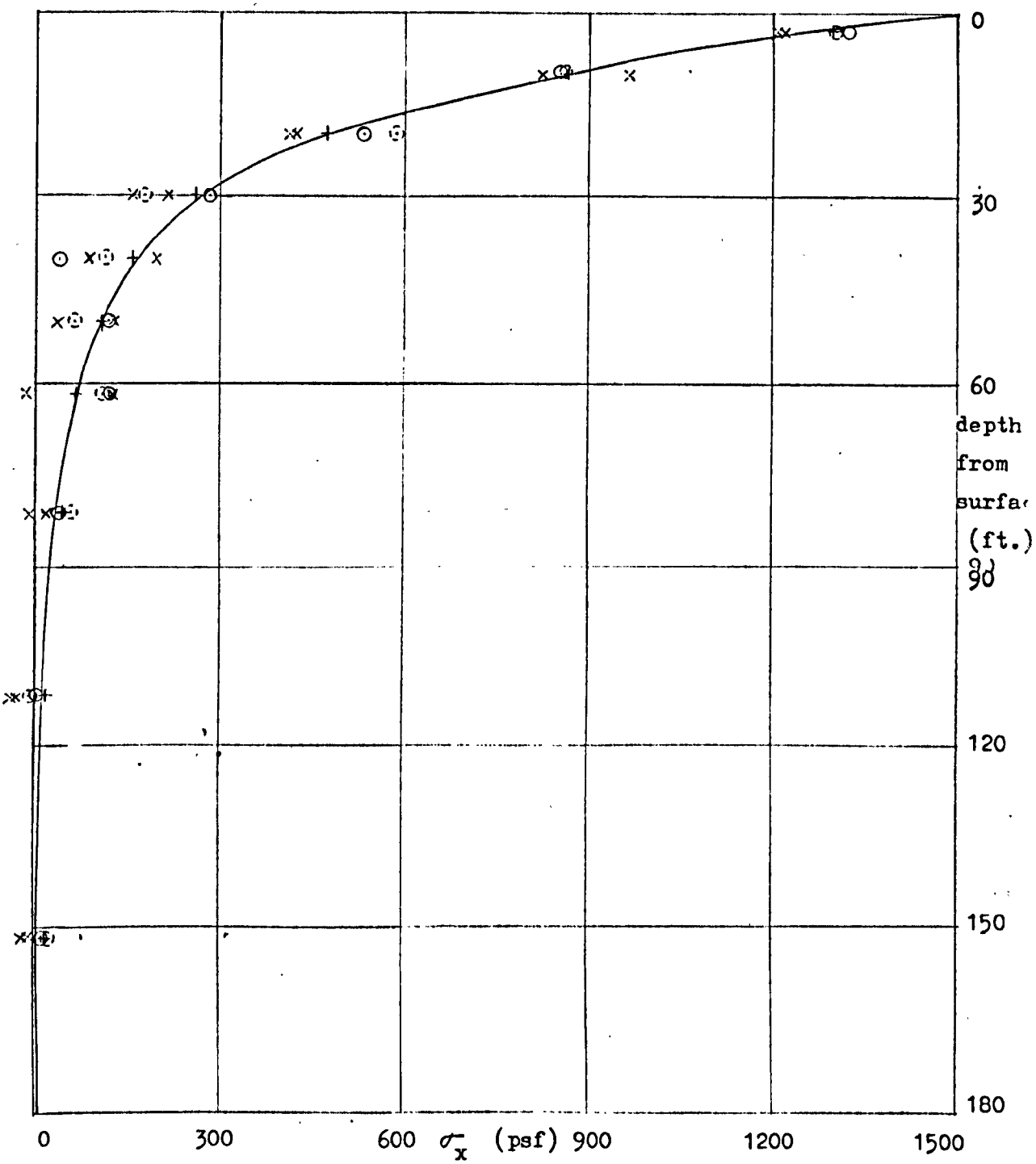

(a) σ_x distributions down centre of strip load p

(Key to symbols in Figs. 24 and 25 :-

- homogeneous (classical solution)
+ - homogeneous (computed)
⊙ - random E, =0·49 ; 1st set ⊙ - 2nd set
× - random E and ; 1st set × - 2nd set)

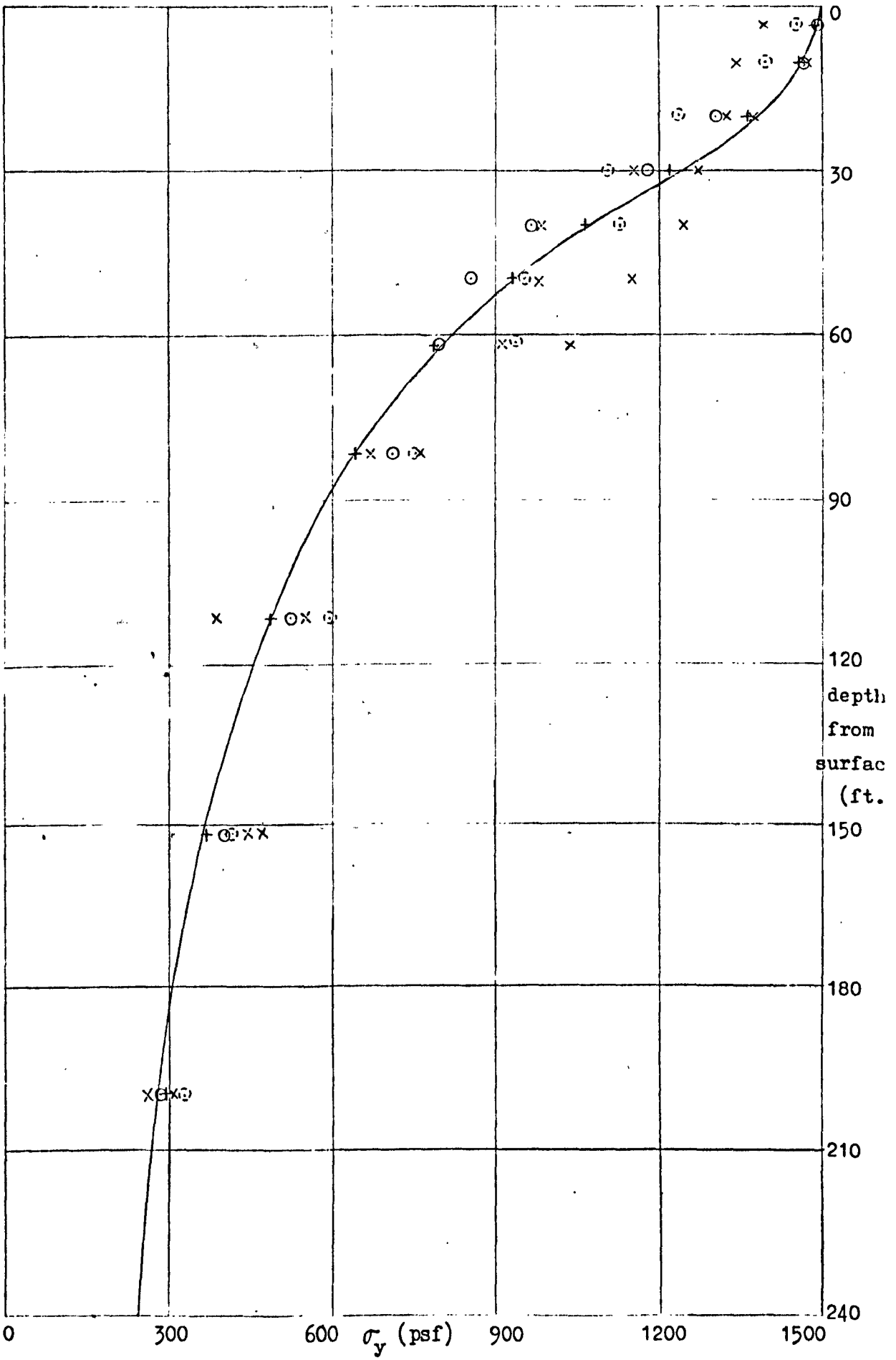

(b) σ_y distributions down centre of strip load

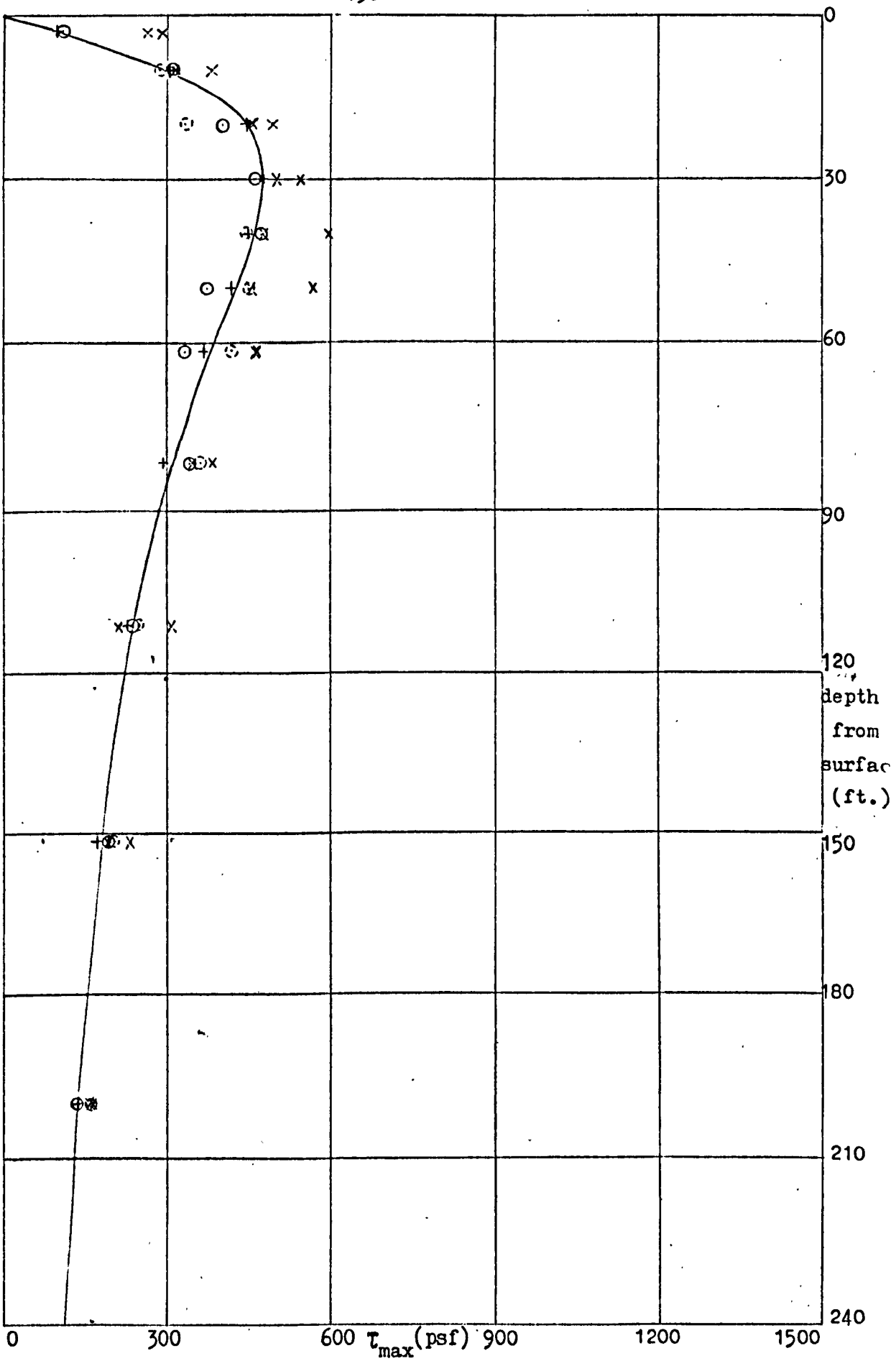

(c) τ_{max} distributions down centre of strip load

Fig. 24. Stress distributions in elastic half-spaces down centre of strip load

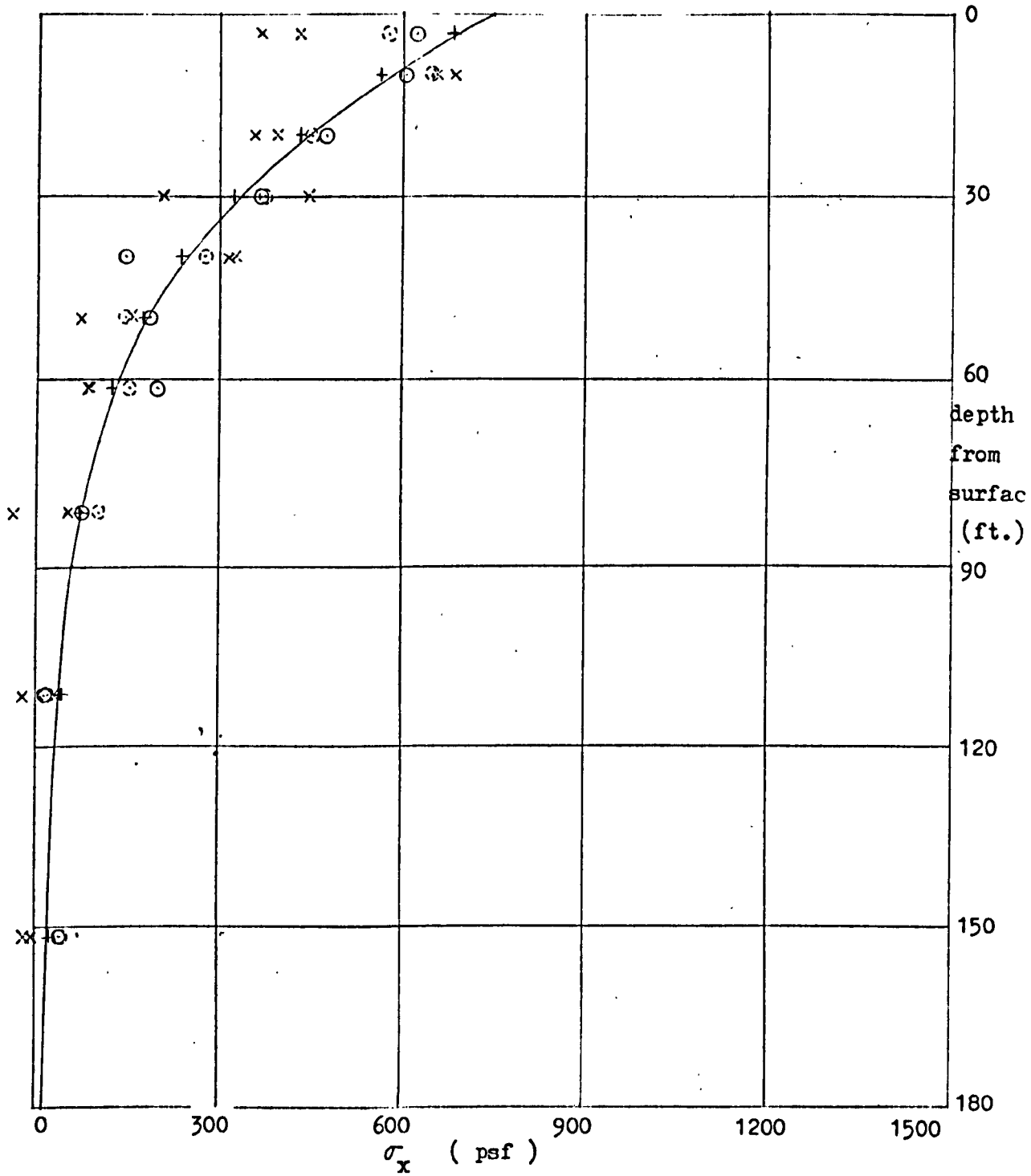

(a) σ_x distributions down edge of strip load

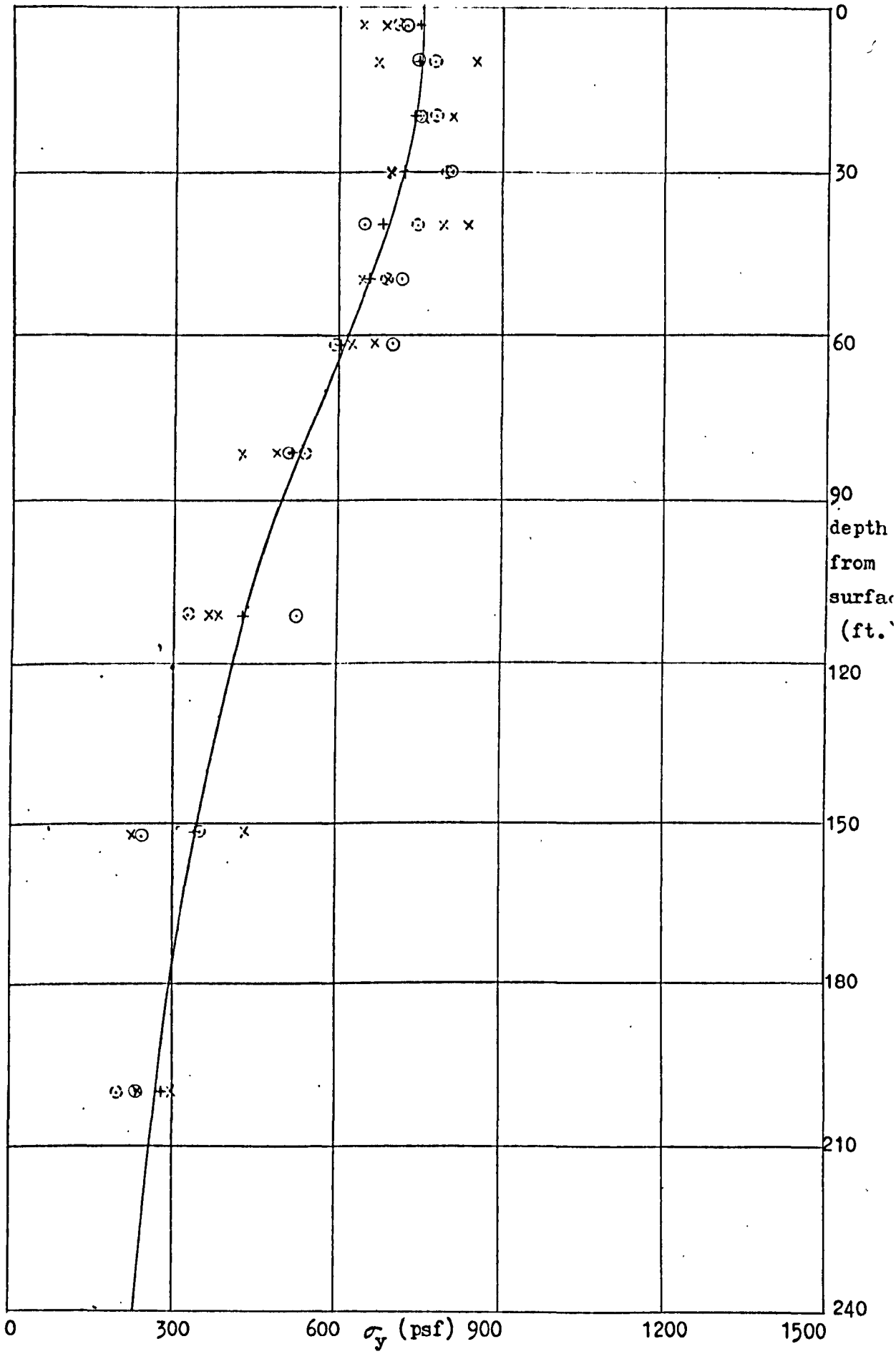

(b) σ_y distributions down edge of strip load

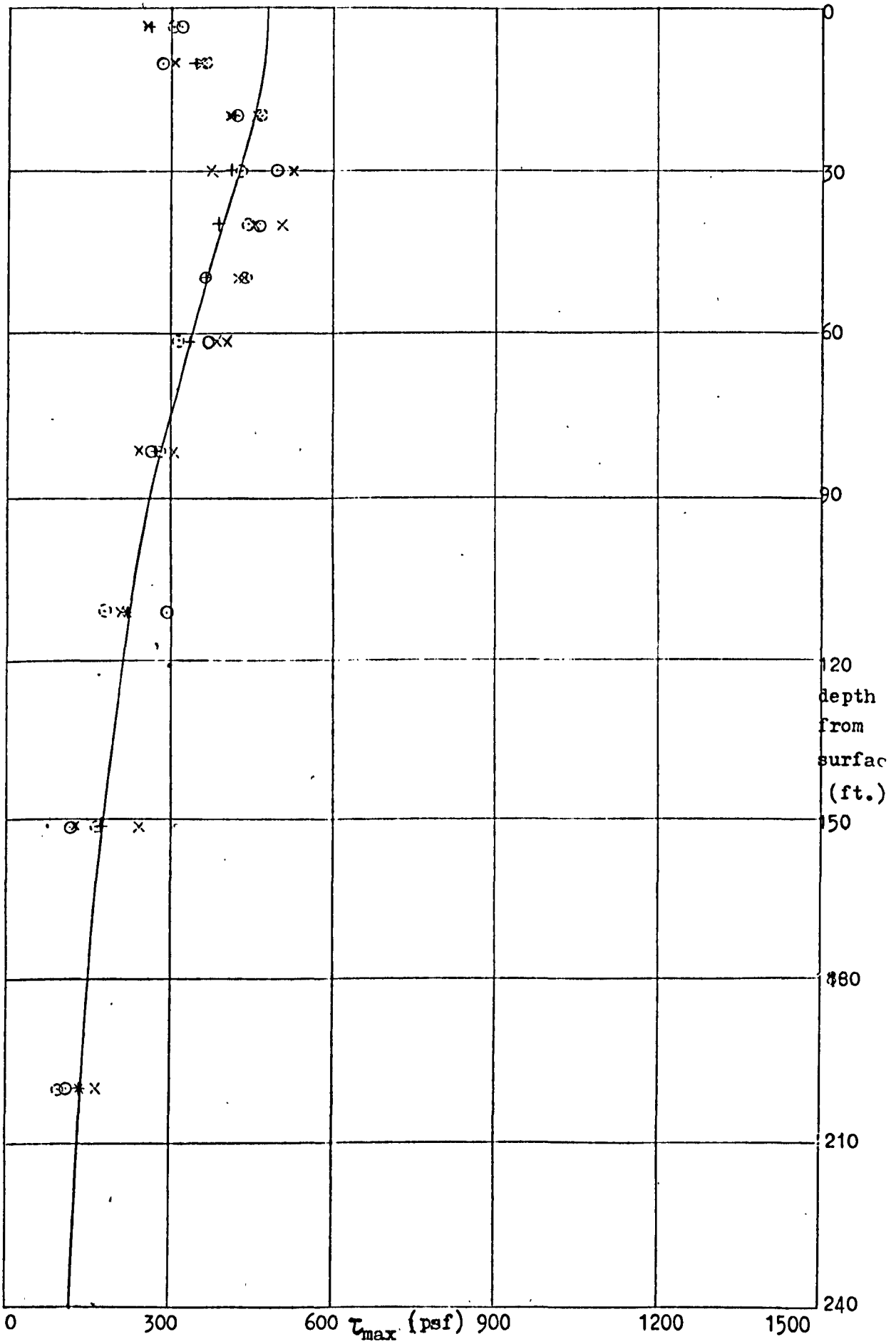

(c) τ_{max} distributions down edge of strip load

Fig. 25. Stress distributions in elastic half-spaces down edge of

Key to symbols in Fig. 26:-

——— - classical solution hand plotted

– – – - classical solution by SYMAP

-·-·- - finite element solution by SYMAP

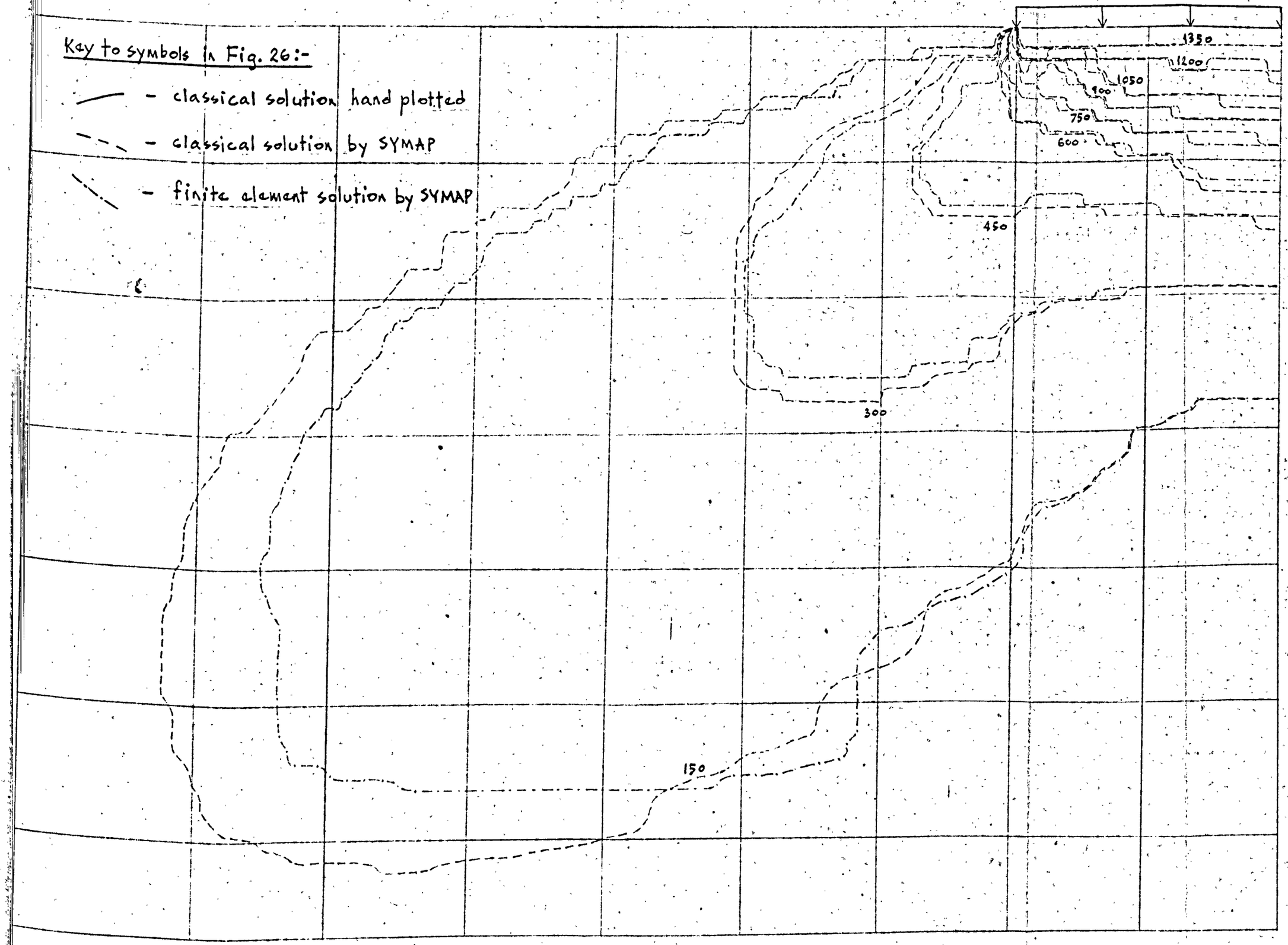

(a) σ_x contours

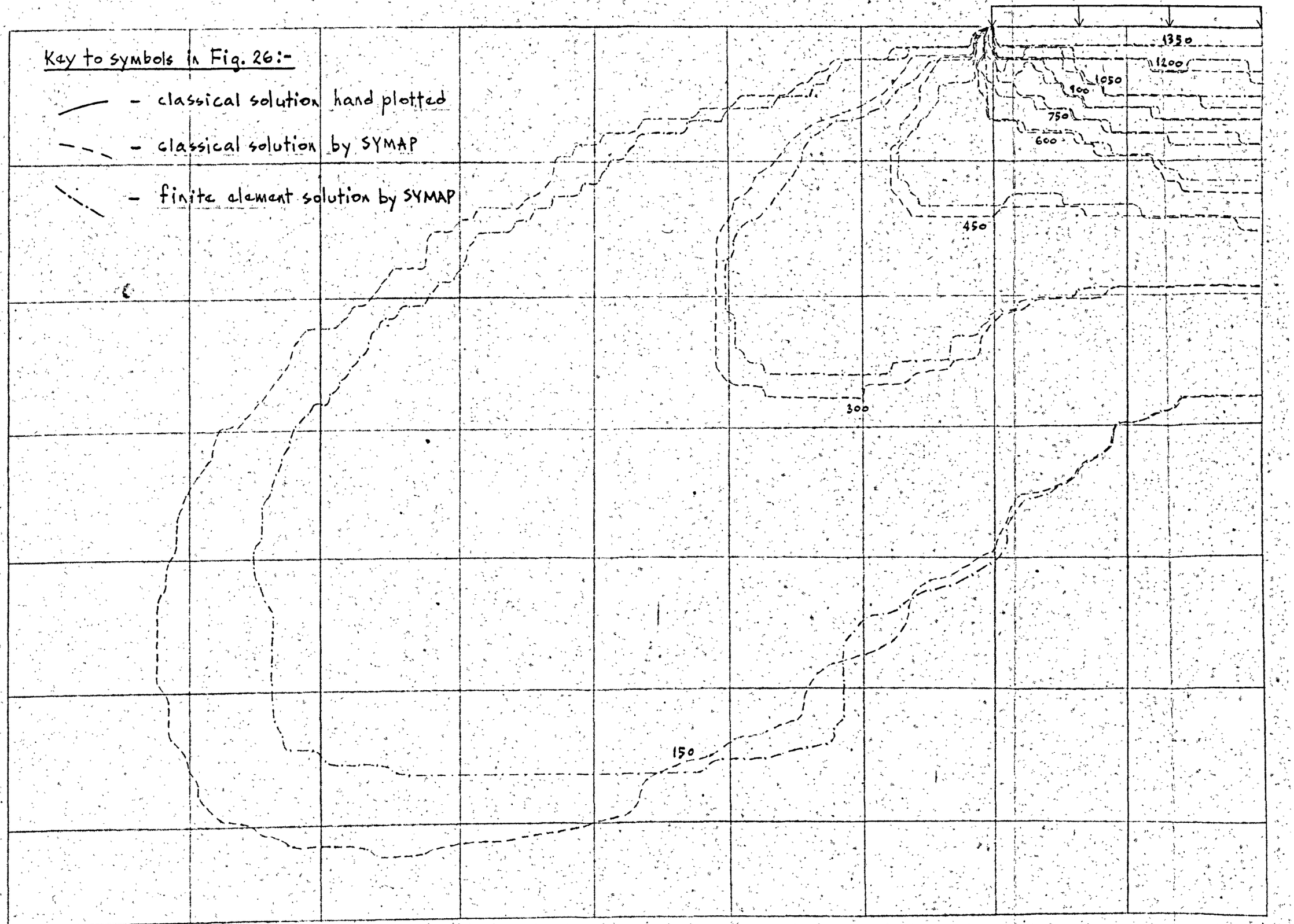

(a) σ_x contours

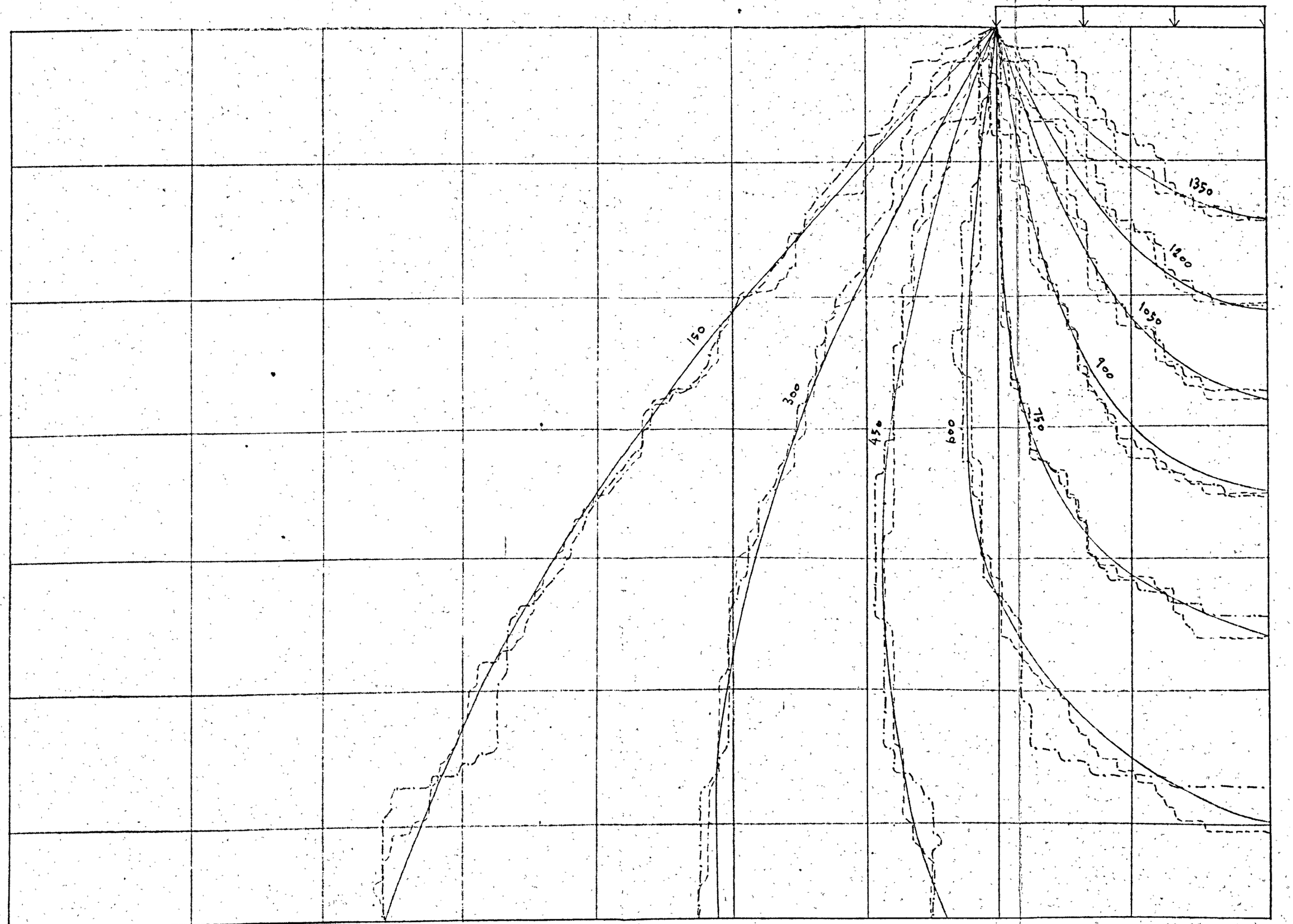

(b) σ_y contours

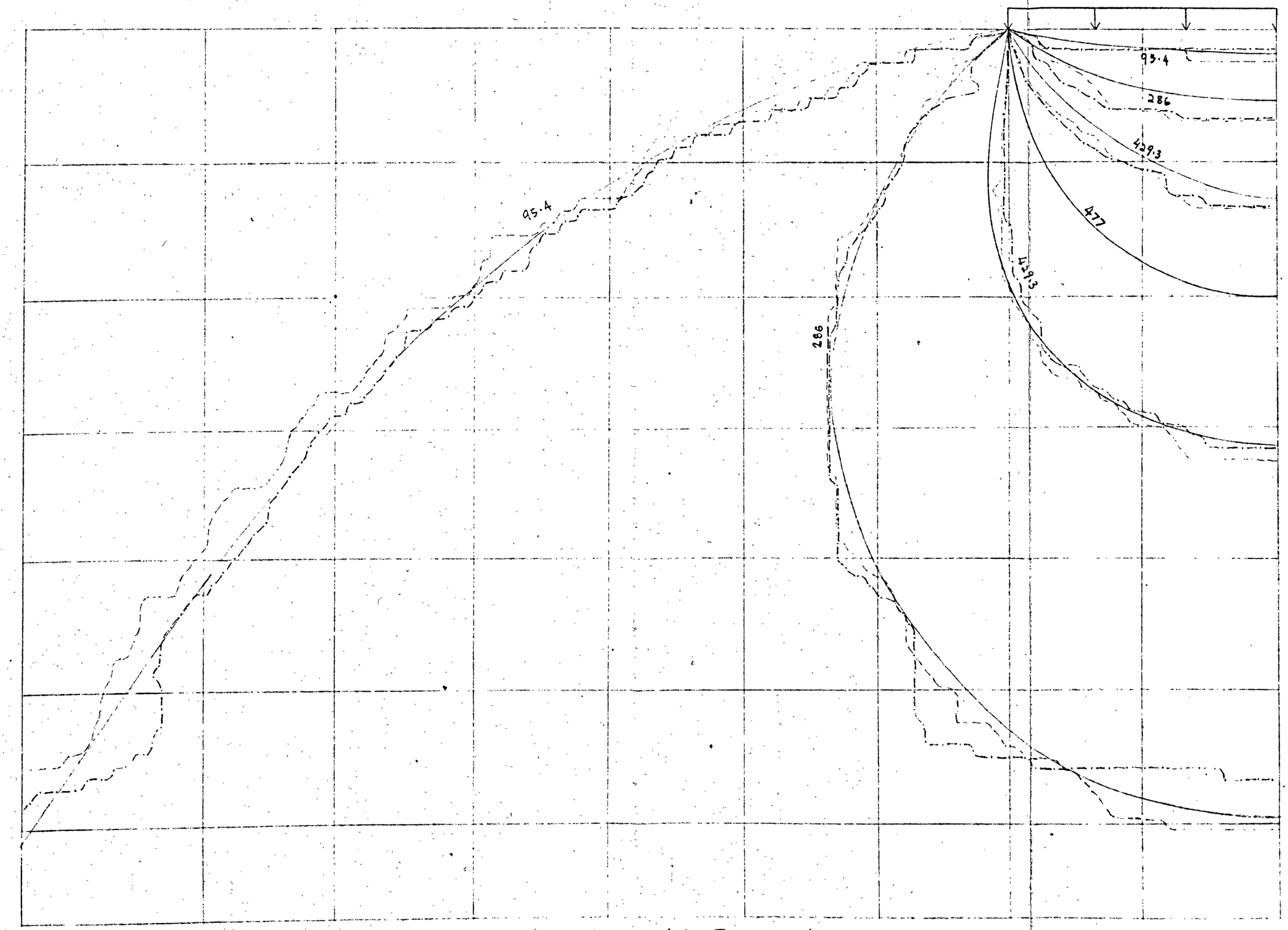

(c) τ_{max} contours

Fig. 26. Stress contours of elastic half-space for working load of 1500 psf by SYMAP (surface data points prescribed) - all figures in psf (HOMOGENEOUS)

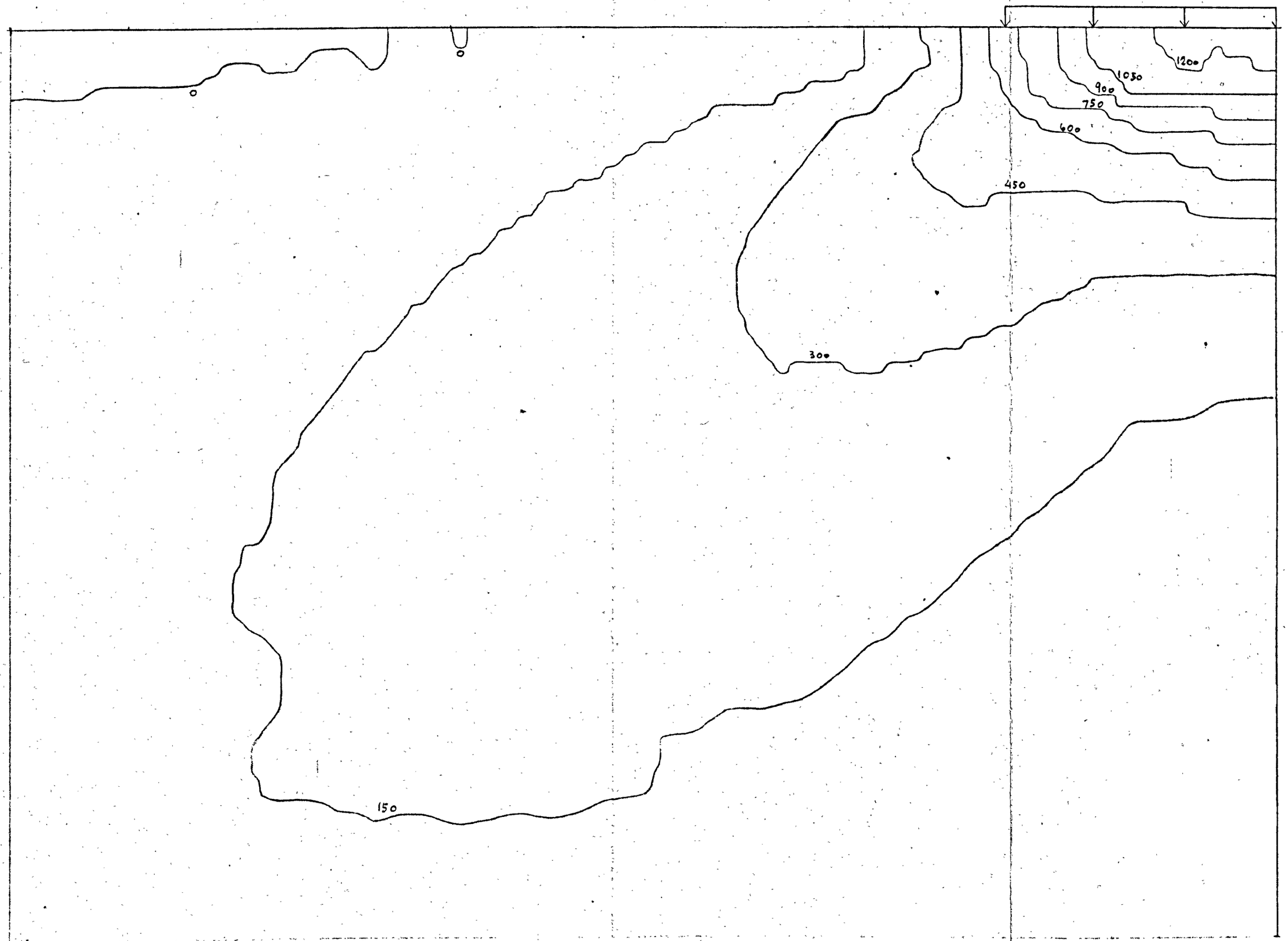

(a) $\bar{\sigma}_x$ contours

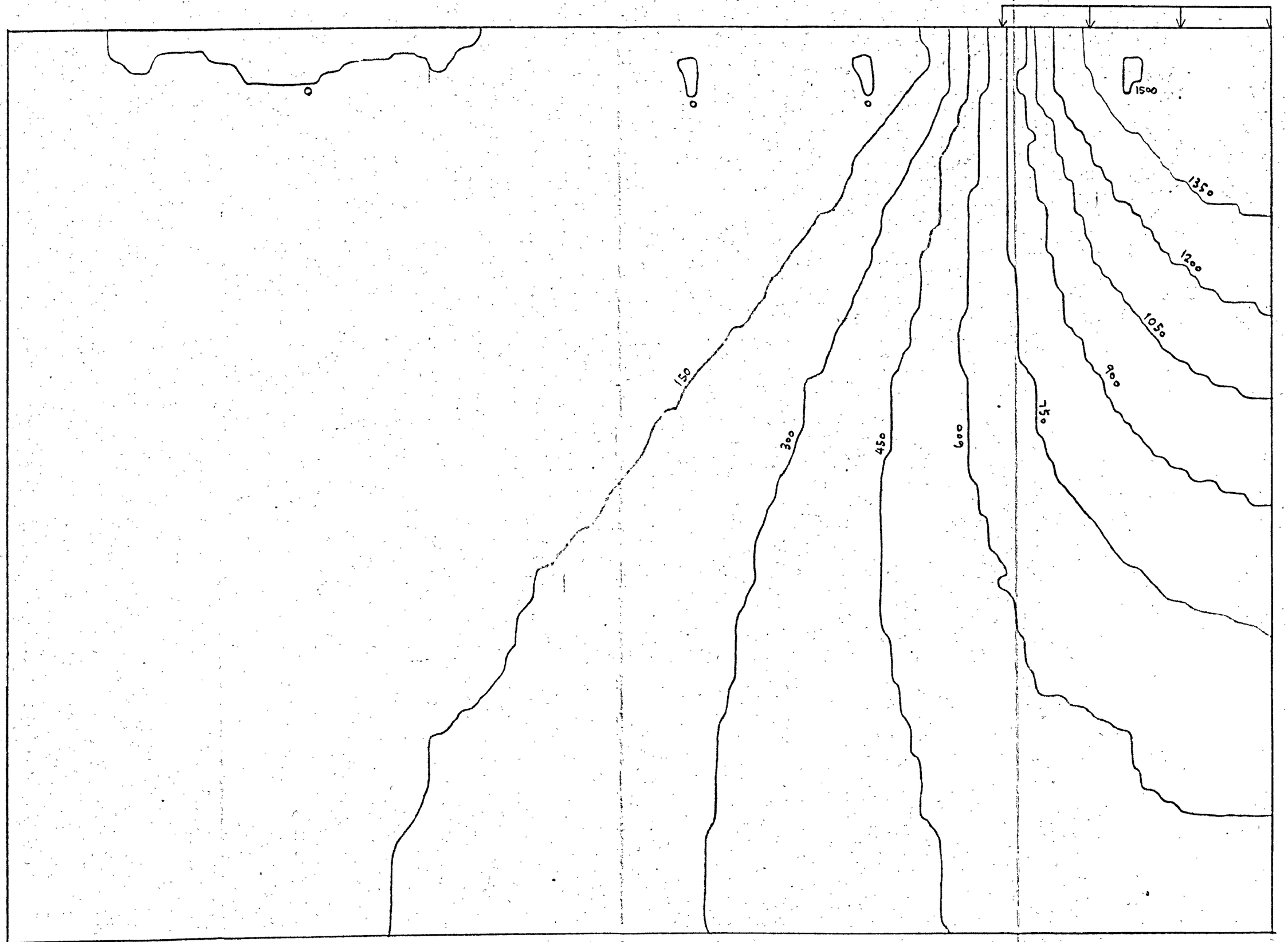

(b) σ_y contours

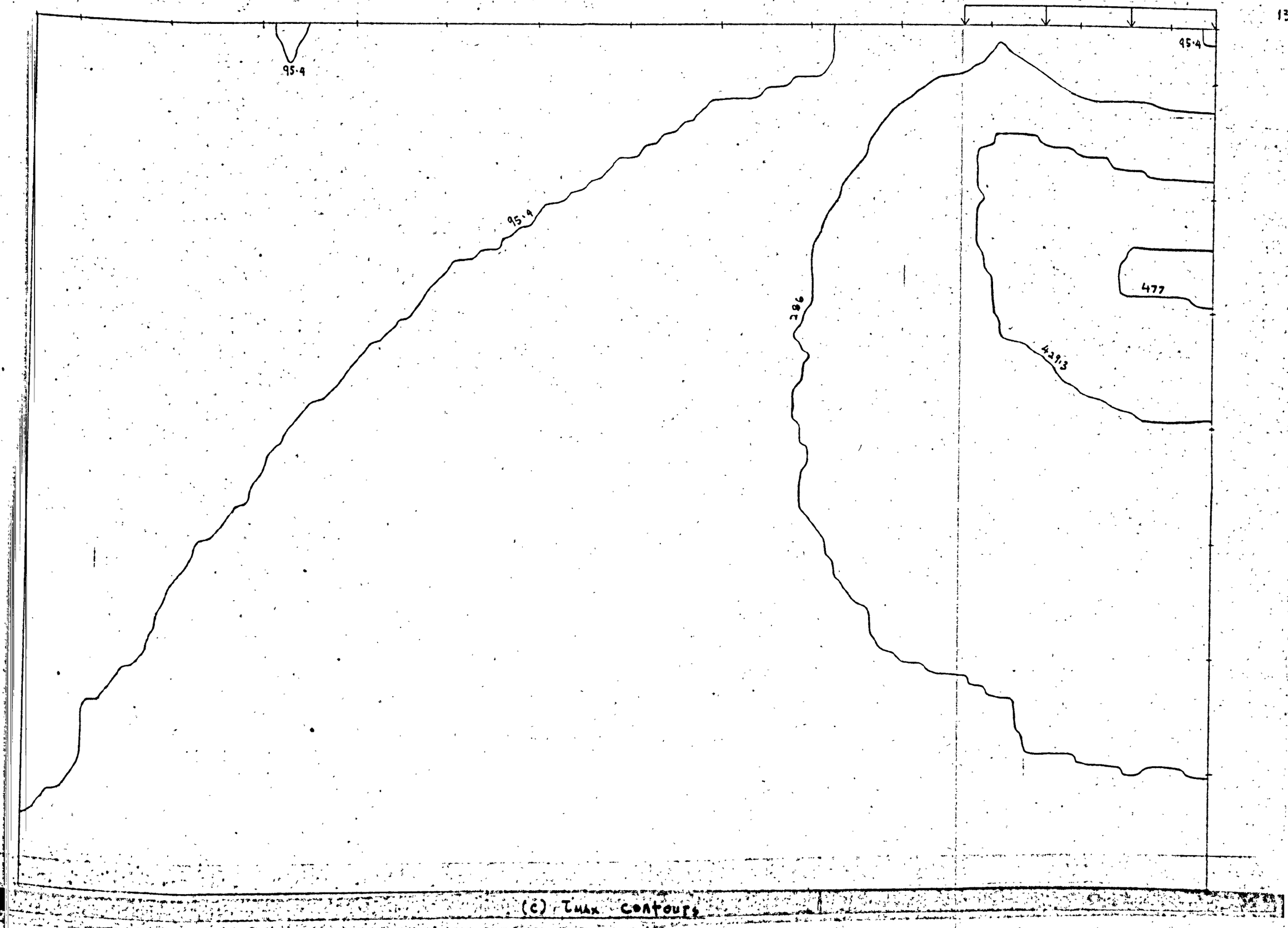

Fig. 27. Stress contours of elastic half-space for working load of 1500 psf by SYMAP (no surface data points prescribed) - all figs. in psf (HOMOGENEOUS)

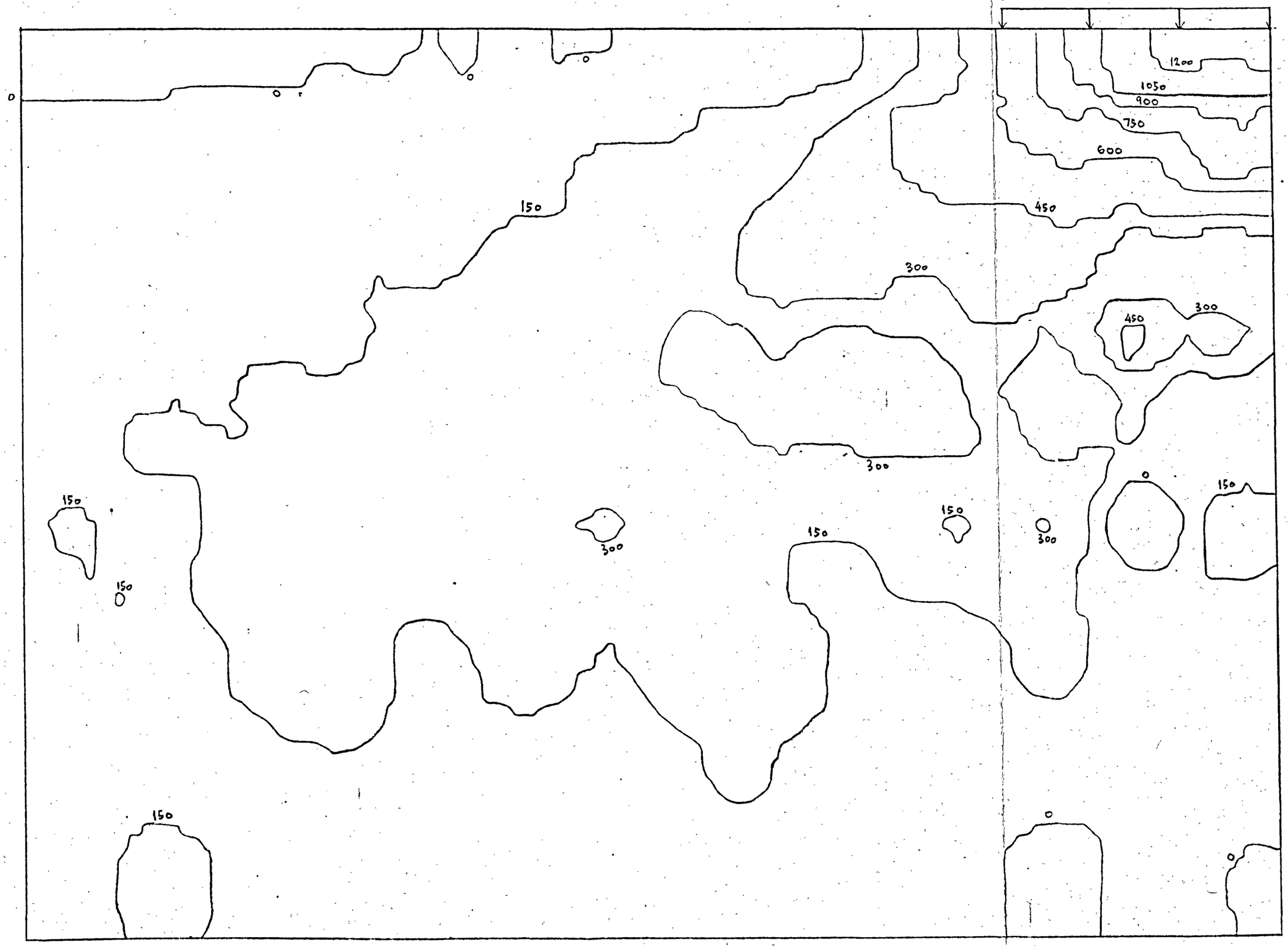

(a) σ_x contours

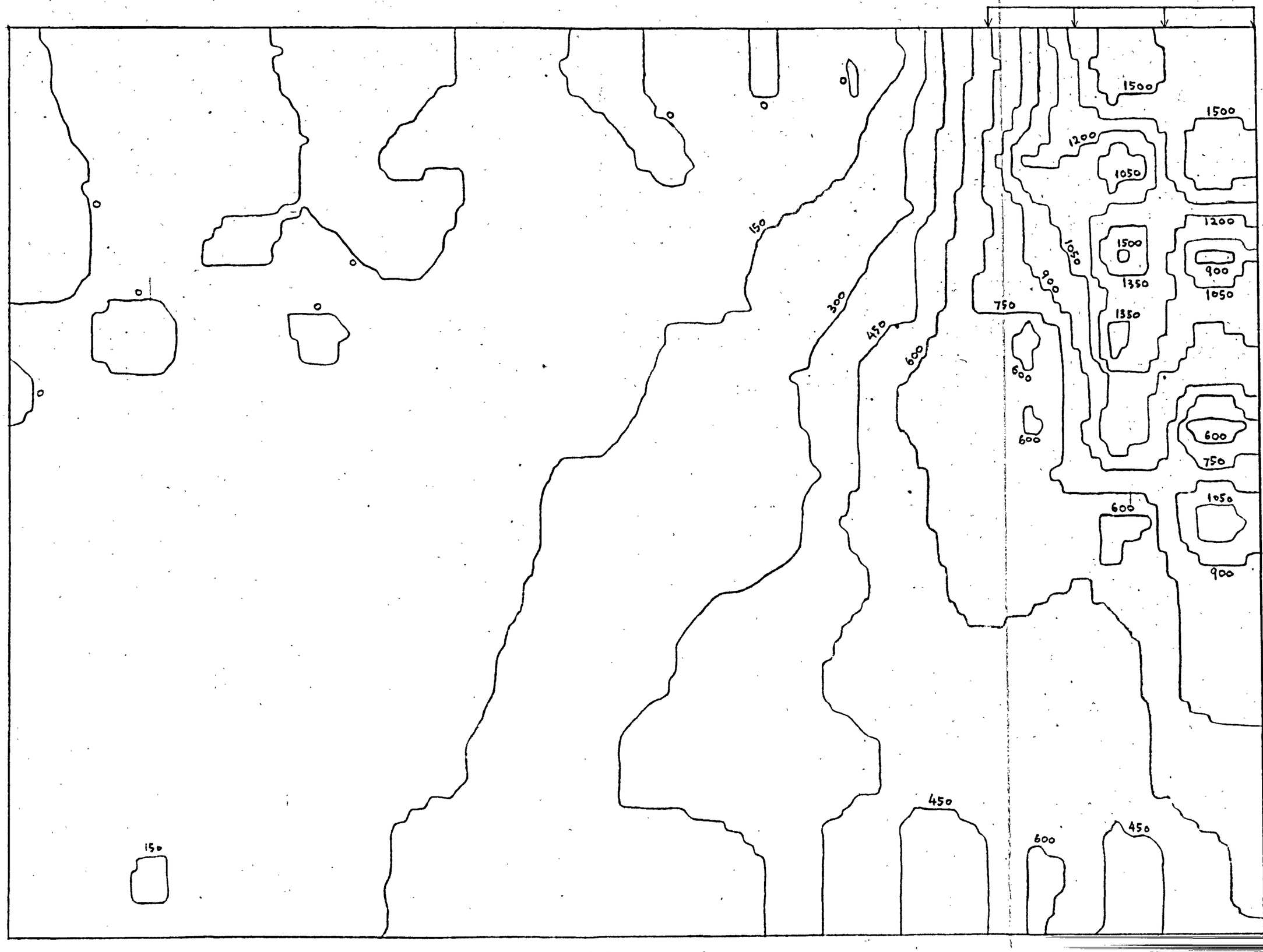

(b) σ_y contours

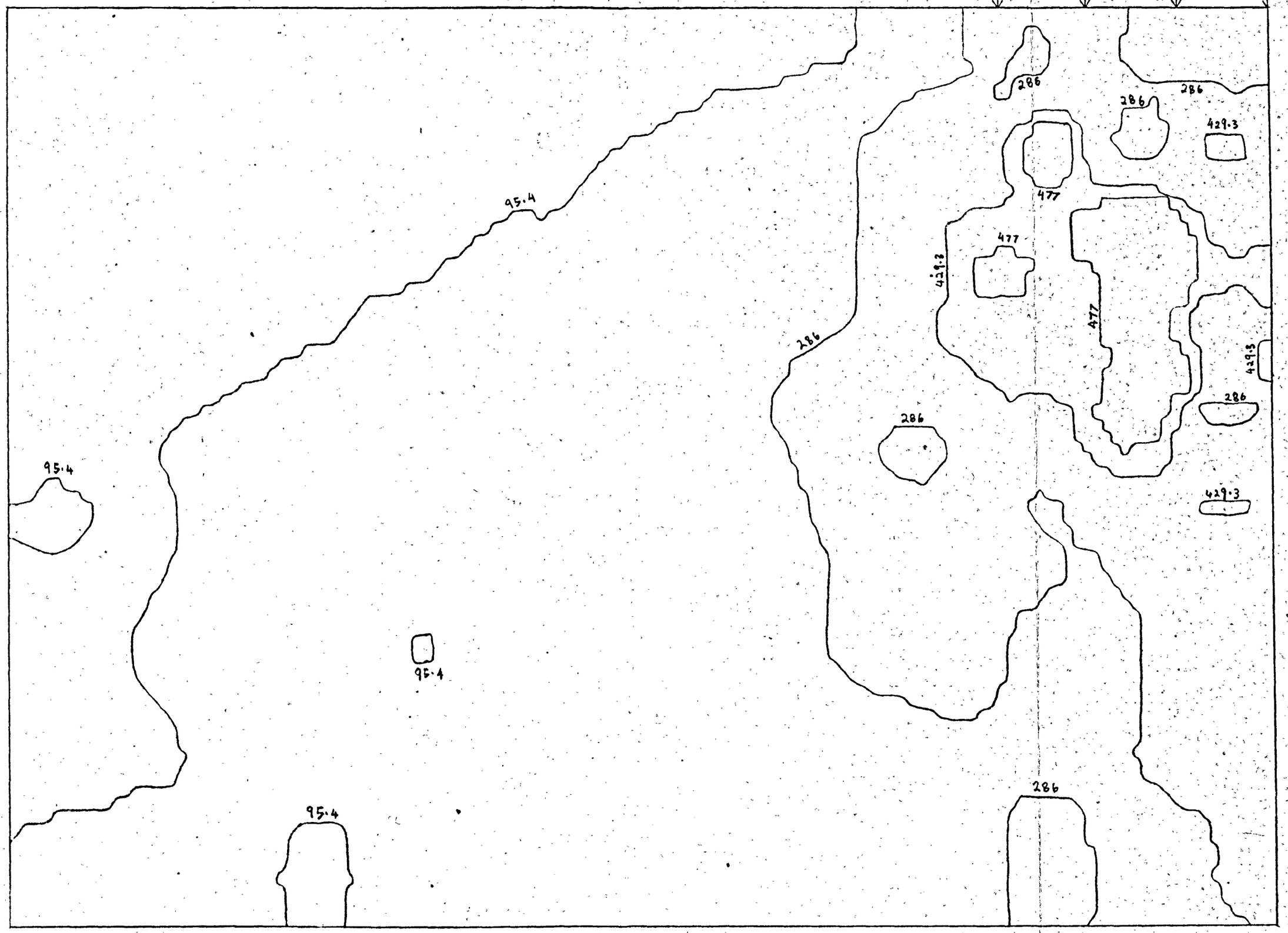

(c) τ_{MAX} contours

Fig. 28. Stress contours of elastic half-space with random Young's Modulus distribution ($\nu = 0.49$) for uniform strip load of 1500 psf by SYMAP (no surface data points prescribed) - all figures in psf

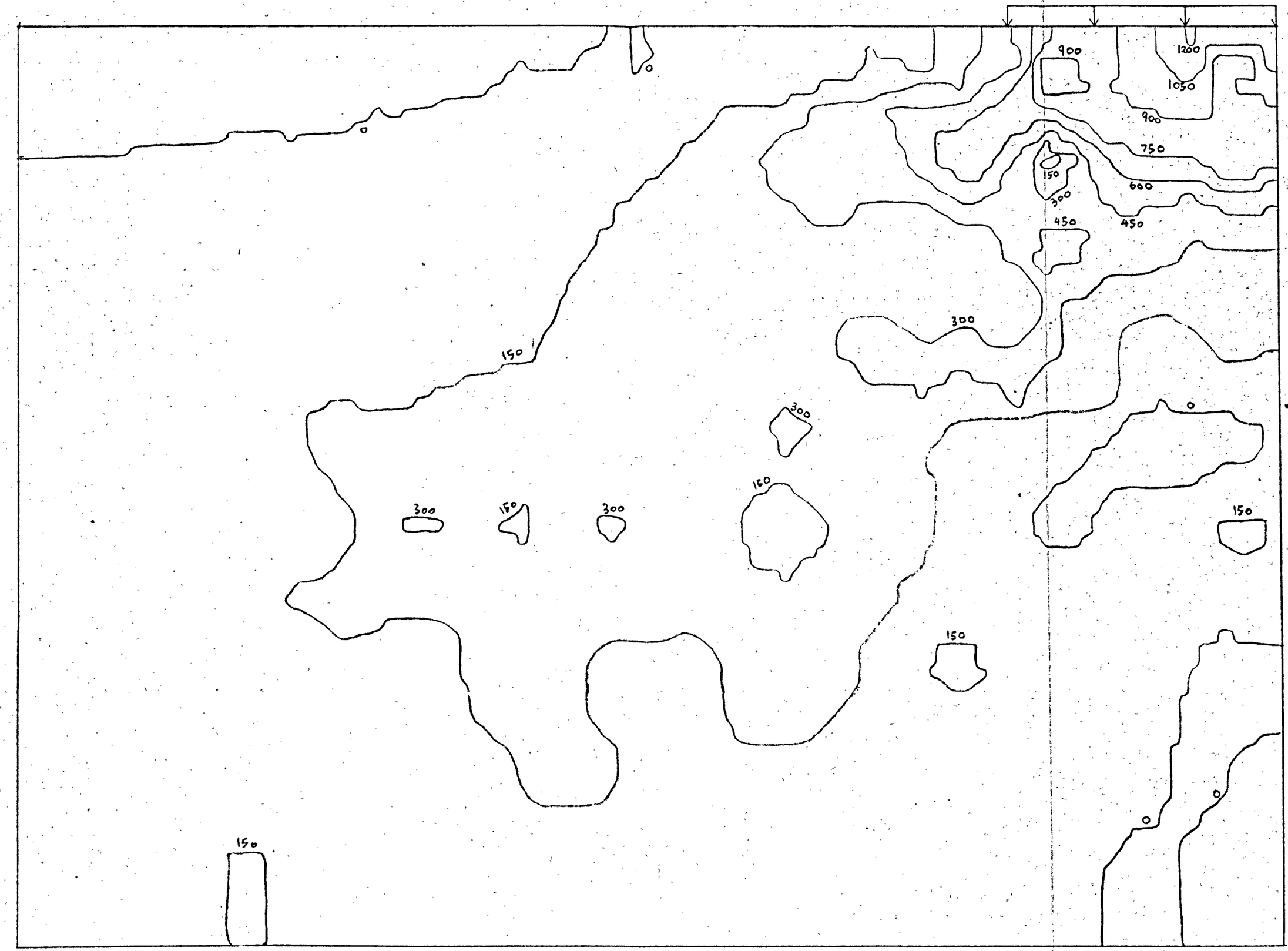

(a) σ_x contours

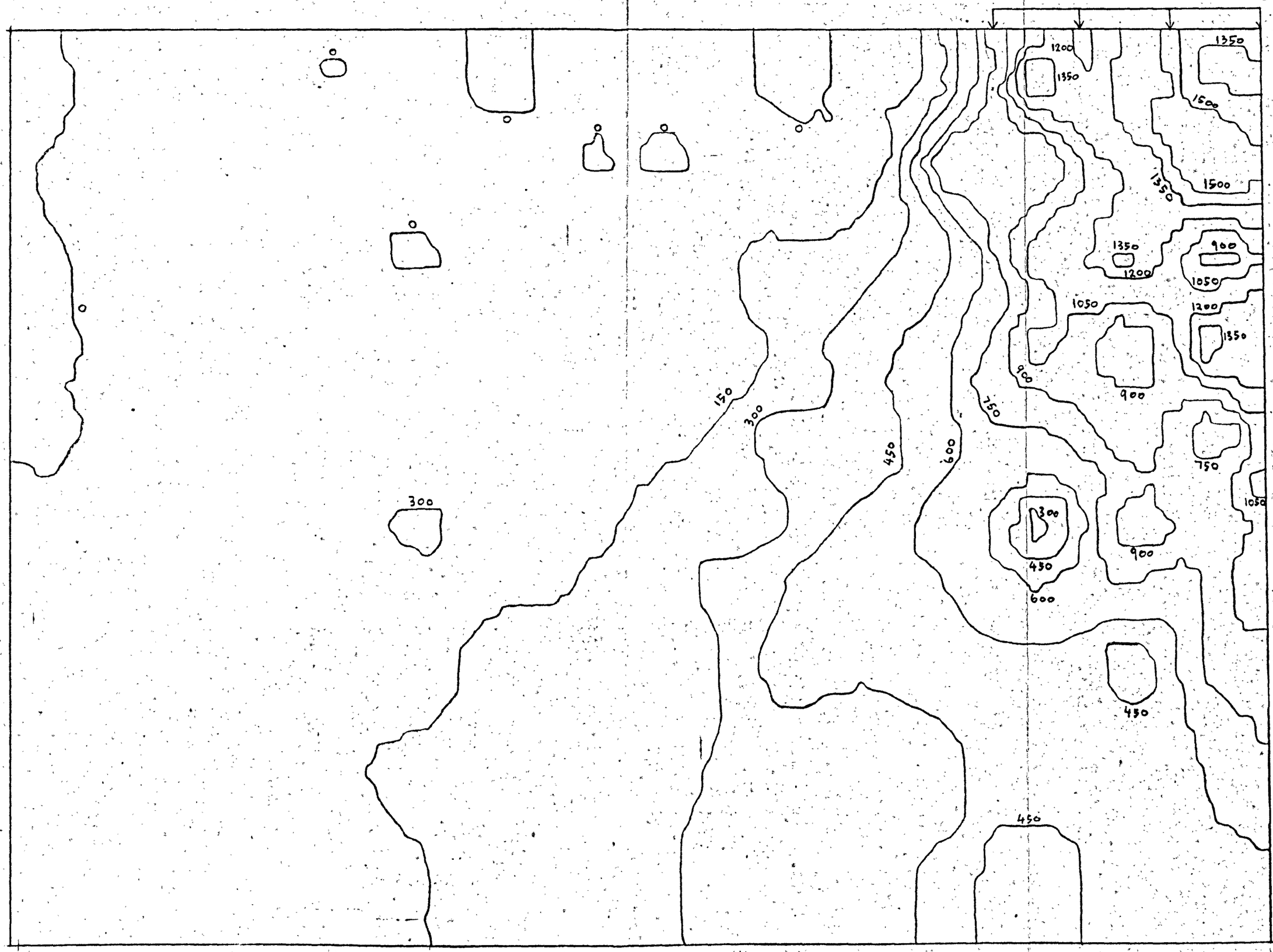

(b) σ_y contours.

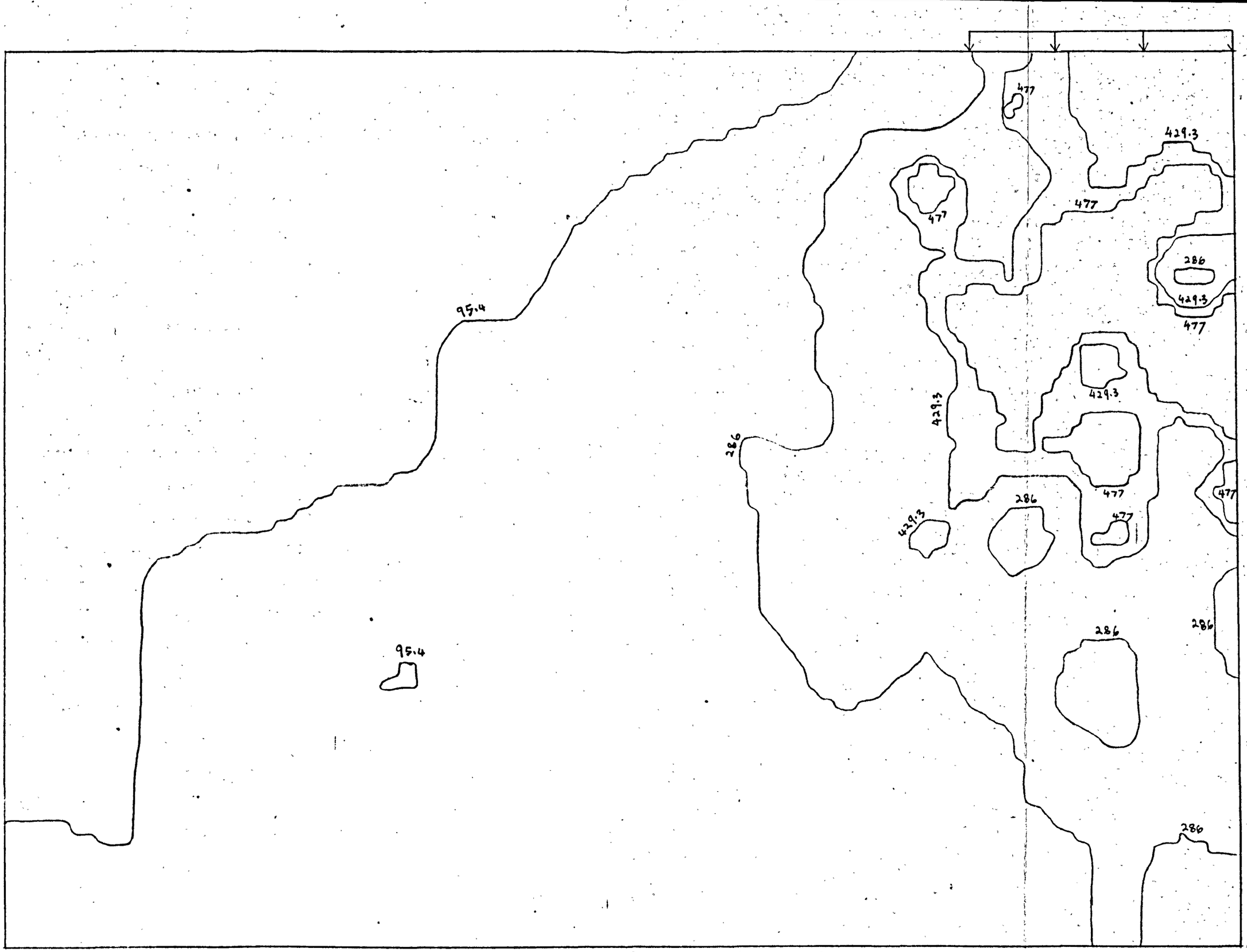

(c) τ_{MAX} contours

Fig. 29. Stress contours for elastic half-space with random Young's Modulus and Poisson's Ratio distribution for uniform strip load of 1500 psf by SYMAP (no surface data points prescribed) – all figures in psf

2.5. The linear elastic, isotropic, homogeneous layer model (flow chart in Section 1.2.7.1.)

Fig. 30(a) shows a linear elastic, isotropic, homogeneous layer idealisation of the practical example of Section 2.2. The idealisation serves as a simple, initial assessment for a working load. The soil properties at mid-depth which are the mean of the range of values are a reasonable choice and they should also approximately correspond to average point values. The same working load of 1500 psf as the half-space problem is adopted here since the presence of the rigid base ought to strengthen the soil body, according to a limit theorem (24). Indeed, it will be shown that the collapse load for the isotropic, homogeneous elastoplastic layer of Section 2.6. is quite insensitive to the proximity of the rigid base.

Fig. 30(b) shows the finite element model adopted for the layer idealisation. The lateral configuration of the half-space is maintained and the lateral rigid boundaries should now have even less effect on the solution. The fine mesh in the vicinity of the strip load for the half-space problem is extended down to the base and even then leads to further economy of computation (10 Bays downwards compared to 20 Bays for the half-space) due to the high load width - to - layer thickness ratio.

The fully-adhesive conditions at the rigid base are correctly modelled by full fixture of the bottom line of joints.

Of several trial assemblages, the one chosen is adjudged to provide the best accuracy - economy combination - with a view to later elastoplastic models.

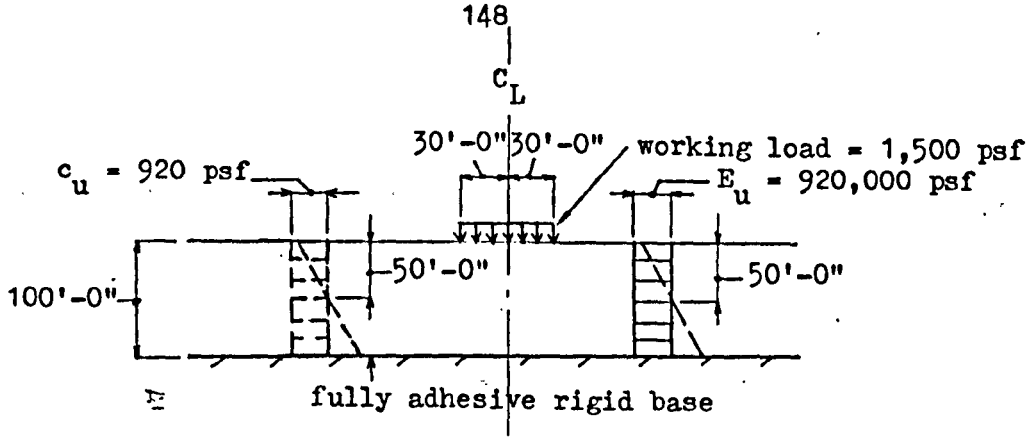

(a) The linear elastic, isotropic, homogeneous layer idealisation

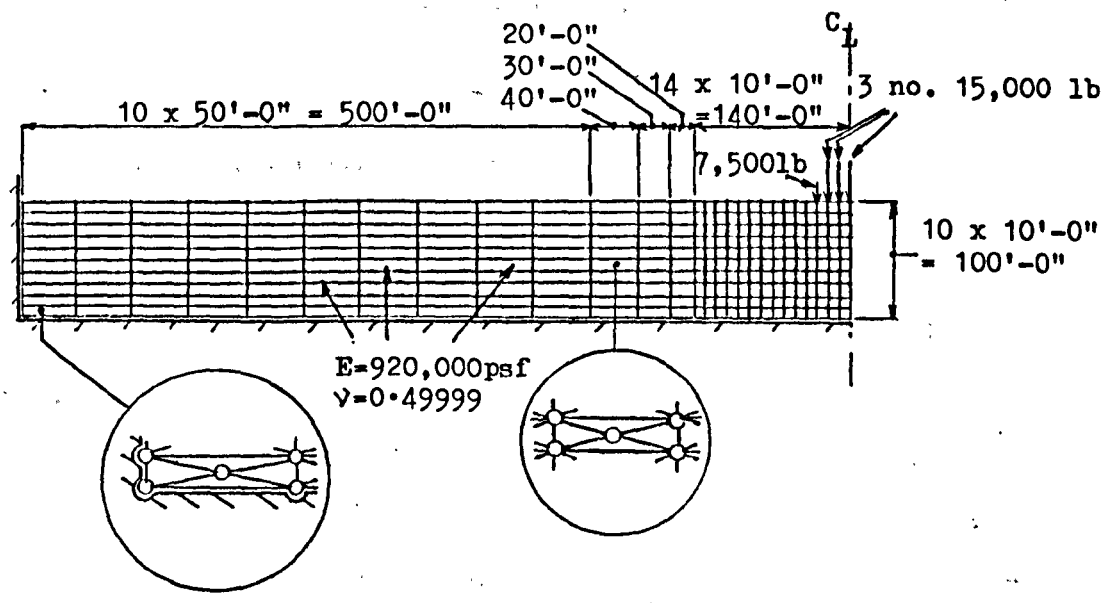

(b) Finite element model for layer idealisation

Fig. 30. A simple assessment for a working load on the layer of Fig. 22

2.5.1. Accuracy of some stresses and surface displacements computed from the finite element model

Figs. 31, 32 and 33 show the stresses down the centre and edge, respectively, of the strip load. The values given by Poulos (10) - obtained by numerical solution - as well as those computed via the finite element model, are plotted. Stresses at the surface, where single-valued, are also plotted: at the centre, σ_x is given by Gibson (41), σ_y is the same as the pressure of the strip, and τ_{max} is given by these with $\tau_{xy} = 0$; at the edge, σ_x (Gibson - (41)) and σ_y are multivalued, although they lead to a single value of τ_{max} ($\tau_{xy} = 0$ as before).

Close agreement between the known and computed stresses is obtained, the latter being generally within ±5% of the former.

The surface displacements are similarly compared in Fig. 34 and, as above, the known (Poulos - (10)) and computed values are in close agreement, the latter being generally within ±2% of the former.

Finally, the stress contours via SYMAP are shown in Fig. 34A ; the surface data points are prescribed to improve the accuracy of the contours in the vicinity of the load.

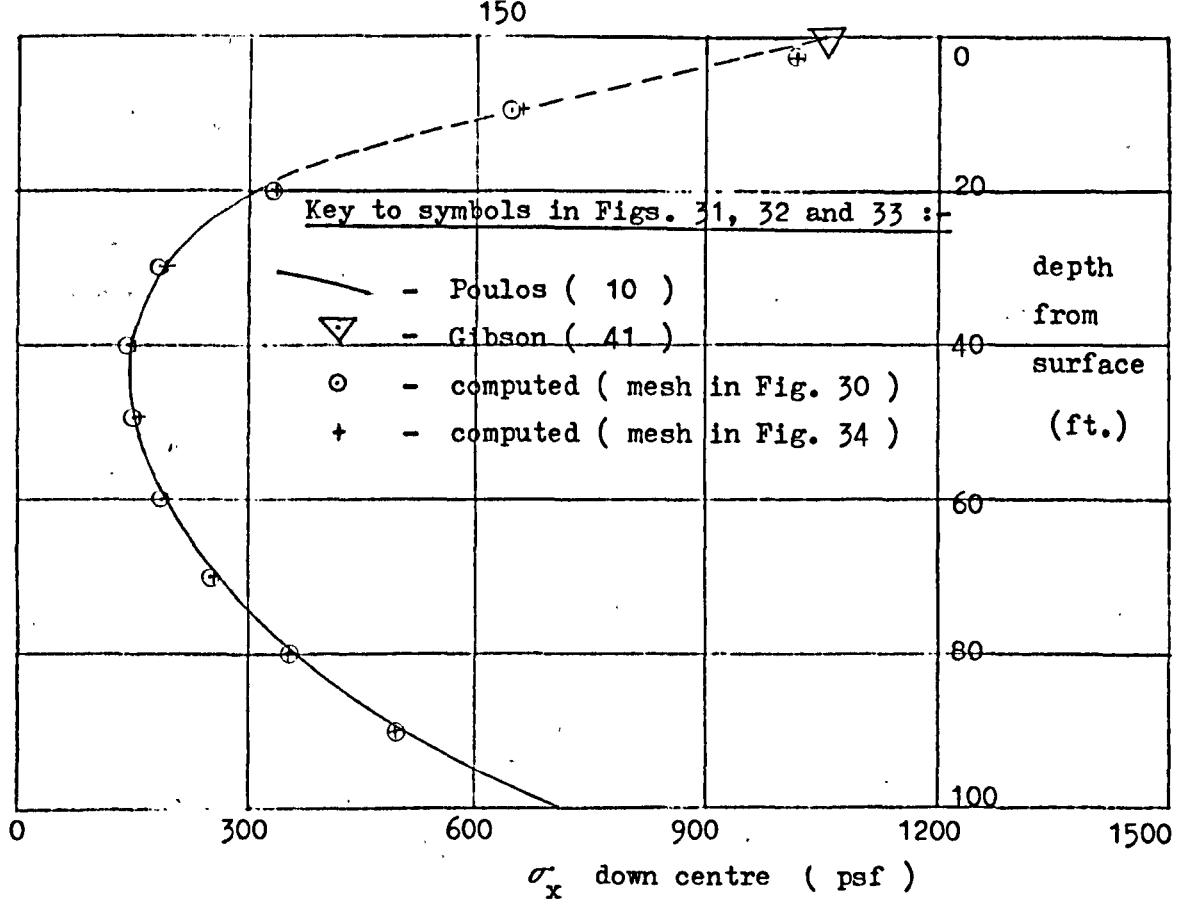

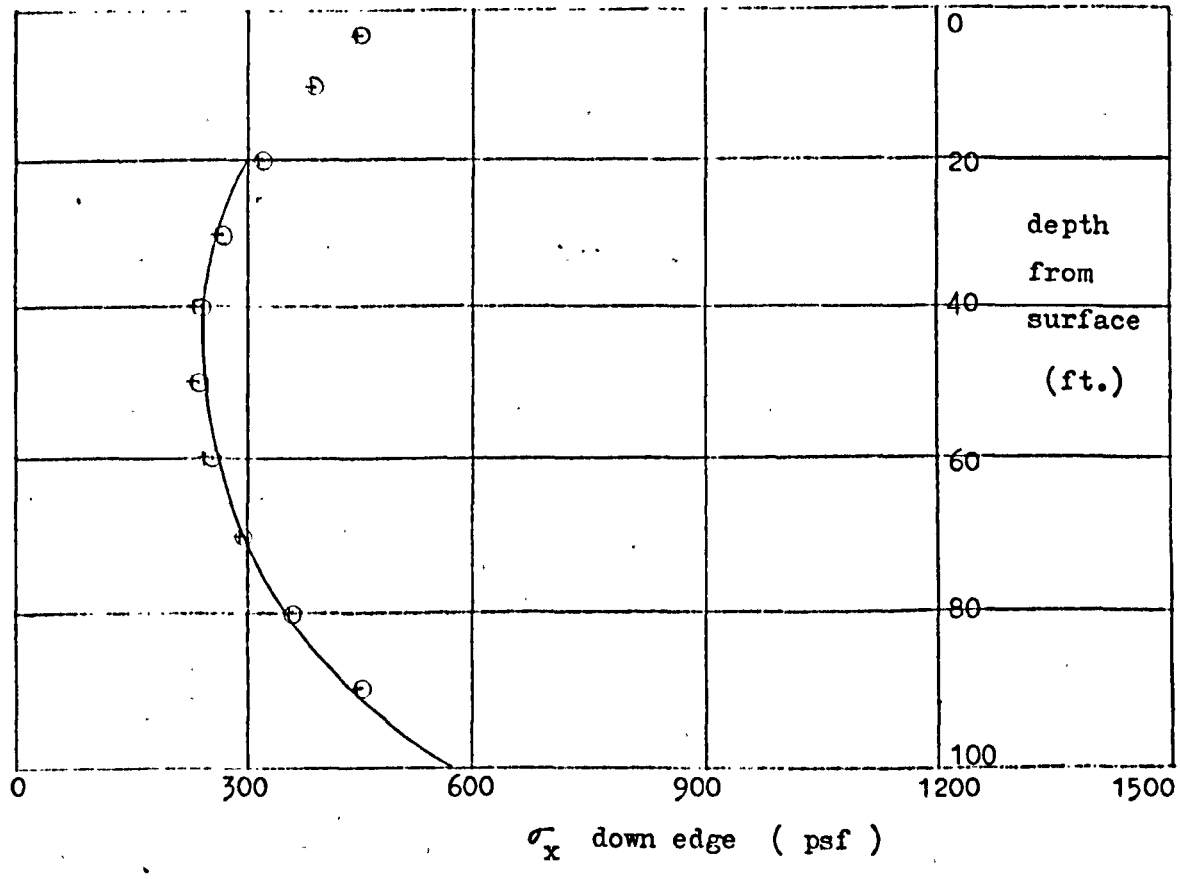

Fig. 31. σ_x distributions down centre and edge of strip load for elastic layer

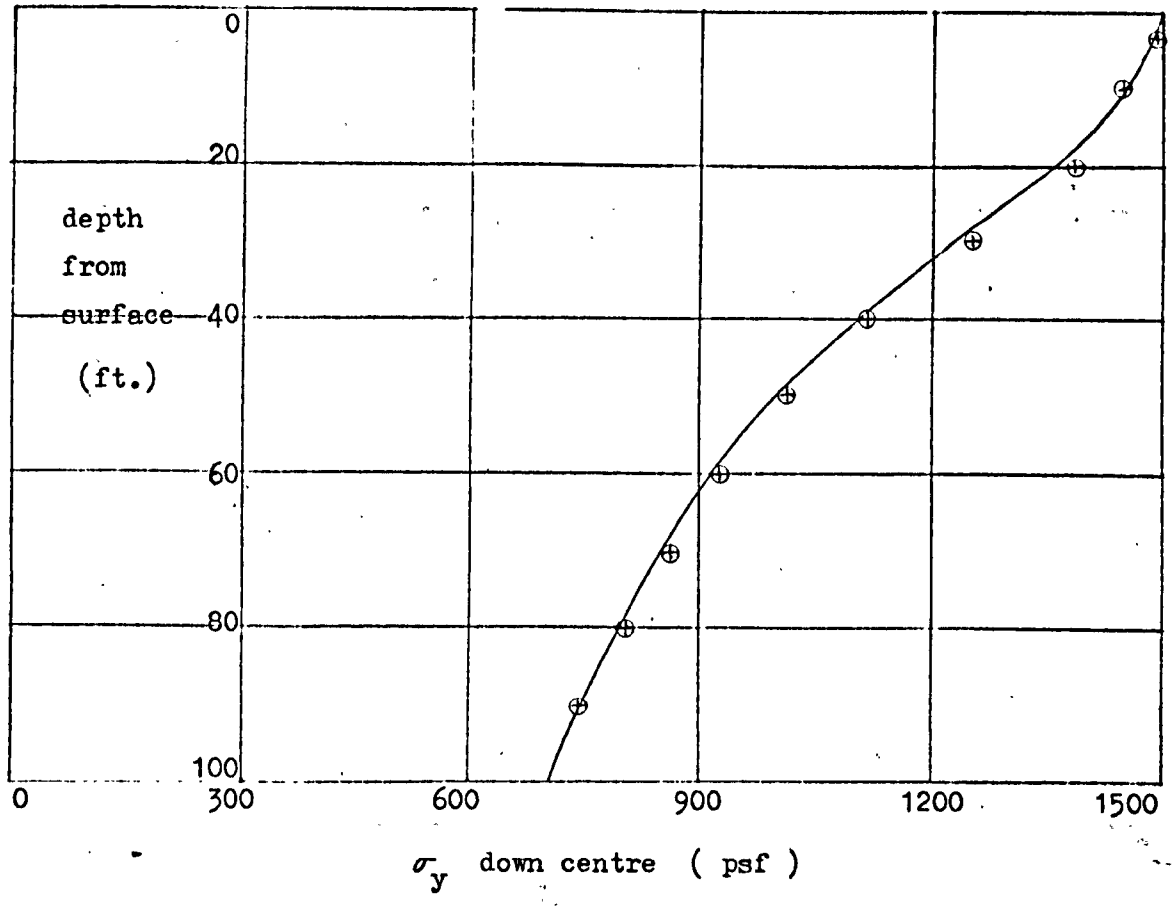

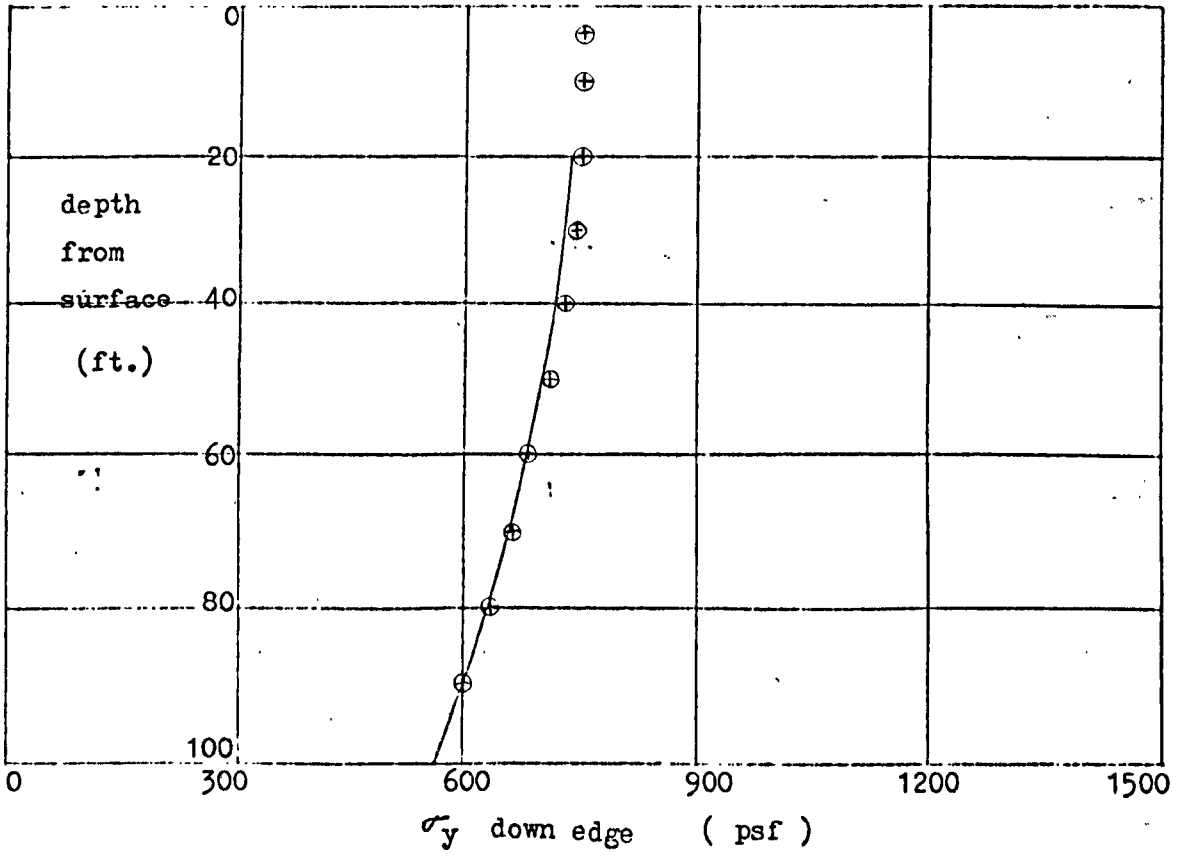

Fig. 32. σ_y distributions down centre and edge of strip load for elastic layer

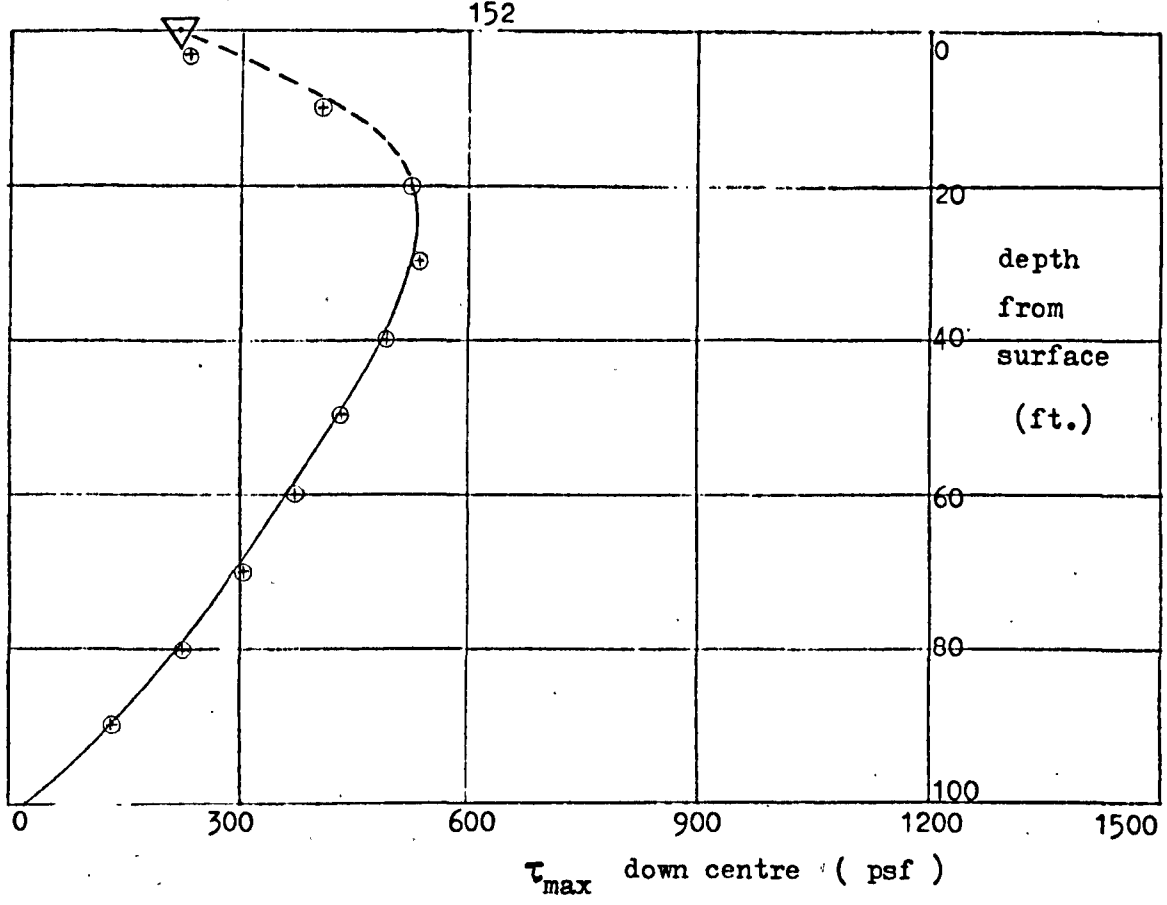

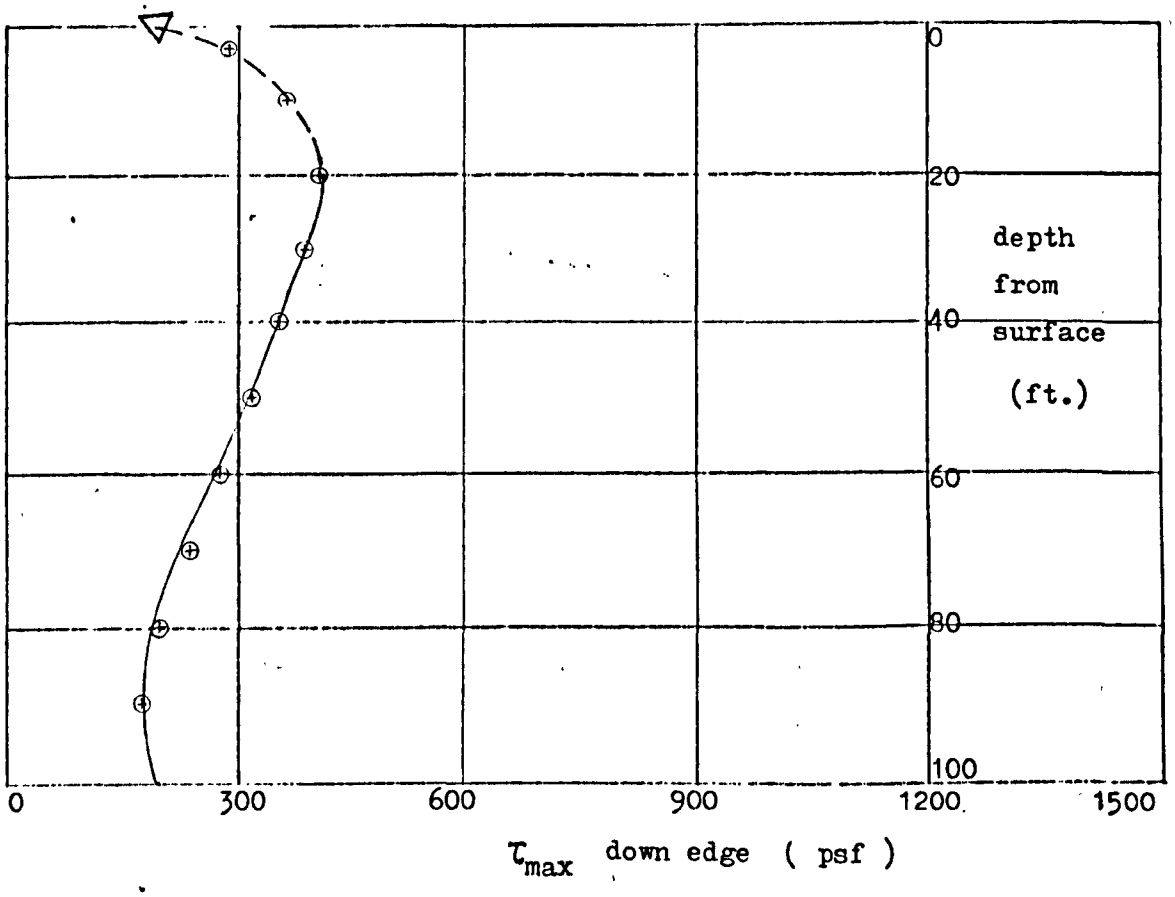

Fig. 33. τ_{max} distributions down centre and edge of strip load for elastic layer

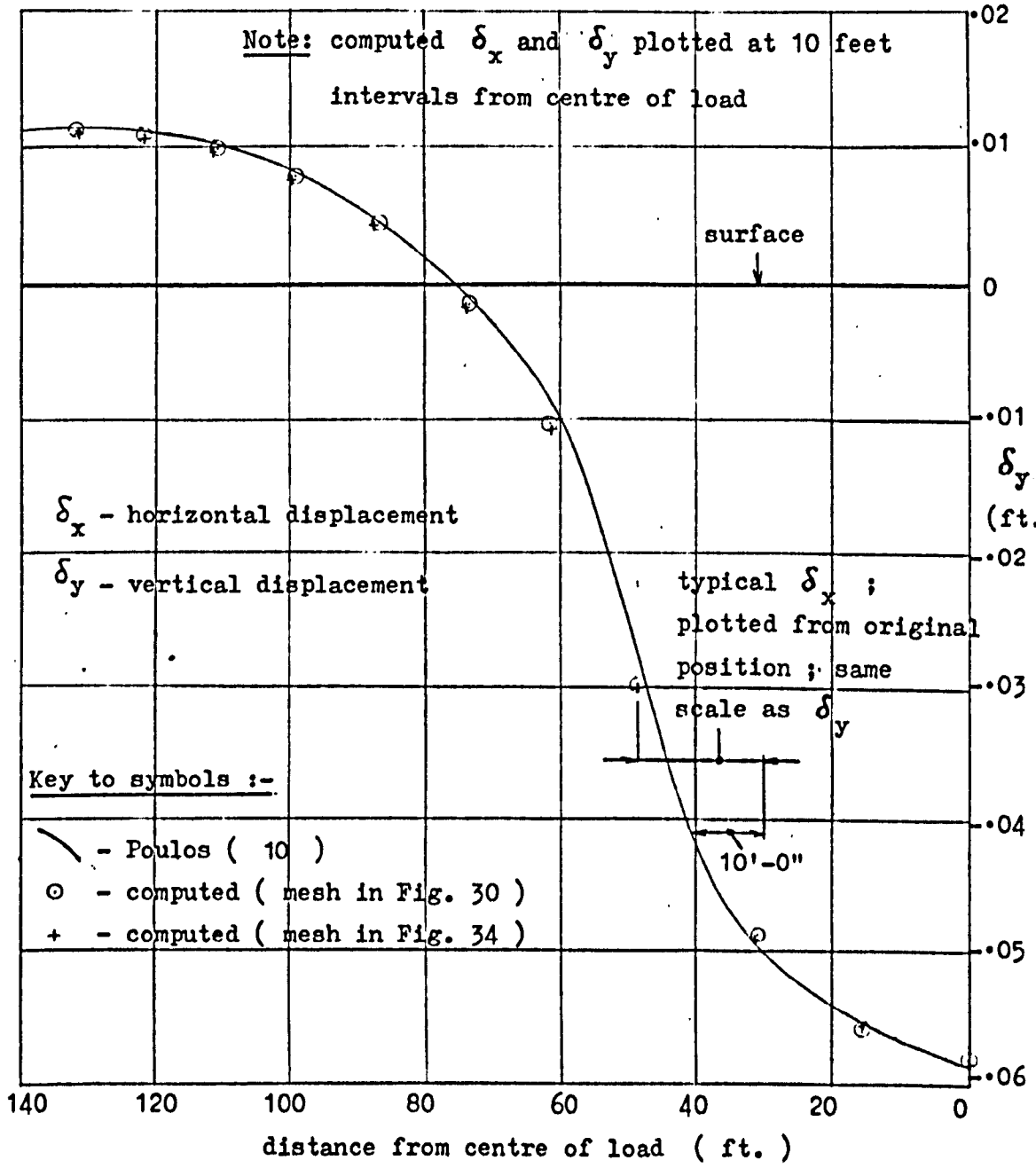

Fig. 34. Surface displacements for elastic layer

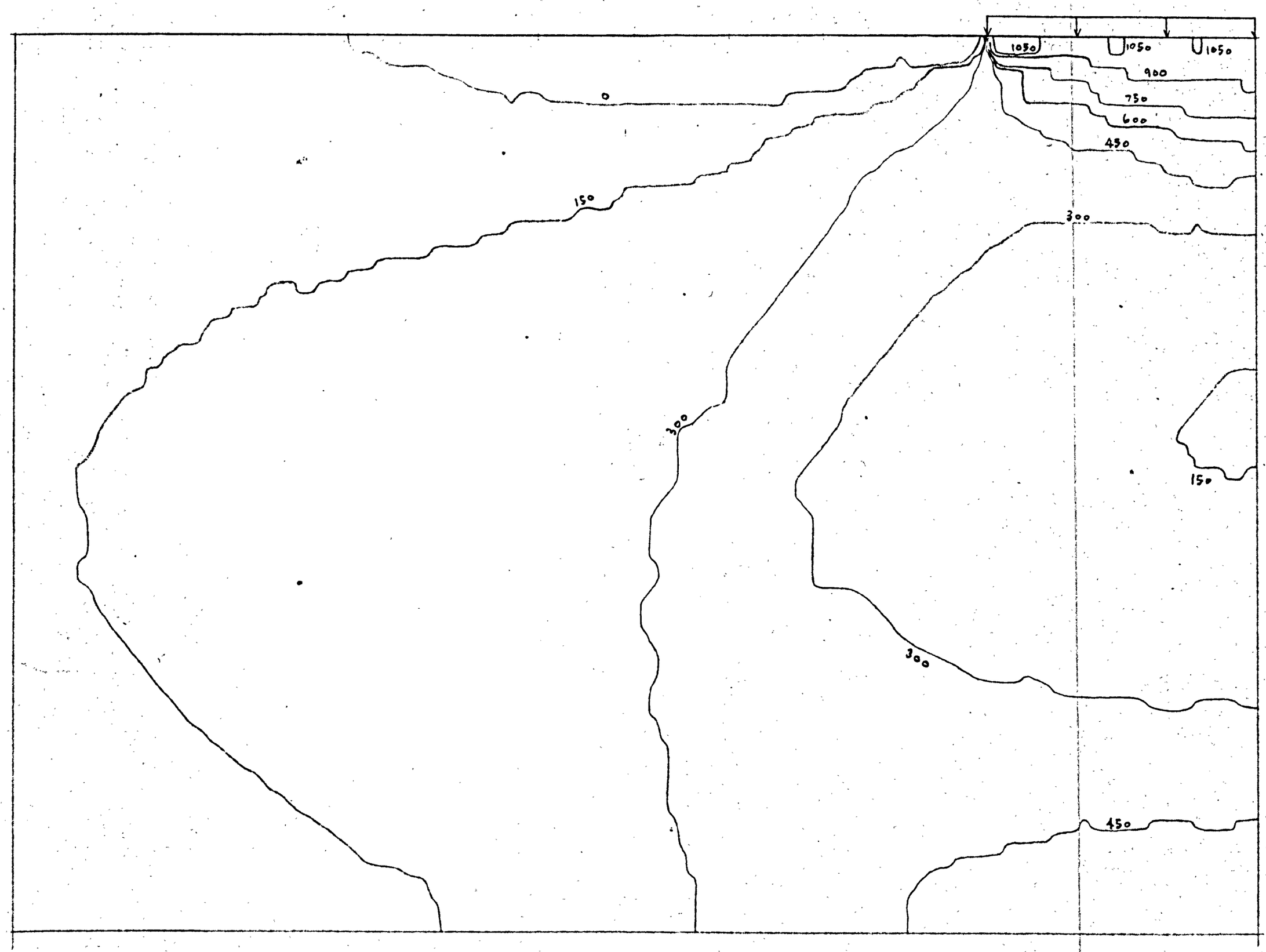

(a) σ_x contours

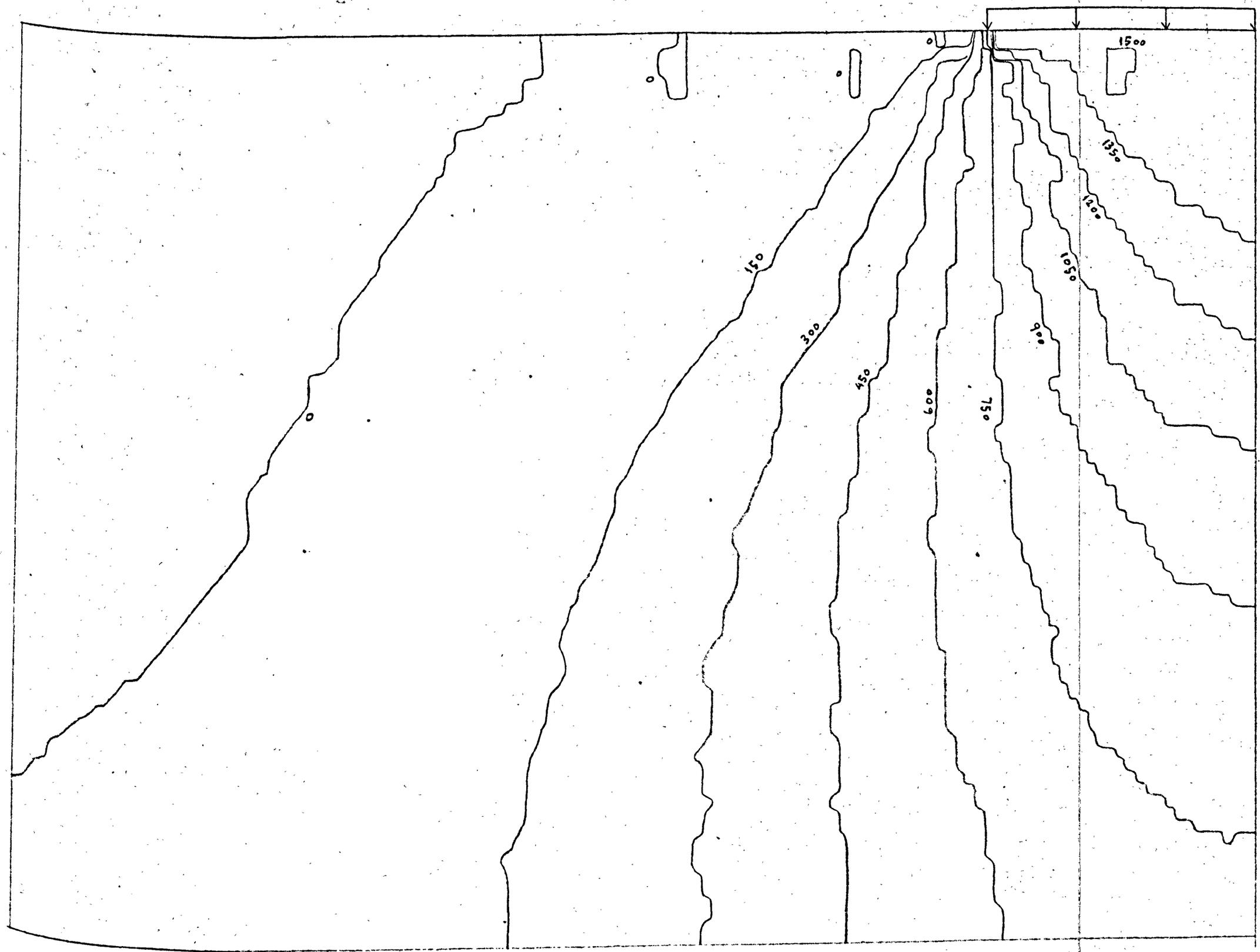

(b) σ_y contours

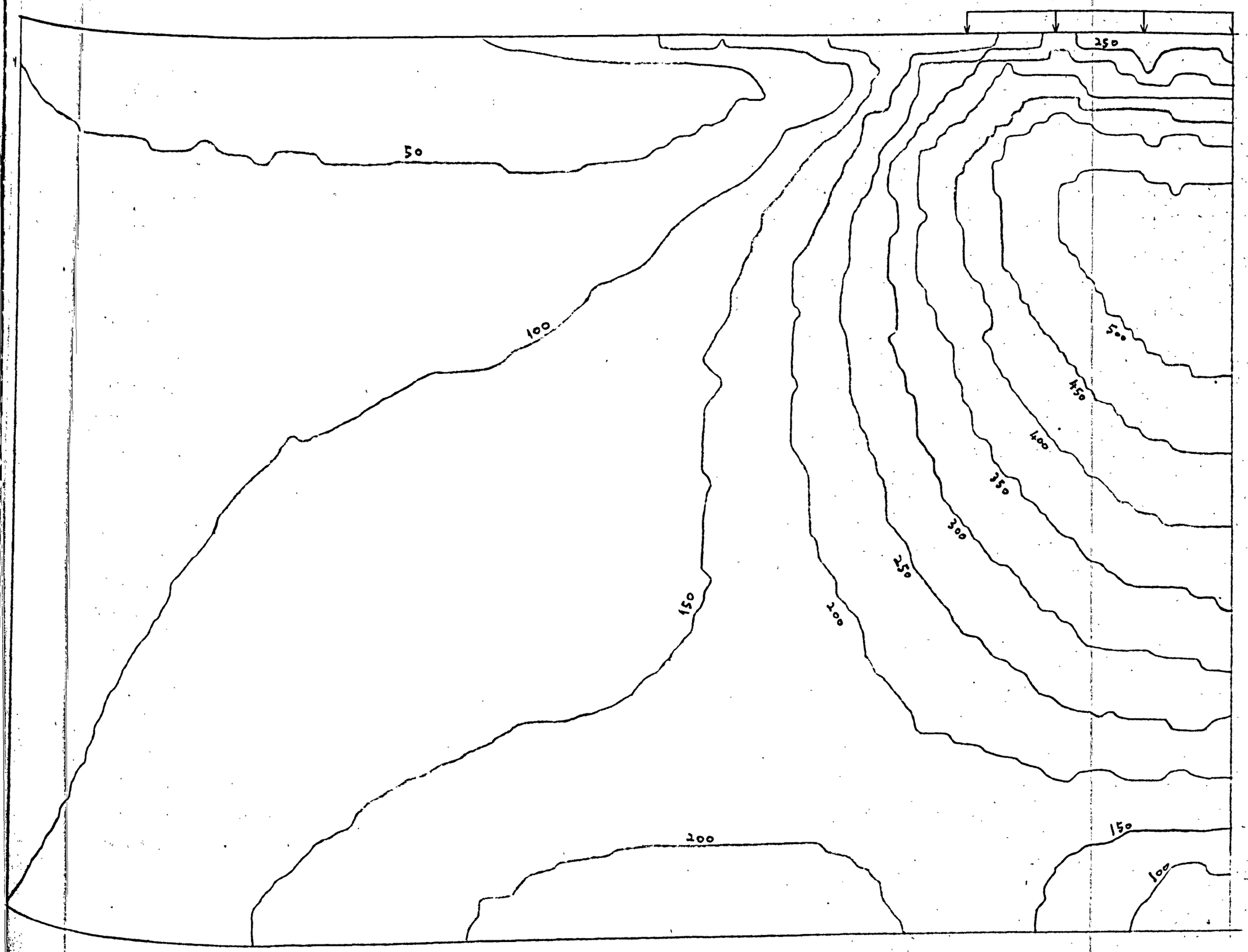

(c) τ_{MAX} contours

Fig. 34A. Stress contours of elastic layer for working load of 1500 psf by SYMAP (surface data points prescribed) - all figures in psf (HOMOGENEOUS)

PART B - A DETAILED STUDY OF THE BASIC ELASTOPLASTIC MODEL

2.6. The linear elastic, perfectly plastic, isotropic, homogeneous layer model (flow chart in Section 1.3.3.1.)

Fig. 35(a) shows a linear elastic, perfectly plastic, isotropic, homogeneous layer idealisation of the practical example of Section 2.2. The idealisation is - as with the elastic layer model of Section 2.5. - a simple, initial assessment of the practical problem, based on average soil properties in the layer. Where it differs, however, is in its ability to model the entire loading range. It thus provides a suitable basis for the following parametric studies, from low working loads to collapse, on the practical problem.

The finite element model for the idealisation is shown in Fig. 35(b). It can be seen that although it retains the configuration given in Fig. 30(b) for the elastic layer in most respects, the lateral extent of the mesh is reduced to make the necessary computational economies when dealing with the plastic phase of the ideal material. Nevertheless, as shown in Figs. 31 - 34, the effect of doing so on accuracy of the elastic solution is insignificant. Furthermore, as mentioned earlier, the computed collapse load is relatively insensitive to reasonably-spaced rigid boundaries and indeed, this reduction in the lateral extent of the mesh is not

accompanied by any significant change in the computed collapse load.

Incidentally, a series of initial checks were made on the accuracy with which the Initial Stress Method models elastoplastic behaviour in some simple problems. Thus, a typical Stack was subject to uniaxial (plane stress and strain) as well as biaxial (plane strain) states of stress. For these, excellent concurrence with the true solutions was obtained not only for the present elastoplastic material but also for Von Mises (42), Drucker-Prager (43) and Mohr-Coulomb (43) materials, involving perfectly plastic, work hardening and work softening behaviour.

The present model is henceforth referred to as the basic model (Fig. 35) since it serves as the basis for comparison with the following parametric studies. Also, since the mesh of Fig. 35(b) models the behaviour of the elastic and plastic phases of the layer accurately, it is adopted as the standard for the following elastoplastic models.

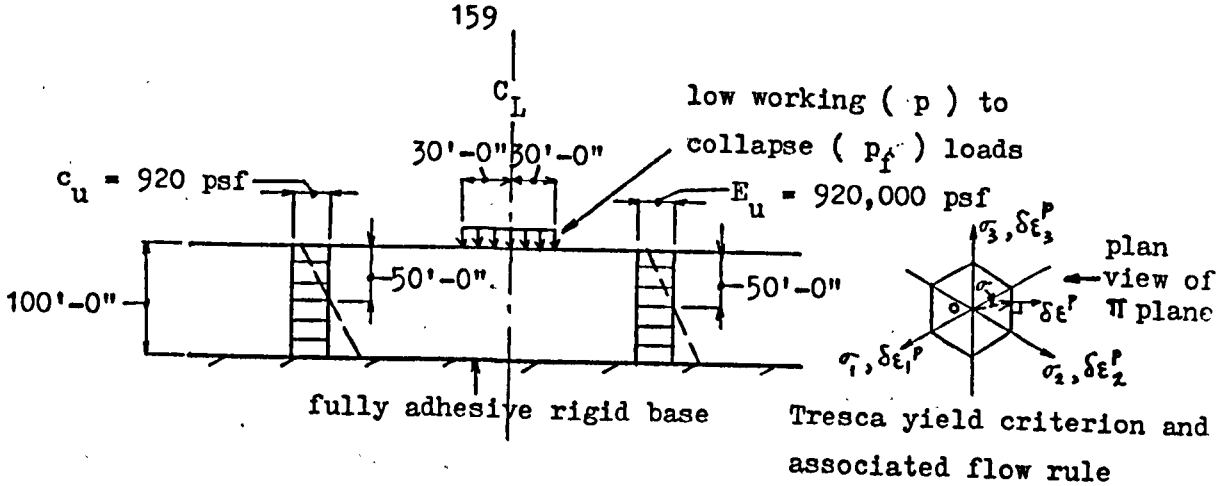

(a) The linear, elastic, perfectly plastic, isotropic, homogeneous layer idealisation

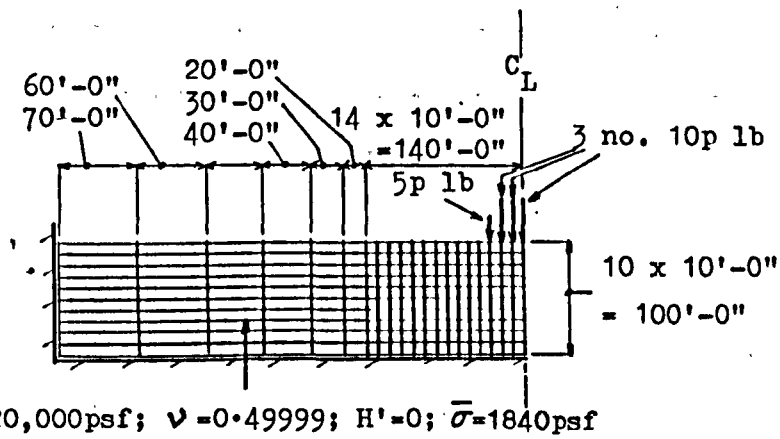

(b) Finite element model of idealisation (see Fig. 30(b) for mesh details)

Fig. 35. A simple assessment of the layer of Fig. 22 for the entire loading range to collapse (basic model)

2.6.1. Growth of the plastic enclave and collapse

As the uniform strip load p (Fig. 35) increases from zero, the layer initially deforms elastically mainly by distorting since the material is virtually incompressible. When p = 2413 psf, however, element X (Fig. 36(a)), which has the highest elastic maximum shear stress value, attains first yield. No plastic flow occurs as yet due to containment by the surrounding elastic material with which the element is compatible. With further loading, there is a general increase in the stresses in the layer although the maximum shear stress of the plastic element X obviously cannot increase. Its elastic distortion is thereby insufficient to maintain compatibility with the surrounding elastic material and thus contained plastic flow ensues until the difference is redressed and equilibrium restored. Still further loading leads to more elements becoming plastic as their maximum shear stresses reach shear strength, with accompanying plastic flow and stress redistribution by a similar process to that above.

In this way, a clearly-defined plastic enclave develops which spreads downwards primarily, to begin with (Fig. 36(a)). This material thus differs from relatively rigid materials like very stiff clays or cemented sands which collapse soon after first yield (37b). Subsequently, the enclave spreads laterally (Fig. 36(c)), and soon after this occurs, it penetrates free surface some way from

the load (Fig. 36(d)) so that it can then flow plastically without inhibition, thus leading to collapse due to the pressure exerted by the strip. Although the enclave had reached the surface adjacent to the strip earlier, no collapse occured since the surface element Y (Fig. 36(c)) was prevented from heaving freely by the elastic body on the left and the strip on the right, to which its two surface joints are connected.

In view of the differences between the maximum shear stress distributions of the elastic layer and the half-space of Sections 2.5. and 2.3., respectively, first yield occurs here at a load less than the well-known value of πc_u for a uniform elastic half-space. What is surprising, however, is that the collapse load of 4900 psf (Fig. 36(d)) obtained in this problem is only 3·5% higher than the Prandtl result, $(\pi+2)\, c_u$, for the half-space (30). Some of this difference is attributable to the general underestimate of stresses by the Finite Element Method so that even less percentage difference is due to strengthening by replacement of the half-space material with the rigid material of the layer problem (according to a limit theorem - (24)).

Indeed, it was found that the collapse load of 4900 psf is quite insensitive to the proximity of the rigid boundaries. Even when the depth to the bottom boundary is only $\frac{1}{3}$ the width of the strip and the growth of the plastic enclave quite different (see also Section 2.7.), no significant change in the collapse load was

detected. This observation lends support to the use of Prandtl's result for layer problems. The lateral boundaries can also be brought to within about 1·5 load widths from the load centre without noticeable change to the value of the collapse load.

In terms of slip line analysis, this suggests that for the present material, a stress extension field that is statically admissible may be devised for bodies with reasonably-spaced boundaries, although the rest of the solution follows the lines of that for the half-space.

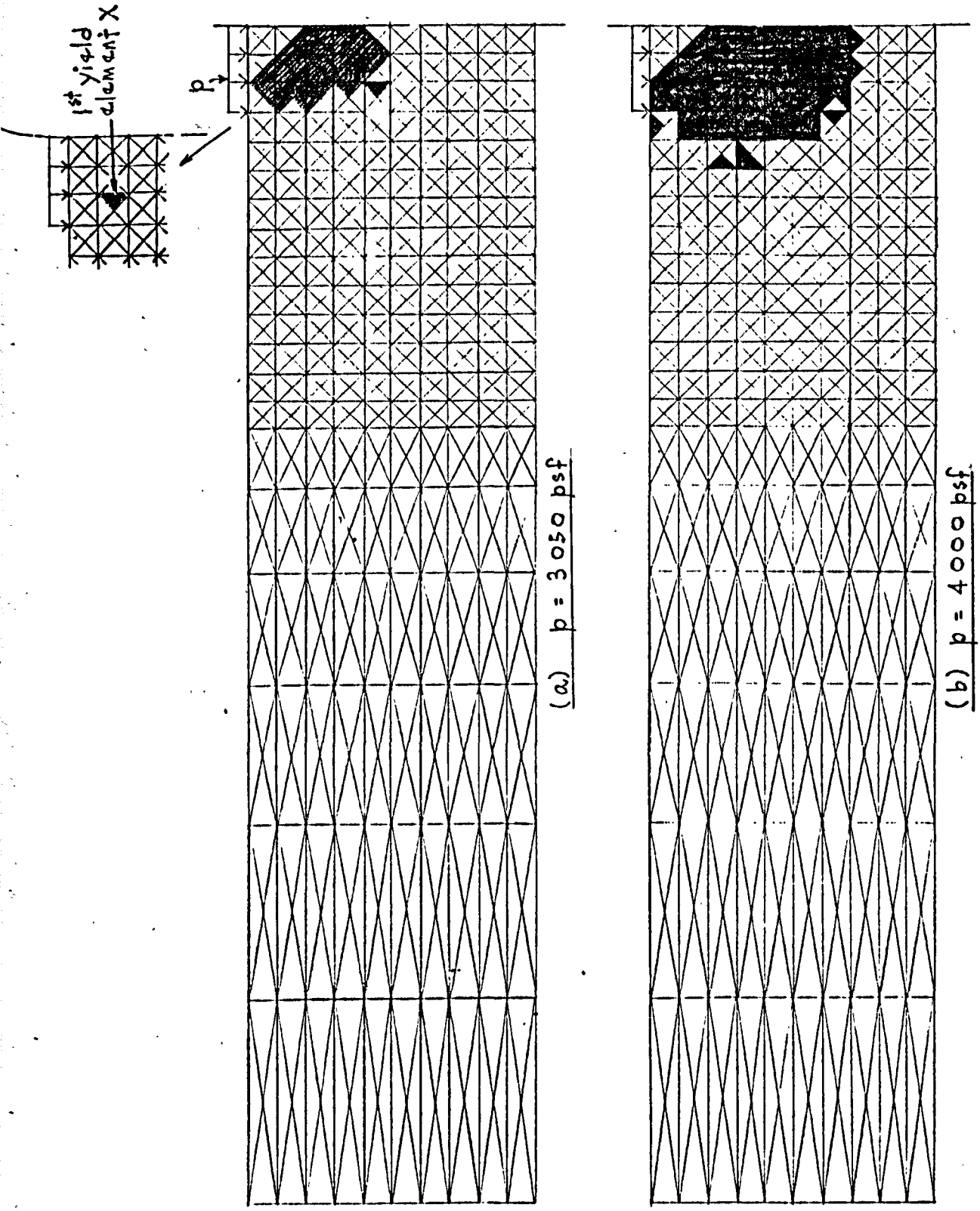
1st yield element X
p
(a) p = 3050 psf
(b) p = 4000 psf

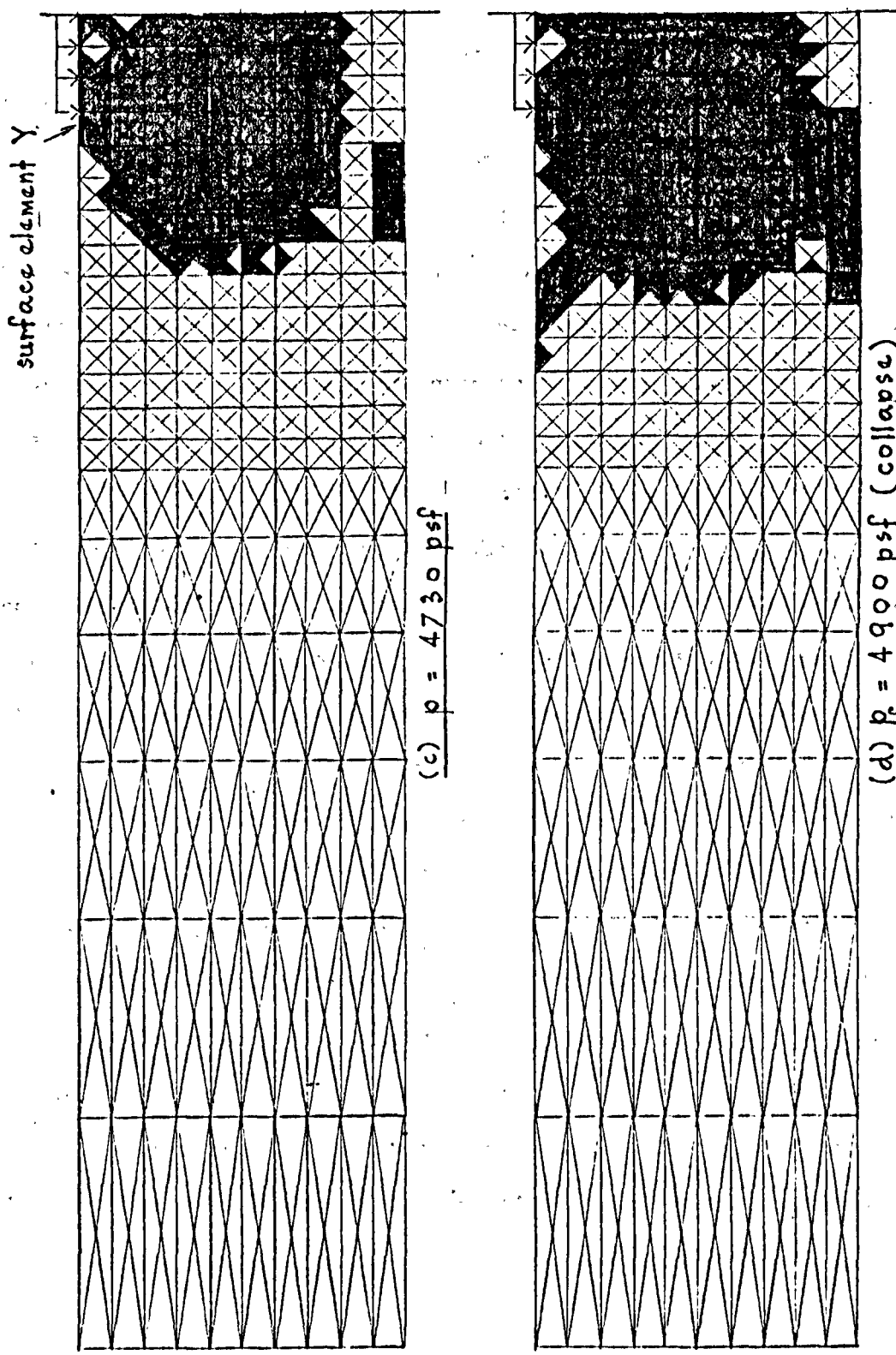

Fig. 36. Growth of the plastic enclave to collapse

2.6.2. Surface and general displacements

Fig. 37 shows the settlement-load plot for joint A (see inset). Up to the first yield load of 2413 psf, the curve is linear elastic. Further loading leads to a gradually steepening curve, becoming more rapid once the plastic enclave spreads laterally. Finally, at the collapse load of 4900 psf, the joint settles by an indefinite amount in the wake of a freely-deforming plastic enclave, and the curve becomes vertical. The curve is characteristic of local shear failure (37c).

Also shown are the settlement-iteration curves at various loads. All curves eventually converge to finite values except that at collapse which rises at a constant rate after some iterations, thus implying indefinite flow. In all subsequent studies, the penetration of the plastic enclave to free surface is supplemented with this constant rate of increase of settlement with iteration to provide a reliable means for detecting when collapse occurs.

The settlement of the surface is shown in Fig. 38. The values at individual joints are plotted and then joined with straight lines, thus reflecting the deformed surface of the assemblage. In a continuum, however, the settlement curve will be a smooth one. The plot at the collapse load pertains to the 200th iteration. The settlement under the strip is reasonably uniform except towards the edge; there, the degree of non-uniformity of settlement is accentuated by increasing

plastic flow so that, just before collapse, the settlement at the centre of the strip is approximately 5 times that at the edge, compared with about twice only when the layer is still elastic.

The settlement curve for the strip is generally dish-shaped thus requiring bottom main steel in the ground slab. There is a slight hog which occurs too near collapse to be of interest in design.

The influence of plastic flow on the magnitude of settlement under the load, prior to collapse, is only moderate. Thus, at a load of 4000 psf, when the plastic enclave is already well-advanced, the settlement accruing from plastic flow, at the centre of the load, is only some 45% of the total settlement; near collapse, it is about 70%. In view of the above, a design bearing capacity based on local shear failure corresponding to the "knee" of the settlement-load curve of Fig. 37(a) may be unduly pessimistic. Indeed, from the structural standpoint, the present slab could theoretically resist the bending moments that occur just before collapse using double reinforcement.

Due to the proximity of the rigid base and the high Poisson's ratio, there is significant elastic heave. The additional settlement arising from plastic flow leads to a corresponding volume of material being squeezed out as additional heave. Note that with increasing plastic flow, there is a tendency for relatively more of this material to accumulate nearer the strip with the result that the positions of the start of and the maximum heave (which becomes considerably more

than for a purely elastic response) both occur closer to it, diminishing left of the maximum more rapidly.

Also plotted in Fig. 38 are the horizontal displacements of the surface joints, which are directed away from the centre of the strip except, of course, the zero displacements at the centre. These, like the settlements show (a) an abrupt change in magnitude (in this case, an increase) towards the edge of the strip and (b) the maximum displacement occurring nearer the strip (coinciding with the point of maximum heave at collapse) and diminishing more rapidly to the left , with increasing plastic flow.

The above observations on the behaviour of the displacements as the layer becomes increasingly plastic can be explained as follows.

When the layer is elastic, the strip settles and the displaced material is gradually turned up to emerge as heave (see Fig. 39). As it becomes plastic, however, the enclave effectively softens the area below the strip and this leads to greater settlements as well as more heave in the vicinity of the strip than from a purely elastic response. The latter effect becomes greatly accentuated when the plastic enclave spreads laterally since the material below the surface adjacent to the strip is then extremely soft. Also, since by then the displacements due to plastic flow are predominant, the mode by which material is displaced as the strip settles becomes relatively more localised around the strip as is evident by comparing Figs. 39(a) and (d). Thus, in order to maintain compatible flow, the abrupt changes in displacements and the relatively greater heave

and lateral displacements in the vicinity of the strip described earlier are required. By the same token, the displacements fade more quickly away from the load with increasing plastic flow.

At collapse, there is a semblance of an area of intense movement in the vicinity of the load that is underlain by a relatively static plastic region, beneath which the material is still elastic - such as associated with slip-line analysis. That is, the displacement-iteration curves in the above area of collapse settle into constant slopes whilst those of the underlying static region converge to finite values. The "bump" in the heave of the final (i.e. collapse) curve of Fig. 38 is, in fact, a manifestation of this behaviour; displaced material continually emerges near the edge of the strip whilst further along the surface in the static region, there is no more heave with iteration.

Fig. 40 which shows the deformed assemblage at various loads provides further illustration of the above behaviour. The lateral extent of the area of intense movement is approximately where the plastic enclave penetrates free surface (Fig. 36(d)). It also roughly agrees with the lateral extent of the Prandtl slip-line field (30).

A final note on the accuracy of the computed displacements. It has already been demonstrated that the computed surface displacements for the elastic layer are generally within an accuracy of about ± 2% of the values calculated by Poulos (10) - see Section 2.5.1. In addition, it is generally in the nature of reasonably structured

finite element assemblages that as the areas of prescribed displacements and external loadings are further removed, the solution improves. It is therefore considered that the above order of accuracy may be presumed to generally apply to the computed displacements for the elastic solution. For the elastoplastic solution, the independent elastic phase of the assemblage will continue to perform with the above accuracy. For the plastic phase, however, no known solutions are available for comparison of displacements. However, a study was made into the effect of altering mesh size on the computed displacements in the elastoplastic range of loading. It was found that the present mesh is sufficiently fine to lead to displacements that will not significantly alter with further refinement (which is an accepted means by which a finite element solution may be improved (38)). It is therefore considered that the displacements obtained in the elastoplastic range of loading will be of the same order of accuracy as in the elastic range. Certainly, the mode of failure - from the displacement point of view - occurs near the expected failure load $(\pi+2)\ c_u$ and is kinematically comparable to those advanced via slip-line methods of analysis.

The same comments generally apply to subsequent elastoplastic models.

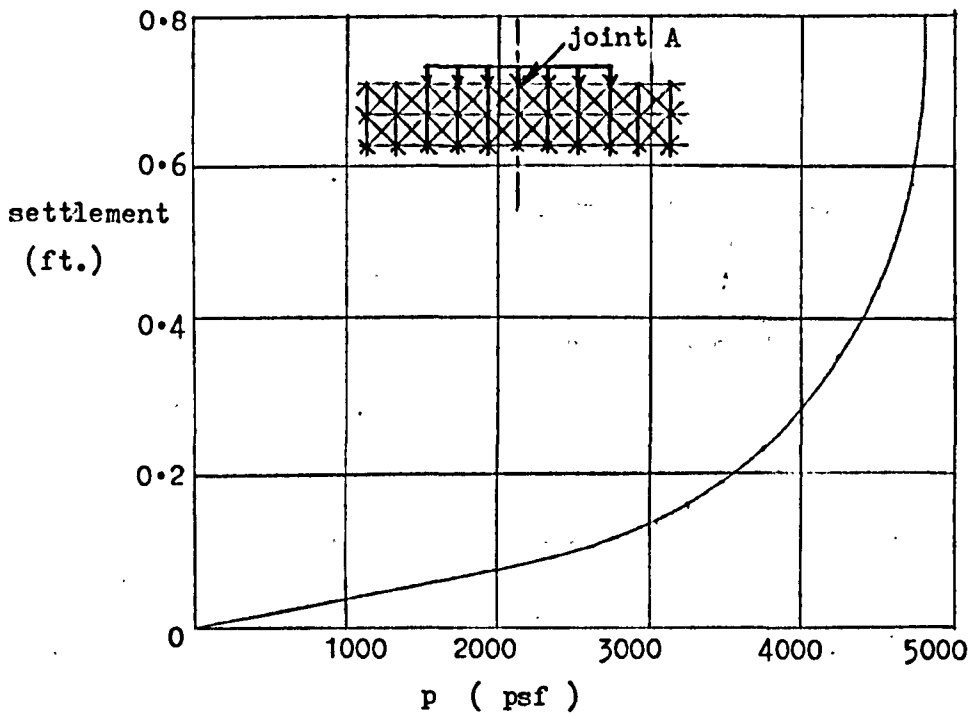

(a) Settlement-load plot

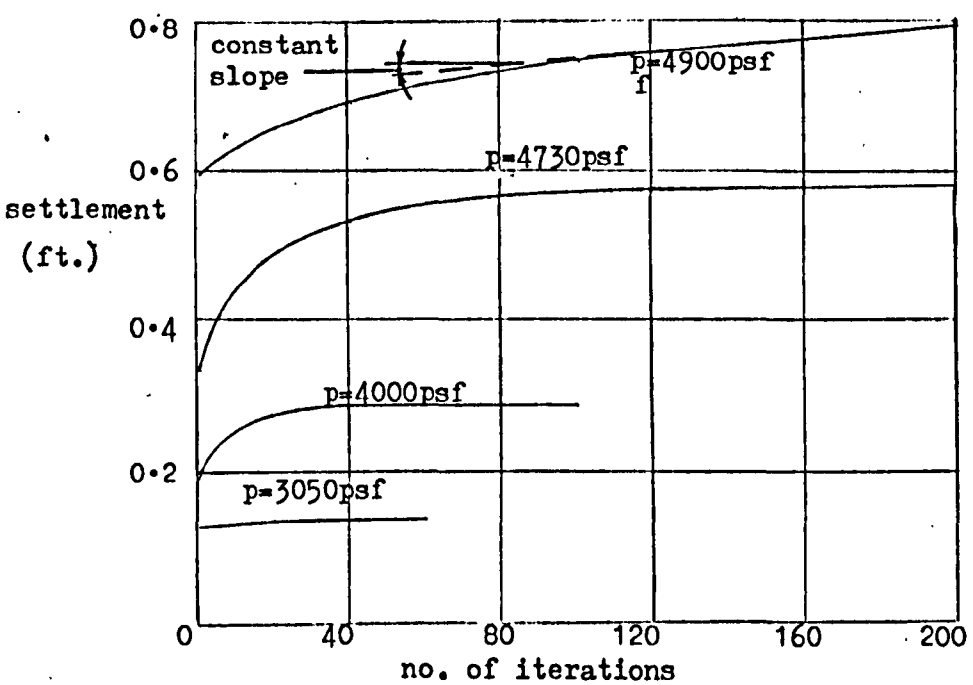

(b) Settlement-iteration plots

Fig. 37. Settlement curves for joint A

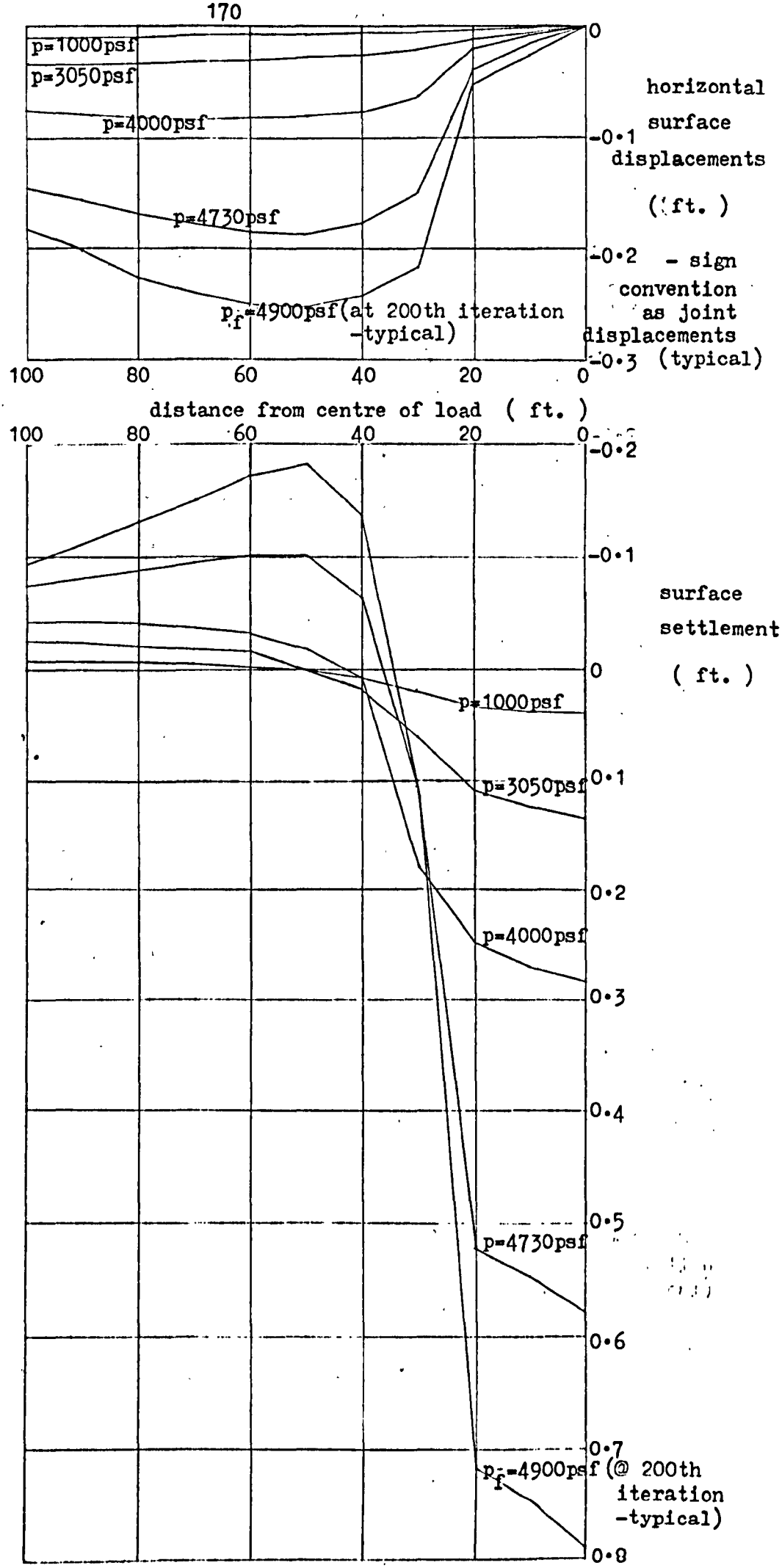

Fig. 38. Surface displacements

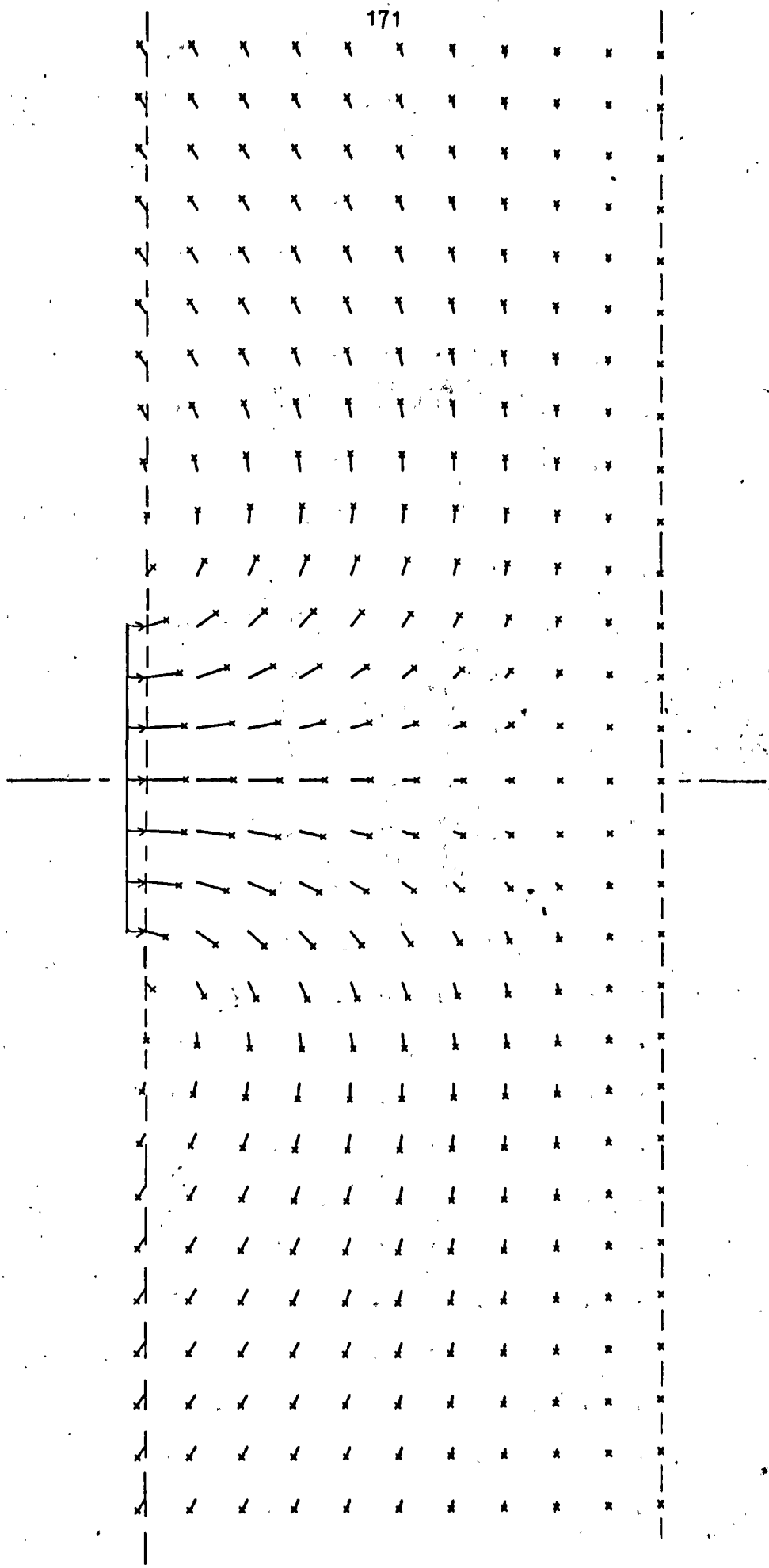

(a) $p = 1000$ psf (magnification 15 x)

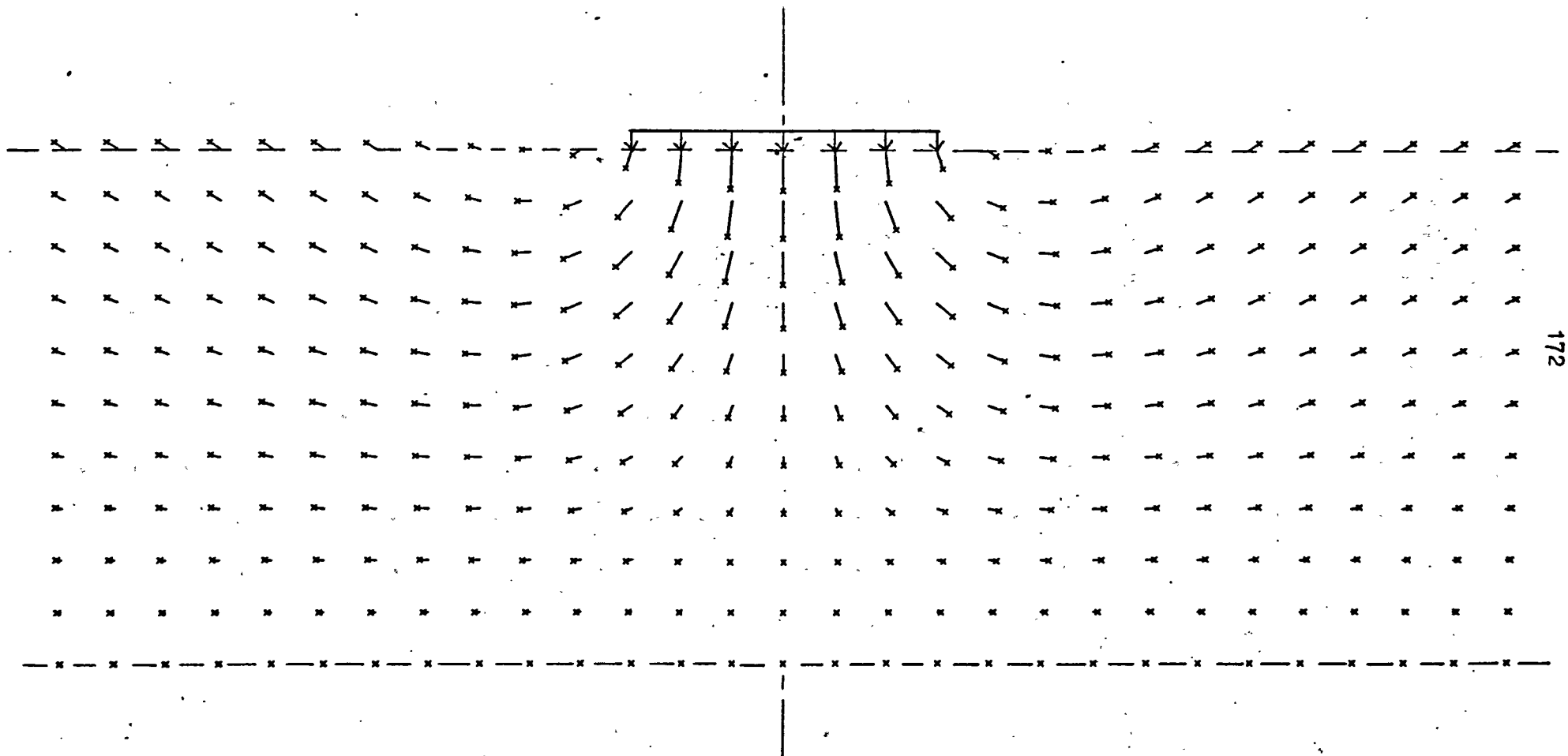

(b) p = 3050 psf (magnification 4·5x)

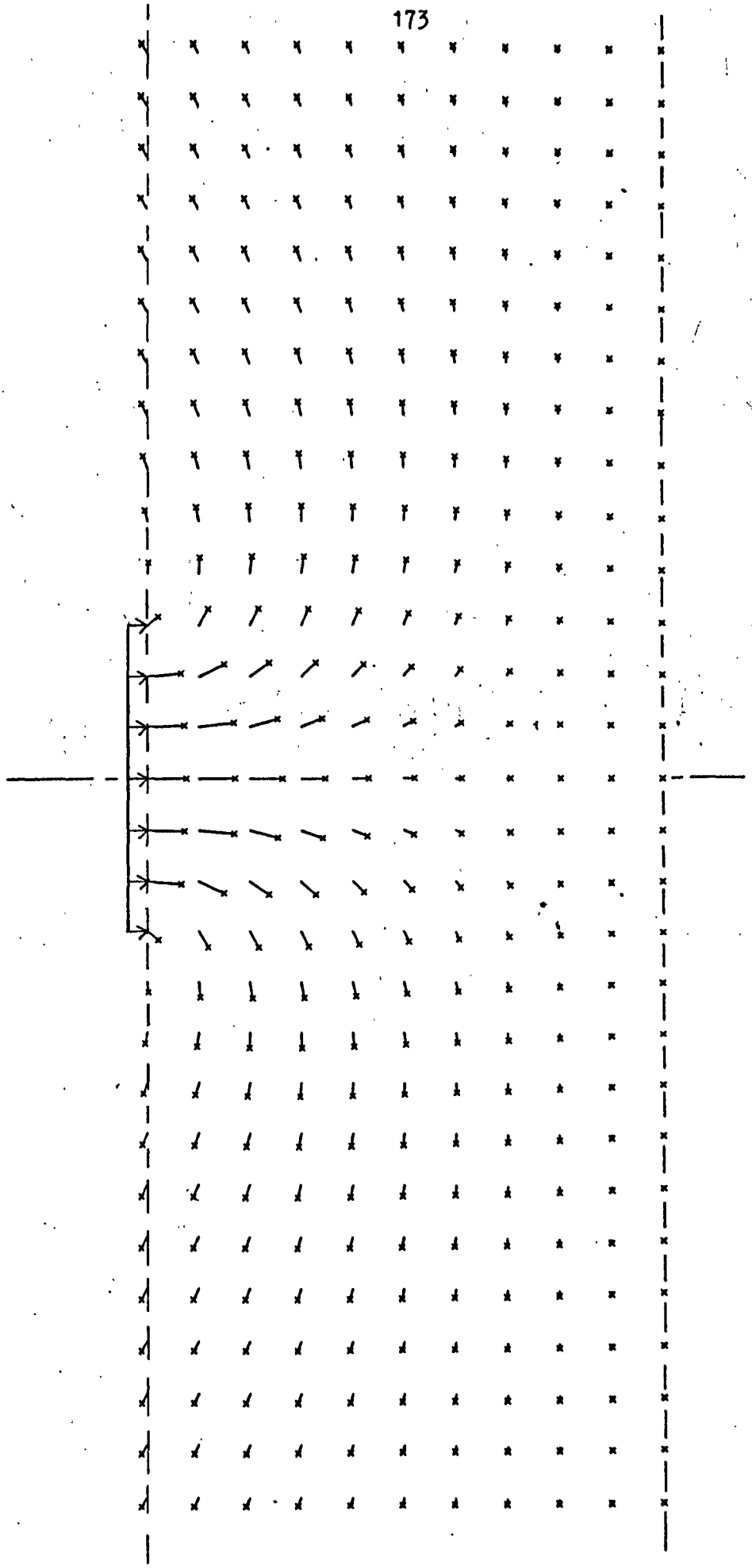

(c) p = 4000 psf (magnification 2x)

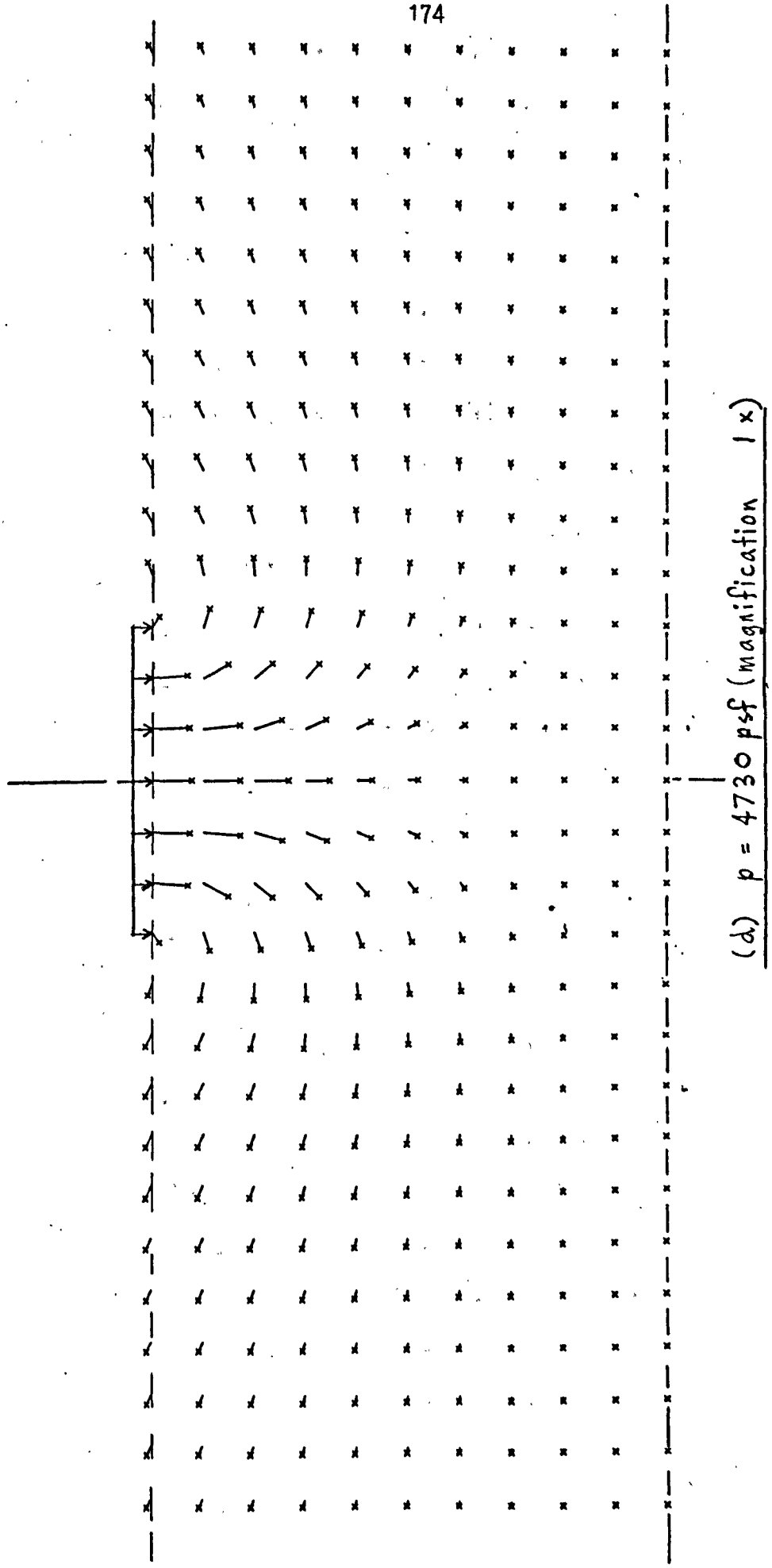

(d) p = 4730 psf (magnification 1x)

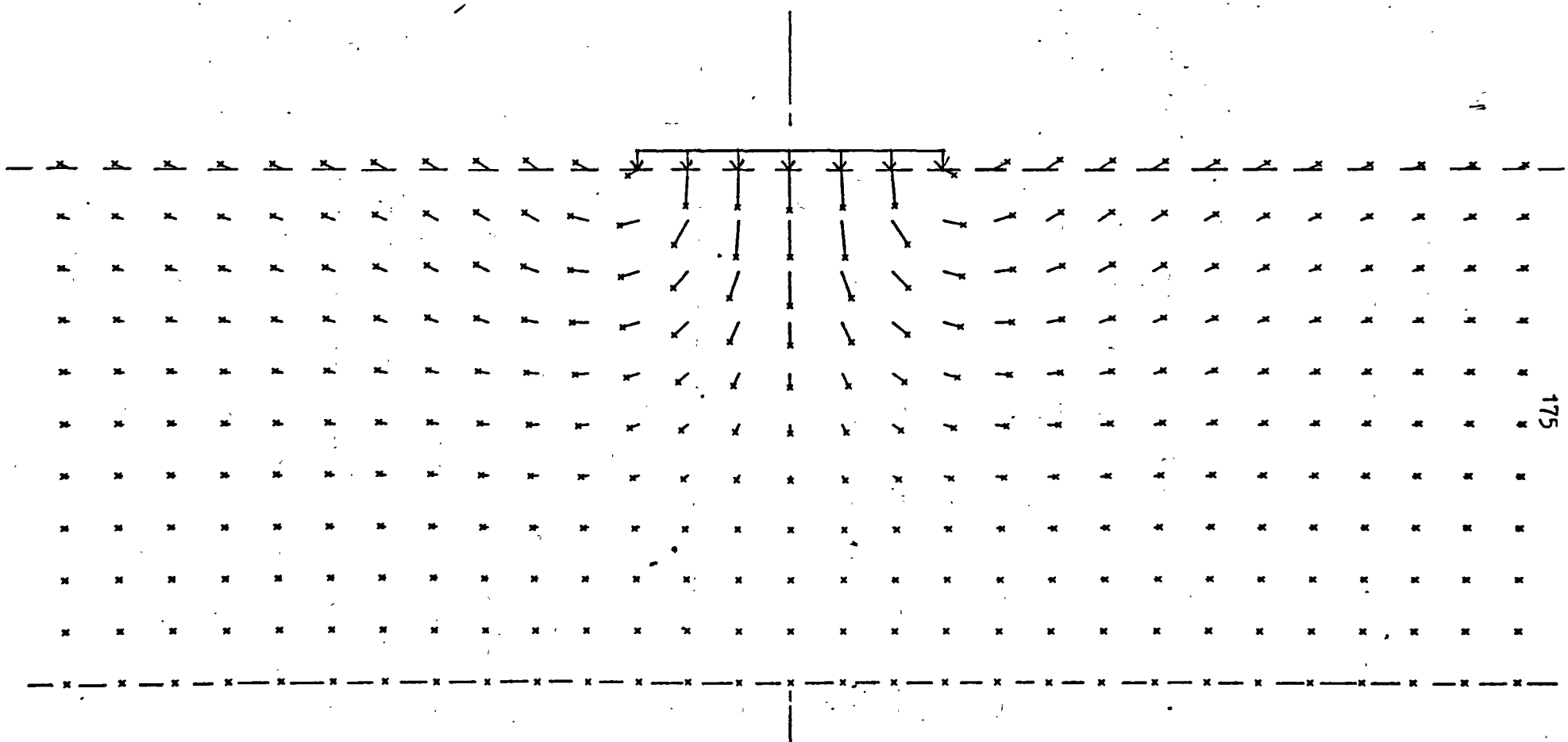

(4) p_f = 4900 psf (magnification 0.75x)

Fig. 39. Joint displacements at various loads (crosses at final positions)

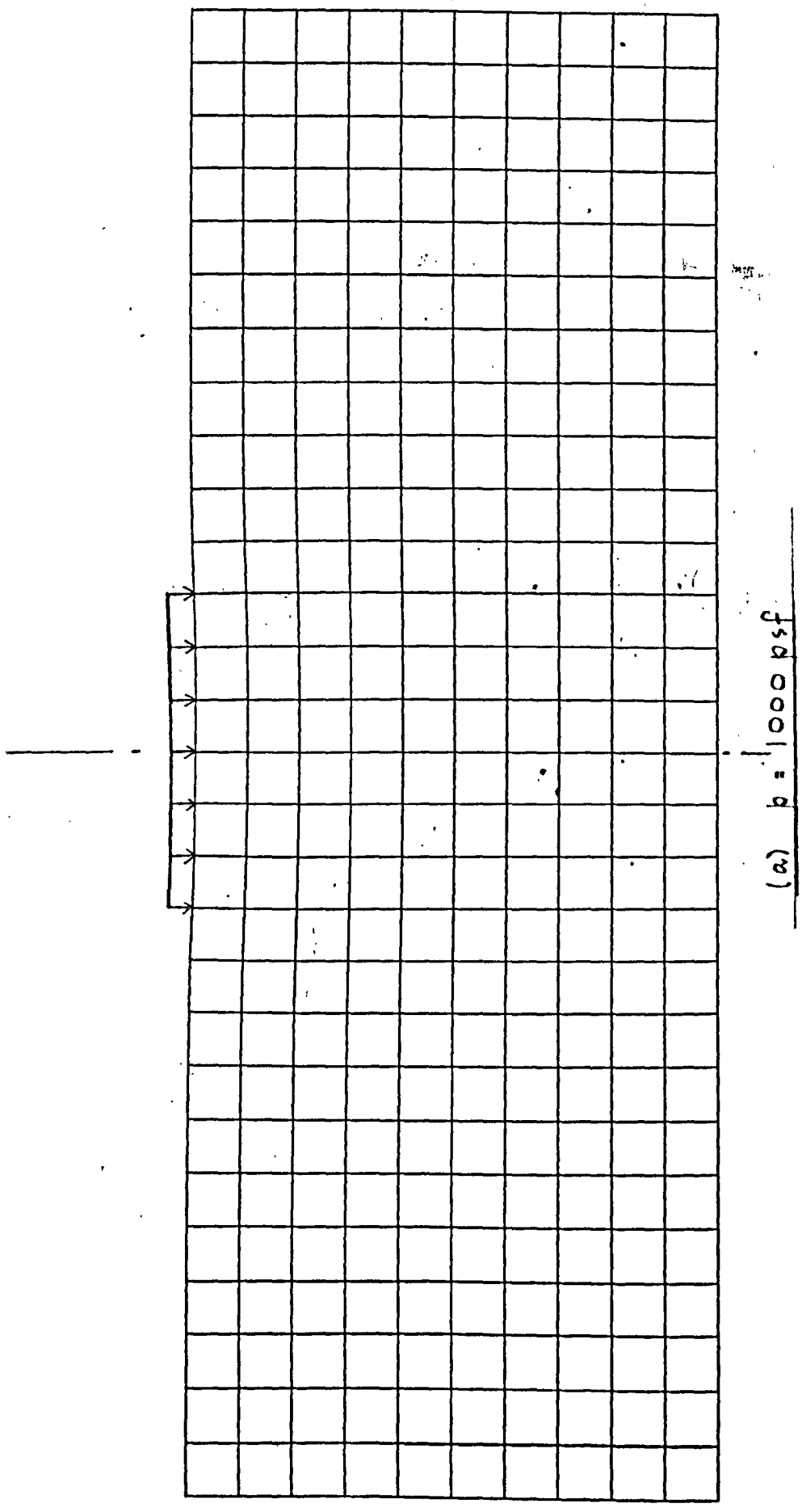
(a) p = 1000 psf

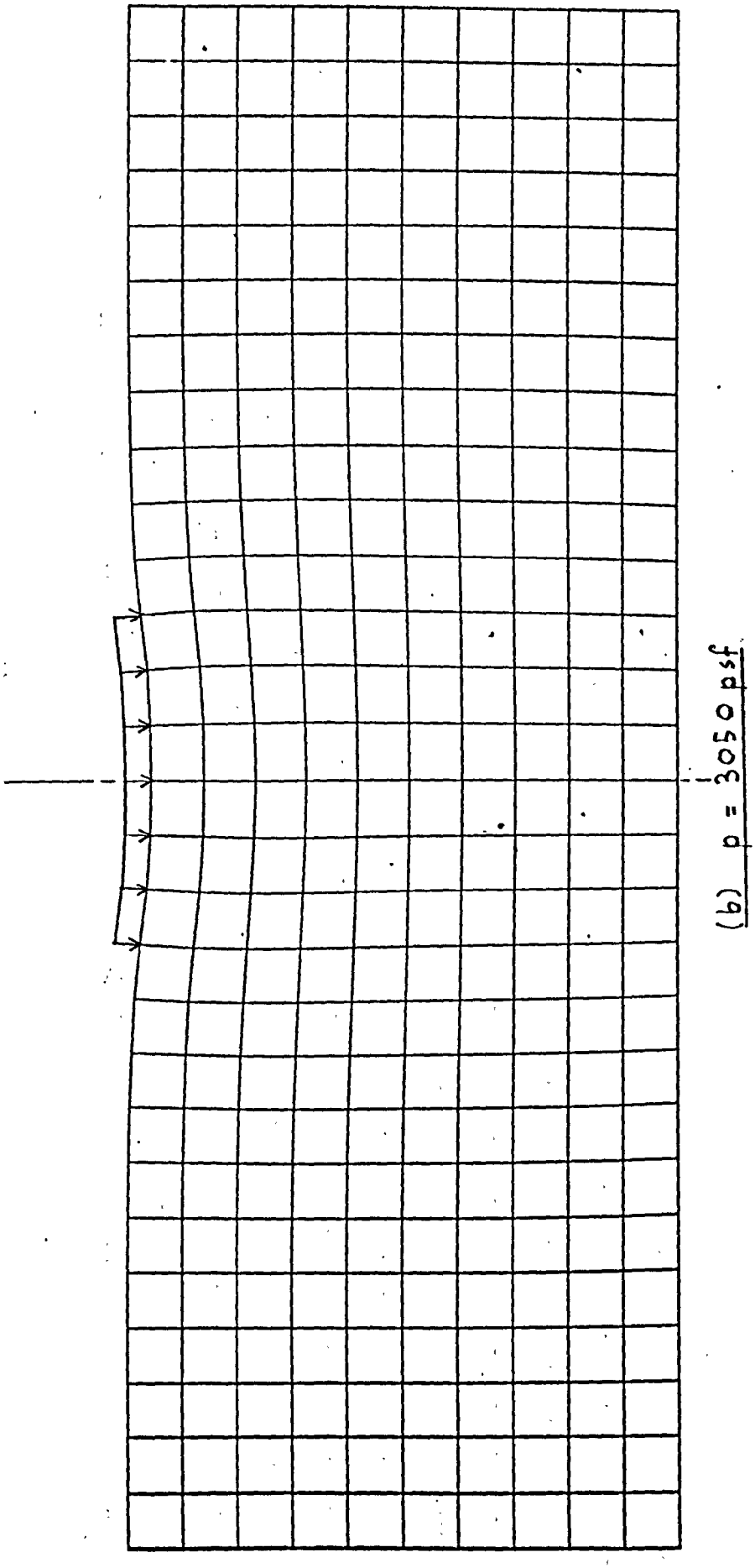

(b) p = 3050 psf

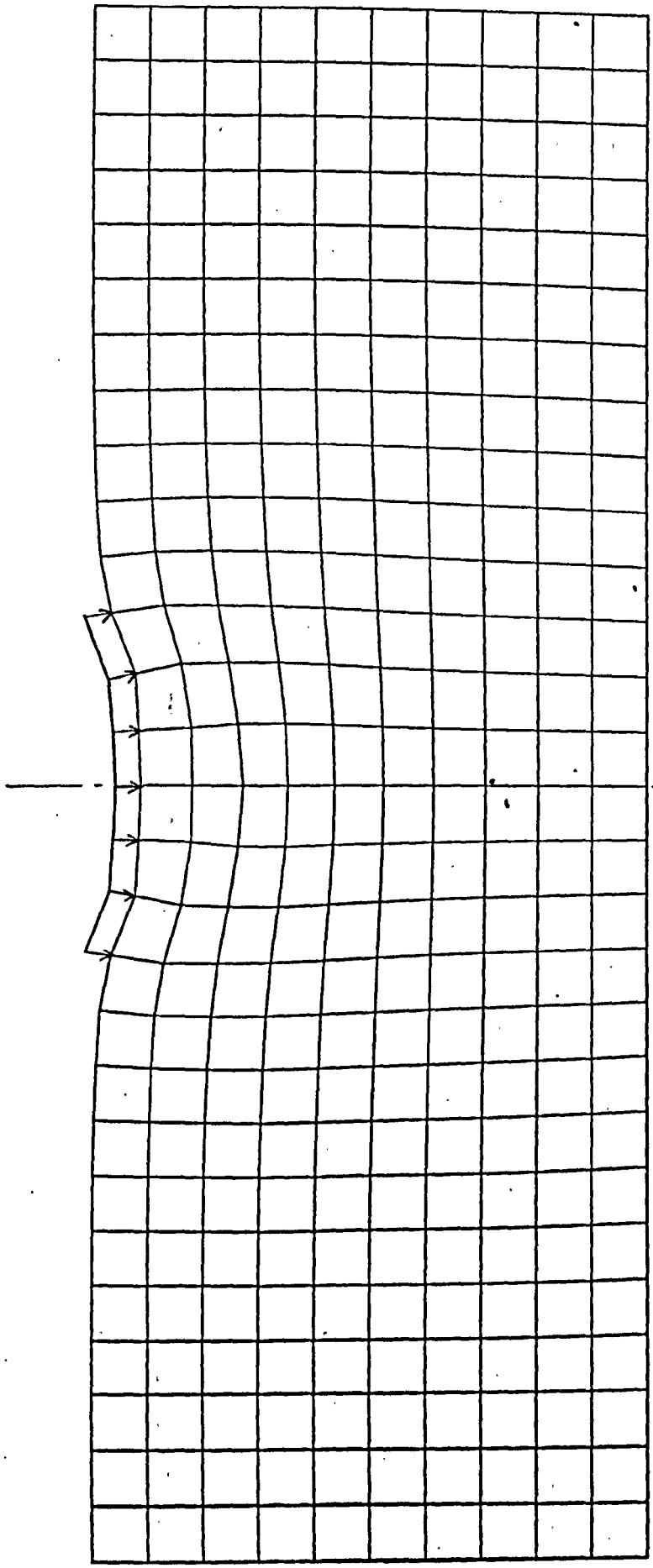

(c) p = 4000 psf

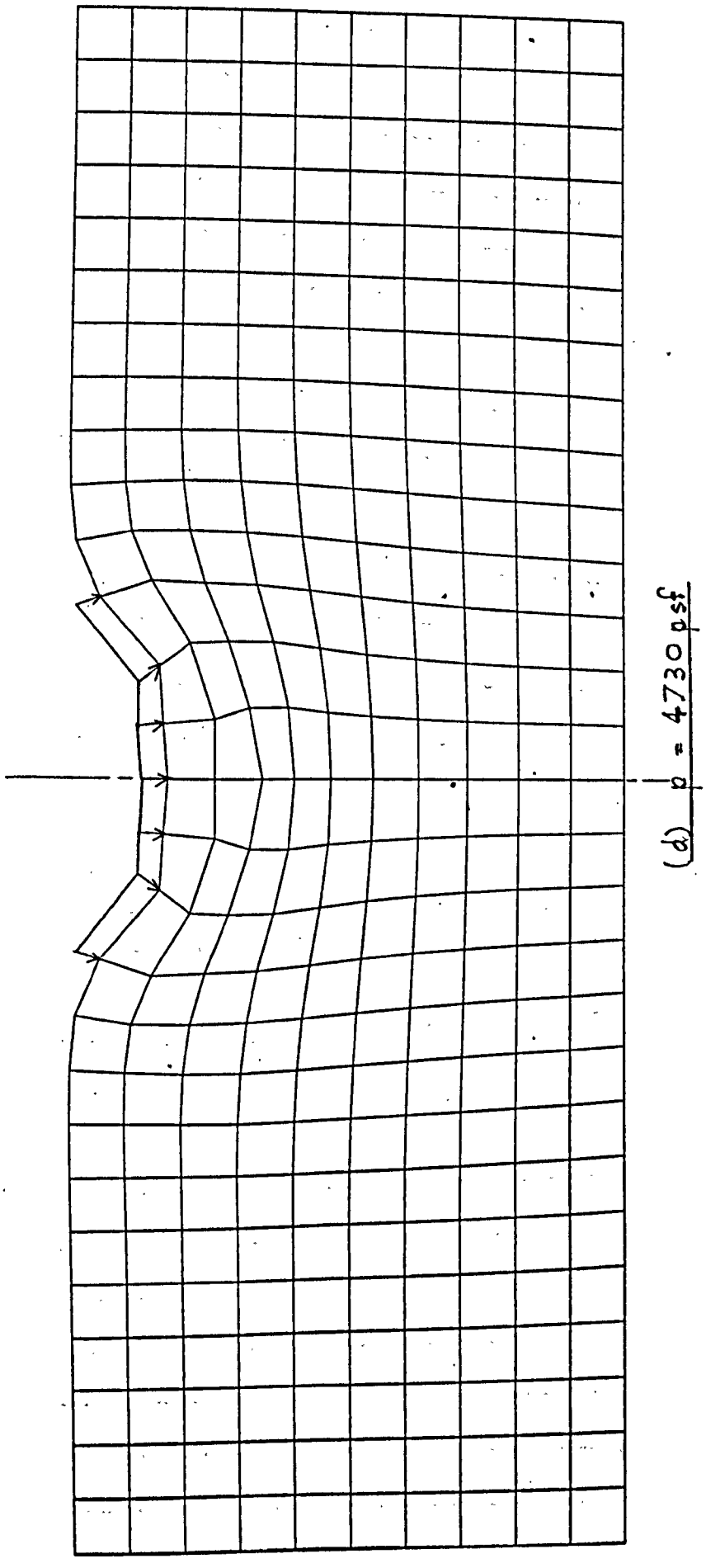

(d) $p = 4730$ psf

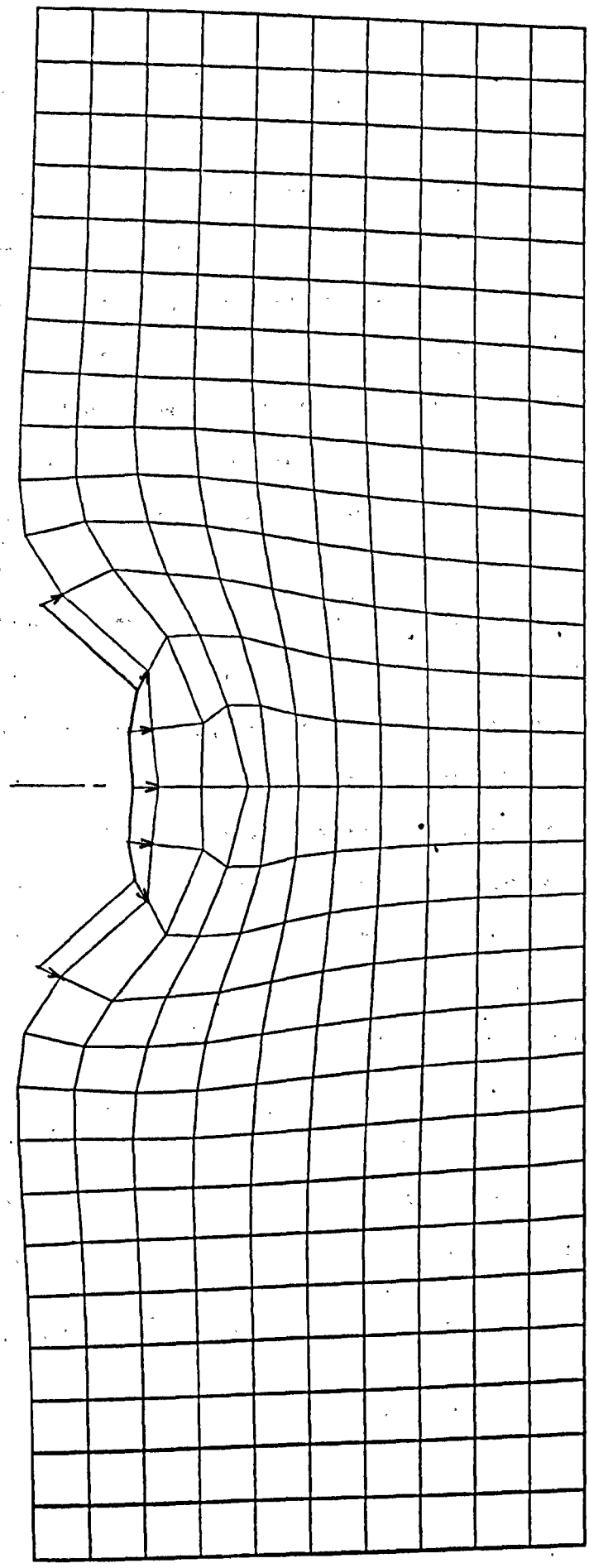

(c) $p_f = 4900$ psf

Fig. 40. General deformation of layer at various loads

2.6.3. Stresses in the layer

Fig. 41 shows the normal stress distribution down the centre and edge, respectively, of the strip load. For the horizontal stress σ_x, it can be seen that increasing the load beyond first yield does not lead to proportionate increase in the stresses prior to yield. Indeed, the normalised horizontal stresses (i.e. σ_x divided by the strip pressure) are extremely sensitive to plastic flow, although becoming generally less so with increasing flow. Part of this sensitivity is featured as considerable variation in the shapes of the horizontal stress - depth curves in the initial stages of plastic flow, although becoming less pronounced towards collapse. The vertical stresses σ_y, on the other hand, increase approximately in proportion to the load right up to collapse. That is, the normalised vertical stresses are relatively insensitive to plastic flow, thus subscribing to the sole use of elastic theory in determining σ_y. The out-of-plane stress σ_z, is approximately $0{\cdot}5(\sigma_x + \sigma_y)$ which is to be expected for this material (see Eqn. 66 with c=0). It thus has a sensitivity to increasing plastic flow that is an average of the sensitivities of σ_x and σ_y.

In elastic consolidation theory, it is well-known that at the undrained stage, the pore pressure increase is equal to the volumetric stress increase $\sigma_v = \frac{1}{3}(\sigma_x + \sigma_y + \sigma_z)$. It can similarly be shown that for the drained $\bar{c} - \bar{\phi}$ material of Chapter 3, the same applies.

Under undrained conditions, there is no volume change. Therefore, the infinitesimal plastic volume change

$$\delta\varepsilon_x^p + \delta\varepsilon_y^p + \delta\varepsilon_z^p = 0$$

Substituting the expressions in Eqn. 73 (pp. 332) into the above equation, we have

$$\lambda\left(\frac{\partial F}{\partial\sigma_x} + \frac{\partial F}{\partial\sigma_y} + \frac{\partial F}{\partial\sigma_z}\right) = \text{Sin}\,\bar{\phi} = 0$$

That is, $\bar{\phi} = 0$

Similarly, the elastic volume change

$$\varepsilon_x^e + \varepsilon_y^e + \varepsilon_z^e = 0$$

so that $\frac{(1-2\bar{\nu})}{\bar{E}}\left(\bar{\sigma}_x + \bar{\sigma}_y + \bar{\sigma}_z\right) = 0$, the elastic drained parameters $\bar{E}$ and $\bar{\nu}$ being described in the drained model of Chapter 3.

Therefore $(\sigma_x - u) + (\sigma_y - u) + (\sigma_z - u) = 0$

where u is the pore pressure so that

$u = \frac{1}{3}(\sigma_x + \sigma_y + \sigma_z) = \sigma_v$ for the prescribed elastoplastic behaviour. It is of interest to note that just as the use of E_u in conjunction with $\nu = 0{\cdot}5$ has been shown to effectively represent undrained behaviour of an elastic soil skeleton (34c), the use of the above relation $\bar{\phi} = 0$ which is based on no change in effective stress (54) can be similarly thought of as being representative

of a $\overline{c} - \overline{\phi}$ material under undrained conditions i.e. with zero volume change.

From the foregoing it can be seen that σ_v, and hence σ_z may be employed here in providing an indication of pore pressure distribution.

For σ_x, the effect of increasing plastic flow is generally to increase the normalised stress down the centre of the strip except near the surface where it remains about the same and towards the bottom of the layer where there is some decrease. Down the edge, a similar trend may be observed. Since, as already mentioned, the normalised vertical stress is relatively insensitive to plastic flow, σ_z may be expected to be similarly influenced by plastic flow as σ_x.

Thus, with increasing plastic flow, pore pressures near the surface will approximately increase in proportion to the applied load. Below that, there will be a marked increase in pore pressure followed by a less than proportionate increase towards the bottom of the layer - i.e. also with increasing plastic flow. Note, however, these remarks pertain only to pore pressures down the centre and edges of the strip. The above changes in emphasis of the initial pore pressures will no doubt have a corresponding effect on the subsequent consolidation process.

As required by theory (43) , constant stress conditions are found to prevail at collapse.

Finally, SYMAP plots of the normalised normal stresses are provided

in Fig. 42 for a more comprehensive study. Again, there is noticeable inaccuracy in the vicinity of the load since no data points are specified at the surface. This, however, may be remedied by extrapolation of stress curves to the surface at various sections of the layer, and adopting the surface values so obtained as data points. Further improvements can be made via the suggestions given in Section 2.3.1. However, the present plots are sufficiently accurate for examining trends - e.g. note the relative insensitivity of the normalised vertical stress over the whole layer in contrast to the widely-differing normalised horizontal stress plots.

A final note on the accuracy of the computed stresses. It has already been demonstrated that the computed stresses down the edges and the centre line of a strip load on the surface of an elastic layer are generally within an accuracy of about ± 5% of the values calculated by Poulos (10) as well as of known values of stresses at the surface of the layer (Section 2.5.1.). From these results which relate in places to areas of potential inaccuracy - e.g. near the load and the rigid base - as well as by inspection of the values of computed stresses in the remaining areas of the elastic layer, experience suggests it would be reasonable to assume that the same order of accuracy as above may be expected in general for the entire assemblage. For the elastoplastic solution, a study was made into the effect of altering the mesh size on the computed stresses. It was found that the present mesh is sufficiently fine to lead to

stresses that will not significantly alter with further mesh refinement. It is therefore considered that the stresses obtained in the elastoplastic range of loading will be of the same order of accuracy as in the elastic range. Certainly, the computed stresses remained constant at the collapse load as they should according to Drucker and Prager (43).

The same comments generally apply to the subsequent elastoplastic models.

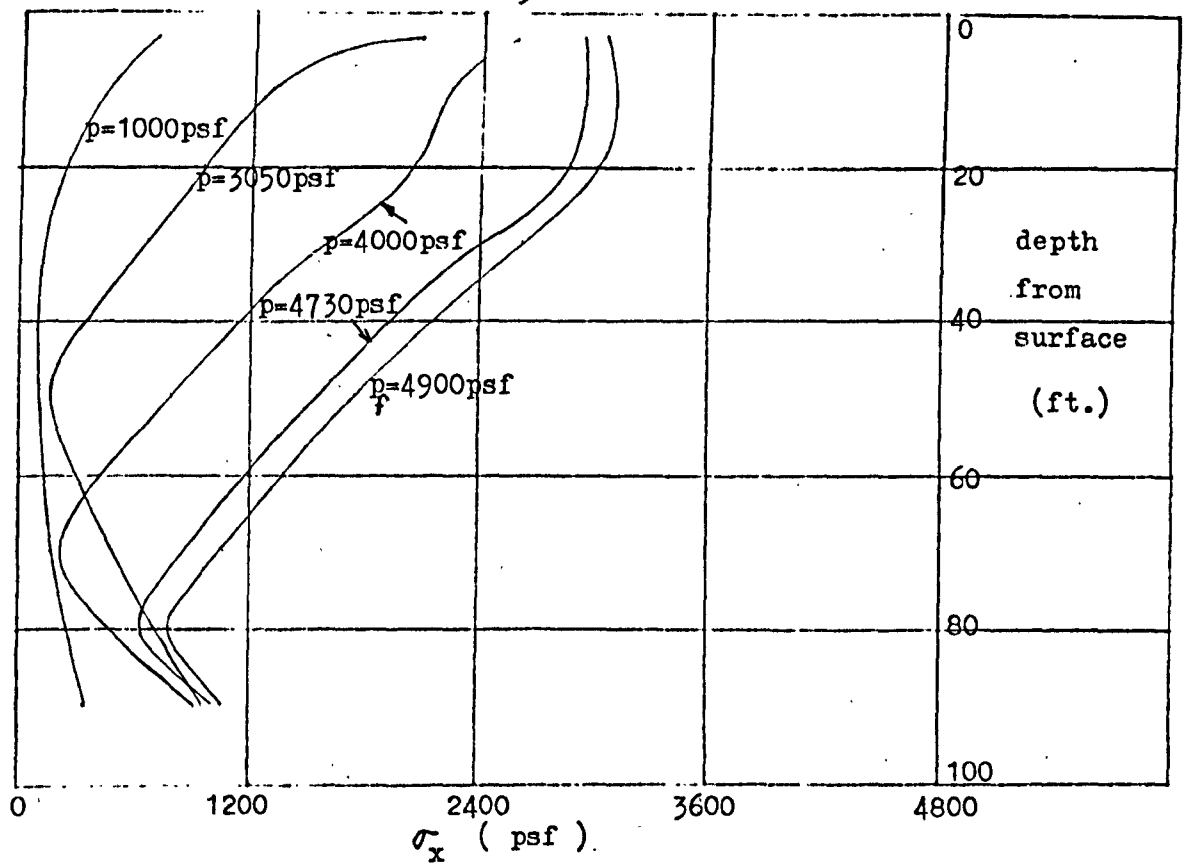

(a) σ_x distributions down centre of strip load

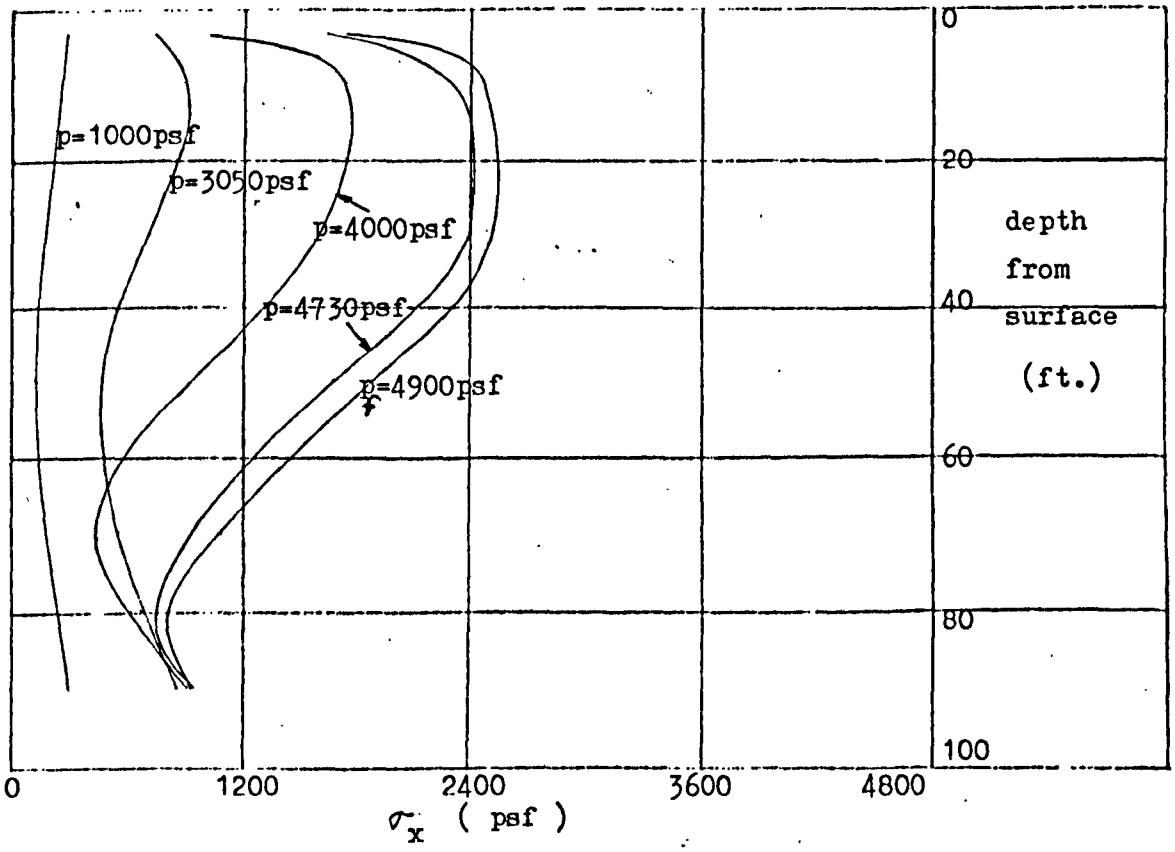

(b) σ_x distributions down edge of strip load

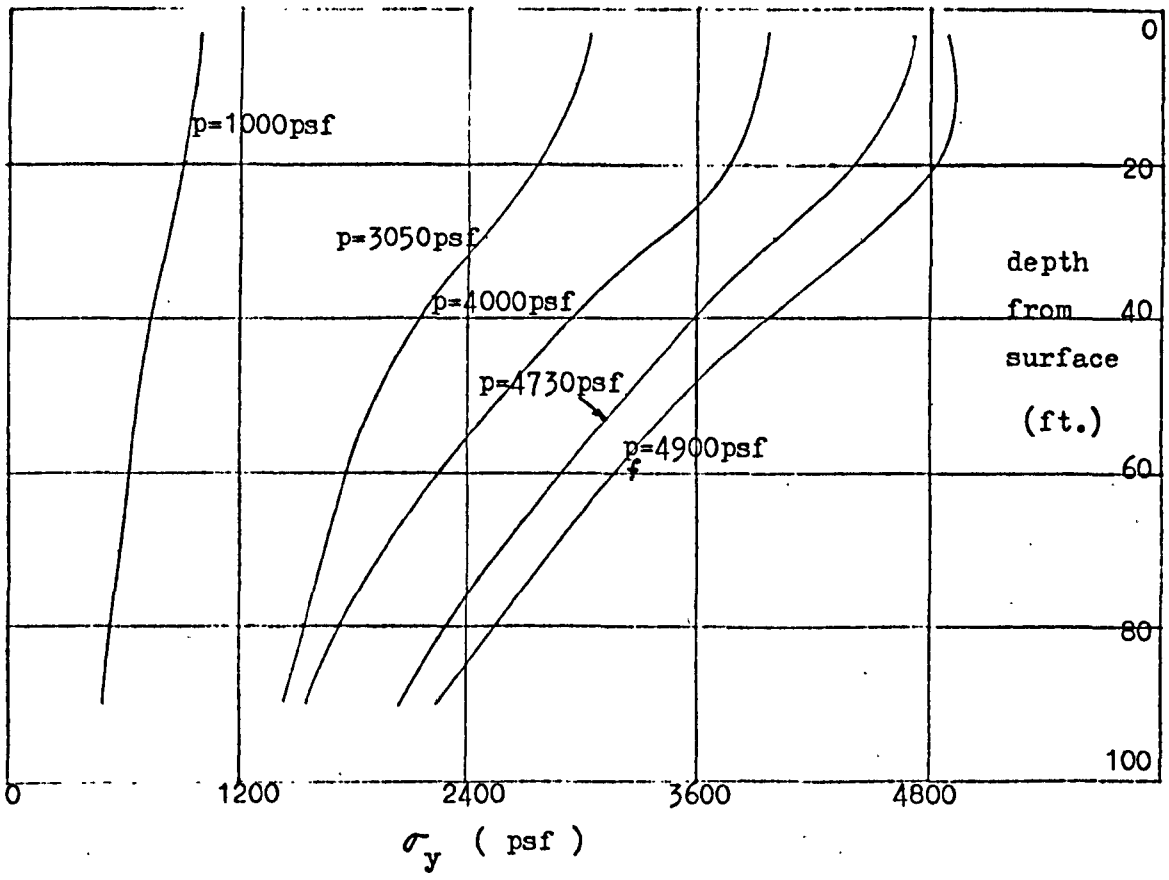

(c) σ_y distributions down centre of strip load

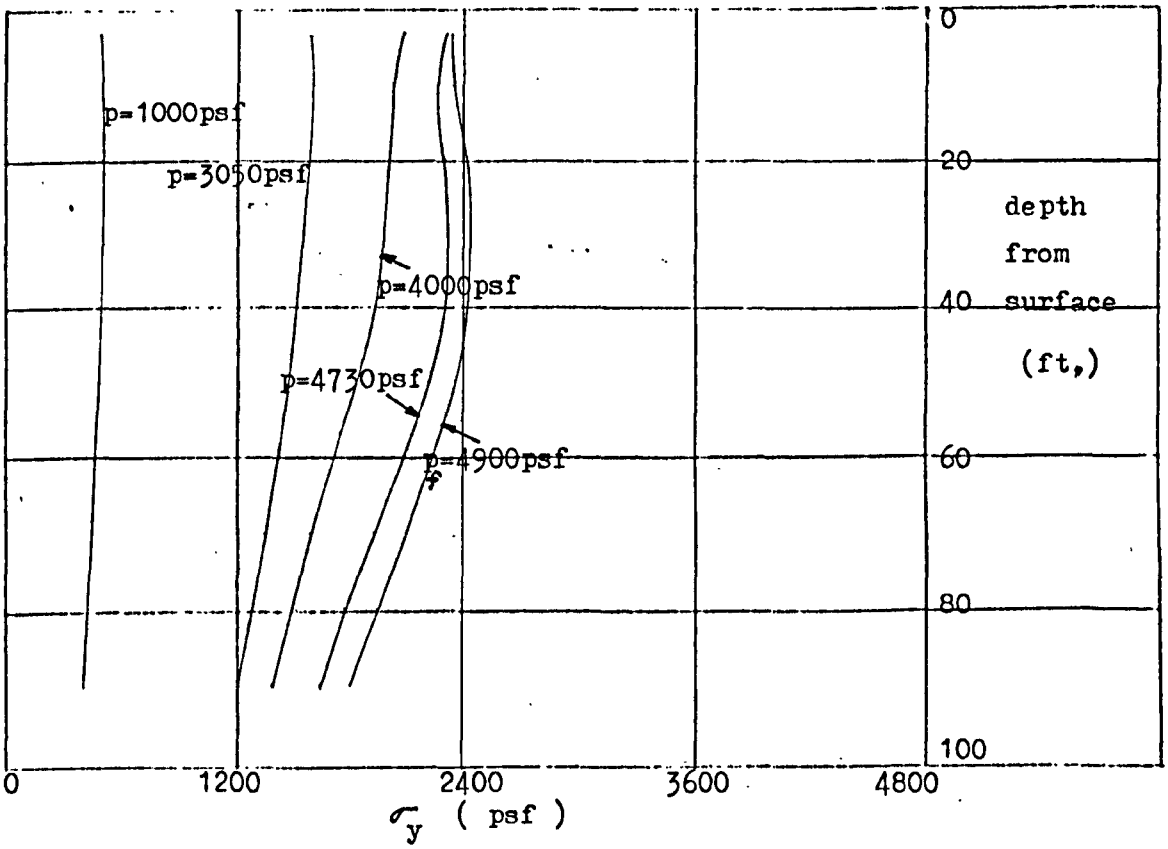

(d) σ_y distributions down edge of strip load

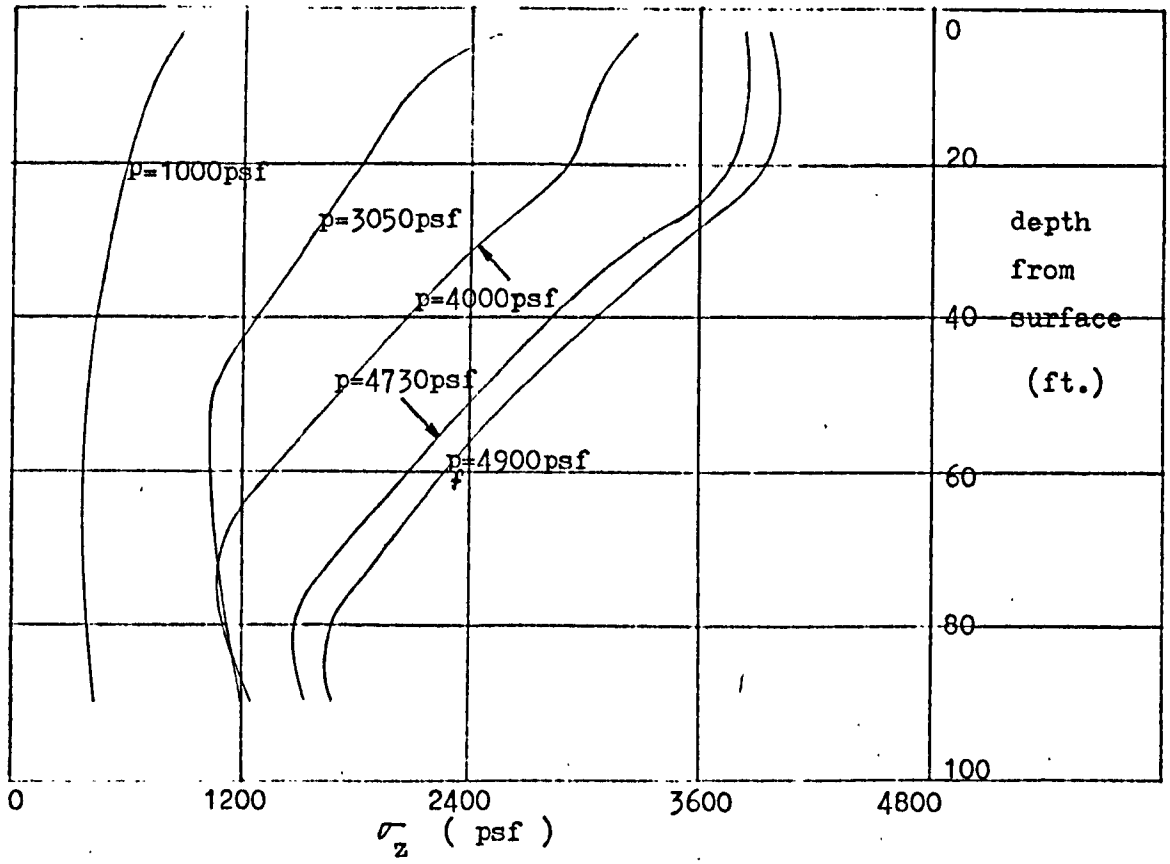

(e) σ_z distributions down centre of strip load

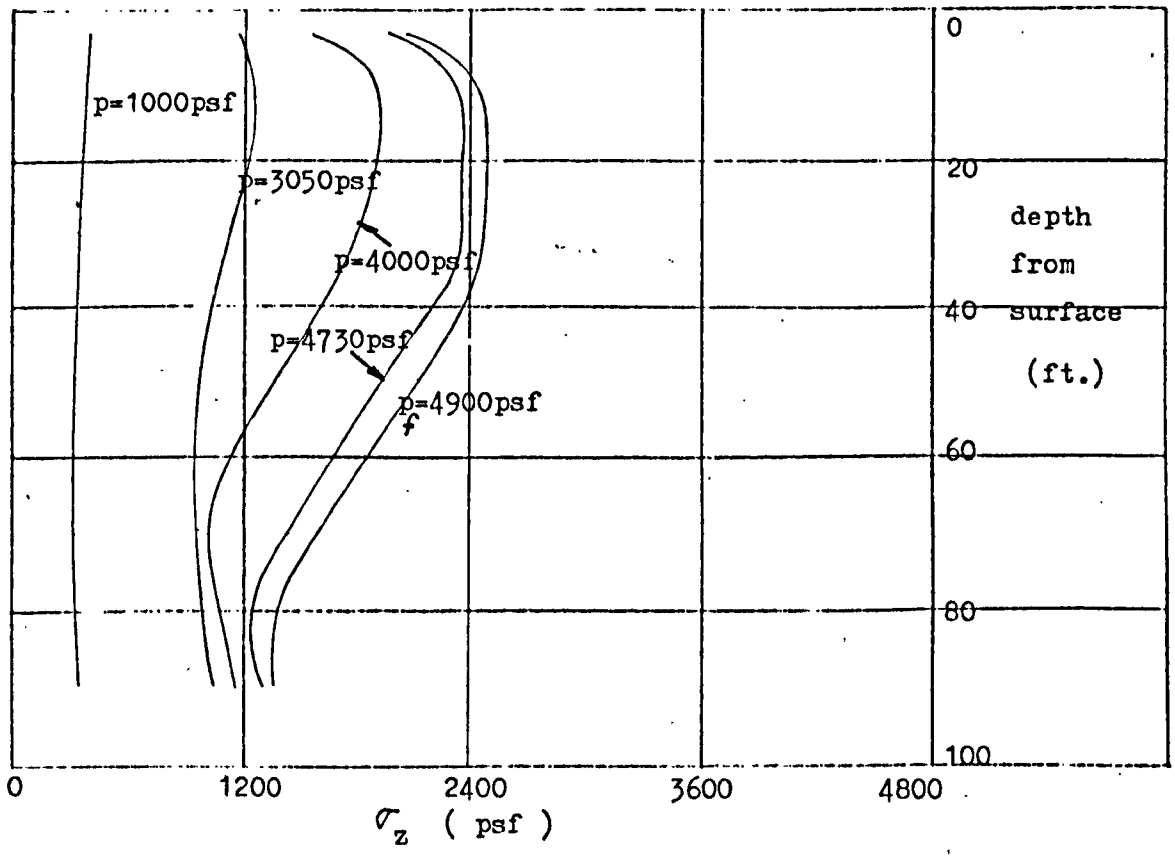

(f) σ_z distributions down edge of strip load

Fig. 41. Normal stress distributions down centre and edge of strip load

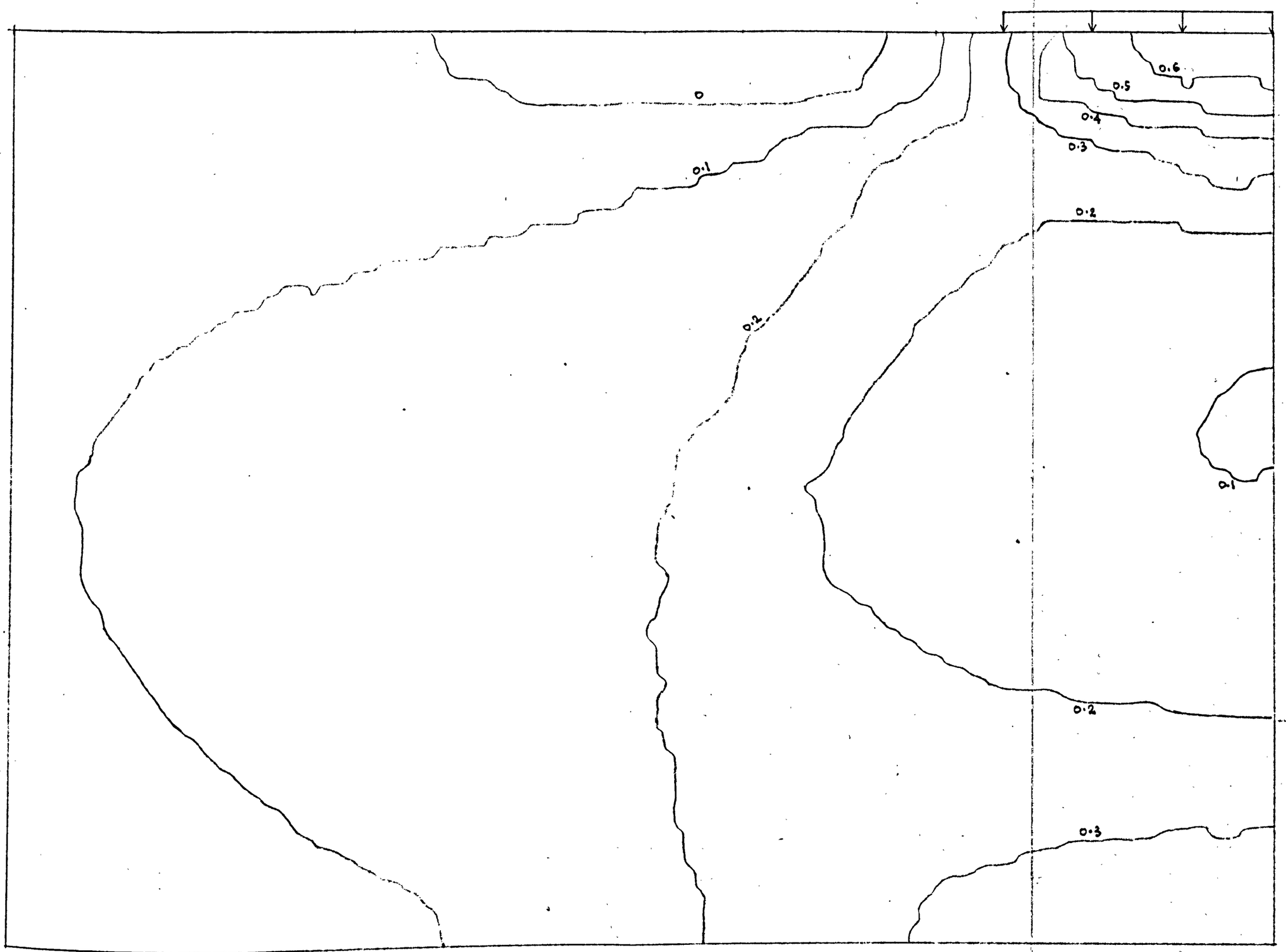

(1a) Normalised σ_x contours for p=1000 psf

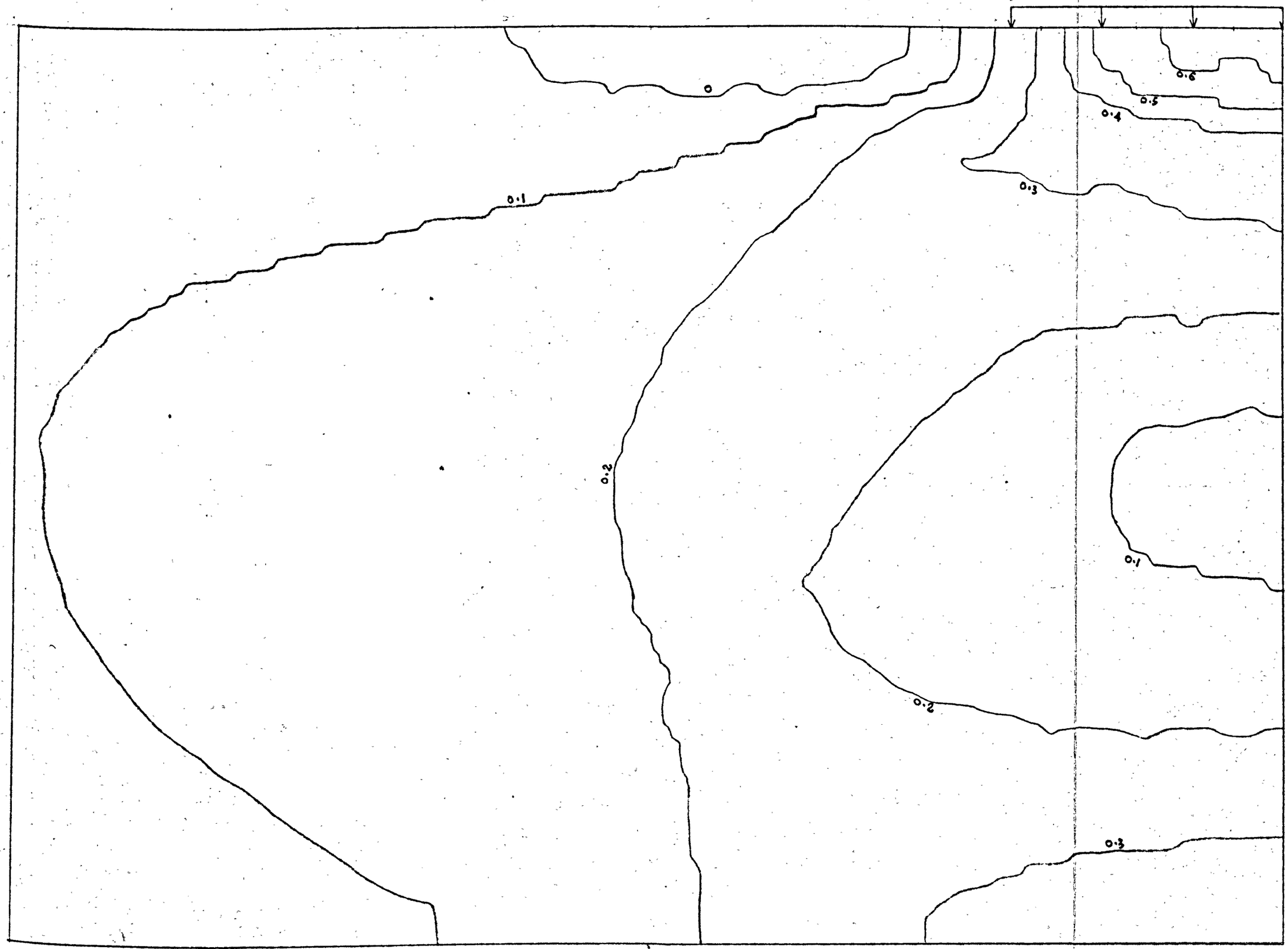

(1b) Normalised σ_x contours for $p = 3050$ psf

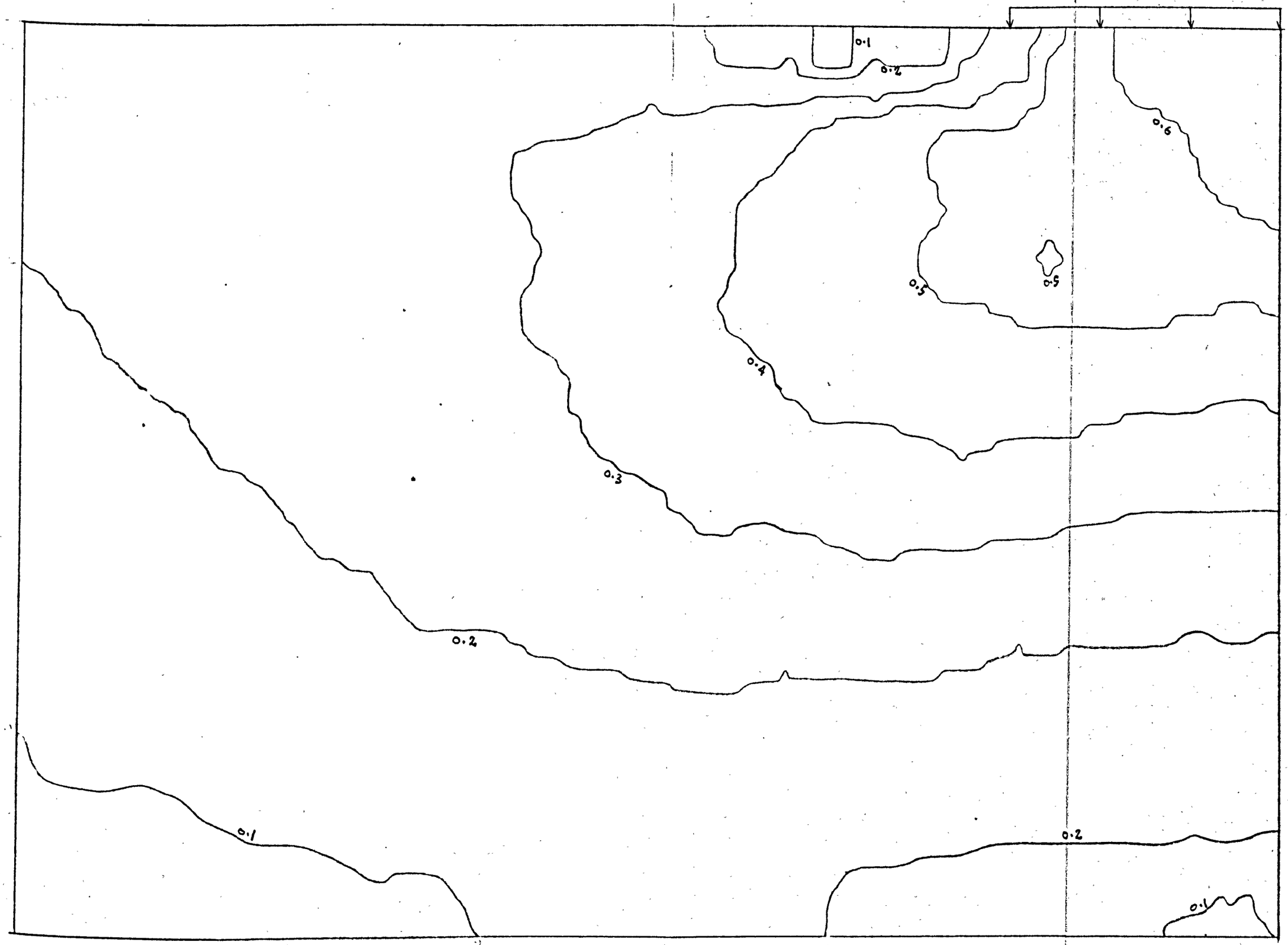

(1d) Normalised σ_x contours for p = 4730 psf

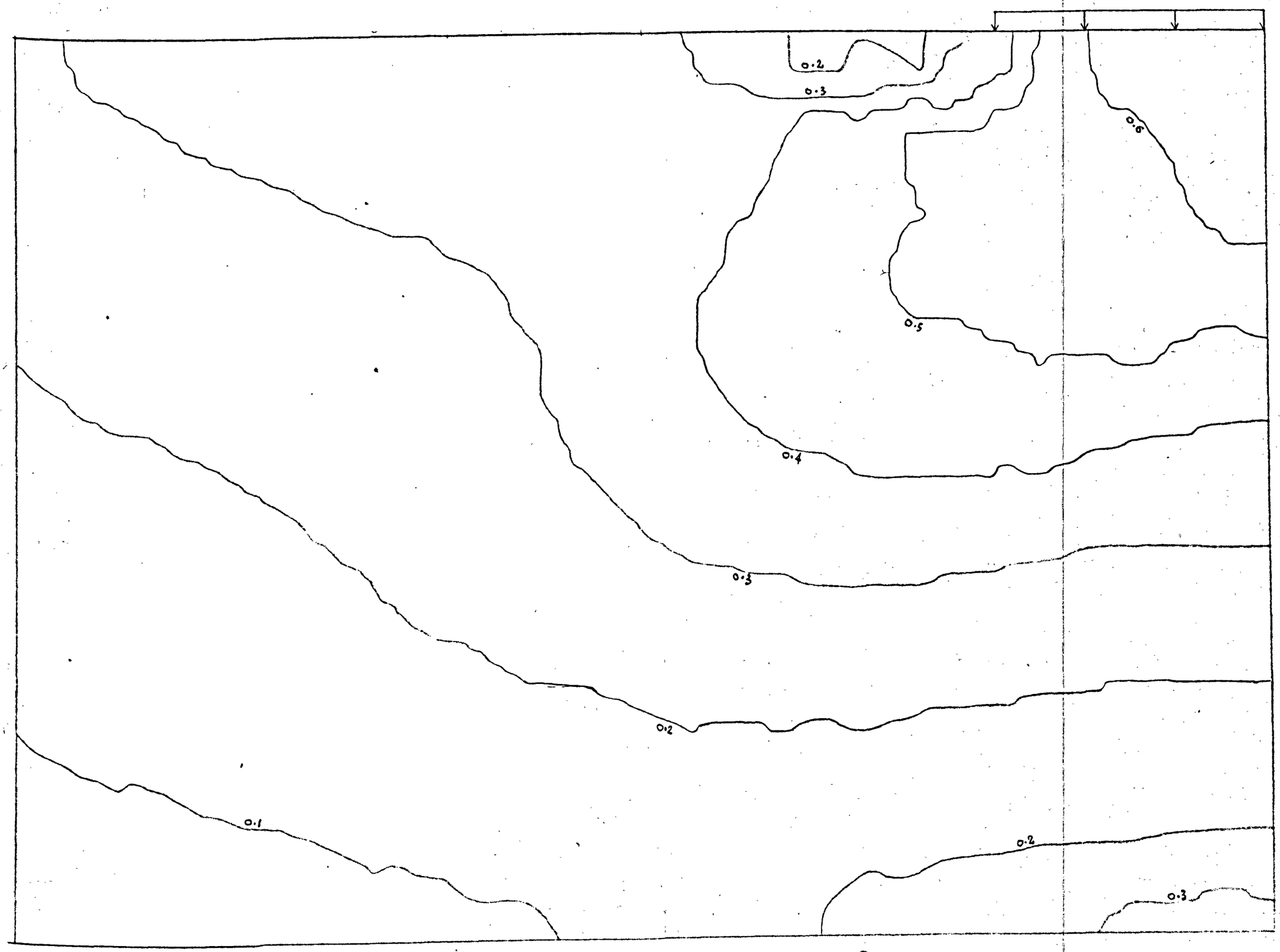

(1c) Normalised $\bar{\tau}_x$ contours for $\bar{p}_f = 4900$ psf

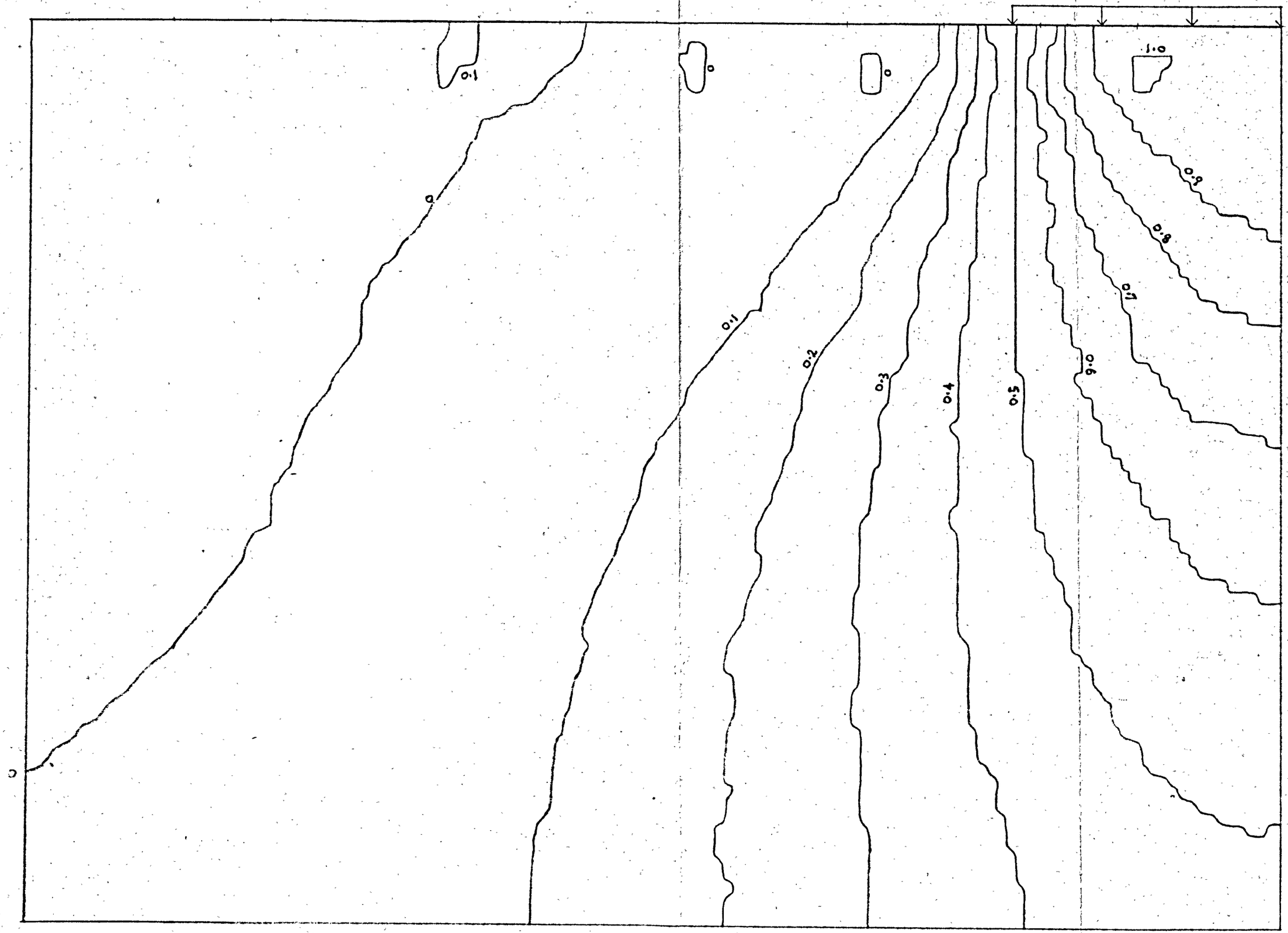

(2a) Normalised σ_y contours for p = 1000 psf

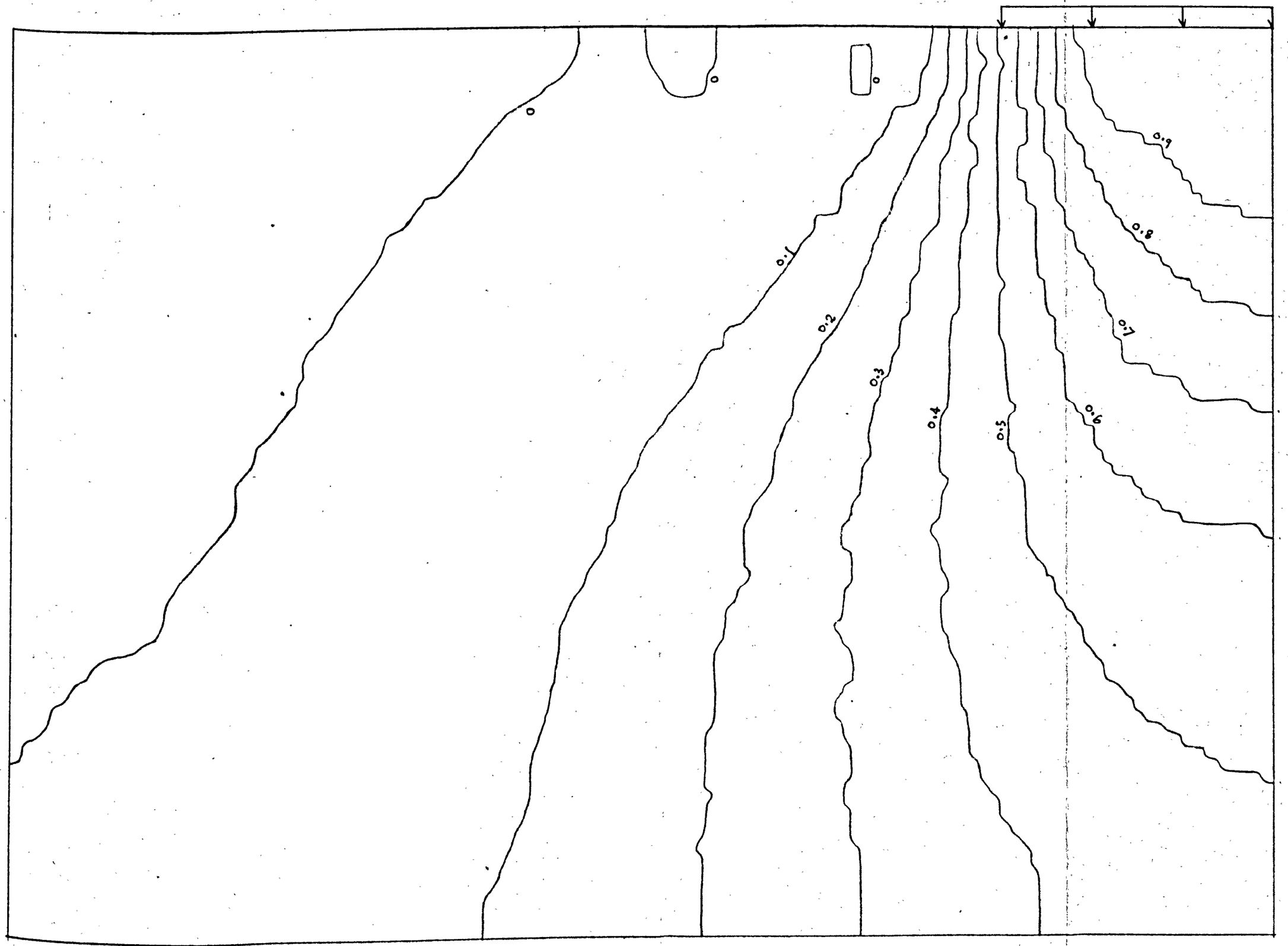

(2b) Normalised σ_y contours for p = 3050 psf

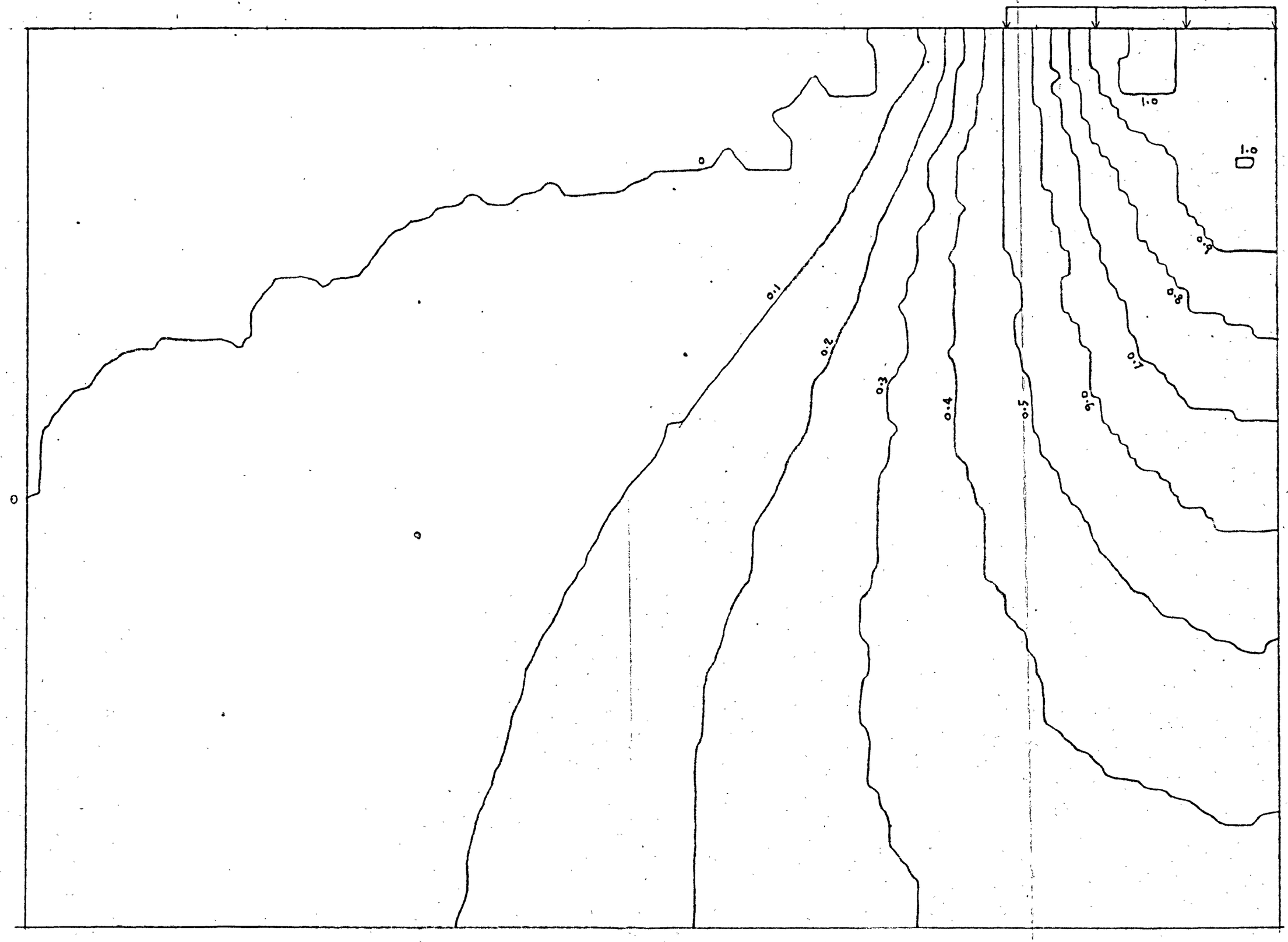

(2c) Normalised σ_y contours for p = 4000 psf

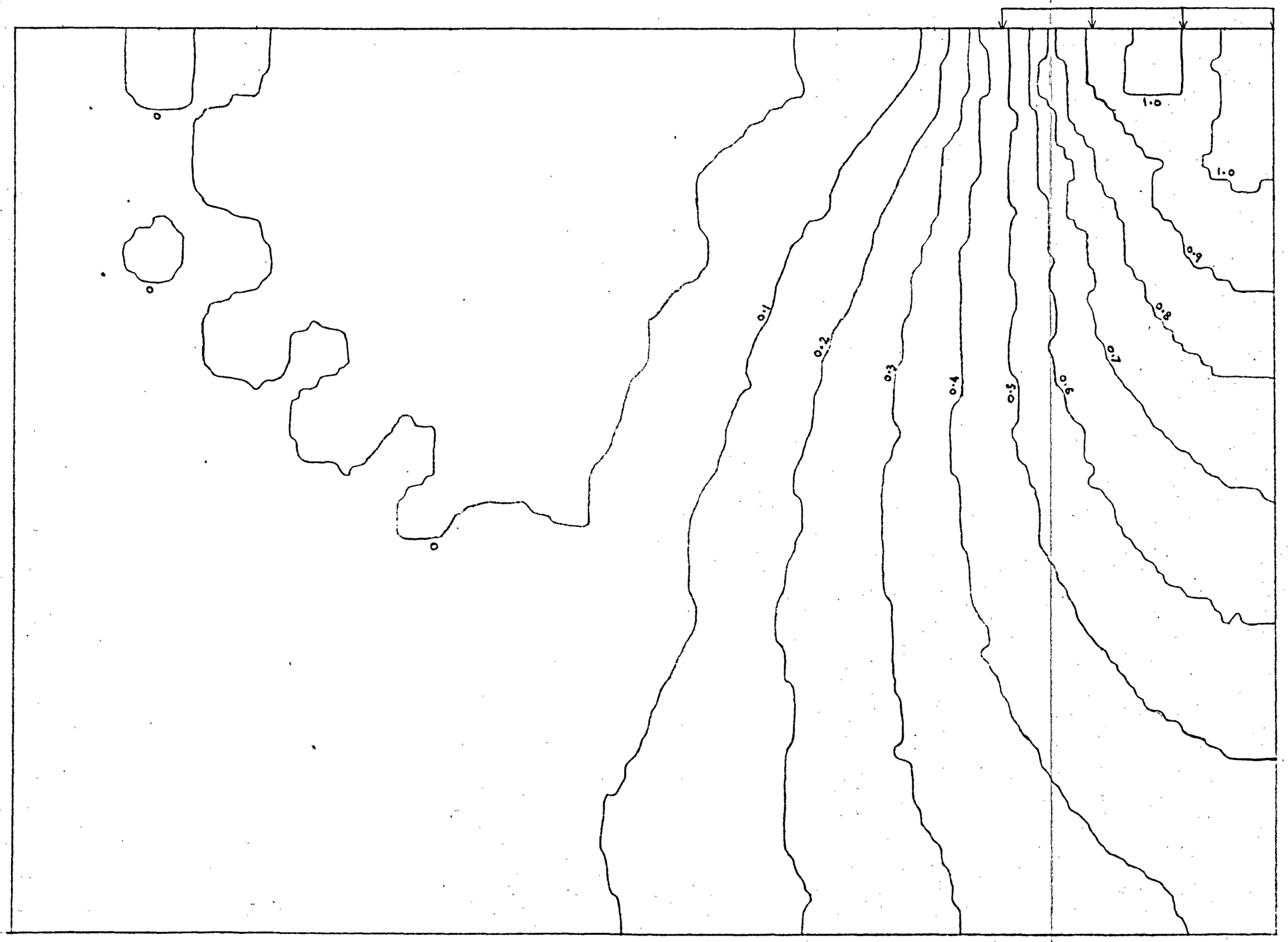

(2d) Normalised σ_y contours for p = 4730 psf

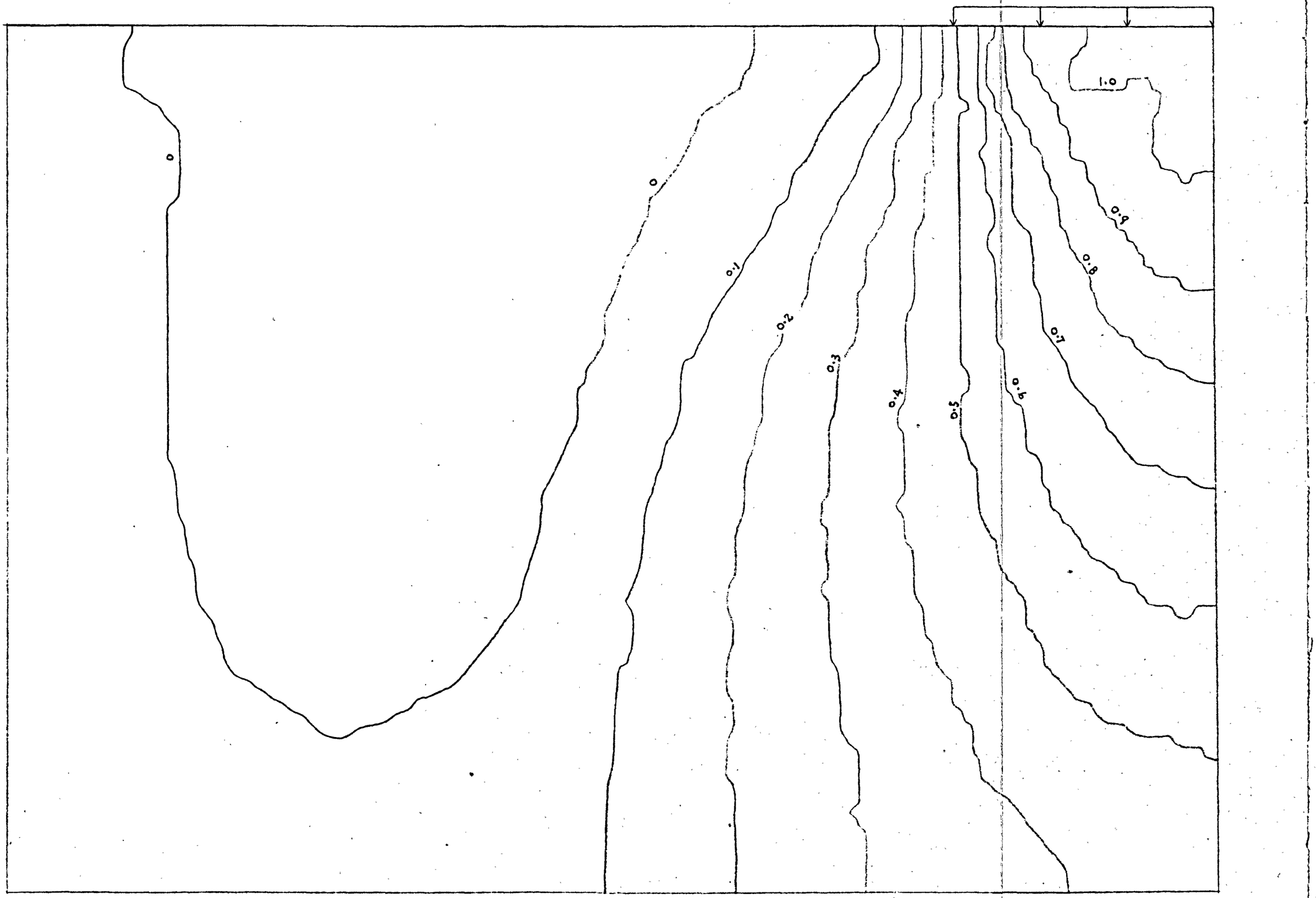

(2c) Normalised σ_y contours for $p_f = 4900$ psf

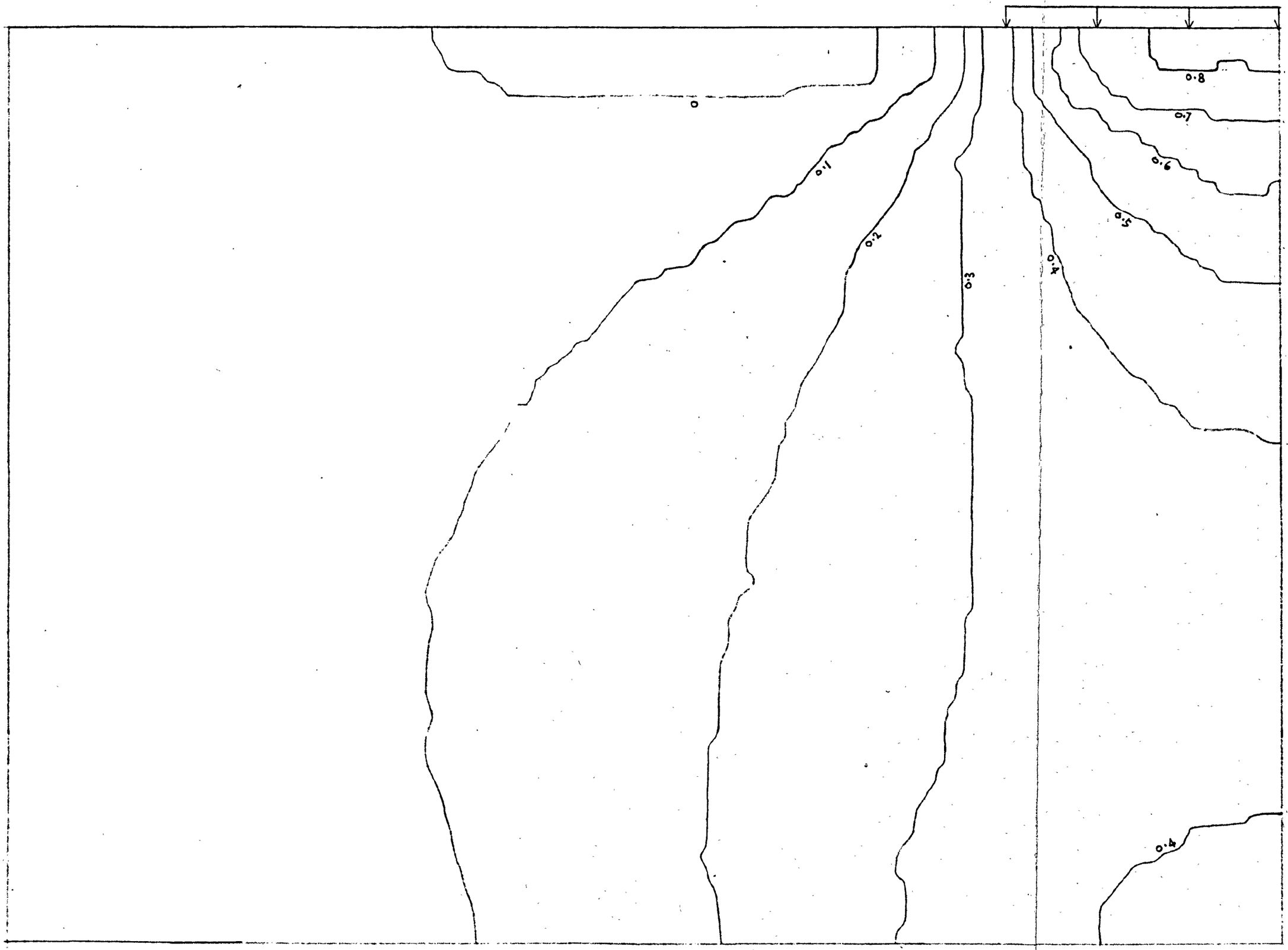

(3a) Normalised σ_z contours for $p = 1000$ psf

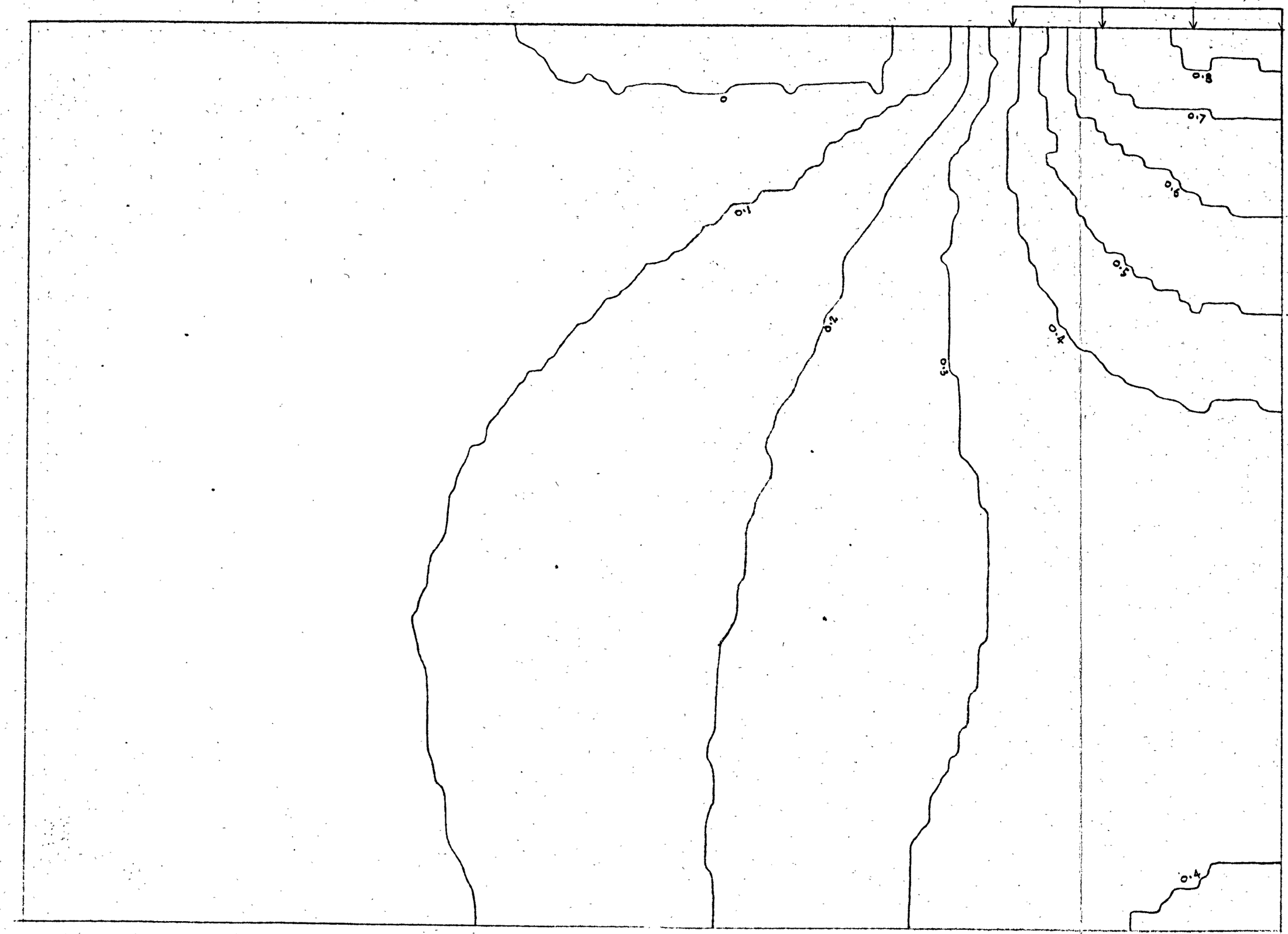

(3b) Normalised σ_z contours for $p = 3050$ psf

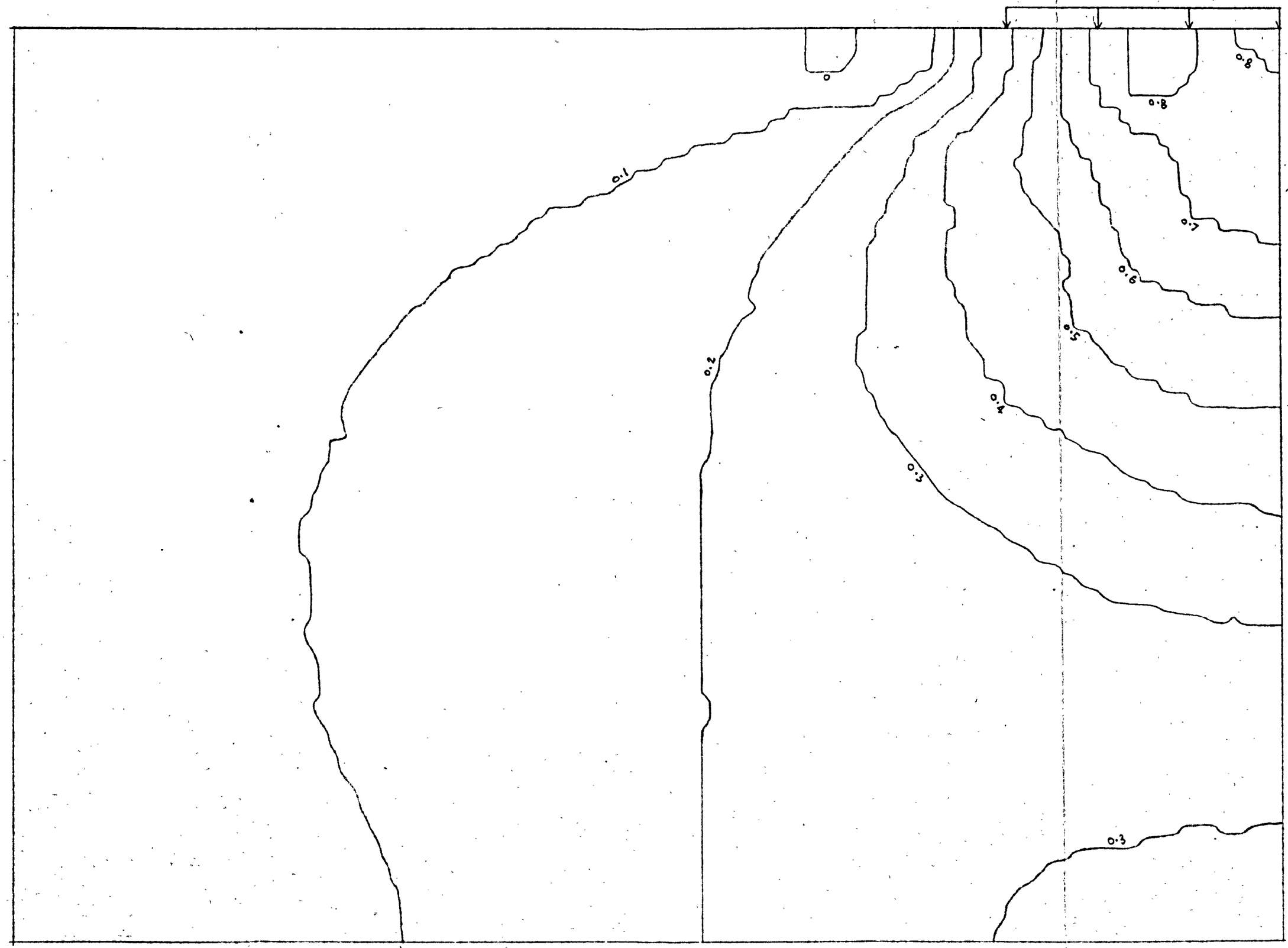

(3c) Normalised σ_z contours for p = 4000psf

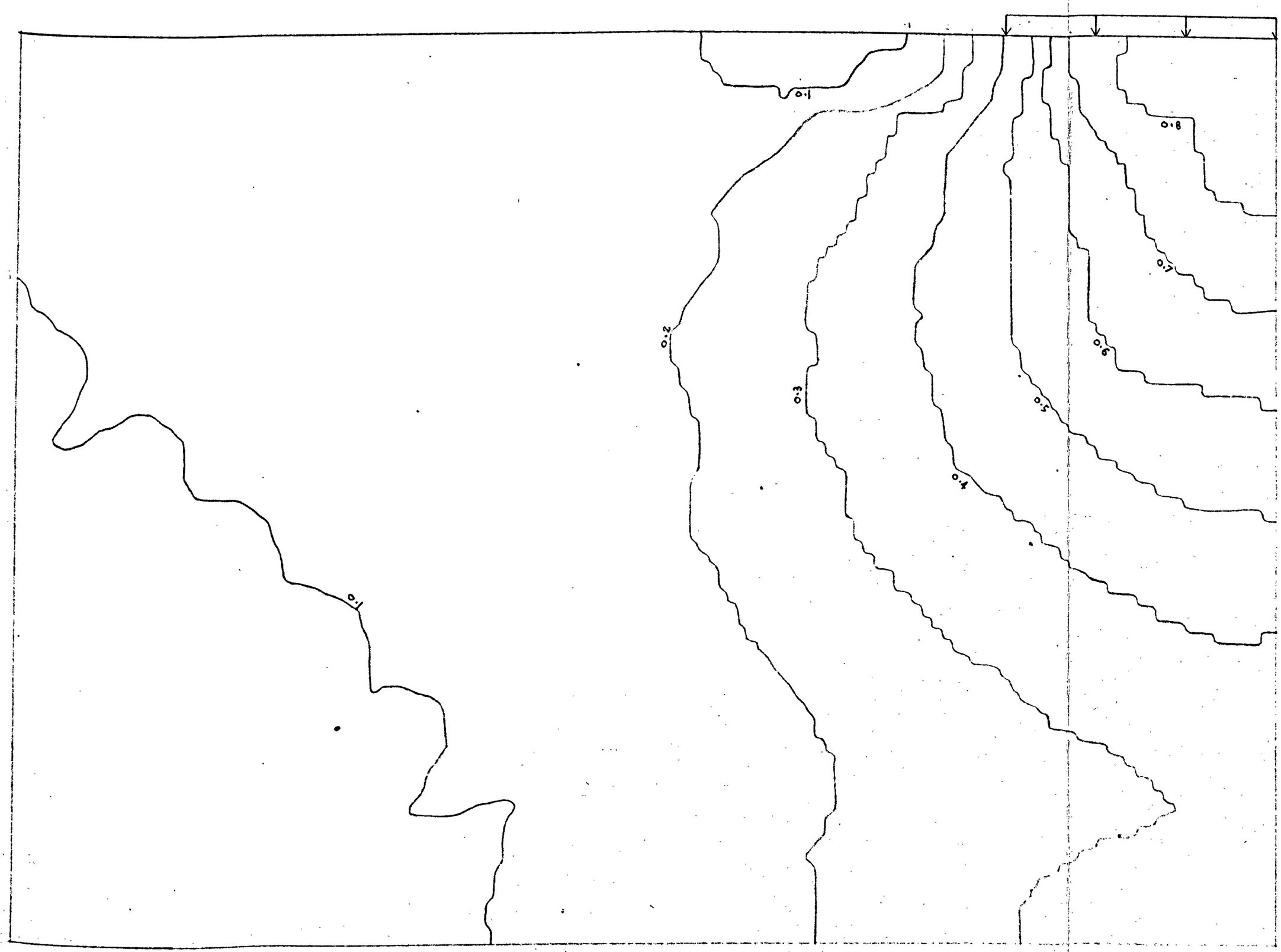

(3d) Normalised σ_z contours for p = 4730 psf

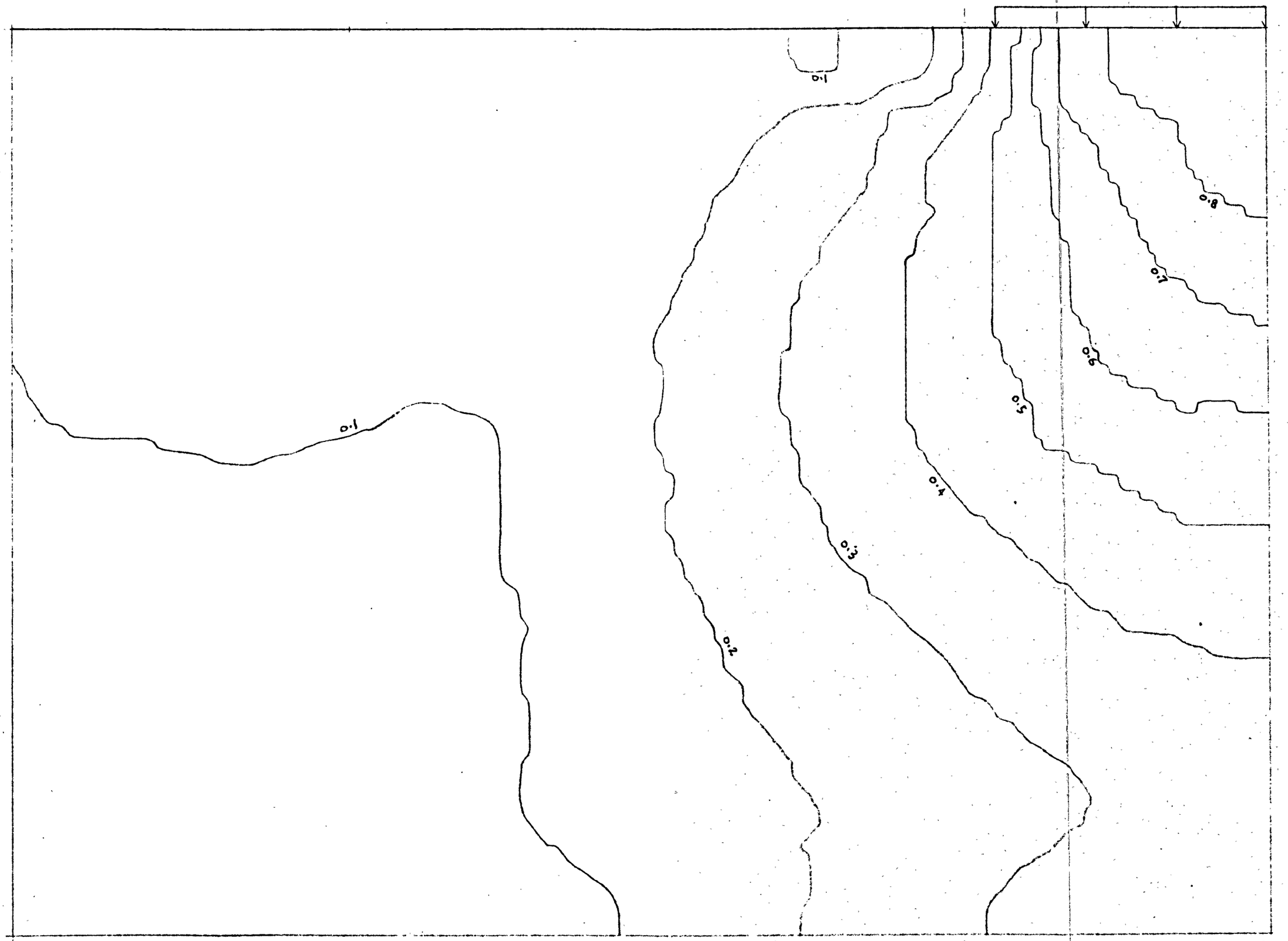

(3a) Normalised σ_z contours for $p_f = 4900$ psf

Fig. 42. Normalised stress contours of elastoplastic layer by SYMAP (no surface data points prescribed) - HOMOGENEOUS

PART C - DETAILED STUDIES OF SEVERAL OTHER ELASTOPLASTIC MODELS

2.7. Effects of variation of layer thickness on the linear elastic, perfectly plastic, isotropic, homogeneous layer model

The relative insensitivity of the collapse load of the present model to the proximity of the rigid base has already been mentioned in the previous section; this is in spite of significant differences in the growth of the plastic enclave, stress distributions and the load at which first yield occurs for various layer thicknesses. The basic model (Section 2.6.) is of sufficient thickness to reflect the general behaviour of a thick layer. Here, by contrast, the behaviour of a thin layer is examined. Fig. 43 shows the idealisation adopted for this purpose. As can be seen, it has the same basis as the basic model.

Fig. 44 shows the growth of the plastic enclave with increasing strip load p. First yield occured at about 900 psf in the element X at the base. This load is a higher proportion of πc_u than that of the basic model which indicates a change from an earlier incidence of first yield (i.e. relative to collapse) as we go from half-space to thick layer, to a later incidence from thick to thin layer. This change should be reflected in the elastic τ_{max} distributions. With increasing p, a plastic enclave develops around the element X, spreading upwards and laterally towards the strip on the right, and to the

adjacent surface on the left. Finally, at p = 1577 psf, the enclave penetrates free surface (nearer the load that the thicker basic model) and collapse occurs. This load is again about 3·5% higher than $(\pi+2)\, c_u$. It is also considerably less than the corresponding value for the basic model which has a bigger c_u value due to its greater depth.

Finally, the proximity of the elastic body to the centre of the strip suggests a Hill-type collapse mechanism (19b) - see also Fig. 47.

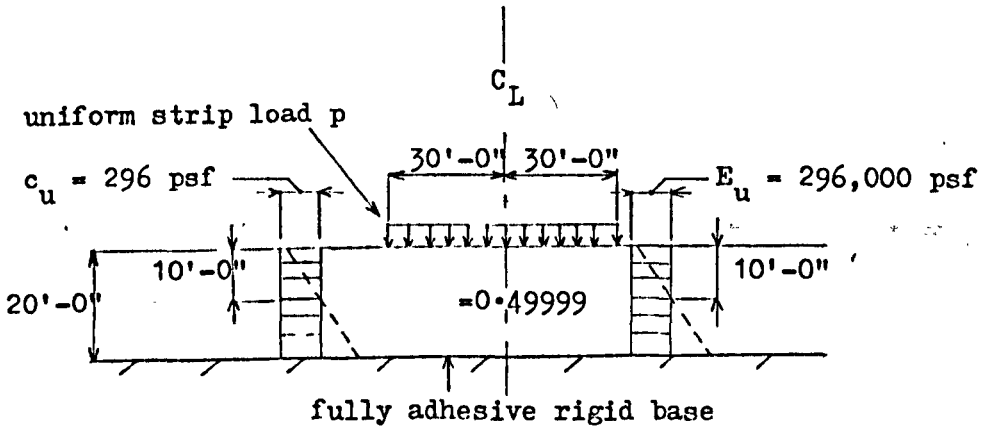

Fig. 43. Thin layer idealisation (Tresca yield criterion and associated flow rule)

PAGE

NUMBERING

AS ORIGINAL

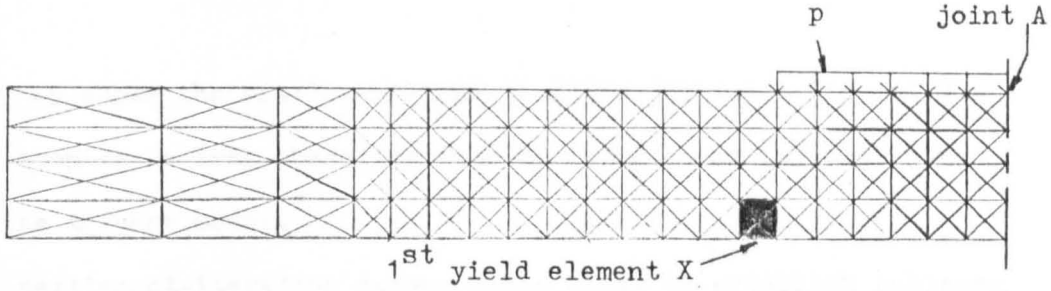

(a) p = 1000 psf

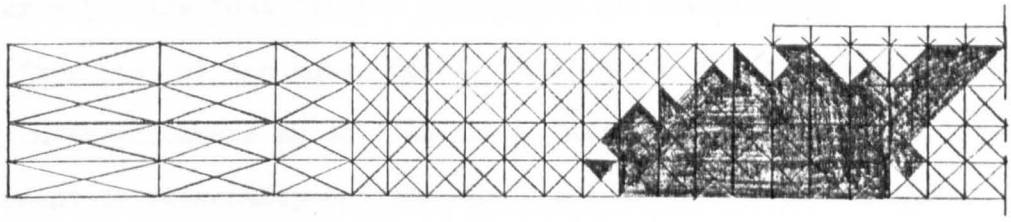

(b) p = 1522 psf

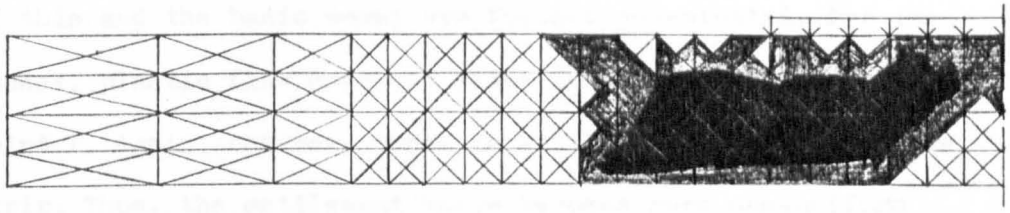

(c) p_f = 1577 psf (collapse)

Fig. 44. Growth of the plastic enclave to collapse

Fig. 45 shows the settlement-load plot for joint A (Fig. 44). It can be seen to be less characteristic of local shear failure than that for the thicker model.

The settlement-iteration curves again serve to establish collapse - i.e. when a curve rises at constant slope so that there can be no convergence.

Fig. 46 shows the surface settlement plots at various loads. The elastic curve (alike that for p = 1000 psf) is considerably different from that of the basic model. This is due to the combination of reduction in thickness as well as the condition of incompressibility. The settlement is reasonably uniform until point P (two-thirds the way along the strip from the centre and where the maximum settlement occurs) when it reduces rapidly until there is little movement at the edge of the strip.

With increasing plastic flow, the differences between the settlement curves of this and the basic model are further accentuated. For the present model, plastic flow does not significantly affect the settlements around point P. Again, however, there is little movement at the edge of the strip. Thus, the settlement curve becomes more non-uniform with increasing plastic flow, the strip hogging more in the central portion and sagging more towards the edge. *

*Towards collapse, a moderate amount of top main steel would be required in the central third of the strip and bottom main steel outwards, to resist the bending moments.

Settlements are considerably less in this case than for the basic model. Thus, the reduction in layer thickness has a greater effect on the magnitude of settlements than the corresponding reduction in rigidity and strength, and indeed, the reduced strength leads to a smaller collapse load thereby restricting the range of plastic flow and its effect on settlement. Local shear failure can be neglected here since the settlement-load curve (Fig. 45) is flatter, and the total settlements considerably smaller than for the basic model.*

The amount of elastic heave relative to elastic settlement is high. This is due to the proximity of the rigid base as well as the condition of incompressibility. Most of this heave is localised around the edge of the strip. Increasing plastic flow leads to a substantial increase in the heave, although unlike the basic model, there is little further localisation of the displacement of material towards the vicinity of the load towards collapse. Thus, the points of incidence of heave (near the edge), and maximum heave do not alter noticeably. By the same token, no marked differences in the behaviour of the horizontal surface displacements with increasing plastic flow is discernable, unlike the basic model.

The lateral extent of the area of intense movement again roughly coincides with the zone of penetration of the plastic enclave

*Also, less reinforcement would be needed since the differential settlements are generally smaller than for the basic model.

to free surface (Fig. 44). The lower boundary of this area is the rigid base.

Fig. 47 shows the general deformation of the thin layer with increasing load. The typical displacement of material from below the strip, laterally, then upwards as heave at collapse can be seen. Note also no noticeable tendency to further localise this movement towards the vicinity of the load with increasing plastic flow, as well as the more restricted extent of the lateral extent of the area of intense movement at collapse.

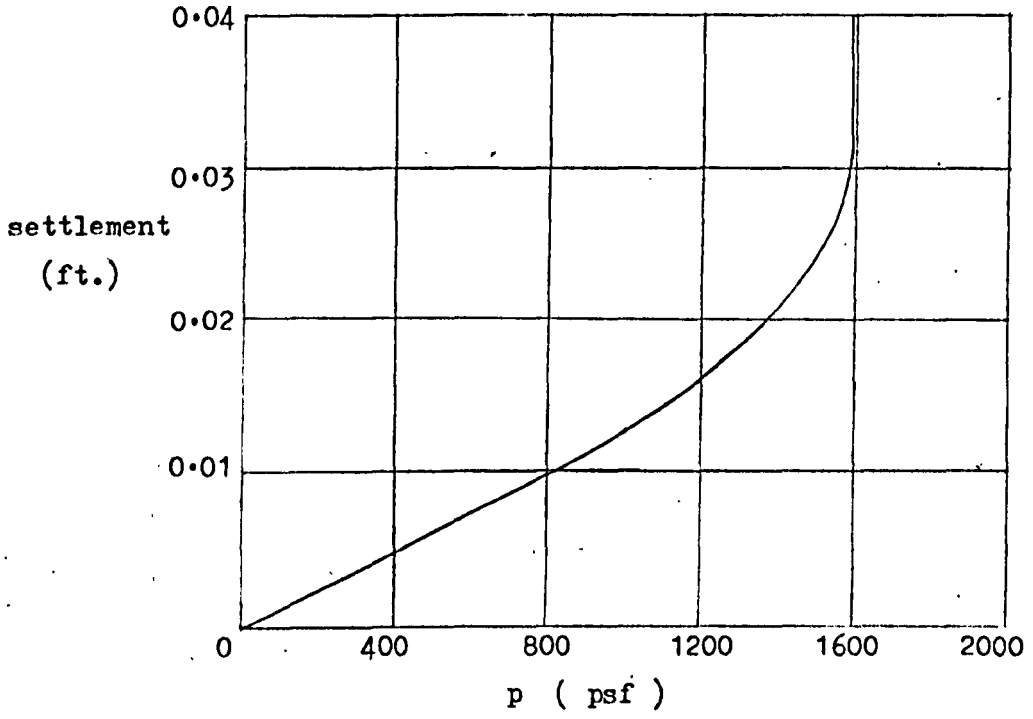

(a) Settlement-load plot

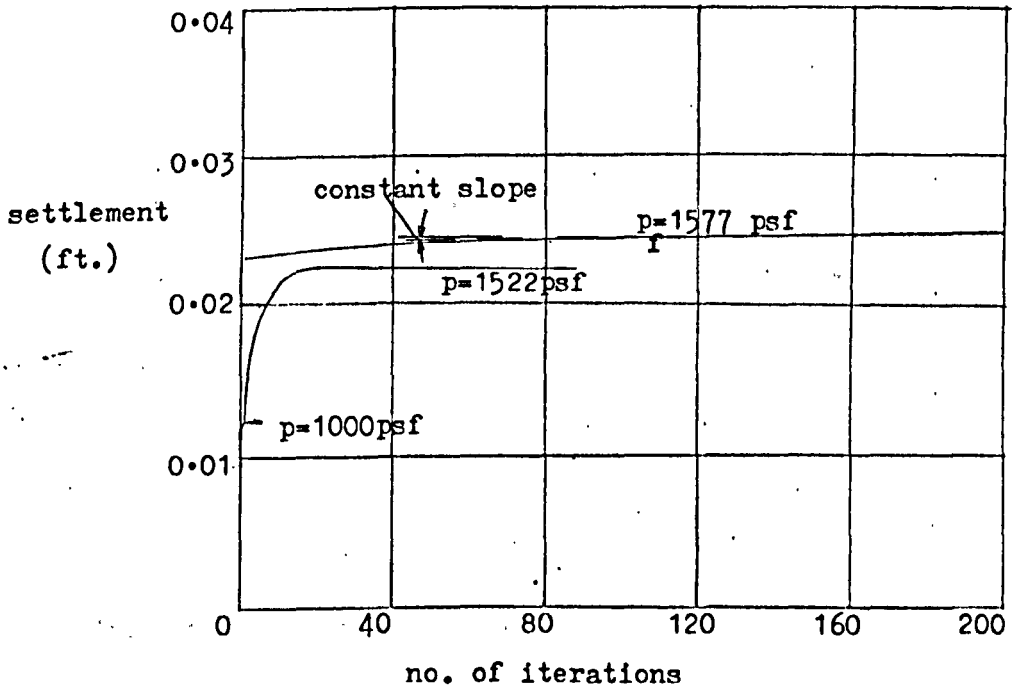

(b) Settlement-iteration plots

Fig. 45. Settlement curves for joint A (see Fig. 44)

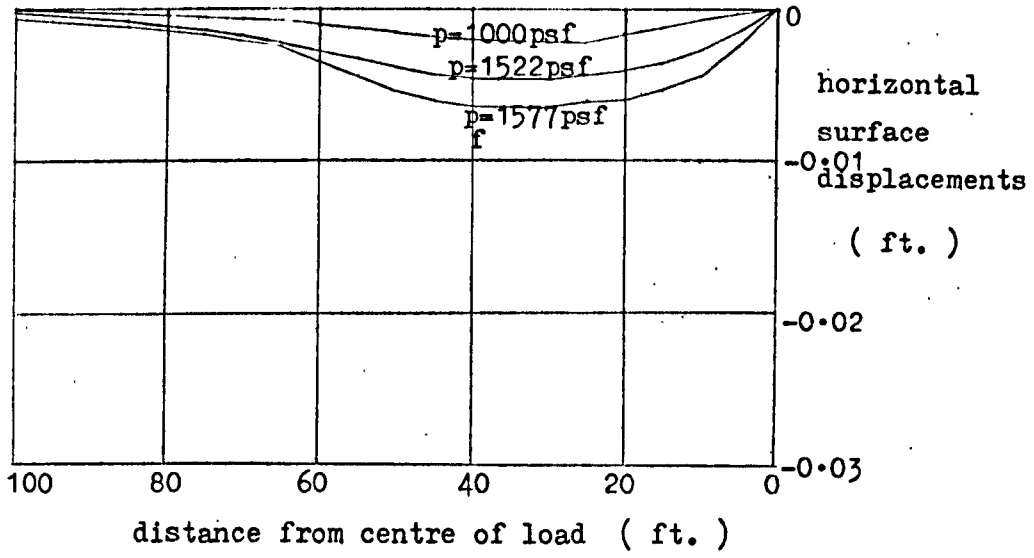

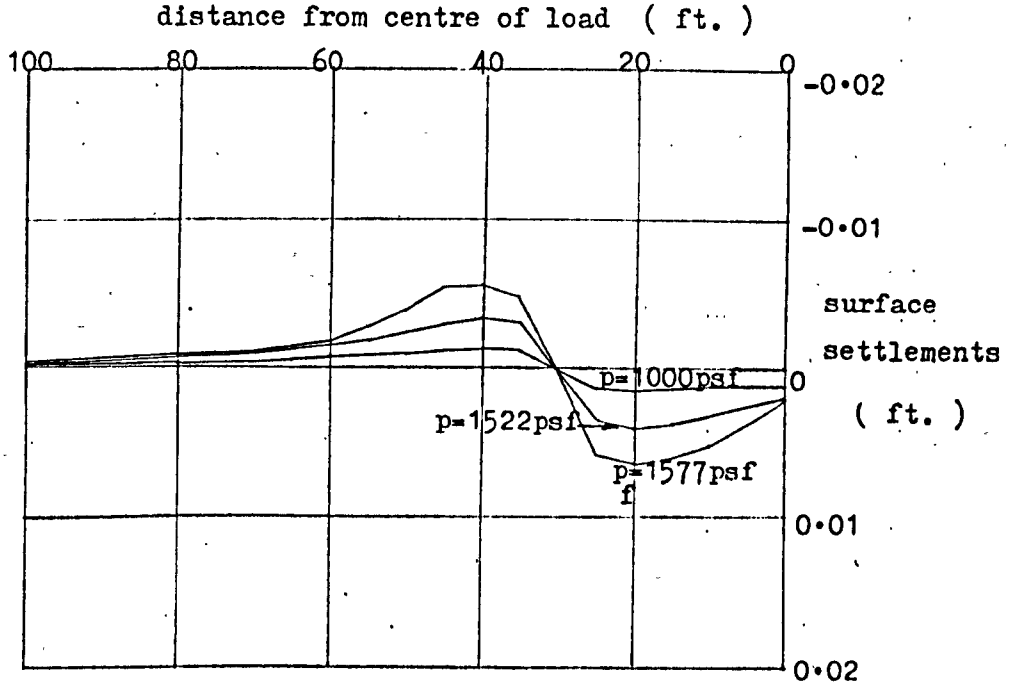

Fig. 46. Surface displacements

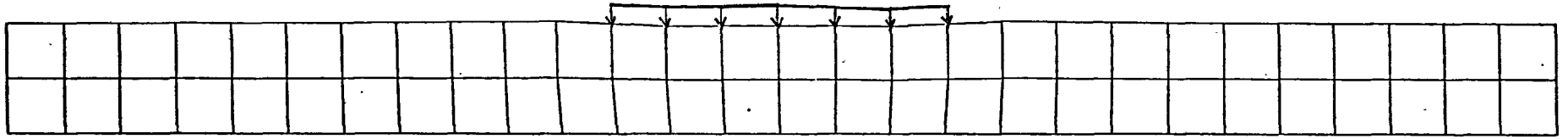

(a) elastic

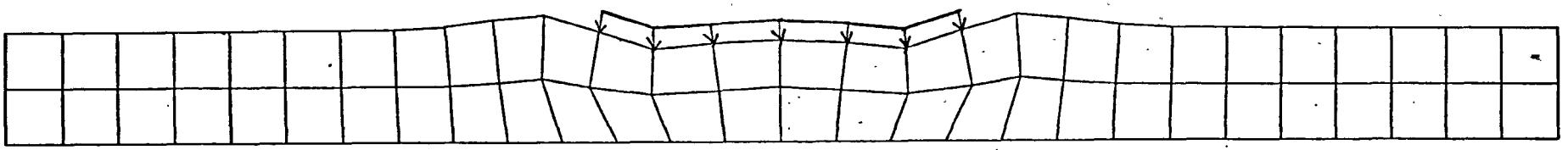

(b) elastoplastic

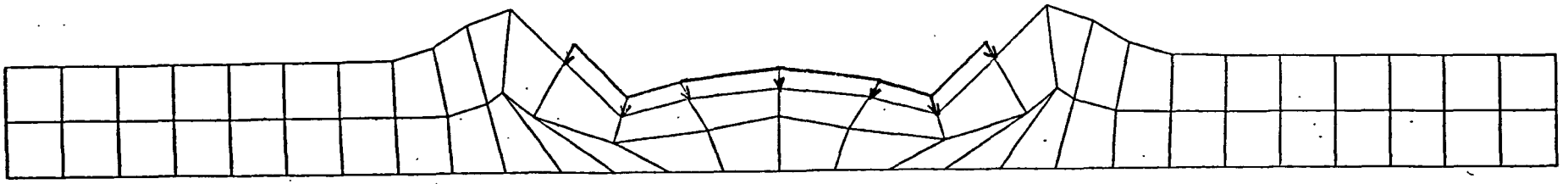

(c) collapse

Fig. 47. General deformation of thin layer at 3 stages of loading

2.8. Inhomogeneity of rigidity and strength about the centre of the strip load (flow chart in Section 1.3.3.2.)

Even if it were assumed that the clay layer of Fig. 22(a) is exceptionally uniform, there will nevertheless be some difference between the average rigidity and strength left of the centre of the load, and right of it, in the real situation. Thus, contrary to the basic model of Section 2.6., the problem is essentially one of inhomogeneity and asymmetry. It would therefore be instructive to ascertain the difference this simple picture of inhomogeneity on either side of the centre of the load would make to the results of the basic model. The clay layer is assumed to be fairly uniform so that the idealisation shown in Fig. 48 is applicable. The degree of inhomogeneity is small and thus the present study will provide an indication of the sensitivity of the results of the basic model to such non-uniformity.

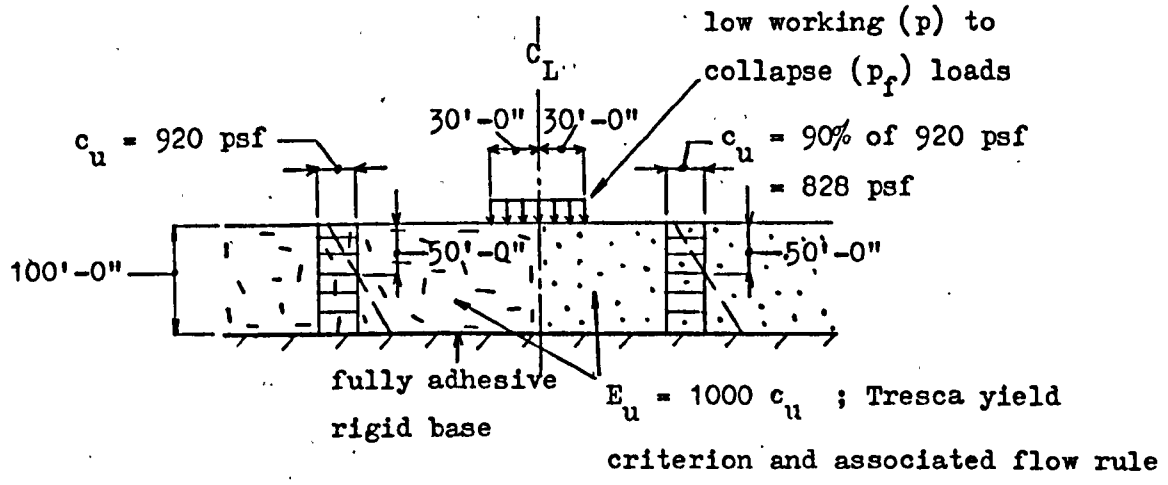

Fig. 48. A simple idealisation for slight degree of inhomogeneity about centre of load.

Fig. 49 shows the growth of the plastic enclave with increasing load p. As expected, first yield occurred in the weaker region at a slightly lower load than for the basic model. Also, subsequent growth of the plastic enclave is predominantly in the weaker half of the layer. At p_f = 4570 psf, the plastic enclave penetrates free surface right of the strip and collapse occurs.

The growth of the enclave in the weaker half of the layer is alike that for the basic model; at collapse, its lateral extent is also roughly equal to that given by Prandtl's slip-line field. The enclave in the stronger half also takes a similar form except that its growth lags behind that in the weaker half so that, at collapse, it has not yet penetrated free surface. Thus, collapse occurs in the weaker region.

The collapse load is approximately half-way between those given by assuming homogeneous layers with the strengths of the two halves respectively. Thus inhomogeneity leads to no radical changes from the behaviour of the basic model, and an average of the two strengths could reasonably be applied to a homogeneous layer in the present context.

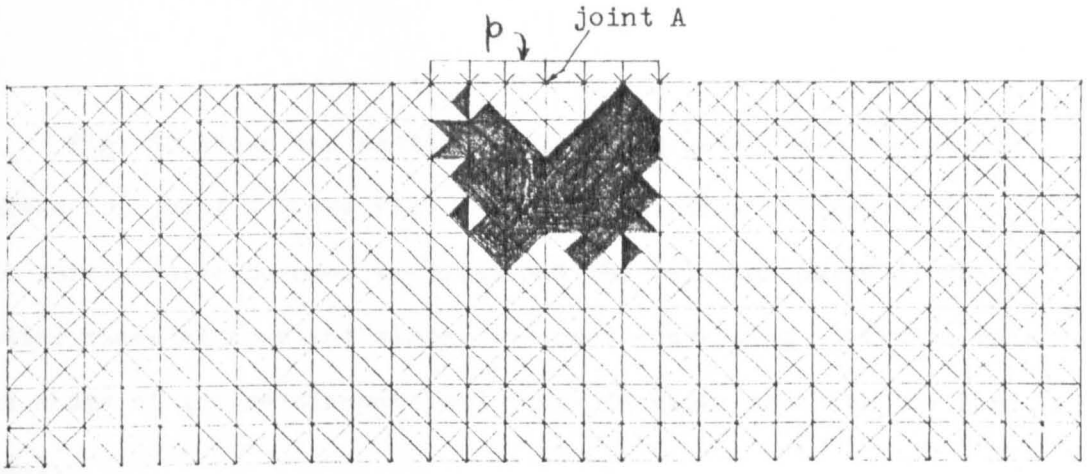

(a) p = 2900 psf

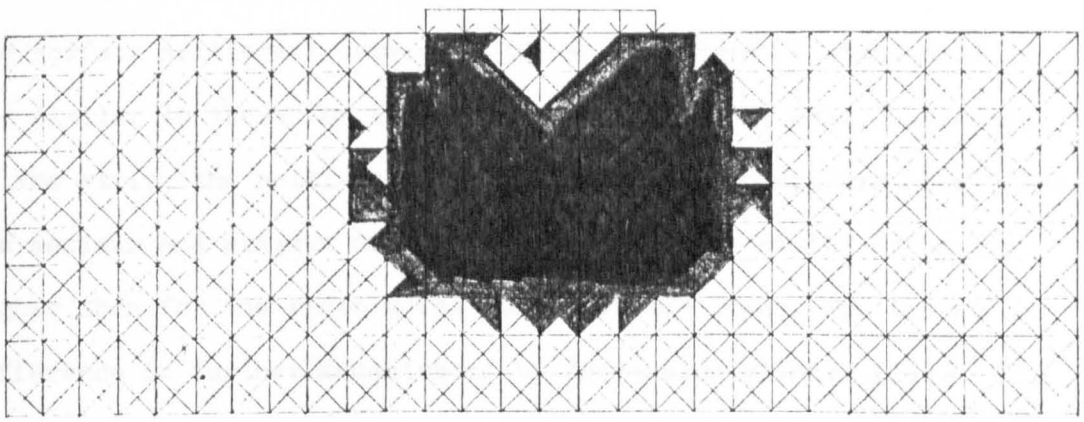

(b) p = 4000 psf

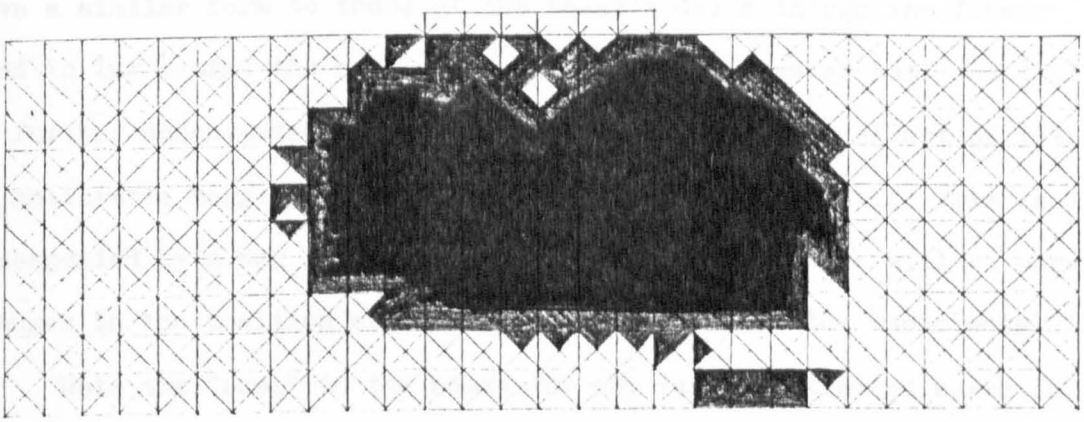

(c) p = 4400 psf

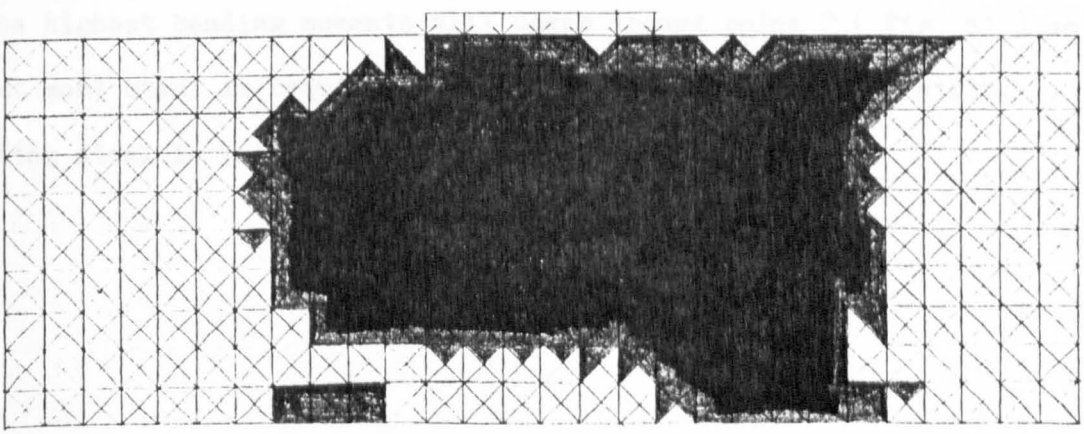

(d) p_f = 4570 psf (collapse)

Fig 49 Growth of the plastic enclave to collapse

Fig. 50 shows the settlement-load and settlement-iteration curves for joint A (see Fig. 49), pin-pointing collapse - i.e. the former curve becomes vertical and the relevant curve of the latter rises at constant slope, the rest converging to finite values. The shape of the settlement-load curve is alike that for the basic model.

Fig. 51 shows the surface displacements at various loads. The surface settlement curves in the weaker region (right half) are similar to those for the basic model. However, near the centre of the strip, the settlements are noticeably more uniform here. Also, the maximum and maximum differential settlements of the strip are higher than for the basic model at comparable loads. The latter difference is further accentuated by increasing plastic flow. * The surface settlement curves in the stronger half of the layer also have a similar form to those of the basic model although the former tend to lag behind the settlement curves for the weaker half and this is further accentuated by increasing plastic flow. The effect of this is noticeable hogging at higher loads in the stronger half. This is accompanied by a sag in the opposite half and thus there will be more changes in the position of main steel here than for the basic model.

Note the "bump" in the heave for the final settlement curve in

*The highest bending moments will occur around point P (Fig. 51) so that most steel is required there. Owing to the sag in the strip, bottom steel is laid.

the right half of the layer found to signify collapse (see basic model). The corresponding curve in the left half indicates an intermediate stage of plastic flow only so no collapse occurs there - as suggested by the plastic enclave earlier.

The horizontal surface displacement curves in both halves also bear close resemblance to those of the basic model. However, an important difference is that the point of zero displacement is no longer at the centre of the strip due to this being a problem of asymmetry. In fact, with increasing plastic flow, more points in the stronger half of the layer begin to displace towards the weaker half. The maximum horizontal surface displacements in the latter region are generally greater than in the former since the progress towards collapse is more advanced.

The similarity between the surface displacement curves here and those of the basic model indicates the lateral extent of the respective areas of intense movement at collapse will be approximately equal. This observation is implicit in the earlier finding that the zones of penetration of the plastic enclave for the two models roughly coincide.

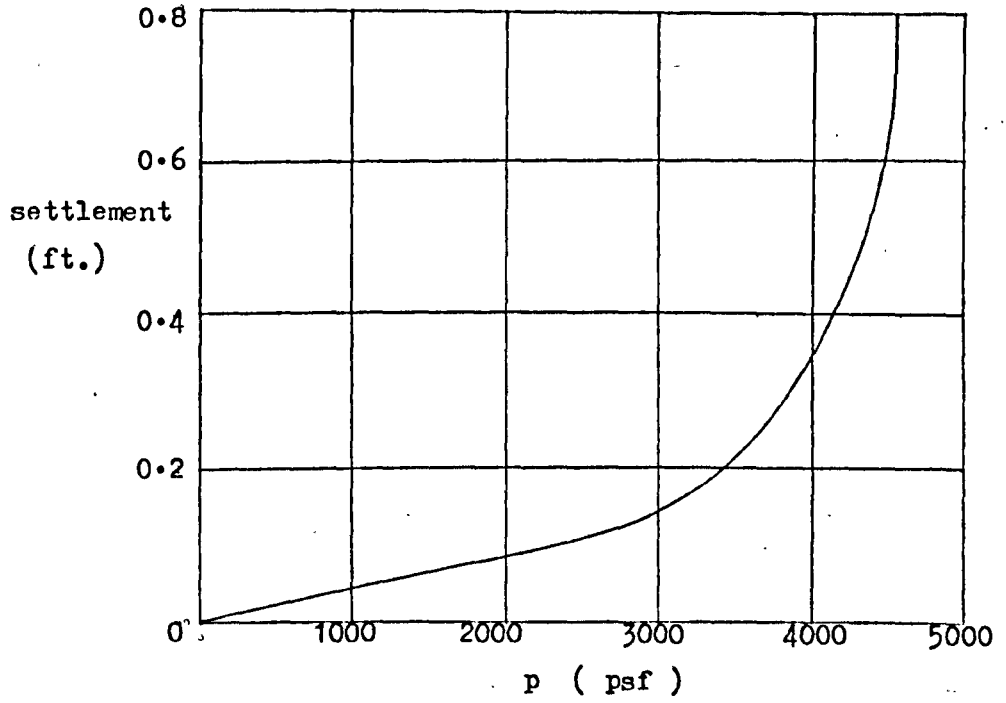

(a) Settlement-load plot

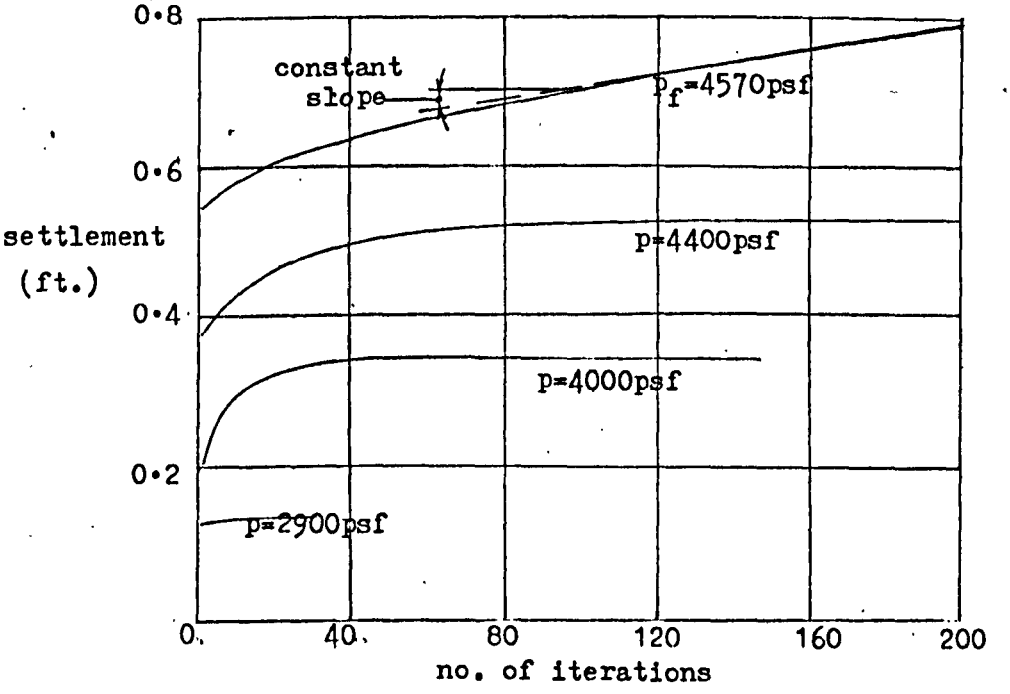

(b) Settlement-iteration plots

Fig. 50. Settlement curves for joint A

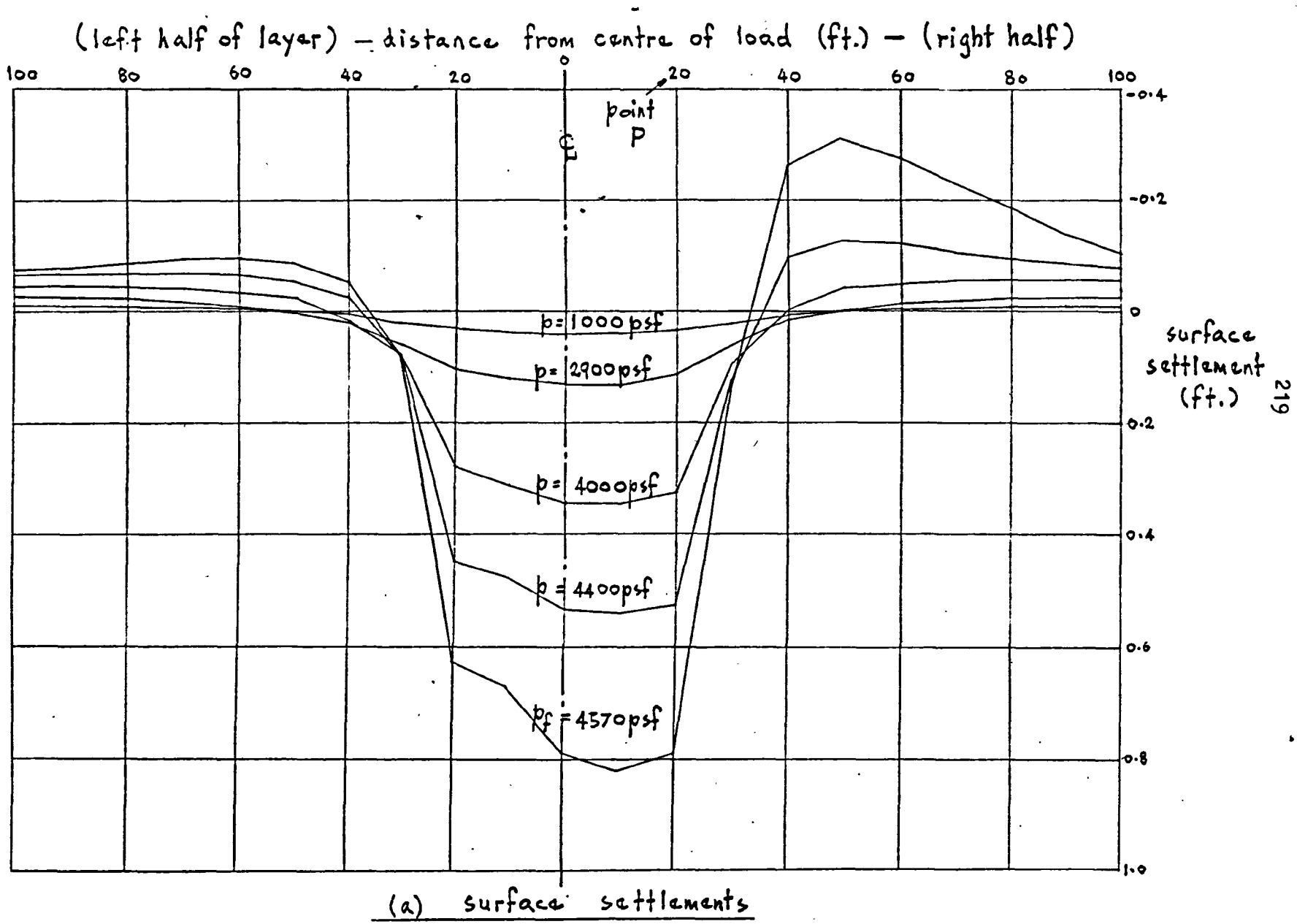

(a) surface settlements

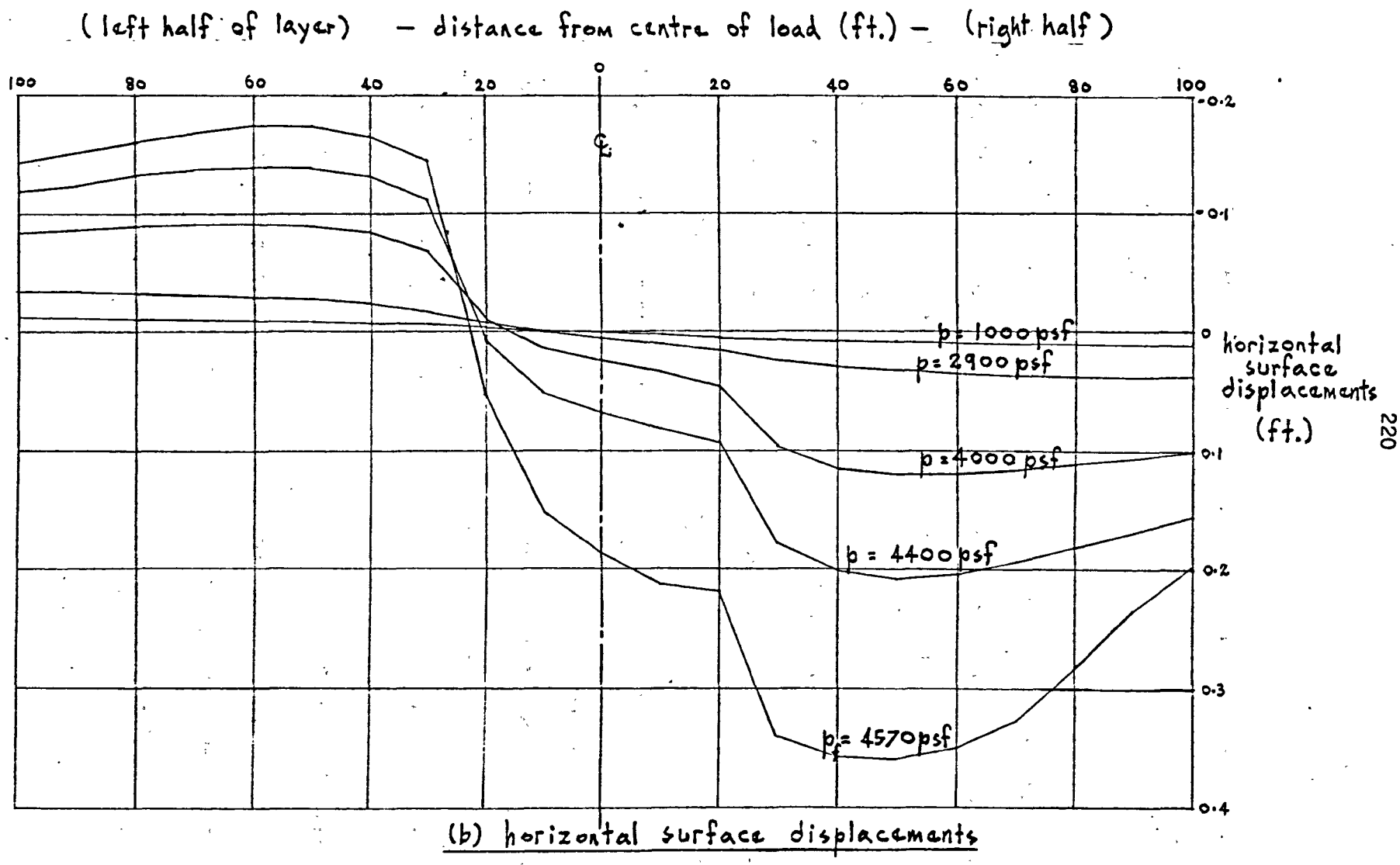

Fig. 51. Surface displacements

Fig. 52 shows the normal stress distributions down the centre and edges of the strip load (both edges are included since asymmetric conditions prevail).

For σ_x , there is a general increase in value above that for the basic model down both edges as well as the centre of the strip, the difference being accentuated by increasing plastic flow. There is little overall difference in σ_x between the two edge distributions - i.e. only local variations occur.

For σ_y , the same type of changes found for σ_x apply down the centre of the strip. Down the left edge, in the harder material, σ_y is generally the same as for the basic model but down the right edge, in the softer material, a decrease in σ_y is found and this is accentuated by increasing plastic flow except towards collapse when an increase occurs. Thus, σ_y down the left edge is greater than down the right at comparable loads, the difference being accentuated by plastic flow except towards collapse when the reverse is true.

Despite the above differences, the trends of the σ_x and σ_y distributions are similar to those of the basic model.

As before, $\sigma_z \doteq \frac{1}{2}(\sigma_x + \sigma_y)$ so the changes in pore pressure arising from the present inhomogeneity may be reasonably represented

by the differences in σ_z between the present and the basic models (i.e. an average of the above changes in σ_x and σ_y).as explained earlier.

Accordingly, we may expect a general increase in pore pressure down the left edge (in the harder material) and centre of the strip, accentuated by plastic flow. Down the right edge (in the softer material), there will be an initial increase and then an increase towards collapse. Thus, pore pressures down the left edge are at first generally higher than down the right, becoming relatively lower towards collapse.

Constant stress conditions are found to prevail at collapse as is to be expected (Section 2.6.3.).

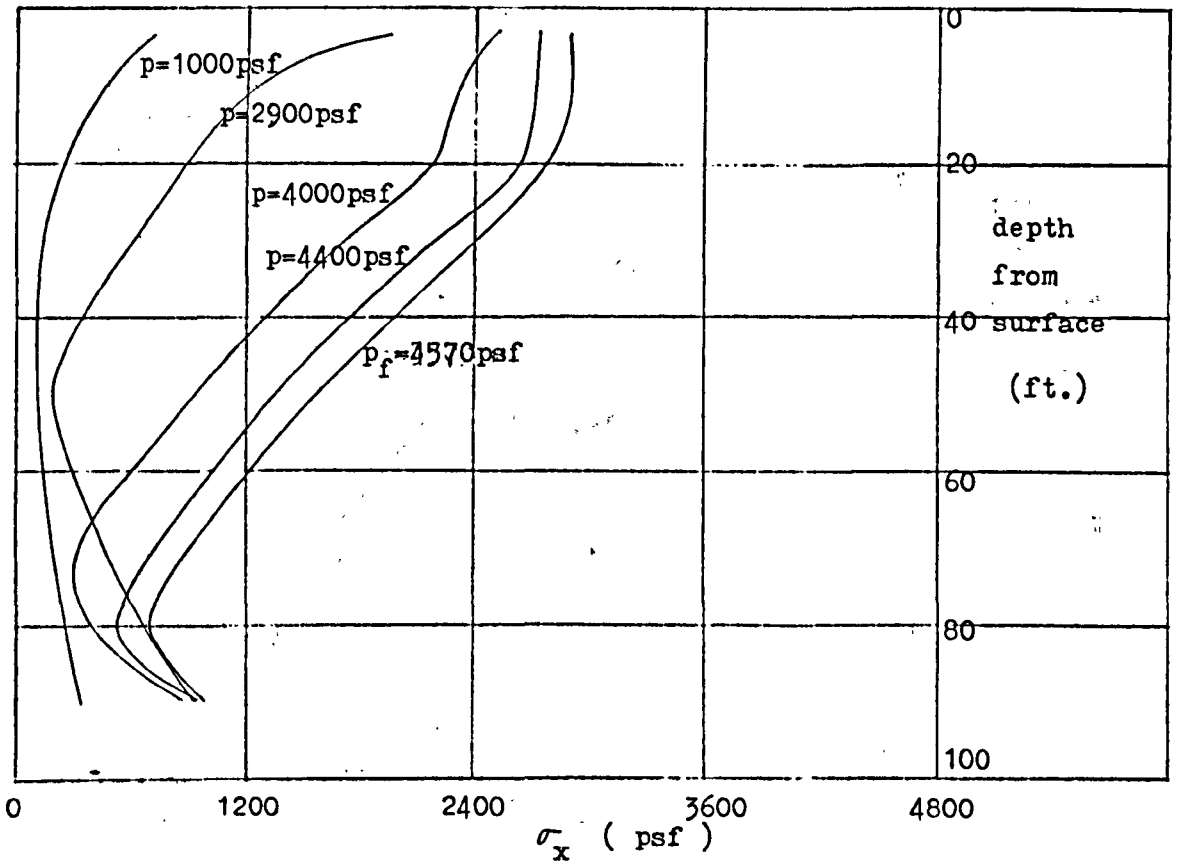

(1a) σ_x distributions down centre of strip load

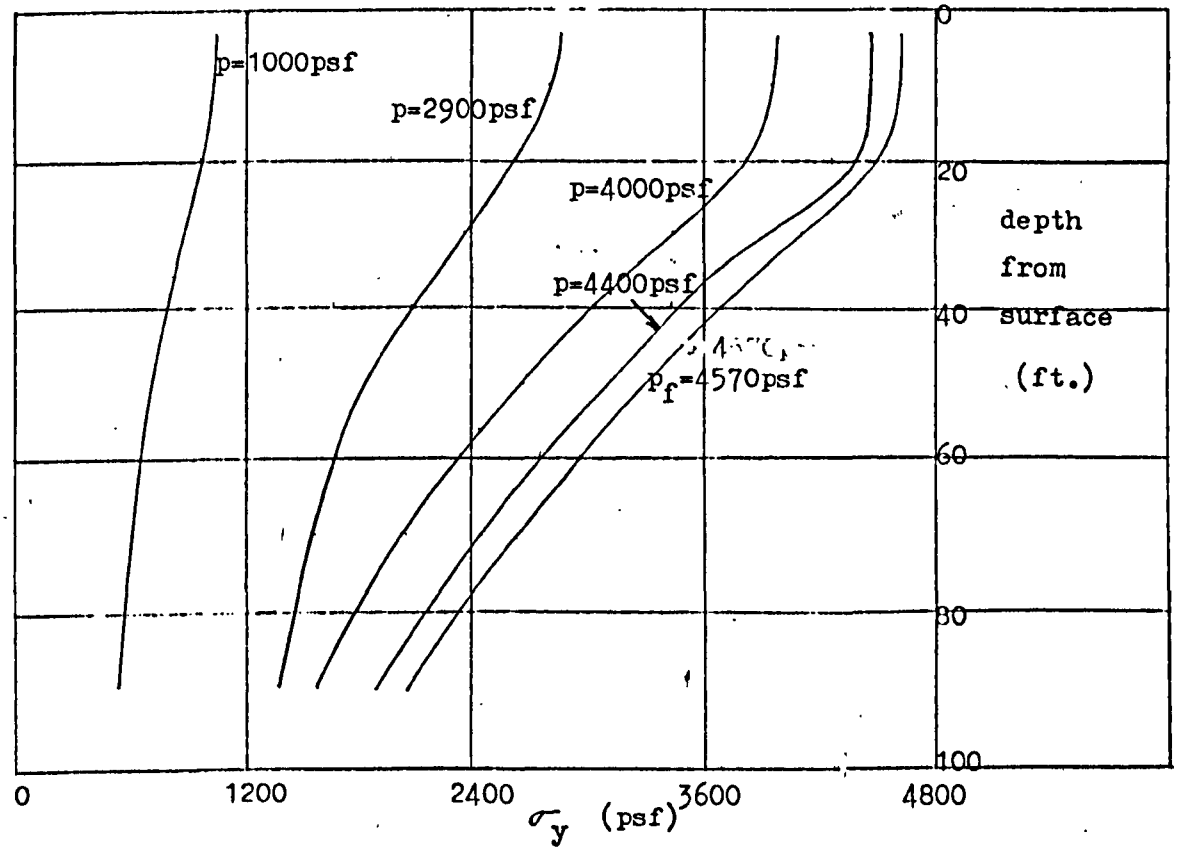

(1b) σ_y distributions down centre of strip load

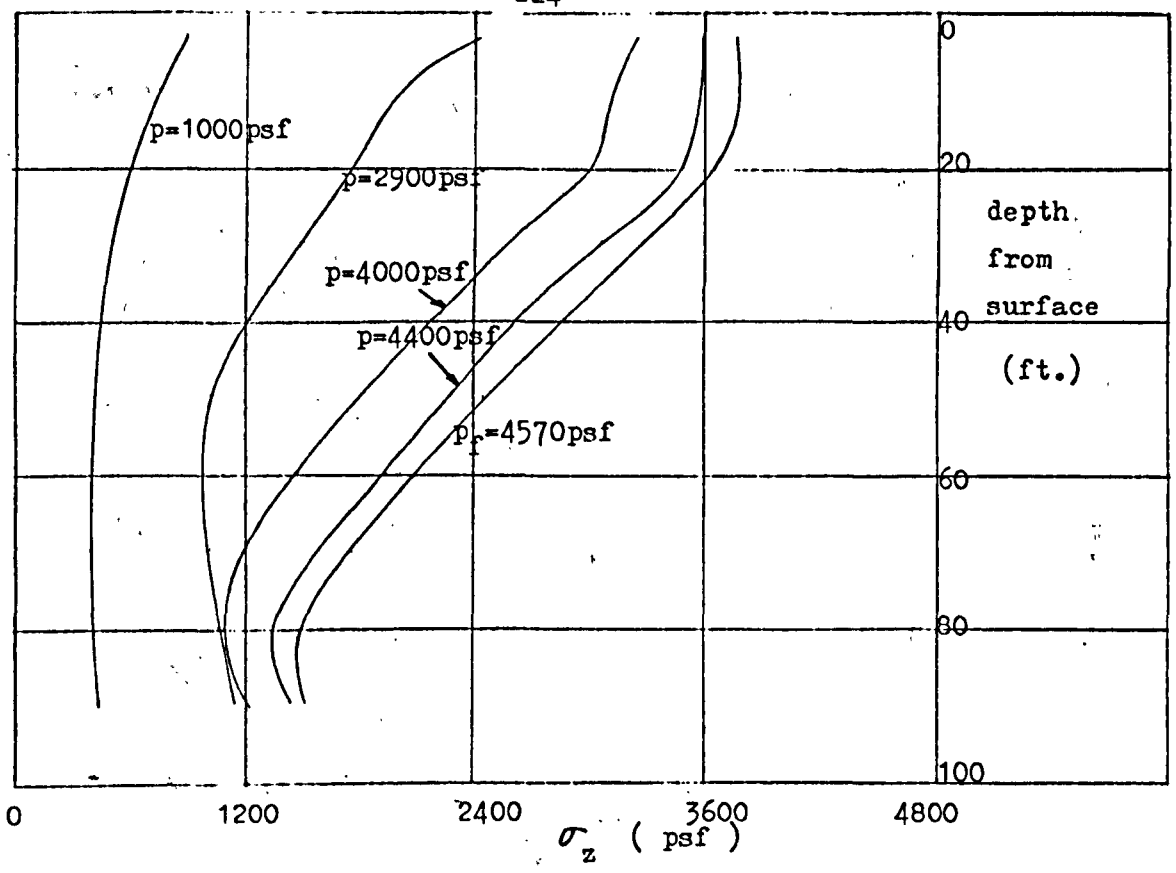

(1c) σ_z distributions down centre of strip load

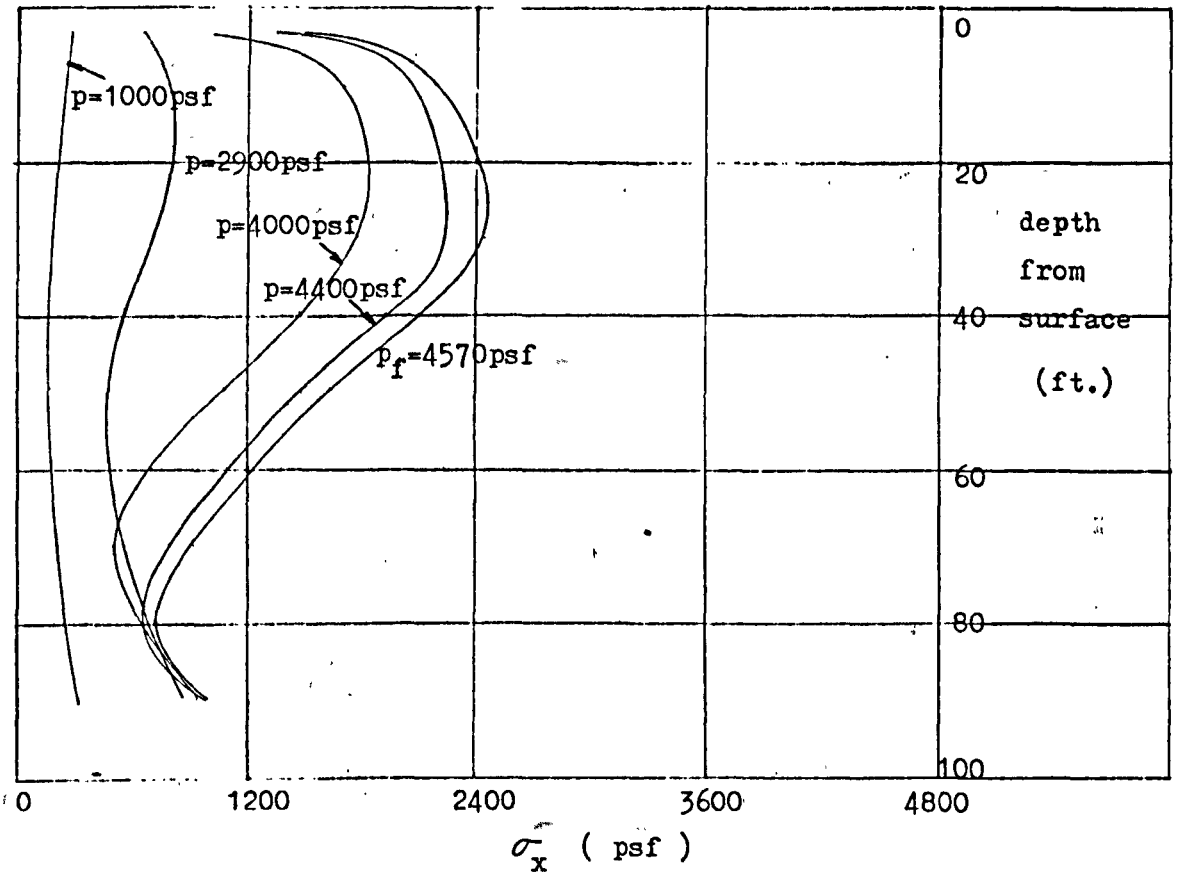

(2a) σ_x distributions down left edge of strip load

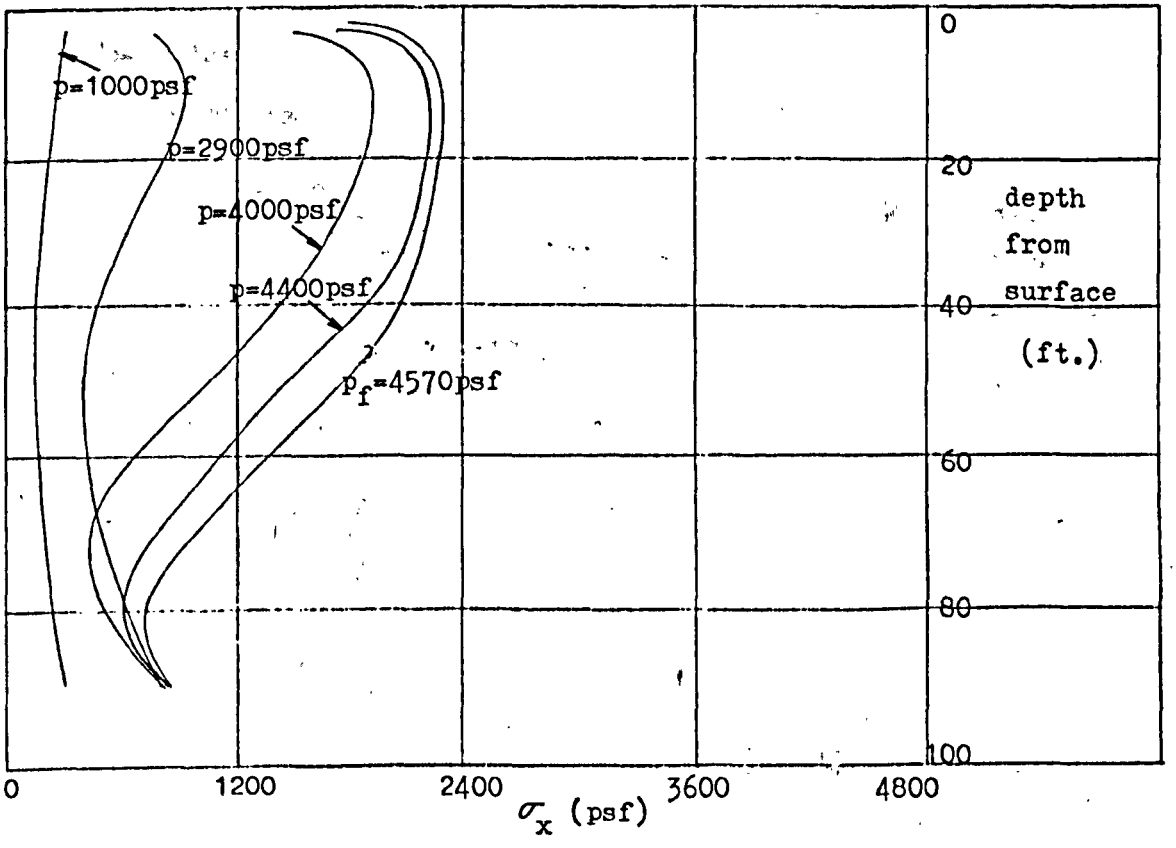

(2b) σ_x distributions down right edge of strip load

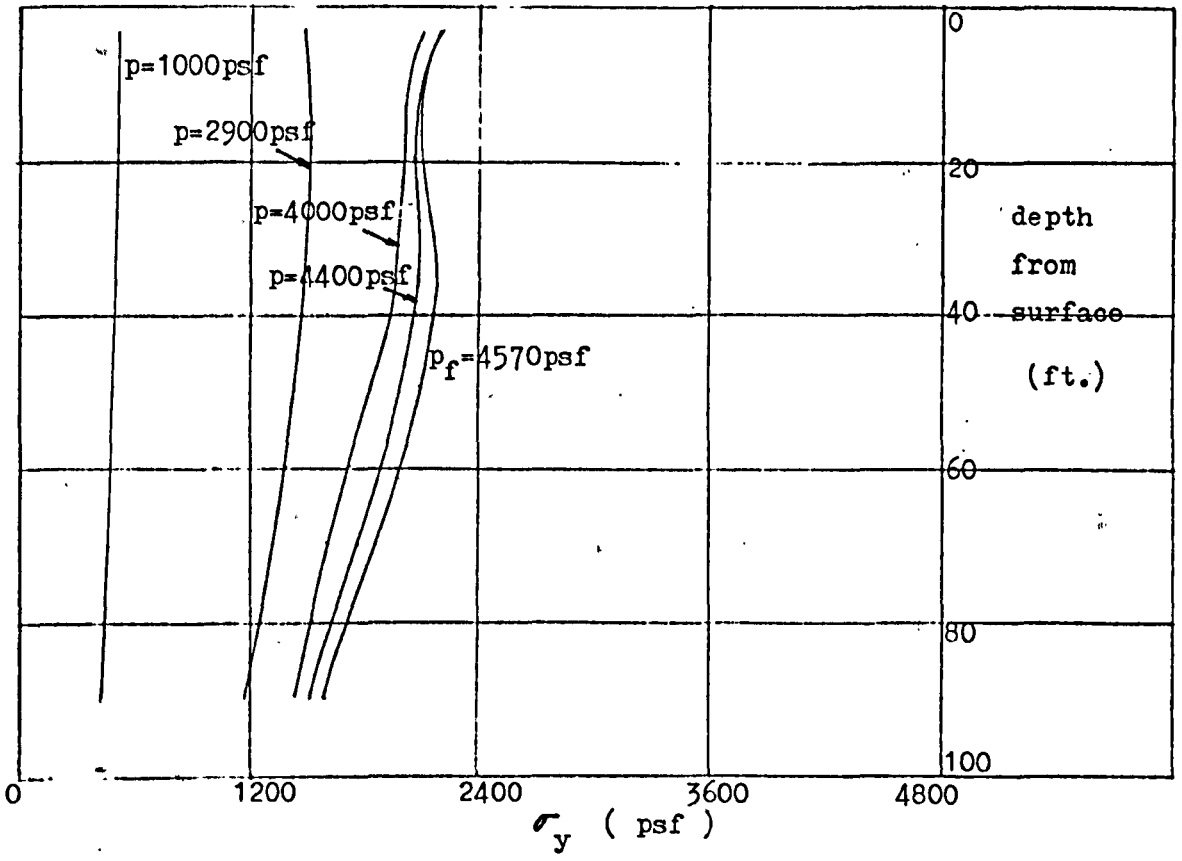

(3a) σ_y distributions down left edge of strip load

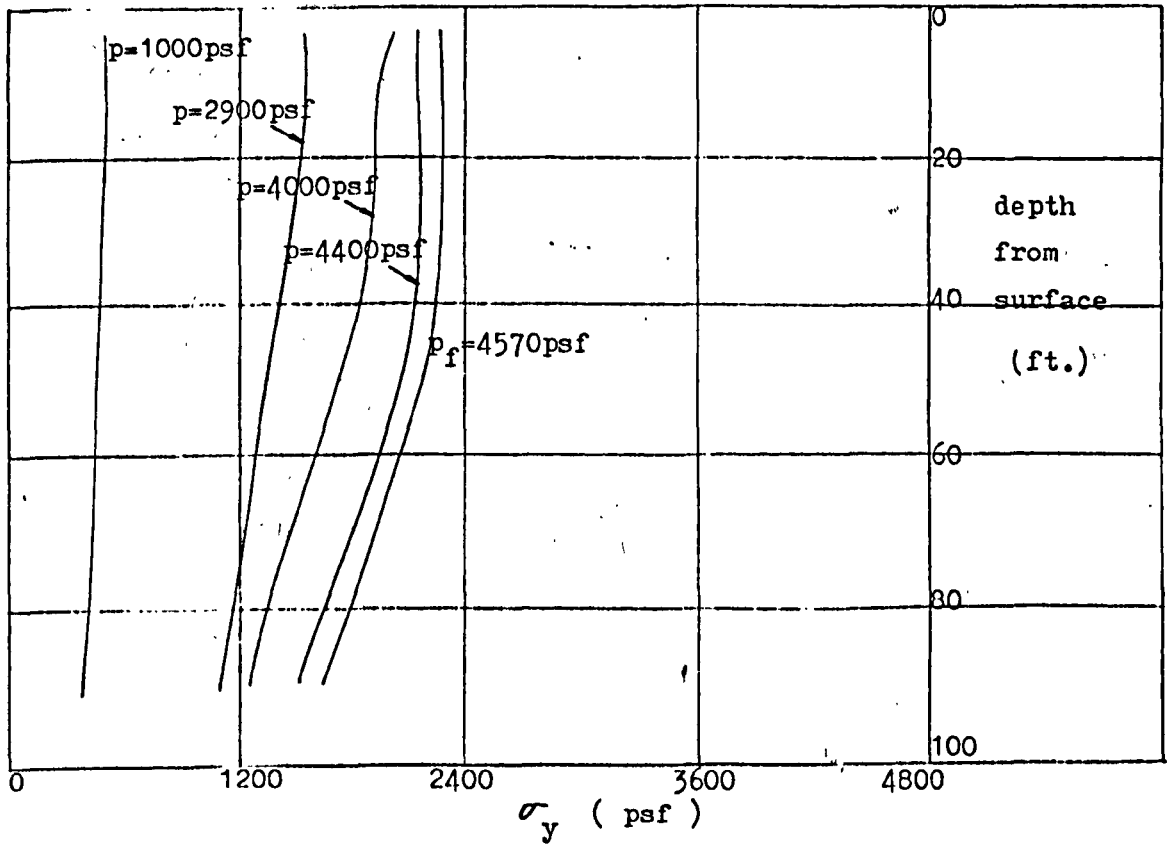

(3b) σ_y distributions down right edge of strip load

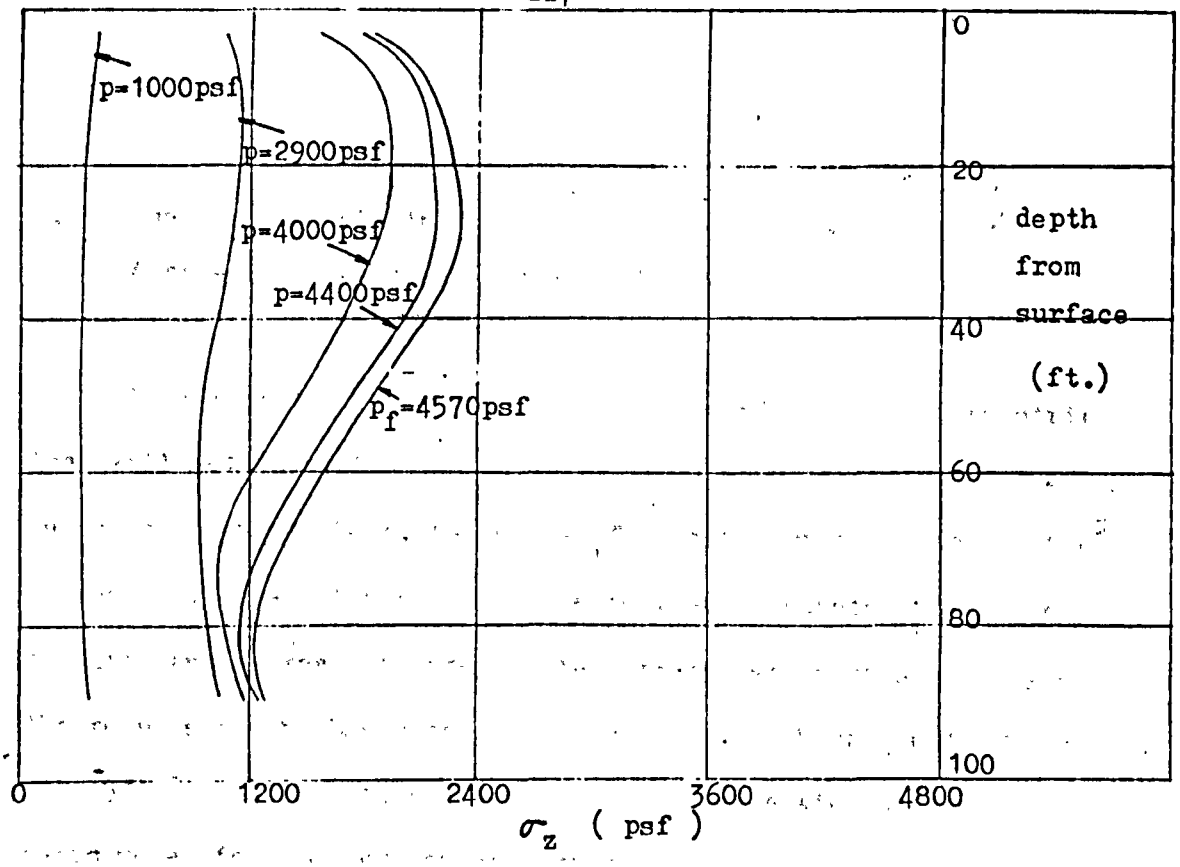

(4a) σ_z distributions down left edge of strip load

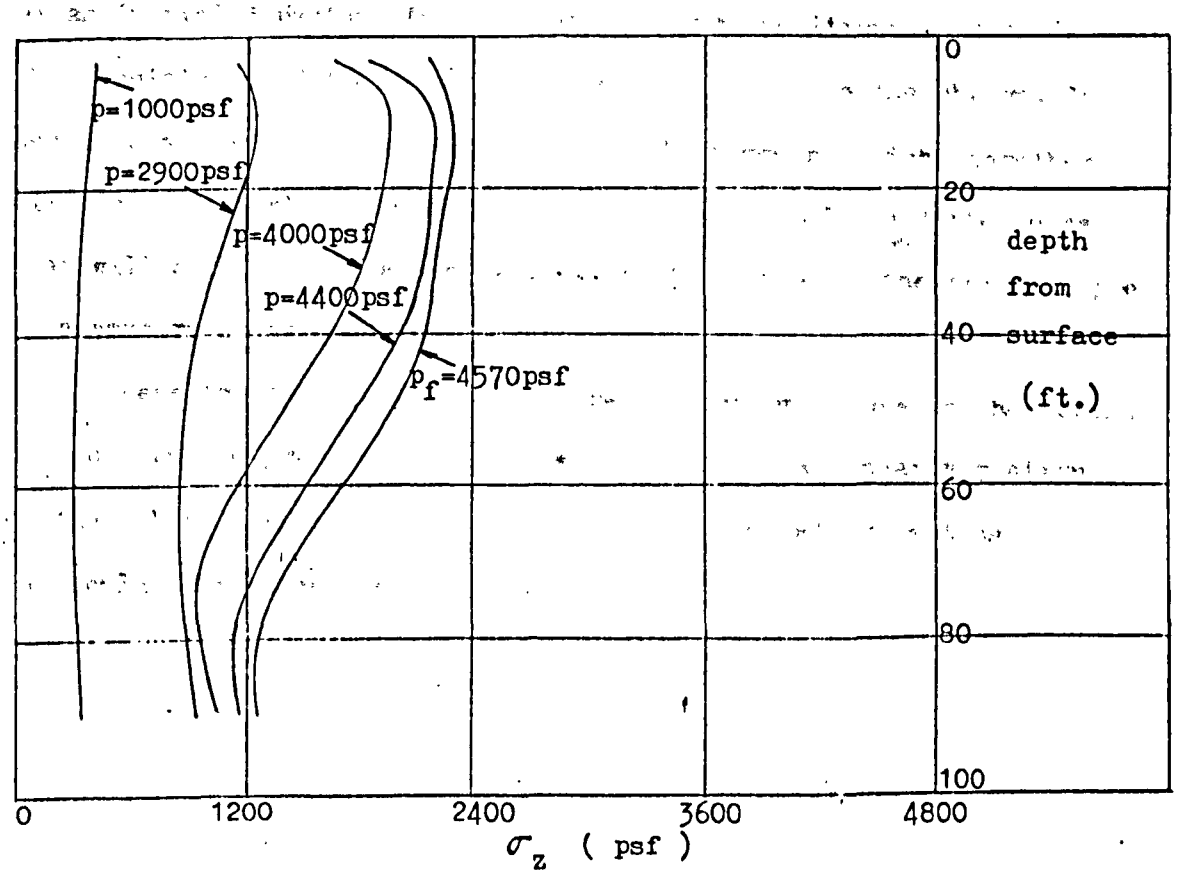

(4b) σ_z distributions down right edge of strip load

Fig. 52. Normal stress distributions down centre and edges of strip load

2.9. Two examples of linear varying strip loading on the layer (flow chart in Section 1.3.3.3.)

By the same token as for the previous study, a uniform strip load will not occur in the real situation: some asymmetry of loading is bound to exist. Here, two cases of linear varying strip loading on the clay layer of Fig. 22(a) are adopted to examine the effects of different degrees of such simple representation of asymmetry on the results of the basic model of Section 2.6. These are shown in Fig. 53, the idealisation for the layer being again that for the basic model for the purpose of comparison.

In the first case, a moderate degree of asymmetry is assumed as an initial departure from uniform loading conditions to ascertain the sensitivity of the results of the basic model to the change. The second case deals with an extreme form of asymmetry which, together with the first, should provide a good indication of the differences that will occur in the above results as the degree of the present type of asymmetry is varied.

These two cases of asymmetry are in widespread use in the design of footings and gravity retaining walls, whereby a linear variation of the subgrade reaction is assumed. The present study is thus particularly relevant to the above problems.

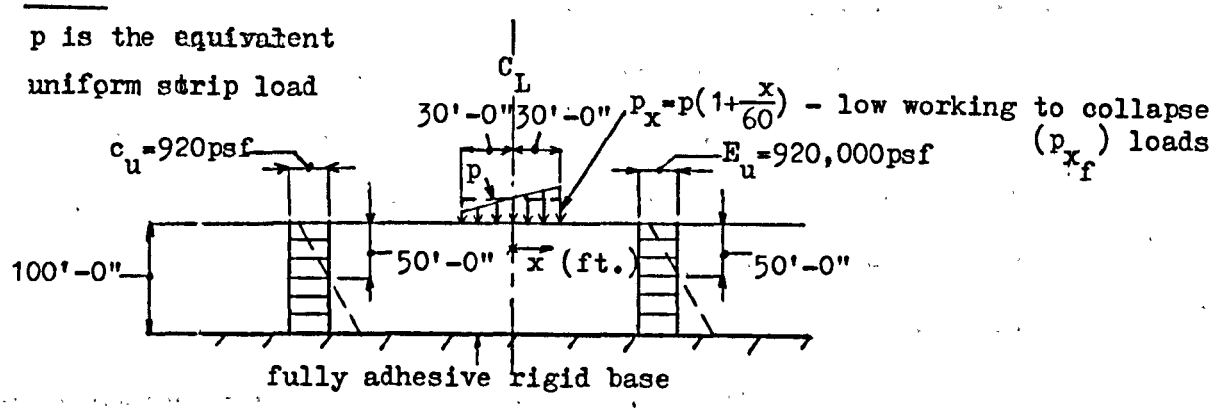

(a) Case 1-moderate asymmetry of loading (Tresca yield criterion and associated flow rule)

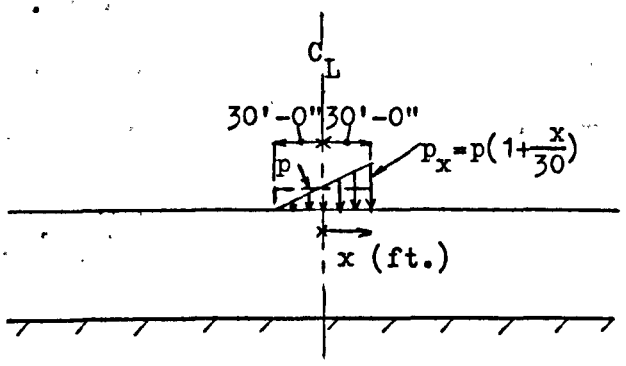

(b) Case 2 - extreme asymmetry of loading (as above except where otherwise shown)

Fig. 53. A simple idealisation for asymmetric strip loading on the clay layer of Fig. 22(a) - see also Fig. 14 of Chapter 1

Fig. 54 shows the growth of the plastic enclave with increasing load (given as the equivalent p value which leads to the same total load) for both cases of asymmetry. It can be seen that the effect of the bias of loading to the right of the centre of the strip has a similar effect to the weakening of that region in the model of Section 2.8. as is to be expected. The effect of the present form of asymmetry in relation to the behaviour of the basic model of Section 2.6. is threefold:-

(a) First yield occurs sooner and in the more heavily-loaded right half of the layer.

(b) At any given load, the growth of the plastic enclave in that right half is more advanced.

(c) Collapse occurs sooner and only in the right half where the enclave penetrates free surface, whilst the left half remains intact. At this stage, the enclave is generally smaller although localised around the strip as usual.

The above differences are further accentuated by increasing the degree of asymmetry.

The collapse load for the basic model is 4900 psf (Fig. 36). For Case 1 loading, this falls to an equivalent value of 4200 psf, which is an approximate 14·25% drop. For Case 2 loading, the equivalent collapse load is only 3300 psf which is an approximate 32·5% drop. These results indicate that for the present model (i.e. with linear varying strip loading), a design based on the maximum pressures not

exceeding the ultimate bearing pressure obtained by assuming uniform strip loading will be conservative from the point of view of the theoretical collapse load. They also suggest that Meyerhof's assumption of an equivalent strip width equal to the strip width minus twice the eccentricity of the resultant from the centre of the strip may not be far out, although leading to an underestimate of the collapse load.

In both Case 1 and 2 loading, the plastic enclave penetrates free surface at about the same distance from the strip. This distance roughly matches the lateral extent of Hill's slip-line field (19b).

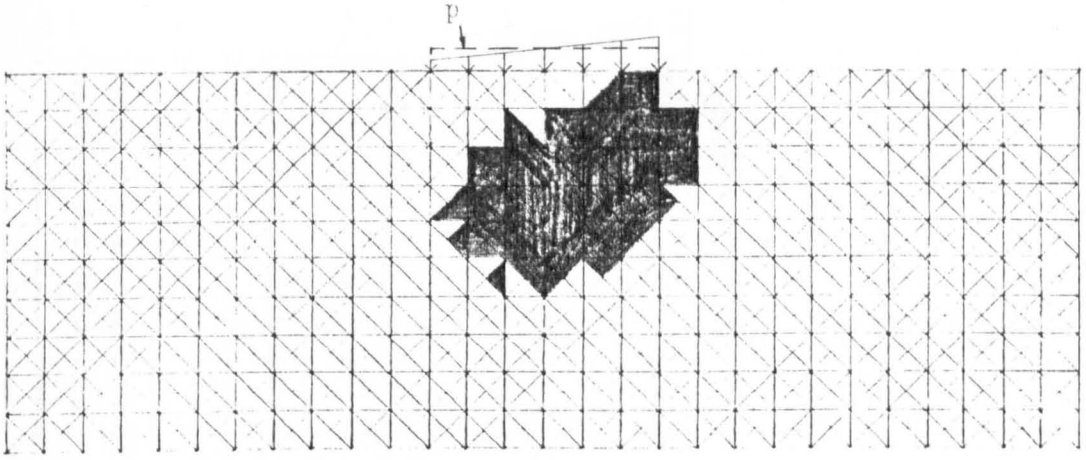

(1a) p = 3050 psf

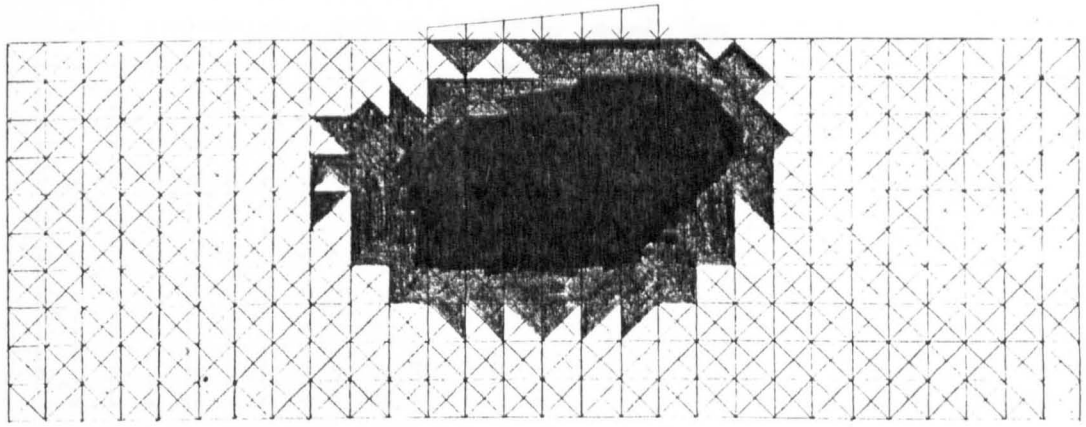

(1b) p = 4000 psf

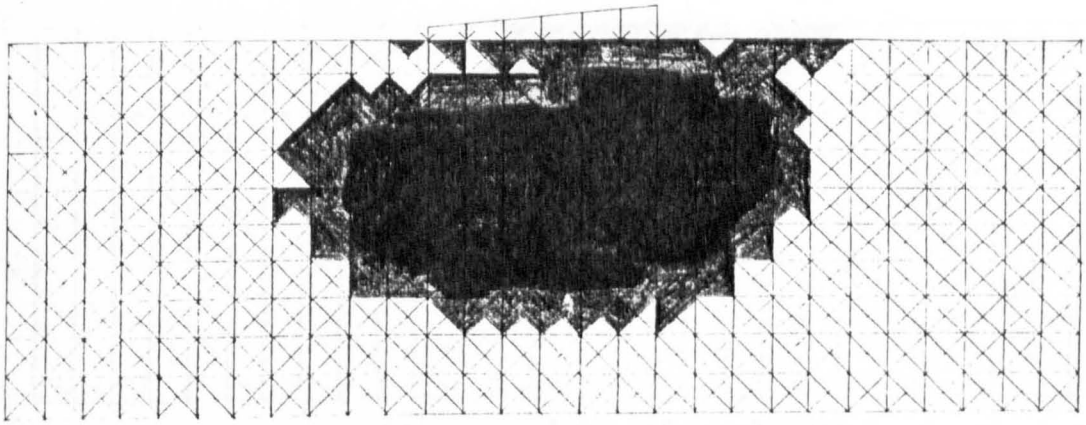

(1c) p_f = 4200 psf (collapse)

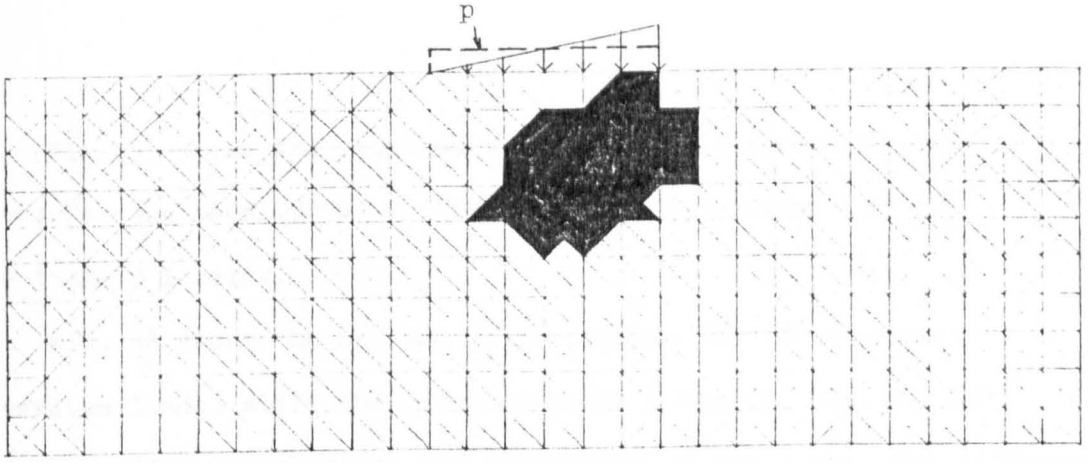

(a) p = 2500 psf

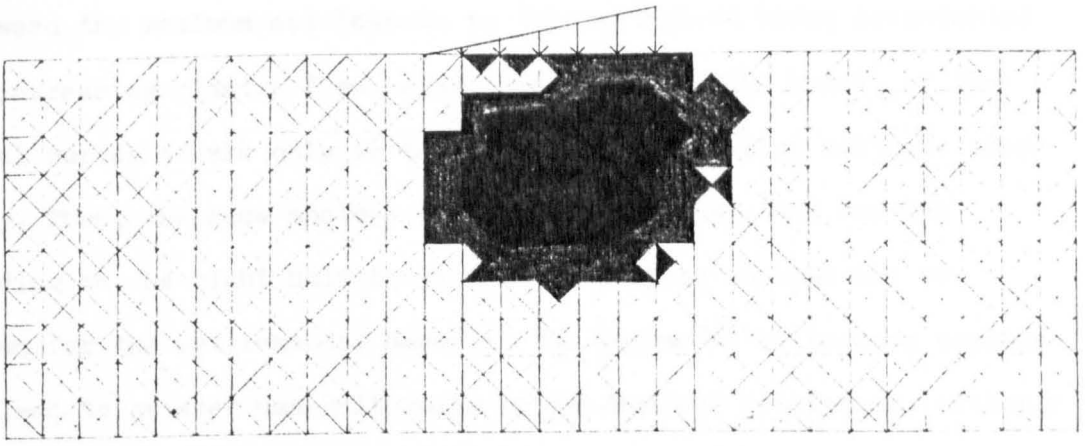

(b) p = 3050 psf

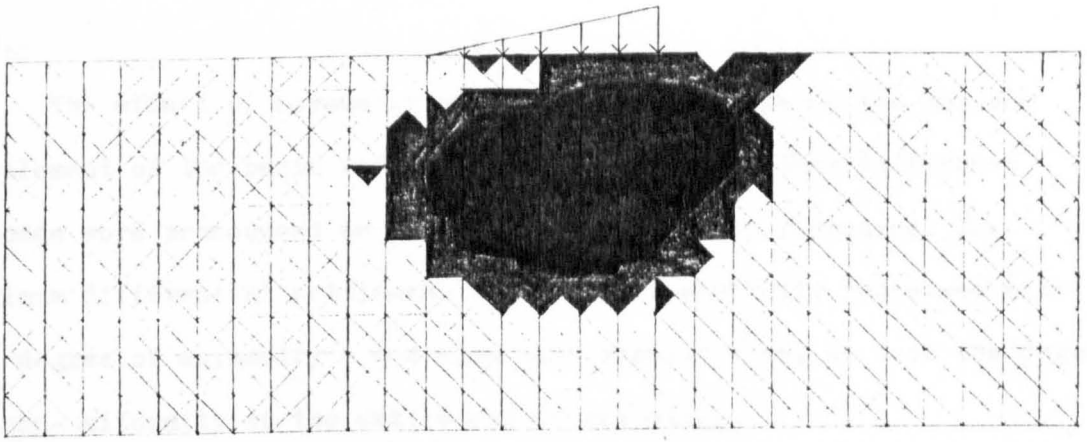

(c) p_f = 3300 psf (collapse)

Fig. 54. Growth of the plastic enclave to collapse (Case 1 - (1a) to (1c) ; Case 2 - (2a) to (2c))

Fig. 55 shows the settlement-load and settlement-iteration curves for the usual joint A. These pin-point collapse for both Case 1 and 2 loading.

Fig. 56 shows the surface displacements for the two cases at various loads. Alike the previous model (Section 2.8.), the maximum settlements occur in the right half of the layer, the difference between the maximum settlements in the two halves being accentuated by increasing plastic flow. Also, the "bump" in the heave for the final curves occurs only in the right half indicating collapse there only. Thus, the same analogy between weakening of, and heavier loading on the right half found for the plastic enclave may be drawn for the settlements. However, the asymmetry of loading appears to lead to greater non-uniformity of the surface settlement, although this may be due to the mild inhomogeneity of the model of Section 2.8.

The effect of asymmetry of loading is to increase the maximum settlement of the basic model at comparable loads; this difference becomes more pronounced as the degree of asymmetry increases. The maximum differential settlement of the strip similarly increases with the degree of asymmetry - and also with plastic flow, as does the degree of non-uniformity of the settlement of the strip.

Maximum bending occurs in the right half of the strip unlike the basic model. With Case 1 loading, some hogging occurs left of this maximum, although it is hardly noticeable; with Case 2 loading, the

hogging there becomes more pronounced. Most of the main steel, however, will be located around the point of maximum bending. Since this is a sag, the steel will be located at the bottom of the slab.

Similar observations may be made for the horizontal surface displacements as for the inhomogeneous model of Section 2.8. However, in the vicinity of the centre of the strip, points right of centre move to the left, this tendency accentuated by increasing the degree of asymmetry - in the inhomogeneous model, points left of centre move towards the right.

Fig. 57 shows the general pattern of joint displacements at different stages of loading. These provide further support for some earlier observations, e.g. note the smaller extent of the area of intense movement than for the basic model at collapse.

Fig. 58 provides a general picture of the deformation of the assemblage. This clearly shows collapse to the right only.

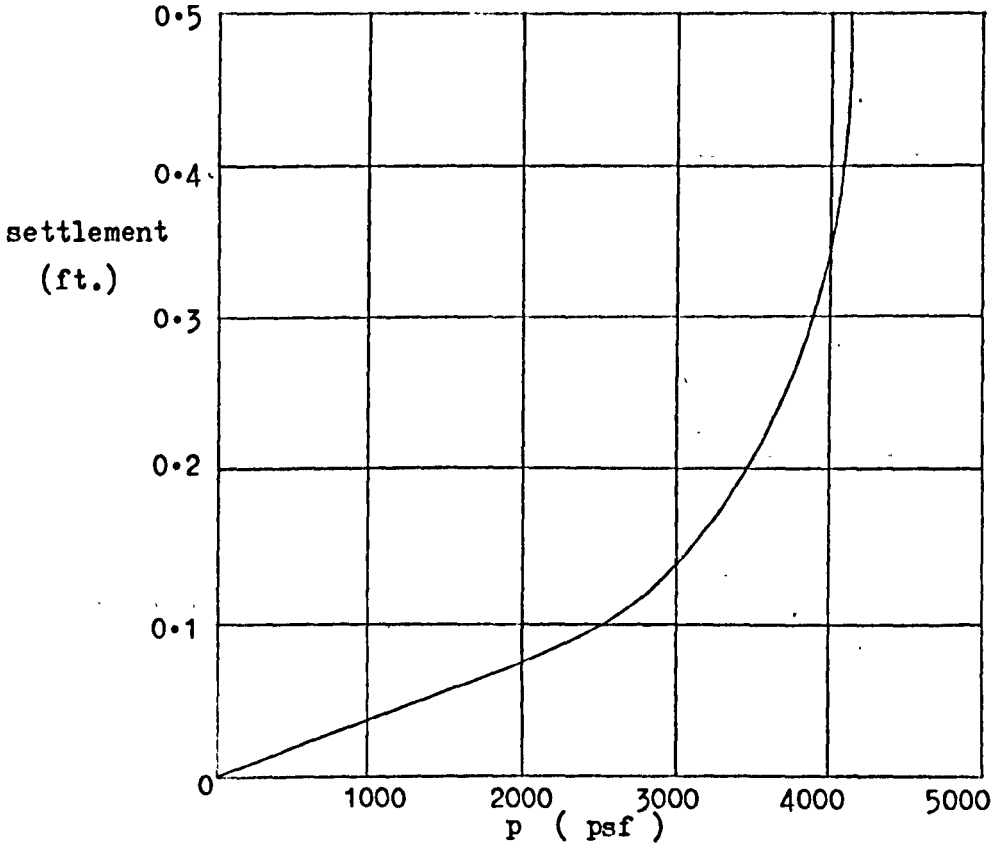

(1a) Settlement-load plot (Case 1)

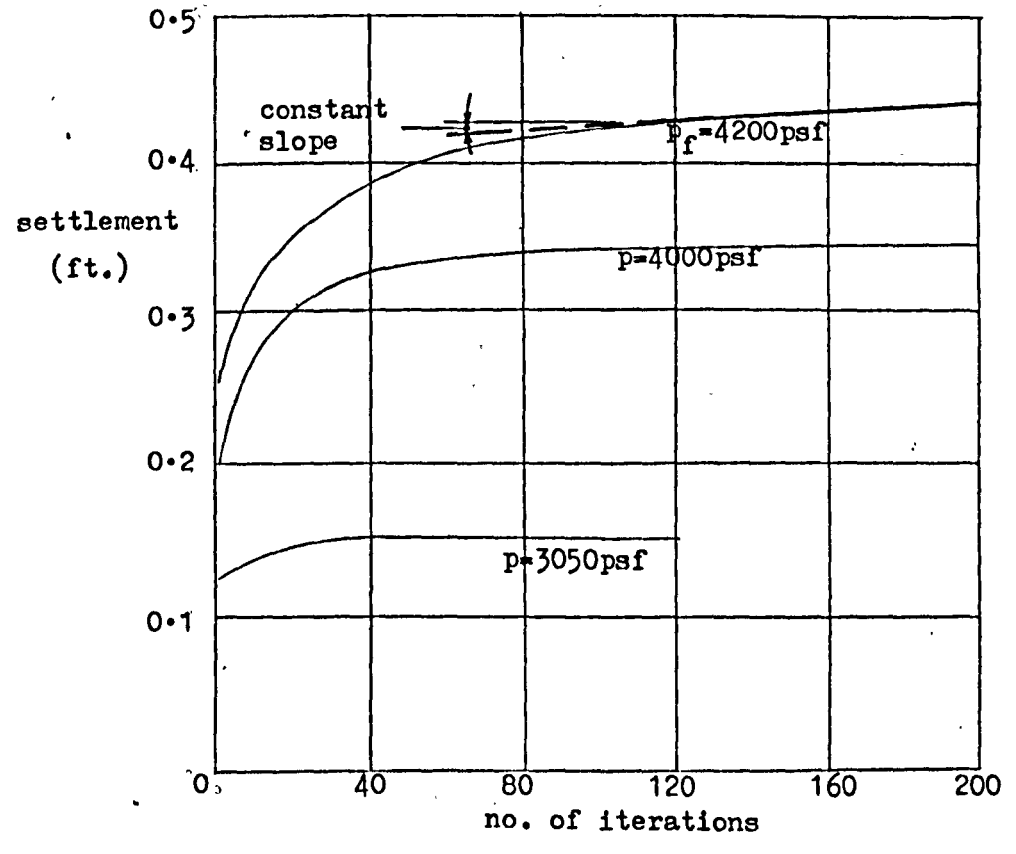

(1b) Settlement-iteration plots (Case 1)

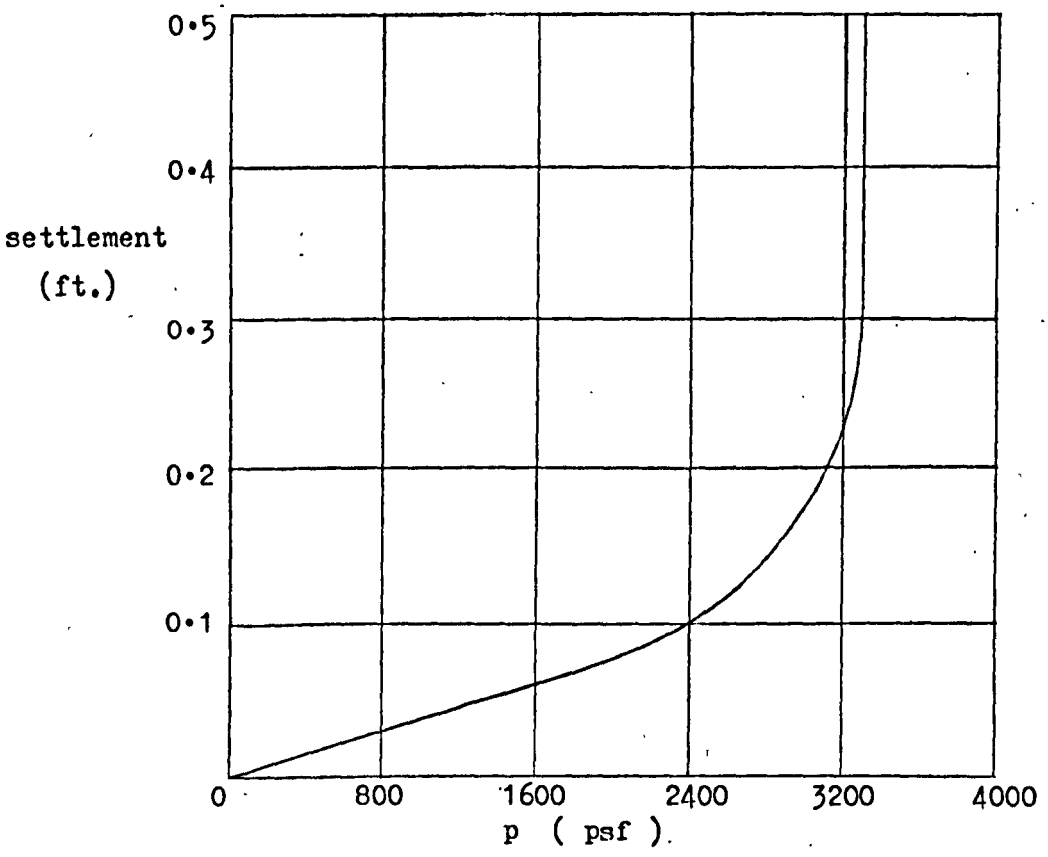

(2a) Settlement-load plot (Case 2)

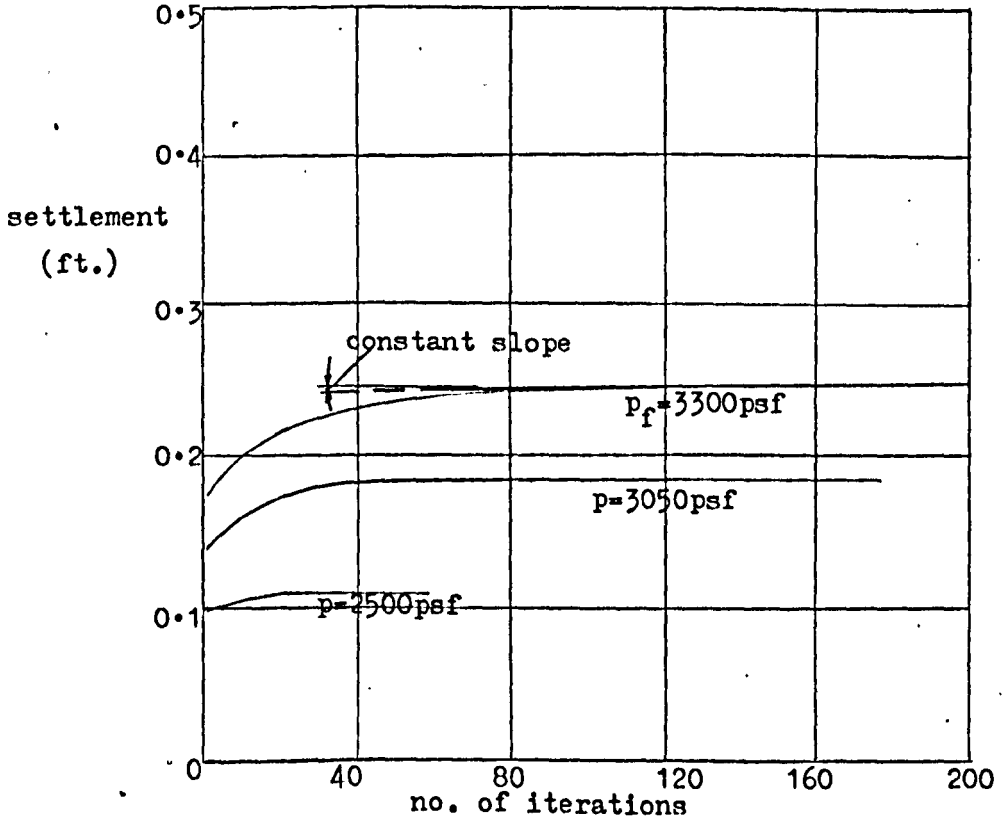

(2b) Settlement-iteration plots (Case 2)

Fig. 55. Settlement curves for joint A

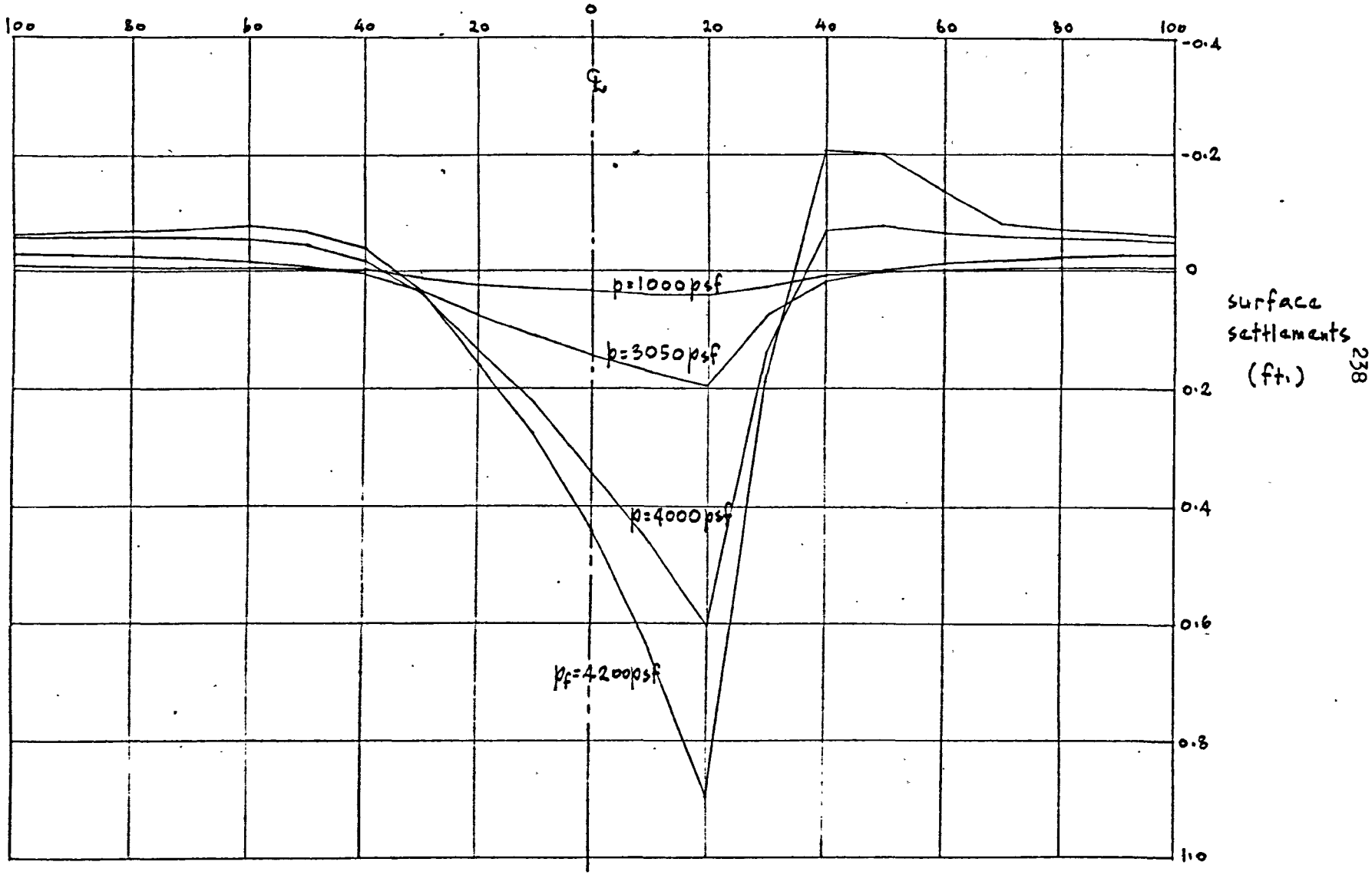

(1a) Surface settlements (Case 1)

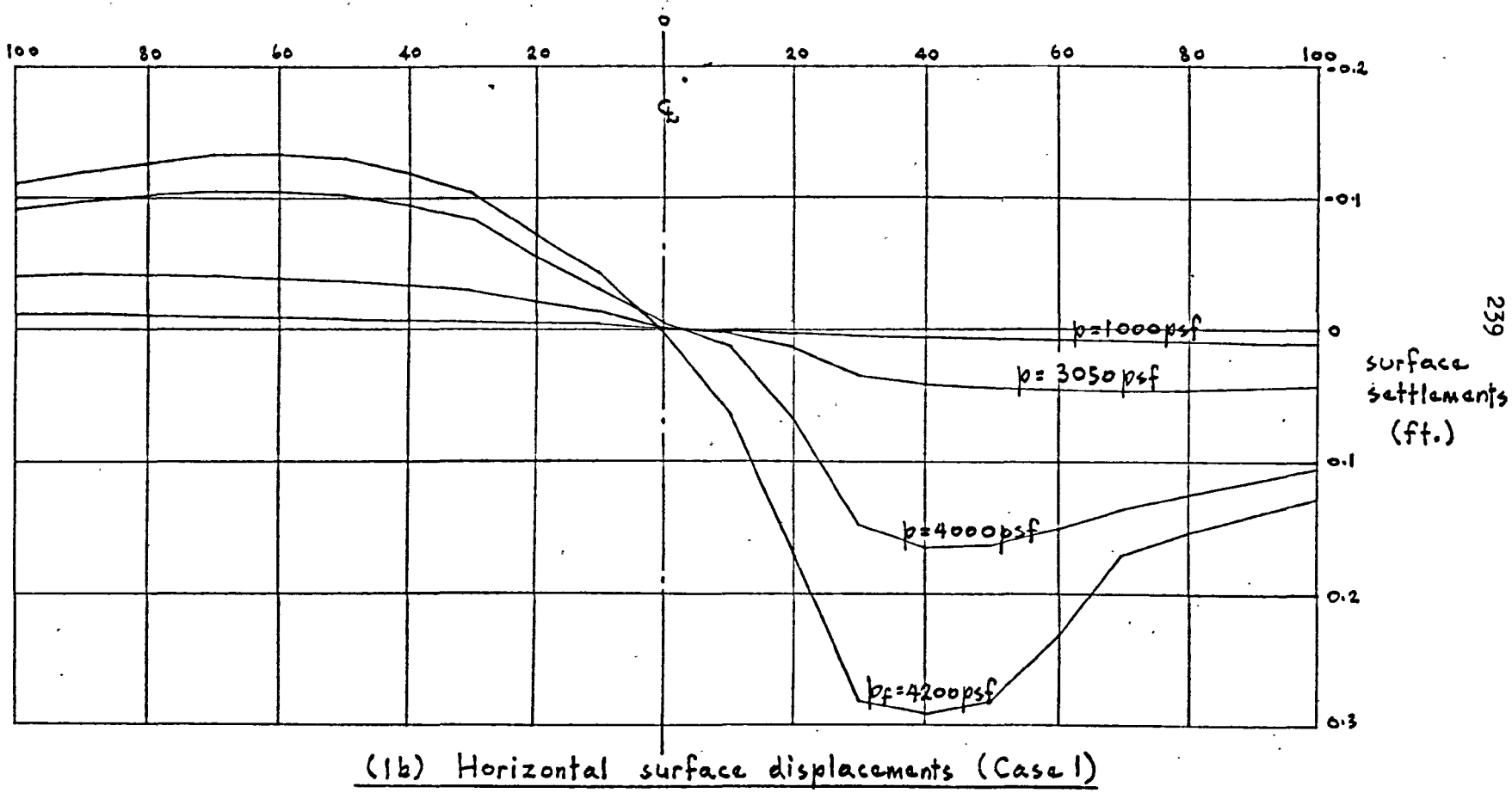

(1b) Horizontal surface displacements (Case 1)

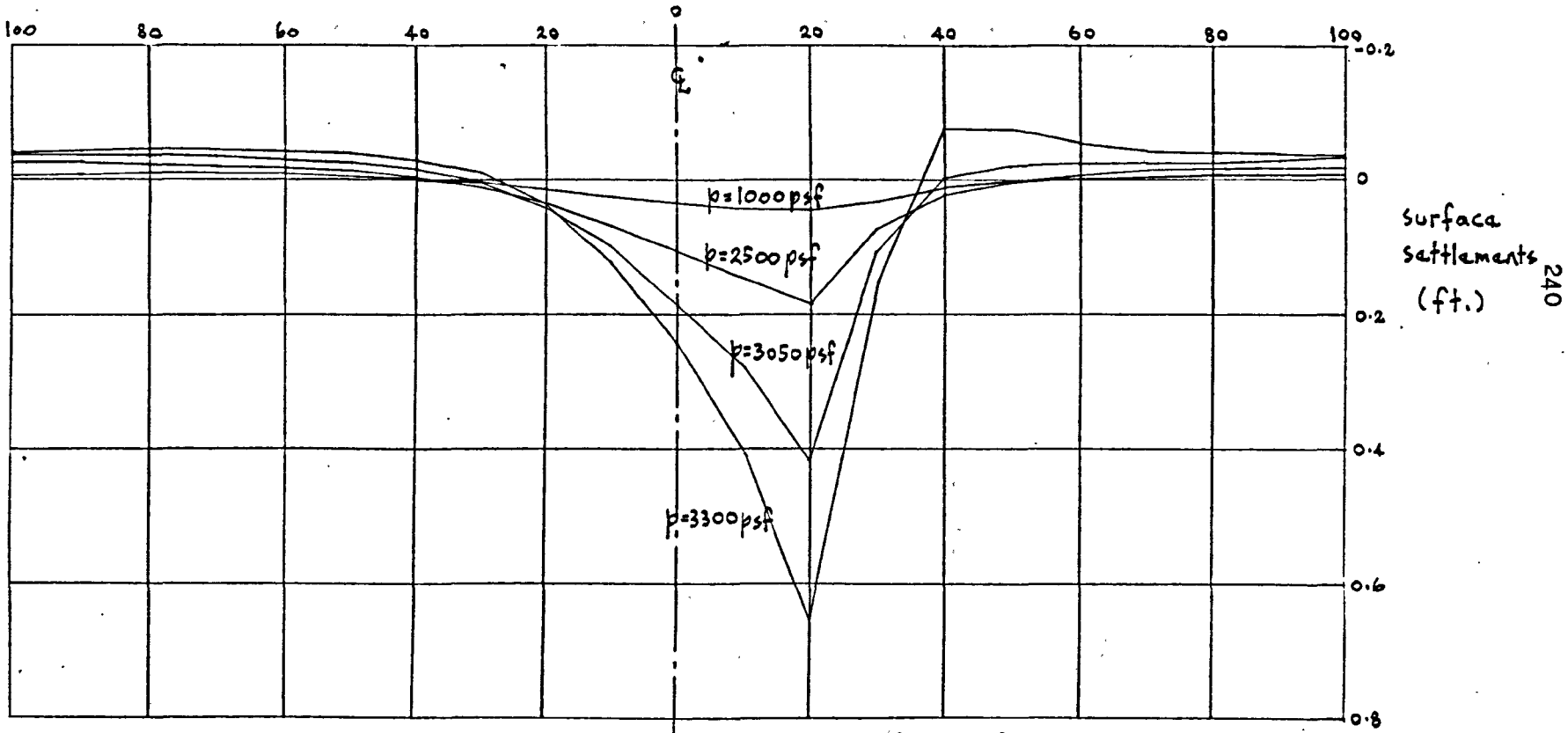

(2a) Surface settlements (Case 2)

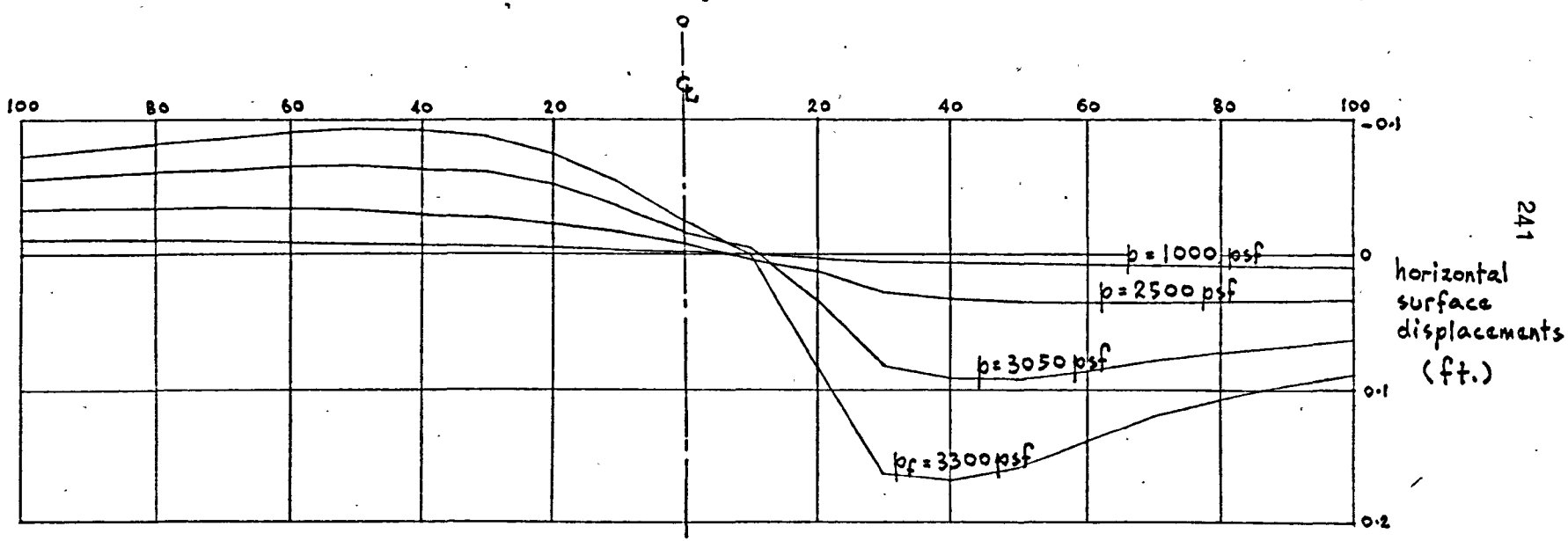

(2b) Horizontal surface displacements (Case 2)

Fig. 56. Surface displacements

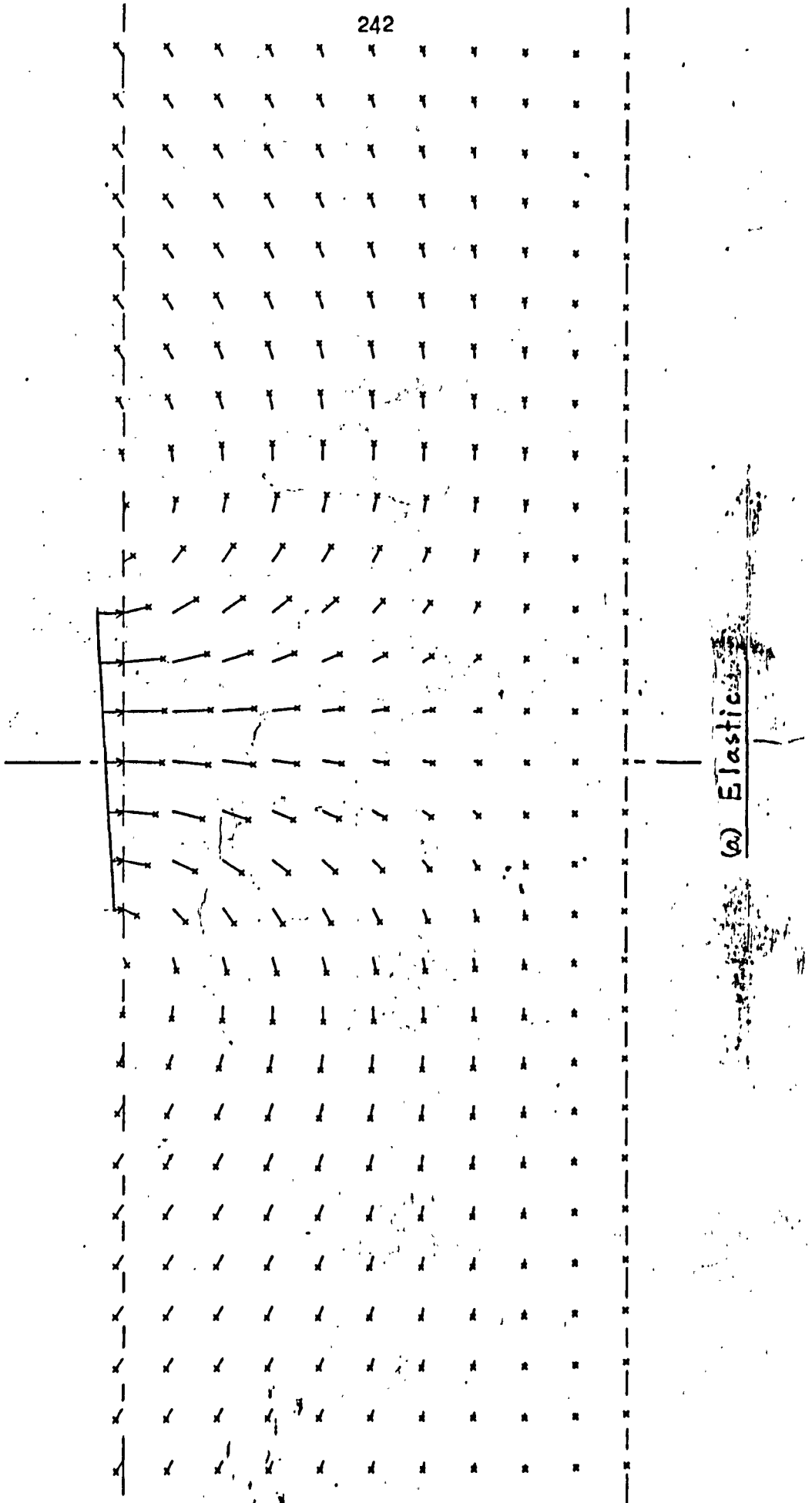

(a) Elastic

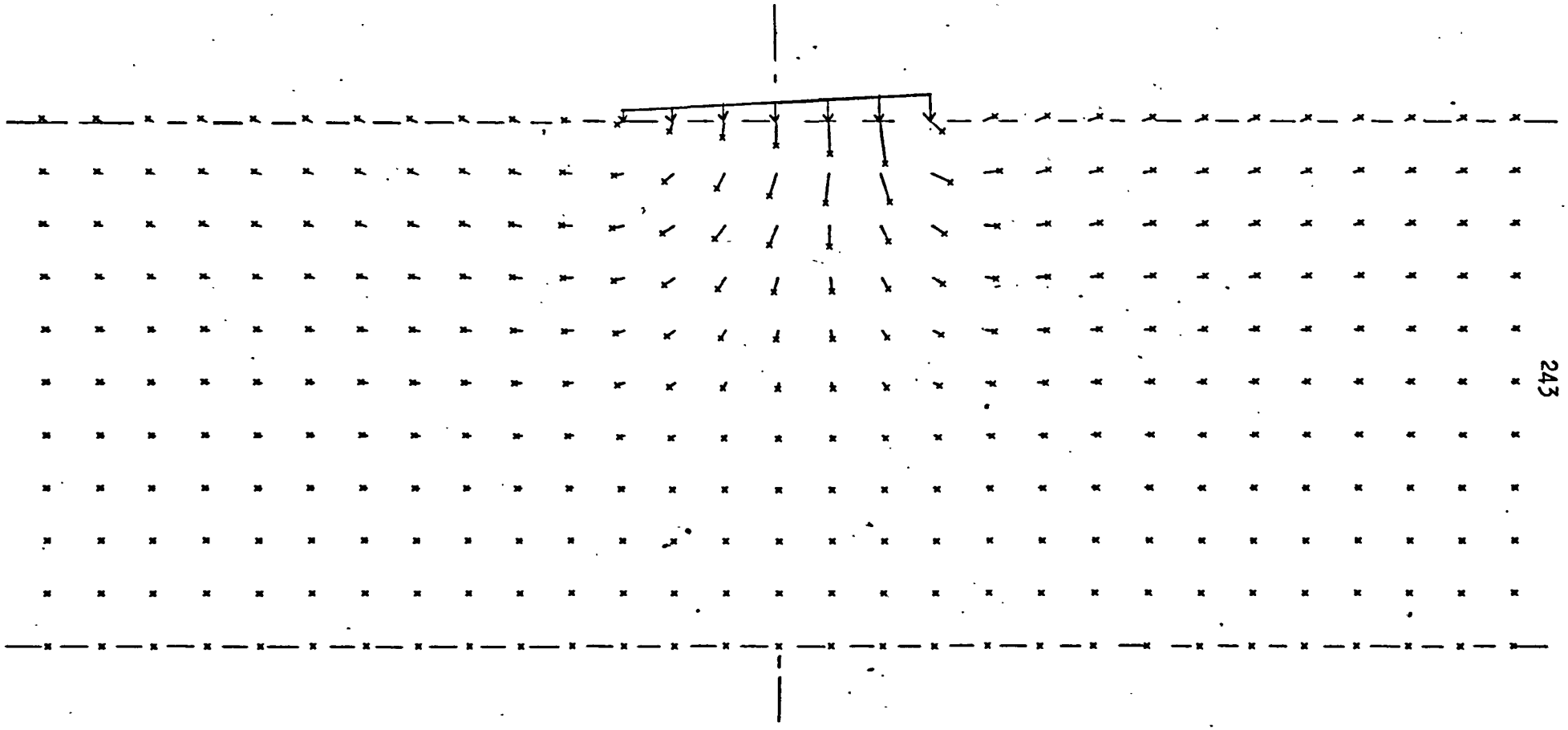

(b) Elastoplastic

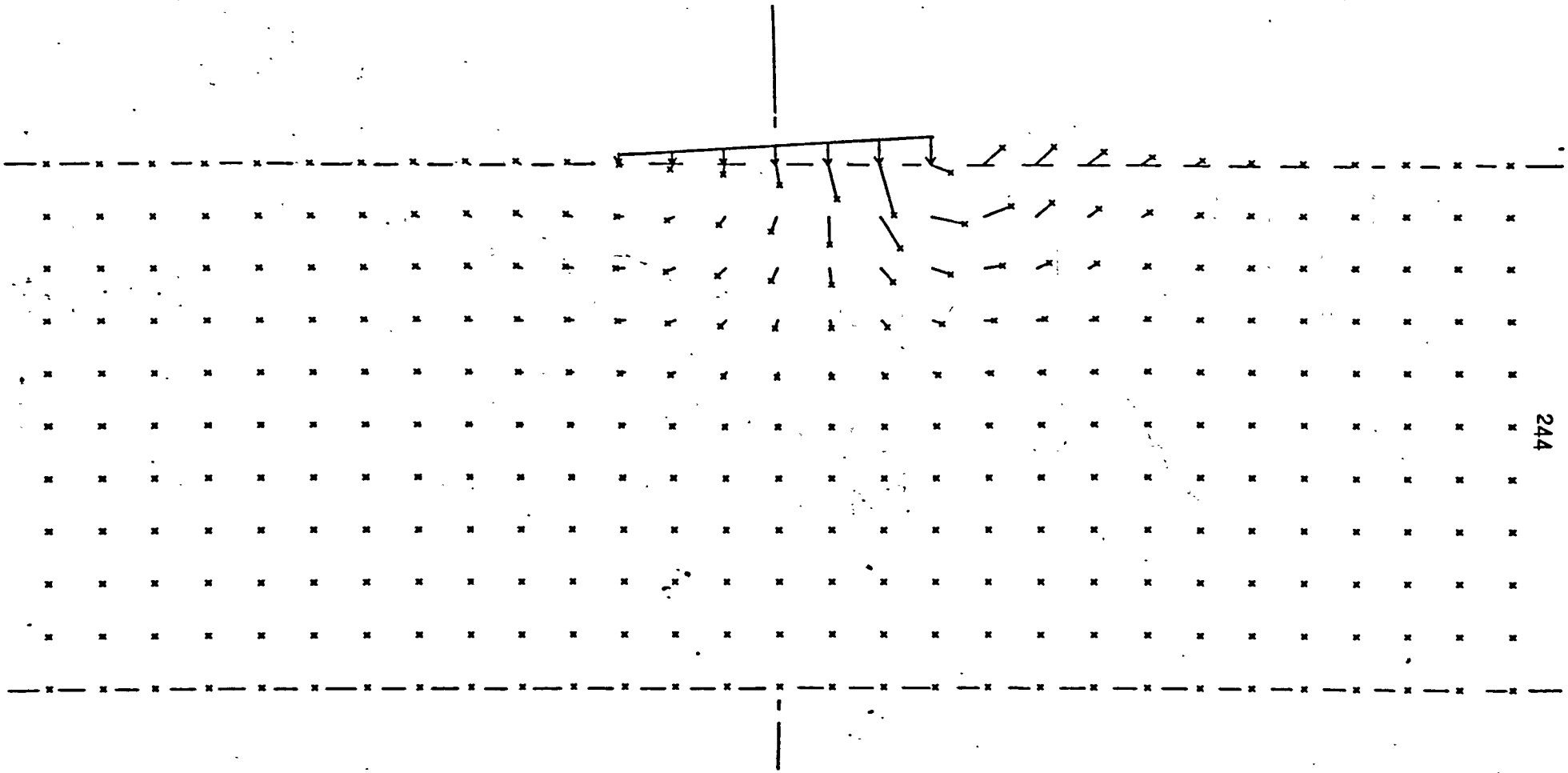

(c) Collapse

Fig. 57. Joint displacements at various loads (crosses at final positions)

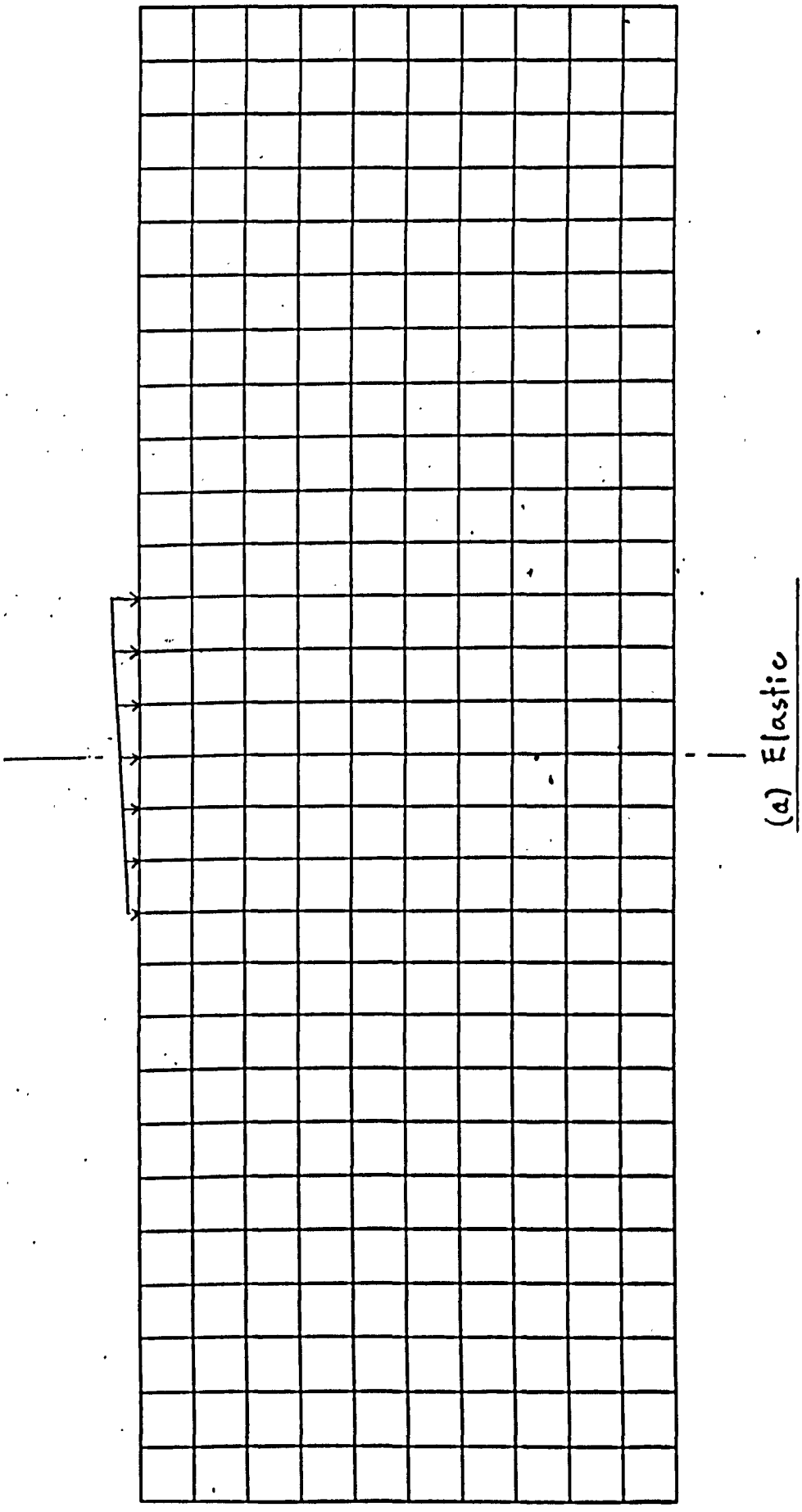

(a) Elastic

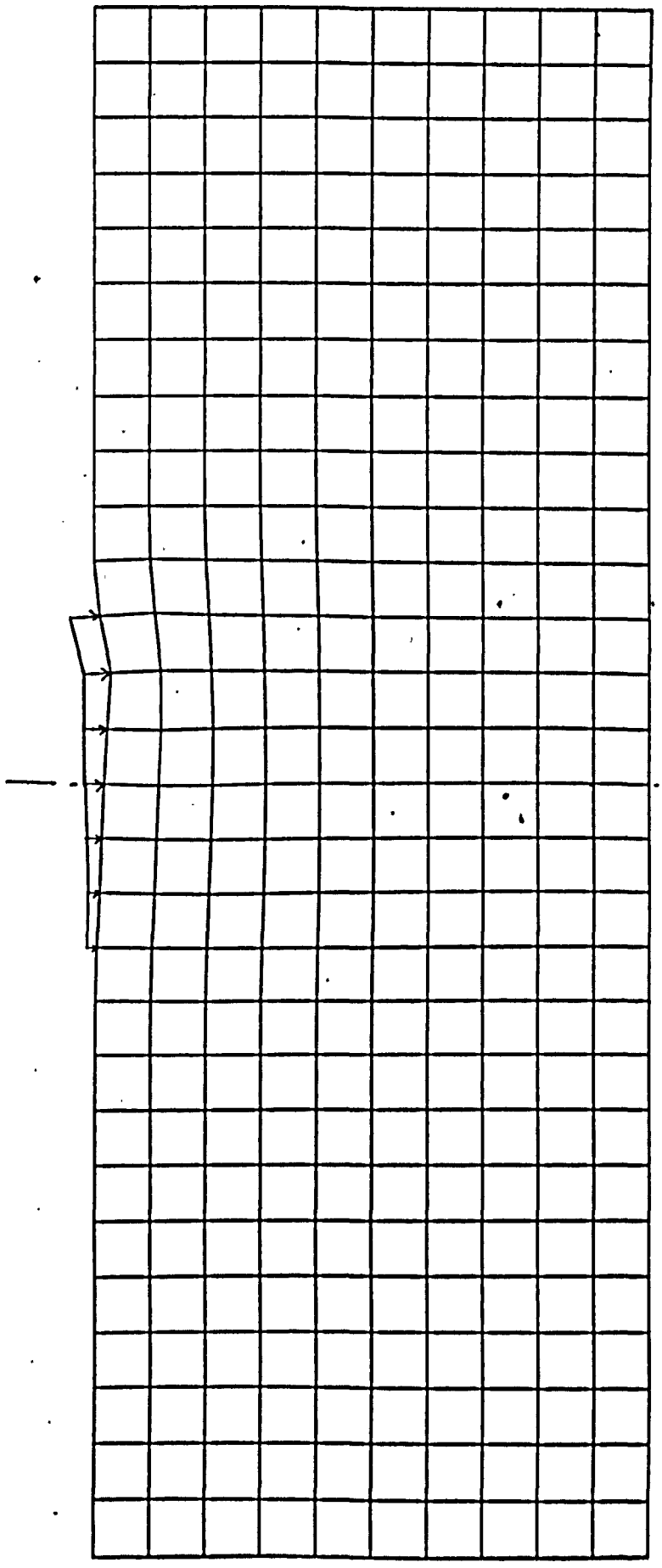

(b) Elastoplastic

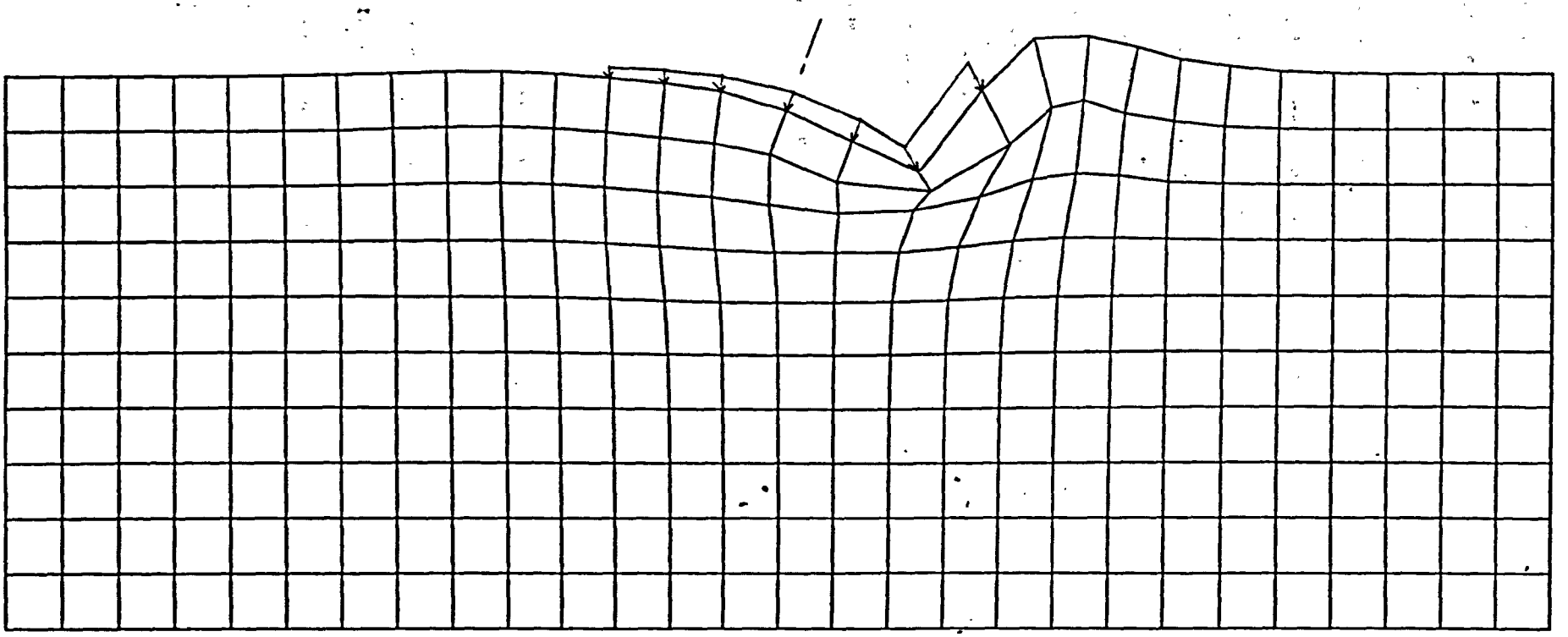

(c) Collapse

Fig. 58. General deformation of layer at various stages of loading

Fig. 58A shows the normal stress distributions down the centre and edges of the strip load for Case 1 and 2 loading, both edge distributions being given since this is a problem of asymmetry.

For σ_x there is little change from the values given by the basic model down the centre of the strip at the elastic stage - i.e. at comparable loads. With plastic flow, however, there is an increase here in the upper region of the layer and a decrease towards the bottom. Near collapse, an increase is found over a greater depth. The influence of further asymmetry is greater increase in the upper region and decrease below. The latter decrease is sufficient to cause tensile stresses to develop around mid-depth in the layer where the stresses are least. Down the left edge of the strip, there is a decrease in σ_x from that of the basic model at comparable loads in the upper region of the layer and an increase around mid-depth which is accentuated by increasing plastic flow. Down the right edge, on the other hand, σ_x increases at the top, accentuated by plastic flow, and decreases below although to a lesser extent towards collapse. The result is that σ_x is less down the left edge than the right (towards which the load is biased) in the upper region of the layer, and greater below.

For σ_y down the centre of the strip, there is an increase at the top and a decrease below although with plastic flow, a general increase develops. The effect of further asymmetry of loading is to

lead to a general decrease initially, followed by an increase at the top and a decrease below with plastic flow. Down the left edge of the strip, σ_y decreases generally from the values of the basic model. Down the right edge, on the other hand, there is an initial general increase followed by an increase at the top and a decrease at the bottom with plastic flow. Thus, σ_y down the lighter left edge is less than down the right, this difference becoming smaller near the bottom of the layer with plastic flow.

As with the inhomogeneous model of Section 2.8., the trends of the σ_x and σ_y distributions are similar to those of the basic model despite the above differences. Also, $\sigma_z \simeq 0{\cdot}5(\sigma_x + \sigma_y)$ so that changes in pore pressure due to asymmetric loading are given by differences in σ_z between the present and basic models , or in other words, the average of the changes described above. Accordingly, we may expect similar pore pressures to those of the basic model down the centre of the strip to begin with, followed by an increase in the upper region of the layer and a decrease below with increasing plastic flow although there will be little change in the latter area towards collapse. Down the lighter left edge, lower pore pressures develop near the top and bottom of the layer and higher pore pressures between - i.e. in the present models.

Constant stress conditions are obtained at collapse as usual.

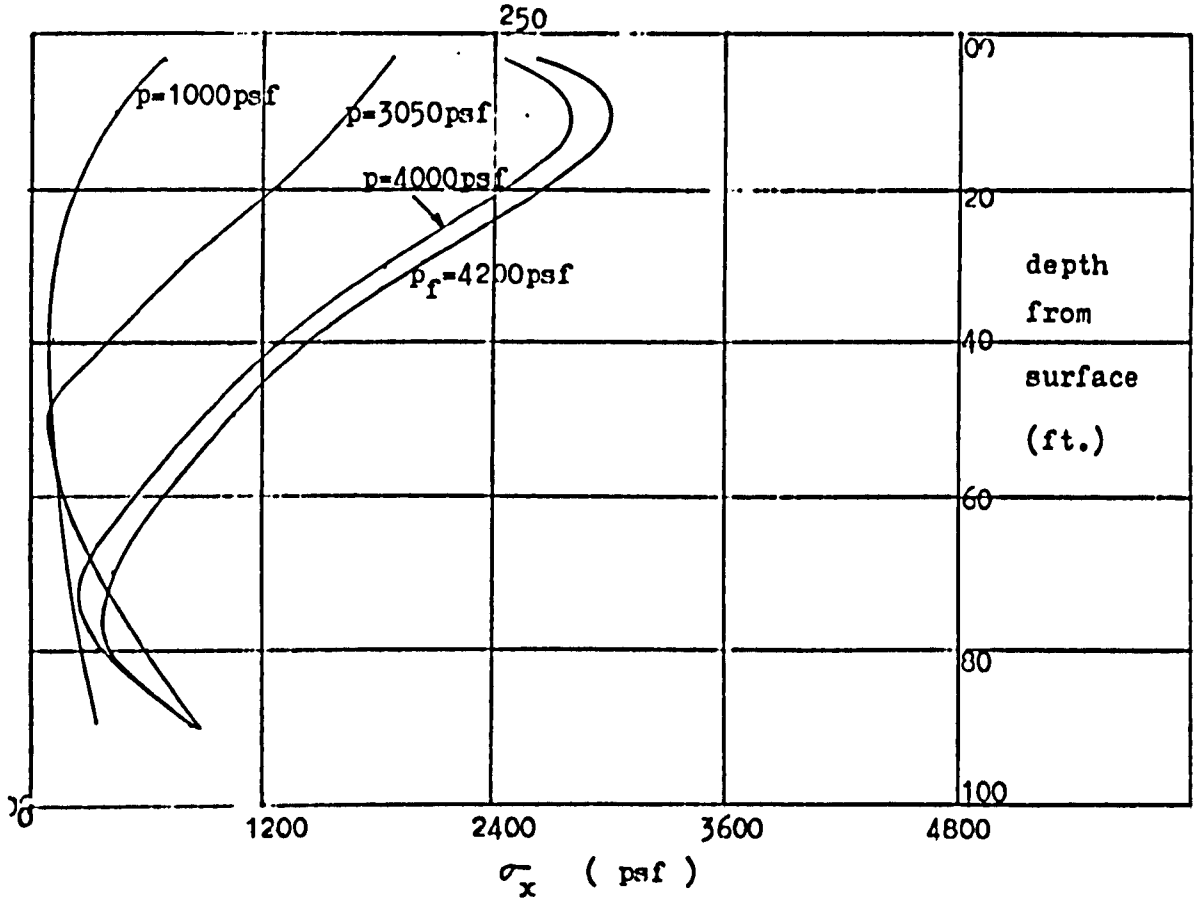

(1a) σ_x distributions down centre of strip load (Case 1)

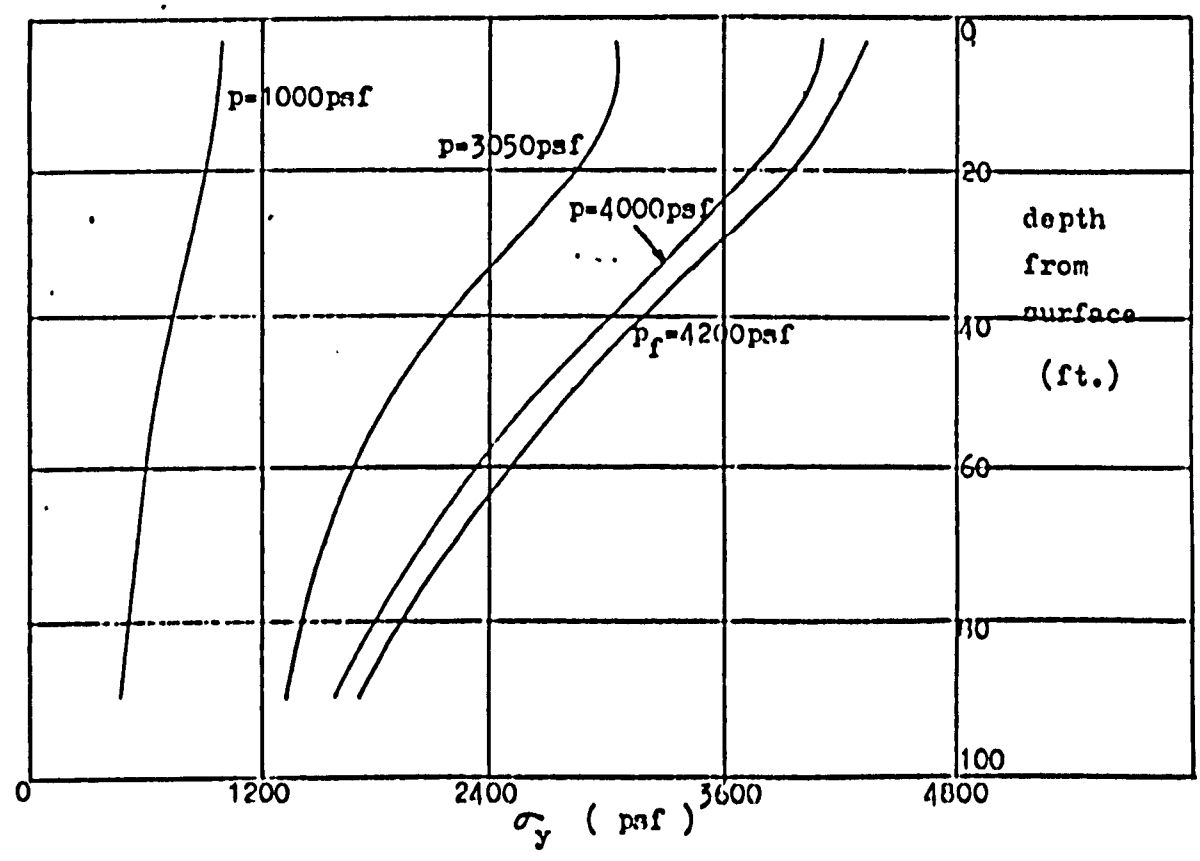

(1b) σ_y distributions down centre of strip load (Case 1)

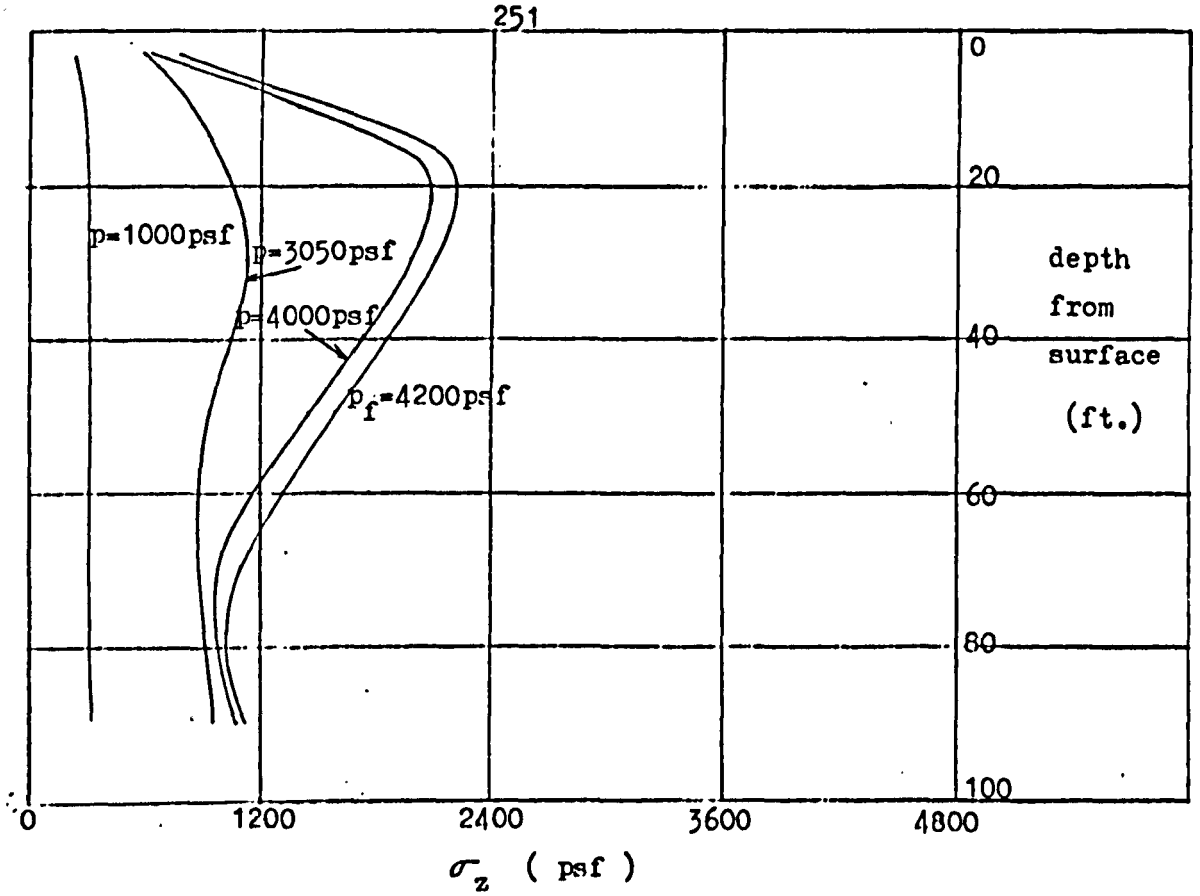

(1c) σ_z distributions down left edge of strip load (Case 1)

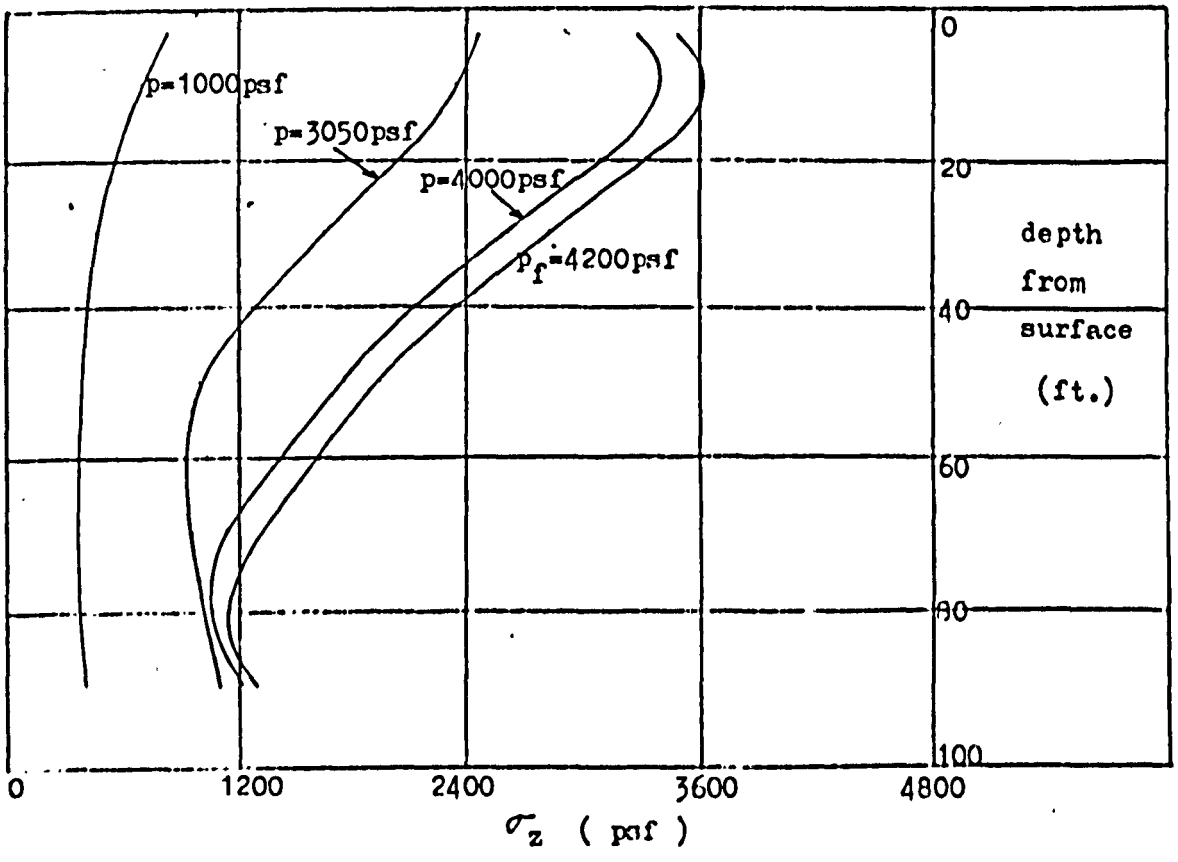

(1d) σ_z distributions down centre of strip load (Case 1)

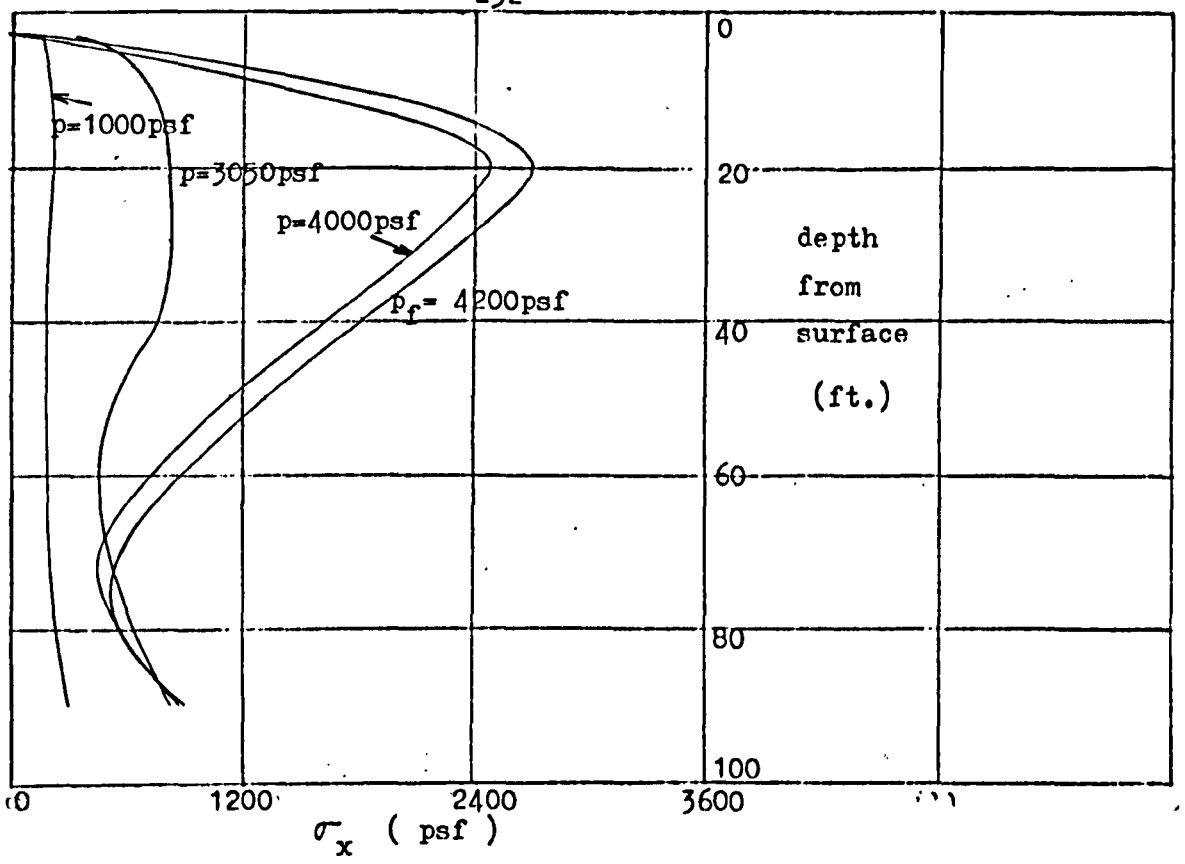

(1e) σ_x distributions down left edge of strip load (Case 1)

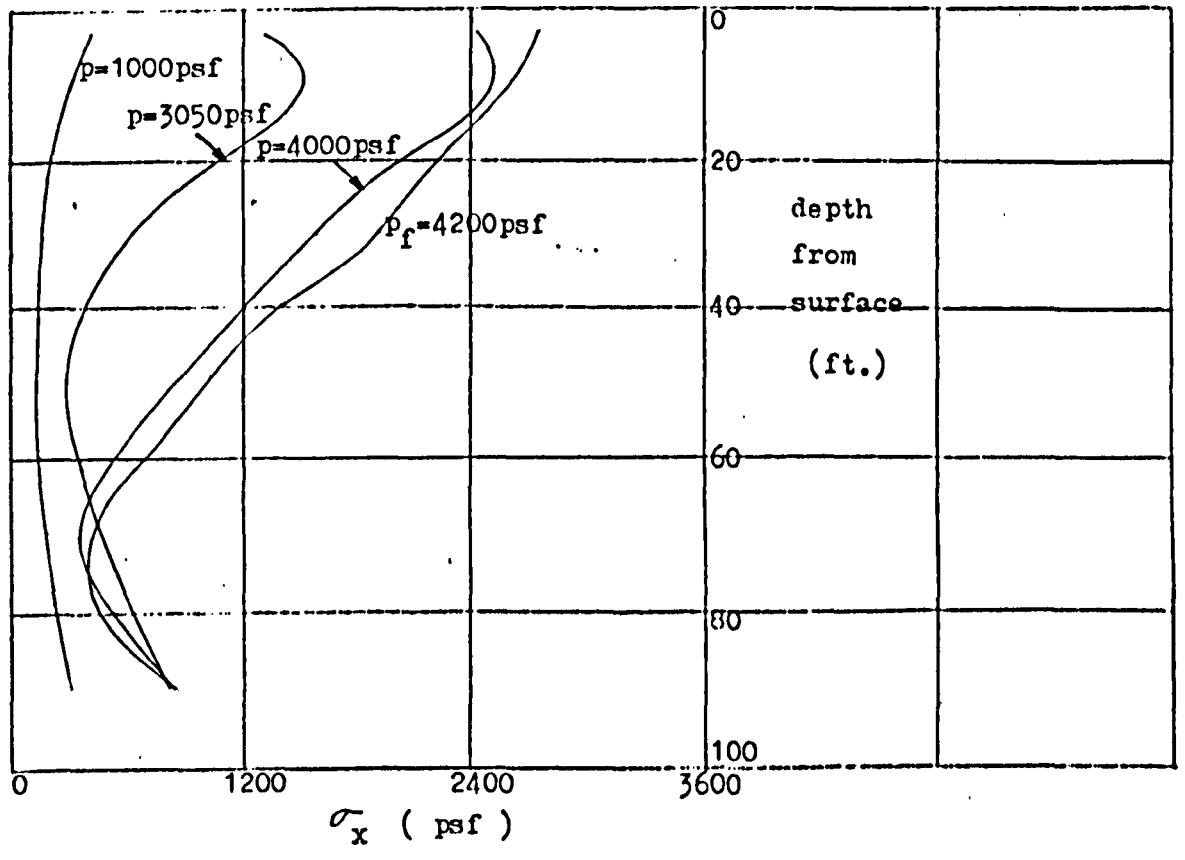

(1f) σ_x distributions down right edge of strip load (Case 1)

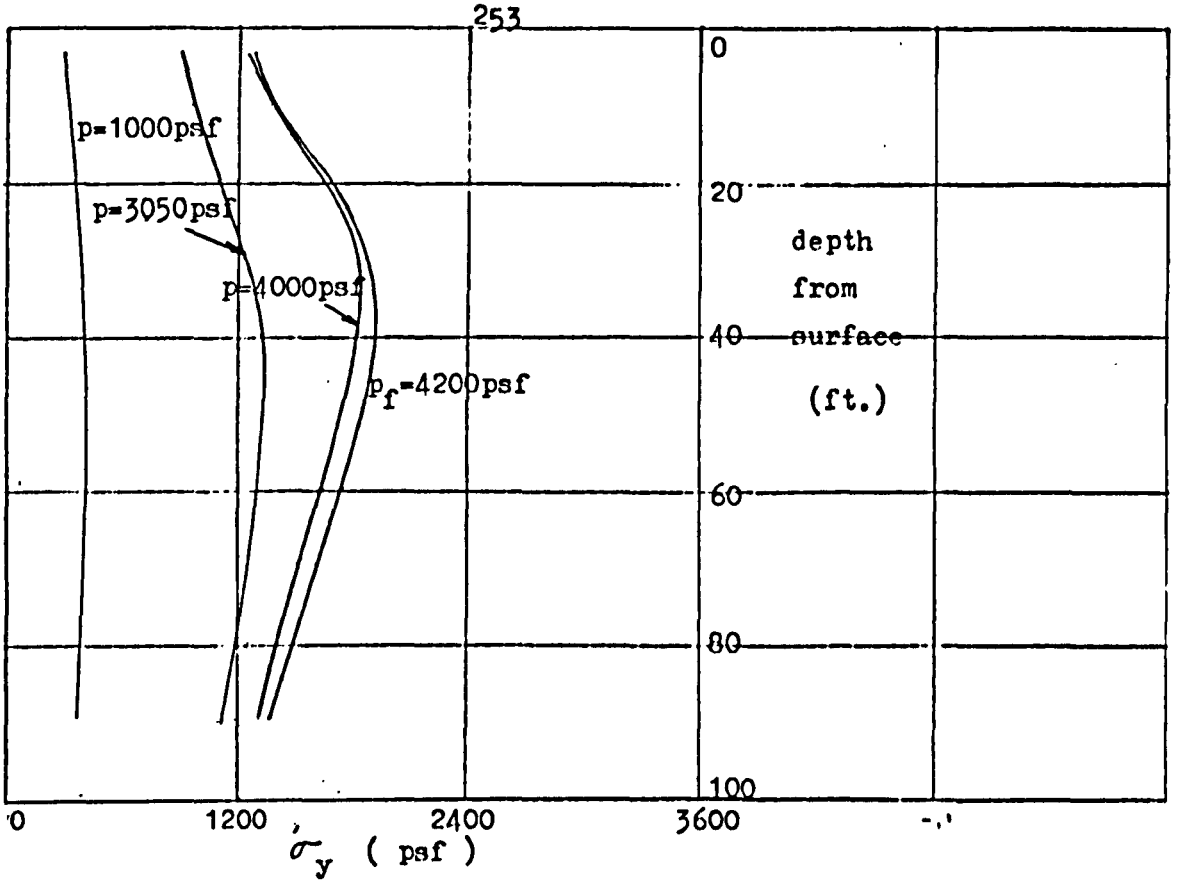

(1g) σ_y distributions down left edge of strip load (Case 1)

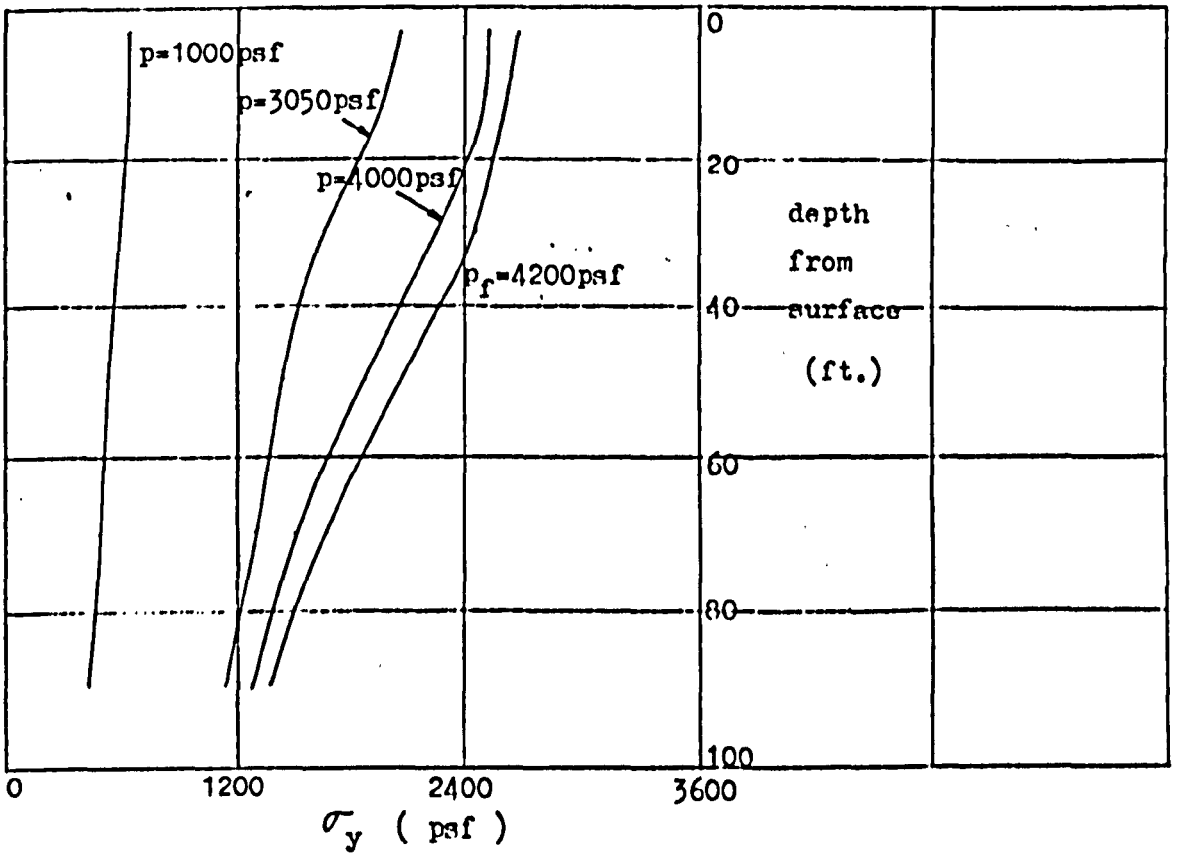

(1h) σ_y distributions down right edge of strip load (Case 1)

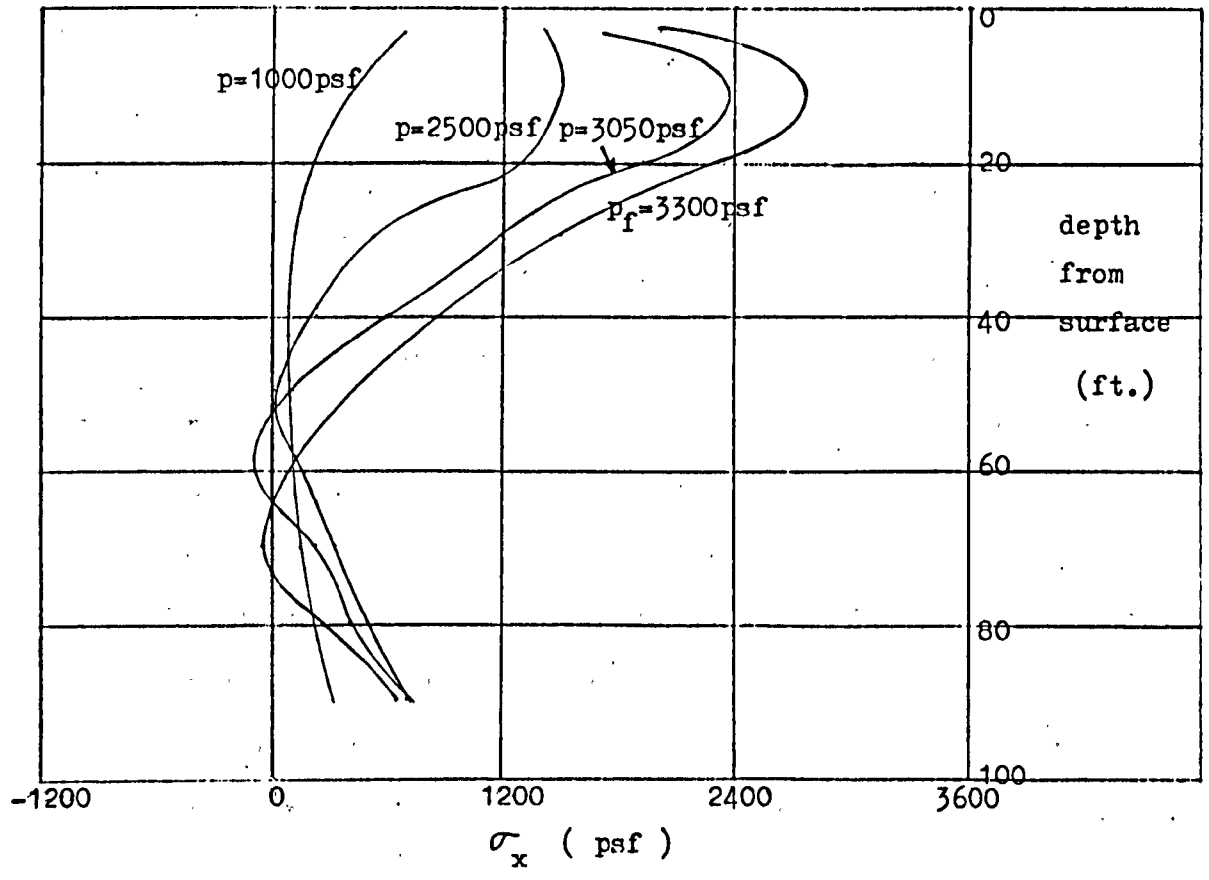

(2a) σ_x distributions down centre of strip load (Case 2)

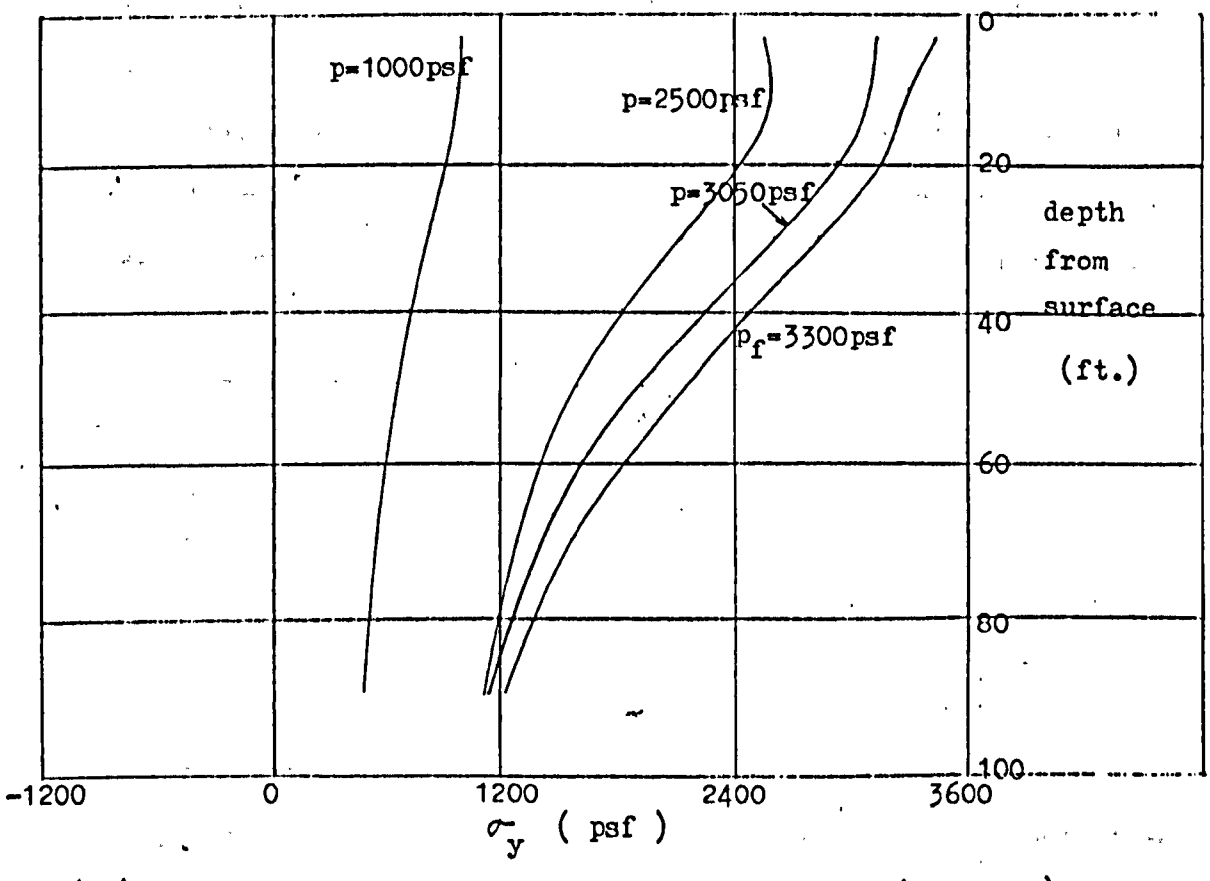

(2b) σ_y distributions down centre of strip load (Case 2)

Fig. 58A. Normal stress distributions down centre and edges of strip load

2.10. Linear variation of rigidity and strength of layer with depth (flow chart in Section 1.3.3.4.)

As mentioned earlier, it is widely held that the undrained rigidity and strength of a saturated, normally consolidated clay layer varies approximately linearly with depth due to the influence of the effective overburden pressure (pp. 111).

Whilst with a small foundation, it may be reasonable to adopt the average point values, the present width of the ground slab requires that a proper account be given of the variation of rigidity and strength with depth.(the following results bear this out).

Indeed the present idealisation was suggested as a suitable representation of the practical problem at the outset and Fig. 22(b) is thus relevant to the present study. A Poisson's Ratio of 0·49999 is adopted.

Note, however, that in view of the requirement for constant material properties in the individual finite elements, an exactly linear distribution of rigidity and strength cannot be reproduced.

Fig. 58B below shows the approximate representation of the linear variations.

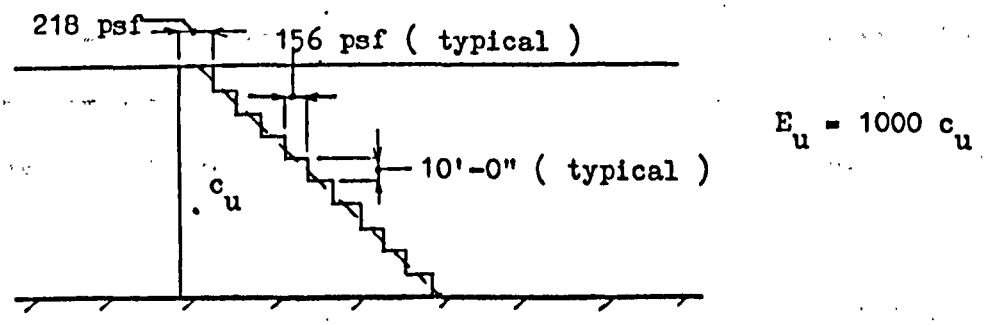

Fig. 58B. Approximations to linear variation of rigidity and strength

Fig. 59 shows the growth of the plastic enclave with increasing load p. First yield occurs at about 950 psf at the surface where the soil is weakest. This load is considerably lower than that for the basic model (i.e. 2413 psf) as would be expected since the strength of the latter corresponds to that at mid-depth here. The subsequent growth of the plastic enclave is also confined to the upper zone of the layer where it is weakest. It thus develops along the surface and when a sufficient area beyond the edge of the strip is covered, collapse occurs. Note that at p =1530 psf, the enclave has a limited lateral extent and is still inhibited by the strip edge on one side, and the elastic body on the other.

Owing to the nature of its development, the enclave in much more localised around the strip than for the basic model. Indeed, its limited size at collapse indicates an extremely restricted area of intense movement in the vicinity of the strip. Also, the proximity of the elastic body to the centre of the strip suggests a Hill type (19b) of collapse mechanism rather than the Prandtl-type of the basic model.

The collapse load of 1615 psf here is considerably less than for the basic model of 4900 psf (i.e. less than $\frac{1}{3}$). This is perhaps not too unexpected since only the strength of a small area of the weaker upper zone need be exceeded to attain the state of collapse. The value of the computed collapse load compares favourably with that obtained by Davis and Booker (28) for a smooth rigid strip using slip-line

analysis. Although their analysis is for a half-space and the contact stress distribution is non-uniform, the results concur to within about 15%.

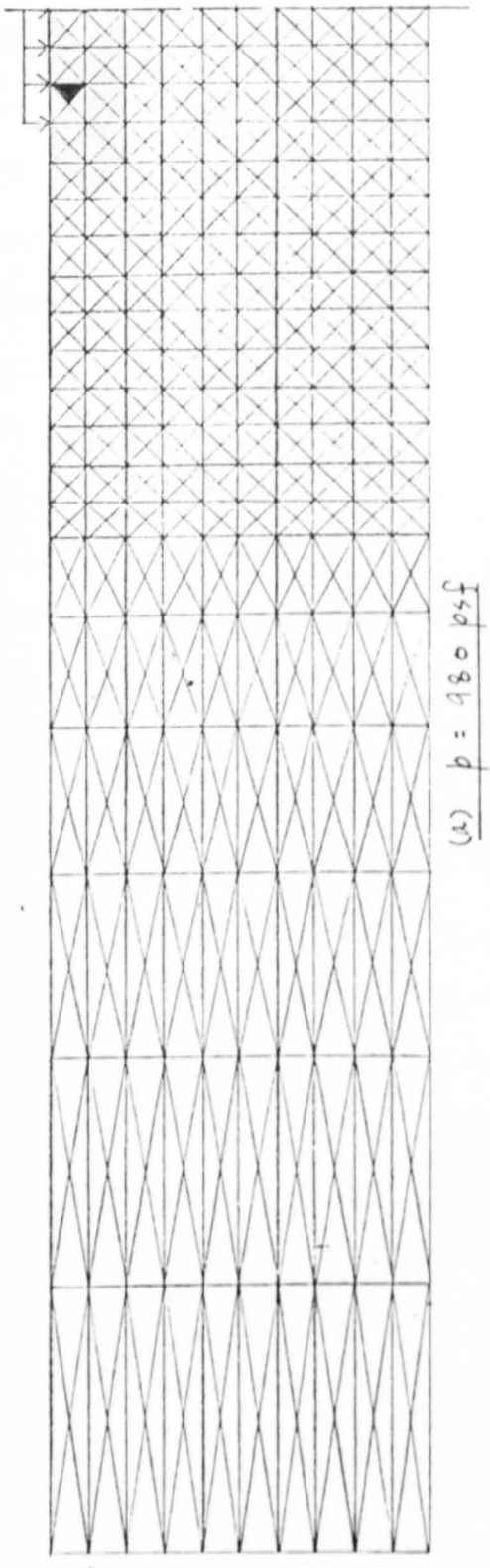

(a) $f_{sp} = 1380\ psf$

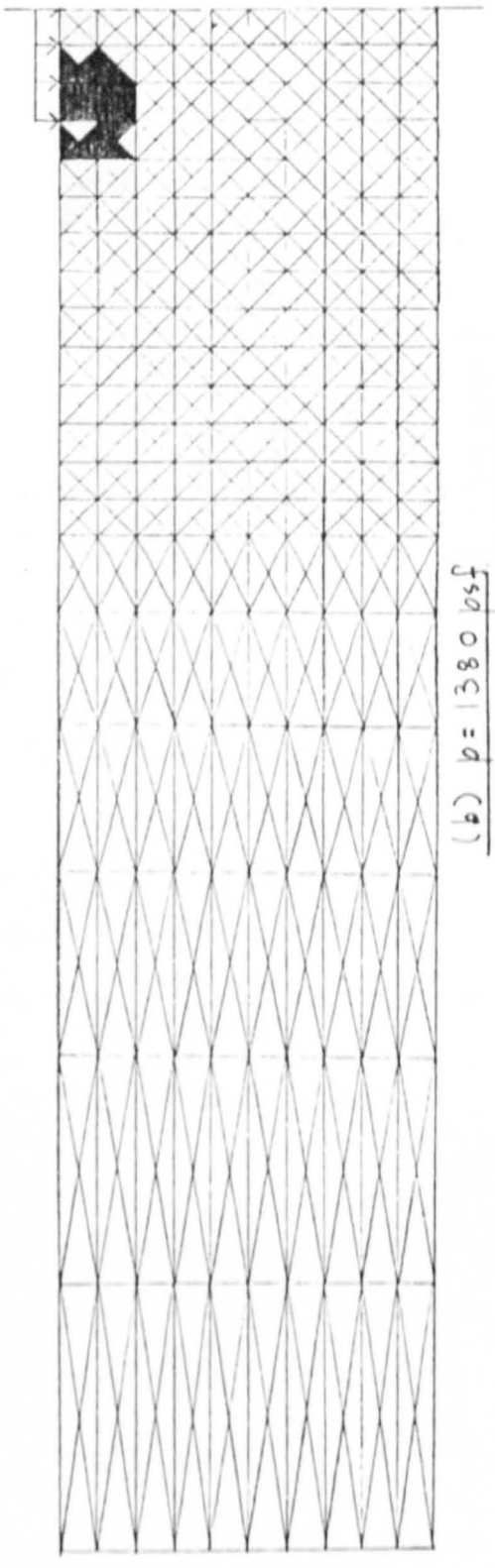

(b) $f_{sp} = 1980\ psf$

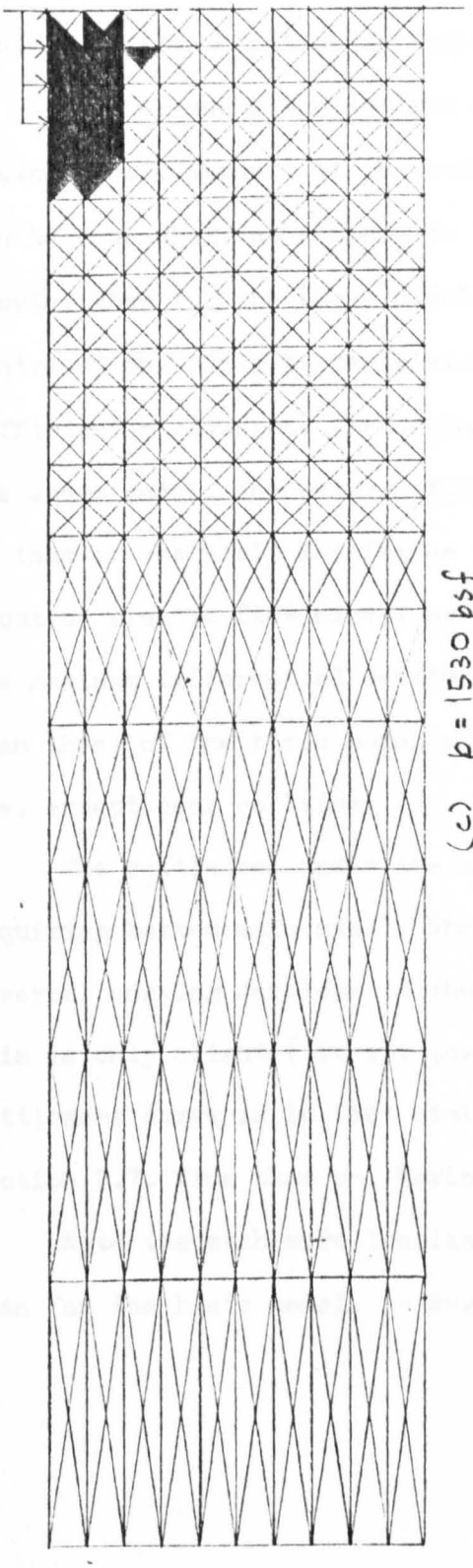

(c) $p = 1530$ psf

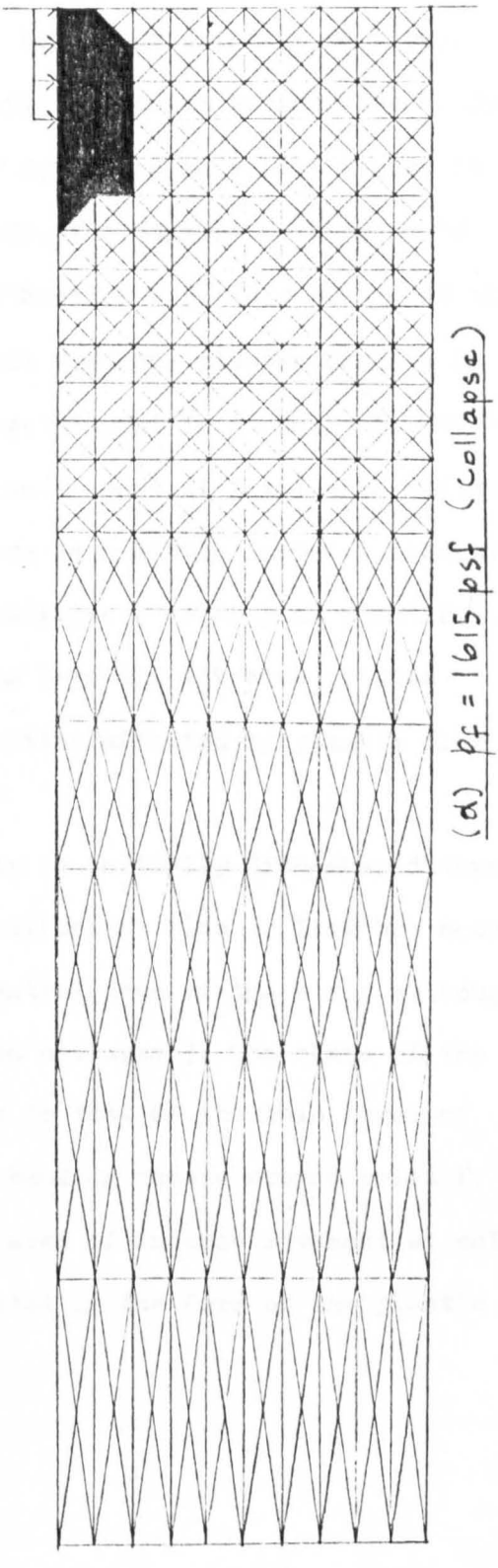

(d) $p_f = 1615$ psf (collapse)

Fig. 59. Growth of the plastic enclave to collapse

Fig. 60 shows the settlement-load and settlement-iteration curves for joint A, pin-pointing collapse. Note the former curve exhibits little local shear failure behaviour prior to collapse.

Fig. 62 shows the surface displacements at various loads. By taking proper account of the softer upper region of the layer, it can be seen that, at comparable loads, the maximum settlement is greater than for the basic model of Section 2.6. This occurs at the centre of the strip to begin with but when the plastic enclave is sufficiently advanced, the maximum settlement is at point P, unlike the above model. The nature of the settlement of joint A is reflected in that of the strip insofar as there is a little increase brought about by plastic flow except near collapse (notably at point P). The maximum differential settlements here are likewise greater than those of the basic model and little affected by plastic flow - i.e. except near collapse.

The settlement under the strip is initially dish-shaped thus requiring bottom main steel. When sufficient plastic flow has occured, however, hogging develops in the central area of the strip although this is only slight (except towards collapse). The shape of the settlement curve is in fact similar to that of the thin layer of Section 2.7. from then on. Maximum bending occurs around point P.

Note the much more localised area of intense movement at collapse than for the basic model, as suggested by the form of the plastic enclave

of Fig. 59 - see also the horizontal surface displacements. Otherwise, the surface displacements show a similar behaviour to those of the basic model.

It is clearly shown here that the lateral extent of the above area approximates the point of penetration to free surface of the plastic enclave (cf. Fig. 59), i.e., where the "bump" in the heave for the final settlement curve begins, left of which there is no further heave with iteration.

The displacements obtained here readily fit into a Hill type of collapse mechanism as suggested earlier.

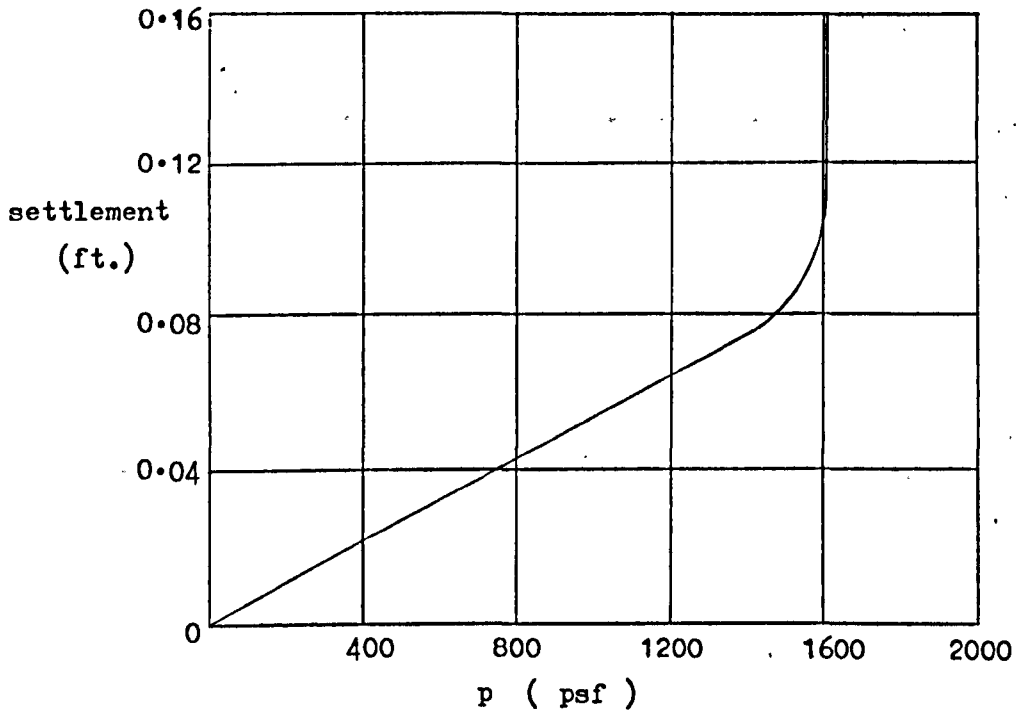

(a) Settlement-load plot

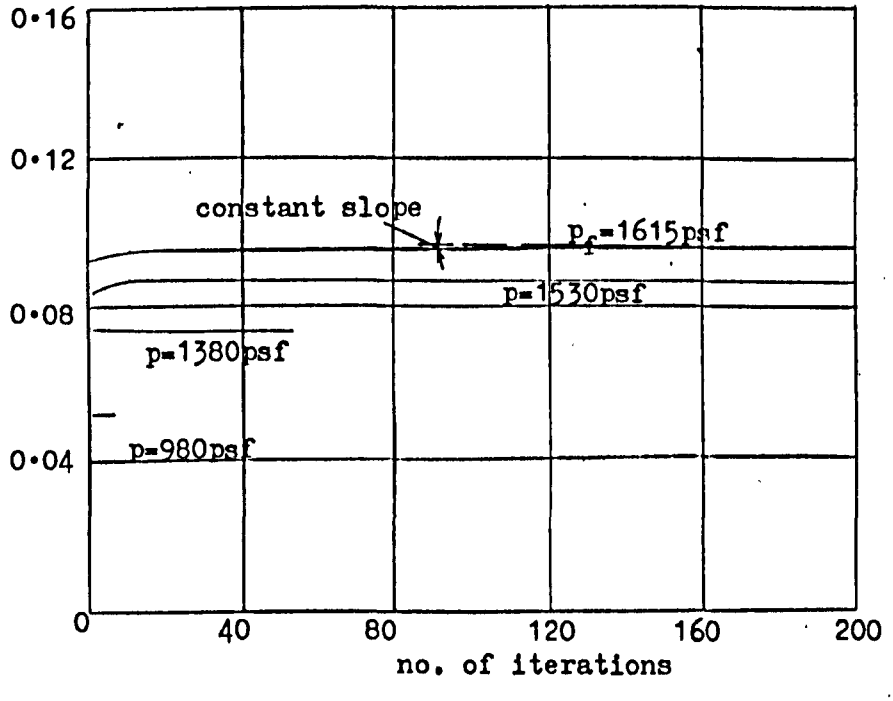

(b) Settlement-iteration plots

Fig. 60. Settlement curves for joint A

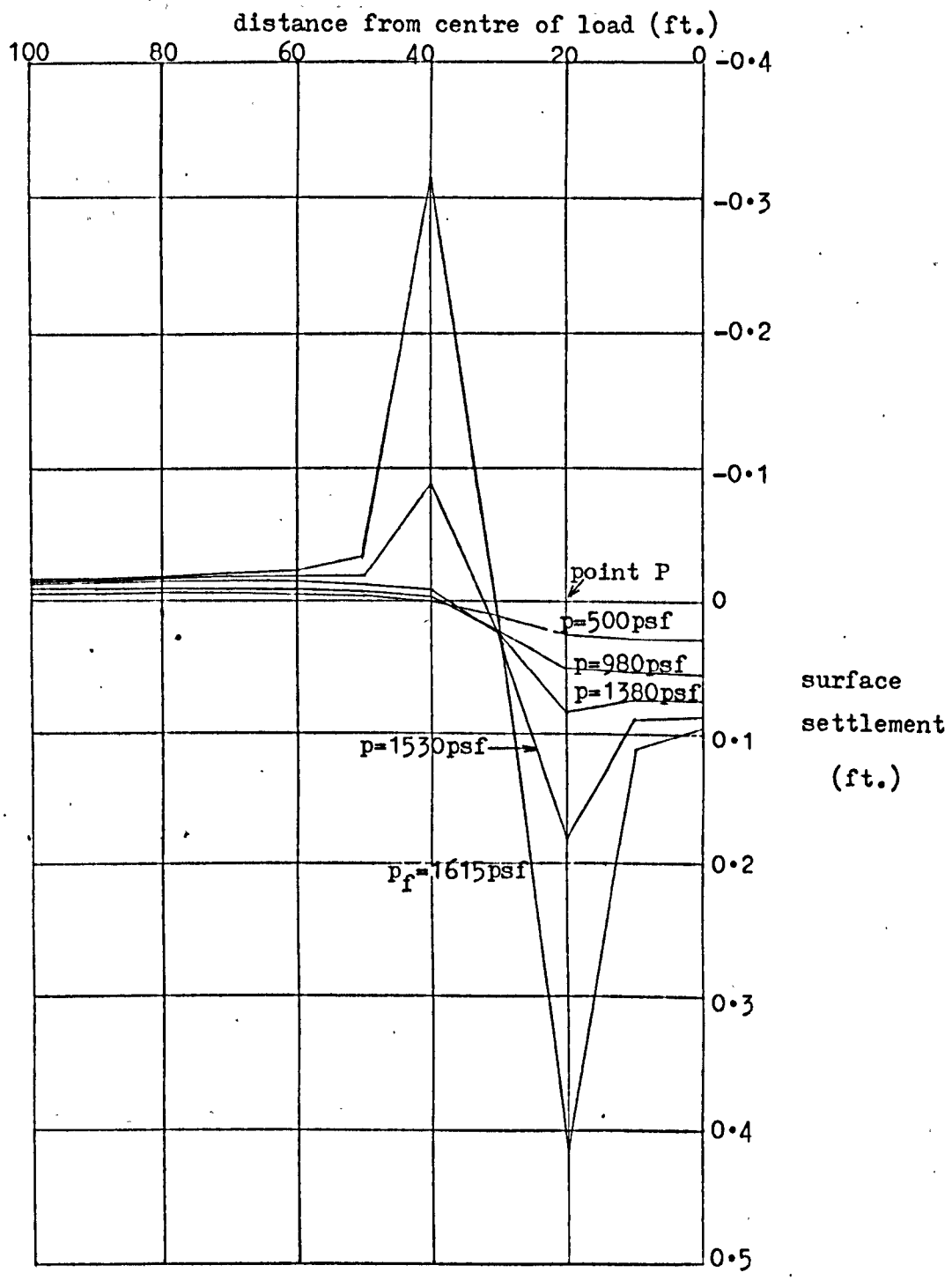
distance from centre of load (ft.)
100
80
60
40
20
0
-0·4
-0·3
-0·2
-0·1
0
0·1
0·2
0·3
0·4
0·5
point P
p=500psf
p=980psf
p=1380psf
p=1530psf
p_f=1615psf
surface
settlement
(ft.)

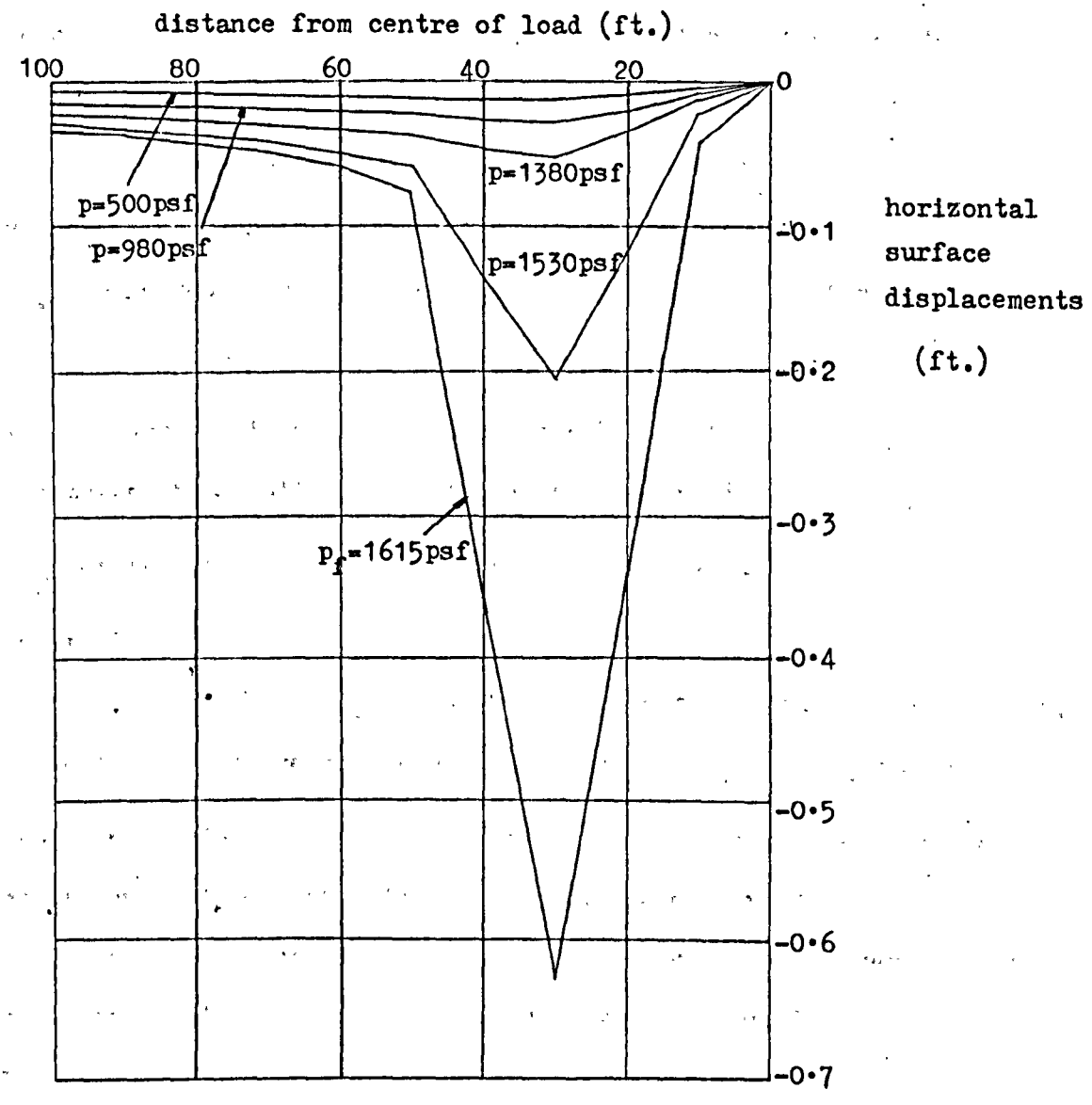

Fig. 62. Surface displacements

Fig. 63 shows the normal stress distributions down the centre and edge of the strip load. For σ_x , there is a general increase in value in the softer upper region of the layer from that of the basic model, down both centre and edge, the difference being accentuated by increasing plastic flow. In the harder lower region, however, σ_x decreases down both centre and edge. For σ_y , the same type of changes occur down the centre but, down the edge, there is an overall increase in stress, that in the harder lower region being accentuated by plastic flow. Otherwise, the trends of the σ_x and σ_y distributions are similar to those of the basic model at comparable loads.

Again, $\sigma_z \doteq 0{\cdot}5(\sigma_x + \sigma_y)$ according to the computations and thus, as usual, the average of the above changes in σ_x and σ_y provides a good indication of the changes in pore pressures arising from the assumption of linear variation of rigidity and strength (i.e. effectively softening the upper half and hardening the lower half of the basic model). Accordingly, we may expect generally higher pore pressures down the centre of the strip in the softer upper region of the layer, accentuated by plastic flow; in the harder lower region on the other hand, there will generally be some decrease in pore pressure from that of the basic model. Down the edge, similar changes in pore pressure to those down the centre of the strip may be expected in the upper region of the layer. Towards the bottom, however, although

a decrease in pore pressure also occurs to begin with, it becomes hardly noticeable with plastic flow.

Constant stress conditions are obtained at collapse as usual.

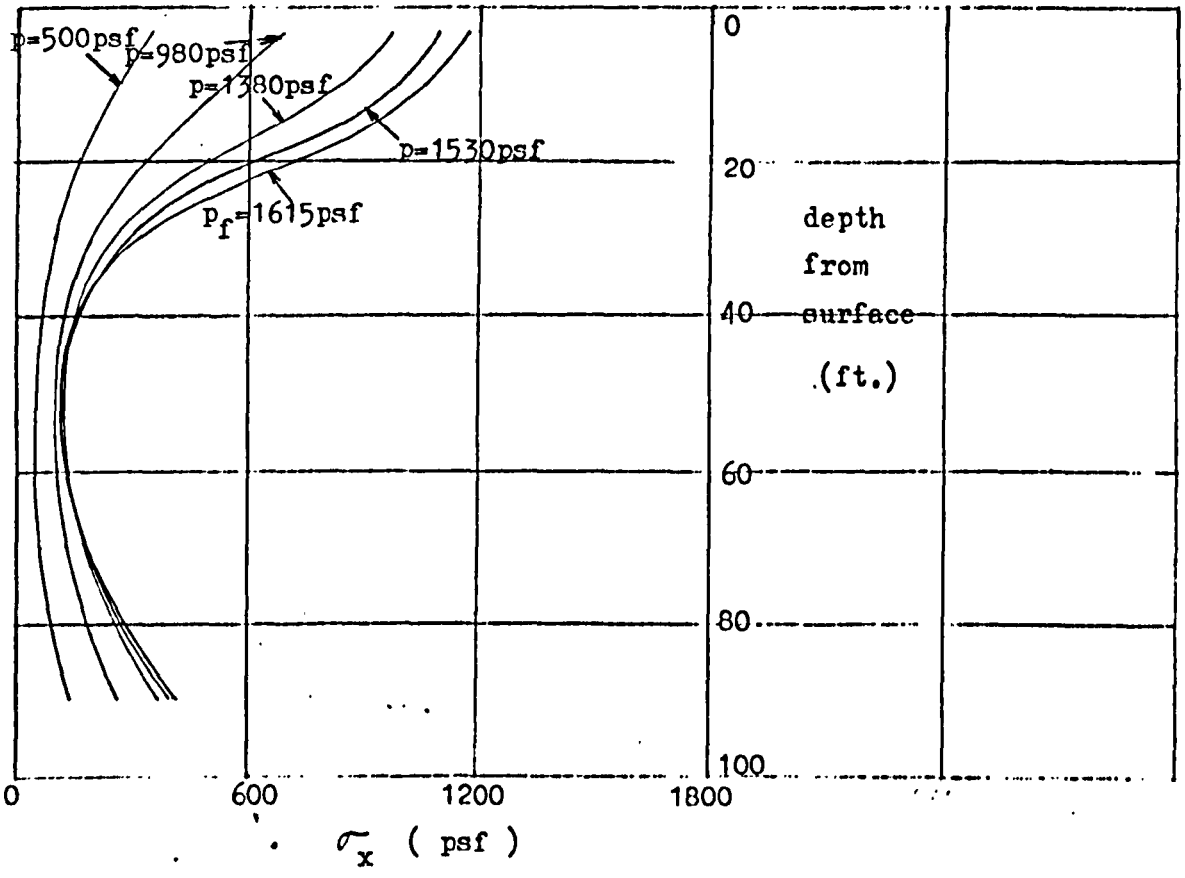

(a) σ_x distributions down centre of strip load

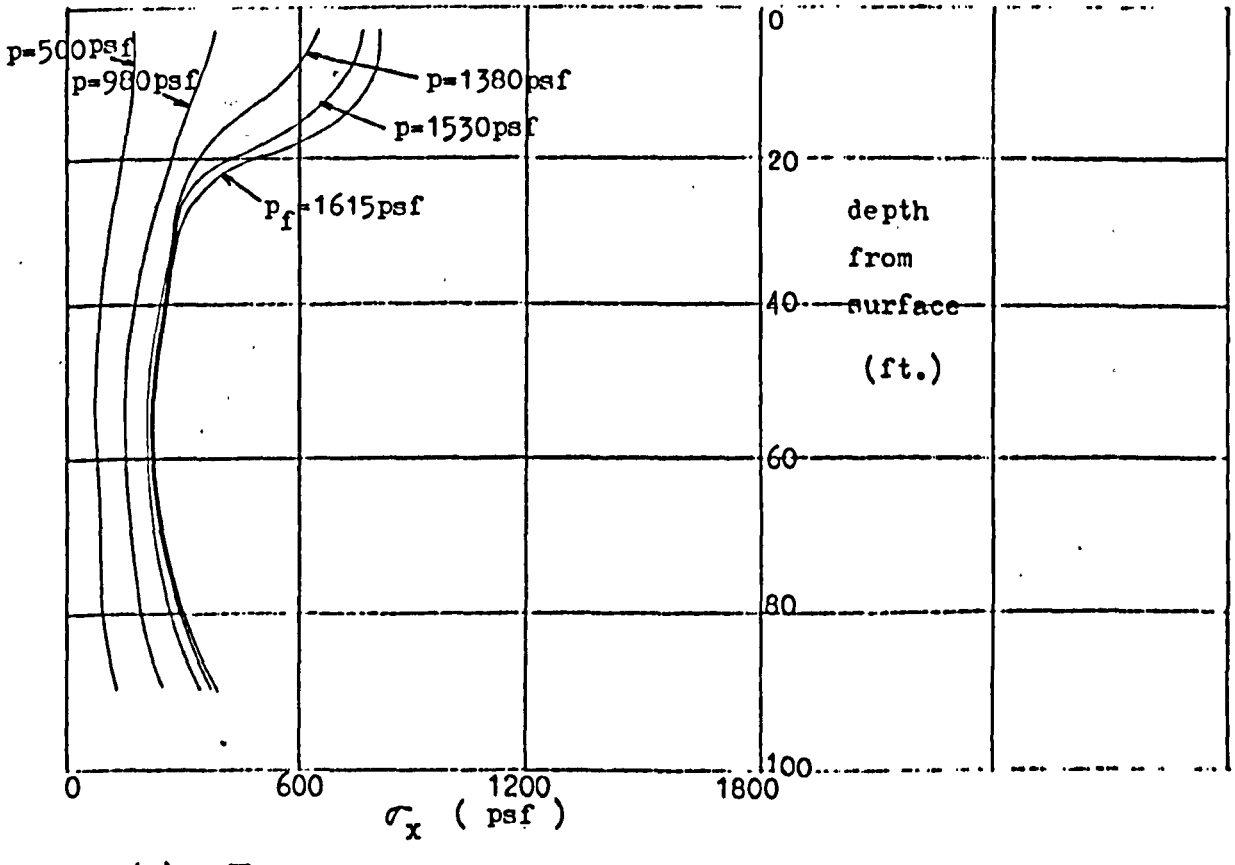

(b) σ_x distributions down edge of strip load

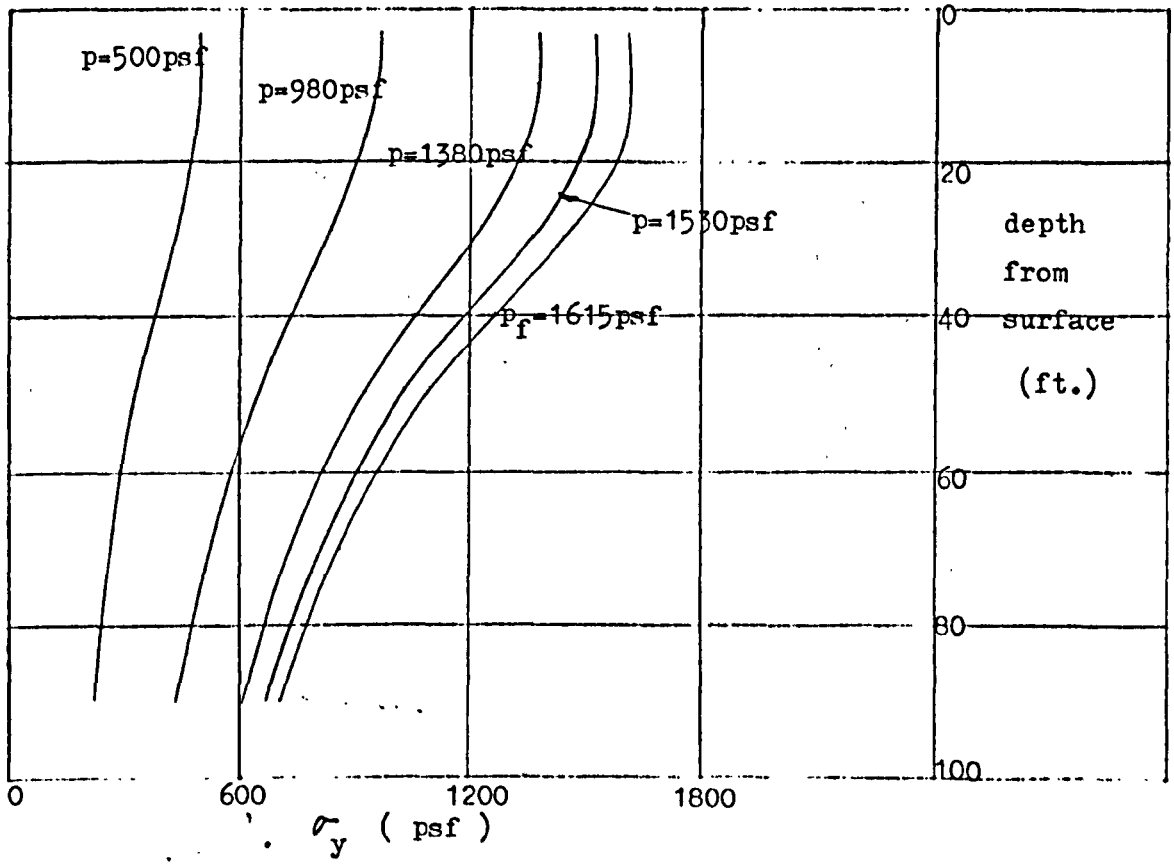

(c) σ_y distributions down centre of strip load

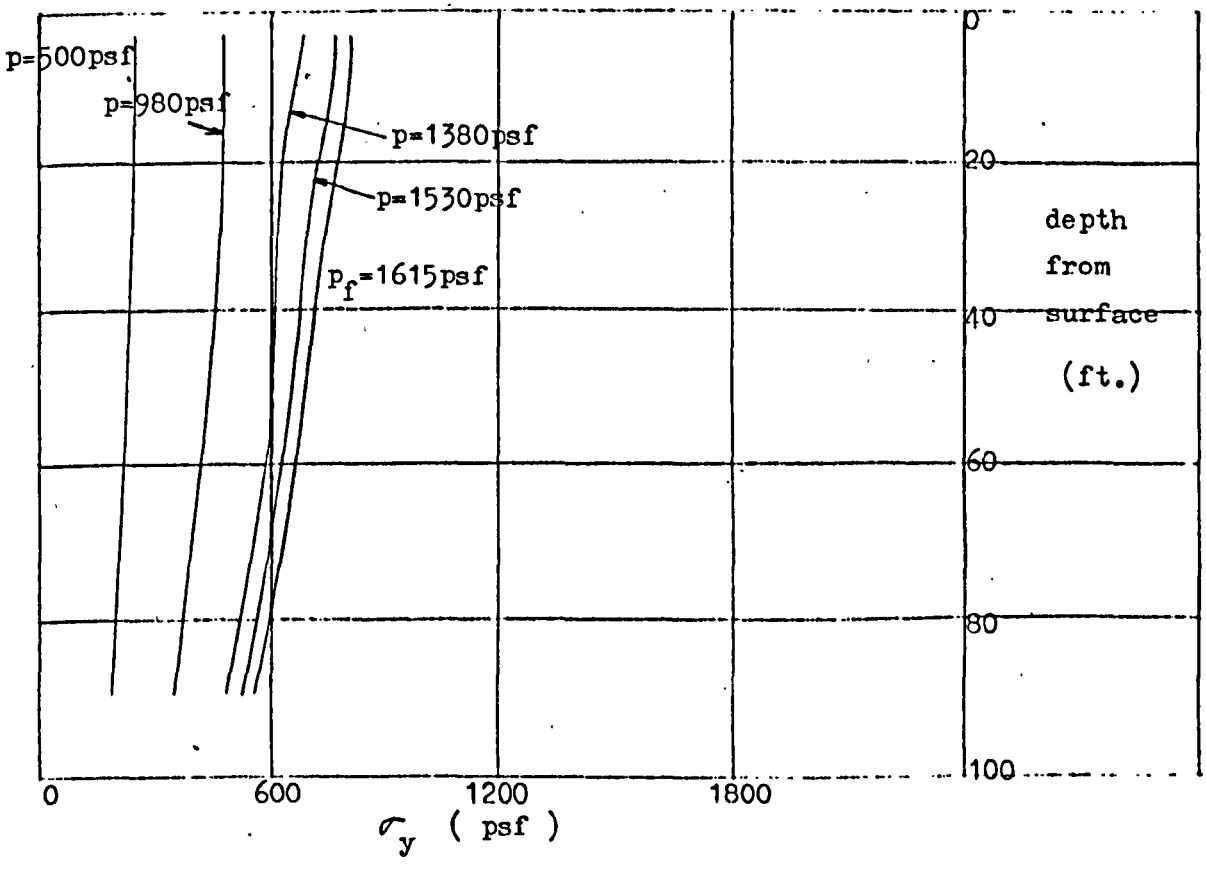

(d) σ_y distributions down edge of strip load

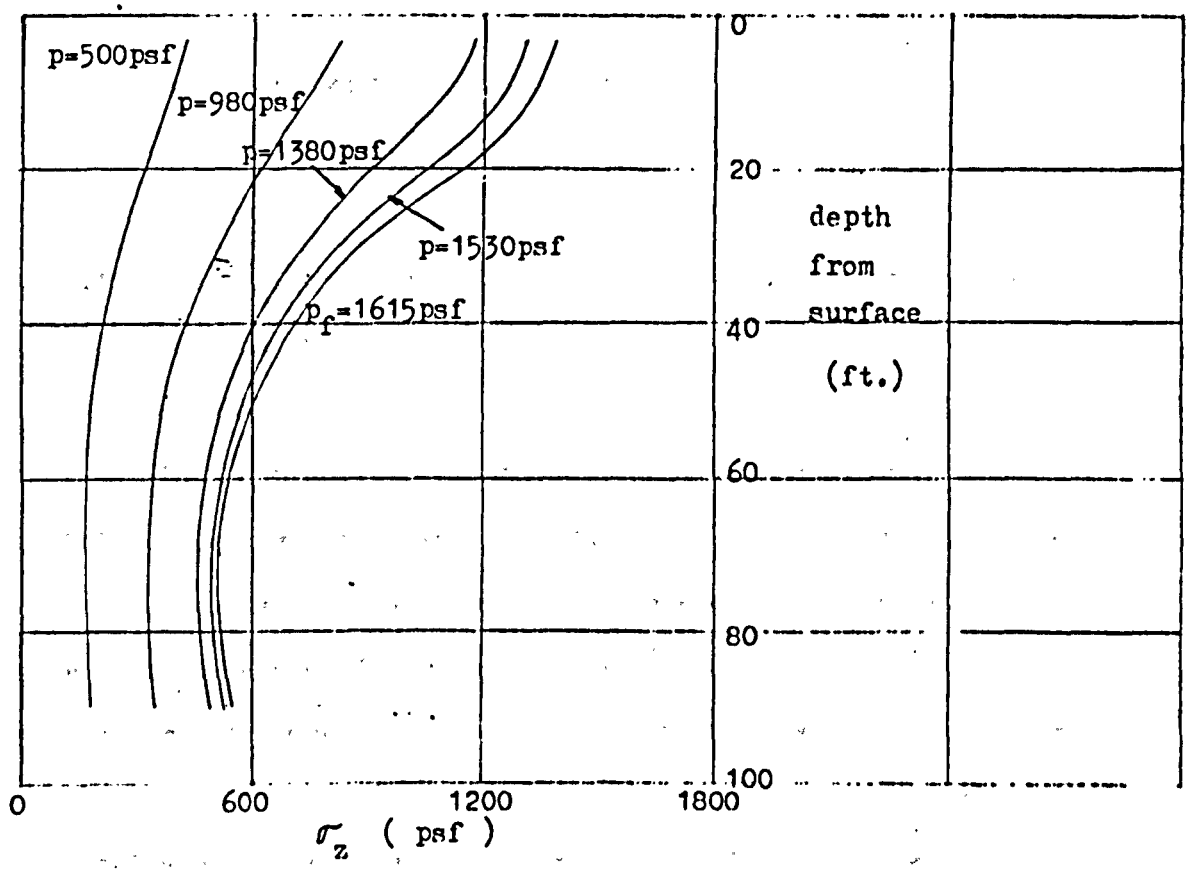

(e) σ_z distributions down centre of strip load

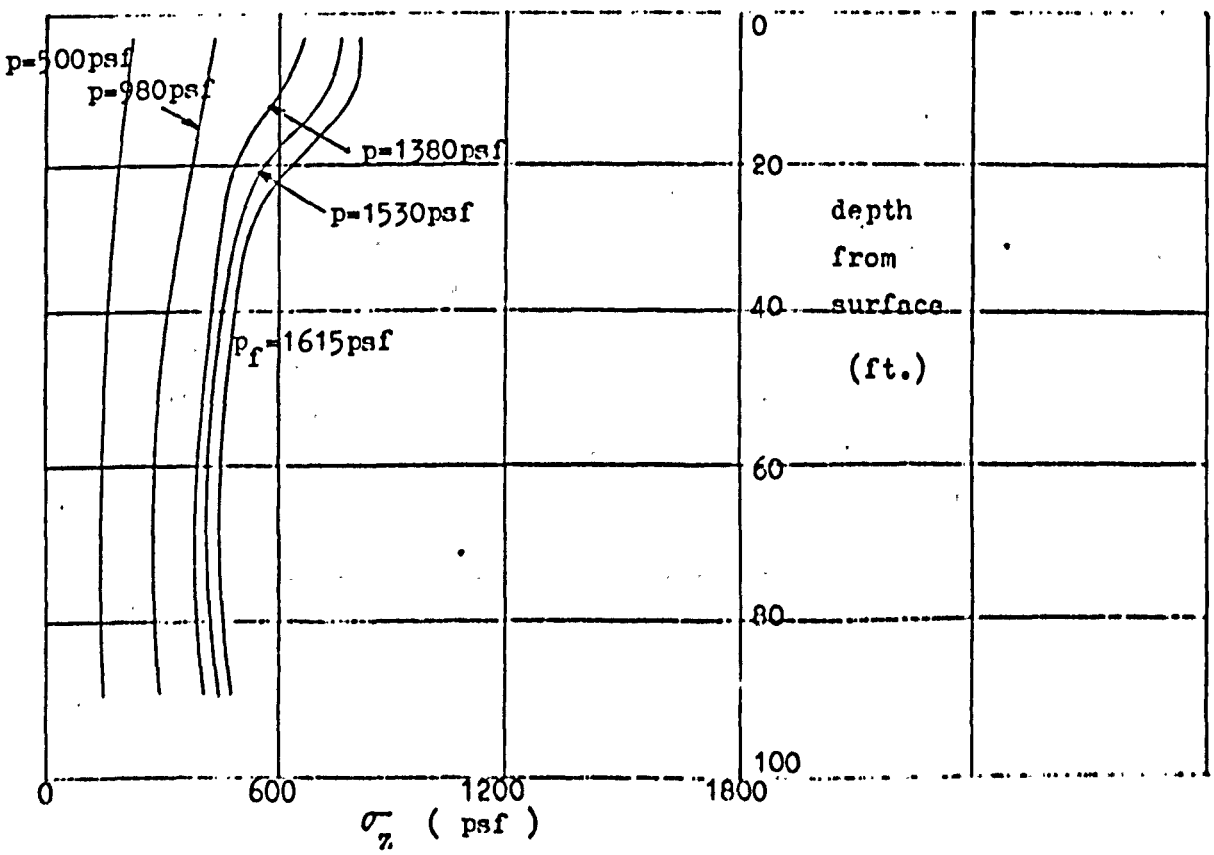

(f) σ_z distributions down edge of strip load

Fig. 63. Normal stress distributions down centre and edge of strip load

PART D - SUGGESTED ELASTOPLASTIC MODELS FOR FURTHER STUDIES

2.11. The effect of a stiff crust at the surface of the layer (flow chart in Section 1.3.3.5.)

In the practical example of Fig. 22, the ground water level falls slightly with time, say. Due to subsequent drying, the soil between the surface and the ground water level overconsolidates, resulting in a stiff crust there with approximately uniform rigidity and strength equal to that at ground water level. Fig. 64 shows the idealisation adopted for studying the effect of the crust on the results of the previous model - which is for ground water level at the surface (i.e. normally consolidated). The idealisation is similar to the one given by Duncan and Dunlop (33).

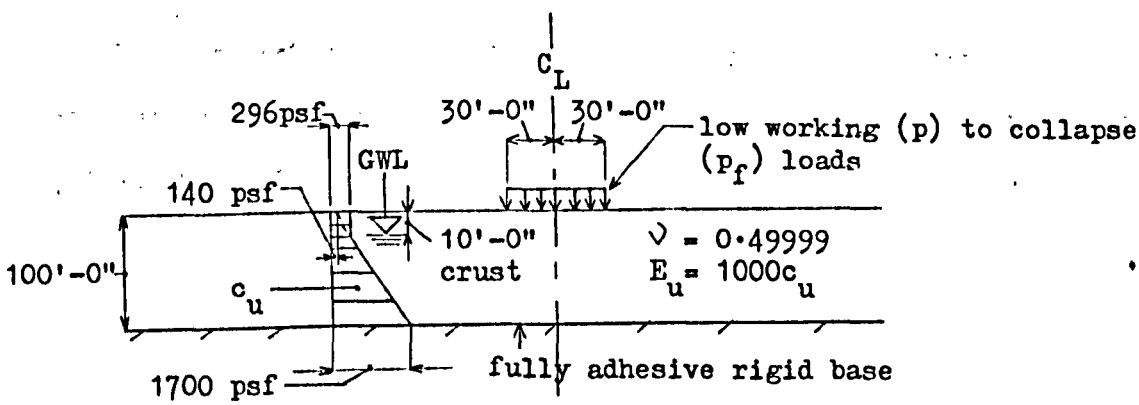

Fig. 64. Idealisation to account for stiff crust at surface of layer of Fig. 22 (Tresca yield criterion and associated flow rule)

Fig. 65 shows the growth of the plastic enclave with increasing load p. First yield occurs in the crust where the material is weakest. The load at first yield is greater than that for the previous model (Section 2.10.) as would be expected since the crust is stronger than the corresponding layer of material of that model. As with the previous model, the subsequent growth of the plastic enclave is confined to the weaker upper region of the layer, collapse occurring when sufficient width of surface clear of the strip (i.e. "free") has yielded. The collapse load of the present model is, however, higher than that of the previous one. This is to be expected since the former is relatively stronger due to the formation of the crust. The higher loads that are sustained here also leads to a greater extent of the plastic enclave than in Section 2.10. although, as with the previous model (and for similar reasons), a Hill-type collapse mechanism that is more localised around the strip than for the basic model is apparent here. The computed collapse load is 1945 psf, some 20% higher than for the previous normally consolidated layer.

The surface displacements as well as the normal stress distributions down the centre and edge of the strip load are presented in Figs. 66 to 68 for examination.

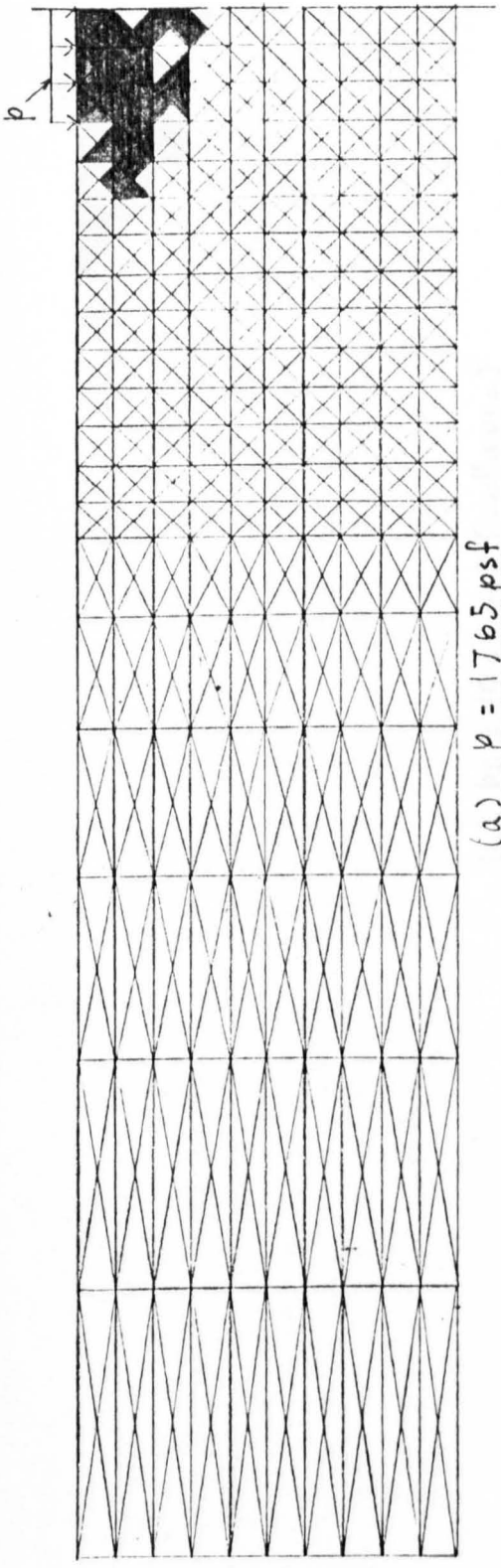

(a) $p = 1765$ psf

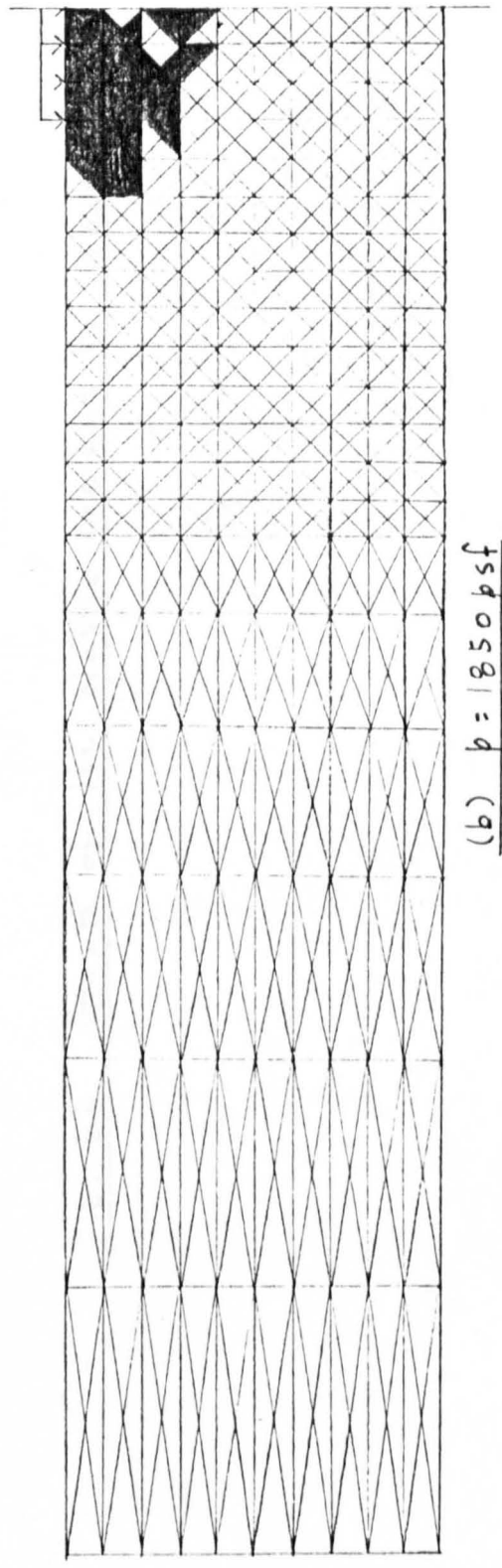

(b) $p = 1850$ psf

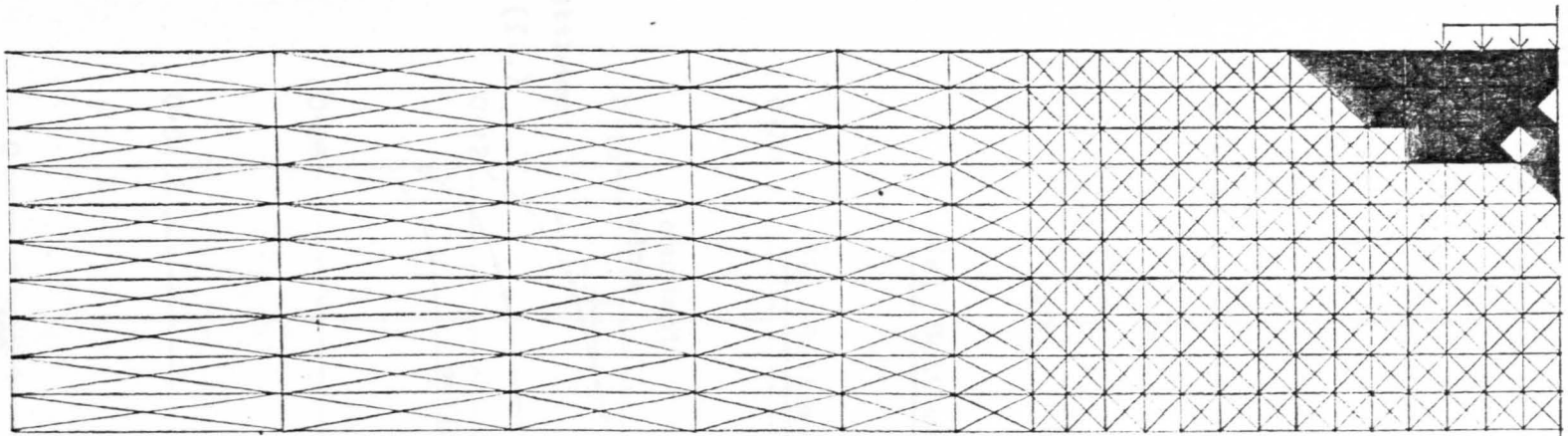

(c) p_f = 1945 psf (collapse)

Fig. 65. Growth of the plastic enclave to collapse

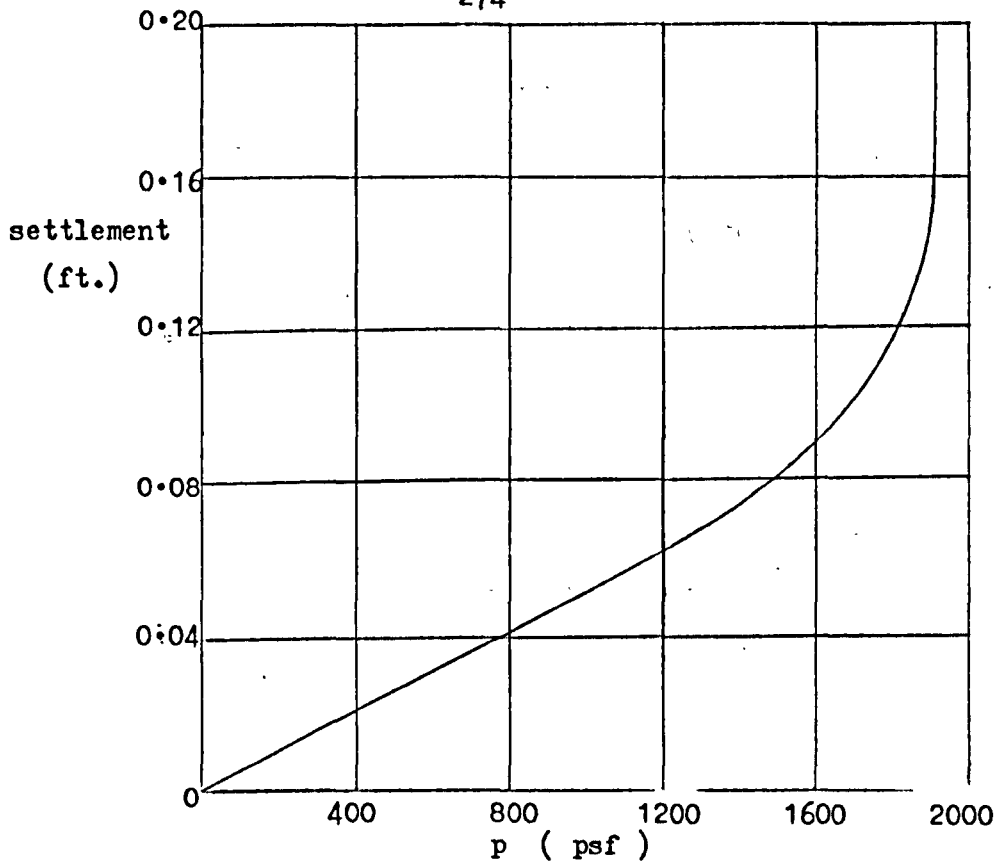

(a) Settlement-load plot

(b) Settlement-iteration plots

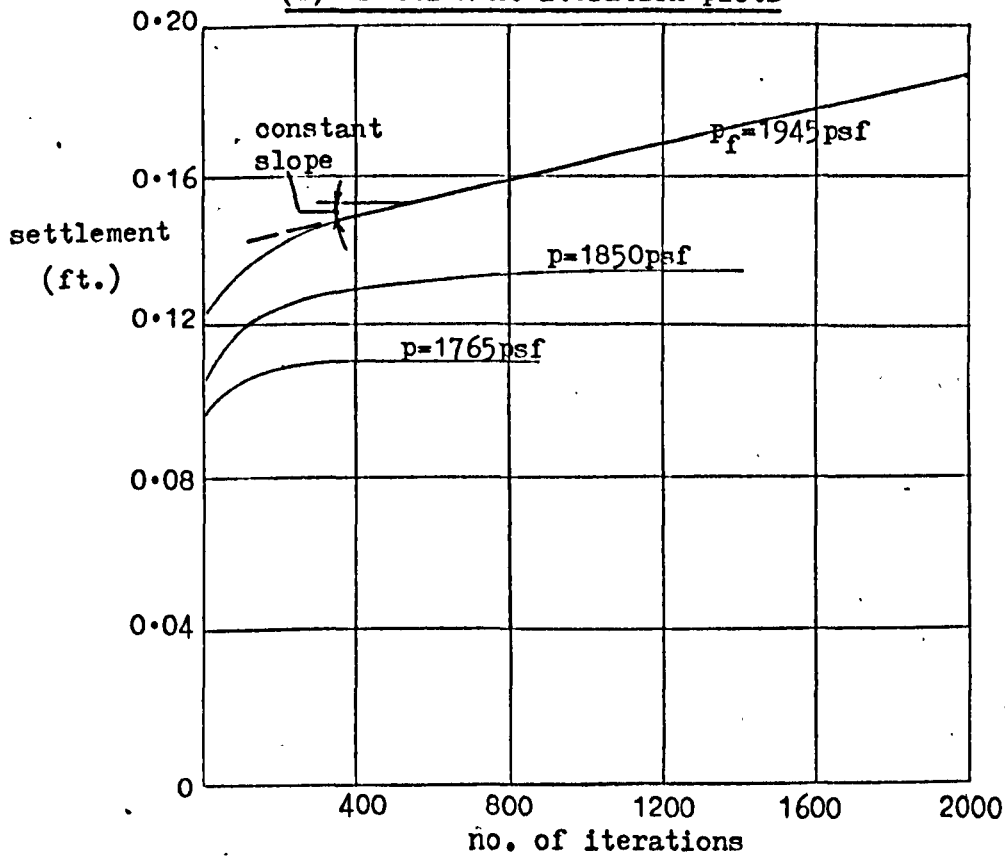

Fig. 66. Settlement curves for joint A

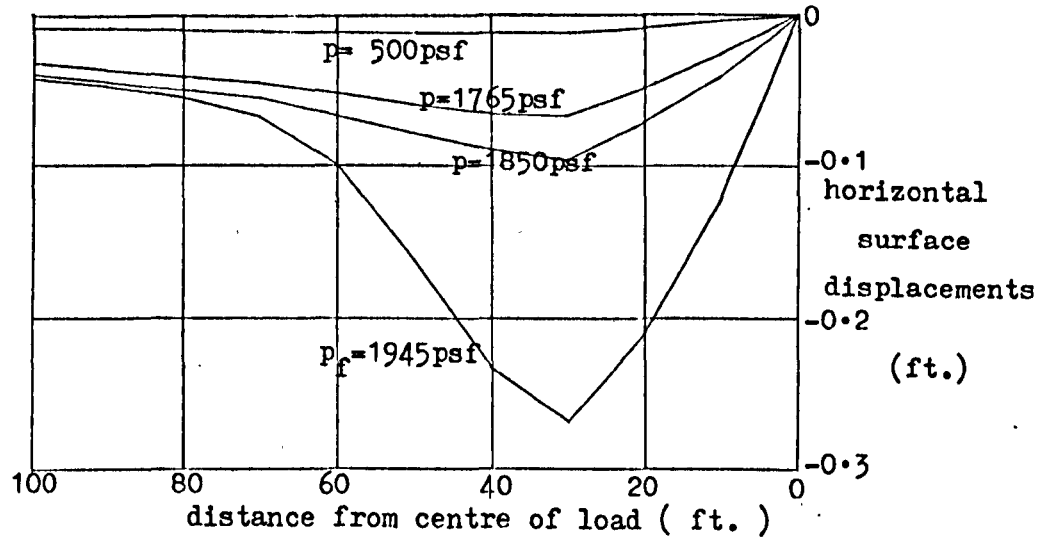

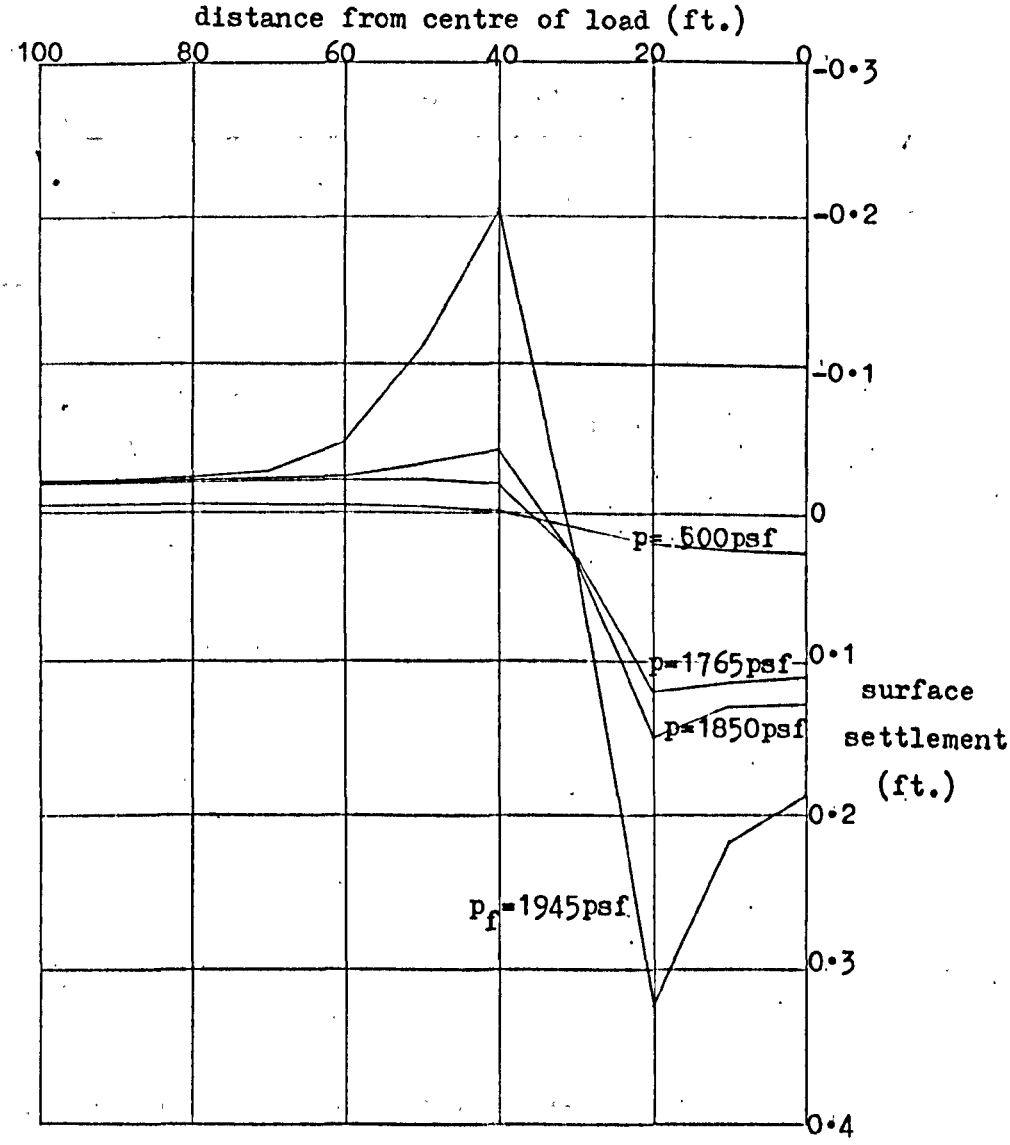

Fig. 67. Surface displacements

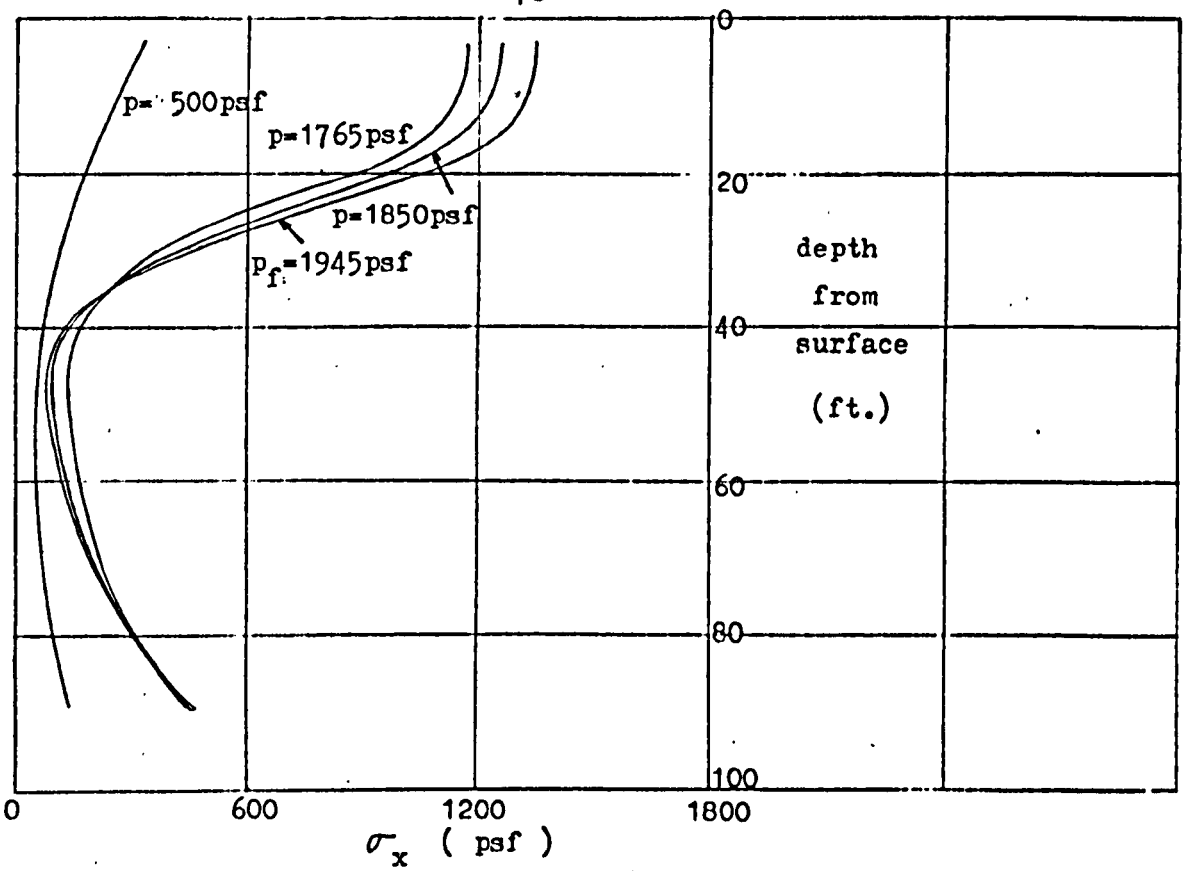

(1a) σ_x distributions down centre of strip load

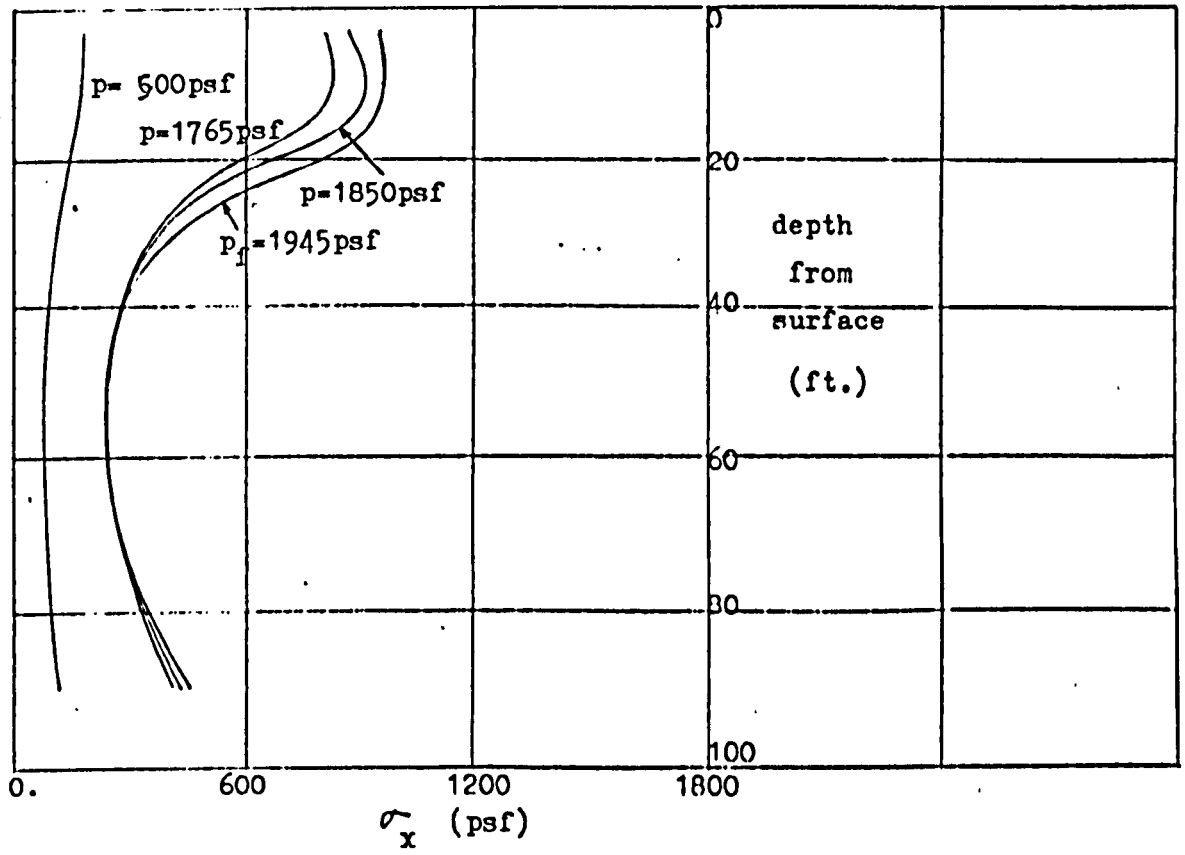

(1b) σ_x distributions down edge of strip load

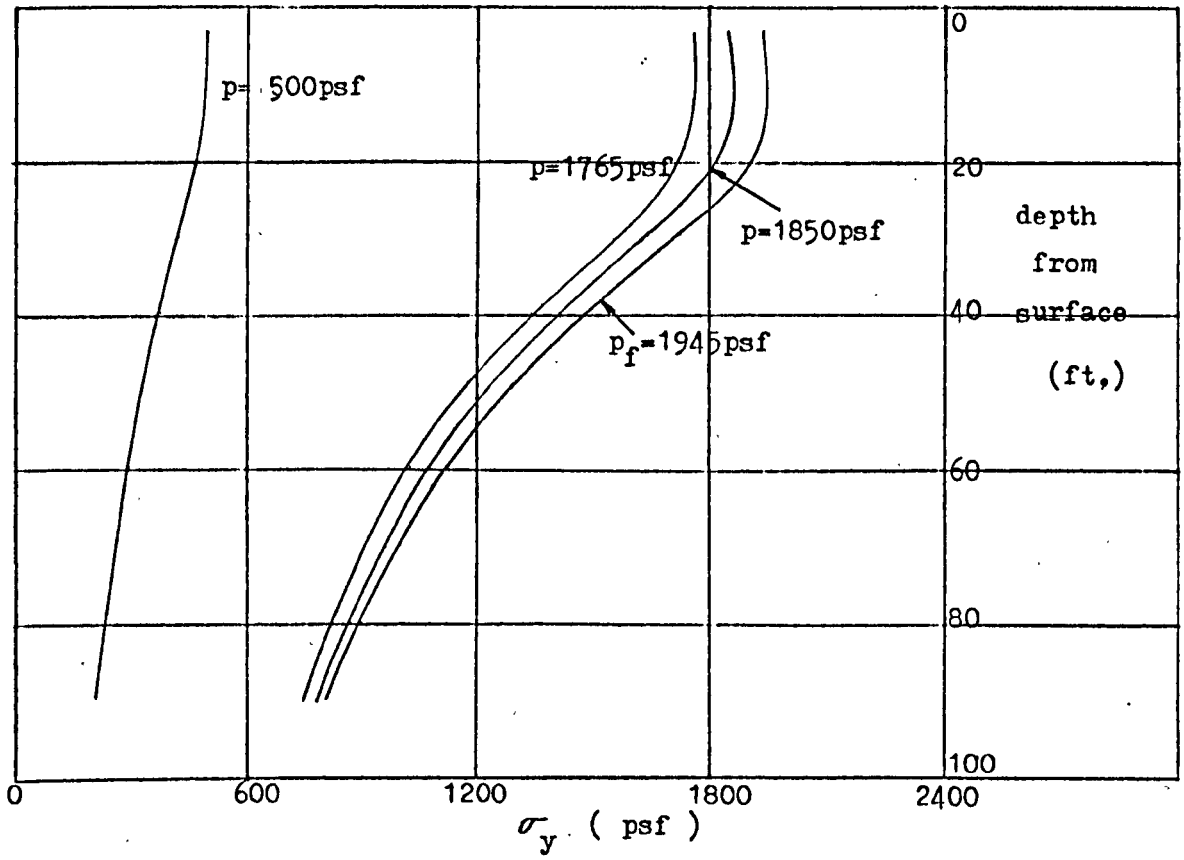

(2a) σ_y distributions down centre of strip load

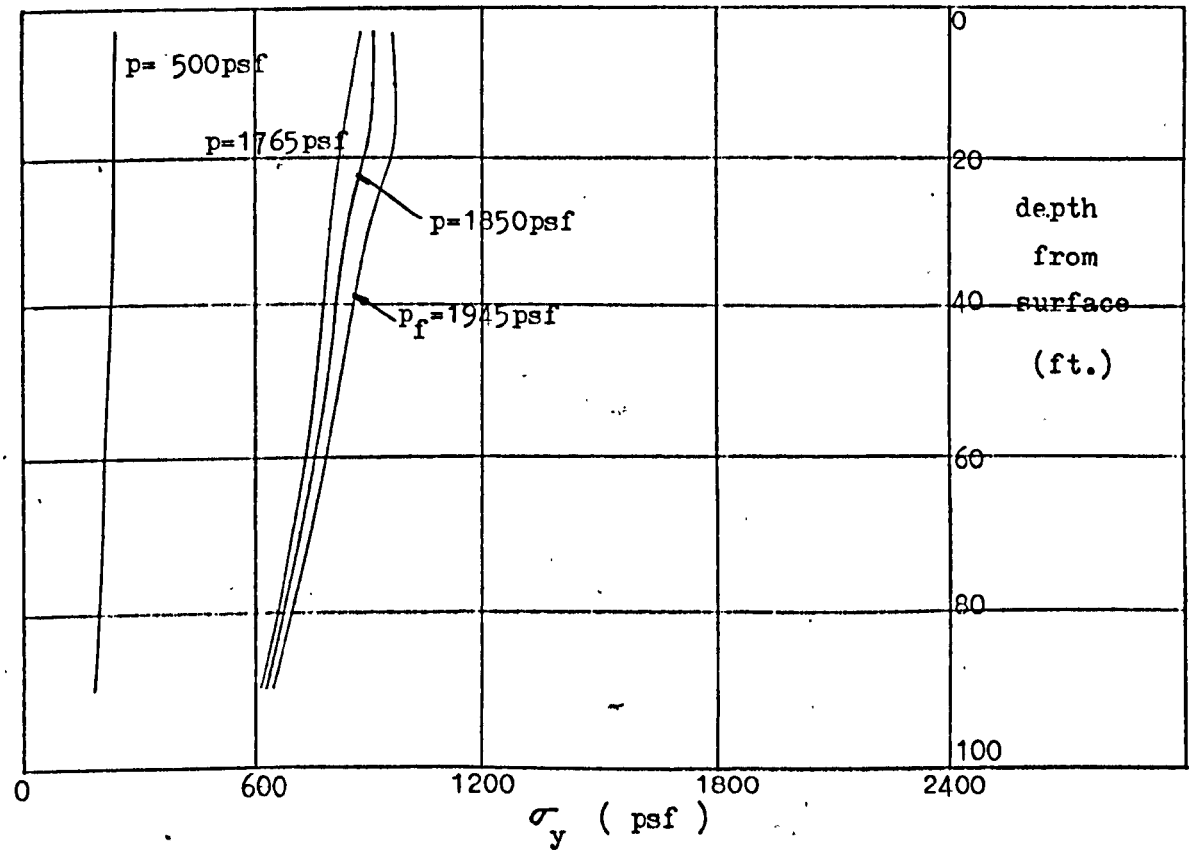

(2b) σ_y distributions down edge of strip load

PAGE

NUMBERING

AS ORIGINAL

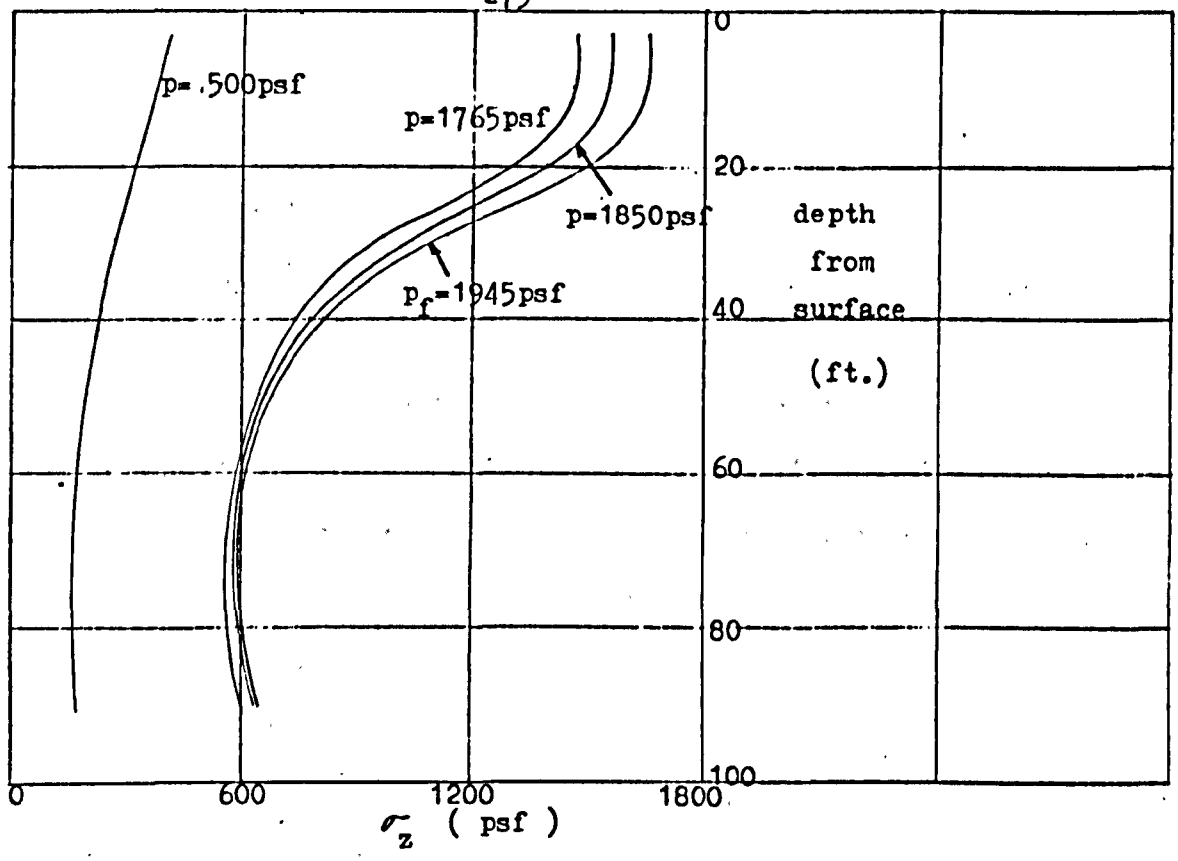

(3a) σ_z distributions down centre of strip load

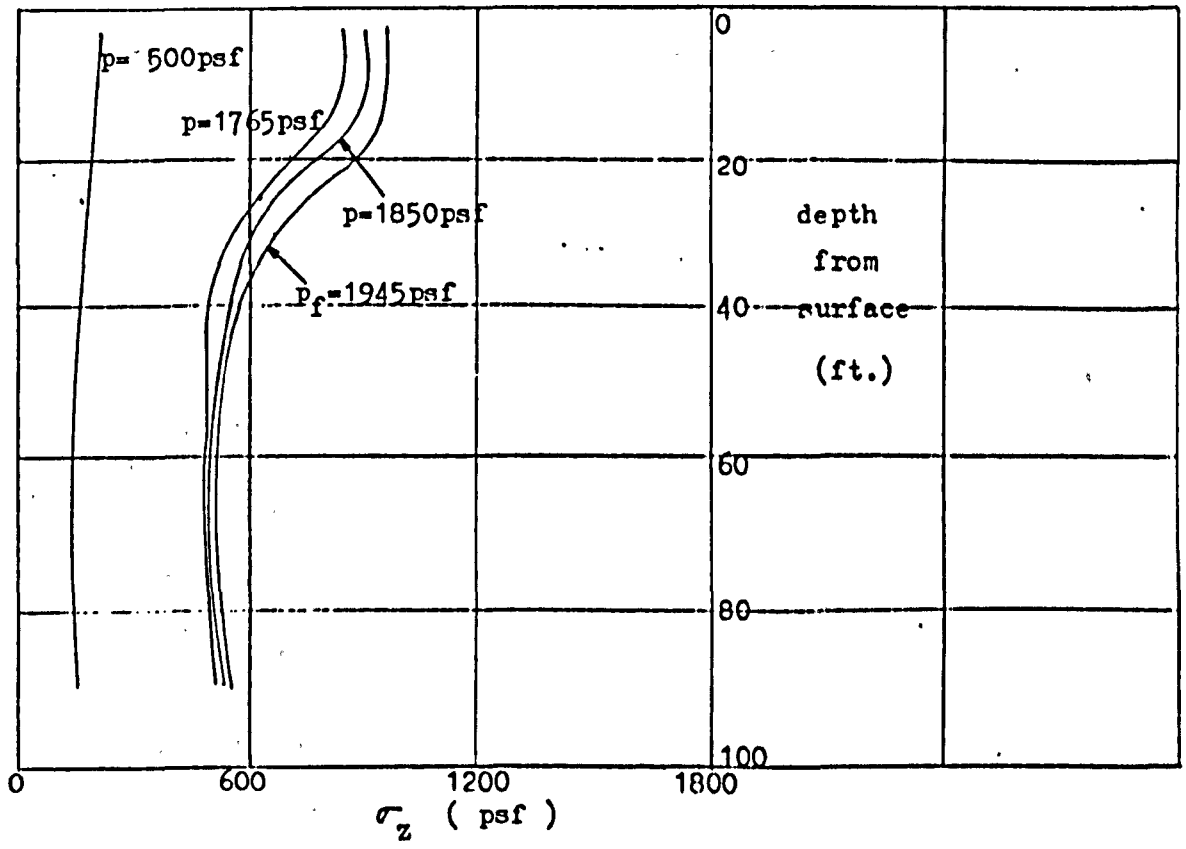

(3b) σ_z distributions down edge of strip load

Fig. 68. Normal stress distributions down centre and edge of strip load

2.12. The effect of an underlying soft layer (flow chart in Section 1.3.3.6.)

Assuming that beneath the clay of the practical example of Fig. 22, a softer layer (i.e. with less rigidity and strength) had initially been laid down on the deep rock stratum, we have the basis for yet another parametric study of practical significance.

The idealisation adopted for this problem is shown in Fig. 69 and it can be seen that (a) the overall thickness of the soil layer is the same as before, assuming sedimentation to a constant level, and (b) a linear variation of rigidity and strength is also assumed for the softer material.

The idealisation is based on an example given by Smith (31) and would suit a silt layer underlying the clay.

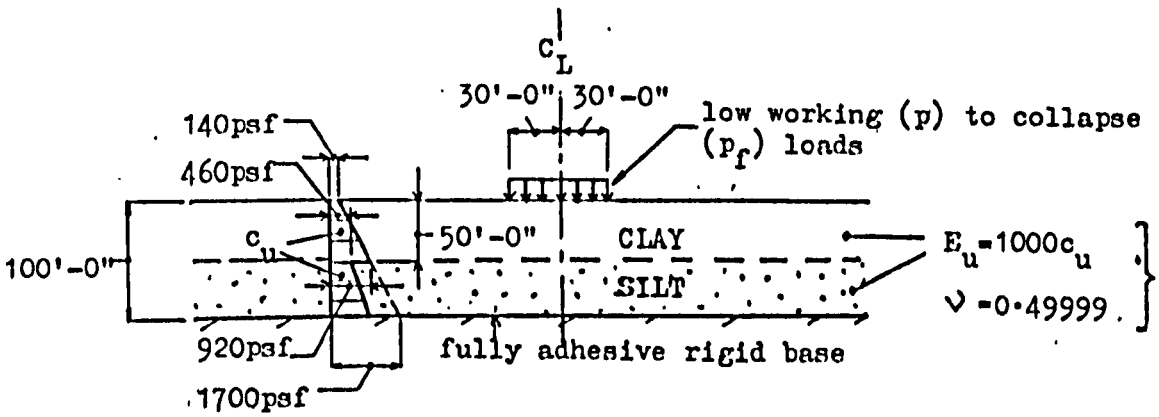

Fig. 69. Idealisation for problem of underlying soft layer (Tresca yield criterion and associated flow rule)

Fig. 70 shows the growth of the plastic enclave with increasing load p. First yield occurs at about the same load in the same surface element as for the model of Section 2.10. Indeed, the replacement of the lower half of that model with the soft layer also leads to little change in the subsequent development of the plastic enclave up to collapse. Thus, the earlier observations (i.e. in Section 2.10.) made on the growth of the plastic enclave - including those on the displacements in the region of collapse - equally apply here. With the same enclave in the same material at collapse, it is to be expected that the computed collapse loads (i.e. 1615 psf) for the present model and that of Section 2.10. are indistinguishable. It has been found, however, that with certain distributions of the material properties in the respective models, their computed collapse loads as well as plastic enclaves can be quite different.

The surface displacements as well as the normal stress distributions down the centre and edge of the strip load are presented in Figs. 71 to 73 for examination.

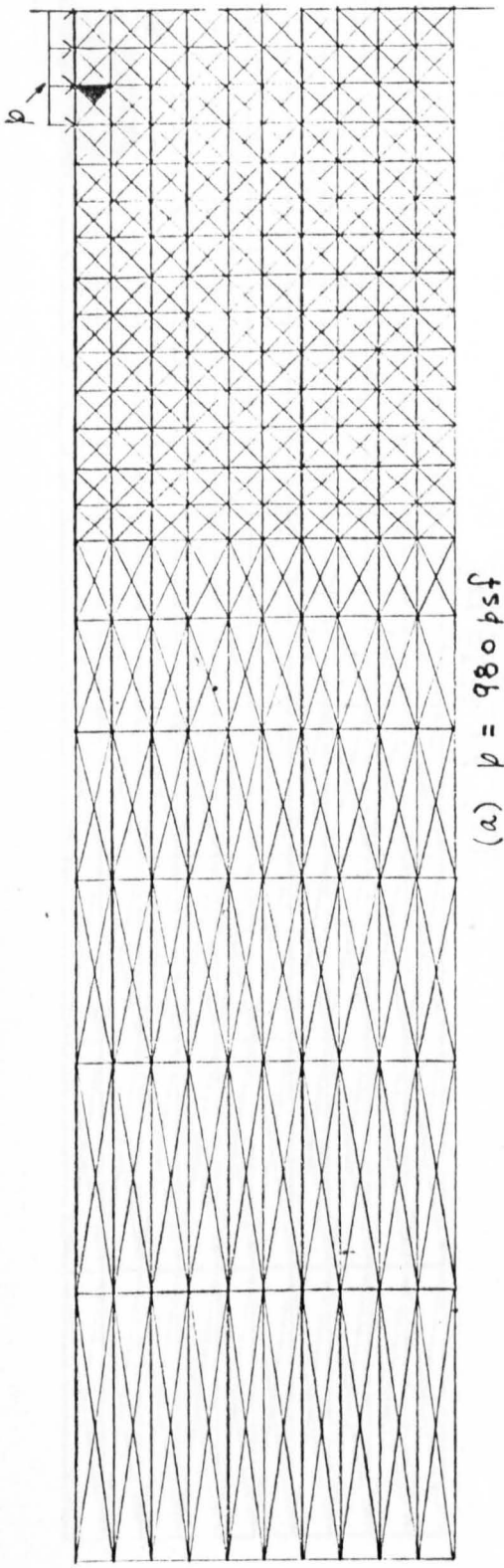

(a) $p = 980$ psf

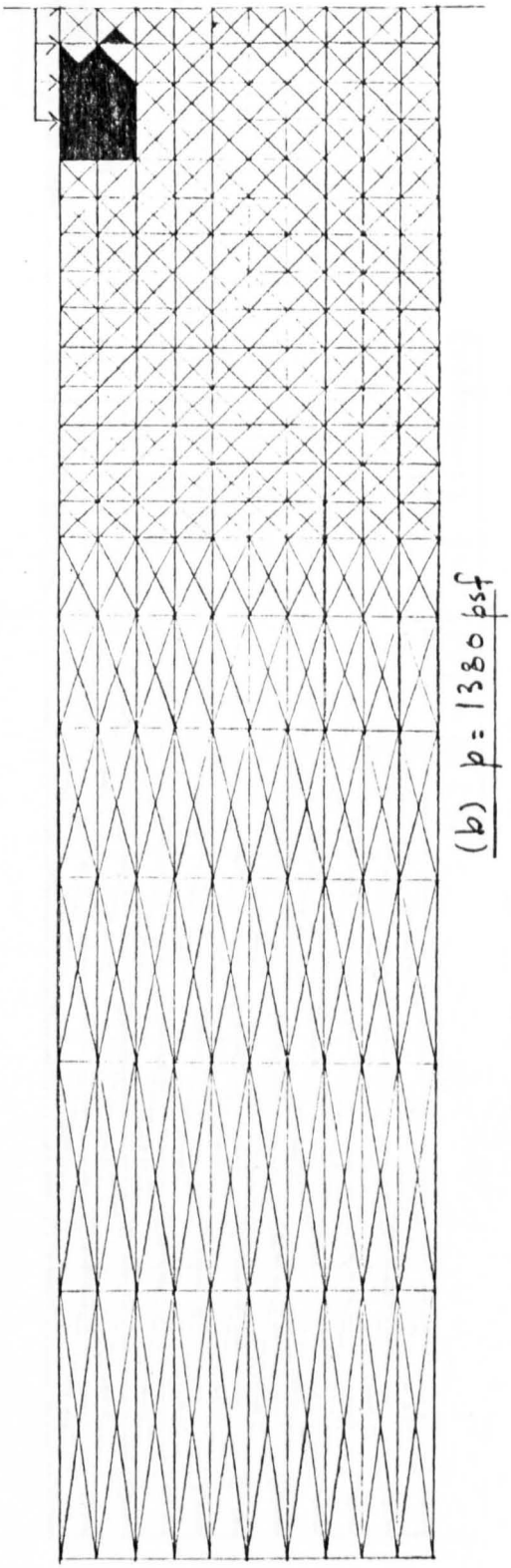

(b) $p = 1380$ psf

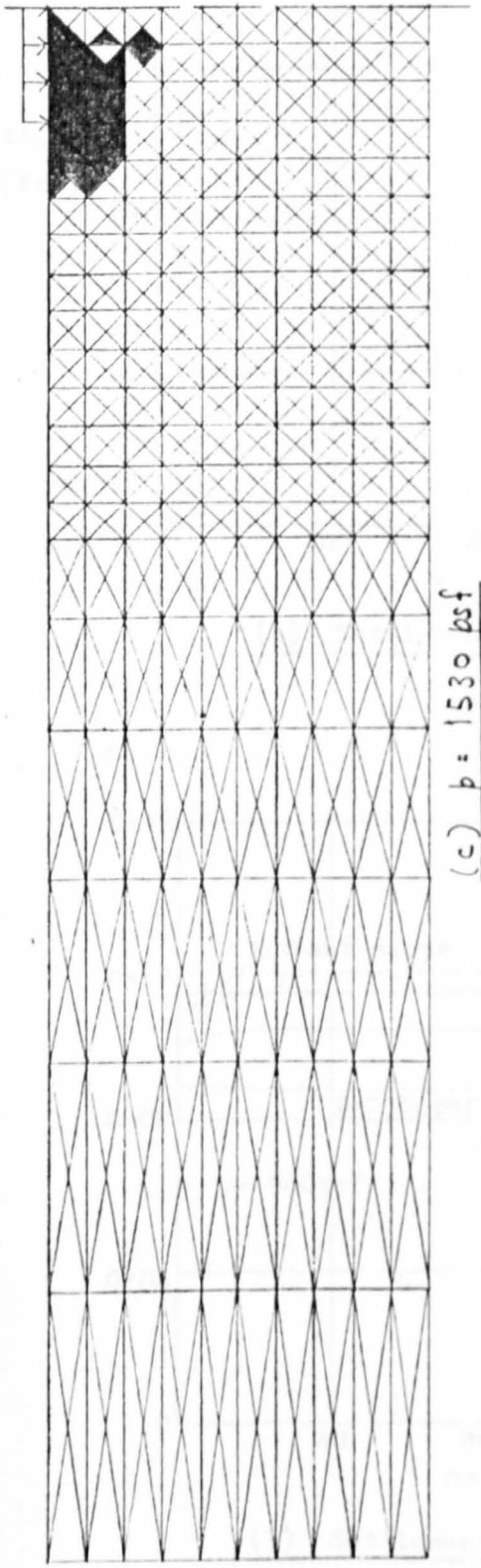

(c) $p = 1530$ psf

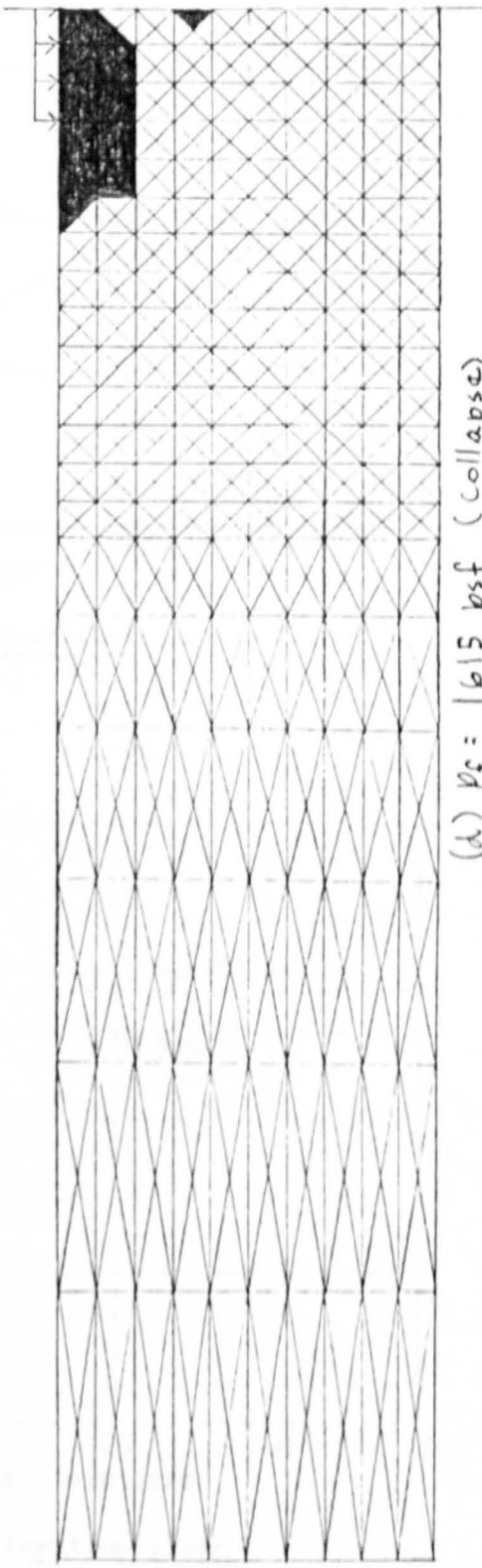

(d) $p_f = 1615$ psf (collapse)

Fig. 70. Growth of the plastic enclave to collapse

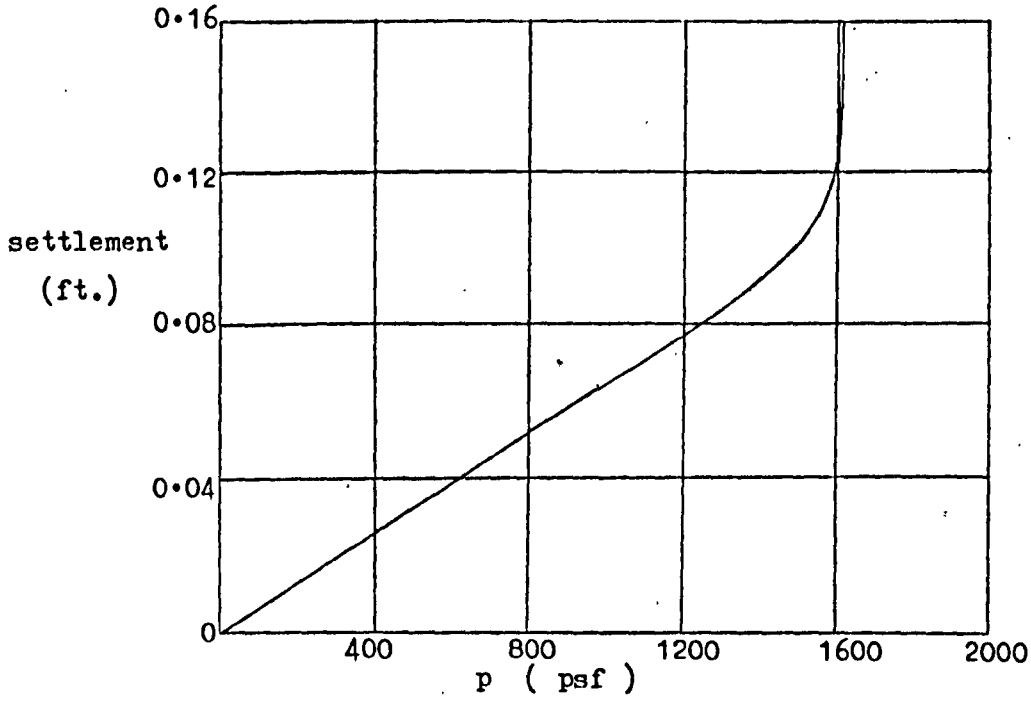

(a) Settlement-load plot

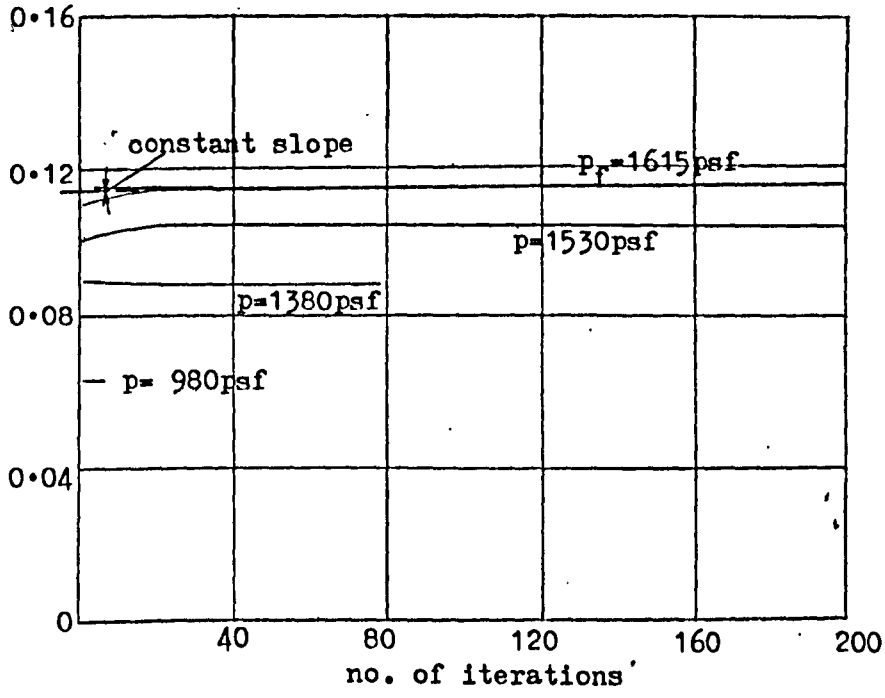

(b) Settlement-iteration plots

Fig. 71. Settlement curves for joint A

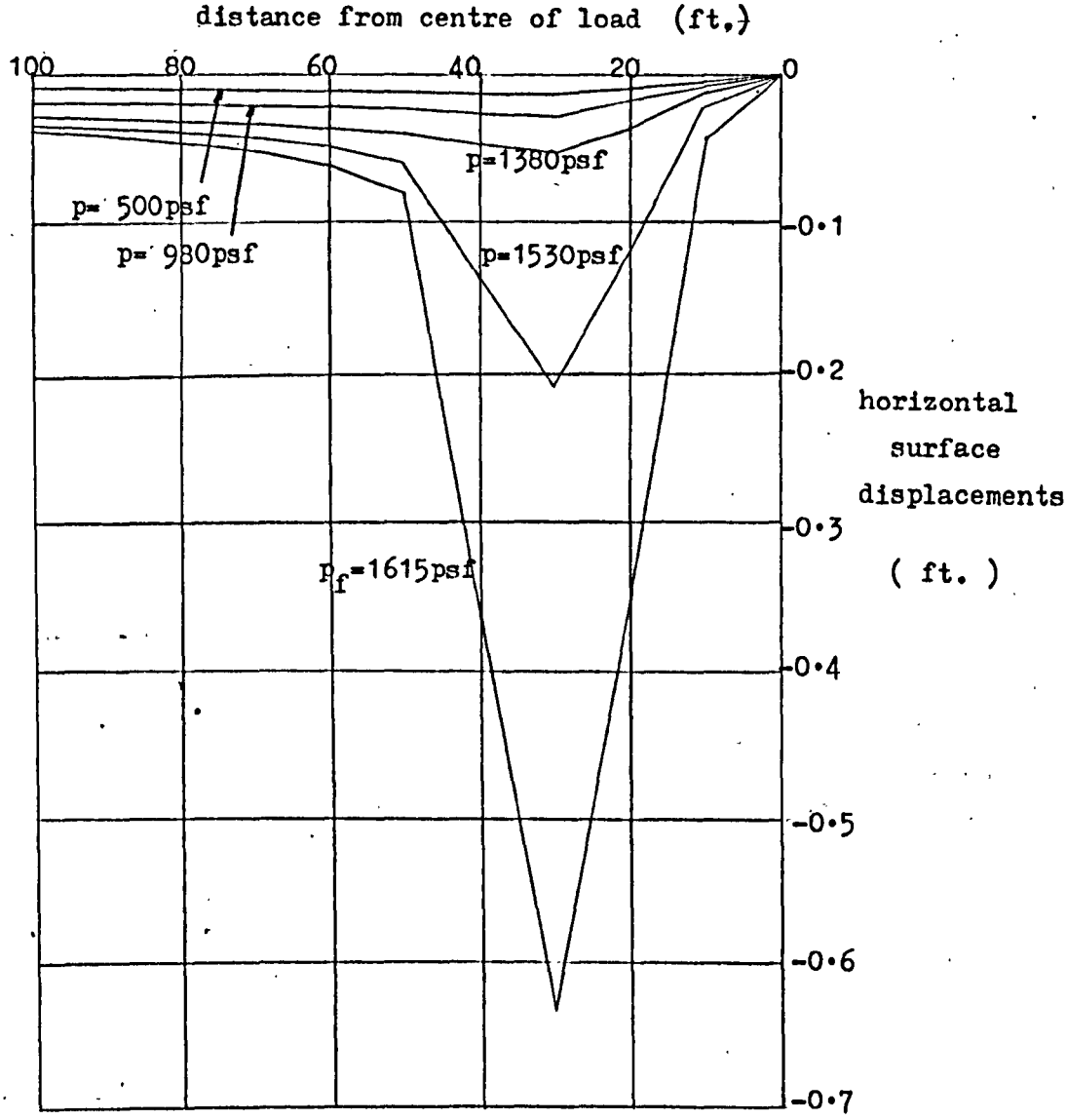
distance from centre of load (ft.)
100
80
60
40
20
0
p= 500psf
p= 980psf
p=1380psf
p=1530psf
p_f=1615psf
-0·1
-0·2
-0·3
-0·4
-0·5
-0·6
-0·7
horizontal surface displacements (ft.)

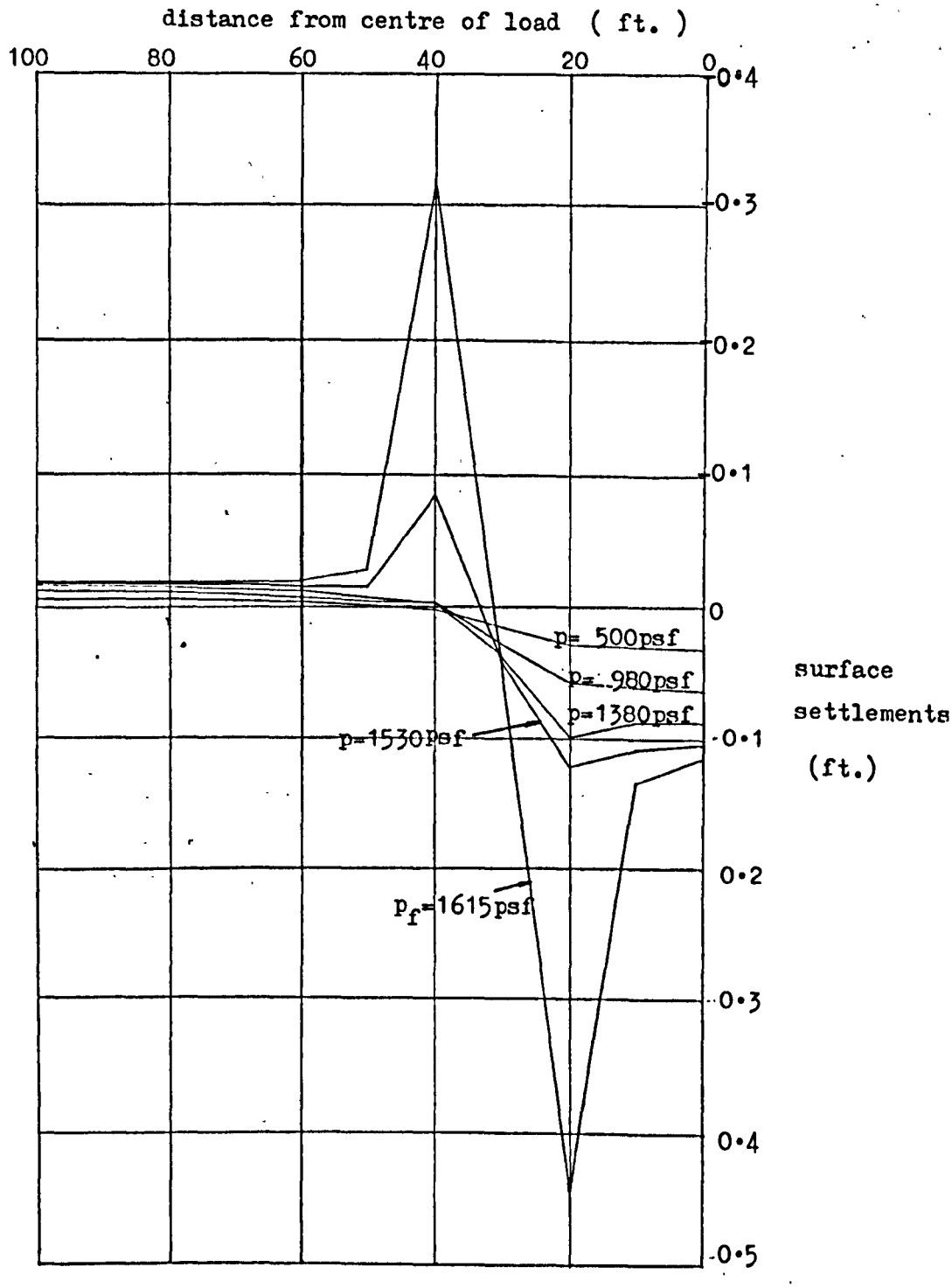

Fig. 72. Surface displacements

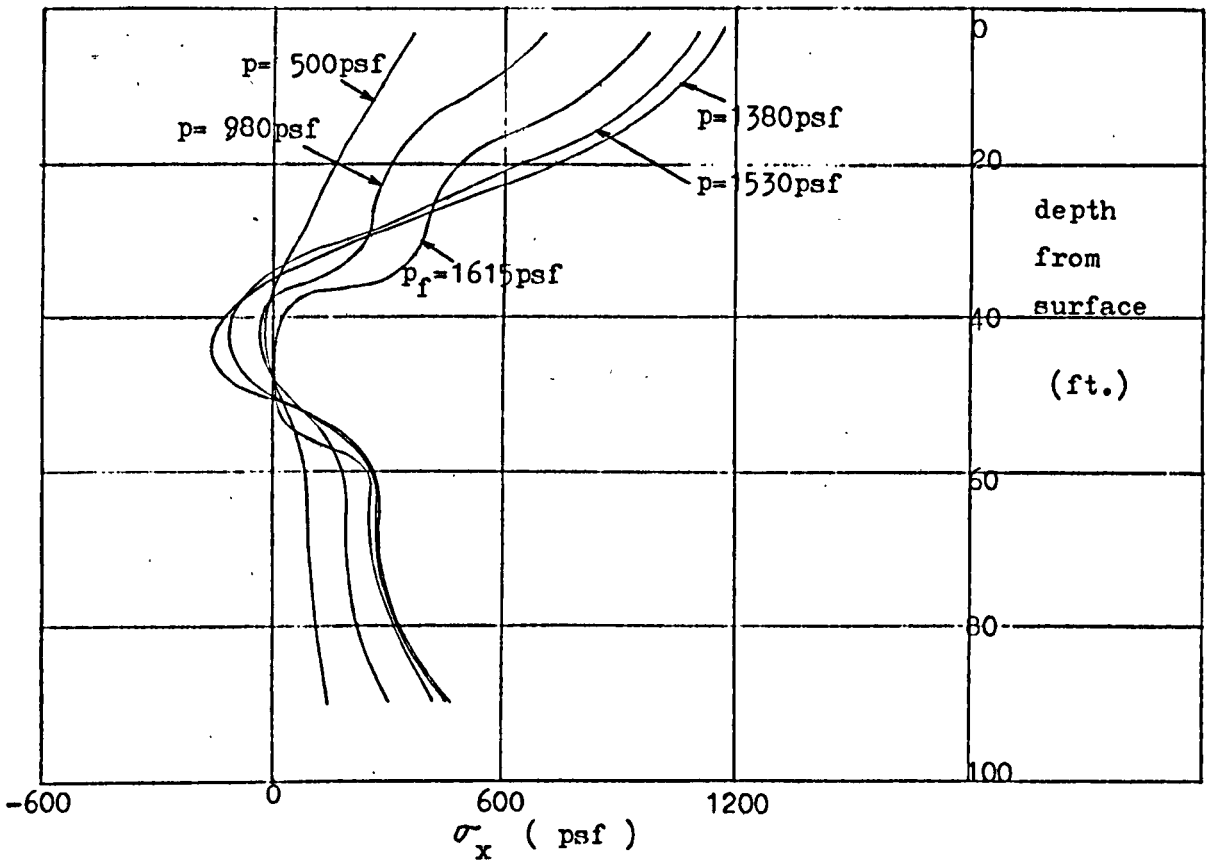

(1a) σ_x distributions down centre of strip load

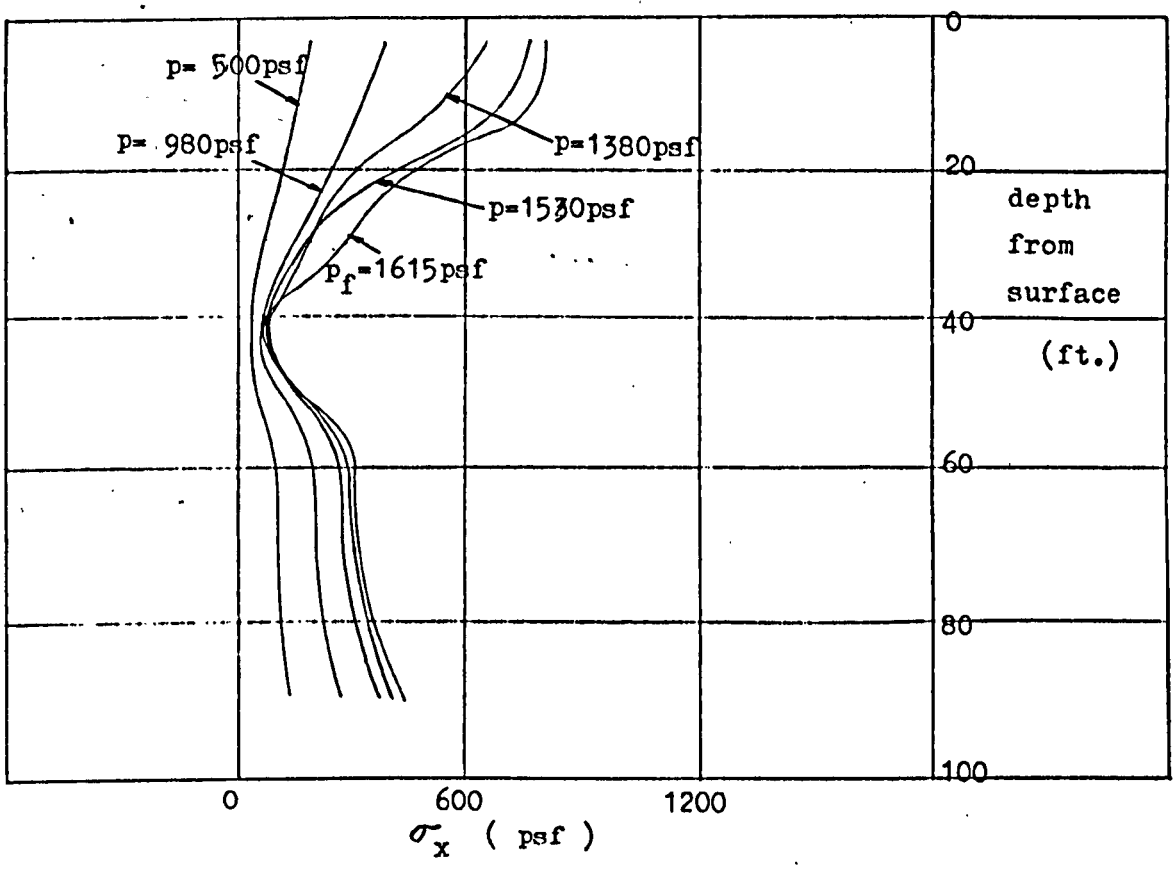

(1b) σ_x distributions down edge of strip load

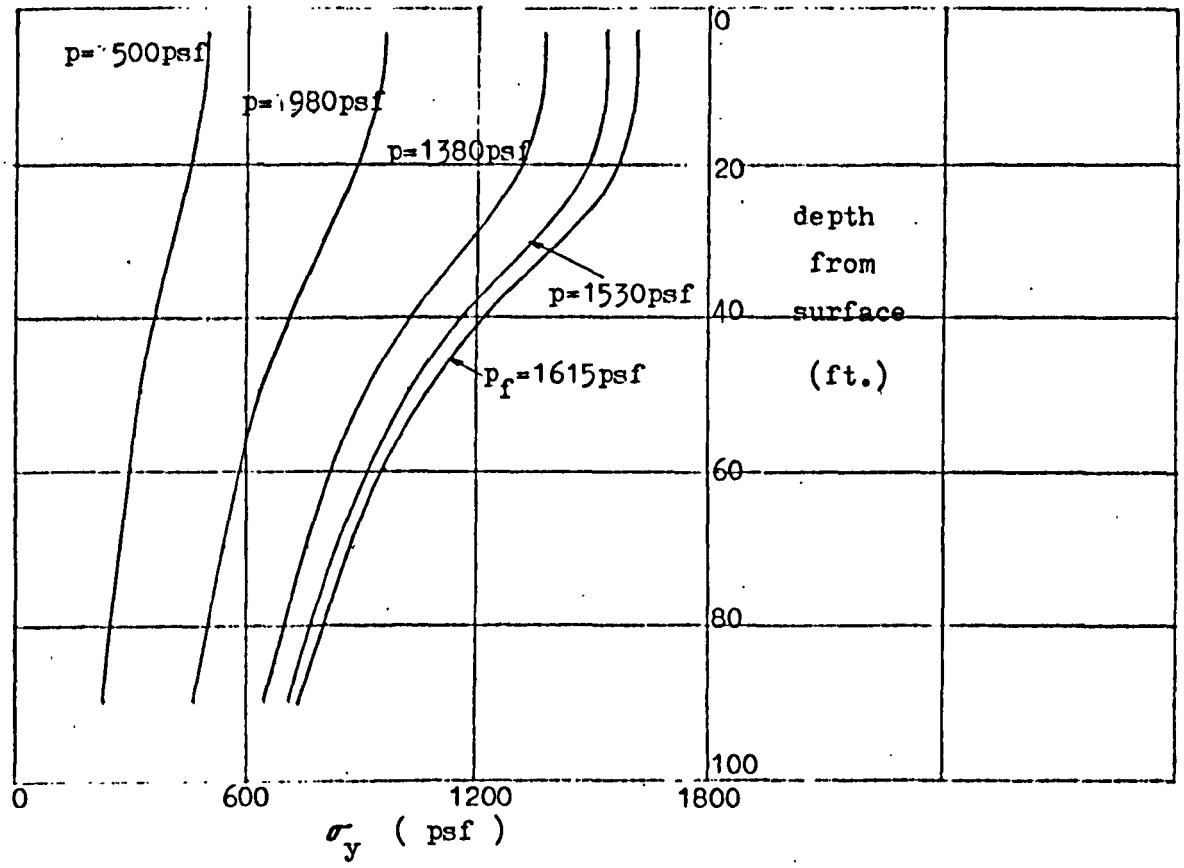

(2a) σ_y distributions down centre of strip load

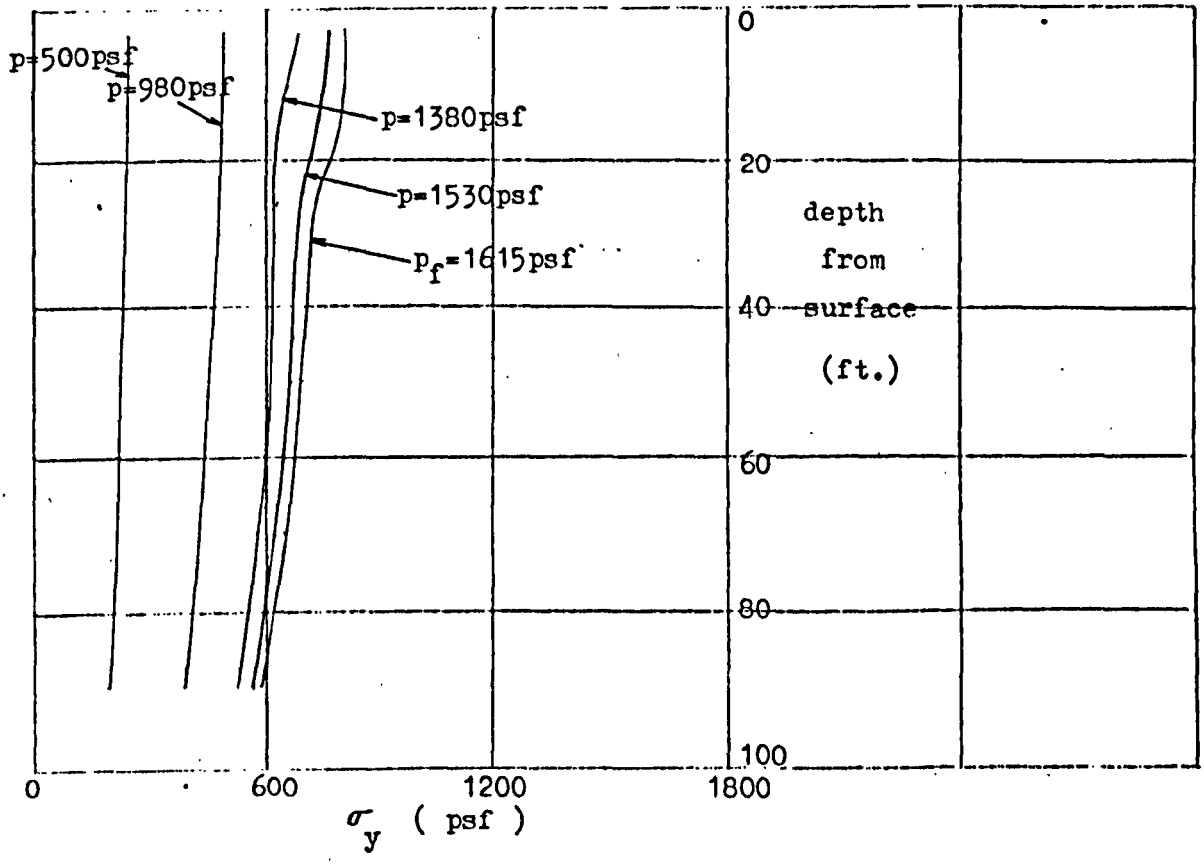

(2b) σ_y distributions down edge of strip load

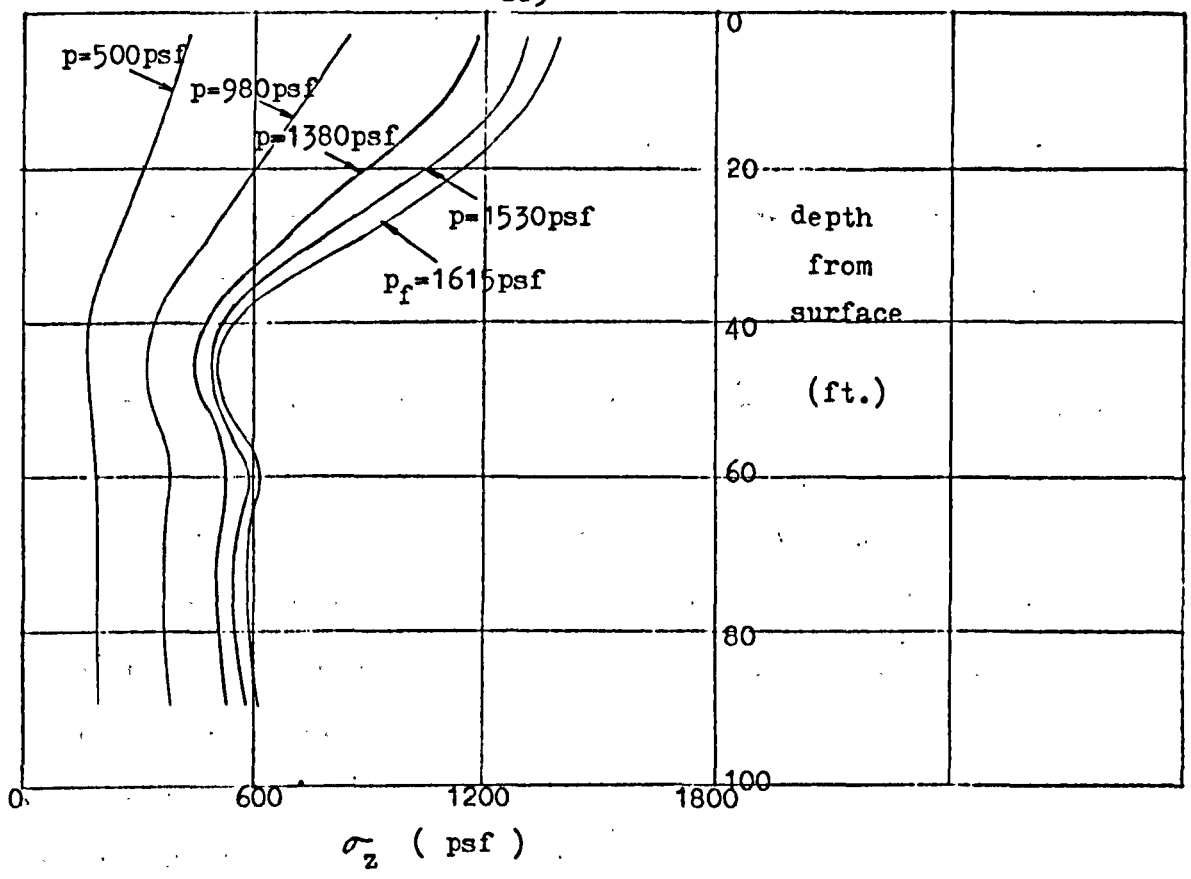

(3a) σ_z distributions down centre of strip load

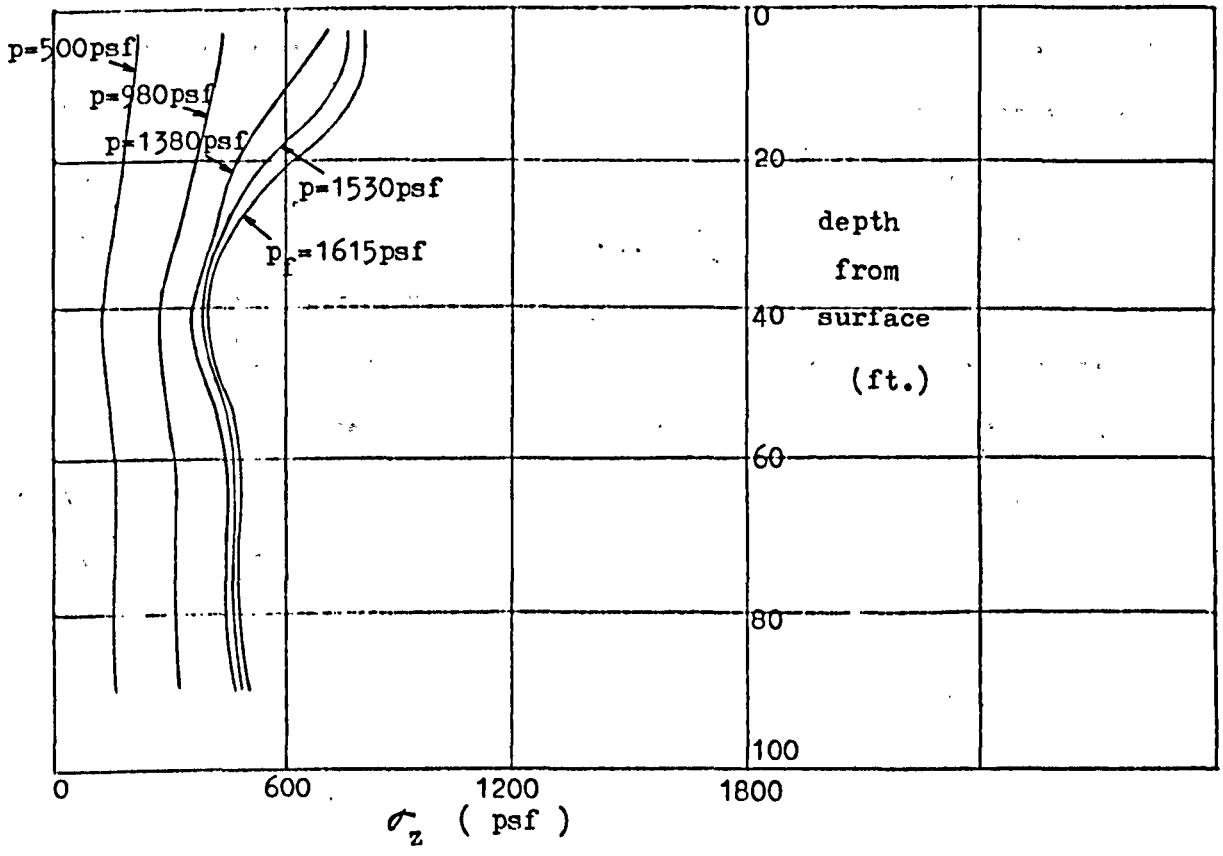

(3b) σ_z distributions down edge of strip load

Fig. 73. Normal stress distributions down centre and edge of strip load

2.13. Random distribution of rigidity and strength in the layer
(flow chart in Section 1.3.2.1.)

The full potential of the finite element approach is exploited here in providing the means for examining the effects of an extreme departure fron the uniform conditions of the basic model on its results - i.e. by assuming random inhomogeneity of rigidity and strength in the layer. Such a distribution can be construed to arise in the following manner.

At a nearby site, a similar layer to that of the practical example of Fig. 22 exists except it has been heavily overconsolidated by removal of overburden throughout its geological history. This leads to a general increase in the strength of the layer, the higher the overconsolidation ratio the greater the percentage increase in strength, with the result that the layer assumes almost uniform strength. By the same token there is a corresponding increase in the rigidity of the layer. Subsequently, the layer is subject to varying degrees of softening as a result of differential pore pressure build-up by consolidation of neighbouring structures, leading to random values of rigidity and strength in the layer. Fig. 74 shows a suitable idealisation for the random inhomogeneous layer so obtained.

The RANF (Section 2.4.) subroutine is again used to generate the random values of rigidity and strength of the individual elements. Due to the relatively large sample, a mean strength of about 920 psf

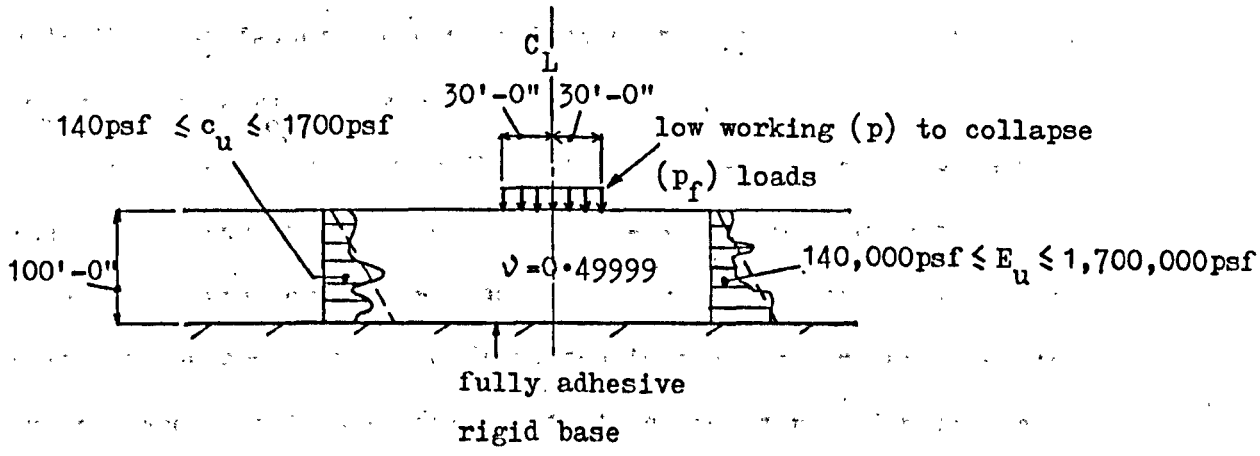

Fig. 74. Idealisation for random inhomogeneous layer (Tresca yield criterion and associated flow rule)

was obtained for the distribution.

Fig. 75 shows the growth of the plastic enclave with increasing load p. First yield occurs at a considerably lower load than that for the basic model of Section 2.6. There is, as for the half-space model (Section 2.4.), a tendency for the maximum shear stresses at the elastic stage to adopt the distribution pattern given by the basic model. In this instance, however, first yield occurs in an element with the most favourable combination of maximum shear stress (high) and shear strength (low).

What is surprising is that although the subsequent growth of the plastic enclave is more irregular - which is to be expected, it still occurs more or less as an entity around the strip load in spite of the considerable differences in the local shear strength in the layer. It thus appears that stress redistribution by the existing enclave to the neighbouring elastic elements continues to play the dominant role in the layer becoming increasingly plastic.

Collapse occurs when the enclave penetrates free surface to the left of the strip at a load of 4280 psf. This is some 12·5% less than for the basic model although with other random distributions of rigidity and strength, differences of +0·4% and -0·5% have been obtained. Indeed, the studies made on this problem suggest that for a large number of distributions, the mean collapse load will be close to that for the basic model. In all cases, the type of development of the plastic enclave described above was also found to apply. In the present problem, there is, on balance, more strength left of the

centre of the strip. The behaviour of the layer thus resembles that of the model of Section 2.8. in certain respects, e.g. collapse occurring to the right.

Once again, it has been found that an assumption of random inhomogeneity can lead to a similar result to that of homogeneity - in this case, approximately average properties seem to apply. This analogy is of obvious practical significance in that soil is inherently non-uniform, sometimes to a high degree.

The surface displacements as well as the normal stress distributions down the centre of the strip load are presented in Figs. 76 to 78 for examination.

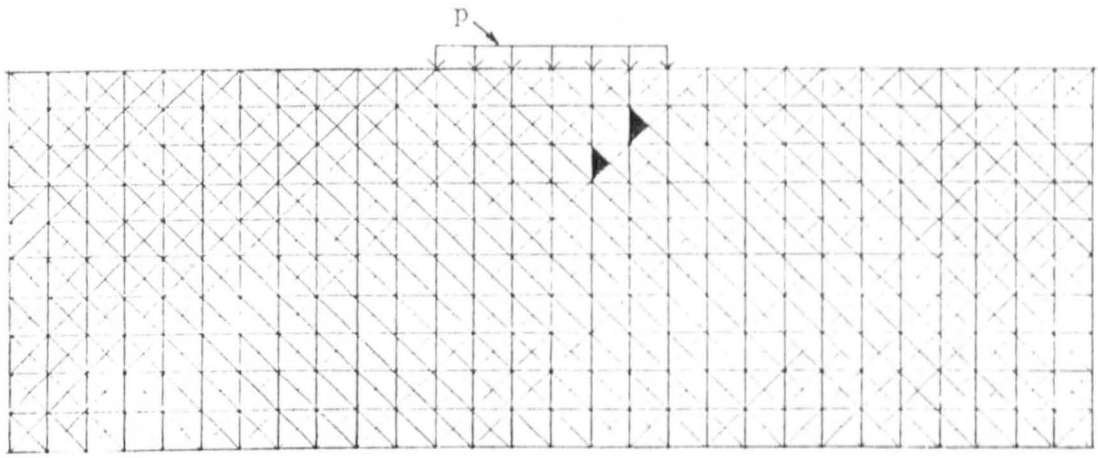

(a) p = 2400 psf

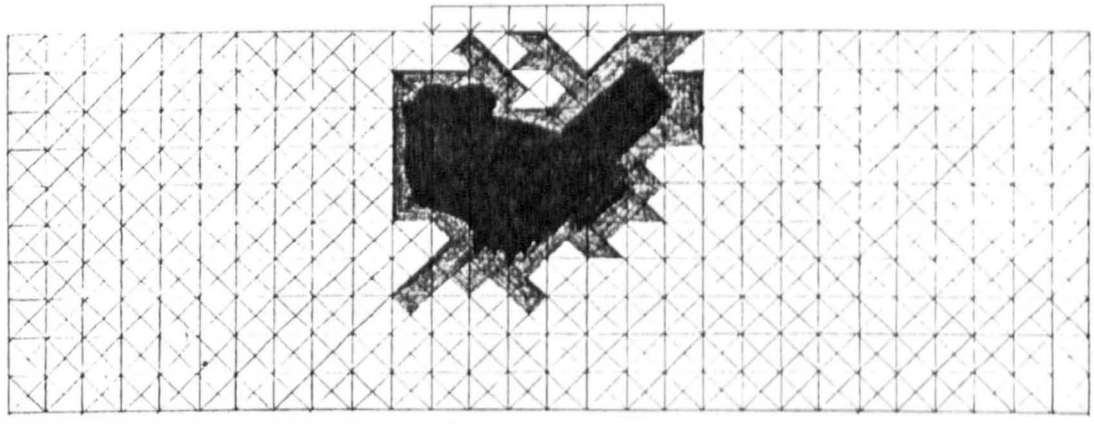

(b) p = 3600 psf

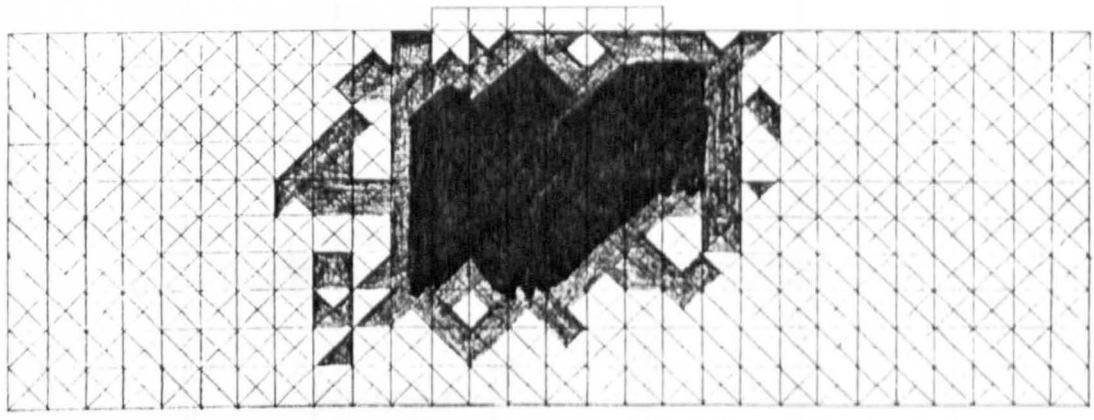

(c) p_f = 4280 psf (collapse)

Fig. 75. Growth of the plastic enclave to collapse

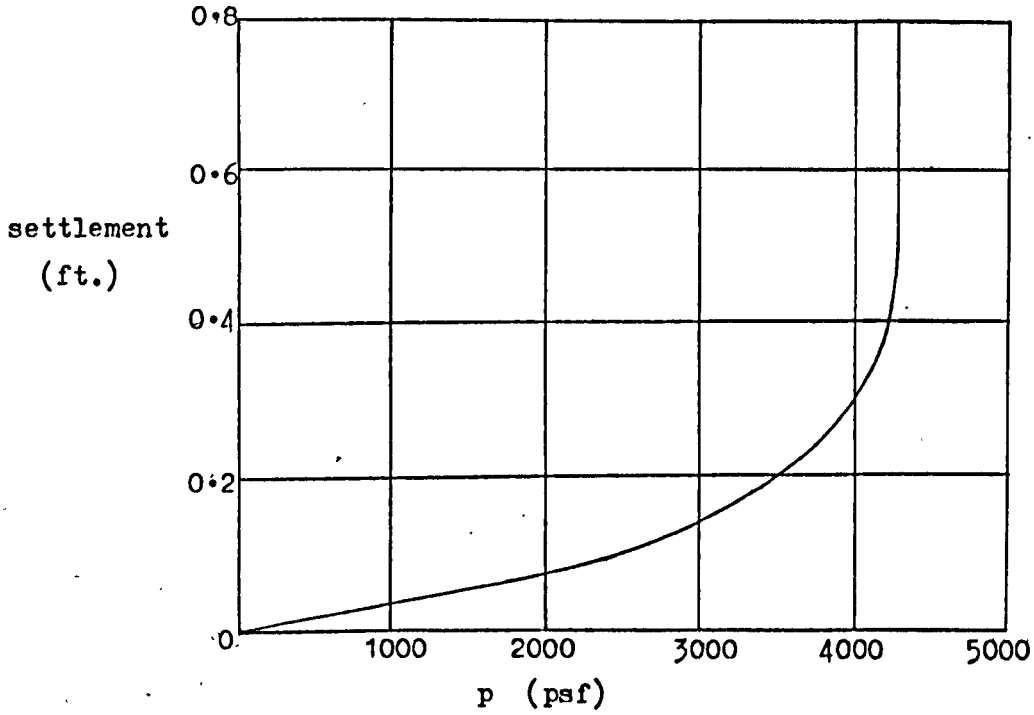

(a) Settlement-load plot

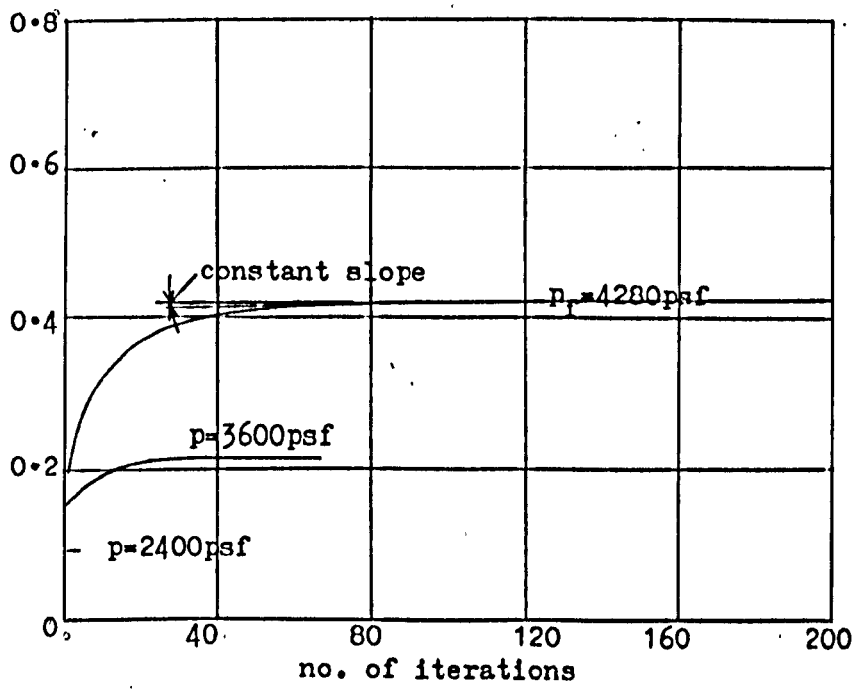

(b) Settlement-iteration plots

Fig. 76. Settlement curves for joint A

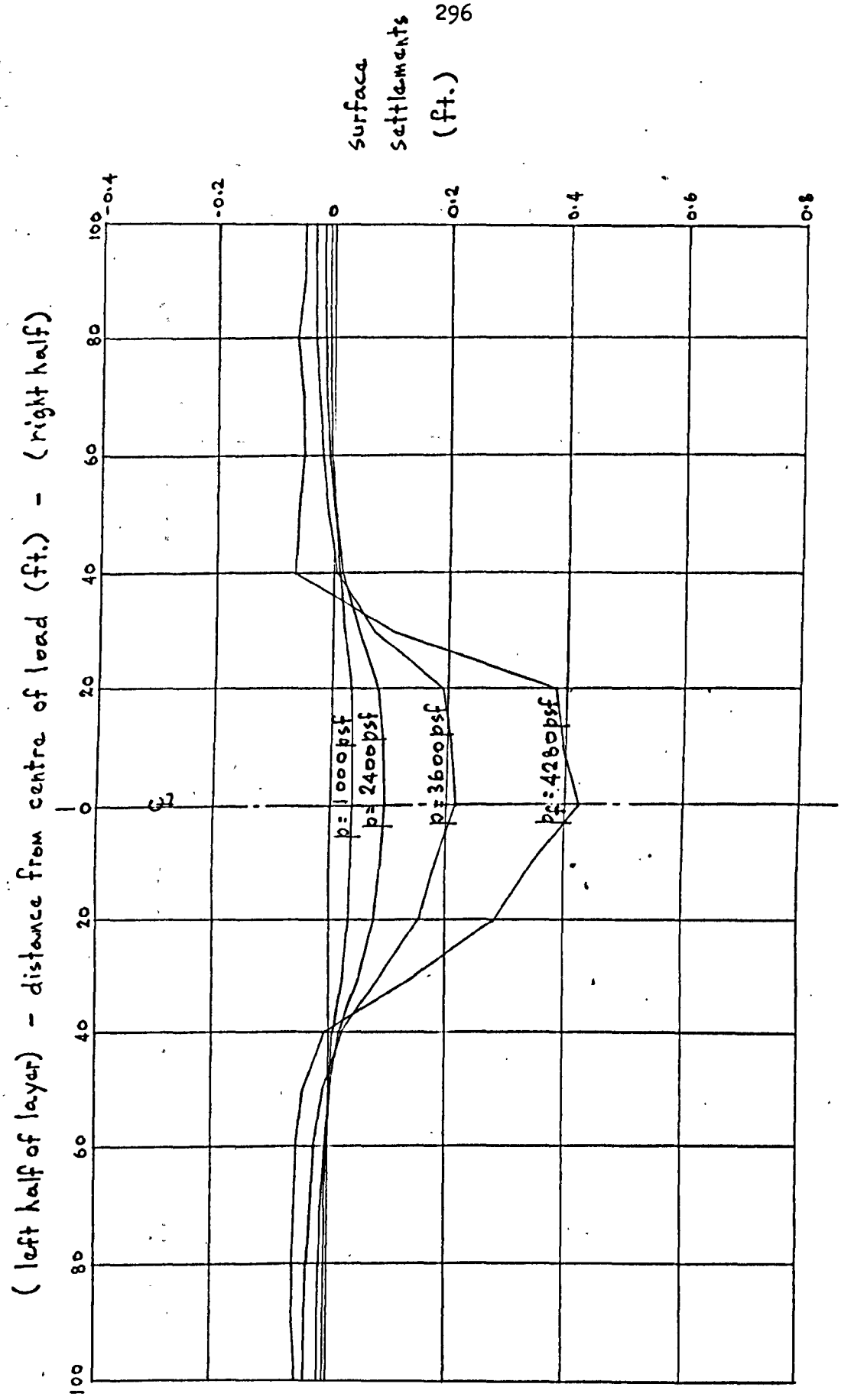
Surface settlements (ft.)
-0.4
-0.2
0
0.2
0.4
0.6
0.8
100
80
60
40
20
0
20
40
60
80
100
(left half of layer) - distance from centre of load (ft.) - (right half)
p = 1000 psf
p = 2400 psf
p = 3600 psf
p = 4280 psf

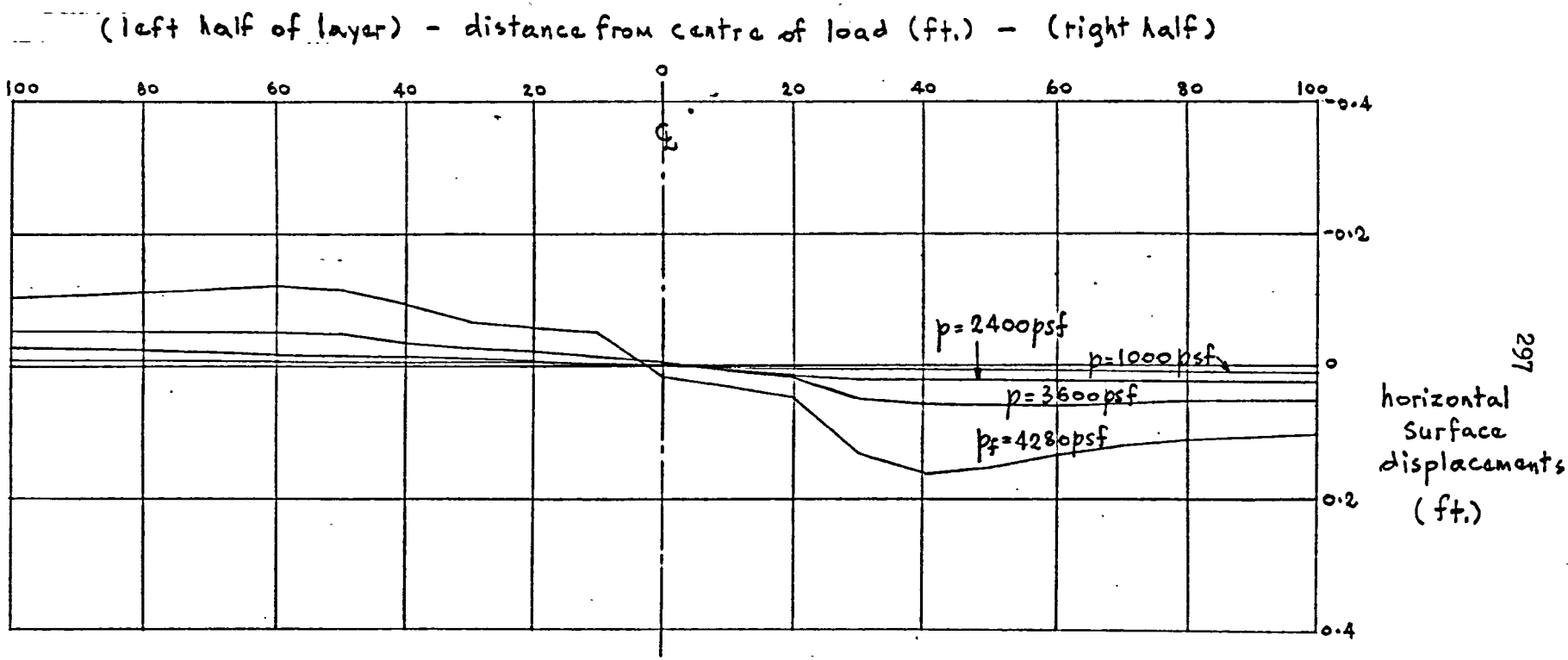

Fig. 77. Surface displacements

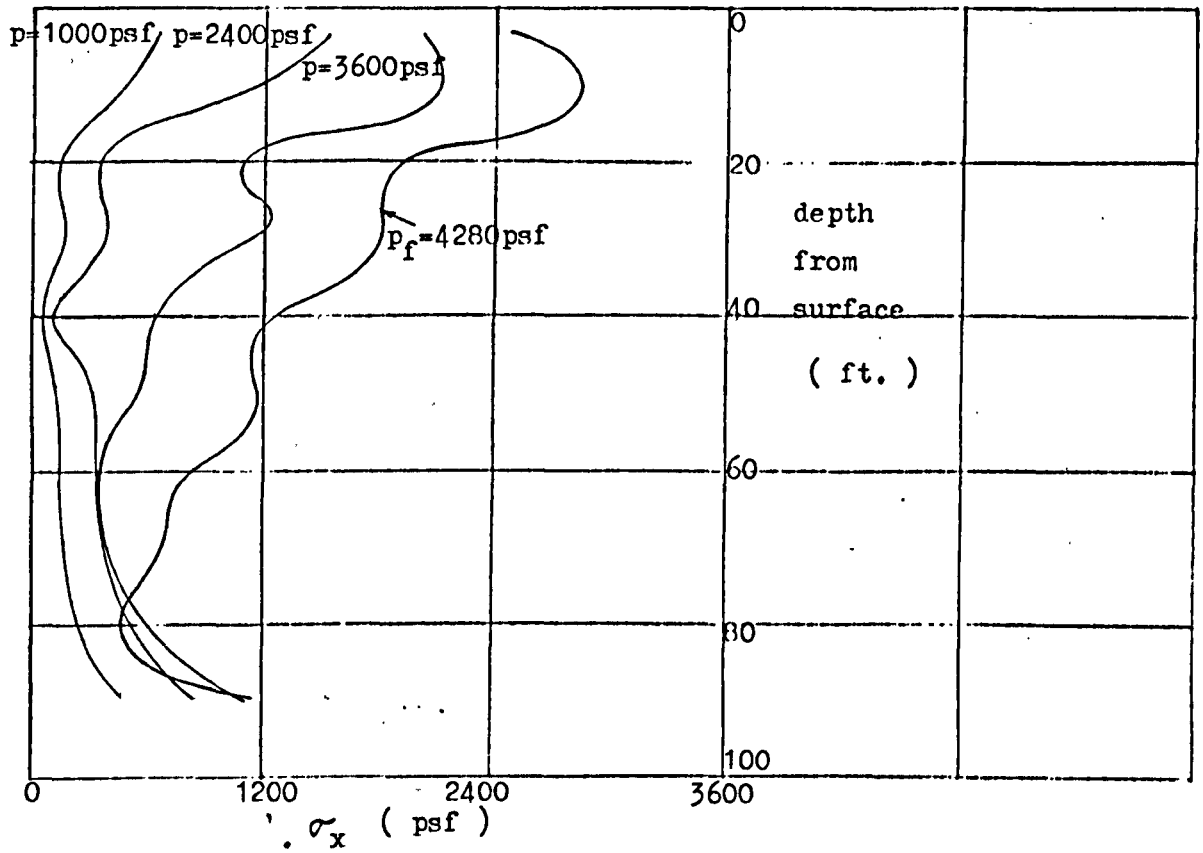

(a) σ_x distributions down centre of strip load

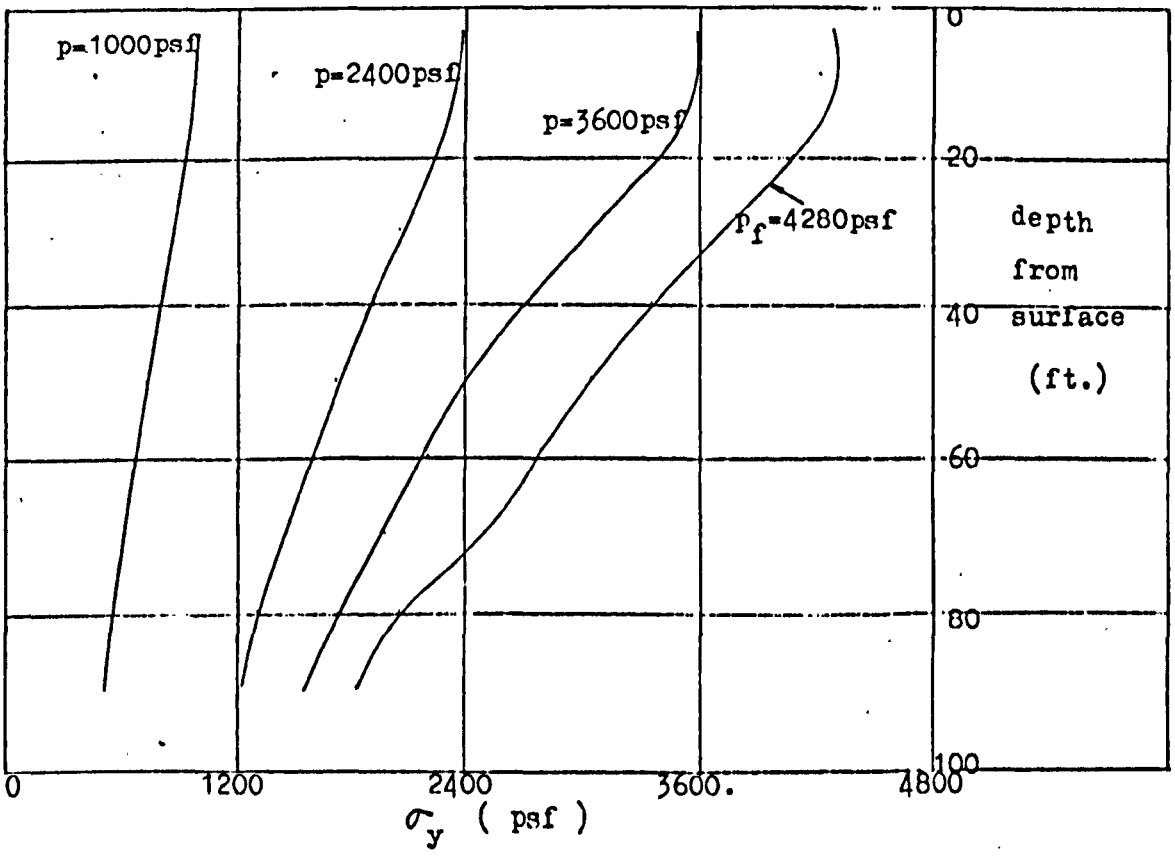

(b) σ_y distributions down centre of strip load

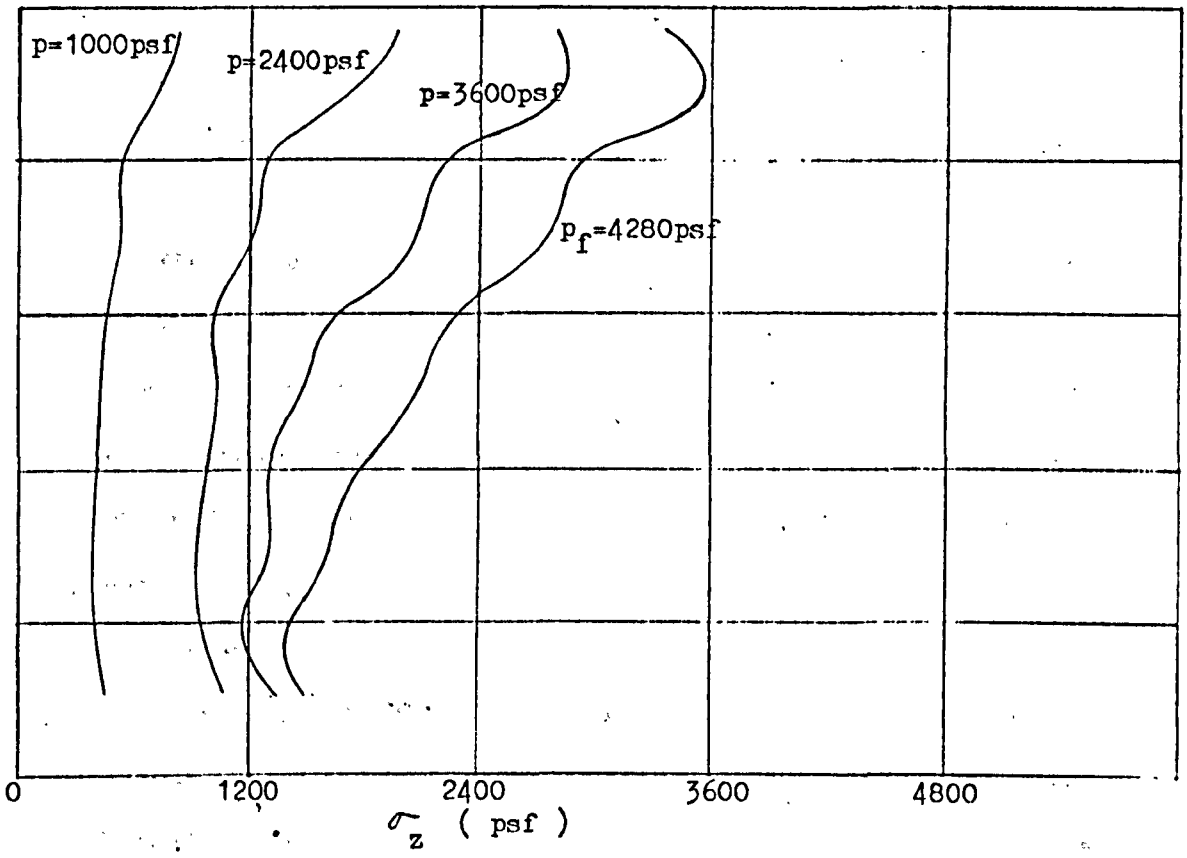

(c) σ_z distributions down centre of strip load

Fig. 78. Normal stress distributions down centre of strip load

2.14. Closer modelling of the triaxial test curve (flow chart in Section 1.4.2.)

Fig. 22(b) shows that the linear elastic, perfectly plastic idealisation of the triaxial test curve hitherto employed can differ significantly from actual constitutive behaviour. Better agreement can, however, be obtained by approximating the curve prior to shear failure as a series of chords representing, initially, linear elastic, and latterly, linear elastoplastic behaviour; perfect plasticity continues to apply at failure.

Only slight modifications are necessary to incorporate the above behaviour into the previous layer models (see Section 1.4.). Such modified models thus remain reasonably simple and therefore provide a suitable basis for similar parametric studies to those of the previous sections.

2.14.1. Shear failure at peak deviator stress

Fig. 79 shows the proposed idealisation for the triaxial test curve of a clay sample taken at mid-depth in the layer of Fig. 22(a). The curve is based on results obtained by Duncan and Dunlop (33) and Bishop (44). The initial linear elastic portion OA occurs where the curve is substantially straight. It is taken to approximate the

early stages of a typical unloading curve; i.e. in terms of plasticity theory, before the Bauschinger effect is manifested. Such an approximation leads to strain recovery on unloading that is a reasonable reflection of observed behaviour. Following first yield, the material work hardens linearly (AB then BC) to provide a close fit to the triaxial test curve. Finally, when peak deviator stress is attained, shear failure is assumed to occur so that the material is then taken to be non-work hardening. Thus, irrecoverable strains are modelled not only at shear failure but also during the intermediate loading range.

Since the following study is to be the first of its kind, the basic model of Section 2.6. is adopted, albeit assuming the present material behaviour.

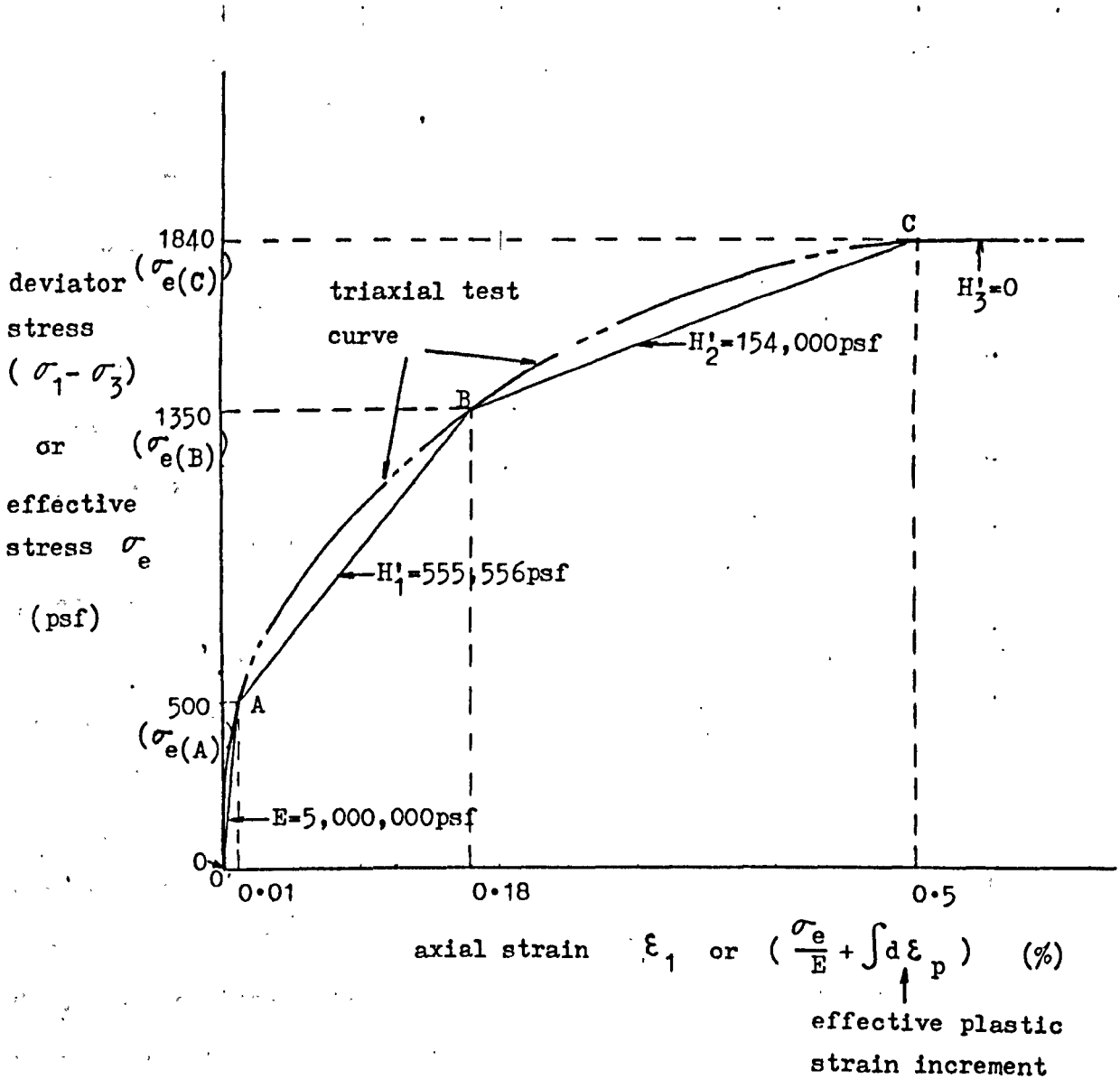

Fig. 79. Elastoplastic idealisation for triaxial test curve for shear failure at peak deviator stress

Fig. 80 shows the growth of the plastic enclave with increasing load p .

First yield occurs at 656 psf which is $\frac{\sigma_{e(A)}}{1840}$ times that for the basic model, $\sigma_{e(A)}$ being the effective stress at state A (i.e. first yield in Fig. 79) and the shear strength of the basic model being $\frac{1}{2}$ of 1840 psf. This is to be expected since the maximum shear stress distribution at the elastic stage is theoretically independent of Young's modulus (10).

A work hardening plastic enclave then develops in much the same way as for the basic model although no collapse occurs when it penetrates free surface since it is then still capable of sustaining load with finite strain. Since the enclave is within state AB, it is less stiff than the outlying elastic material.

With further loading, the first yield element is the first to go into state BC. The enclave at state AB continues to develop whilst another enclave which is at state BC grows within it in similar fashion though obviously lagging. Subsequently, the same element reaches state C- .. - i.e. becomes perfectly plastic - first and an enclave in the same state develops around it, again in similar fashion to that in state AB - and hence BC - though lagging behind both enclaves which are increasing in size meantime.

Finally, at 6200 psf, the perfectly plastic enclave penetrates free surface and is no longer able to sustain the strip with finite

deformation. That is, collapse occurs. Note that this load is some 27% higher than that for the basic model (i.e. 4900 psf). However, the enclaves shown are limited to a maximum of 200 iterations only. A computation was conducted for p = 5300 psf up to 500 iterations for which the limit of the perfectly plastic enclave obtained is shown dashed in Fig. 80(d). There is the suggestion that if the iterations are carried far enough, collapse may occur at that smaller load which is only some 8% higher than that for the basic model.

There is thus a possibility that the notion of path independence of the collapse load for the elastic, perfectly plastic material of the basic model (which is well-known) may be extended to include the present elastoplastic material. Indeed, other computations based on similar elastoplastic materials were found to support this view.

The surface displacements as well as the normal stress distributions down the centre and edge of the strip load are presented in Figs. 81 to 83 for examination.

Key to state of elements:-

- elastic (OA)
- $H_1' = 555,556$ psf (AB)
- $H_2' = 154,000$ psf (BC)
- perfectly plastic (C-..)

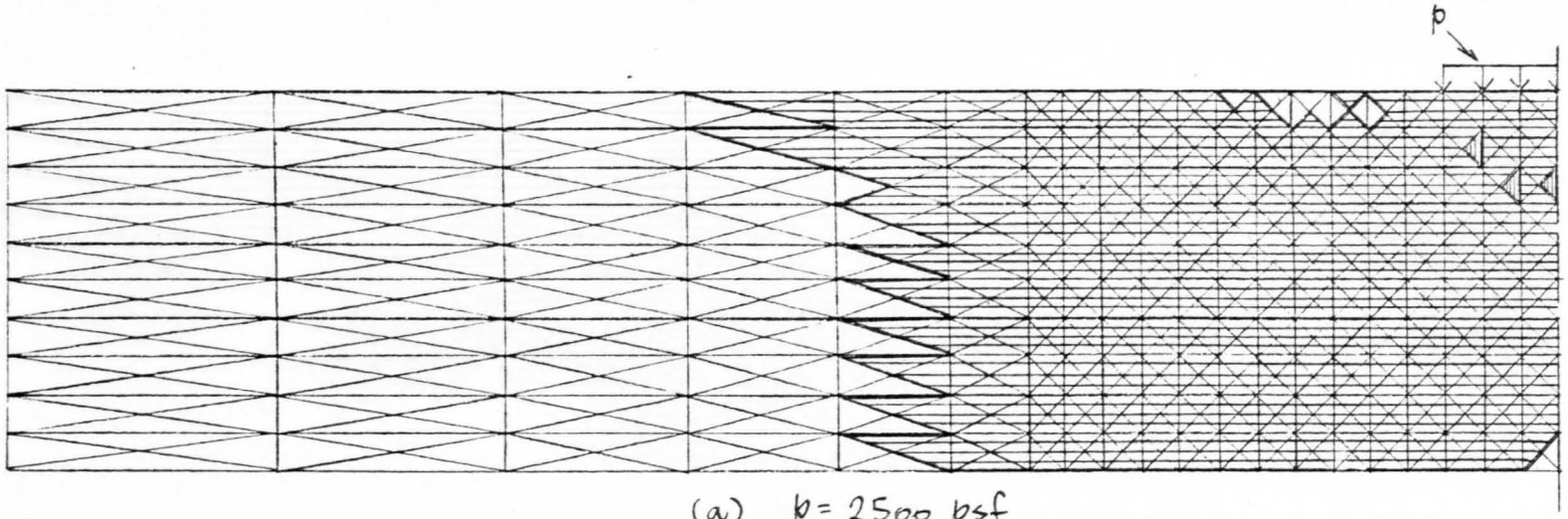

(a) $p = 2500$ psf

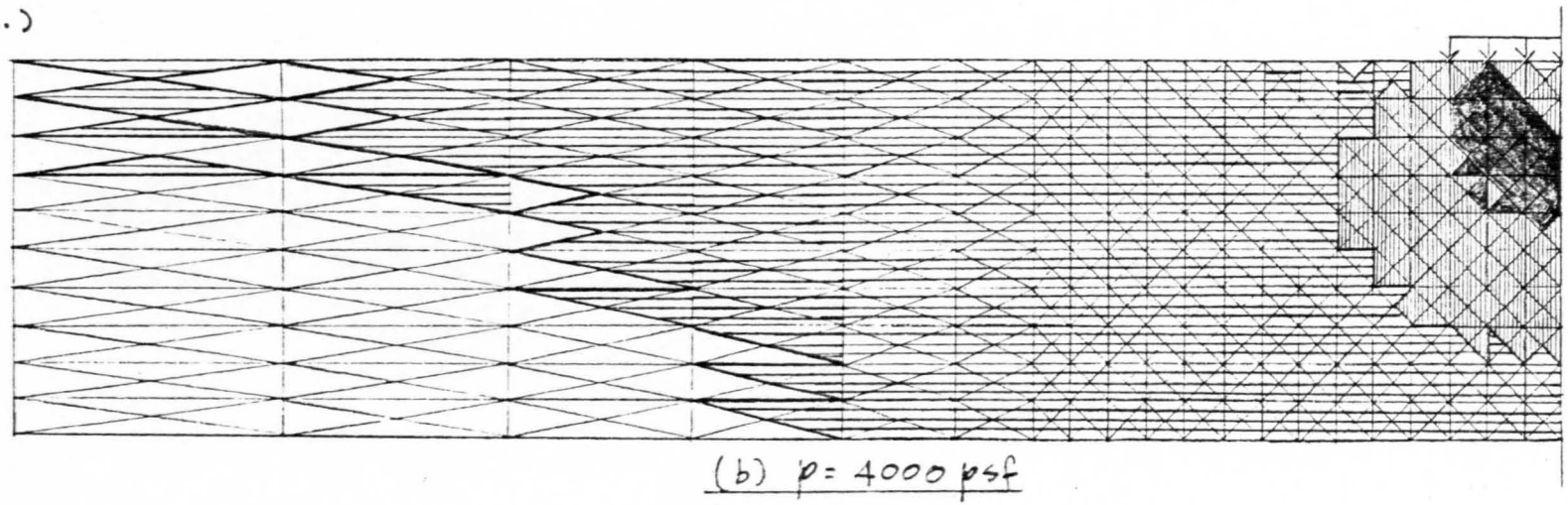

(b) $p = 4000$ psf

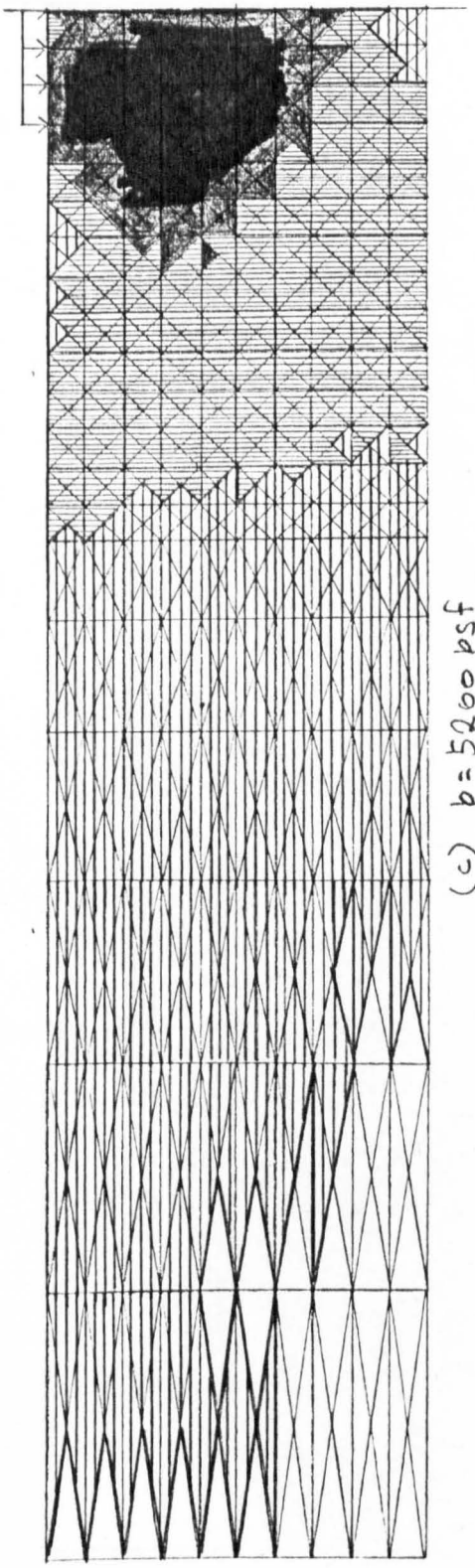

(c) $p = 5200$ psf

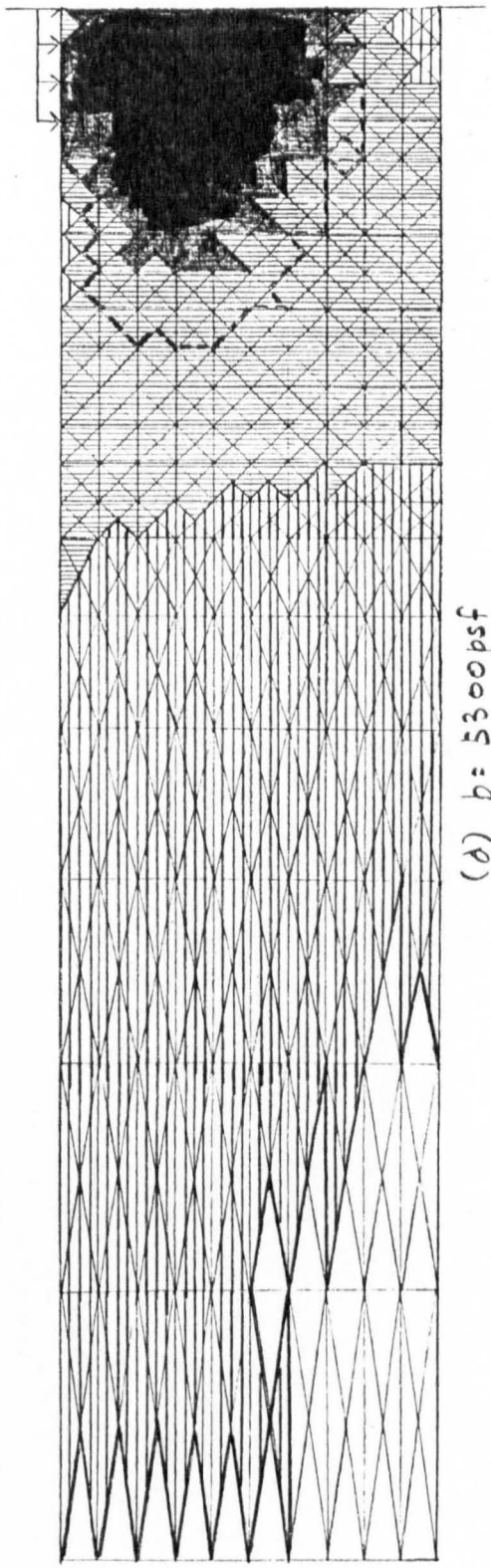

(d) $p = 5300$ psf

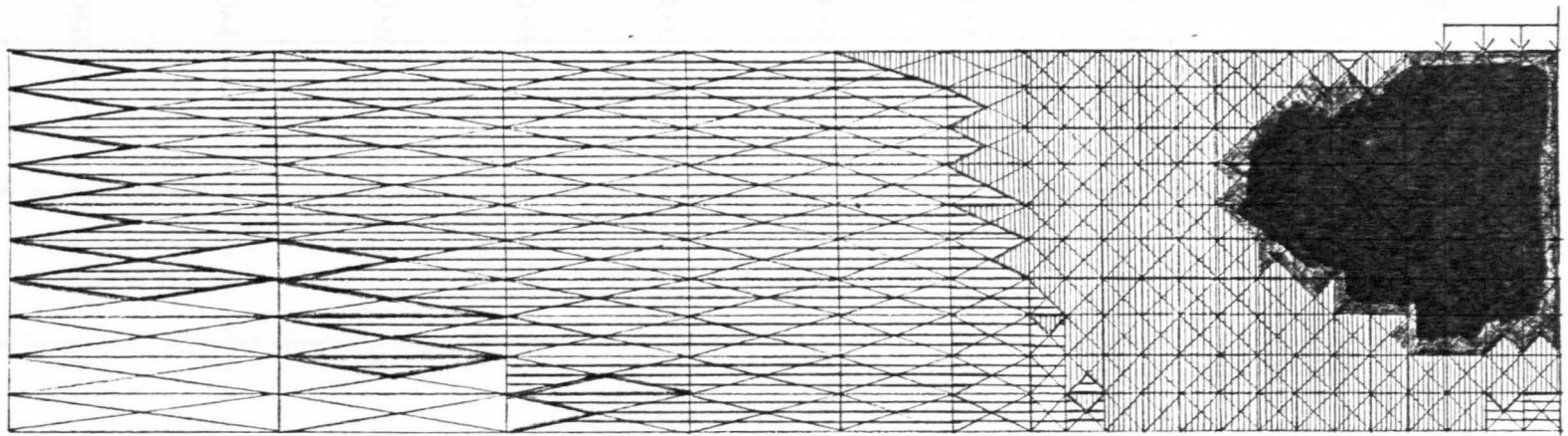

(e) $p = 5700$ psf

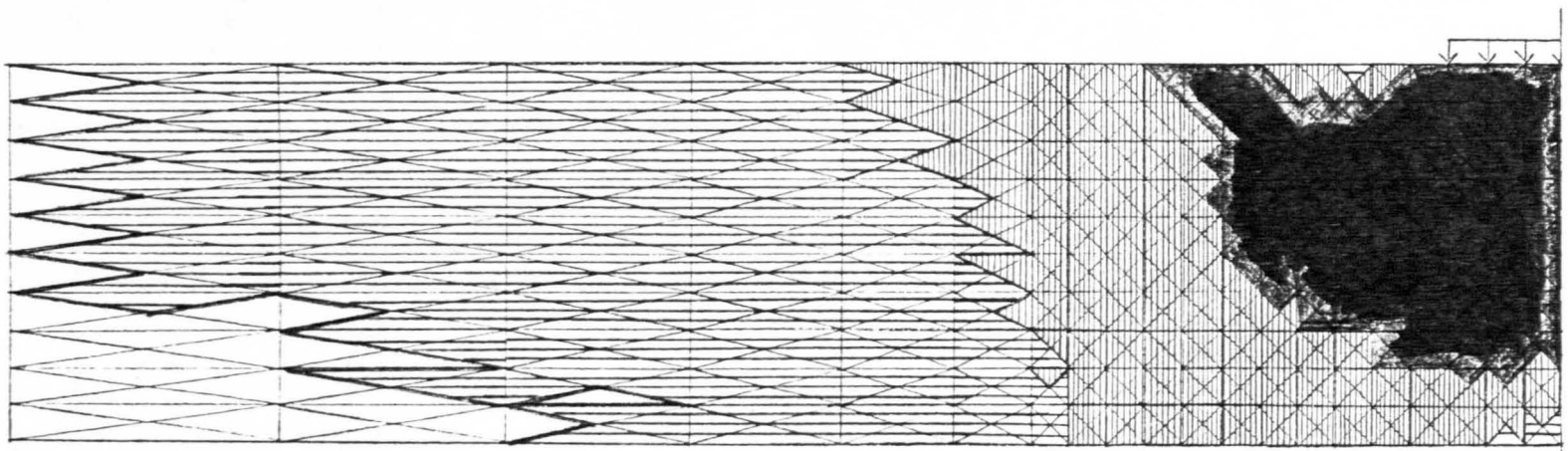

(f) $p_f = 6200$ psf (collapse)

Fig. 80. Growth of plastic enclave to collapse

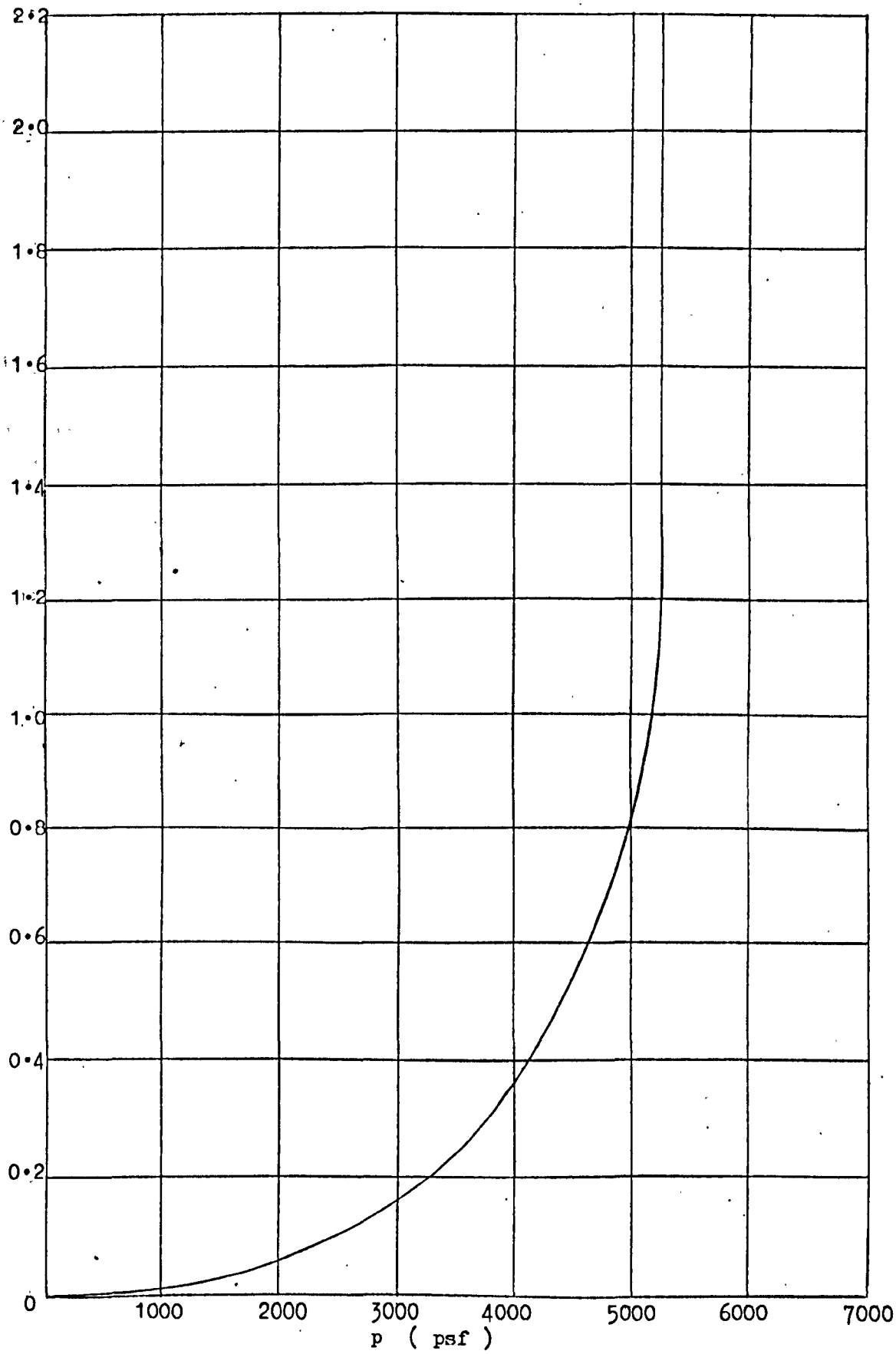

(a) Settlement-load plot

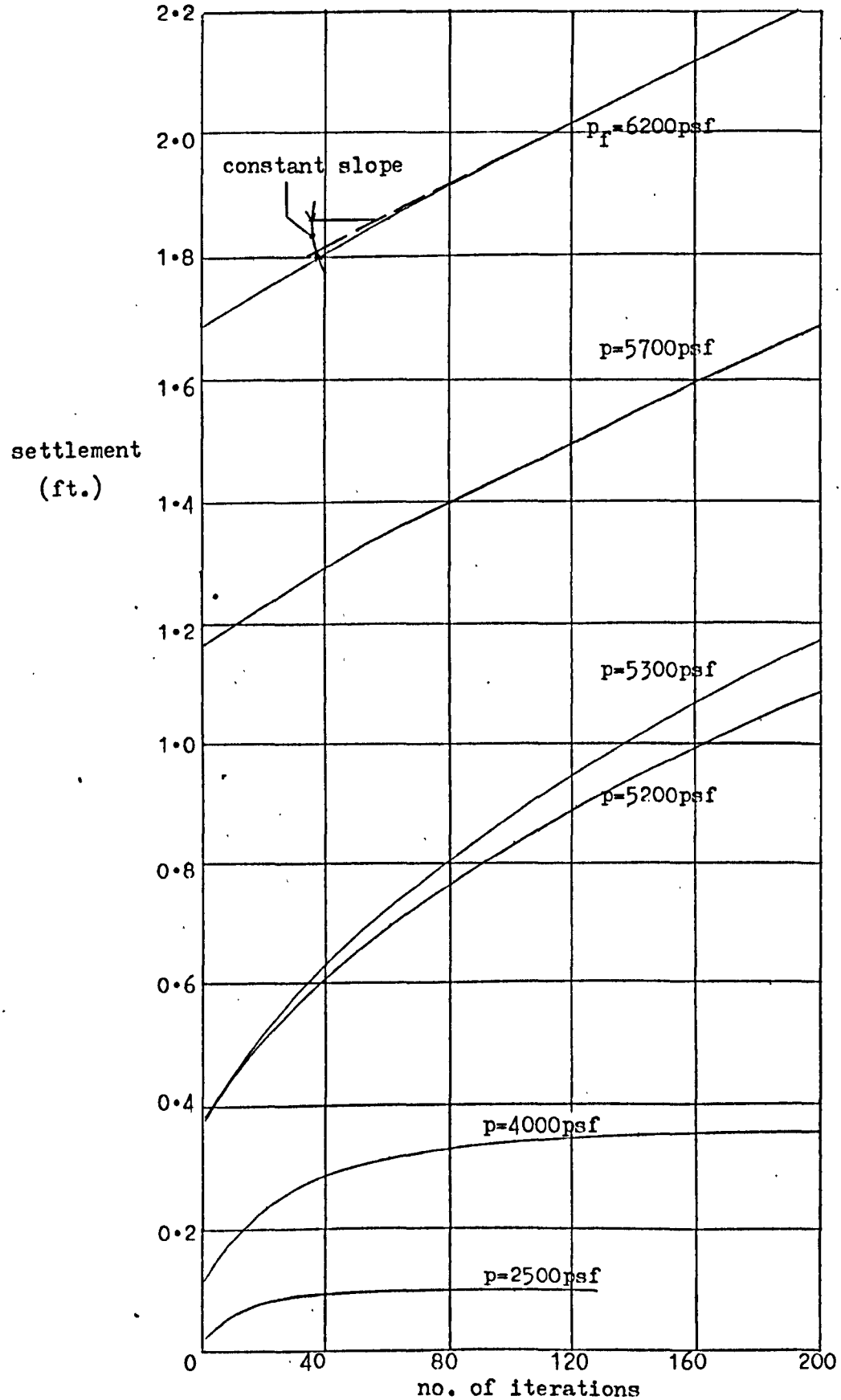

(b) Settlement - iteration plots

Fig. 81. Settlement curves for joint A

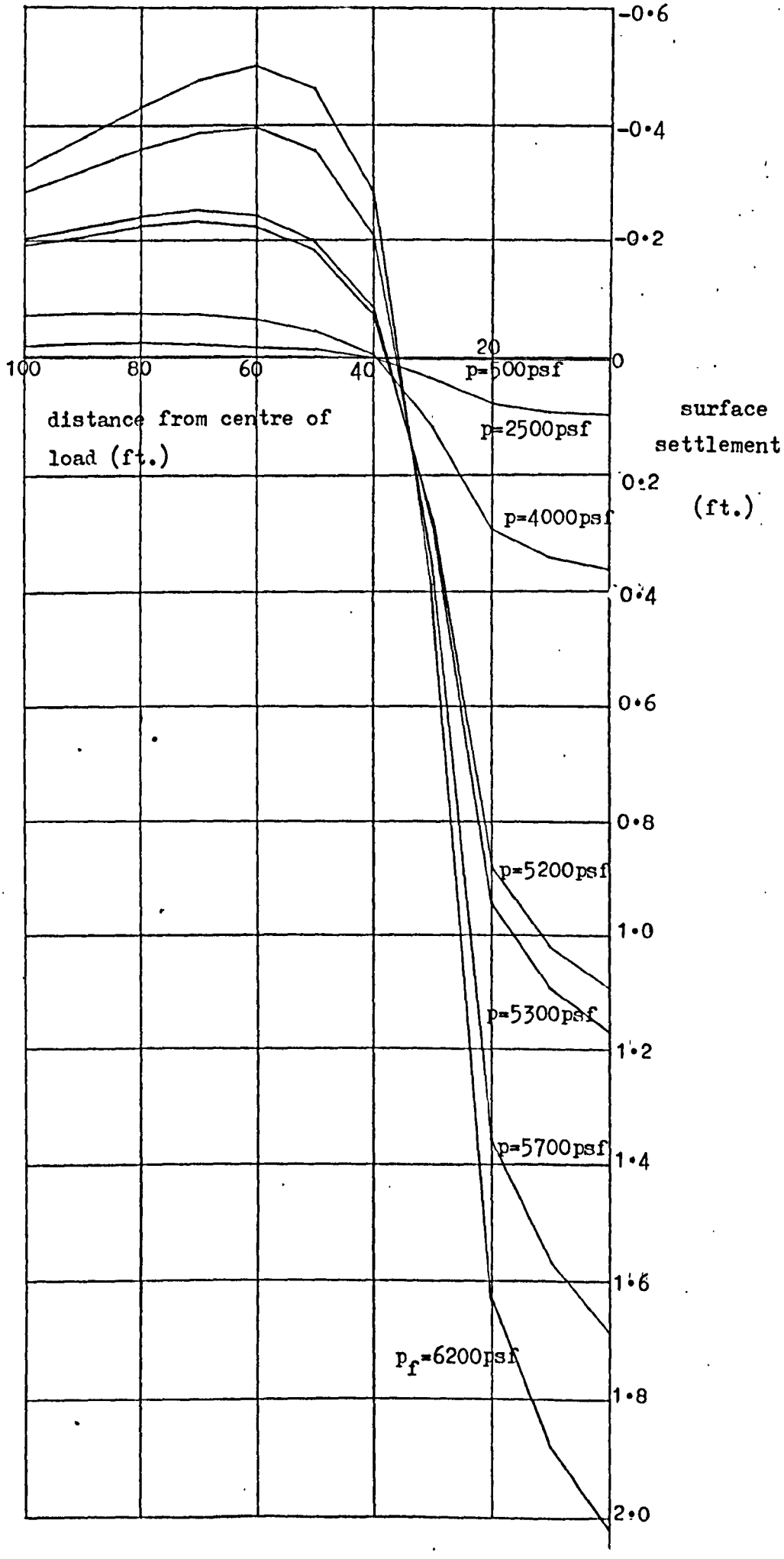
-0·6
-0·4
-0·2
0
0·2
0·4
0·6
0·8
1·0
1·2
1·4
1·6
1·8
2·0
100
80
60
40
20
0
distance from centre of load (ft.)
surface settlement (ft.)
p=500psf
p=2500psf
p=4000psf
p=5200psf
p=5300psf
p=5700psf
p_f=6200psf

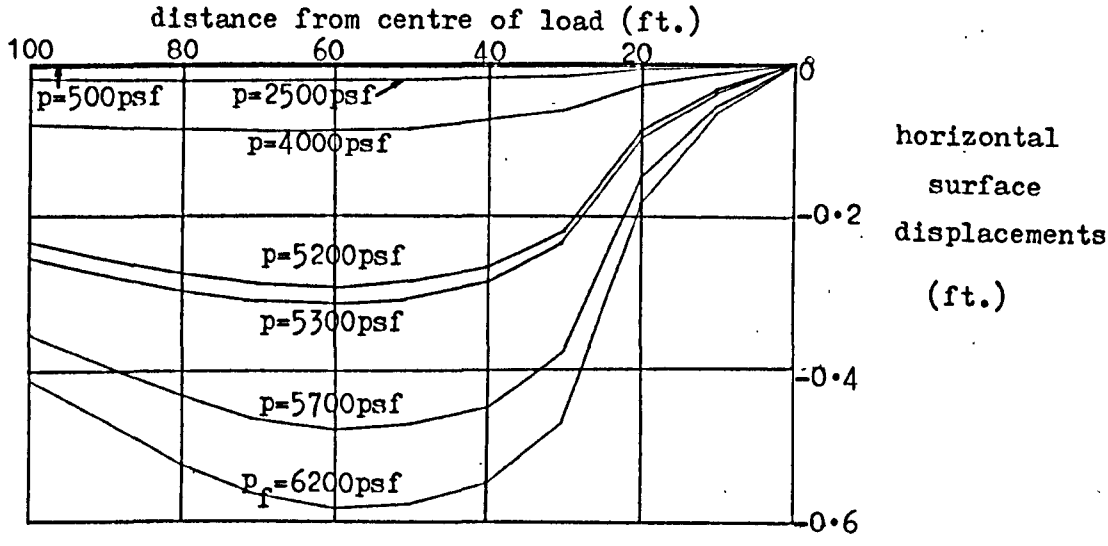

Fig. 82. Surface displacements

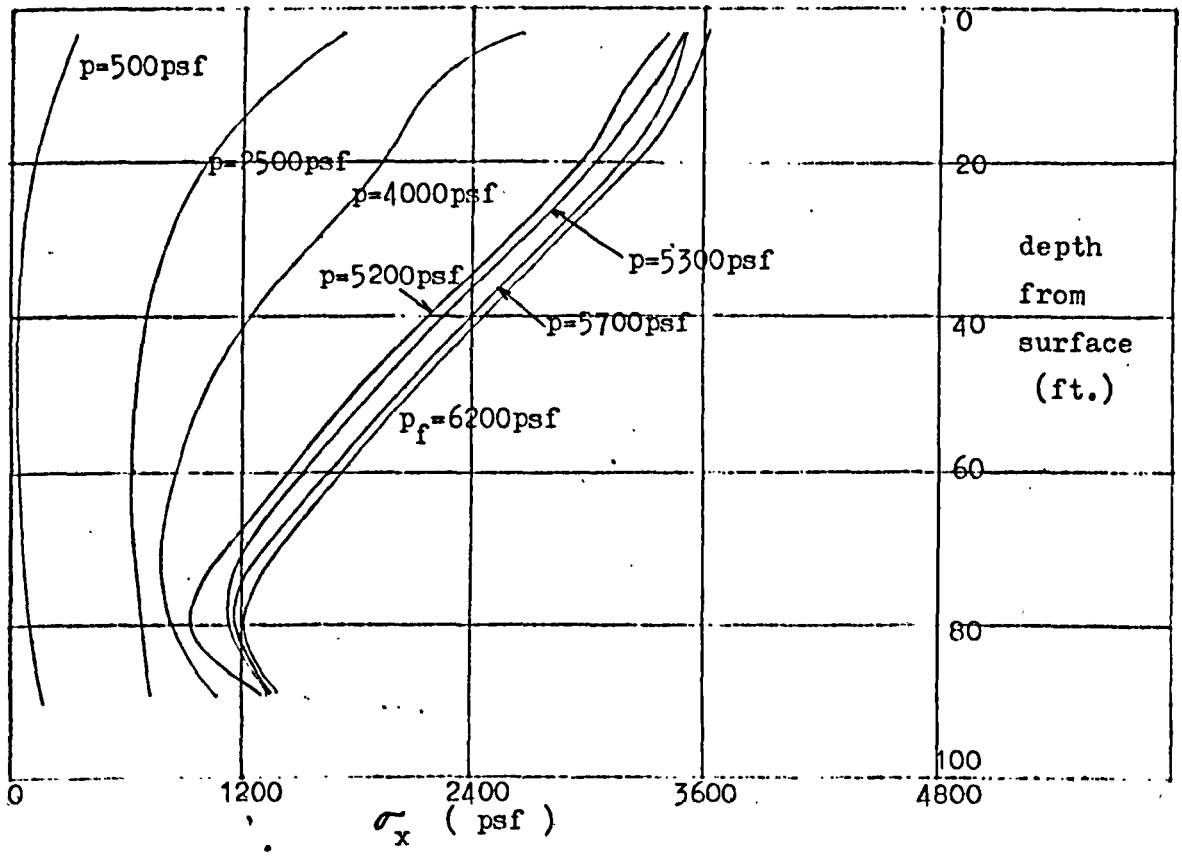

(a) σ_x distributions down centre of strip load

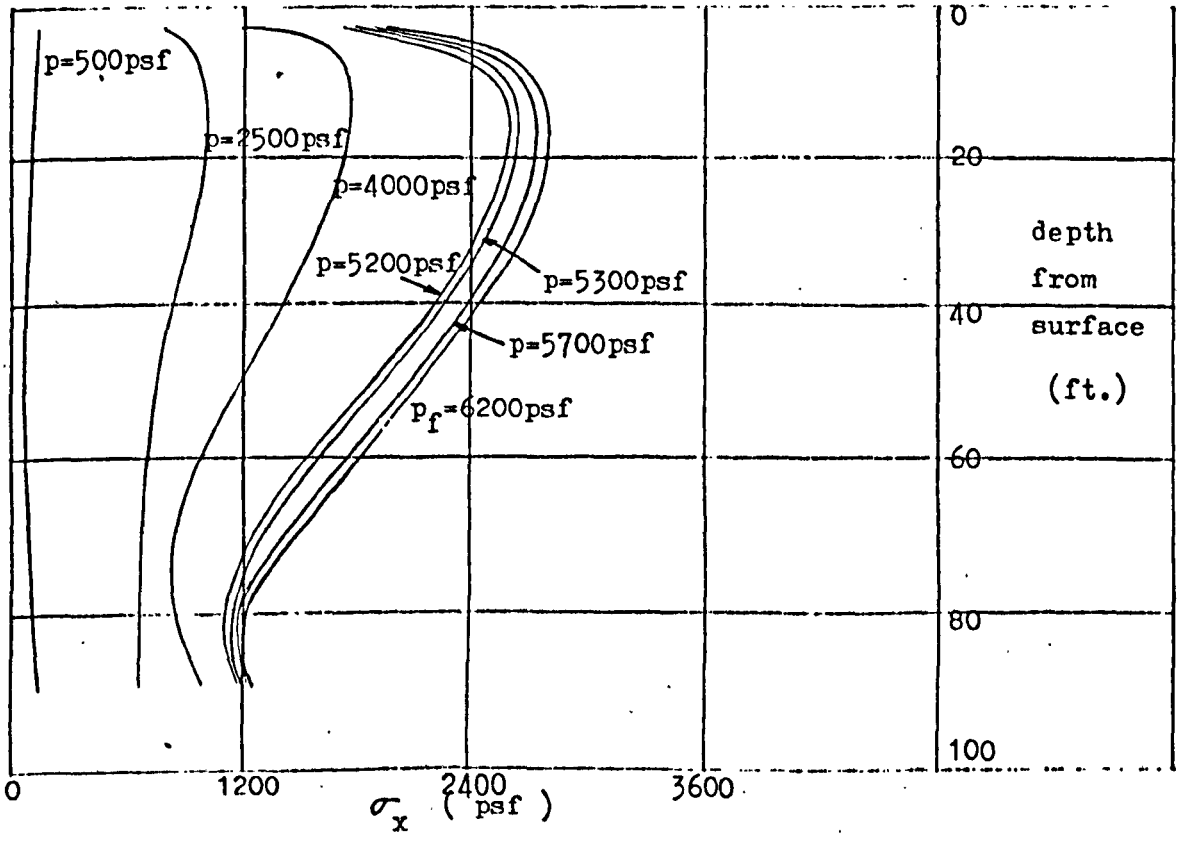

(b) σ_x distributions down edge of strip load

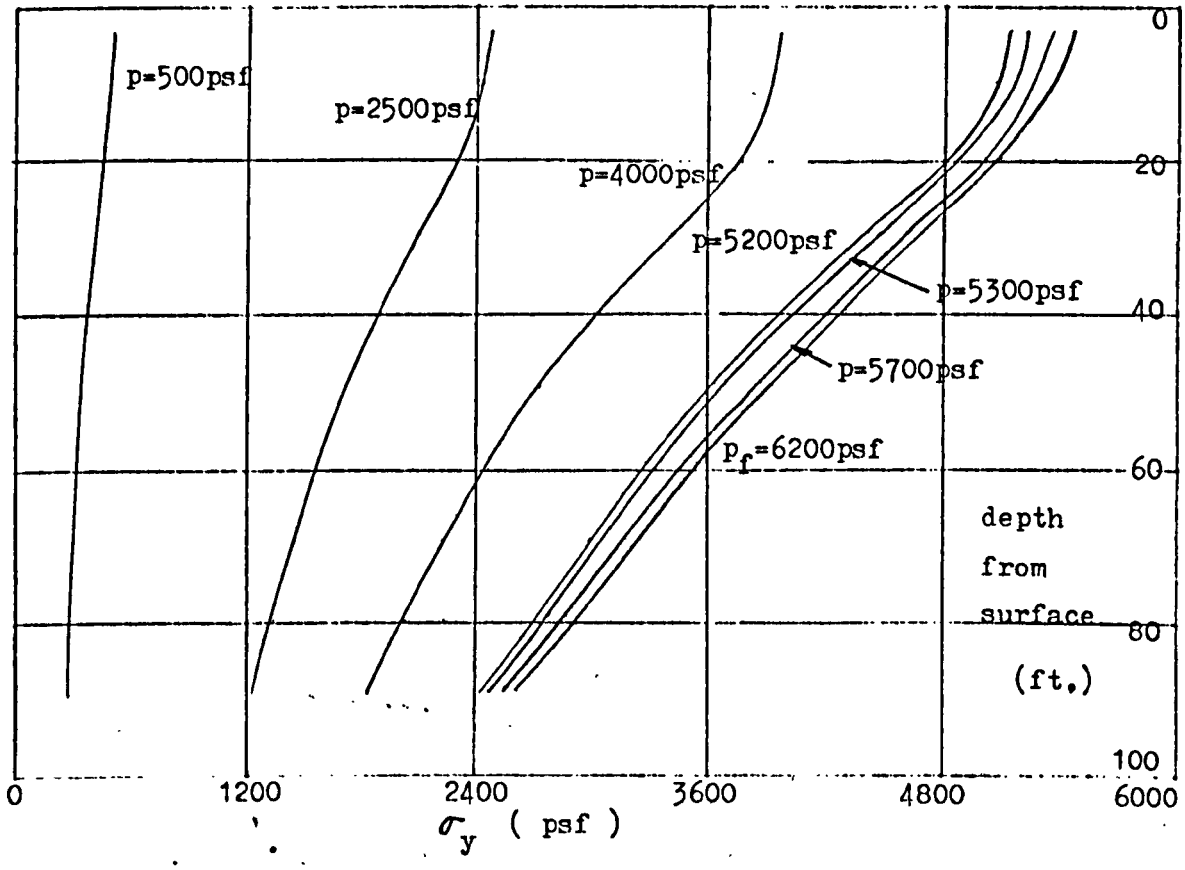

(c) σ_y distributions down centre of strip load

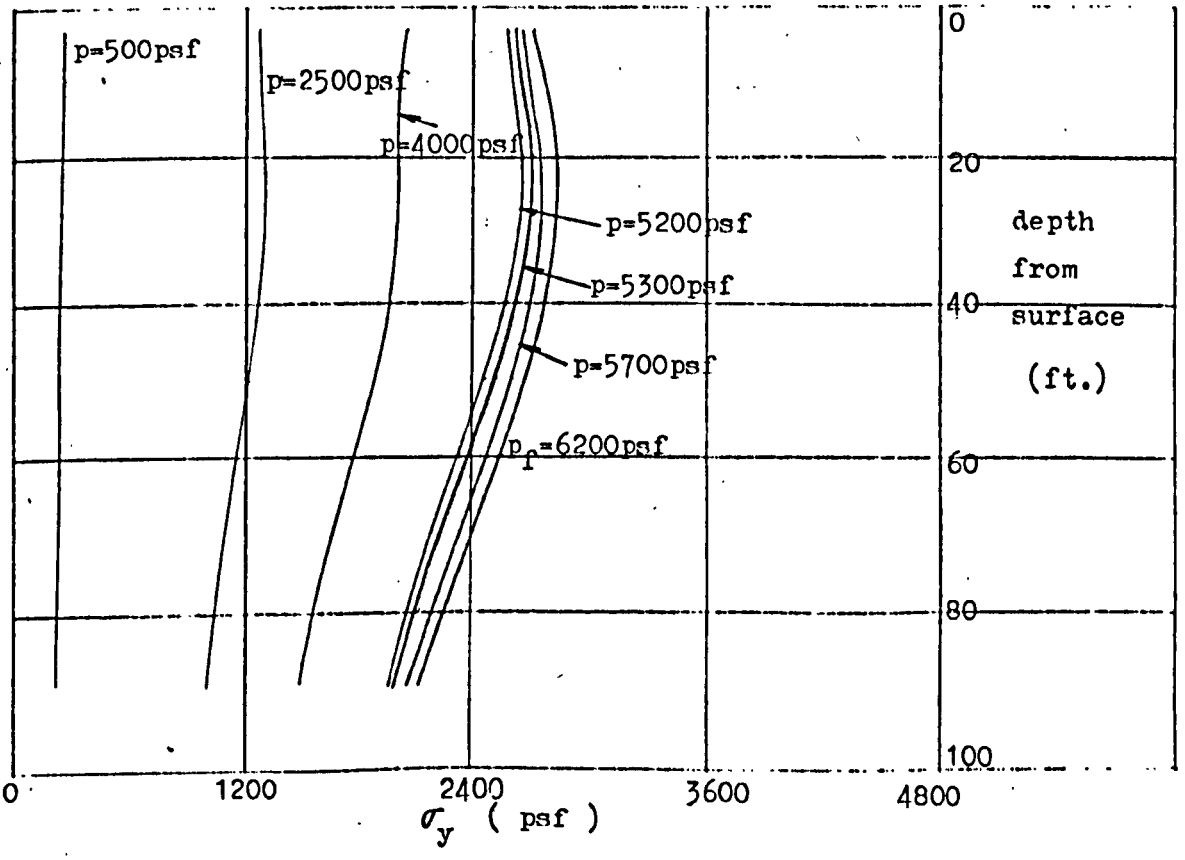

(d) σ_y distributions down edge of strip load

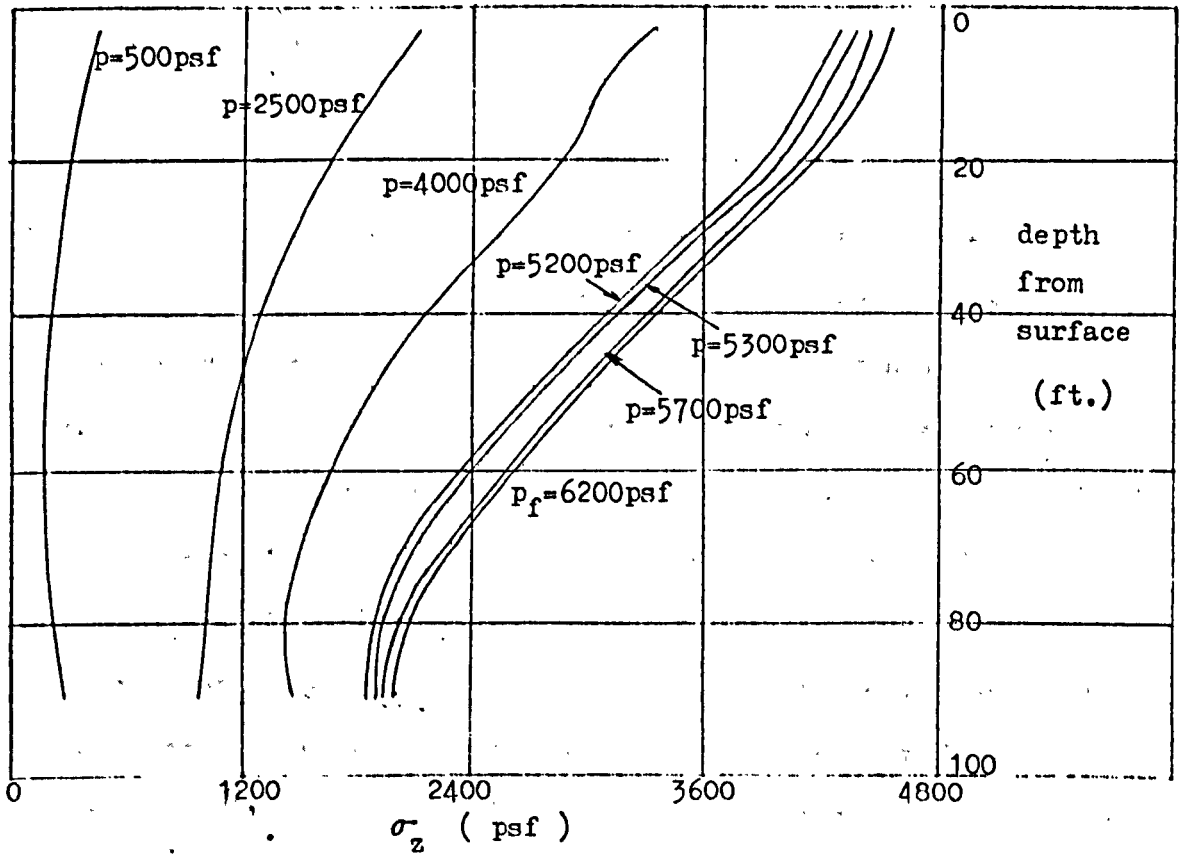

(e) σ_z distributions down centre of strip load

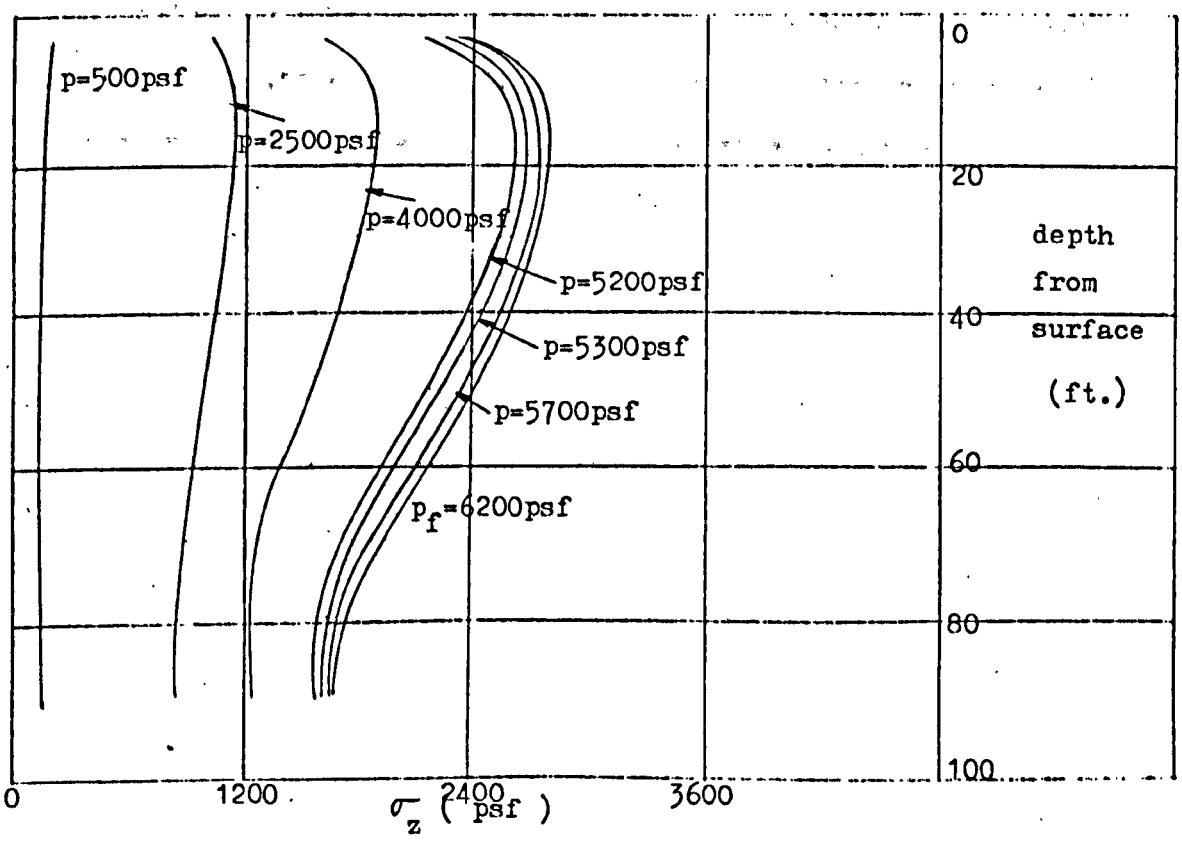

(f) σ_z distributions down edge of strip load

Fig. 83. Normal stress distributions down centre and edge

2.14.2. Post-peak softening

The previous study has been based on shear failure at peak deviator stress whereas it has been found that some post-peak softening generally occurs in undrained triaxial tests on normally consolidated as well as overconsolidated saturated clays (44). Fig. 84 shows the actual continuation of the triaxial test curve post peak based on the results obtained by Bishop (44) and a choice of sensitivity appropriate to the type of clay of the practical example of Fig. 22(a). Strictly speaking, the use of negative linear elastoplastic behaviour (CD) in conjunction with an associated flow rule is not a proper reflection of work softening in the context of plasticity theory (see pp. 101a). Nevertheless it does provide a simple means for studying post-peak behaviour. As in the previous model, (Section 2.14.1.), ultimate shear failure is modelled as non-work hardening. Also, by the same token as before, the following study is based on the basic model of Section 2.6. albeit with the present material behaviour.

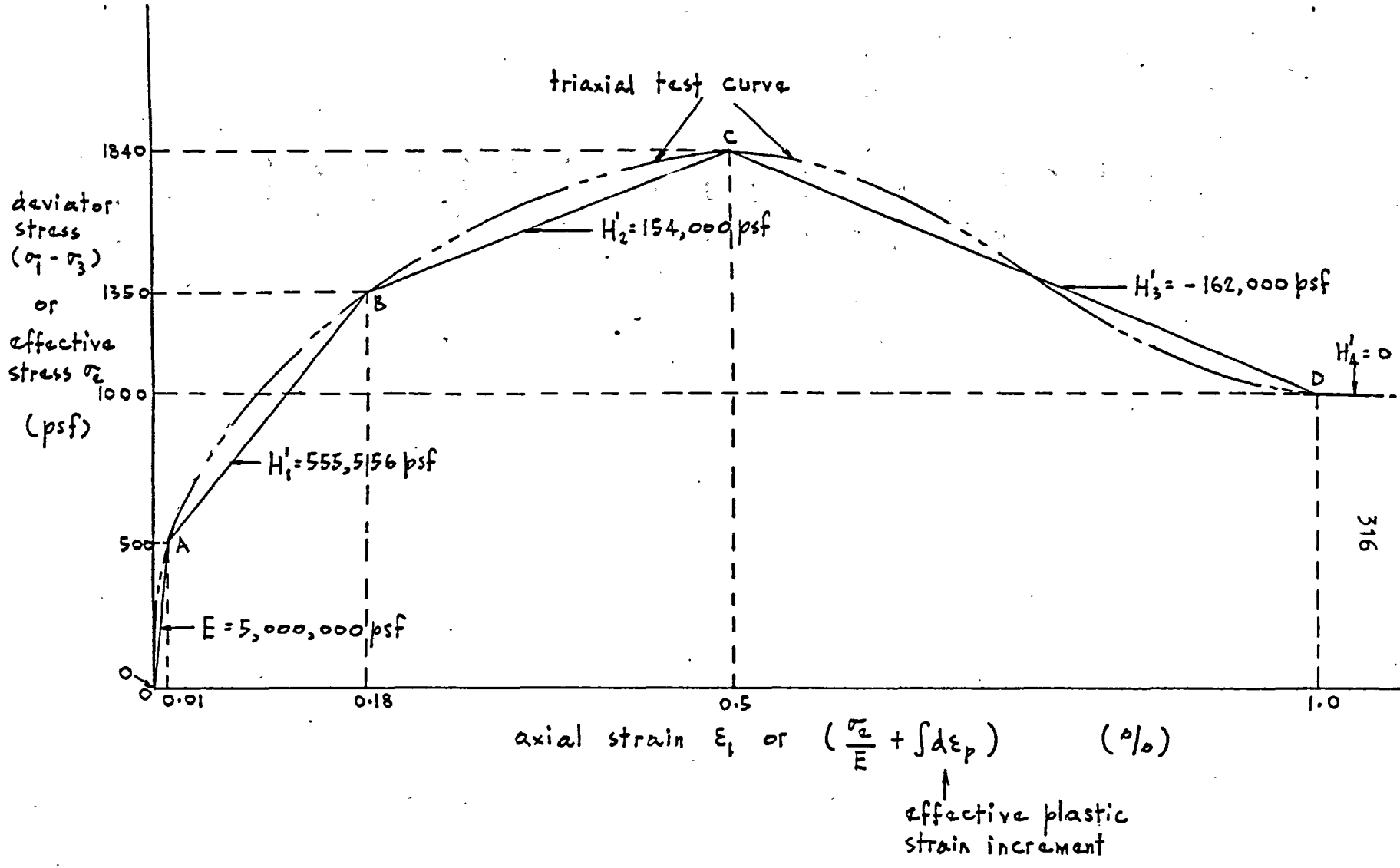

Fig. 84. Elastoplastic idealisation for triaxial test curve with post-peak softening

Fig. 85 shows the growth of the plastic enclave with increasing load p. Since the triaxial test curve is the same as for the previous model (Section 2.14.1.) up to peak strength (cf. Figs. 79 and 84), the remarks in Section 2.14.1. until the first yield element attains state C also apply here. The subsequent development of the plastic enclave and the conditions by which collapse is attained are, however, quite different here from those that have applied hitherto.

Further deformation of the above element due to additional loading leads to some stress reduction as it softens. This, in turn, leads to an increase in stress of the neighbouring elements for equilibrium. The softening has thus two effects: (a) more elements are brought nearer peak stress and (b) the layer deforms more than for the model of Section 2.14.1. at the same load. With further loading, more elements soften and become perfectly plastic after sufficient deformation. These elements, which are in the most advanced region from the outset - i.e. plastically speaking, form an enclave around the first to soften, as would be expected. By a similar process to the above, this enclave, representing an area of considerable stress reduction, causes a correspondingly wider surrounding area to be brought near peak stress for equilibrium, and much more deformation in the layer to maintain compatability than for the model of Section 2.14.1 at comparable loads. Finally, at a load of 4000 psf, events in the enclave appear to overtake those in the surrounding material so that the former undergoes

a continuing process of stress reduction with accompanying deformation without check by the latter. Large displacements thus occur characteristically of collapse.

The collapse load is therefore about +11% of that required to attain peak strength locally and -18% of that of the basic model. It would thus be unduly pessimistic to adopt the residual strength in the latter model from the point of view of collapse load.

The surface displacements as well as the normal stress distributions down the centre and edge of the strip load are presented in Figs. 86 to 88 for examination.

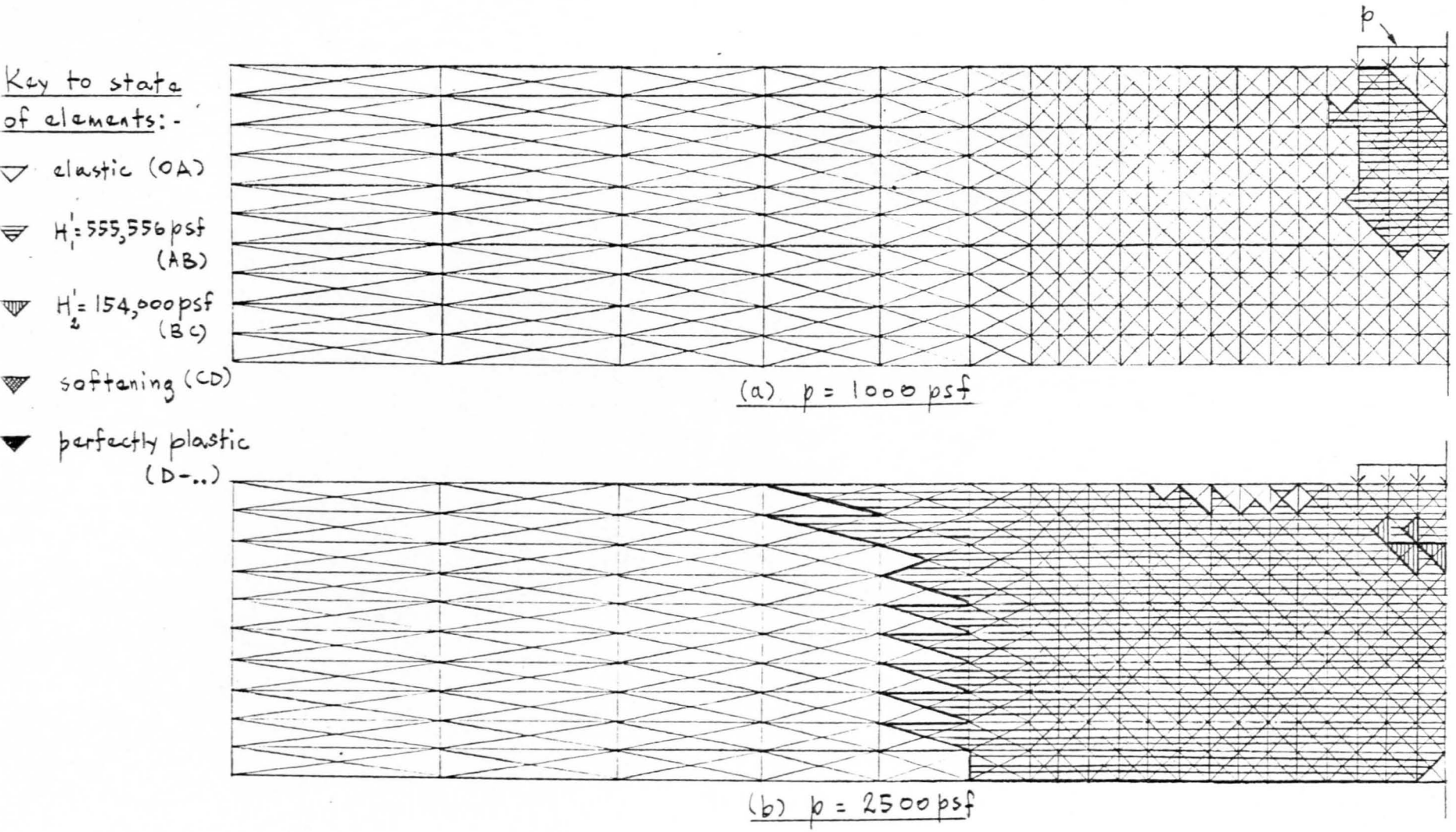
Key to state of elements:-
elastic (OA)
$H_1' = 555,556$ psf (AB)
$H_2' = 154,000$ psf (BC)
softening (CD)
perfectly plastic (D-..)
p
(a) p = 1000 psf
(b) p = 2500 psf

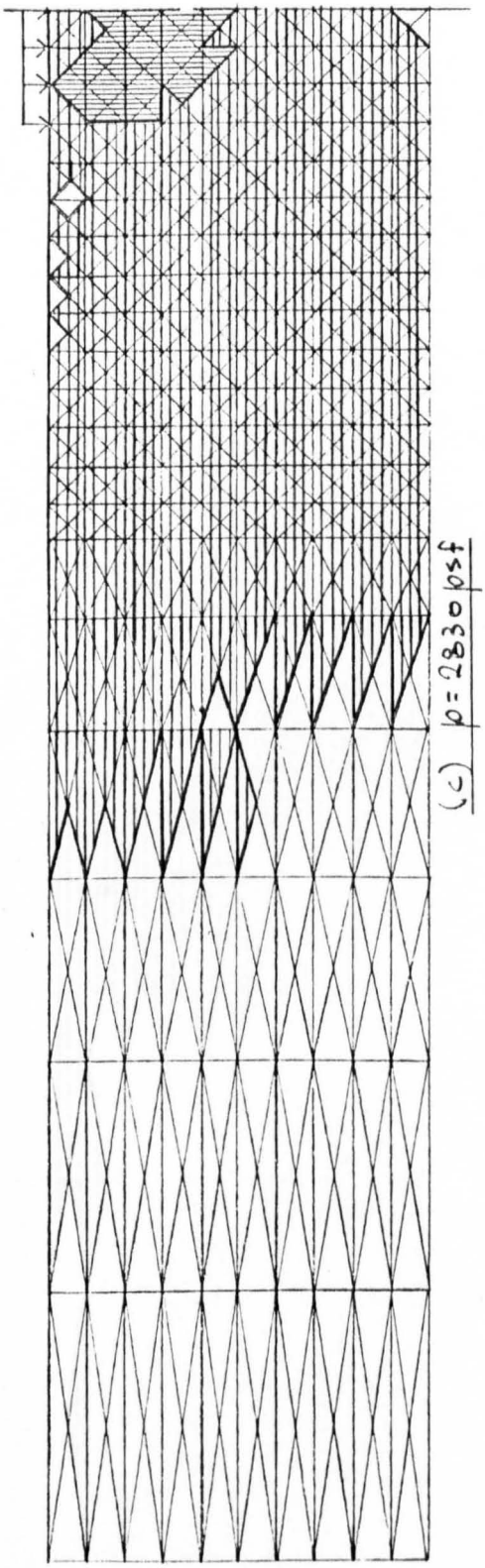

(c) $p = 2830$ psf

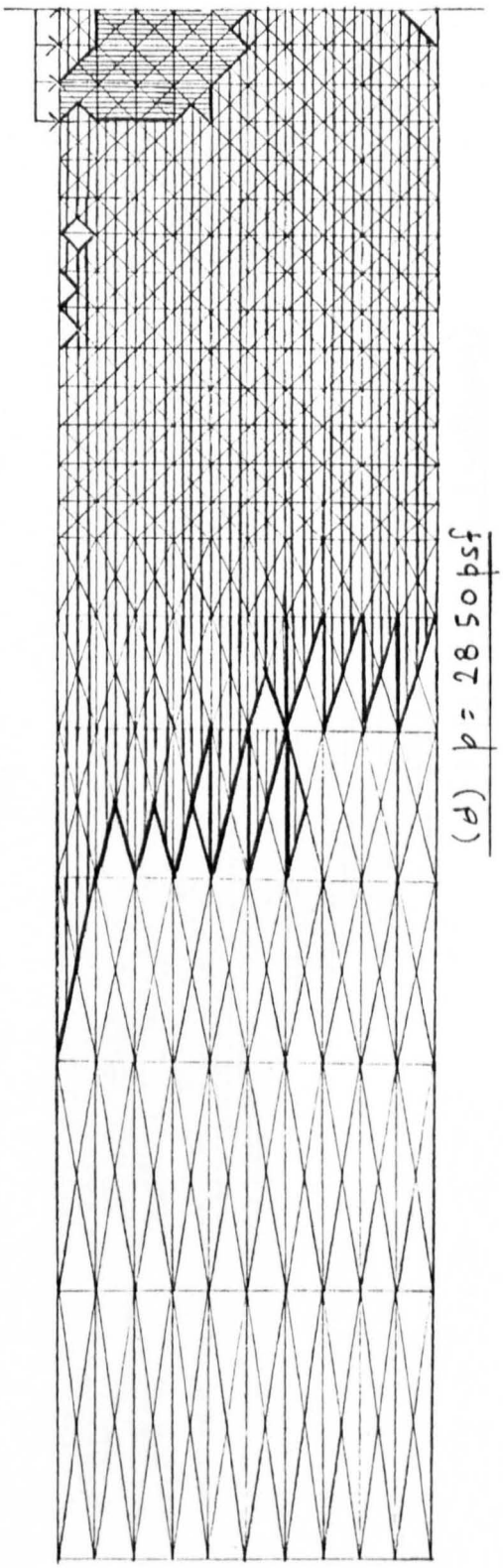

(d) $p = 2850$ psf

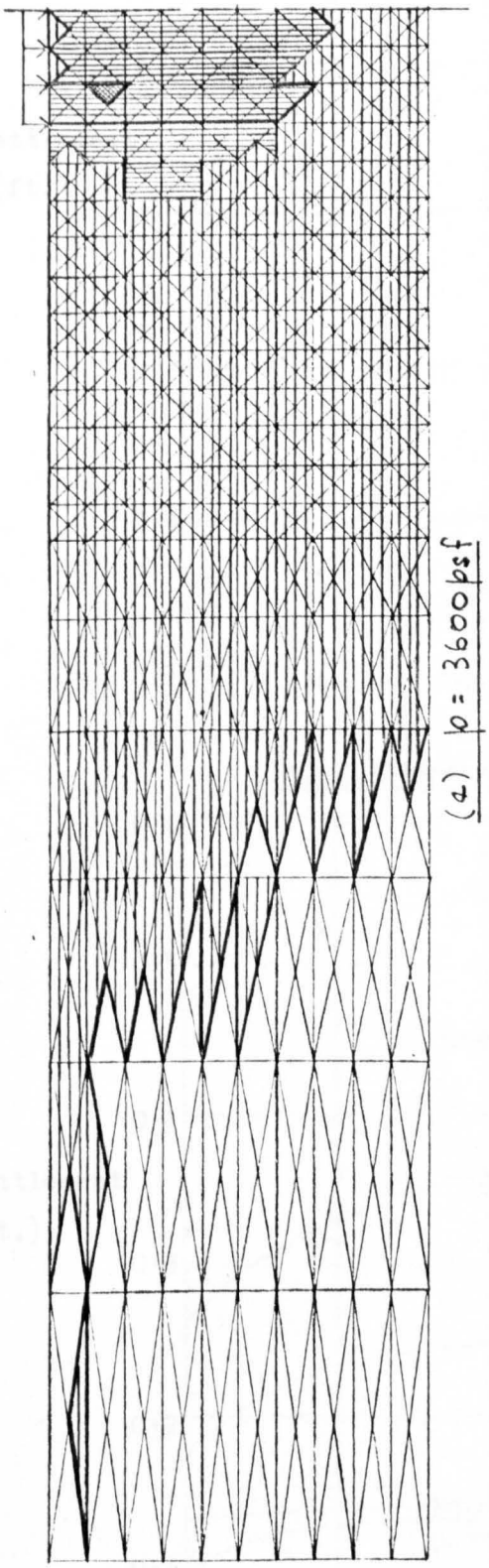

(e) $p = 3600$ psf

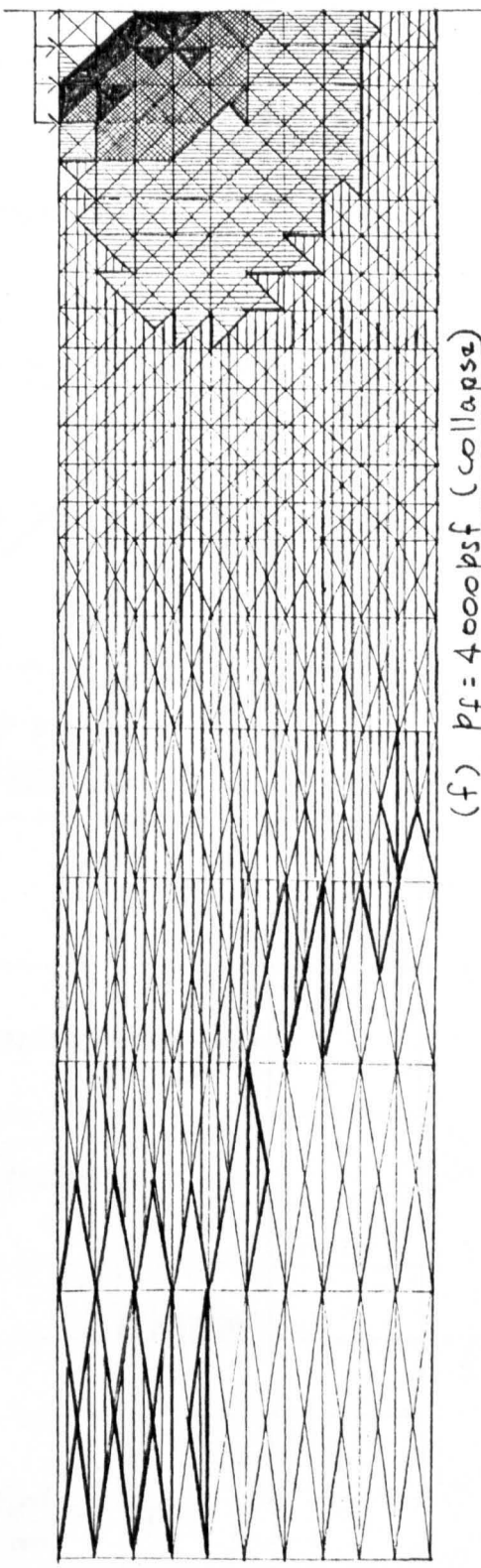

(f) $p_f = 4000$ psf (collapse)

Fig. 85. Growth of the plastic enclave to collapse

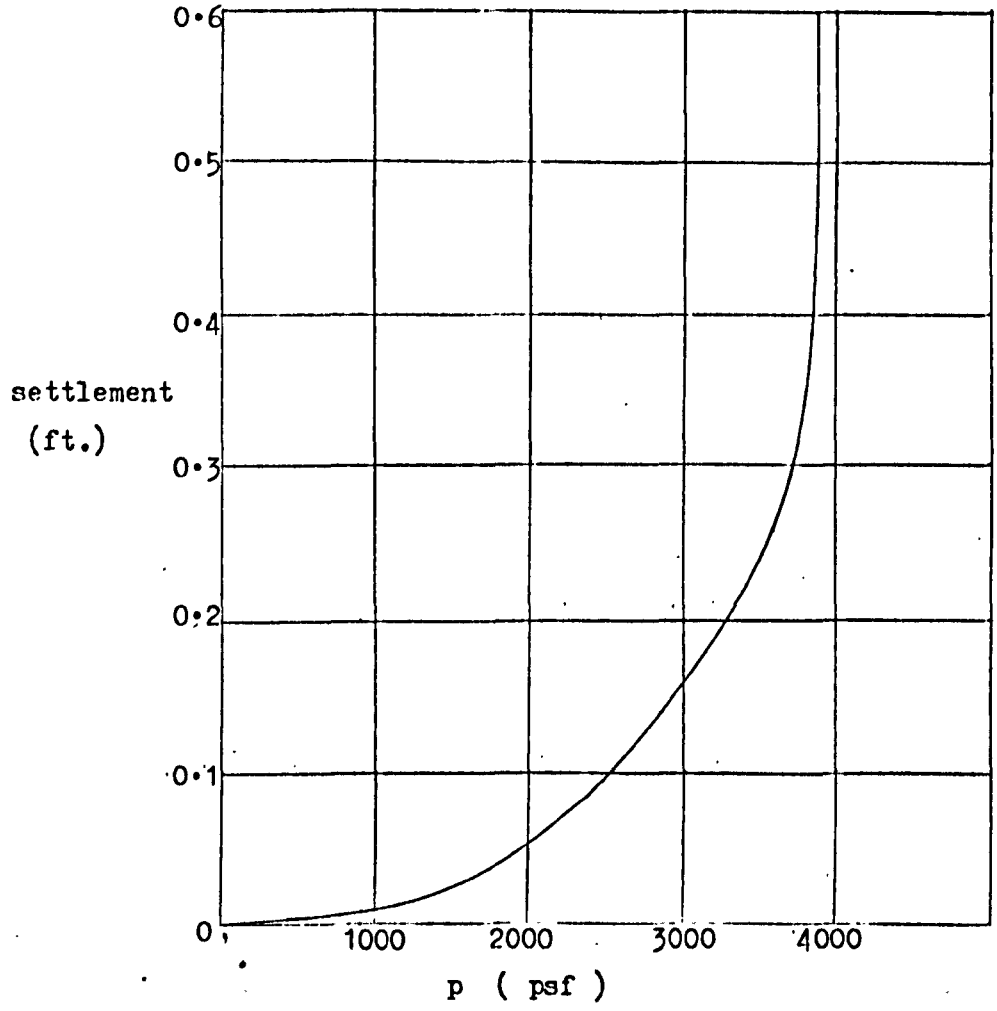

(a) Settlement-load plot

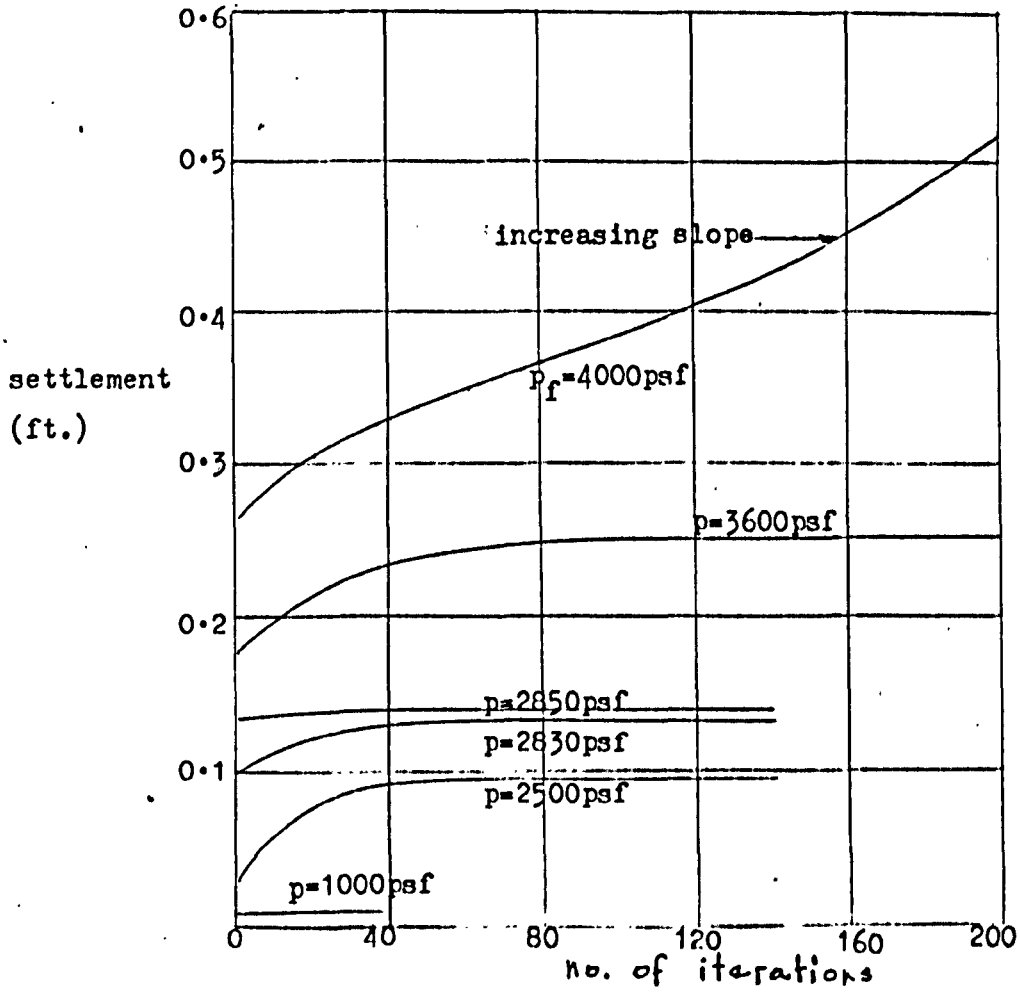

(b) Settlement-iteration plots

Fig. 86. Settlement curves for joint A

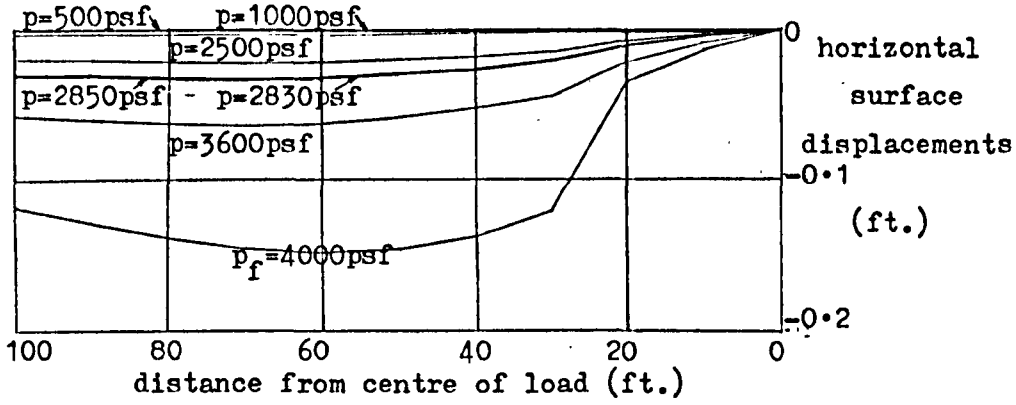

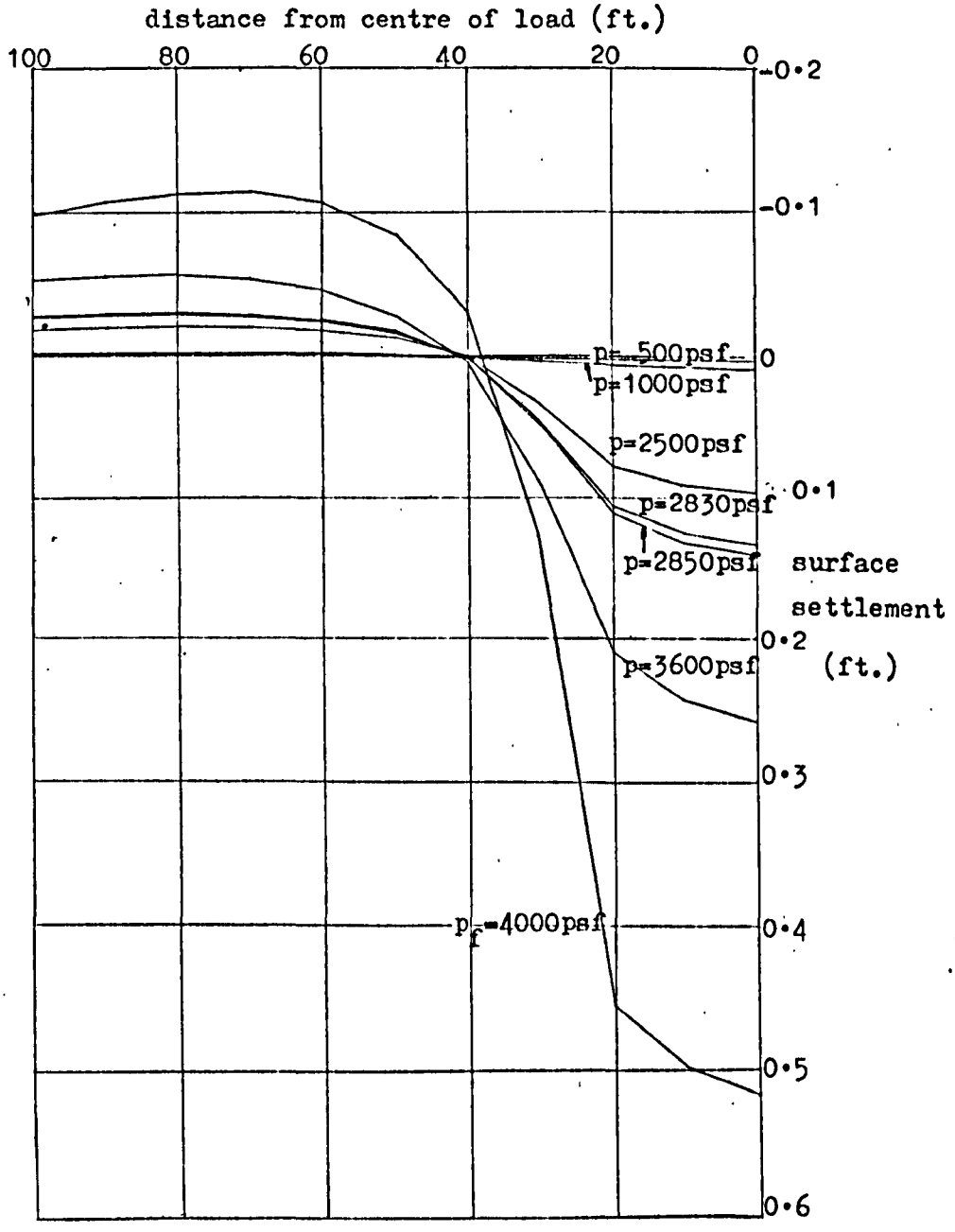

Fig. 87. Surface displacements

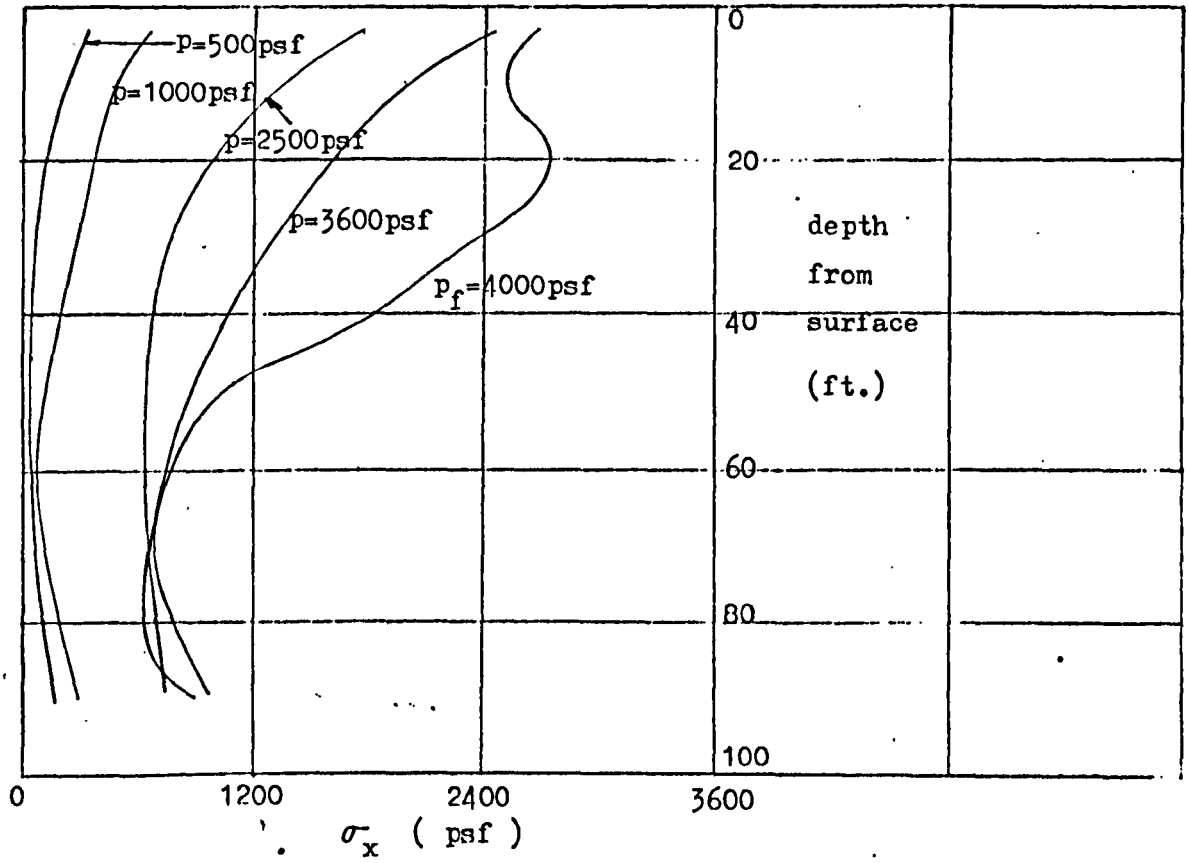

(a) σ_x distributions down centre of strip load

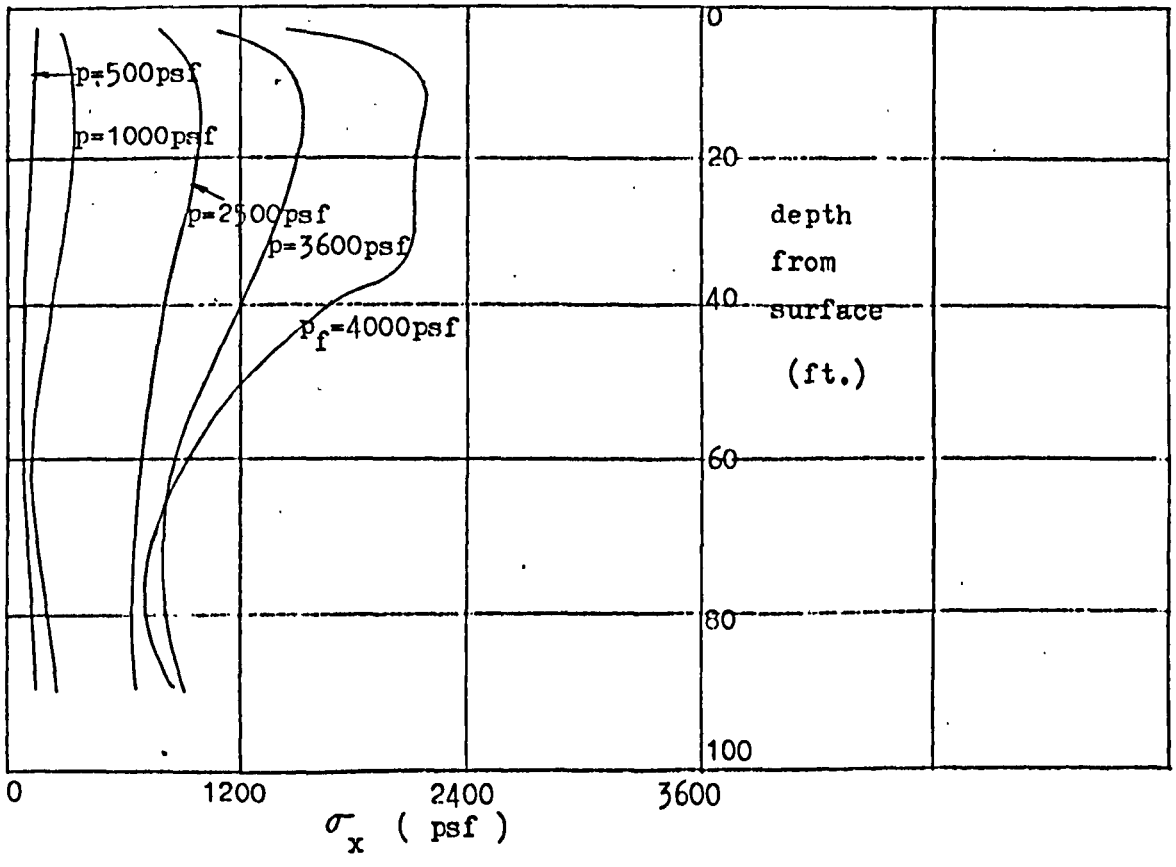

(b) σ_x distributions down edge of strip load

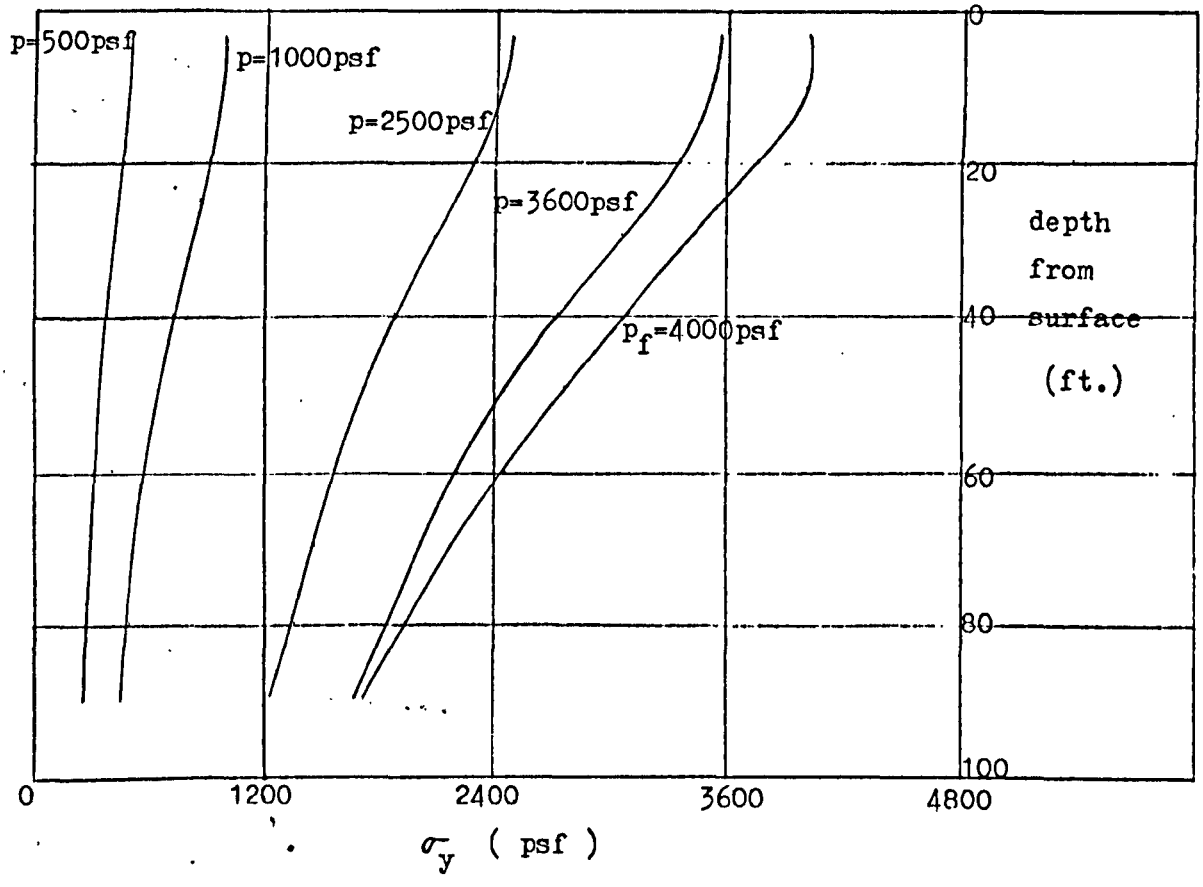

(c) σ_y distributions down centre of strip load

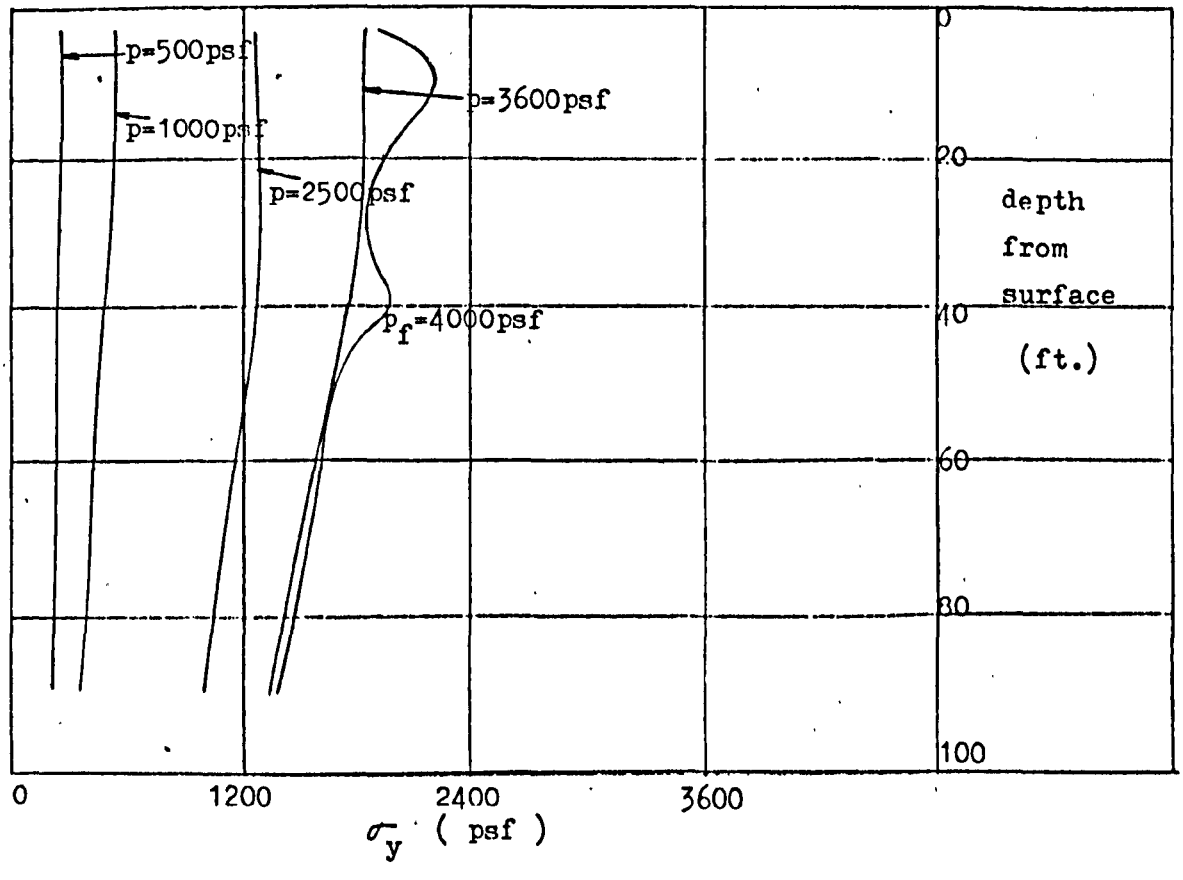

(d) σ_y distributions down edge of strip load

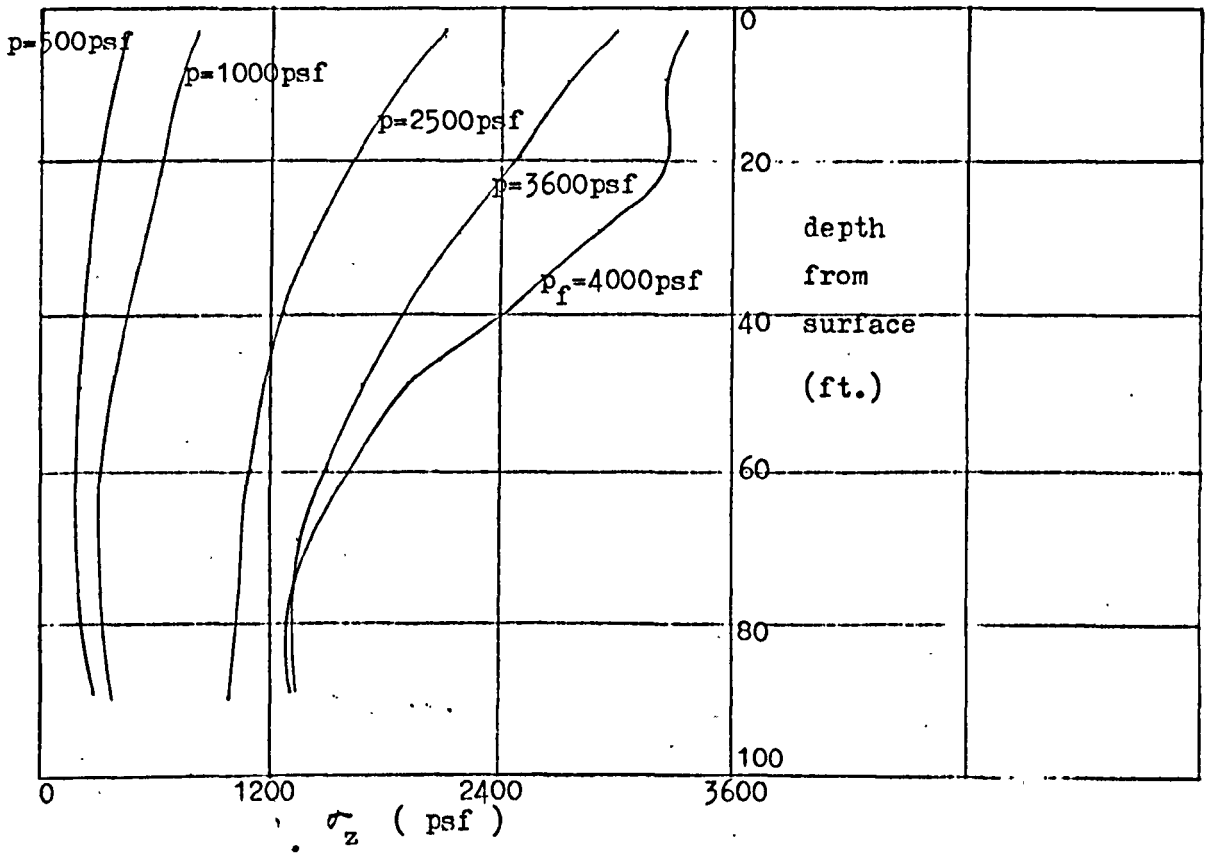

(e) σ_z distributions down centre of strip load

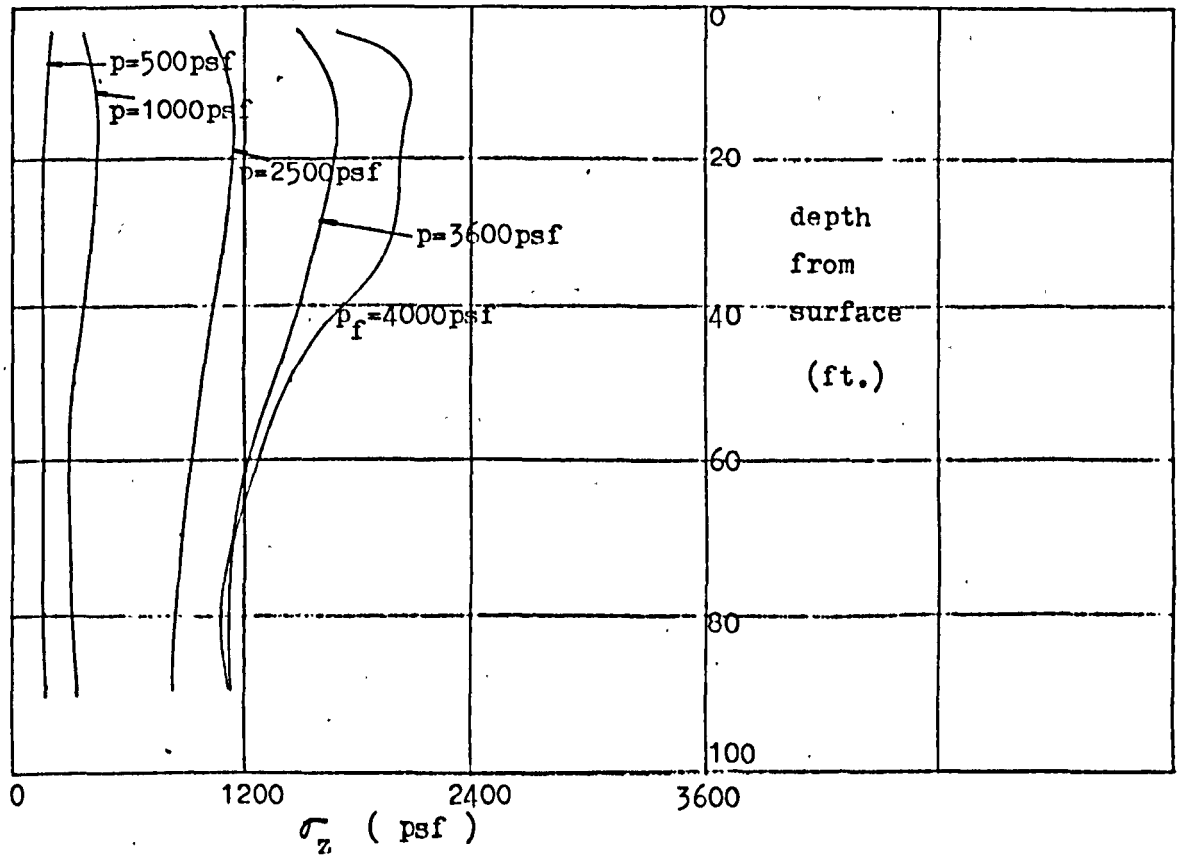

(f) σ_z distributions down edge of strip load

Fig. 88. Normal stress distributions down centre and edge of strip load

CHAPTER 3

DRAINED STRIP LOADING ON A CLAY LAYER, A VERTICAL CUT PROBLEM AND SOME PROPOSED FURTHER STUDIES

3.1. Introduction

When studying the failure of cohesive-frictional bodies of soil such as some drained clays, due to strip loading, it is customary to idealise the material behaviour as elastic-rigid, perfectly plastic, and obeying the Mohr-Coulomb yield criterion (purely frictional soils are treated as special instances of zero cohesive strength). By adopting a linear elastic phase instead, the resulting material could provide a useful basis for parametric studies on drained settlement and bearing capacity of the soil body, over the entire loading range, along the lines of the undrained studies of Chapter 2.

For this purpose, the necessary adaptations to the elastoplastic models of Chapter 1 to incorporate the alternative Mohr-Coulomb yield criterion are indicated herein.

The assumption of an associated flow rule in the derivation is, however, at odds with observed volume changes, i.e. approximately zero volume change in the ultimate condition. Although this may not be a serious flaw from the point of view of determining

the collapse load (45), a derivation based on a non-associated flow rule (possibly in conjunction with a changing Poisson's ratio.) may be necessary to render a proper account of the deformational behaviour of the material at all stages of loading.

Another problem is the inability to model the irrecoverable strains that inevitably accompany increasing mean pressure. The spherical end-cap of Drucker et al. (46) and the bullet-shaped, and latterly, ellipsoidal yield surfaces of Roscoe et al. (47), are examples that provide for such behaviour.

Nevertheless, it would be a useful initial step to ascertain whether the present numerical approach can model accurately simple behaviour for which a known result exists. Accordingly, the problem of uniform strip loading on an isotropic, homogeneous layer of linear elastic, perfectly plastic material with a Mohr-Coulomb yield criterion and an associated flow rule, to which a classical solution for the collapse load is applicable, is studied.

For this purpose an example of the above loading on a drained, overconsolidated clay layer, based on the practical problem of Chapter 2, is devised.

The results will be shown to be promising, and the next step is to implement any necessary modifications - as suggested above - before conducting parametric studies along the lines proposed. The initial study also provided some useful experience of the behaviour over the entire loading range.

Whilst slip-line analyses have been restricted to the collapse of homogeneous half-spaces on grounds of the difficulties in arriving at a rigorous mathematical solution, the numerical model, on the other hand, can deal with material non-uniformities and boundary conditions over a wide range.

Next, "Reduced Stack Addition" is developed to deal with the vertical cut problem. As before, the accuracy of the numerical method is checked against a known solution - in this case, of the critical height. For this purpose, an idealisation of the undrained layer of Chapter 2 is adopted.

Again, the results are promising, thus justifying further undrained as well as drained parametric studies on vertical cuts in soil bodies. By this method, the behaviour of the vertical cut at heights less than critical (i.e. prior to collapse) may also be studied.

Adaptations to the "Stack Addition" procedure of Chapter 1 to deal with other important soil mechanics boundary value problems - e.g. earth dams, embankments, tunnels, etc. - are next outlined. This widens the scope for further parametric studies.

Finally, other important soil mechanics topics are discussed within the present context.

3.2. Uniform strip loading on an isotropic, homogeneous layer of linear elastic, perfectly plastic material obeying the Mohr-Coulomb yield criterion and its associated flow rule

3.2.1. A practical example and the soil mechanics idealisation

At a neighbouring, alternative site for the warehouse of Chapter 2, a clay layer similar to the one shown in Fig. 22 exists, say, except it is overconsolidated as a result of the removal of some overburden at an earlier stage of its geological history.

The effect of overconsolidation is to increase E_u. Also, because the overconsolidation ratio decreases with depth, there is a corresponding decrease in the rate of increase of E_u (34d). Nevertheless, according to Ladd (48), for the factor of safety of 1.5 adopted against shear failure, it is reasonable to assume no significant change in the E_u distribution of Fig. 22 due to overconsolidation.

Fig. 89 illustrates a simple initial assessment of the practical problem based on the idealisation of Section 2.6. Drained loading is effected by application of the storage load at a rate that is slow compared with the rate of consolidation of the layer. The drained Young's modulus $\bar{E}$ is taken to be $2E_u(1+\bar{\nu})/3$ (34c) at mid-depth, and a drained Poisson's ratio, $\bar{\nu} = 0{\cdot}3$, is appropriate for this clay (34e). Based on values given by Lambe (34f) a cohesion $\bar{c} = 150$ psf

and a friction angle. $\bar{\phi} = 18^{\circ}$. are adopted.

The finite element mesh for the Tresca models of Chapter 2 is used. It was shown to model the elastic as well as the plastic behaviour fairly well and leads to close agreement with the Prandtl collapse load for a c-ϕ material.

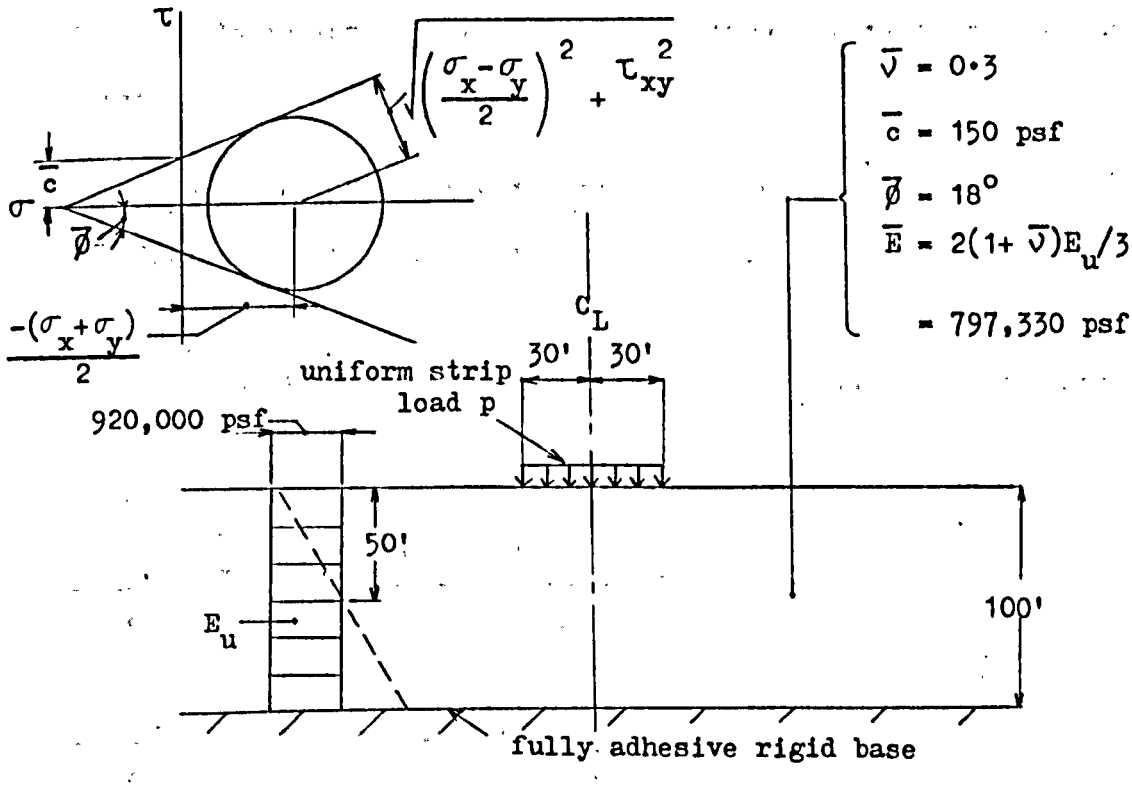

Fig. 89. A simple idealisation of the drained problem

3.2.2. Adaptations to the elastoplastic models of Chapter 1 to incorporate the alternative Mohr-Coulomb yield criterion and its associated flow rule .

When applying the Initial Stress Method, only the expressions for F, A and $\left\{\frac{\partial F}{\partial \{\bar{\sigma}\}}\right\}$ need be altered, in general, when replacing one type of elastoplastic material of the present category with another (see pp. 81 ,).

For a Mohr-Coulomb yield criterion, and reverting to the terminology of Chapter 1, we have,

$$F = \left(\frac{\sigma_x+\sigma_y}{2}\right)\sin\bar{\phi} + \sqrt{\left(\frac{\sigma_x-\sigma_y}{2}\right)^2 + \tau_{xy}^2} - \bar{c}\cos\bar{\phi} \quad \ldots\ldots (\ 72\ ) \text{ - see}$$

Fig. 89 , so that

$$\frac{\partial F}{\partial \sigma_x} = \tfrac{1}{2}\left\{\sin\bar{\phi} + \frac{\tfrac{1}{2}(\sigma_x-\sigma_y)}{\sqrt{\tfrac{1}{4}(\sigma_x-\sigma_y)^2 + \tau_{xy}^2}}\right\},$$

$$\frac{\partial F}{\partial \sigma_y} = \tfrac{1}{2}\left\{\sin\bar{\phi} - \frac{\tfrac{1}{2}(\sigma_x-\sigma_y)}{\sqrt{\tfrac{1}{4}(\sigma_x-\sigma_y)^2 + \tau_{xy}^2}}\right\},$$

$$\frac{\partial F}{\partial \tau_{xy}} = \frac{\tau_{xy}}{\sqrt{\tfrac{1}{4}(\sigma_x-\sigma_y)^2 + \tau_{xy}^2}} \quad \text{and} \quad \frac{\partial F}{\partial \sigma_z} = 0 \quad \ldots\ldots (\ 73\ ).$$

The expressions of Eqn. 73 are the plane strain equivalents of $\left\{\frac{\partial F}{\partial \{\bar{\sigma}\}}\right\}$ (see pp. 67), and, by a similar procedure to that outlined

in pp. 68 to 70, it can be readily shown that $A = -H' = 0$ for a perfectly plastic material.

Thus, to obtain the present model, only the above changes need be made to the elastoplastic model of Section 2.6. By the same token, the same changes could be applied to the other elastoplastic models of Chapter 1 to obtain corresponding Mohr-Coulomb models.

A note of caution must be sounded here: the above choice of F is not based on the equivalent stress. This makes no difference to the yield criterion since $F = 0$, and neither does it invalidate the use of the expressions of Eqn. 73 since the resulting difference, which is simply a constant, can be considered to be absorbed into λ, which is later eliminated. There is, however, an effect on A, whose derivation in Chapter 1 is now complicated by the existence of two material constants in the yield criterion. Nevertheless, this does not affect the validity of $A = 0$ for perfect plasticity, stated earlier.

The ability of the present numerical approach to deal with other perfectly plastic, elastoplastic materials of the present category was also assessed.

By adopting a von Mises material in a problem similar to that of Section 2.6., the collapse load $p_f = (\pi + 2)\, c_u$ was again overestimated by less than 4%. However, unlike the Tresca material where the c_u value is 0·5 times the uniaxial yield stress, c_u for the von Mises material must be taken as $1/\sqrt{3}$ times the uniaxial yield stress. This result thus supports the view that since the same slip-

line field applies to both materials, the same collapse load will be obtained (23c).

A Drucker-Prager material (43) was also adopted in the problem and was found to lead to no significant difference from the Mohr-Coulomb collapse load obtained by Prandtl (30), thus subscribing to the assertion by Drucker and Prager (43) that their yield surface is a proper (i.e. a reasonable) generalisation of Mohr-Coulomb behaviour. This is in spite of Bishop's assertion (49) that the Drucker-Prager material can lead to an overestimation of strength.

The flexiblity of the choice of F , mentioned earlier, was also tested. For the above Drucker-Prager problem, $\overline{\phi}$ was set to zero, effectively leading to the assumption of a von Mises material, although with F not based on effective stress. Nevertheless, the same collapse load as that for F based on effective stress was obtained.

In these material studies, the same boundary insensitivity mentioned in Section 2.6. was found.

3.2.3. Adaptations to the flow chart of Section 1.3.3.1. for the Mohr-Coulomb model of Section 3.2.

Block	Adaptations
H1	Set $F(\sigma') = \frac{(\sigma'_x + \sigma'_y)}{2} \operatorname{Sin} \bar{\phi} + \frac{1}{2}\sqrt{(\sigma'_x - \sigma'_y)^2 + \tau'^2_{xy}}$
H2	Deleted
H3	Is $F(\sigma') - \bar{\sigma} \leqslant 10^{-11}$
H4	Set $F(\sigma_o) = \frac{(\sigma_{o_x} + \sigma_{o_y})}{2} \operatorname{Sin} \bar{\phi} + \frac{1}{2}\sqrt{(\sigma_{o_x} - \sigma_{o_y})^2 + \tau^2_{o_{xy}}}$
H5	Deleted
H6	Is $F(\sigma_o) - \bar{\sigma} < -10^{-11}$
I1	Set $s = \bar{\sigma} / F(\sigma_o)$
J2	Deleted
J3	Deleted
J4	Calculate $\left\{\frac{\partial F}{\partial \{\sigma\}}\right\}$
J8	Deleted
J9	Set $\{\sigma_o\} = \{\sigma_o\} + \{\Delta\sigma_1\}$
J10	Calculate and accumulate initial stresses $\{\Delta\sigma''\}$
J15	Is $\lvert F(\sigma') - \bar{\sigma} \rvert \leqslant 10^{-11}$?

3.2.4. Growth of the plastic enclave and collapse

Fig. 90 shows the growth of the plastic enclave with increasing load. First yield occurred at about 600 psf in an element beneath and near to the load. With further loading, a well-defined plastic enclave develops and spreads downwards initially, then laterally. The lateral spread is substantially in the lower half of the layer, and this is attributable to the relatively low Poisson's ratio. At 2060 psf, the enclave penetrates the free surface some way from the load so that it can then deform freely. As a result, collapse occurs due to pressure exerted by the strip.

The enclave had, in fact, reached the surface earlier but was still contained by the strip and the elastic body respectively on either side.

The above collapse load is only some 5% higher than the Prandtl result,

$$\bar{c}\cot\bar{\phi}\left\{e^{\pi\tan\bar{\phi}}\tan^2(45^\circ+\frac{\bar{\phi}}{2})-1\right\},$$

for the half-space (30). As some of this difference may be attributed to the underestimate of stresses by the numerical method, the strengthening by replacement of the half-space material with rigid boundaries is thus marginal. Indeed, the collapse load is quite insensitive to the proximity of reasonably spaced boundaries, thus supporting the use of the Prandtl result for less extensive bodies of soil.

By contrast to its purely cohesive counterpart, the present

cohesive-frictional model has a plastic enclave of far greater lateral extent at collapse.

Furthermore, the existence of compressive stresses increases the strength against local shear failure, thus deferring first yield. By the same token, further increases in the compressive normal stresses at collapse lead to a relatively higher collapse to first yield load ratio.

Finally, there is a more gradual development between the onset of a predominantly lateral spread of the plastic enclave and collapse.

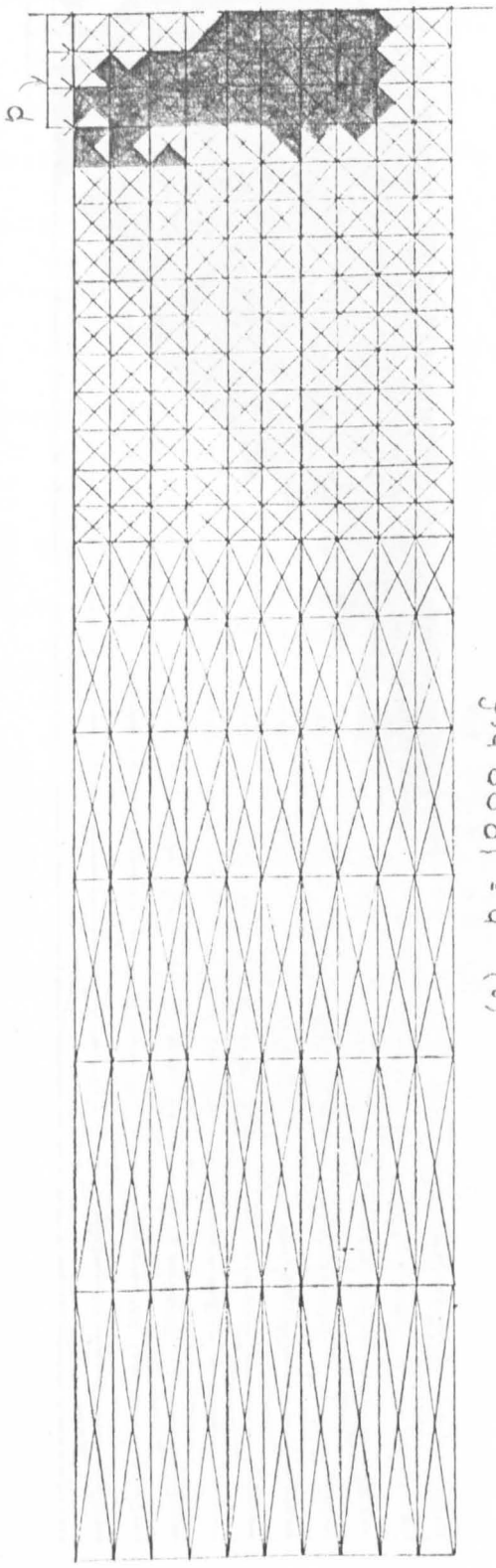

(a) $p = 1000$ psf

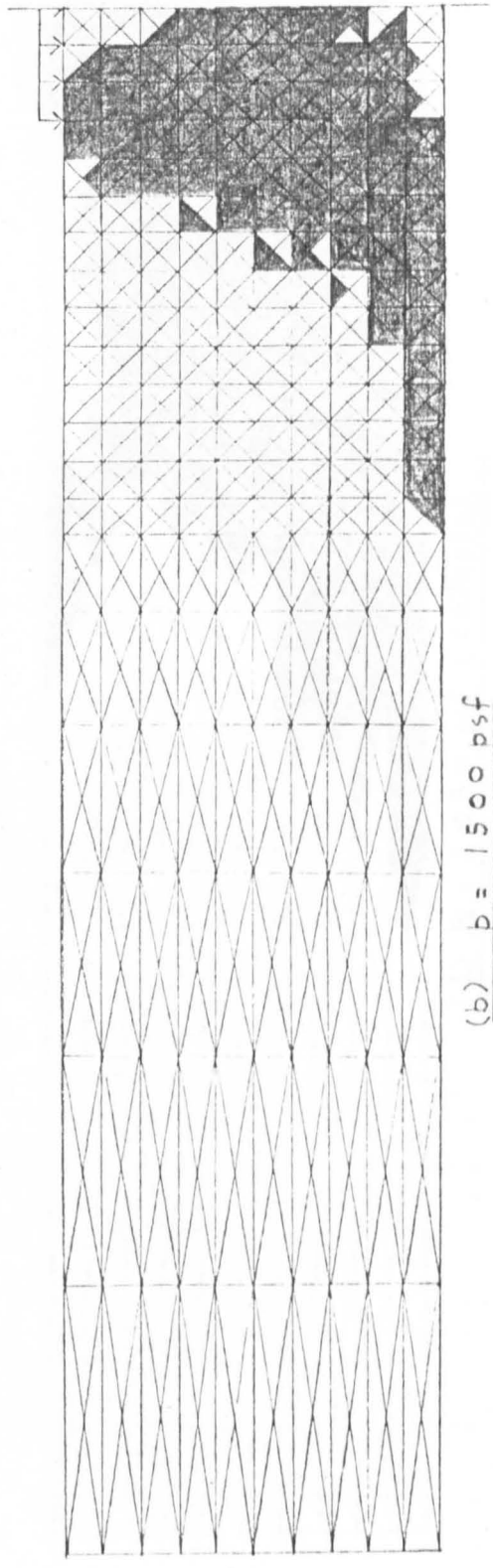

(b) $p = 1500$ psf

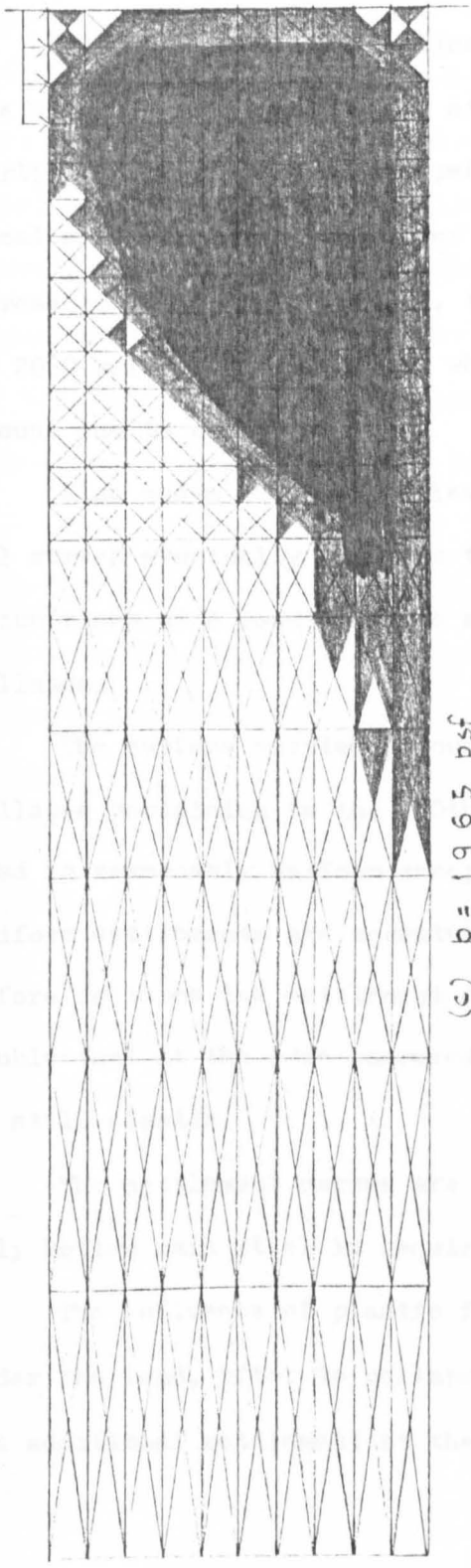

(c) $p = 1965$ psf

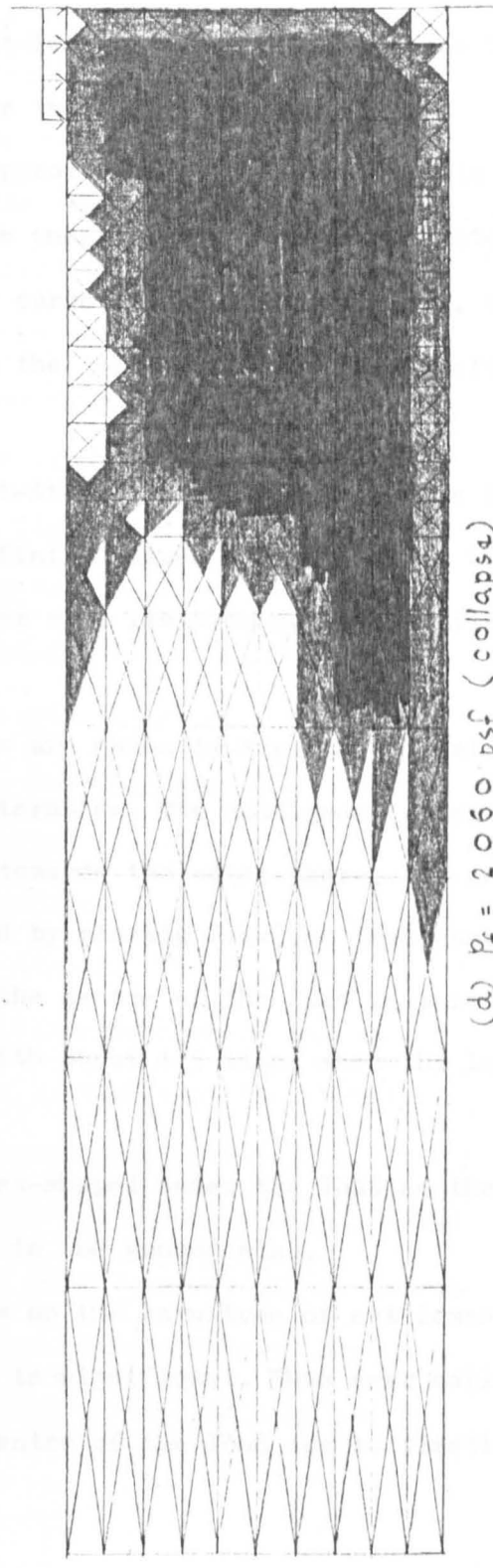

(d) $p_f = 2060$ psf (collapse)

Fig. 90. Growth of the plastic analysis to collapse

3.2.5. Surface displacements

Fig. 91 shows the settlement-load plot for joint A (see inset). The curve steepens noticeably after the initial linear elastic portion (first yield at 600 psf approximately), characteristic of local shear failure. Soon after the onset of a predominantly lateral spread of the plastic enclave, the curve steepens more rapidly, and at 2060 psf, becomes vertical when the joint settles by an indefinite amount due to collapse.

Also shown are the settlement-iteration curves at various loads. All curves eventually converge to finite values except that at 2060 psf which rises at a constant rate after some iterations, thus confirming collapse.

The surface settlement curves are shown in Fig. 92 , that at collapse pertaining to the 200th iteration. The settlement under the load is reasonably uniform except towards the edge; there, the non-uniform settlements are accentuated by plastic flow, so that just before collapse the settlement at the centre of the load is more than double that at the edge compared with about 1·5 times when the layer is still elastic.

The settlement curves are dish-shaped under the load so that only bottom main steel is required in the ground slab.

The influence of plastic flow on the magnitude of settlements under the load, prior to collapse, is significant. Thus near collapse, the additional settlement at the centre of the load due to plastic

flow is about 50% of the total settlement. However, a design bearing capacity on the basis of local shear failure at the "knee" of the settlement-load curve of Fig. 91 would be unduly pessimistic since even when approaching collapse the bending moments in the slab arising from the present settlements can be readily resisted. The above results also show that the influence of plastic flow on the magnitude of settlement and the differential settlements of the load in the present model is less pronounced than that found for the corresponding purely cohesive model of Section 2.6.

Despite the proximity of the rigid base, there is little heave when the layer is still elastic due to the relatively low Poisson's ratio. As the layer becomes increasingly plastic, however, substantial heave develops. More displaced material tends to accumulate nearer the load as plastic flow increases and consequently, the positions of the start of and the maximum surface heave move towards the load, steadily diminishing left of the maximum.

Initially, when the layer is elastic, the horizontal surface displacements around the strip are directed towards its centre (where the horizontal displacement is zero), with very small outward displacements farther away. With increasing plastic flow, however, these displacements become very small under the strip, followed by an abrupt change towards its edge, and large outward displacements outside the strip. Also, the point of maximum outward displacement occurs nearer the load, gradually diminishing to the left, as for the heave;

towards collapse, it coincides with the point of maximum heave.

The above behaviour of the surface displacements as the layer becomes more plastic, viz., the

(a) abrupt change in direction around the edge of the strip,

(b) relatively more heave and outward horizontal displacements occurring nearer the strip, and gradually diminishing away from it, and

(c) reduction in inward horizontal displacements under the strip, and subsequent reversal in direction,

may, as with the cohesive model of Section 2.6., be attributed to the tendency to localise the displacement of material.

At collapse, this material settles under the load, moves laterally, then finally emerges as surface heave in a restricted area outside of which is a relatively static region of plastic, underlain by elastic material. A similar behaviour is predicted by slip-line analysis. As with the cohesive model, the lateral extent of the region of intense movement is approximately where the enclave emerges from the free surface and is thereby relatively wider; it roughly agrees with the lateral extent of Hill's (19b) slip-line field.

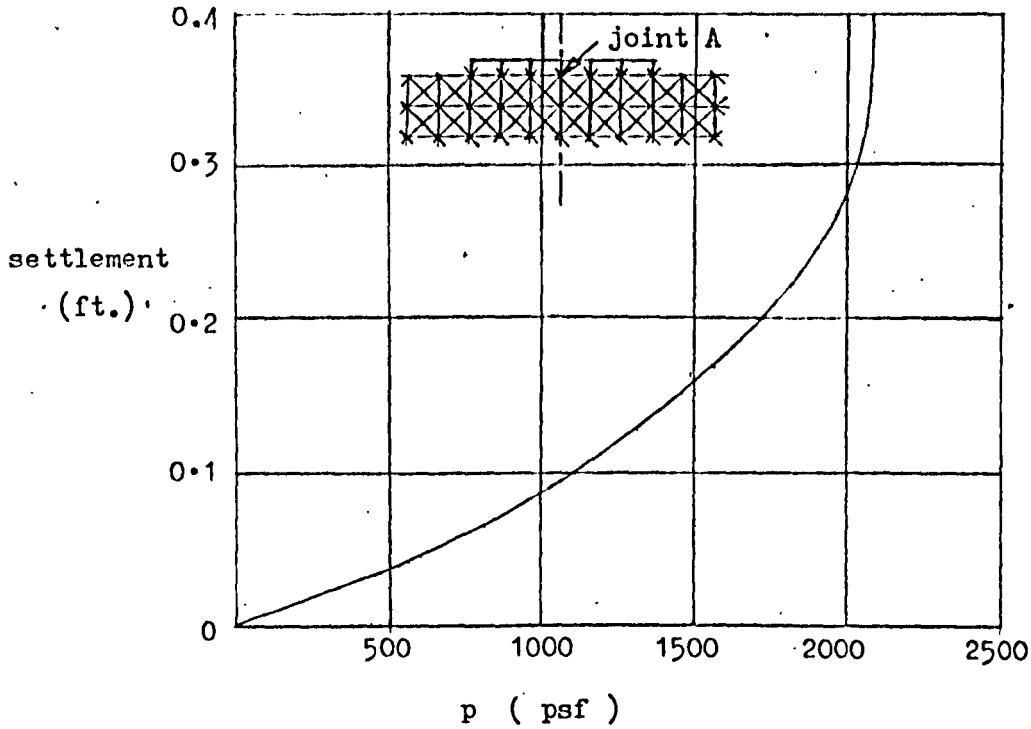

(a) Settlement-load plot

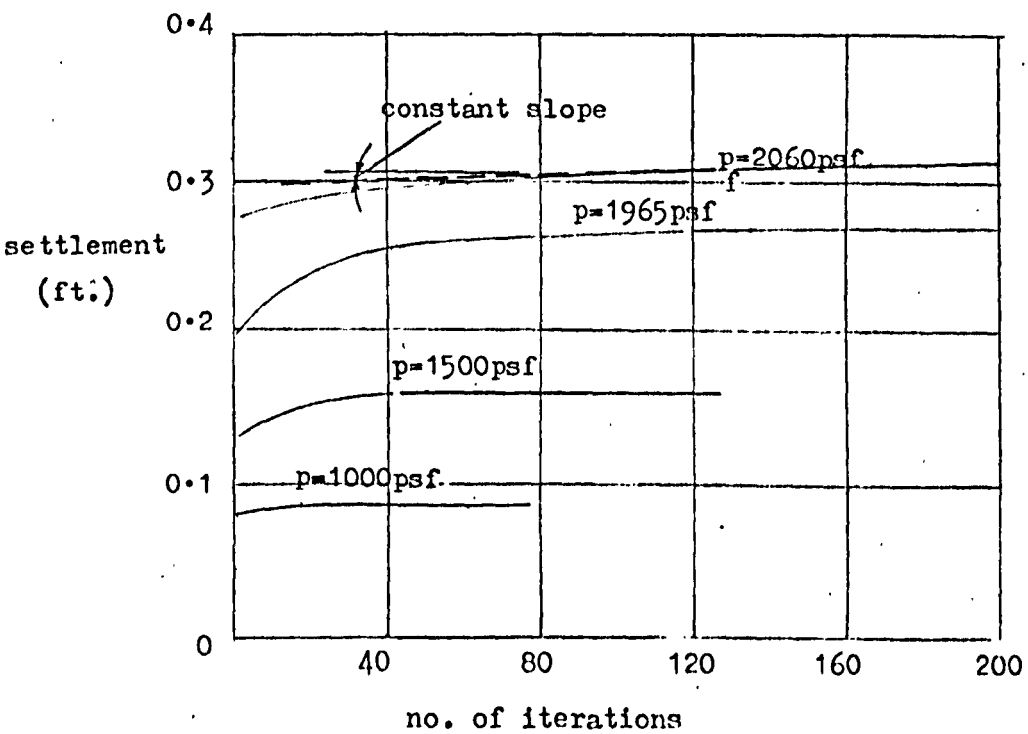

(b) Settlement-iteration plots

Fig. 91. Settlement curves for joint A

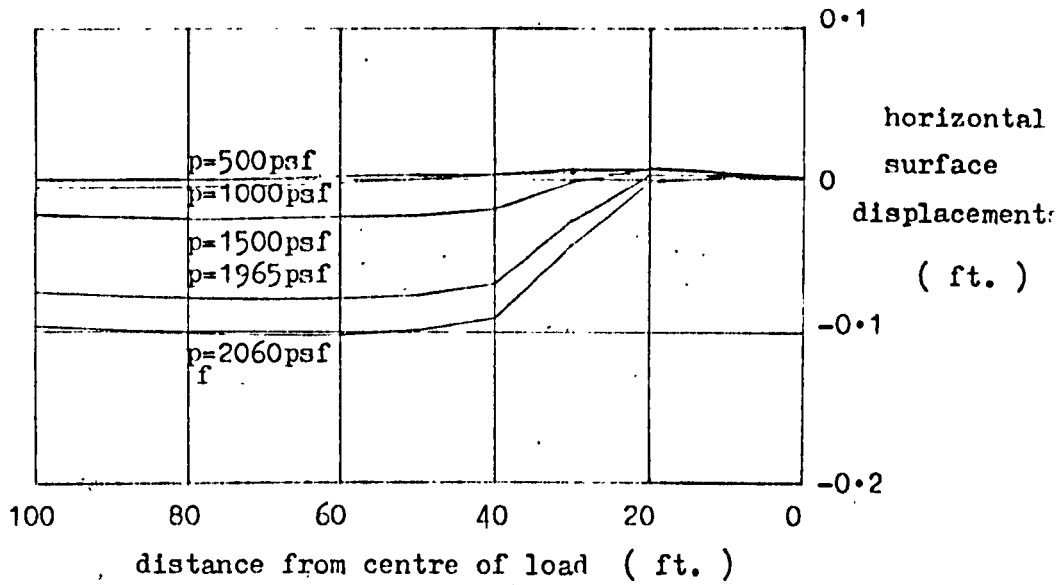

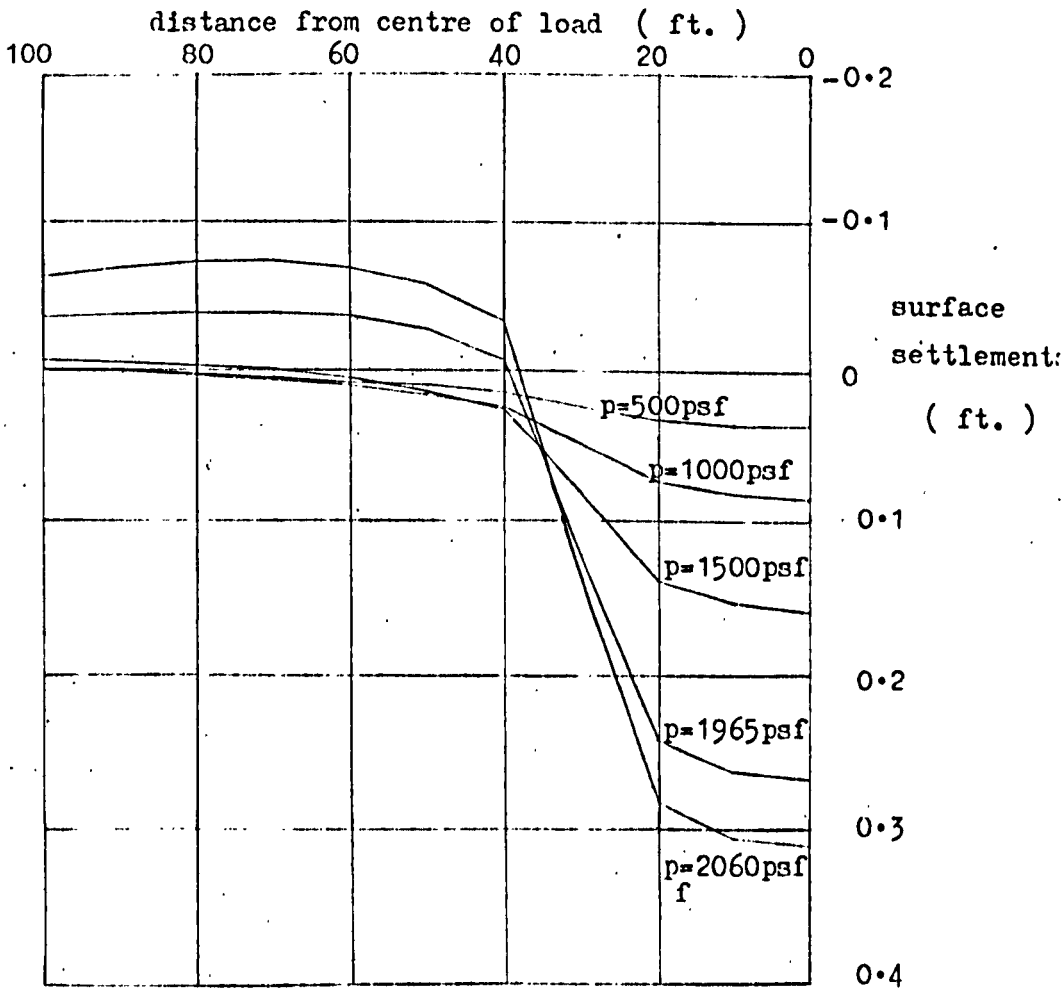

Fig. 92 . Surface displacements

3.2.6. Some stress distributions

Fig. 93 shows the normal stress distributions down the centre and edge respectively, of the strip load. The normalised horizontal stresses are the most sensitive to plastic flow, although becoming generally less so with increasing flow. The shapes of the stress-depth curves vary considerably in the initial stages of plastic flow, but as this increases, the variation becomes noticeably smaller. The normalised vertical stresses are, as usual, relatively insensitive to plastic flow, the vertical stresses, when the layer is still elastic, increasing approximately in proportion to the load right up to collapse. The normalised out-of-plane stresses have a sensitivity that is between the above two stresses, and thus also the normalised volumetric stresses. This is because $\sigma_z = \nu(\sigma_x + \sigma_y)$ by the same token as in Section 2.6.3.

The elastic stress-depth curves, and the manner in which they vary with increasing plastic flow, are broadly similar to those of the corresponding cohesive model. Also, as required by theory (43), constant stress conditions prevail at collapse.

The weight of the soil has not been included in the present model although the stress changes may be quite different when the overburden pressures and lateral stresses at rest are incorporated into the model as initial stresses. The same applies to the displacements of the previous section. Even if these initial stresses lead only to an

isotropic state of stress, there will be a general increase in strength, thus affecting the plastic flow, and consequently stress redistribution. Indeed, the collapse load of the present model is unrealistically small, even less than for the cohesive model of Section 2.6., although it is generally accepted that, with drainage, there should be an overall strengthening of the soil. However, if it is assumed that $K_o=1$ here (i.e. with weight included), the substantial increase in mean stress will lead to a higher collapse load.

In the cohesive model, on the other hand, an isotropic stress increase has no effect on the state of yield. In fact, it is implicit in Chapter 2 that $K_o=1$ so that, to obtain total stresses, it is simply necessary to add the initial stresses to the plotted stress increments. The shapes of the stress curves shown thus remain unchanged and the displacements still apply.

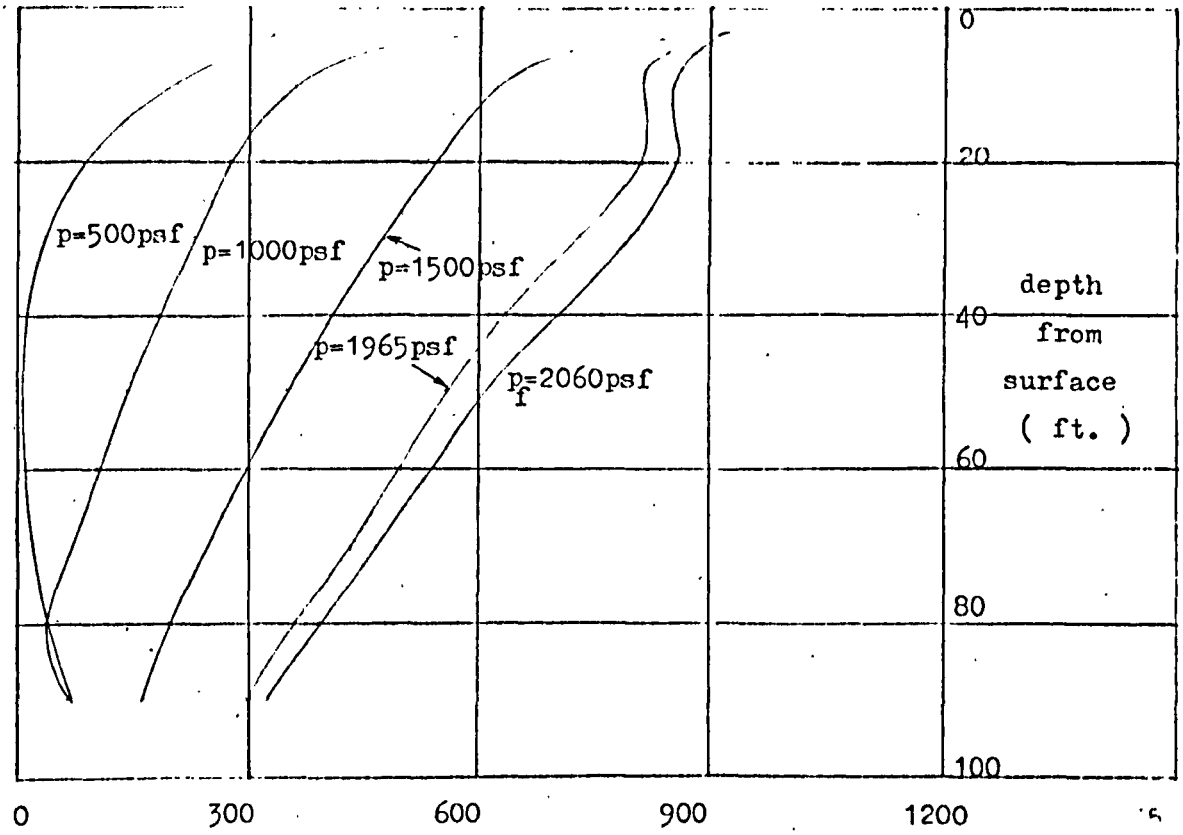

(a) σ_x distributions down centre of strip load (psf)

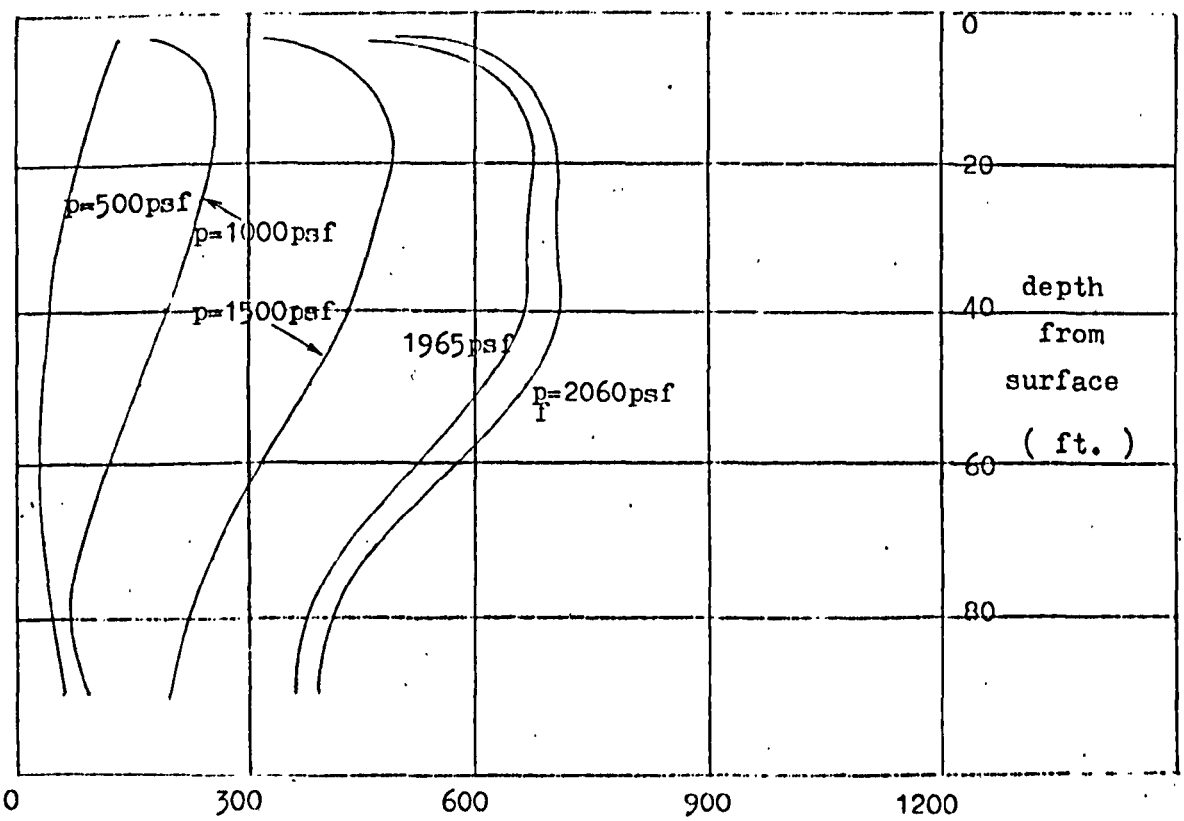

(b) σ_x distributions down edge of strip load (psf)

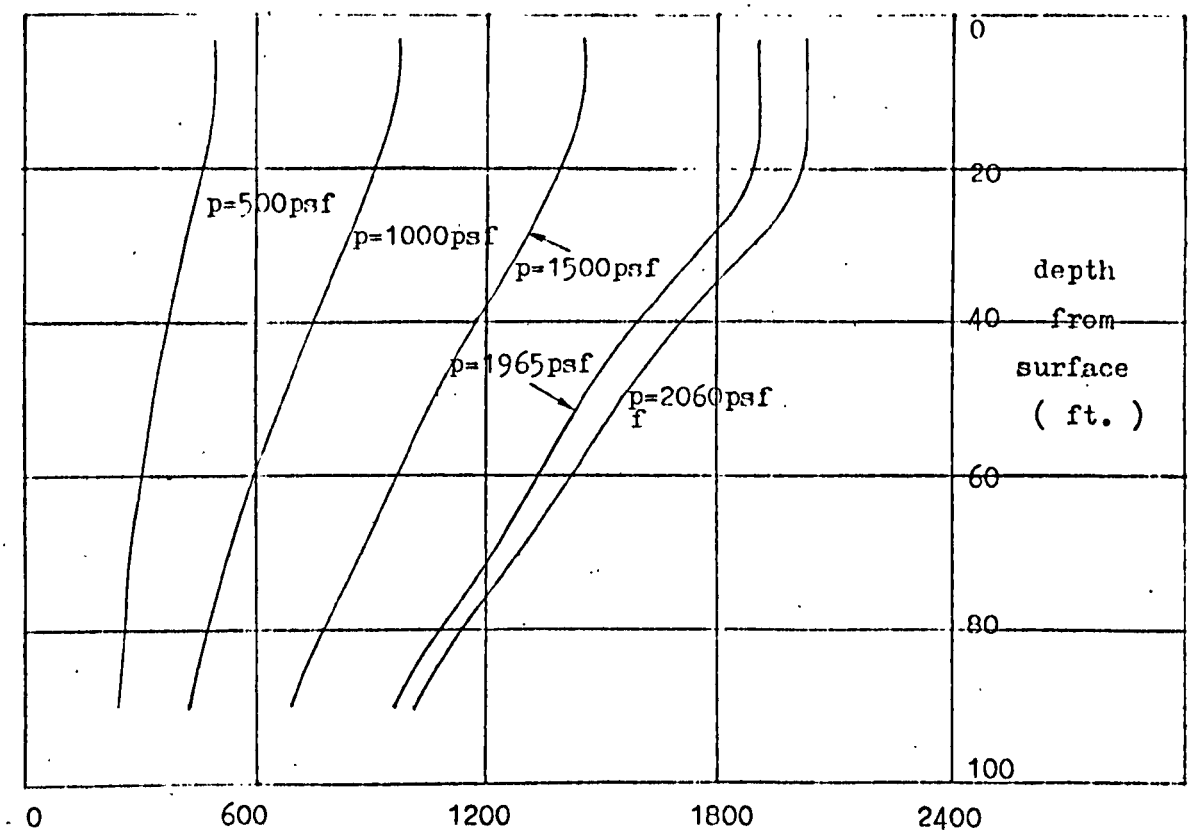

(c) σ_y distributions down centre of strip load (psf)

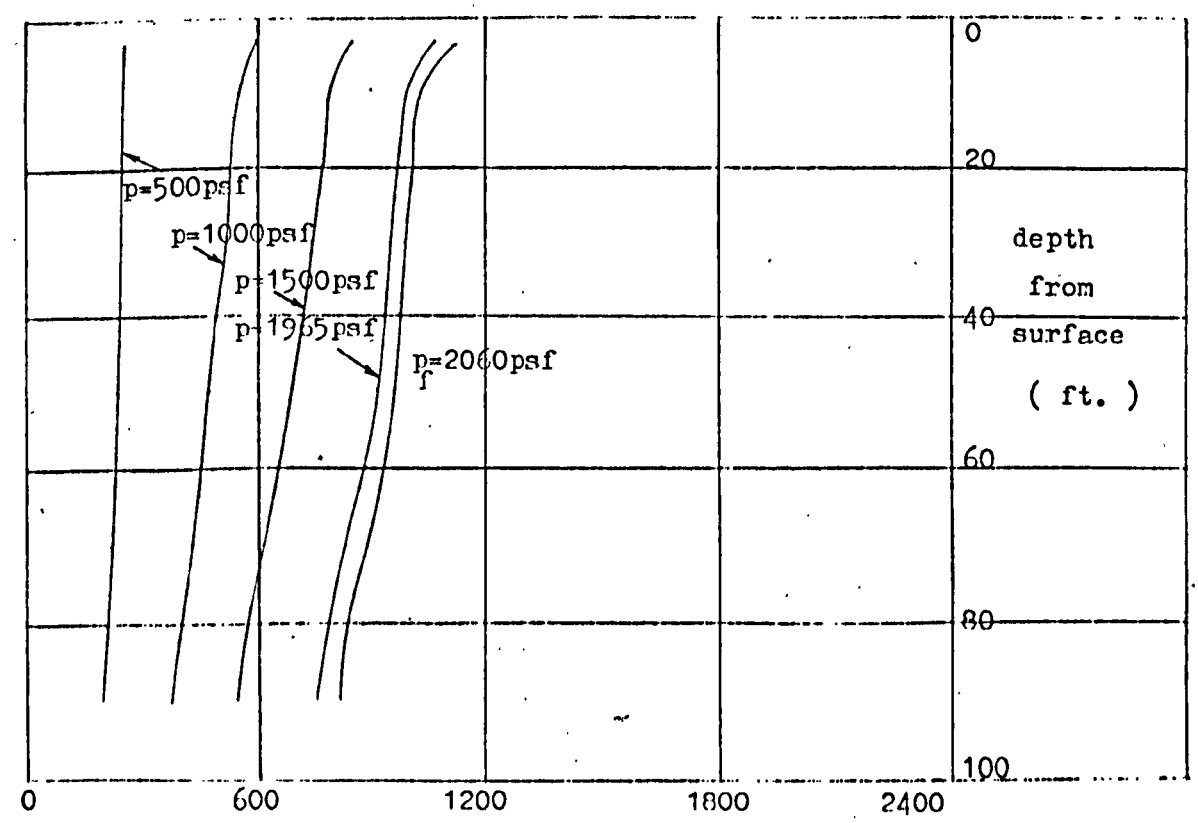

(d) σ_y distributions down edge of strip load (psf)

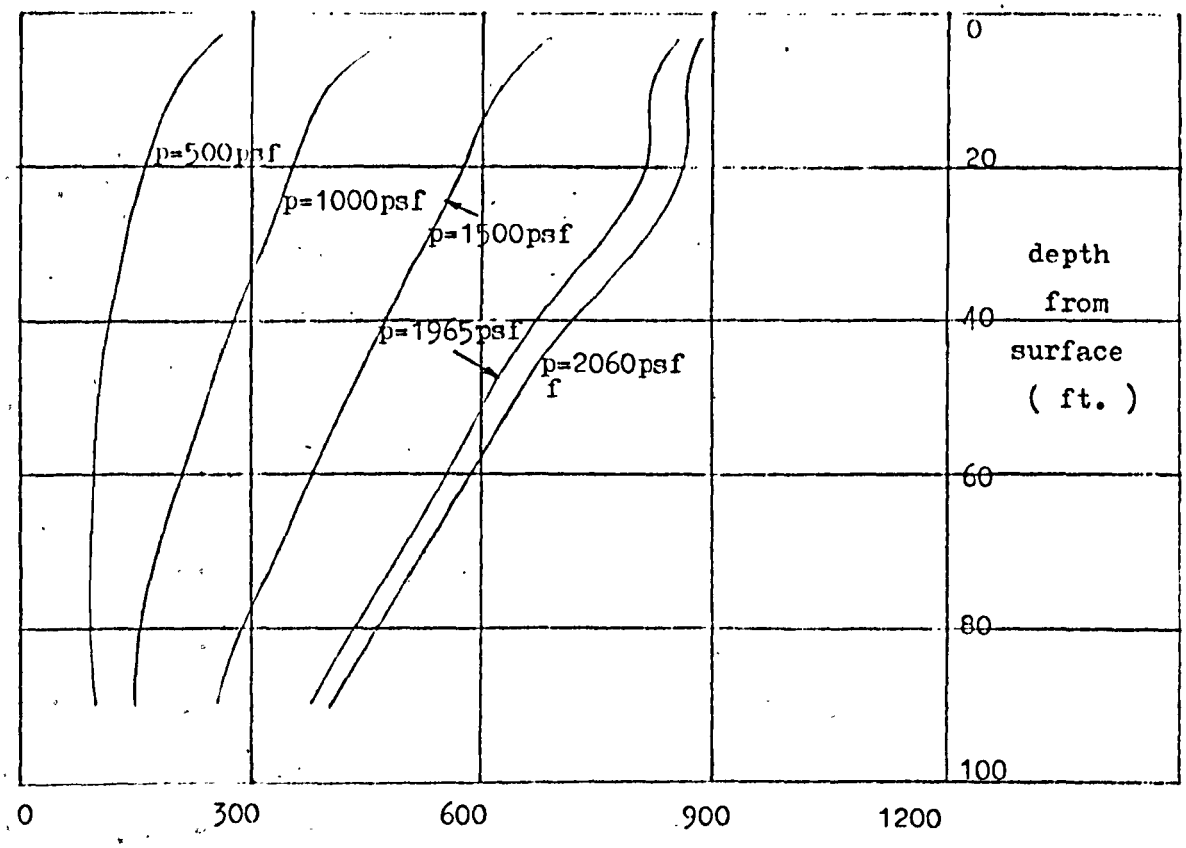

(e) σ_z distributions down centre of strip load (psf)

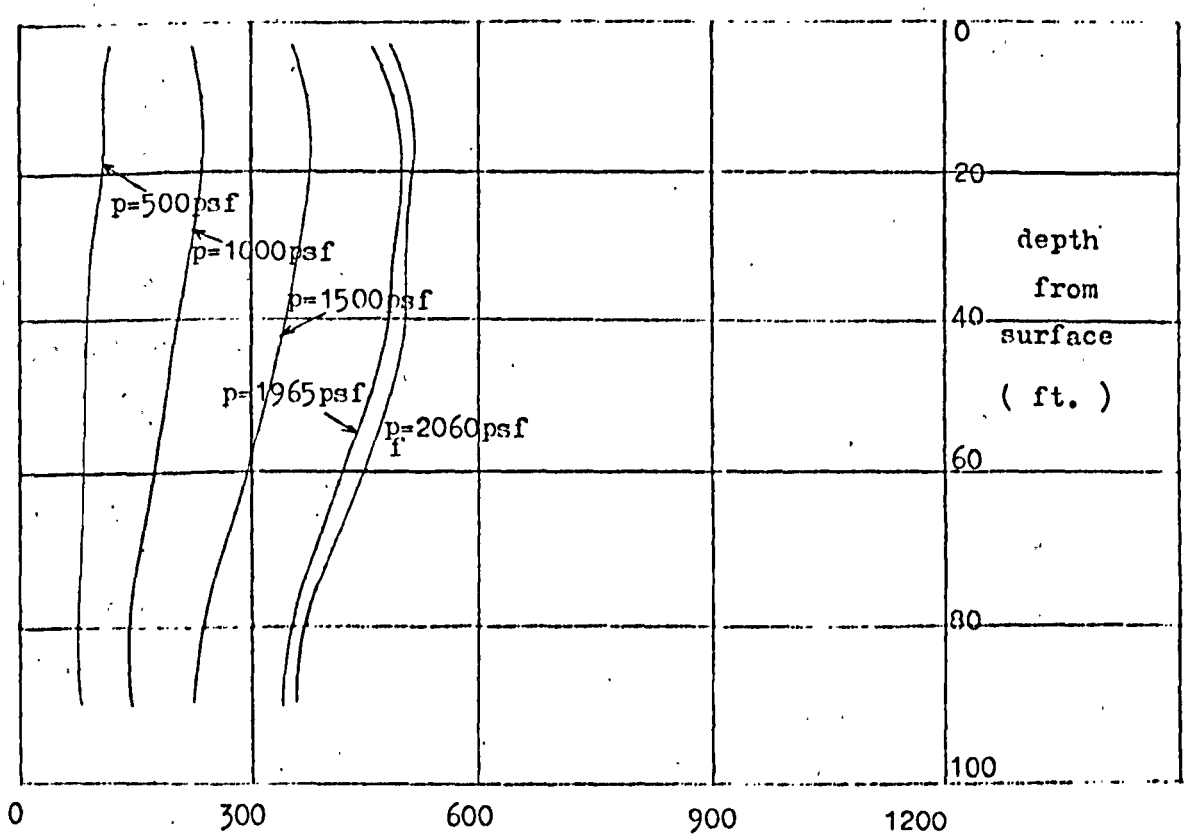

(f) σ_z distributions down edge of strip load (psf)

Fig. 93. Normal stress distributions down centre and edge of strip load

3.3. A vertical cut in an isotropic, homogeneous body of linear elastic, perfectly plastic material obeying the Tresca yield criterion and its associated flow rule

3.3.1. A practical example, the soil mechanics idealisation, and the finite element model

Fig. 94 shows a simple model of a vertical cut in the clay layer of Fig. 22 (Chapter 2) based on the idealisation of Section 2.6. As the problem is one of undrained loading under self-weight the analysis is based on total stresses. A bulk density of 125 psf, as suggested by Duncan and Dunlop (33), is assigned to the saturated clay.

Also shown is the finite element model adopted in the analysis. This has a rather limited mesh size although, as explained later, it is adequate for the present purpose of obtaining a good result of the critical height.

It is obvious that ordinary "Stack Addition" cannot be applied to the model although, with suitable modification, the procedure can be retained in essence; this is demonstrated in the following section.

It will be noted that gradual excavation of the cut is not allowed for. Also, the initial overburden stresses are not specified. However, for the present perfectly plastic material, the collapse conditions can be studied without need for reference to the actual stress path leading to collapse (23a).

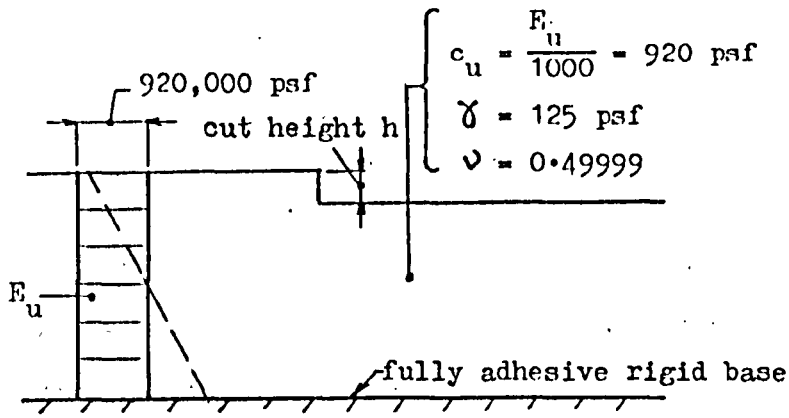

(a) A simple idealisation

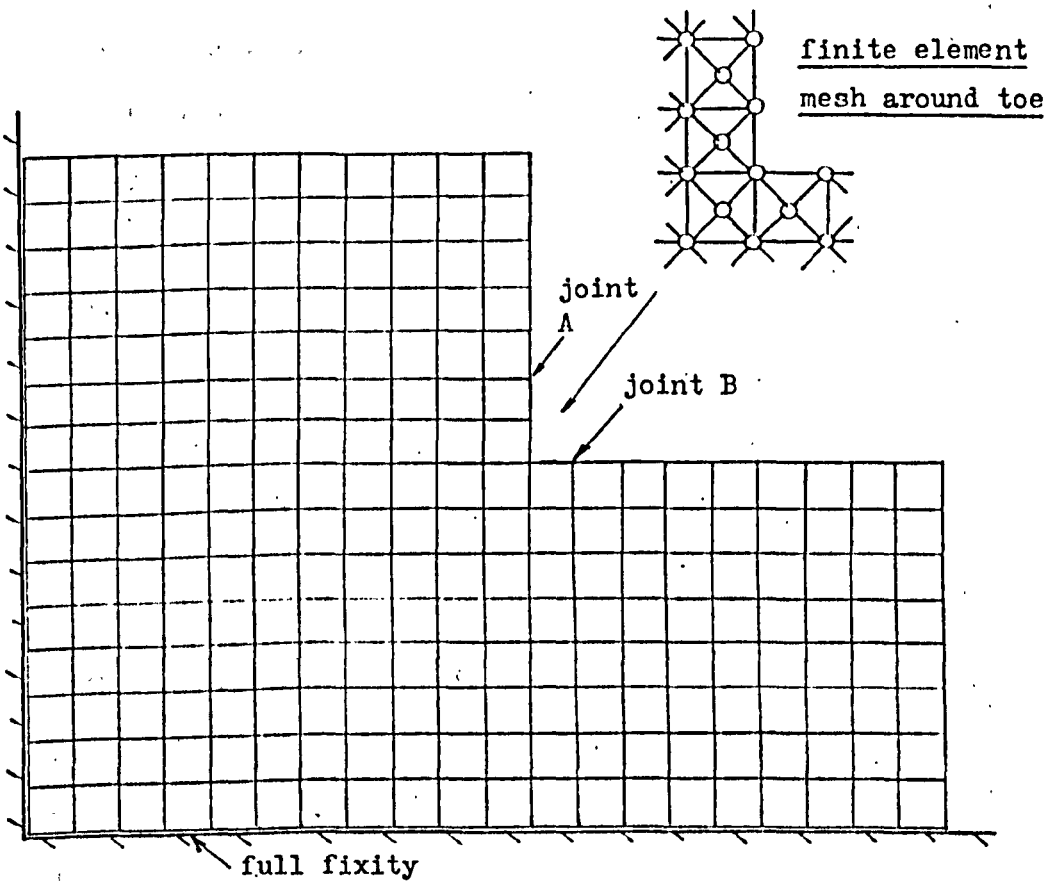

(b) Finite element model

Fig. 94. The soil mechanics idealisation and finite element model of the vertical cut problem

3.3.2. "Reduced Stack Addition" for the vertical cut

It is evident from Fig. 95 that "Stack Addition", as outlined in Chapter 1, is not applicable once the face of the vertical cut is reached - there, two dissimilar Stacks have to be "added". Thus, "Reduced Stack Addition", a slightly modified version of "Stack Addition" that retains its computational advantages, was devised to deal with the vertical cut problem.

The modifications entail essentially (i) alternative expressions to the otherwise standard ones given by Eqns. 40 to 43 (pp. 46), for the line of joints at the face as well as for the following line of joints, and (ii) distinguishing between the standard expressions that apply to the Stacks left of the face, and those of the shorter Stacks to the right, as follows:-

Reverting to the terminology of Chapter 1, and dealing in "equivalent" terms (pp. 42), we have, at joint x' (Fig. 95),

$$\{p_x\} = [R_{(x-1)}]^T\{q_{(x-1)}\} + [K_{R(x-1)}]\{q_x\} + [X][K''_{L(x)}]\{q''_x\} + [X][R''_{(x)}]\{q''_{x+1}\} \quad \ldots\ (74),$$

for equilibrium (cf. Eqn. 26 with r=x).

The double prime refers to the influence of the shorter Stack which does not affect the face joints, except the bottom one, so that the matrix [X] has to be included to maintain the order of the load vector. The triple prime relates to the "reduced" joint, x+1 "'.

Notes:

$\{p_x\} = \begin{bmatrix}[0]\\[I]\end{bmatrix}\{p''_x\} = [X]\{p''_x\}$, where $[0]$ is a $\{2xd_1 \times 2x(d_2+1)\}$ matrix

of zeros, and $[I]$ is a unit matrix of order $2x(d_2+1)$. Also, $\{q''_x\} = [X]^T\{q_x\}$

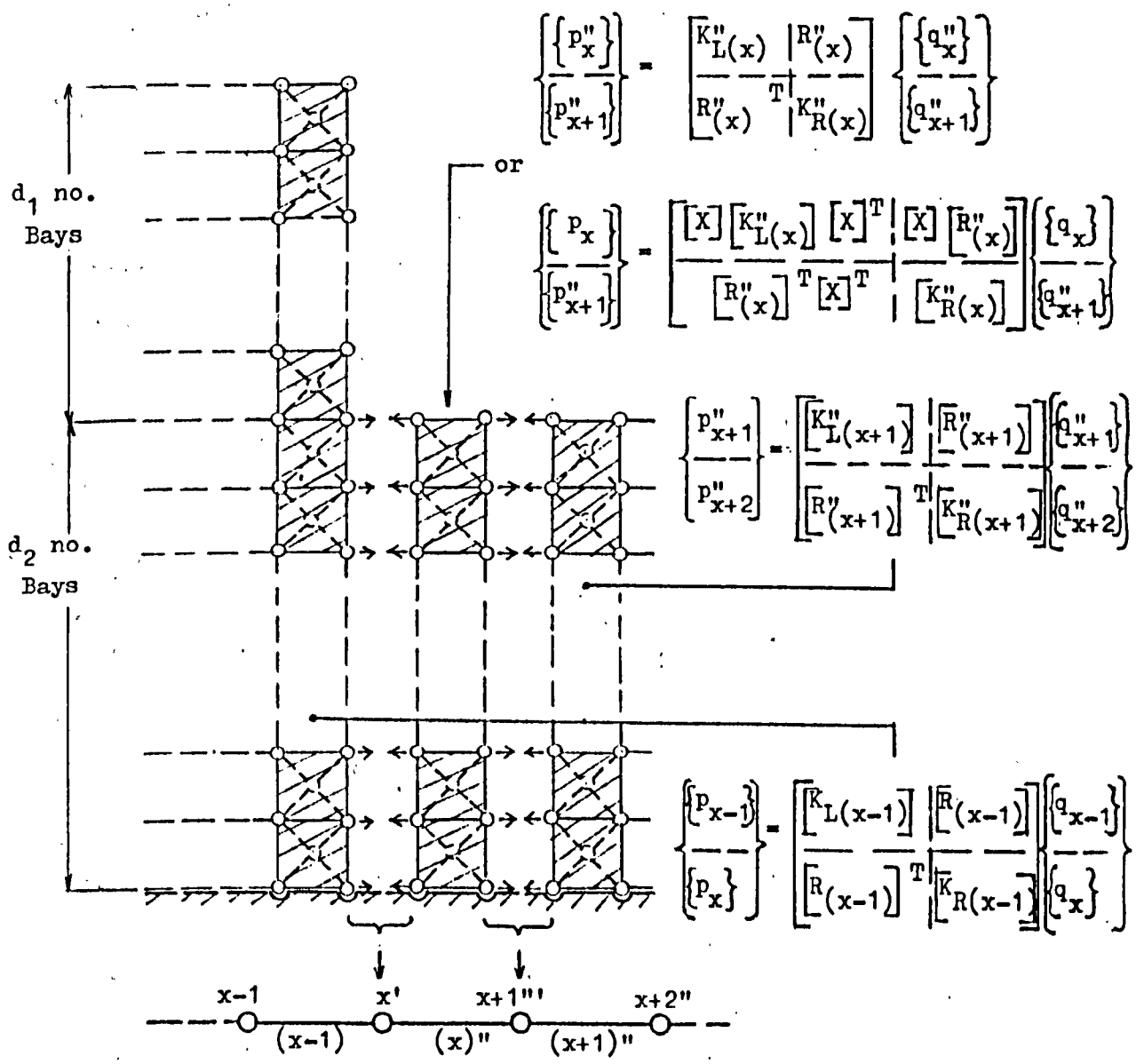

Fig. 95. "Reduced Stack Addition"

Next, the displacements of joint x', i.e., $\{q_x\}$, are obtained in the usual manner; thus, substituting for the displacements of joint x-1 (r=x-1 in Eqn. 40), i.e.,$\{q_{x-1}\}$, in Eqn. 74, we have,

$$\{p_x\} = [R_{(x-1)}]^T ([F_{(x-1)}]\{h_{x-1}\} + [T_{(x,x-1)}]\{q_x\}) + [K_{R(x-1)}]\{q_x\}$$

$$+ [X][K''_{L(x)}]\{q''_x\} + [X][R''_{(x)}]\{q''_{x+1}\} \quad ; \text{ i.e.,}$$

$$([R_{(x-1)}]^T [T_{(x,x-1)}] + [K_{R(x-1)}])\{q_x\} + [X][K''_{L(x)}]\{q''_x\} = \{p_x\} -$$

$$[R_{(x-1)}]^T [F_{(x-1)}]\{h_{x-1}\} - [X][R''_{(x)}]\{q''_{x+1}\} .$$

Next, $\{q''_x\}$ is expressed in terms of $\{q_x\}$ since it is necessary to deal with the whole line of joints at the face to obtain the solution.

Accordingly, we now have,

$$([R_{(x-1)}]^T [T_{(x,x-1)}] + [K_{R(x-1)}]) \{q_x\} + [X][K''_{L(x)}][X]^T \{q_x\} =$$

$$\{p_x\} - [R_{(x-1)}]^T [F_{(x-1)}]\{h_{x-1}\} - [X][R''_{(x)}]\{q''_{x+1}\} \text{ , since } \{q''_x\} =$$

$[X]^T \{q_x\}$ (Fig. 95); i.e.,

$$([X][K''_{L(x)}][X]^T + [K_{R(x-1)}] + [R_{(x-1)}]^T [T_{(x,x-1)}]) \{q_x\} =$$

$$(\{p_x\} + [T_{(x,x-1)}]^T \{h_{x-1}\}) - [X][R''_{(x)}]\{q''_{x+1}\} \text{ , whereupon,}$$

$\{q_x\} = [F'_{(x)}]\{h_x\} + [T'_{(x+1,x)}]\{q''_{x+1}\}$ .... (75), where

$[F'_{(x)}] = ([X][K''_{L(x)}][X]^T + [K_{R(x-1)}] + [R_{(x-1)}]^T [T_{(x,x-1)}])^{-1}$

.... (76), $\{h_x\} = \{p_x\} + [T_{(x,x-1)}]^T \{h_{x-1}\}$ .... (77), and

$[T'_{(x+1,x)}] = -[F'_{(x)}][X][R''_{(x)}]$ .... (78). the single prime relating to the joint at the face, x' (cf. Eqns. 40 to 43).

Moving on to the next joint, $x+1$, we have, for equilibrium (Fig. 95),

$$\{p''_{x+1}\} = [R''_{(x)}]^T \{q''_x\} + [K''_{R(x)}]\{q''_{x+1}\} + [K''_{L(x+1)}]\{q''_{x+1}\} + [R''_{(x+1)}]\{q''_{x+2}\} \quad \ldots\ldots (79).$$

As before, it is necessary to work in terms of $\{q_x\}$, so we re-write,

$$\{p''_{x+1}\} = [R''_{(x)}]^T [X]^T \{q_x\} + [K''_{R(x)}]\{q''_{x+1}\} + [K''_{L(x+1)}]\{q''_{x+1}\} + [R''_{(x+1)}]\{q''_{x+2}\} :$$

Next, substituting for $\{q_x\}$ (Eqn. 75), we have,

$$\{p''_{x+1}\} = [R''_{(x)}]^T [X]^T ([F'_{(x)}]\{h_x\} + [T'_{(x+1,x)}]\{q''_{x+1}\}) + [K''_{R(x)}]\{q''_{x+1}\} + [K''_{L(x+1)}]\{q''_{x+1}\} + [R''_{(x+1)}]\{q''_{x+2}\}$$

$$= ([K''_{L(x+1)}] + [K''_{R(x)}] + [R''_{(x)}]^T [X]^T [T'_{(x+1,x)}])\{q''_{x+1}\} - [T'_{(x+1,x)}]^T \{h_x\} + [R''_{(x+1)}]\{q''_{x+2}\} .$$

Thus, finally,

$$\{q''_{x+1}\} = [F'''_{(x+1)}]\{h'''_{x+1}\} + [T'''_{(x+2,x+1)}]\{q''_{x+2}\} \quad \ldots\ldots (80), \text{ where}$$

$$[F'''_{(x+1)}] = ([K''_{L(x+1)}] + [K''_{R(x)}] + [R''_{(x)}]^T [X]^T [T'_{(x+1,x)}])^{-1} \quad \ldots\ldots (81),$$

$$\{h'''_{x+1}\} = \{p'''_{x+1}\} + [T'_{(x+1,x)}]^T \{h_x\} \quad \ldots\ldots (82), \text{ and}$$

$$[T'''_{(x+2,x+1)}] = -[F'''_{(x+1)}][R''_{(x+1)}] \quad \ldots\ldots (83).$$

The above two sets of modifications to the otherwise standard Eqns 40 to 43, and due regard to the change in order of the various matrices once joint x+1"' is past, when using the above equations, are the only differences to "Stack Addition" as outlined in Chapter 1, when solving the vertical cut problem.

It should also be noted that the loading on the assemblage no longer resembles those employed hitherto; instead, all 3 joints of every finite element will be subject to the same vertical concentrated load due to self-weight (see Eqn. 12). This, however, makes no difference to the solution procedure outlined in pp. 46 to 53 , which is quite general.

3.3.2.1. Adaptations to the flow chart of Section 1.3.3.1. for the vertical cut problem of Section 3.3.

Block	Adaptations
D10	Calculate the stiffness matrix of the Stack, taking note of its height (Section 1.2.5.2., 1.2.5.3. & 1.2.5.4.)
D10 (Sub-block 4.1)	Is this Stack the first one to the left of the cut face? (Yes: Go to Sub-block 4.2; No: Go to Sub-block 4.3)
D10 (Sub-block 4.2)	Calculate $\left[F_{(r)}\right]$ and $\left[T_{(r+1,r)}\right]$ according to Eqns. 76 & 78 respectively and store on disk. Go to Sub-block 5.
D10 (Sub-block 4.3)	Is this Stack at the base of the cut? (Yes: Go to Sub-block 4.4; No: Go to Sub-block 5)
D10 (Sub-block 4.4)	Calculate $\left[F_{(r)}\right]$ and $\left[T_{(r+1,r)}\right]$ according to Eqns. 81 & 83 respectively and store on disk. Go to Sub-block 5
E1	Set up load vectors for all columns of nodes from body forces due to self-weight only
F2 (Sub-block 6.1)	Is this column of nodes on the cut face? (Yes: Go to Sub-block 6.2; No: Go to Sub-block 6.3)

Block	Adaptations
F2 (Sub-block 6.2)	Calculate $\{h_r\}$ according to Eqn. 77 and store. Go to Sub-block 9
F2 (Sub-block 6.3)	Is this column of nodes the first to the right of the cut? (Yes: Go to Sub-block 6.4; No: Go to Sub-block 7)
F2 (Sub-block 6.4)	Calculate $\{h_r\}$ according to Eqn. 82 and store. Go to Sub-block 9.
F7 (Sub-block 3.1)	Is this column of nodes on the cut face? (Yes: Go to Sub-block 3.2; No: Go to Sub-block 4)
F7 (Sub-block 3.2)	Calculate $\{q_r\}$ according to Eqn. 75 and store. Go to Sub-block 6
F9 (Sub-block 2.1)	Obtain $\{p_e\}$ from body forces acting at the middle node of the bay
F9 (Sub-block 3)	Calculate $\{q_e\}$ using $\{p_e\}$ just obtained
F9 (Sub-block 10)	Print and store $\{\gamma\}$, $\{\sigma\}$ & σ_z in $\{\Delta\varepsilon'\}$, $\{\Delta\sigma'\}$ & $\Delta\sigma'_z$ respectively
G1	Deleted
K18	Is KK < 500?
L2	Finish
L3 - L8	Deleted

3.3.3. Growth of the plastic enclave; displacements and collapse of the vertical cut

Fig. 96 shows the growth of the plastic enclave with increasing height of the cut. First yield occurs around the toe when the height is about 7 feet - i.e. $0{\cdot}95\,\frac{c_u}{\gamma}$. With further increase in height, a well-defined plastic enclave develops and spreads downwards as a thin strip. From a height of about 14·75 feet ($2\,\frac{c_u}{\gamma}$) onwards, the enclave begins to spread laterally and upwards into the bank on the left as well as towards the bottom of the cut on the right. A few finite elements near the rigid boundaries also become plastic.

Towards collapse, the distribution of the enclave suggests either Terzaghi's "base failure" or a "bank failure" (37d) will occur. However, neither collapse mode takes place. Instead, some finite elements along the lower boundary of the enclave in the bank begin to unload elastically so that additional shear has to be borne by the region beneath the bottom of the cut. This appears to act as a trigger mechanism for collapse in part of the latter region; the weight of material adjacent to the toe acts as if it were a strip load, below which the material flows downwards, sideways thence upwards as surface heave, as for the model of Section 2.6. This volume of material is displaced to the right, the weight of the bank on the left acting as a surcharge preventing a similar movement to the left (see Fig. 98) . Thus, no sliding failure involving the bank occurs, the latter remaining

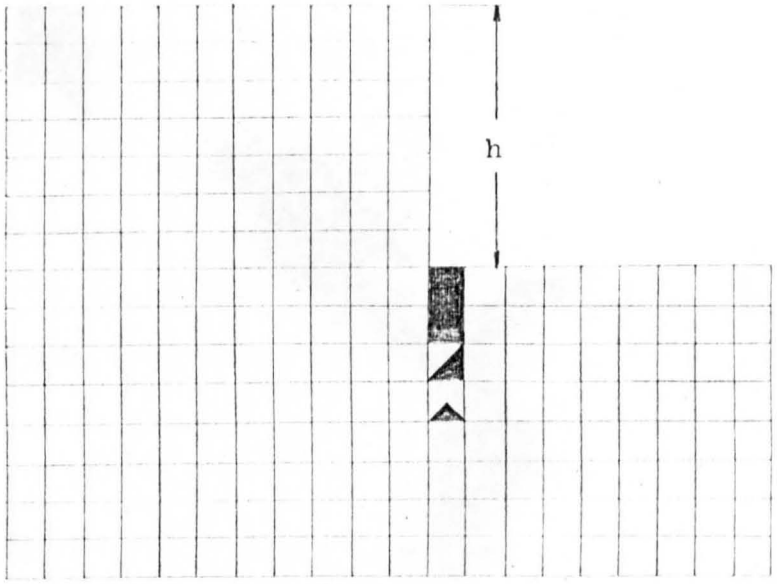

(a) $h = \frac{c_u}{\gamma}$

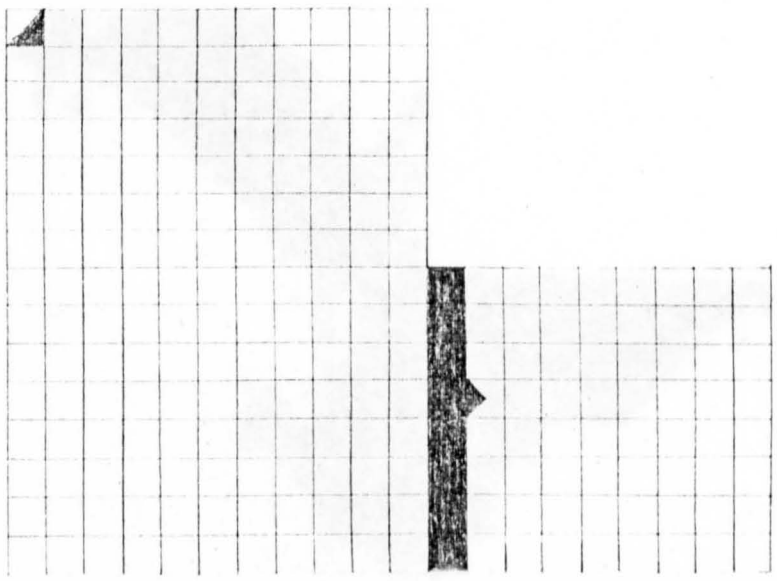

(b) $h = 2\frac{c_u}{\gamma}$

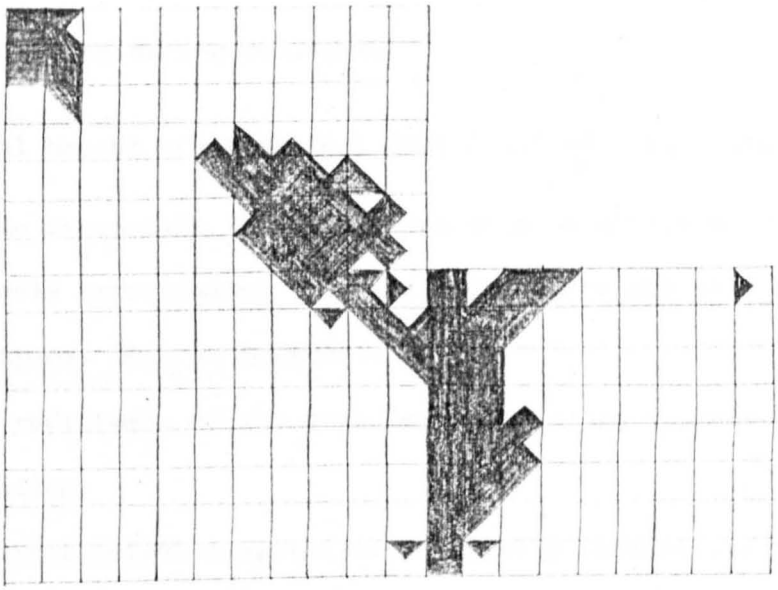

(c) $h = 3\,\frac{c_u}{\gamma}$

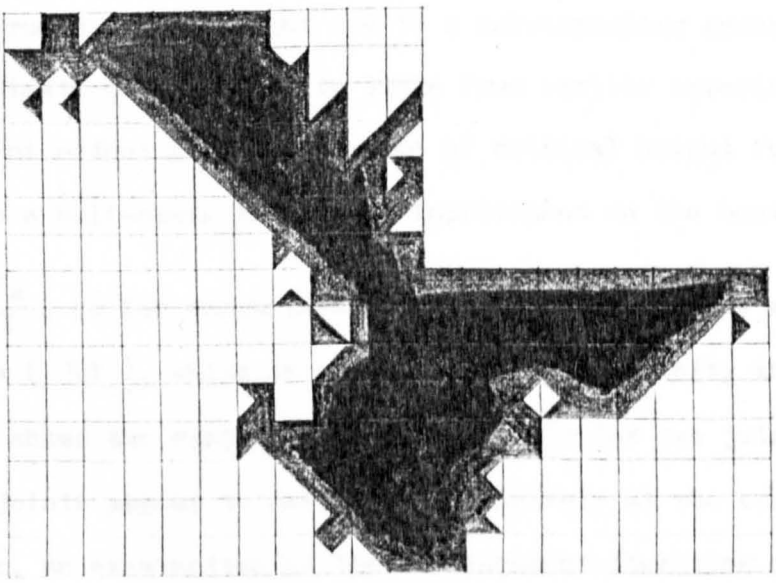

(d) $h_c = 3{\cdot}6\,\frac{c_u}{\gamma}$ (collapse)

Fig. 96 . Growth of the plastic enclave to collapse

relatively motionless during collapse.

A critical height of about 26·5 feet ($3.6 \frac{c_u}{\gamma}$) was obtained. As before, it is reasonable to assume that this result is an upper bound that closely approximates the true critical height of a vertical cut in a half-space. This is because:-

(a) further refinement of the mesh leads to little improvement in the solution,

(b) the critical height computed is relatively insensitive to the location of reasonably spaced boundaries which when farther removed lead to a slight reduction in the above height; this is attributable to replacement with weaker material, according to a limit theorem (23b), and

(c) the present numerical method leads to a slight overestimate of the true critical height due to a corresponding general underestimate of stresses, to judge from earlier experience.

Thus, the present method provides a value of critical height for a vertical cut in a half-space that is an improvement on the best upper bound of $3{\cdot}83 \frac{c_u}{\gamma}$, so far encountered. The latter is given by a slip circle analysis (50), which is consistent with plasticity theory.

Fig. 97 shows the displacement-height plots for two joints at the cut. Both joints appear to displace indefinitely at the critical height. However, an examination of the displacement-iteration plots reveals convergence to finite values for joint A (the bank being

relatively stationary at collapse), whereas joint B, which is in the region of collapse, displaces indefinitely, as the eventual constant rate of descent of the vertical displacement-iteration curve suggests. The latter joint first rises due to elastic heave, the rate of ascent increasing with height of cut due to lost ground through progressive yielding. At collapse, there is an abrupt reversal in the displacement-height plot of that joint as it sinks indefinitely in the wake of uninhibited plastic flow in the region of collapse as described earlier.

Fig. 98 shows the overall deformation of the cut at some stage of collapse, thus illustrating various features in the above discussion.

Although the mesh adopted is obviously too restricted to represent accurately a cut in the clay layer of Fig. 94 in all respects, nevertheless, the above account still holds true in general terms; indeed, the critical height should be fairly accurate. For accurate displacements and stresses, however, further extension of the mesh is required, although it is probably sufficiently fine.

Fig. 97. Displacement curves for joints A and B (refer to Fig. 94)

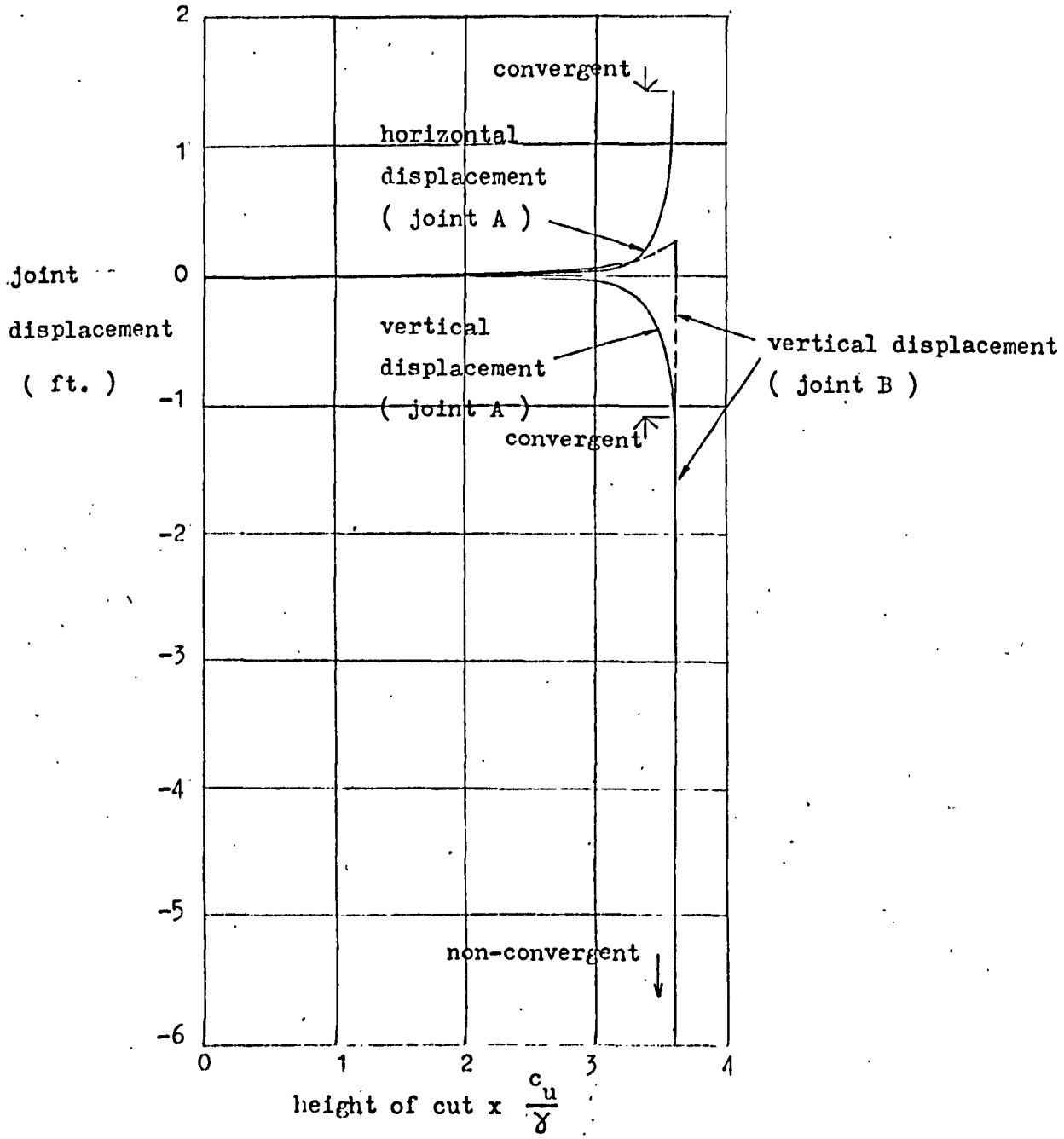

(a) Displacement-height plots

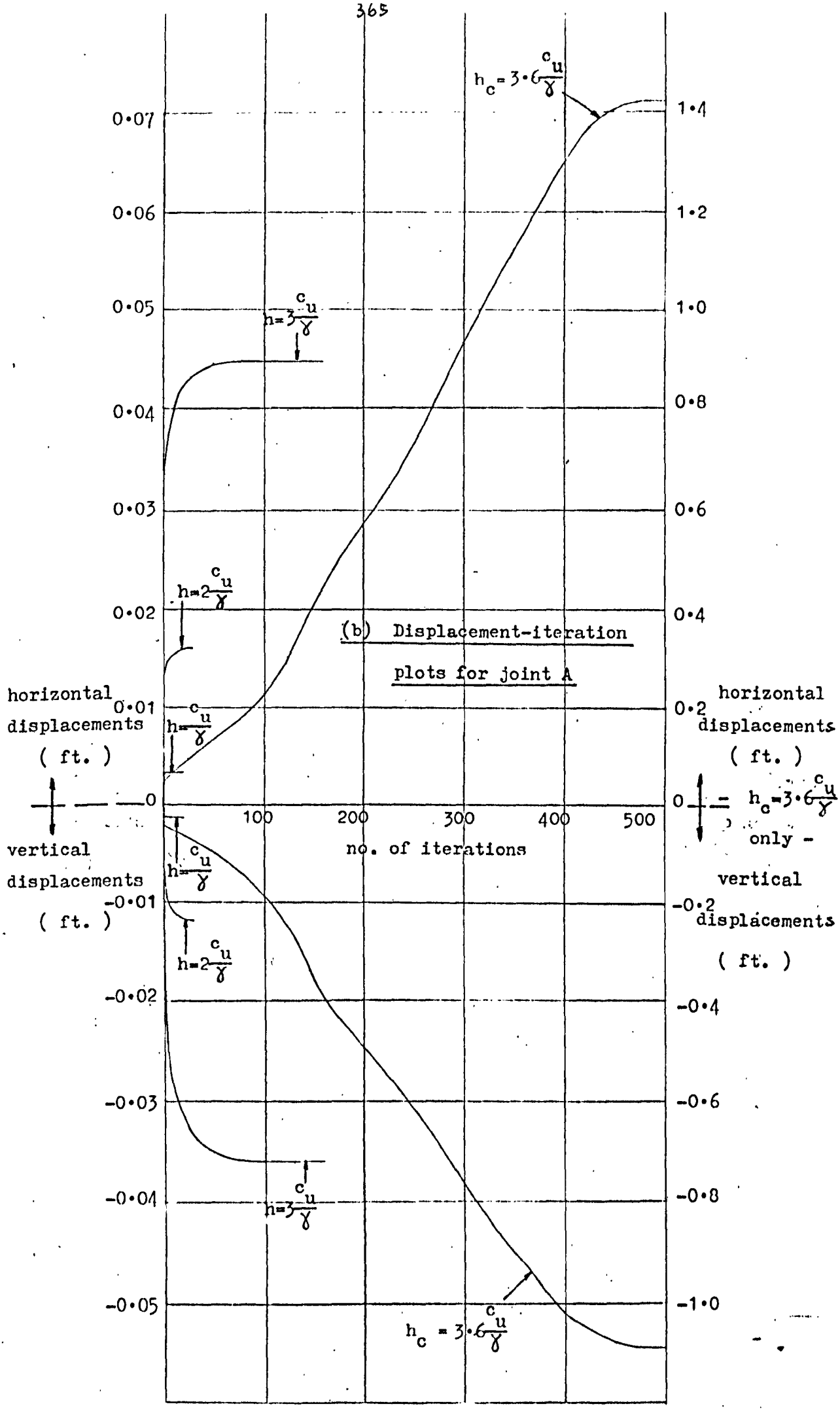

(b) Displacement-iteration plots for joint A

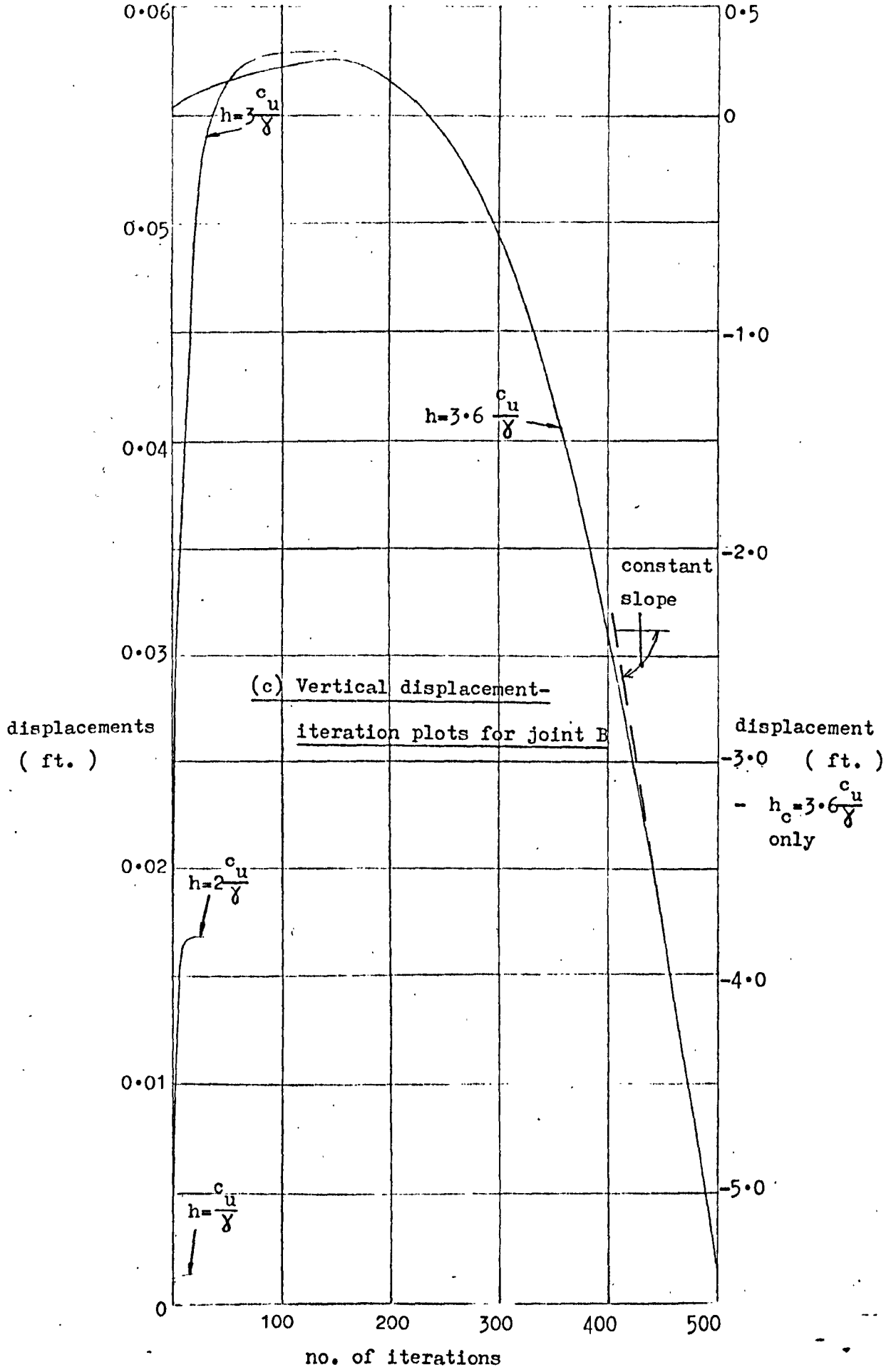
0·06
0·05
0·04
0·03
0·02
0·01
0
0·5
0
-1·0
-2·0
-3·0
-4·0
-5·0
$h=3\frac{c_u}{\gamma}$
$h=3{\cdot}6\frac{c_u}{\gamma}$
$h=2\frac{c_u}{\gamma}$
$h=\frac{c_u}{\gamma}$
constant slope
(c) Vertical displacement-iteration plots for joint B
displacements (ft.)
displacement (ft.)
$h_c=3{\cdot}6\frac{c_u}{\gamma}$ only
100
200
300
400
500
no. of iterations

Fig. 98. General deformation of vertical cut at collapse

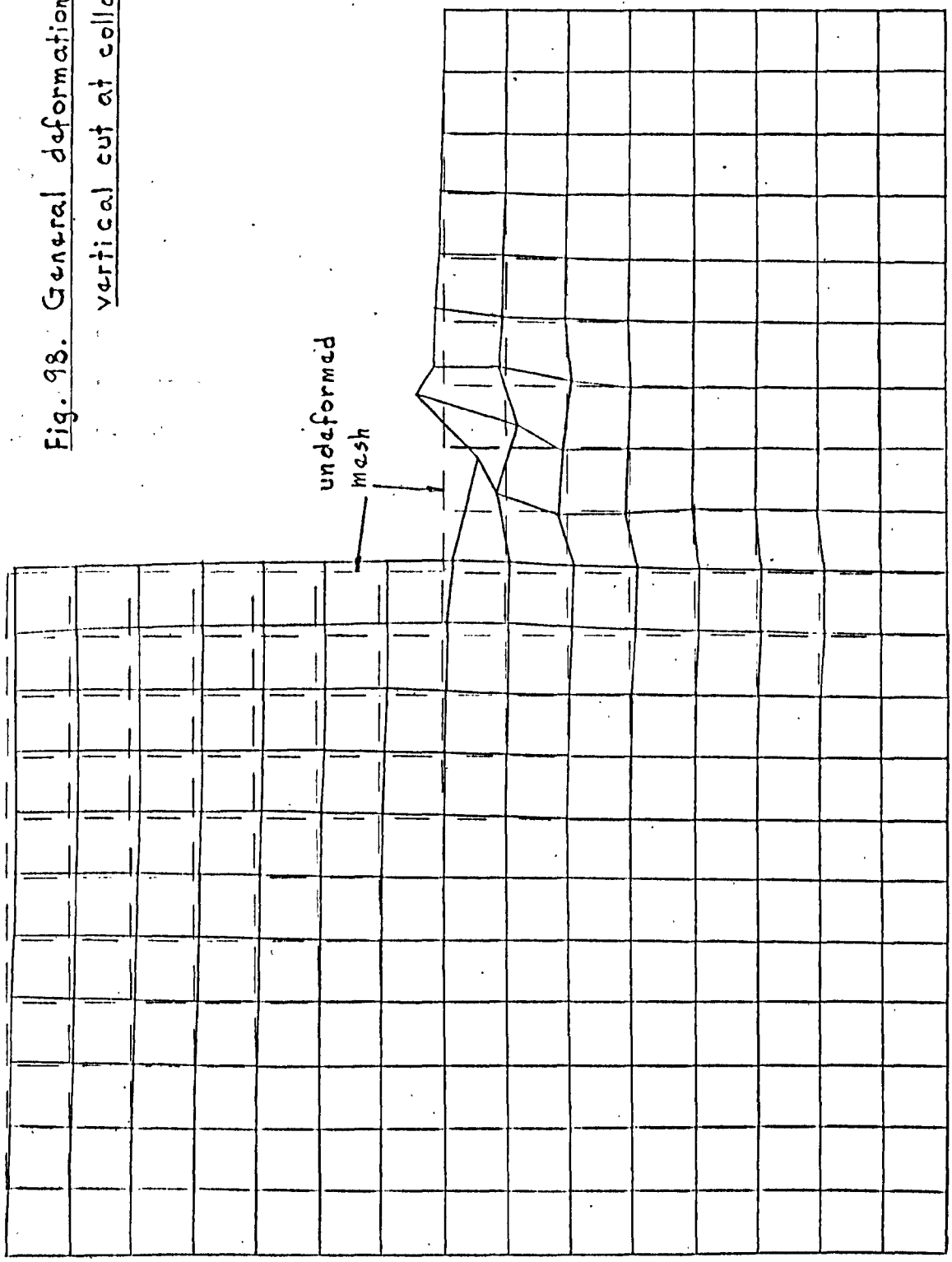

3.4. Modifications to "Stack Addition" for some boundary value problems

Figs. 99 and 100 illustrate suitable finite element meshes for studying the behaviour of an embankment and a circular underground opening respectively, due to self-weight loading, using a modified version of "Stack Addition".

For the embankment, "Stack Addition" is carried out for all lines of joints preceeding the crest. At the crest, however, the relevant right Stack has a reduced right line of joints, and this leads to two modifications essentially, viz. :-

(a) The top Bay of the right Stack is triangular and therefore its stiffness matrix, when condensed, relates to only 3 joints - at the apices.

(b) The relevant $[R]$, and hence $[T]$ matrices reduce in size.

By the same token, further reductions in the order of the relevant load, displacement and component stiffness matrices occur when considering successive lines of joints, with consequent reductions in the order of the $[F]$, $[T]$ and $\{h\}$ matrices used in the solution procedure. However, in this instance, no $[X]$ type matrix ("Reduced Stack Addition") is required, the difference being that there is no abrupt change in the number of joints in any one line, that is connected to the relevant right and left Stacks respectively. Thus the form of the underlying equations for "Stack Addition" as outlined in Chapter 1 applies intact here; the only difference is that from the crest, down

slope, progressively smaller matrices are generally involved. Once the line of joints following the toe of the slope is reached, however, normal "Stack Addition" is resumed, except that shorter Stacks are then "added".

The solution procedure for the tunnel is similar. In this case, however, two mirror-image triangular condensed Bays occur from the start of the tunnel (approximated as a series of chords). From there on, the number of joints along any one line reduces so that, as before, smaller matrices are involved in the solution procedure. Once past the centre of the tunnel, the number of joints, and hence the order of the relevant matrices steadily increases until the opposite side of the tunnel is reached. Subsequent lines of joints are then subject to ordinary "Stack Addition", the Stacks being of the same size as those prior to the start of the tunnel.

From these two examples and the vertical cut problem, it is obvious that other soil mechanics problems of plane strain can be readily dealt with in similar fashion, viz. earth dams, retaining walls to backfill, etc. Furthermore, the similarity of the finite element formulation of plane strain and axisymmetric problems, respectively, provides the basis for extending this solution procedure to deal with the latter problems.

In problems of symmetry, less computing resources are expended by using the procedure presented by the Author (9), involving reflection about the line of symmetry.

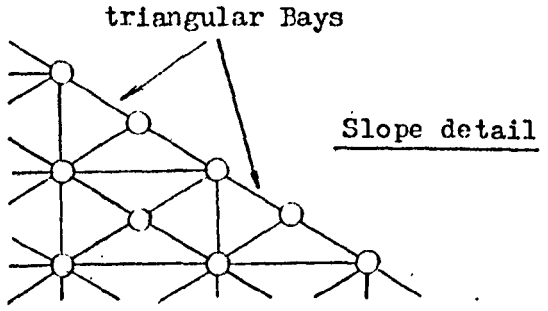

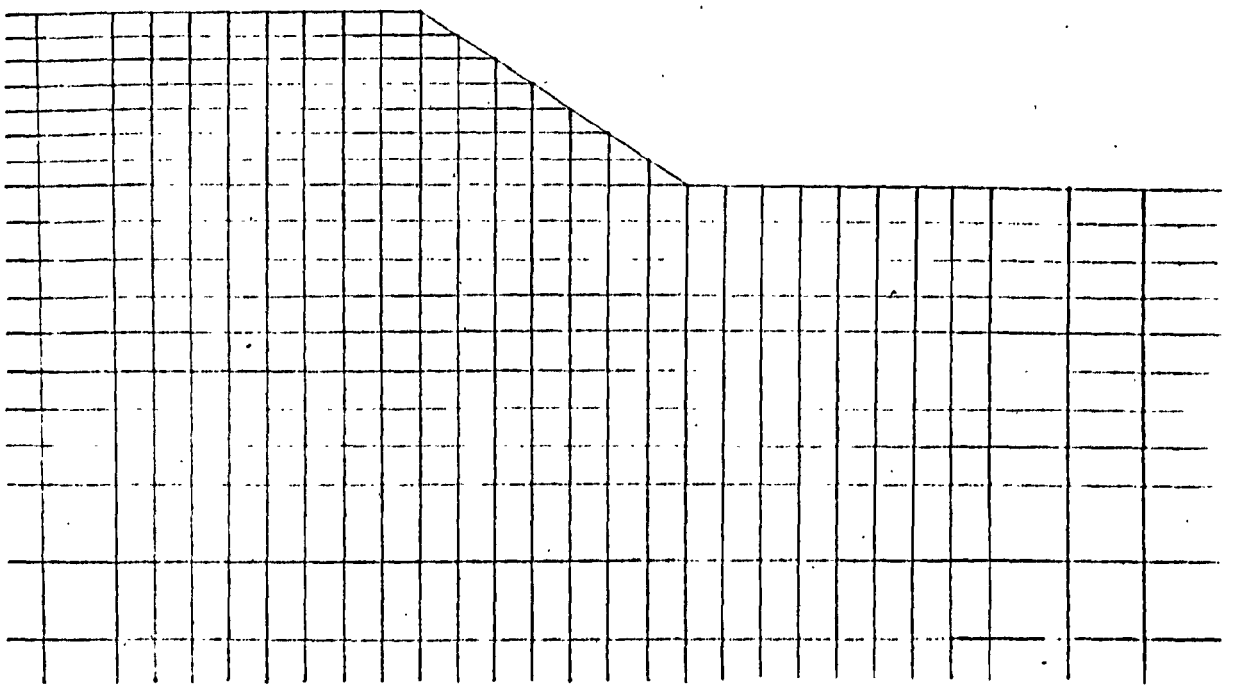

Fig. 99 . Proposed mesh for embankment problem

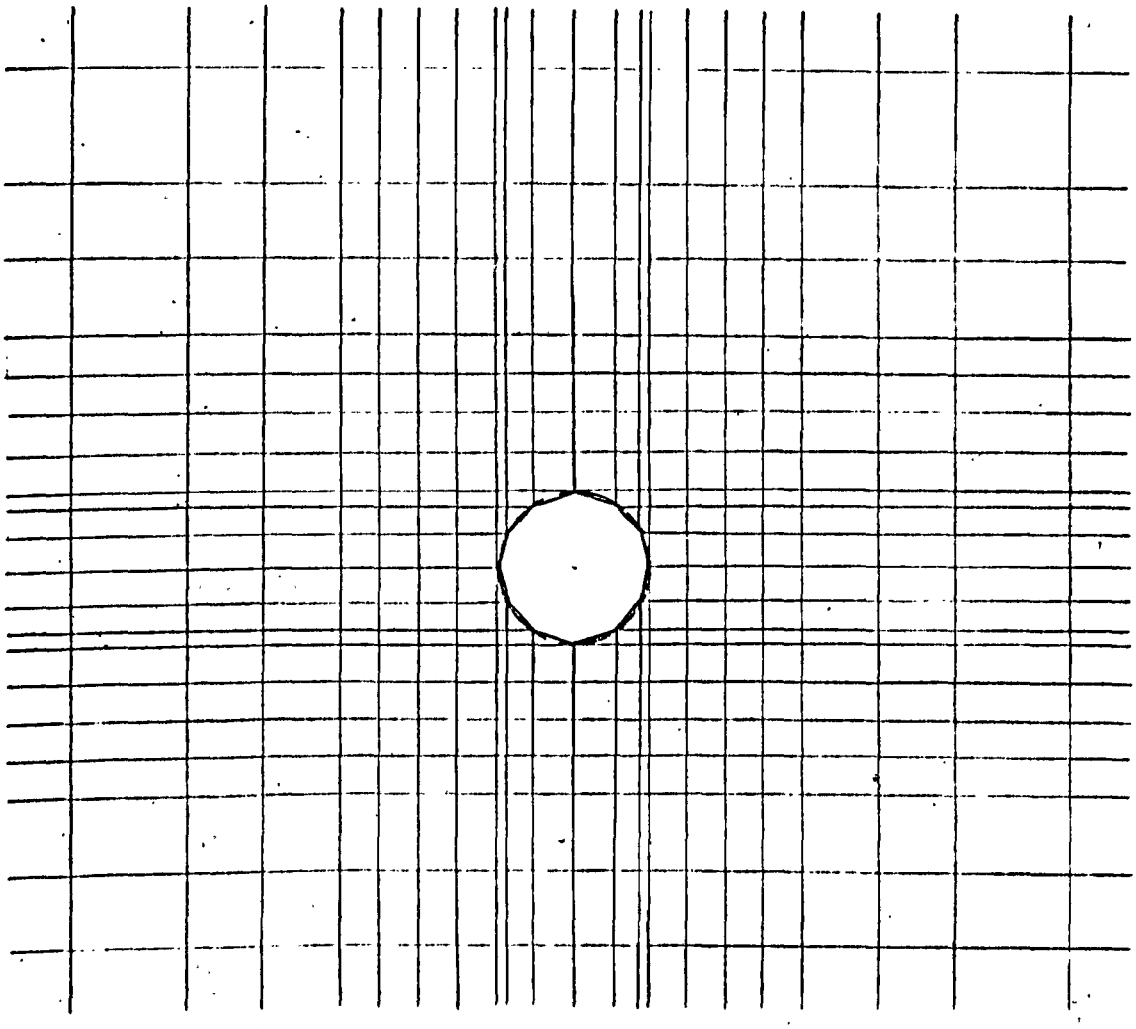

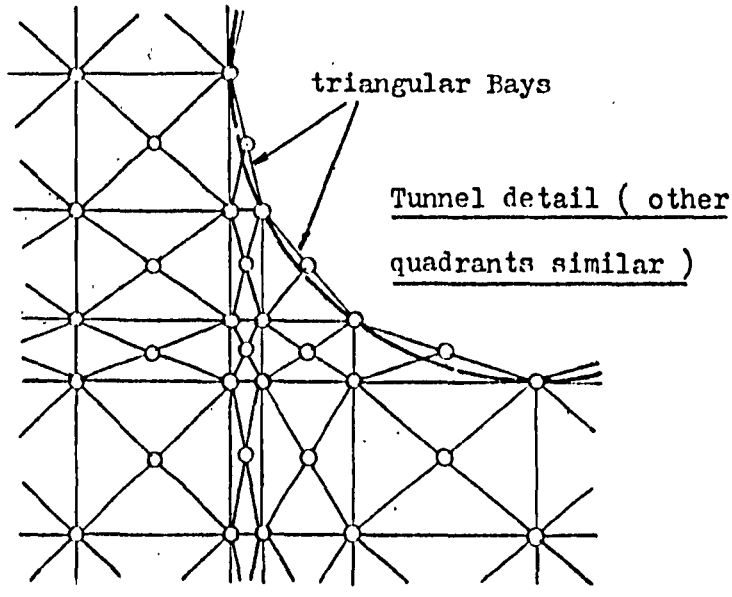

Fig. 100. Proposed mesh for circular underground opening problem

3.5. Some suggested topics for further study

The adoption of a non-associated flow rule to improve modelling of volume changes in drained soil obeying the Mohr-Coulomb yield criterion, has been mentioned. Thus, for a perfectly plastic material, the provision for normality of the plastic strain increment vector to the isotropic stress line ensures zero volume change during local shear failure, as required. For this purpose, the formulation by Davis (45) of the constitutive behaviour provides a suitable basis for numerical solution via a modified version of the present Initial Stress Method. The required modification is to the elastoplastic stress-strain increment matrix, as outlined by Nayak and Zienkiewicz (51), and leads to a plastic potential that is distinct from the yield surface.

A better model of drained behaviour would account for the rate of volume change as the plastic material work hardens. This requires a corresponding rotation of the plastic strain increment vector to a final no-volume-change condition at failure. In addition, as proposed earlier, the yield surface might be modified to cater for the irrecoverable strains arising from increases in mean pressure.

Chapter 2 presented some settlements that occur at the end of construction. With the passage of time, however, the soil consolidates so that larger total, and possibly, differential settlements develop. The consolidation settlements may be determined as follows.

The magnitude of consolidation settlements may be taken to be the difference in settlements given by the perfectly plastic undrained models of Chapter 2 and corresponding drained models such as the one in Section 3.2. (but with weight included), the above models representing the initial and final conditions respectively. Path-dependency of the final strains, since the material is now elastoplastic, means that this is not strictly true, although it is believed this discrepancy is not serious (34g).

To determine the rate of consolidation, 1- or psuedo 3-dimensional consolidation analyses may be employed, using the normal stress distributions given in Chapter 2 and those from the drained models. The presence of the rigid base (i.e. displacement boundary condition) as well as the sensitivity of the normalised normal stresses to plastic flow, in general, requires that some a priori time-dependency of the total stresses be established in the case of psuedo 3-dimensional consolidation; with 1-dimensional consolidation, however, the relative insensitivity of the normalised vertical stresses makes the choice a simple one. In the latter case, the vertical stresses at the edges and centre of the load are probably sufficient to determine the maximum settlement, and the greatest differential settlement (a smooth curve drawn between). In the former, however, more comprehensive stress plots using SYMAP will be required.

Further refinement to the above approach could be included, e.g. the adoption of a non-associated flow rule in the drained model to give zero volume change during local shear failure. However, to

obtain a consistent approach, true 3-dimensional consolidation is required - the general lack of coupling of the magnitude and progress of consolidation settlement of the 1- and psuedo 3-dimensional analyses is not assumed in this case. A further extension to this work would thus be to employ an elastoplastic soil skeleton based on a satisfactory drained model (such as suggested earlier) in a true 3-dimensional consolidation analysis. In the above consolidation studies, the finite element formulation of Christian and Boehmer (52) is likely to be useful.

Yet another important topic is the limited ability of soil to take tension. Drucker and Prager (43) have outlined a modified version of the Mohr-Coulomb yield criterion that precludes the development of tension, and this provides a suitable basis for such a study along present lines. They also showed that the upper bound for the critical height of a vertical cut can fall below the probable true value for the "intact" model, when tension is precluded.

Finally, the inherent anisotropy of soil that is attributable to the nature of the sedimentation process is another worthwhile subject for study. Although anisotropy in elastic soils is readily dealt with using the Finite Element Method, no such procedure has been encountered for plastic anisotropy. Nevertheless, the formulation presented by Booker and Davis (53) appears promising as a possible staging point for the study of elastoplastic anisotropy along present lines.

APPENDIX

THE MASTER FLOW CHART

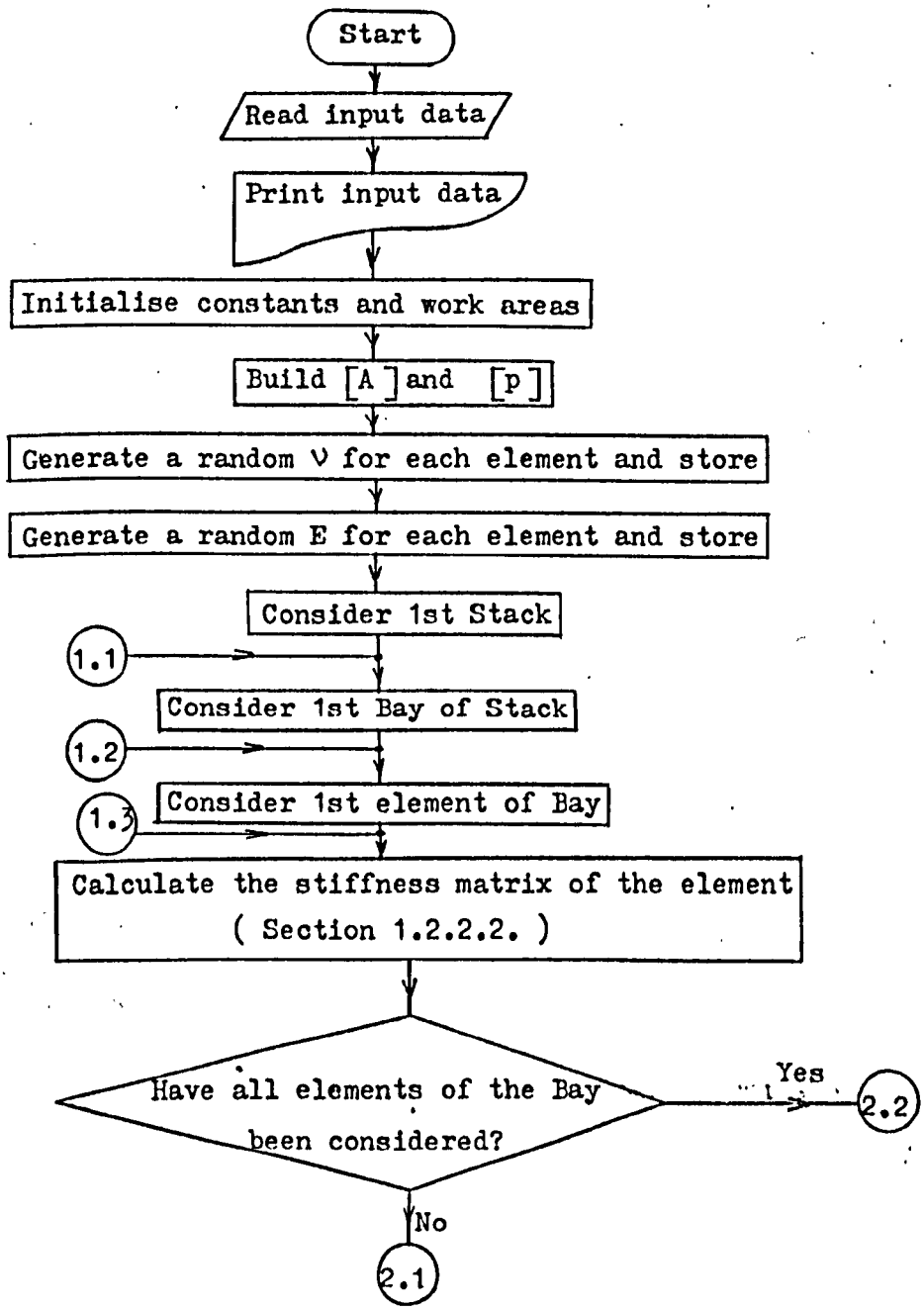

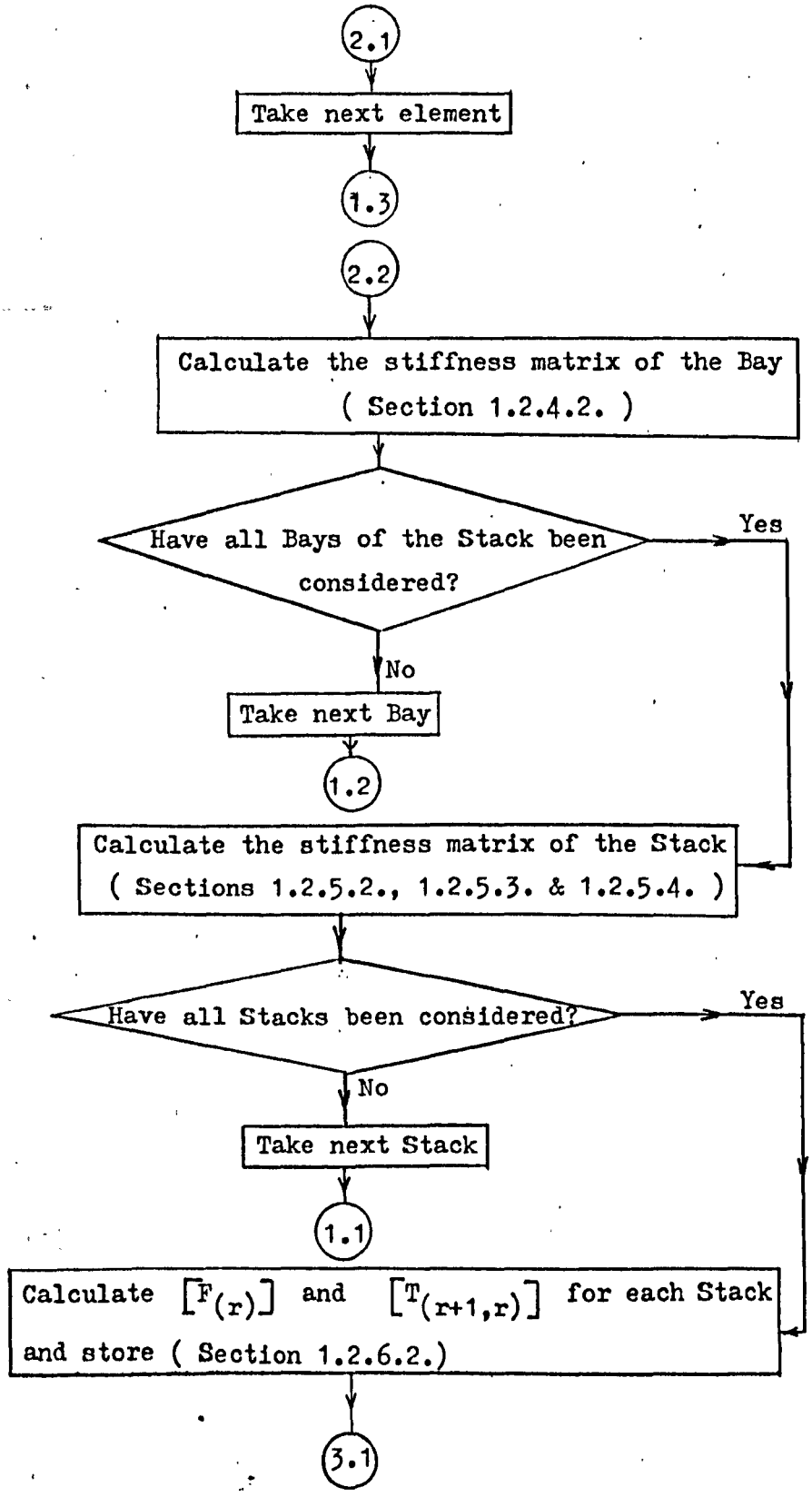
2.1
Take next element
D
6
1.3
2.2
Calculate the stiffness matrix of the Bay
(Section 1.2.4.2.)
7
Have all Bays of the Stack been considered?
Yes
8
No
Take next Bay
9
1.2
Calculate the stiffness matrix of the Stack
(Sections 1.2.5.2., 1.2.5.3. & 1.2.5.4.)
10
Have all Stacks been considered?
Yes
11
No
Take next Stack
12
1.1
Calculate [F(r)] and [T(r+1,r)] for each Stack and store (Section 1.2.6.2.)
13
3.1

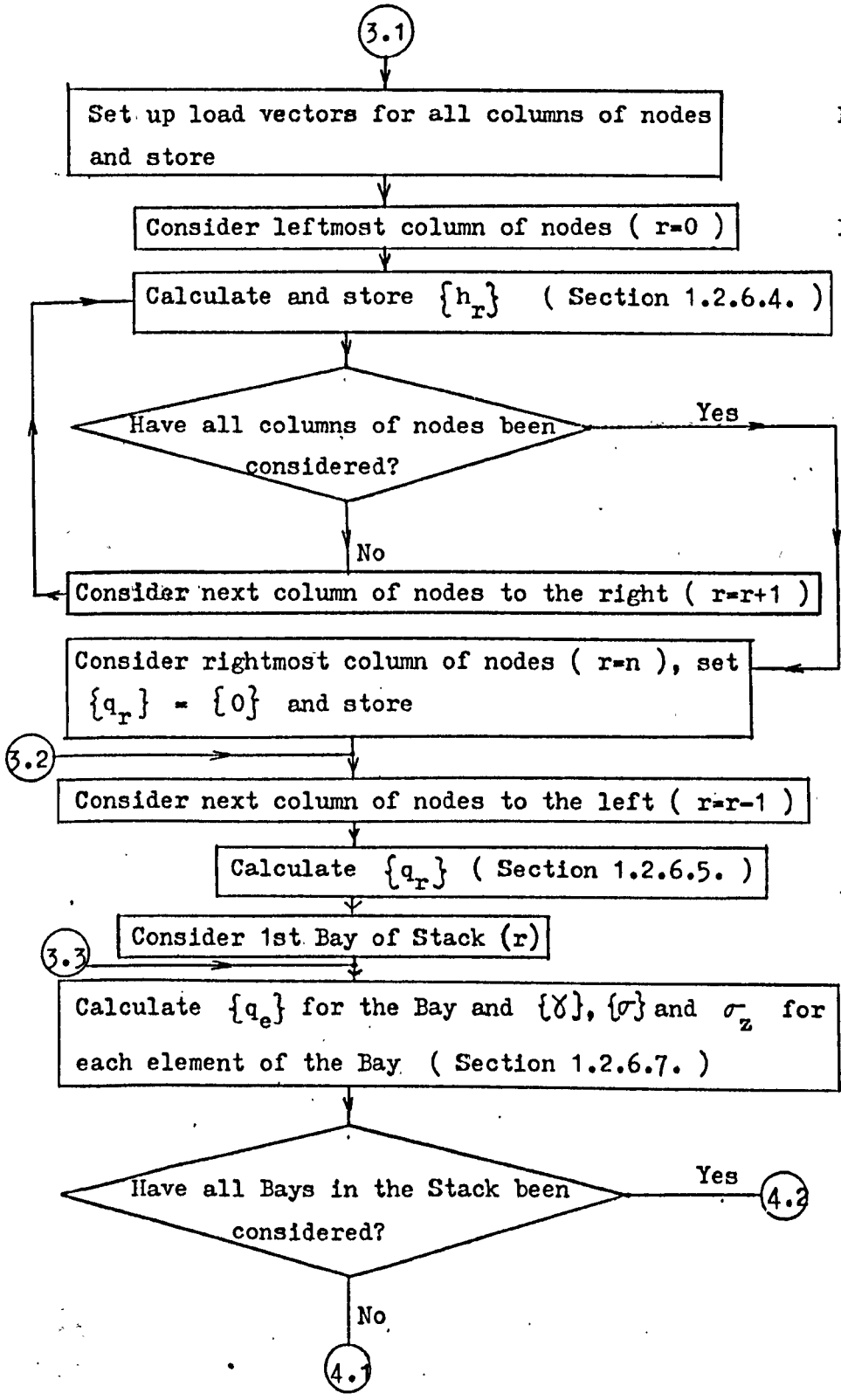
3.1
Set up load vectors for all columns of nodes and store
E
1
Consider leftmost column of nodes (r=0)
F
1
Calculate and store $\{h_r\}$ (Section 1.2.6.4.)
2
Have all columns of nodes been considered?
Yes
3
No
Consider next column of nodes to the right (r=r+1)
4
Consider rightmost column of nodes (r=n), set $\{q_r\} = \{0\}$ and store
5
3.2
Consider next column of nodes to the left (r=r-1)
6
Calculate $\{q_r\}$ (Section 1.2.6.5.)
7
Consider 1st Bay of Stack (r)
8
3.3
Calculate $\{q_e\}$ for the Bay and $\{\gamma\}$, $\{\sigma\}$ and σ_z for each element of the Bay (Section 1.2.6.7.)
9
Have all Bays in the Stack been considered?
Yes
4.2
10
No
4.1

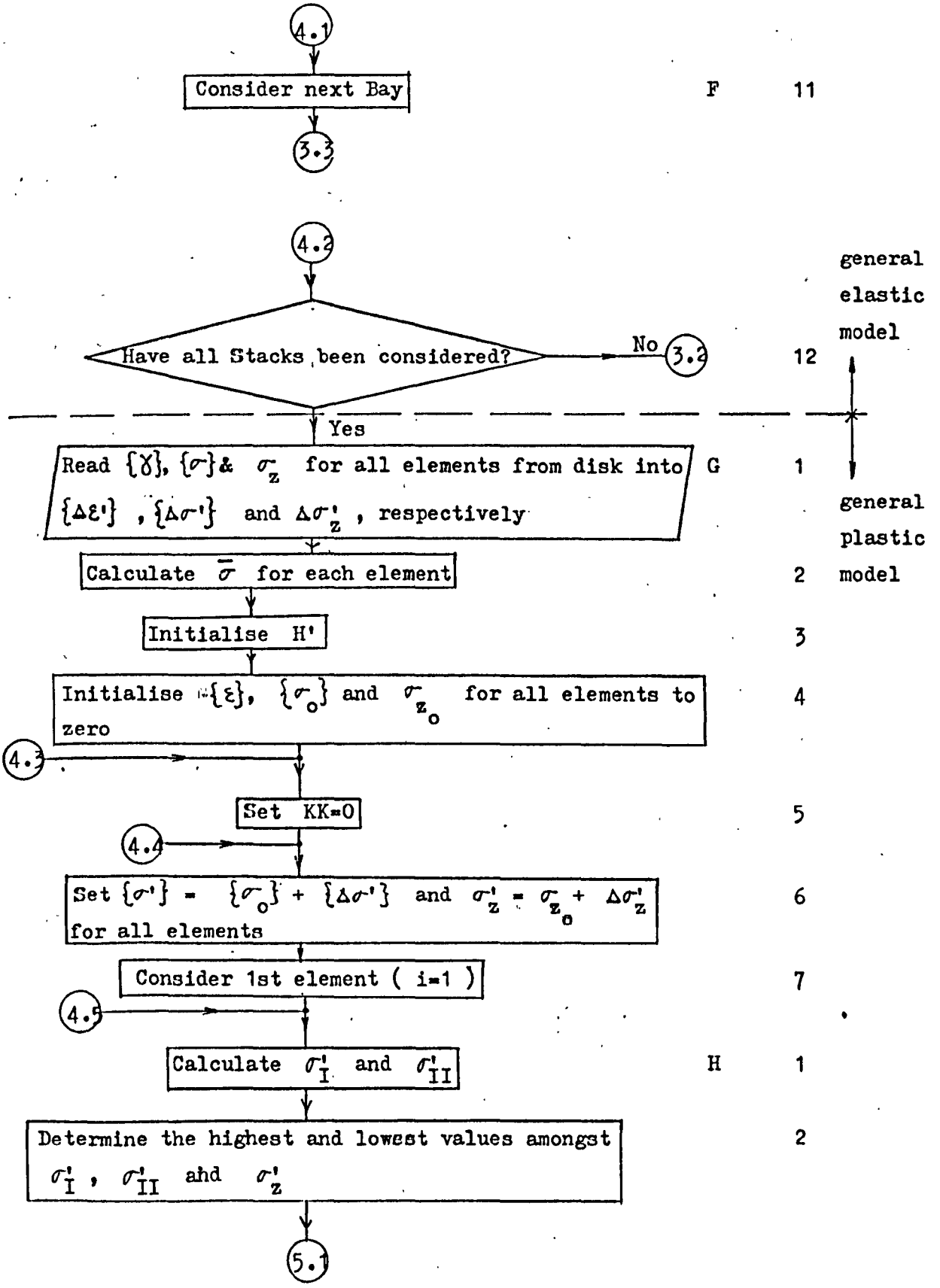
4.1
Consider next Bay
F 11
3.3
4.2
general elastic model
Have all Stacks been considered?
No
3.2
12
Yes
Read {γ}, {σ}& σz for all elements from disk into {Δε'} , {Δσ'} and Δσ'z , respectively
G 1
general plastic model
Calculate σ̄ for each element
2
Initialise H'
3
Initialise {ε}, {σo} and σzo for all elements to zero
4
4.3
Set KK=0
5
4.4
Set {σ'} = {σo} + {Δσ'} and σ'z = σzo + Δσ'z for all elements
6
Consider 1st element (i=1)
7
4.5
Calculate σ'I and σ'II
H 1
Determine the highest and lowest values amongst σ'I , σ'II and σ'z
2
5.1

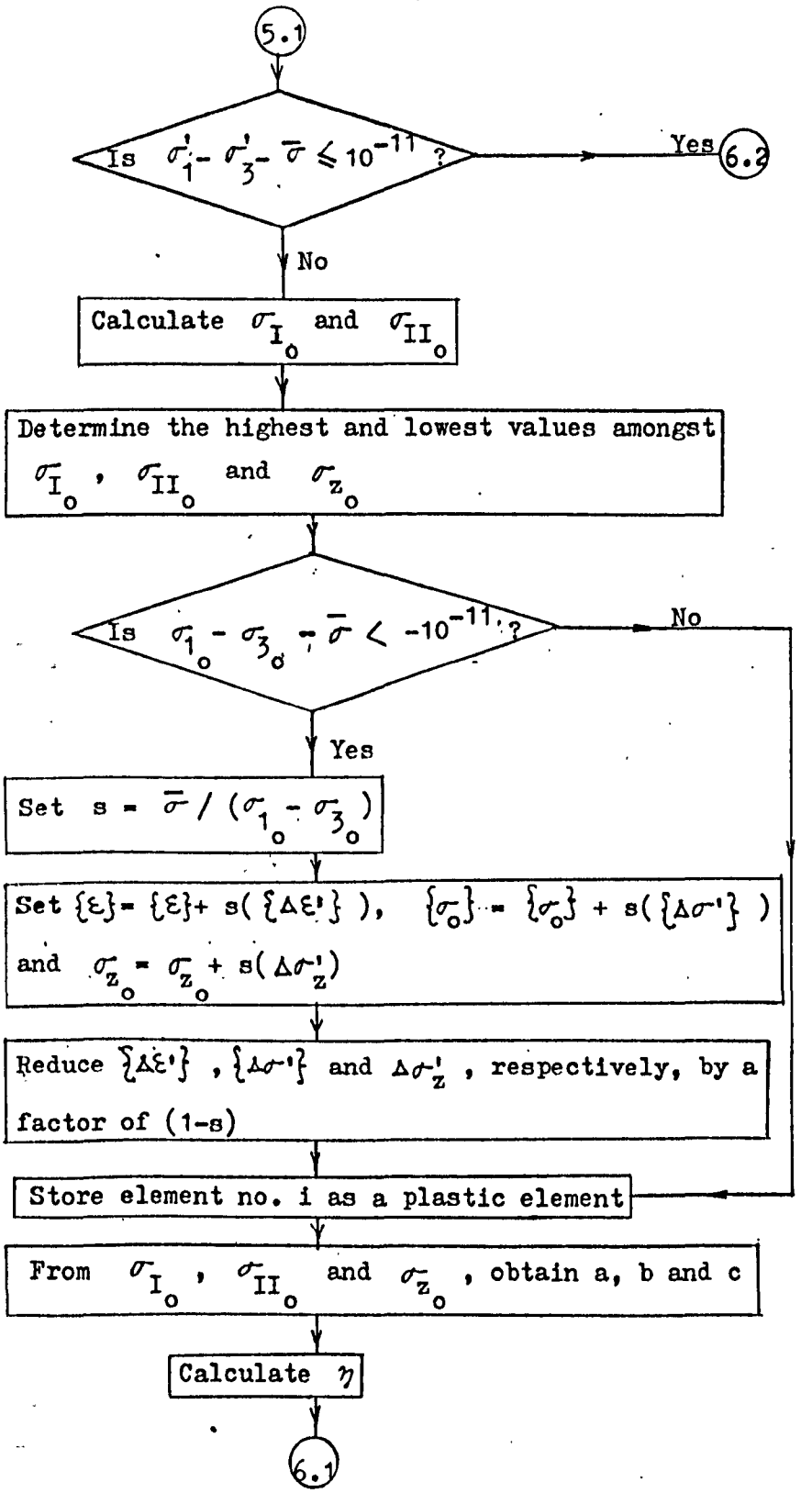

	H	3
4		
5		
6		
	I	1
2		
3		
	J	1
2		
3		

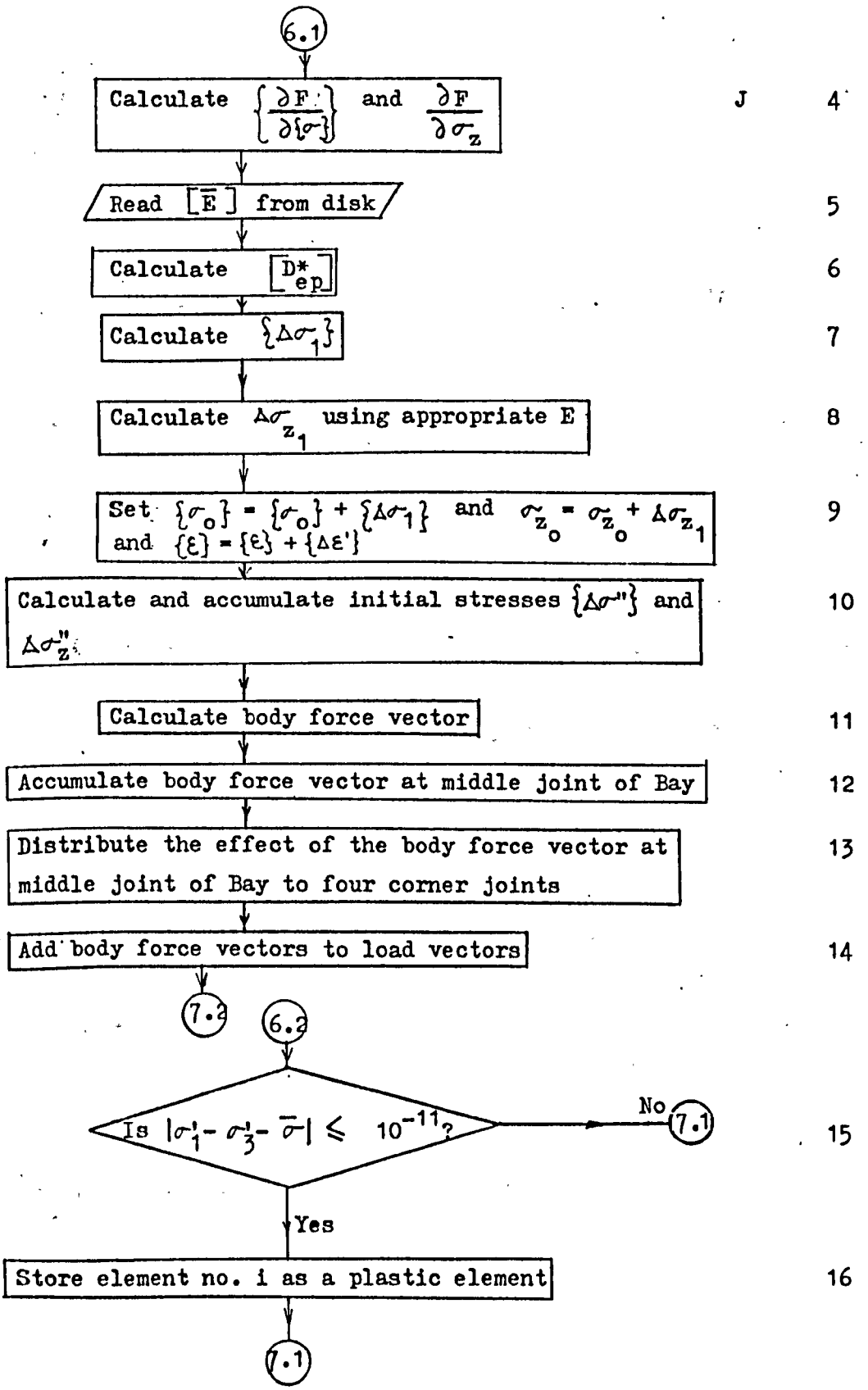
6.1
Calculate $\left\{\frac{\partial F}{\partial \{\sigma\}}\right\}$ and $\frac{\partial F}{\partial \sigma_z}$
J
4
Read $[\bar{E}]$ from disk
5
Calculate $[D^*_{ep}]$
6
Calculate $\{\Delta\sigma_1\}$
7
Calculate $\Delta\sigma_{z_1}$ using appropriate E
8
Set $\{\sigma_o\} = \{\sigma_o\} + \{\Delta\sigma_1\}$ and $\sigma_{z_o} = \sigma_{z_o} + \Delta\sigma_{z_1}$ and $\{\varepsilon\} = \{\varepsilon\} + \{\Delta\varepsilon'\}$
9
Calculate and accumulate initial stresses $\{\Delta\sigma''\}$ and $\Delta\sigma''_z$
10
Calculate body force vector
11
Accumulate body force vector at middle joint of Bay
12
Distribute the effect of the body force vector at middle joint of Bay to four corner joints
13
Add body force vectors to load vectors
14
7.2
6.2
Is $|\sigma'_1 - \sigma'_3 - \bar{\sigma}| \leq 10^{-11}$?
No
7.1
15
Yes
Store element no. i as a plastic element
16
7.1

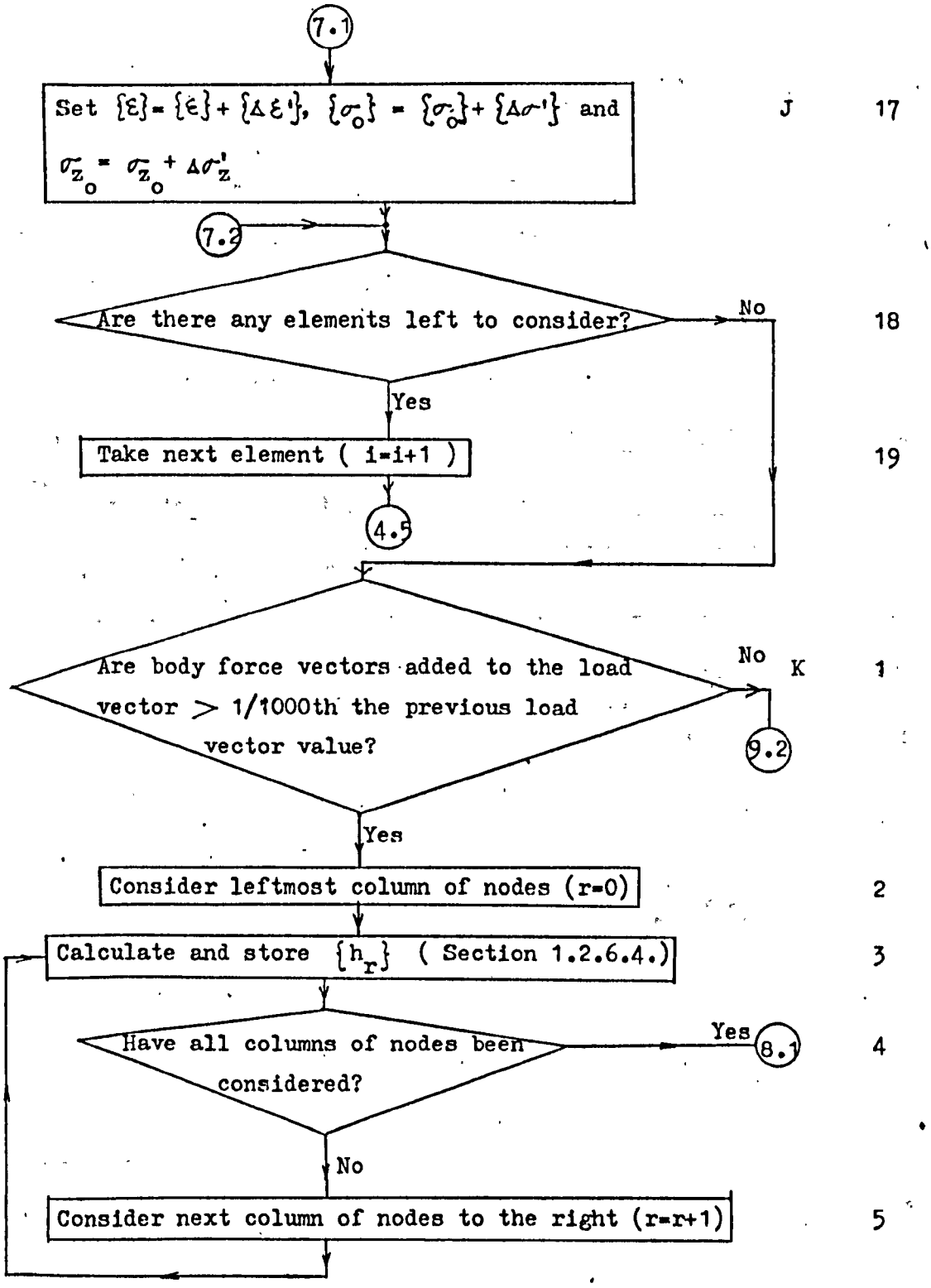
7.1
Set $\{\varepsilon\} = \{\epsilon\} + \{\Delta\varepsilon'\}$, $\{\sigma_o\} = \{\sigma_o\} + \{\Delta\sigma'\}$ and
$\sigma_{z_o} = \sigma_{z_o} + \Delta\sigma'_z$
J 17
7.2
Are there any elements left to consider?
No 18
Yes
Take next element (i=i+1) 19
4.5
Are body force vectors added to the load vector > 1/1000th the previous load vector value?
No K 1
9.2
Yes
Consider leftmost column of nodes (r=0) 2
Calculate and store $\{h_r\}$ (Section 1.2.6.4.) 3
Have all columns of nodes been considered?
Yes 8.1 4
No
Consider next column of nodes to the right (r=r+1) 5

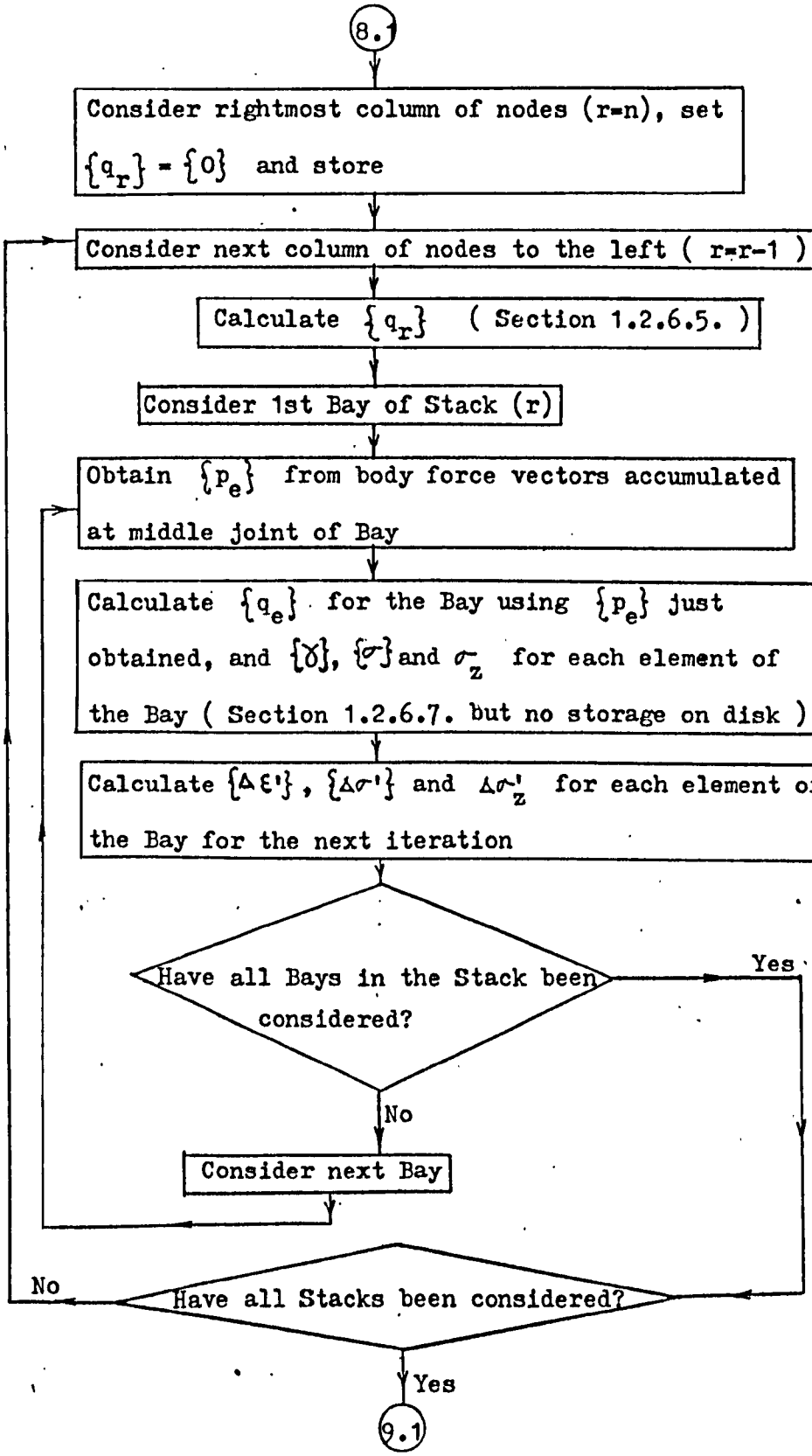
8.1
Consider rightmost column of nodes (r=n), set $\{q_r\} = \{0\}$ and store
K .6
Consider next column of nodes to the left (r=r-1)
7
Calculate $\{q_r\}$ (Section 1.2.6.5.)
8
Consider 1st Bay of Stack (r)
9
Obtain $\{p_e\}$ from body force vectors accumulated at middle joint of Bay
10
Calculate $\{q_e\}$ for the Bay using $\{p_e\}$ just obtained, and $\{\gamma\}$, $\{\sigma\}$ and σ_z for each element of the Bay (Section 1.2.6.7. but no storage on disk)
11
Calculate $\{\Delta\varepsilon'\}$, $\{\Delta\sigma'\}$ and $\Delta\sigma'_z$ for each element of the Bay for the next iteration
12
Have all Bays in the Stack been considered?
Yes
13
No
Consider next Bay
14
No
Have all Stacks been considered?
15
Yes
9.1

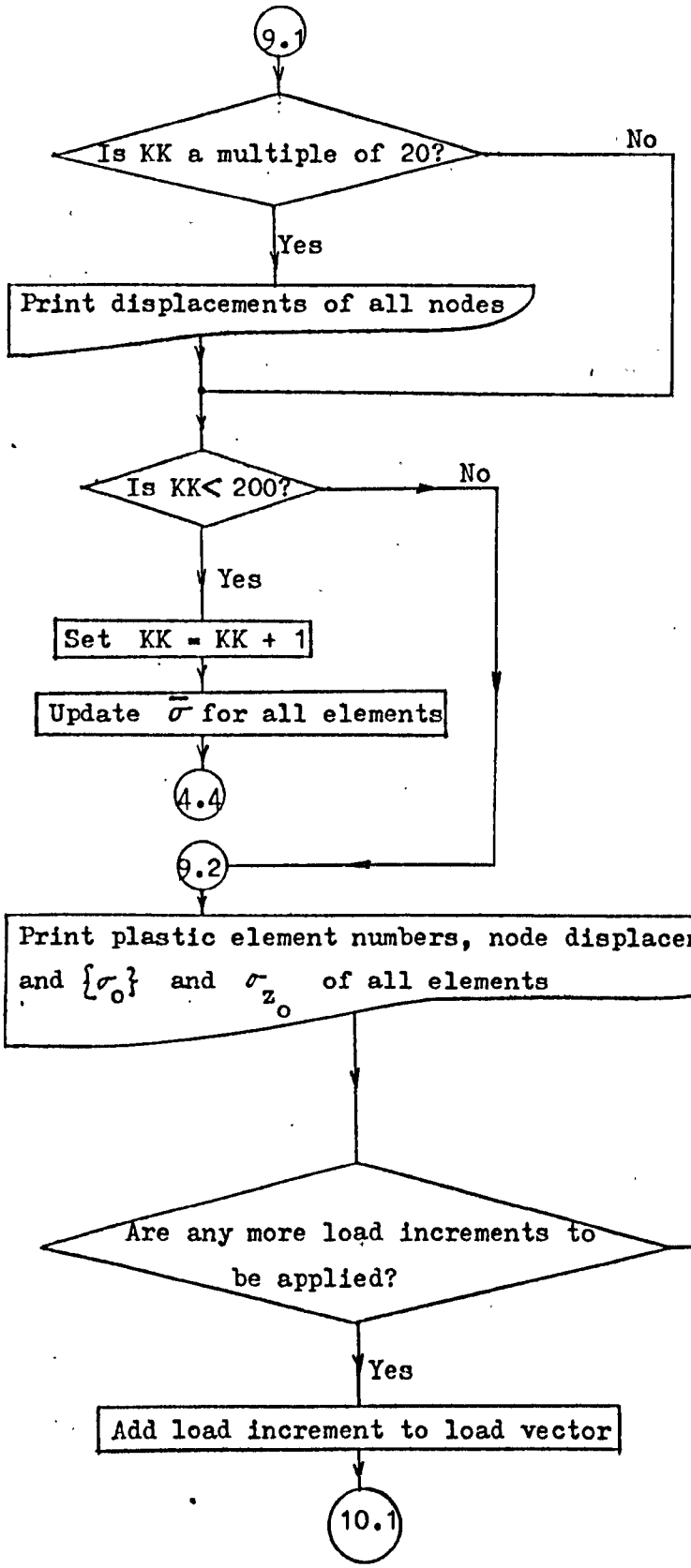

K		16
		17
		18
		19
		20
L		1
		2
		3

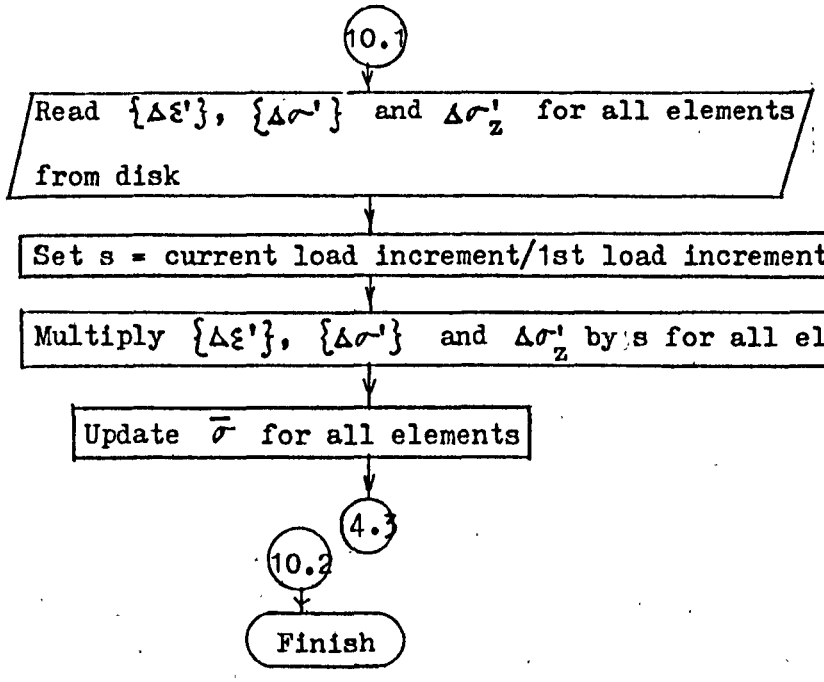
10.1
Read {Δε'}, {Δσ'} and Δσ'z for all elements from disk
L
4
Set s = current load increment/1st load increment
5
Multiply {Δε'}, {Δσ'} and Δσ'z by s for all elements
6
Update σ̄ for all elements
7
4.3
10.2
Finish
8

BIBLIOGRAPHY

1. Roscoe, K.H. (1969). Some soil mechanics concepts and the possibility of their wider application. Paper 81, Proc. Int. Conf. Struct., Solid Mech. Engng Des. civ. Engng Mater., University of Southampton.

2. Rowe, P.W. (1971). Theoretical meaning and observed values of deformation parameters for soil. Stress-strain Behaviour of Soils, Roscoe Memorial Symposium, 143-194. Henley-on-Thames: Foulis.

3. Smith, I.M. (1971). Plane plastic deformation of soil. Stress -strain Behaviour of Soils, Roscoe Memorial Symposium, 548-563. Henley-on-Thames: Foulis.

4. Burland, J.B. (1973). The finite element method in geotechnics. BGS Discussion, Institution of Civil Engineers.

5. Smith, I.M. & Kay, S. (1971). Stress analysis of contractive and dilative soil. Proc. Am. Soc. Civ. Engrs 97, SM7, 981-997.

6. Zienkiewicz, O.C. (1971). The finite element method in engineering science. New York: McGraw Hill. 521 pp.

7. Desai, C.S. (1972). Theory and applications of the finite element method in geotechnical engineering. Proc. Symp. on the applications of the finite element method in geotechnical engineering, Vicksburg, USA, 3-80.

8. Zienkiewicz, O.C., Valliappan, S. & King, I.P. (1969). Elasto-plastic solutions of engineering problems-'initial stress', finite element approach. Int. Jnl Num. Meth. Engng 1, 75-100.

9. Lo, K.W. (1970). The analysis of plane strain in an infinite elastic layer overlying a rigid base. M.Sc. dissertation, University of London.

10. Poulos, H.G. (1967). Stresses and displacements in an elastic layer underlain by a rough rigid base. Geotechnique 17, No. 4, 378-410.

11. Herrmann, L.R. (1965). Elasticity equations for incompressible and nearly incompressible materials by a variational theorem. J. Am. Inst. Aeronaut. Astronaut. 3, No. 10, 1896-1900.

12. Mroz, Z. (1963). Non associated laws in plasticity. J. Mec. & Phys. Appli. 2, 21-41.

13. Drucker, D.C. (1959). A definition of stable inelastic material. J. Appl. Mech., Trans. A.S.M.E. 26, 101-106.

14. Zienkiewicz, O.C. & Valliappan, S. (1969). Analysis of real structures for creep, plasticity and other complex constitutive laws. Proc. Int. Conf. Struct., Solid Mech. Engng Des. civ. Engng Mater. University of Southampton.

15. Zienkiewicz, O.C. & Naylor, D.J. (1971). The adaptation of critical state soil mechanics theory for use in finite elements. Stress-strain Behaviour of Soils, Roscoe Memorial Symposium, 537-547. Henley-on-Thames: Foulis.

16. Havner, K.S. (1968). On convergence of iterative methods in plastic strain analysis. Int. J. Solids Struct. 4, 491-508.

17. Smith, I.M. (1970). Incremental numerical solution of a simple deformation problem in soil mechanics. Geotechnique 20, No. 4, 357-372.

18. Mendelson, A. (1968). Plasticity: theory and application. New York: Macmillan, 70-134.

19. Hill, R. (1950). The mathematical theory of plasticity. Oxford University Press, (a) 128-160, (b) 254-255

20. Timoshenko, S.P. & Goodier, J.N. (1951). Theory of elasticity. New York: McGraw-Hill, 15-34.

21. Høeg, K. (1972). Finite element analysis of strain-softening clay. Jnl Soil Mech. Fdns Div. Am. Soc. Civ. Engrs 98, SM1, 43-58.

22. Gibson, R.E. & Sills, G.C. (1971). Some results concerning the plane deformation of a non-homogeneous elastic half-space. Stress-strain Behaviour of Soils, Roscoe Memorial Symposium, 564-572. Henley-on-Thames: Foulis.

23. Calladine, C.R. (1969). Engineering plasticity. Pergamon Press, (a) 83-94, (b) 93-116. (c) 194-213.

24. Prager, W. (1959). An introduction to plasticity. Massachusetts: Addison-Wesley.

25. Gibson, R.E. (1974). The analytical method in soil mechanics. Geotechnique 24, No. 2, 115-140.

26. Davis, E.H. & Christian, J.T. (1970). Bearing capacity of anisotropic cohesive soil. Research Report No. R149; The University of Sydney.

27. Davis, E.H. & Booker, J.R. (1971). The bearing capacity of strip footings from the standpoint of plasticity theory. Research Report No. R170, The University of Sydney.

28. Davis, E.H. & Booker, J.R. (1973). The effect of increasing strength with depth on the bearing capacity of clays. Geotechnique 23, No. 4, 551-563.

29. Carrier, W.D., III & Christian, J.T. (1973). Rigid circular plate resting on a non-homogeneous elastic half-space. Geotechnique 23, No. 1, 67-84.

30. Prandtl, L. (1920). "Über die Härte" Plastischer Koerper. Goettinger Nachr., Math. Phys. Kl., 74-85.

31. Smith, G.N. (1971). Elements of soil mechanics for civil and mining engineers. London: Crosby Lockwood, 217-238.

32. Bishop, A.W. (1971). Shear strength parameters for undisturbed and remoulded soil specimens. Stress-strain Behaviour of Soils, Roscoe Memorial Symposium, 3-58.

33. Dunlop, P. & Duncan, J.M. (1970). Development of failure around excavated slopes. Jnl Soil Mech. Fdns Div. Am. Soc. Civ. Engrs 96, SM2, 471-493.

34. Lambe, T.W. & Whitman, R.V. (1969). Soil Mechanics. New York: Wiley, (a) 151-161, (b) 195-497, (c) 435, (d) 458, (e) 491, (f)310, (g) 374-387.

35. Skempton, A.W. (1951). The bearing capacity of clays. Building Research Congress, England.

36. Poulos, H.G. & Davis, E.H. (1974). Elastic solutions for soil, and rock mechanics. New York: Wiley, 249-251.

37. Terzaghi, K. (1951). Theoretical soil mechanics. New York: Wiley, (a) 376-377, (b) 384, (c) 119-120, (d) 145-155.

38. Zienkiewicz, O.C. & Cheung, Y.K. (1967). The finite element method in structural and continuum mechanics. New York: McGraw-Hill, 35-37.

39. Gilbert, J.C. (1974). SYMAP: geographic mapping on lineprinter: user's guide. University of London Computer Centre, Bulletin B4·8/5.

40. Gilbert, J.C. (1971). Random number generators. University of London Computer Centre, Bulletin 5·2/3.

41. Gibson, R.E. (1974). Private communication.

42. Mises, R. von (1928). Mechanik der plastischen Formaenderung von Kristallen. Z. angew. Math. Mech. 8, 161-185.

43. Drucker, D.C. & Prager, W. (1952). Soil mechanics and plastic analysis or limit design. Q. Appl. Math. 10, 157-165.

44. Bishop, A.W., Webb, D.L. and Lewin, P.I. (1965). Undisturbed samples of London clay from the Ashford Common shaft: strength -effective stress relationships. Geotechnique 15, 1-31.

45. Davis, E.H. (1968). Theories of plasticity and the failure of soil masses. Soil mechanics selected topics.(Ed. by I.K. Lee). Sydney: Butterworths, 341-380.

46. Drucker, D.C., Gibson, R.E. and Henkel, D.J. (1955). Soil mechanics and work hardening theories of plasticity. Proc. Am. Soc. Civ. Engrs 81, Separate 798, Transactions A.S.C.E. 122, 338-346 (1957).

47. Roscoe, K.H. and Burland, J.B. (1968). The generalised stress -strain behaviour of Wet Clay. Engineering Plasticity (Ed. by J. Heyman and F.A. Leckie). Cambridge University Press, 535-609.

48. Ladd, C.C. (1964). Stress-strain modulus of clay in undrained shear. Jnl. Soil Mech. Fdns Div. Am. Soc. Civ. Engrs 90, SM5, 127-156.

49. Bishop, A.W. (1966). Strength of soils as engineering materials. 6th Rankine Lecture. Geotechnique 16, 89-130.

50. Taylor, D.W. (1948). Fundamentals of soil mechanics. New York: Wiley, 406-479.

51. Nayak, G.C. and Zienkiewicz, O.C. (1972). Elastoplastic stress analysis - a generalisation for various constitutive relations including strain softening. Int. Jnl. Num. Meth. Engng 5, 113 -135.

52. Christian. J.T. and Boehmer, J.W. (1970). Plane strain consolidation by finite elements. Jnl. Soil Mech. Fdns Div. Am. Soc. Civ. Engrs 96, SM4, 529-549.

53. Booker, J.R. and Davis, E.H. (1970). A general treatment of plastic anisotropy under conditions of plane strain. Research Report No. R152, The University of Sydney.

54. Scott, C.R. (1969). An introduction to soil mechanics and foundations. London: Applied Science Publishers Ltd., 121-151.